UC San Diego
UC San Diego Electronic Theses and Dissertations

Title

Rhenium and manganese bipyridine tricarbonyl catalysts for the electrochemical reduction of carbon dioxide

Permalink

Author

Sampson, Matthew Dean

Publication Date

2015

Peer reviewed|Thesis/dissertation

UNIVERSITY OF CALIFORNIA, SAN DIEGO

Rhenium and manganese bipyridine tricarbonyl catalysts for the electrochemical

reduction of carbon dioxide

A dissertation submitted in partial satisfaction of the requirements for the degree of

Doctor of Philosophy

in

Chemistry

by

Matthew Dean Sampson

Committee in charge:

      Professor Clifford P. Kubiak, Chair
      Professor Seth M. Cohen
      Professor Michael Galperin
      Professor Melvin Y. Okamura
      Professor Michael J. Sailor

2015

This dissertation of Matthew Dean Sampson is approved, and it is acceptable in quality and form for publication on microfilm and electronically:

_____

_____

_____

_____

_____
Chair

University of California, San Diego

2015

DEDICATION

To my family – your support has been vital to my success.

EPIGRAPH

In wisdom gathered over time I have found that every experience is a form of

exploration.

Ansel Adams

TABLE OF CONTENTS

LIST OF FIGURES

LIST OF TABLES

ACKNOWLEDGEMENTS

I have been extremely fortunate to have a supportive family, an amazing girlfriend, and great friends, coworkers, and mentors during my PhD studies. I would not be here writing this dissertation if it weren't for the help and support from all of these people. Given that, there are too many people to thank here, so I apologize in advance to anyone I've inevitably forgotten.

I'll start out by thanking the love of my life and the girl that's been right by my side for the last 4+ years. Brooke, I can't thank you enough for all of your support and for all you have sacrificed over these years. I am forever grateful that you stopped your life in IL and moved out to CA to join me during my first year. I'm certain that if you wouldn't have moved out, that I wouldn't have made it this far. Thank you for always dragging me outdoors for a walk to the beach, encouraging me to pursue my hobbies and dreams, and for providing me with a much needed break from science every day. Your positive outlook on life continues to inspire me everyday. You are my best friend, the best happy hour partner, and the best adventure partner. I love all of the moments we have shared since moving out to CA, and I wouldn't have wanted to spend those moments with anyone else. I can't wait for the next steps of our journey back in IL.

I also wouldn't be here today without the loving support of my family. Mom and Dad, who would've guessed you two would raise two scientists? I can't thank you enough for all you've done for me over these years. Since day one, you both have encouraged me to pursue my interests, even if it hasn't always aligned with your own.

Your constant encouragement, care, and optimism have been absolutely vital to my ability to get this PhD. I know it was hard to have your kids on opposite sides of the country for a while, and I'm glad we are all finally going to be back in the Midwest. And to my sister, Lauren, and my brother in-law, Derek – although it's been difficult to stay close living across the country from one another, I've appreciated each and every time we've spent together. You both have been great role models and great encouragement through this process. You are going to make amazing parents, and I can't wait to live close to see little Dean grow up. I love you all so much – thank you for your continued support. I would also like to acknowledge Brooke's parents and brother – Vicki, Craig, and Andrew. Thanks so much for welcoming me with open arms into your family. You all have been incredibly supportive, generous, and caring throughout these years.

I've been lucky to have a great group of loving friends, both here in CA and back in IL, that have been by my side in this adventure of getting a PhD. Thank you all for keeping me sane, healthy, and happy – I love each and every one of you. First, I'd like to thank my friends here in CA. Kara and Dan, thanks for allowing me to live with you guys for our first year of grad school. I will never forget that house in PB, and I couldn't have ask for better roommates after moving across the country to start grad school. We had so much fun, maybe too much fun at times, and I thank you both for each day we've spent together. Kara, I'm so glad you moved down the street from us in La Jolla, so we could continue those great times from our first year. Kara and Matt, thanks for showing us around Tijuana, for being our tiki drink partners at

Mandarin House, for those Shack nights, and for the camping trips (even if some divine force tried to derail them each time). You guys are the best, and I hope we continue to stay in touch as the years go on. Clare, Cliff, and Mark Boerneke – thanks for all of the great times here in San Diego. Matt Grant, Sara, Kirby, and Jen – thanks for being 'the friends up north' and for all the great adventures.

To my friends back in IL, thanks for staying in touch over these years and continuing to be great support. John (Filla), Justin, and Jackie – thanks for being the best friends anyone could ever hope for. I will never forget our backpacking trip to Yosemite. I'm glad that I was with all of you to experience that beauty and experience what true exhaustion really feels like. I can't wait for the adventures to come in the future. Justin, I can't wait to start homebrewing with you every weekend when I move back to IL. Jeremy, Justin (J Lee), and Adam – thanks for always making time to meet up in the city when I was back in IL, and thanks for the great ski trips. You guys make me laugh more than anyone, and I can't wait for more fun nights in the city soon. Shilpy and Pavan, thanks for your support and encouragement over the years. I'm excited to grow closer when we move back to IL.

During my PhD studies, I've been fortunate to be part of many fruitful collaborations. My success during the last four years would not have been possible without the help of great collaborators. In particular, I'd like to thank Dr. Daniel Friebel and Prof. Anders Nilsson at Stanford for help at SLAC National Accelerator Center and with X-ray Absorption Spectroscopy experiments – especially, Daniel for spending many long nights with us at the beamline. I'd like to thank Dr. Christoph

Riplinger, Dr. John Keith (now Prof.), and Prof. Emily Carter at Princeton for many computational collaborations. I'd also like to thank Dr. Ian Sharp and Prof. Heinz Frei at Lawrence Berkeley National Laboratory for (1) purchasing equipment to allow us to perform stopped-flow IR spectroscopy experiments and (2) allowing me to spend many long days hogging one of your gloveboxes and your stopped-flow instrument. Thanks to Doug Agnew and Prof. Josh Figueora for help with computational chemistry, help with EPR experiments, and many helpful discussions. I'd like to thank Dr. Honghan Fei and Prof. Seth Cohen for having the insight to put some of our molecular catalysts in metal-organic frameworks. This collaboration has opened the door for a new research project that I hope continues into the future. I'd also like to thank Dr. Idan Hod, Prof. Omar Farha, and Prof. Joseph Hupp at Northwestern for another great collaboration on metal-organic frameworks. Finally, thanks to Dr. Curtis Moore and Prof. Arnold Rheingold for help with many, many single crystal X-ray crystallography experiments over the years.

I can't thank Cliff enough for all he's done for me over the past four years. I couldn't have asked for a better advisor and a better mentor. Cliff, thanks for allowing me to pursue the research that I wanted to pursue. Cliff sent me on many research trips – to Stanford, Berkeley, Caltech, and Northwestern to name a few – and these trips provided me with unique experiences to collaborate, network, learn from others, and run exciting experiments. These experiences made my grad school journey so much more interesting and fulfilling. Cliff also allows his students to be involved in every aspect of academic life, including writing your own papers, helping with grant writing,

submitting and revising technical papers, and attending a variety of conferences. Cliff gives his students the freedom to both struggle and thrive on their own, which teaches us an unprecedented amount of skills, which we normally would not learn with other management techniques. Sometimes students can struggle with this freedom, but in the end it turns them into a better scientist and a better person. Cliff is also brilliant – he is one of the smartest people I've ever had the privilege to work with. And, his jokes and stories are fascinating (even when you've heard them for the third or fourth time). Cliff, thank you for being who you are, for providing me with so much support, and teaching me how to be a competent scientist.

Now, I'd like to acknowledge the people that I spent the most time with over the last four years, the Kubiak Research Group. I owe all of you so much for the great times, intelligent conversations, and experimental help. I'm going to thank some of you individually (in no particular order), but I want you all to know that I appreciate each and every one of you. First of all, thanks to Benson and Smieja who got me up to speed on the lab's CO_2 reduction work and all things electrochemistry and gloveboxes – my success in grad school started with you guys. Thanks to Dr. Kyle "Kylefinder" Grice (now Prof. Grice) for keeping all of us up to speed on recently published papers (seconds after they hit the ASAP page) and not letting anything stand in your way to get us those papers (not even the 4th floor bathroom...). But seriously, Kyle, you probably taught me more than anyone did during my first two years in lab, thank you. Thanks to Gabe for showing me that sometimes (only sometimes, Cliff) it's OK to start your day in lab after noon, as long as your research doesn't suffer. You taught me

that grad school can be (and should be) fun. Gabe, you have been one of the funniest, kindest, and most helpful people over the past four years. Jesse, thanks for the headbanging, the pub trips, and most of all, thanks for bringing us Pubsketball (https://www.youtube.com/watch?v=meMfNdALMQ8). I think everyone knows that we both have a future in film making if this science thing doesn't end up working out. To Mark Llorente, thanks for always declining Jesse's invitation to play basketball, and for getting us all that $$$. Doud, thanks for all the pub trips and for organizing Ocho de Mayo every year (even if it did always occur in June or July). And thanks for graduating so the students can finally enjoy Taco Villa. To Jane, thanks for being so outspoken and keeping us all honest. I will never be able to listen to Adele or Beach House without both cringing and thinking about you. Also, thanks for being my desk neighbor all of those years. Tram, thanks for sharing my passion for food with me, and to Tram and Alissa, thank you both for making the best damn birthday cake anyone has ever received. Thanks to Charlie (Dr. Machan) for becoming my brewing buddy and for always trying to get the group to go out to a brewery together (even if no one ever came with us...). Thanks for having that ridiculous laugh and for all the sing alongs in lab. Steven, thanks for keeping the beer fridge stocked, throwing all of those awesome parties, and showing me what a Catermelon is. Oh, and I'm sorry for almost blowing your arm off by that exploding KC_8 flask (what doesn't kill us makes us stronger, right?). Reineke, thanks for being a wildcard and teaching us to always sit down while going to the bathroom in the middle of the night. Thanks for popping open a beer at noon with me on all of those Wednesdays. To Melissa, thanks for being my

xxxiii

stalker and for being the girl in lab that was always willing to hang with the guys. Oh, and thanks for showing us what "wine drunk" really means. Jason, thanks for being a champ. Eddie, thanks for living your undergrad years to the fullest. David, thanks for showing me that yo-yoing, of all things, can be mesmerizing. Alma, thanks for never judging us too hard. To Tyler, Daphne, Gwen – thanks for being the young ones (in grad school years) and for being eager to take over the reins.

To finish this off, I'd like to thank a few miscellaneous things that made my time in San Diego so much more enjoyable. Thanks to the breweries of San Diego County (specifically, Green Flash, Ballast Point, AleSmith, Modern Times, Stone, Societe, and The Lost Abbey) for making me love beer more than any sane man should. Thank you Bird Rock Coffee Roasters for providing the best damn coffee I've ever had – I'm going to miss you so much. Thanks to The Coffee Cup and açai bowls for being my breakfasts of choice. Thanks to Porter's Pub for many great nights and for showing me what bad beer tastes like – I hope a new pub (a good pub) opens up on campus soon. Thank you Don Bravo and Don Carlos for being my neighborhood taco shops and for providing me with a delicious California burrito whenever I needed it. Thanks to Windansea Beach for being that gorgeous getaway down the street for the past three years. And finally, thanks to Yosemite National Park, Sequoia National Park, and Big Sur for providing me with the best, most beautiful escapes from grad school. California was the best choice for grad school solely due to the proximity to those national treasures.

CHAPTER SPECIFIC ACKNOWLEDGEMENTS

Much of the material for this chapter comes directly from a manuscript entitled: "The Electronic States of Rhenium Bipyridyl Electrocatalysts for CO_2 Reduction as Revealed by X-ray Absorption Spectroscopy and Computational Quantum Chemistry" by Eric E. Benson, Matthew D. Sampson, Kyle A. Grice, Jonathan M. Smieja, Jesse D. Froehlich, Daniel Friebel, John A. Keith, Emily A. Carter, Anders Nilsson, and Clifford P. Kubiak, which has been published in *Angew. Chem. Int. Ed.*, **2013**, 52, 4841–4844. http://dx.doi.org/10.1002/anie.201209911. The dissertation author is the primary co-author of this manuscript.

Much of the material for this chapter comes directly from a manuscript entitled: "Direct Observation of the Reduction of Carbon Dioxide by Rhenium Bipyridine Catalysts" by Matthew D. Sampson, Jesse D. Froehlich, Jonathan M.

Much of the material for this chapter comes directly from a manuscript entitled: "Photocatalytic CO_2 Reduction to Formate Using a Mn(I) Molecular Catalyst in a Robust Metal-Organic Framework" by Honghan Fei, Matthew D. Sampson, Yeob Lee, Clifford P. Kubiak, and Seth M. Cohen, which has been published in *Inorg. Chem.*, **2015**, 54, 6821–6828. http://dx.doi.org/10.1021/acs.inorgchem.5b00752. The dissertation author is a primary co-author of this manuscript.

Much of the material for this chapter comes directly from a manuscript entitled: "Fe-Porphyrin-Based Metal-Organic Framework Films as High-Surface Concentration, Heterogeneous Catalysts for Electrochemical Reduction of CO_2" by Idan Hod, Matthew D. Sampson, Pravas Deria, Clifford P. Kubiak, Omar K. Farha, and Joseph T. Hupp, which has been published in *ACS Catal.*, **2015**, 5, 6302–6309. http://dx.doi.org/ 10.1021/acscatal.5b01767. The dissertation author is a contributing author of this manuscript.

Chapter 9. The material in this chapter is unpublished work.

VITA

2015   Doctor of Philosophy, University of California, San Diego

2013   Master of Science, University of California, San Diego

2011   Bachelor of Science, University of Illinois at Urbana-Champaign

PUBLICATIONS

Sampson, M. D.; Kubiak, C. P. "Manganese Electrocatalysts with Bulky Bipyridine Ligands: Utilizing Lewis Acids to Promote Carbon Dioxide Reduction at Low Overpotentials." **2015**, *Submitted*.

Hod, I.; Sampson, M. D.; Deria, P.; Kubiak, C.P.; Farha, O. K.; Hupp, J. T. "Fe-Porphyrin Based MOF Films as High-Surface-Concentration, Heterogeneous Catalysts for Electrochemical Reduction of CO_2." *ACS Catal*. **2015**, 5, 6302-6309

Hod, I.; Deria, P.; Bury, W.; Mondloch, J. E.; Kung, C.-W.; So, M.; Sampson, M. D.; Peters, A. W.; Kubiak, C. P.; Farha, O. K.; Hupp, J. T. "A Porous Proton-Relaying, Metal-Organic Framework Material that Accelerates Electrochemical Hydrogen Evolution" *Nature Comm*. **2015**, 6, 8304.

Sampson, M.D.; Kubiak, C.P. "Electrocatalytic Dihydrogen Production by an Earth-abundant Manganese Bipyridine Catalyst." *Inorg. Chem*. **2015**, 54, 6674.

Fei, H.; Sampson, M.D.; Lee, Y.; Kubiak, C.P.; Cohen, S.M. "Photocatalytic CO_2 Reduction to Formate Using a Mn(I) Molecular Catalyst in a Robust Metal-Organic Framework." *Inorg. Chem*. **2015**, 54, 6821.

Machan, C.W.; Sampson, M.D.; Kubiak, C.P. "A Molecular Ruthenium Electrocatalyst for the Reduction of Carbon Dioxide to CO and Formate." *J. Am. Chem. Soc*. **2015**, 137, 8564.

Reineke, M. H.; Sampson, M. D.; Rheingold, A. L.; Kubiak, C. P. "Synthesis and Structural Studies of Nickel(0) Tetracarbene Complexes with the Introduction of a New Four-Coordinate Geometric Index, τ_δ." *Inorg. Chem*. **2015**, 54, 3211-3217.

Riplinger, C.; Sampson, M. D.; Ritzmann, A. M.; Kubiak, C. P.; Carter, E. A. "Mechanistic Contrasts between Manganese and Rhenium Bipyridine Electrocatalysts for the Reduction of Carbon Dioxide." *J. Am. Chem. Soc*. **2014**, 136, 16285-16298.

Machan, C. W.; Sampson, M. D.; Chabolla, S. A.; Dang, T.; Kubiak, C. P. "Developing a mechanistic understanding of molecular electrocatalysts for CO_2 reduction using Infrared Spectroelectrochemistry." *Organometallics*. **2014**, 33, 4550-4559.

Sampson, M. D.; Nguyen, A. D.; Grice, K. A.; Moore, C. E.; Rheingold, A. L.; Kubiak, C. P. "Manganese Catalysts with Bulky Bipyridine Ligands for the Electrocatalytic Reduction of Carbon Dioxide: Eliminating Dimerization and Altering Catalysis." *J. Am. Chem. Soc*. **2014**, 136, 5460-5471.

Sampson, M. D.; Froehlich, J. D.; Smieja, J. M.; Benson, E. E.; Sharp, I. D.; Kubiak, C. P. "Direct observation of the reduction of carbon dioxide by rhenium bipyridine catalysts." *Energy Environ. Sci*. **2013**, 6, 3748-3755.

Benson, E. E.; Sampson, M. D.; Grice, K. A.; Smieja, J. M.; Froehlich, J. D.; Friebel, D. Keith, J. A.; Carter, E. A.; Nilsson, A.; Kubiak, C. P. "The Electronic States of Rhenium Bipyridyl Electrocatalysts for CO_2 Reduction as Revealed by X-ray Absorption Spectroscopy and Computational Quantum Chemistry." *Angew. Chem. Int. Ed*. **2013**, 52, 4841-4844.

Grice, K. A.; Gu, N. X.; Sampson, M. D.; Kubiak, C. P. "Carbon monoxide release catalyzed by electron transfer: Electrochemical and spectroscopic investigations of [Re(bpy-R)(CO)4](OTf) complexes relevant to CO2 reduction." *Dalton Trans*. **2013**, 42, 8498-8503.

Smieja, J. M.; Sampson, M. D.; Grice, K. A.; Benson, E. E.; Froehlich, J. D.; Kubiak, C. P. "Manganese as a substitute for rhenium in CO2 reduction catalysts: The importance of acids." *Inorg. Chem*. **2013**, 52, 2484-2491.

ABSTRACT OF THE DISSERTATION

Rhenium and manganese bipyridine tricarbonyl catalysts for the electrochemical

reduction of carbon dioxide

by

Matthew Dean Sampson

Doctor of Philosophy in Chemistry

University of California, San Diego, 2015

Professor Clifford P. Kubiak, Chair

Electrocatalytic reduction of carbon dioxide (CO_2) is a profoundly challenging problem that is of interest, not only as a means of counteracting unsustainable emissions of CO_2, but also as a method for the development of renewable fuels. Rhenium and manganese bipyridine tricarbonyl complexes are among the most active and robust catalysts for proton-coupled CO_2 reduction to carbon monoxide (CO). X-ray Absorption Spectroscopy studies are reported to reveal the electronic ground state of the Re catalysts, which help explain origins for high selectivity for CO_2 reduction over proton reduction. Stopped-flow mixing in tandem with rapid-scan IR

spectroscopy is utilized to probe the direct reaction of the Re catalysts with CO_2, observing, for the first time, the binding of CO_2 to these catalysts.

Manganese bipyridine catalysts are desirable, in comparison with their Re analogs, due to the earth-abundance of Mn and the ability for these catalysts to operate at lower overpotentials. One distinct difference between these Mn catalysts and their Re counterparts is a high tendency for dimerization after one-electron reduction, which contributes to the potential necessary to access their active state and to limiting their catalytic activity. Synthetic modification of the bipyridine ligand (by adding bulky mesityl groups) is used to completely eliminate dimerization for these Mn complexes, allowing the active catalyst to be generated at a 300 mV more positive potential than in typically Mn bipyridine complexes. CO_2 reactivities in the presence of weak Brønsted acids, strong Brønsted acids, and Lewis acids have been explored in order to encourage this bulky Mn catalyst to reduce CO_2 at low overpotentials. Mechanistic tools, including IR-spectroelectrochemistry, are described to gain insight into these unique catalytic processes.

In order to further enhance stability and facilitate product separation, the use of metal-organic frameworks (MOFs) is explored as a means of anchoring molecular catalysts on a heterogeneous platform. A Mn bipyridine catalyst attached to a highly robust Zr(IV)-based MOF is used to enhance photochemical CO_2 reduction. By utilizing an iron porphyrin catalyst, anchored into the linkers of a MOF thin film, we demonstrate, in a proof of principle, electrochemical CO_2 reduction by this heterogenized molecular catalyst.

Chapter 1

Motivation and means for the electrocatalytic reduction of carbon dioxide towards the production of liquid fuels.

1.1 Declining Supplies of Fossil Fuels and Unsustainable Emissions of Carbon Dioxide

A dramatic increase in global fuel consumption coupled with unsustainable emissions of carbon dioxide (CO_2) has led to one of the greatest challenges of our modern era – the development of renewable, CO_2-neutral fuels.[1] In recent years, tremendous efforts have been made to develop technologies for solar and wind power; however, the energy sources for these technologies suffer from intermittent

availability. Therefore, research in energy storage, particularly storage in chemical bonds, is essential to the sustainability of these technologies. To counteract the intrinsic availability problem of solar and wind energy, the electricity generated from these sources can be stored in chemical bonds, such as liquid fuels generated from CO_2 reduction. These renewable fuels can be utilized on demand to drive an engine or produce electricity in a fuel cell. Artificial photosynthetic systems are currently being developed that couple CO_2 reduction and water (H_2O) oxidation and are driven by solar energy.[2] By harnessing solar energy, these systems will provide a route to carbon-neutral energy, helping to counteract our unsustainable CO_2 emissions. Production of renewable fuels through CO_2 reduction can also provide a fuel source capable of incorporation into existing infrastructure. This fuel source will help replace declining supplies of fossil fuels (Figure 1.1).

Figure 1.1 Worldwide oil production (separated by region) since 1930, with future estimates projected to 2050. Figure taken with permission from Ref. 3.

CO_2 is a notorious greenhouse gas, released by both natural and artificial processes. In 2014, the Intergovernmental Panel on Climate Change (IPCC) released their Fifth Assessment Report, which states, "Human influence on the climate system is clear, and recent anthropogenic emissions of greenhouse gases are the highest in history. Cumulative emissions of CO_2 largely determine global mean surface warming by the late 21st century and beyond. Continued emission of greenhouse gases will cause further warming and long-lasting changes in all components of the climate system."[4] Since the beginning of the industrial era, a significant increase in anthropogenic CO_2 emissions has occurred (see Figure 1.2b) originating primarily from the world's reliance on petroleum for fuels and commodity chemicals.[4] As a result, in recent years, atmospheric CO_2 concentrations have reached unprecedented levels going back over 800,000 years (Figure 1.2a).[5] Atmospheric CO_2 levels will continue to increase into the future, with projections estimating levels around ~550 ppm (for lower emissions scenarios) to over 900 ppm (for higher emissions scenarios) (Figure 1.2a). The increased levels of CO_2 in the atmosphere has caused, and will continue to cause, warming of the climate system. This "global warming" is indisputable, and many of the observed changes are unprecedented over tens to thousands of years. Since these unsustainable, anthropogenic CO_2 emissions of recent decades have originated in large part from fossil fuel use, there is a high need for the development of renewable, CO_2-neutral fuels. Even if anthropogenic emissions of CO_2 are stopped, the effects of climate change will be felt for centuries.[4] A commercially

viable, CO_2-neutral fuel source will help mitigate these effects and help avoid further damage to our climate.

Figure 1.2 (a) Atmosphere carbon dioxide (CO_2) concentrations (in ppm) over time from 800,000 years before present. Atmospheric CO_2 levels from 2008 and estimated levels from 2100 using higher and lower emissions scenarios are indicated. Data is taken from the IPCC Fourth Assessment Report, and the figure is reproduced from Ref. 5. (b) Global anthropogenic CO_2 emissions since 1850 from the burning of fossil fuels, cement production, and flaring (grey) as well as from forestry and other land use (gold). Emissions of CO_2 are given in Gigatons of CO_2 per year ($GtCO_2$ yr^{-1}). Figure is reproduced from Ref. 4.

1.2 Thermodynamic and Kinetic Considerations for Carbon Dioxide Reduction

As previously stated, one promising route to the production of renewable, chemical fuels is via the electrocatalytic reduction of CO_2. In order to make this electrocatalytic process CO_2-neutral, the electricity required can be generated from photoexcitation in a semiconductor or from an applied external voltage, where the latter could originate from a renewable source, such as wind turbines or photovoltaics.[6-9] Other than electrocatalytic processes, there are also other means to perform CO_2 reduction, including heterogeneous CO_2 reduction[7,10-13], CO_2 hydrogenation,[14-16] and photochemical CO_2 reduction.[15,17-18]

Returning CO_2 to a useful state by activation and reduction is an energetically and kinetically challenging processes. The direct, one-electron reduction of CO_2 to the $CO_2^{\bullet-}$ radical anion possesses a very high thermodynamic penalty (approximately -1.9 V vs. NHE),[19] primarily due to the large reorganizational energy required to bend the linear CO_2 molecule to form $CO_2^{\bullet-}$. Proton-coupled, multi-electron reductions of CO_2 are much more favorable in terms of thermodynamics, as these processes form thermodynamically stable molecules. These thermodynamic considerations are summarized in E1.1–E1.6 (potentials are referenced vs. NHE, pH 7 aqueous solution, 25 °C, 1 atm gas pressure, 1 M other solutes).[18,20] Since the reductions of CO_2 shown in E1.1–E1.5 are proton-coupled processes, it's important to consider the thermodynamics of the reduction of protons to dihydrogen (H_2) as well (E1.7). Specifically, the reduction of protons to H_2 is either thermodynamically favored or thermodynamically neutral as compared to the proton-coupled CO_2 reductions.

$$CO_2 + 2H^+ + 2e^- \rightarrow CO + H_2O \qquad E° = -0.53 \text{ V} \qquad \textbf{(E1.1)}$$

$$CO_2 + 2H^+ + 2e^- \rightarrow HCO_2H \qquad E° = -0.61 \text{ V} \qquad \textbf{(E1.2)}$$

$$CO_2 + 4H^+ + 4e^- \rightarrow HCHO + H_2O \qquad E° = -0.48 \text{ V} \qquad \textbf{(E1.3)}$$

$$CO_2 + 6H^+ + 6e^- \rightarrow CH_3OH + H_2O \qquad E° = -0.38 \text{ V} \qquad \textbf{(E1.4)}$$

$$CO_2 + 8H^+ + 8e^- \rightarrow CH_4 + 2H_2O \qquad E° = -0.24 \text{ V} \qquad \textbf{(E1.5)}$$

$$CO_2 + e^- \rightarrow CO_2^{\bullet-} \qquad E° = -1.90 \text{ V} \qquad \textbf{(E1.6)}$$

$$2H^+ + 2e^- \rightarrow H_2 \qquad E° = -0.38 \text{ V} \qquad \textbf{(E1.7)}$$

In addition to these thermodynamic considerations, there are also crucial kinetic concerns dealing with CO_2 reduction. In general, although the higher multi-proton coupled reductions of CO_2 (E1.3–E1.5) are thermodynamically more favorable than the two-proton, two-electron reductions of CO_2 (E1.1–E1.2), it is kinetically challenging to form and break a large number of chemical bonds, in addition to assembling nuclei in close proximity to one another, in order to convert the CO_2 molecule into more complex and energetic products. Because of these kinetic challenges, the direct conversion of CO_2 to even the simplest chemical fuel, methanol (CH_3OH), is incredibly challenging. To this date, no single homogeneous electrocatalyst is capable of reducing CO_2 to CH_3OH or beyond. Reducing CO_2 via two-proton, two-electron processes is much more facile, and thus, most of the research on homogeneous electrocatalysts is centered on optimizing and improving upon these processes. As previously mentioned, the two-electron reduction of protons to H_2 (E1.7) is thermodynamically favored over the two-electron reductions of CO_2 to either CO or formic acid (HCO_2H) (E1.1, E1.2). Therefore, any catalyst one chooses to facilitate this process must have a kinetic preference for engaging CO_2 over a proton.

Including the aforementioned direct reduction of CO_2, there are three main strategies to convert CO_2 to chemical fuels (Figure 1.3). Due to the kinetic challenges associated with the direct conversion of CO_2 to a chemical fuel (such as CH_3OH), the two most promising strategies for this conversion are either via tandem catalysis or via syngas production and further use of existing Fisher-Tröpsch technologies. In tandem catalysis, CO_2 reduction proceeds stepwise, via sequential two-electron reductions,

using a different catalyst for each reduction step. Here, CO_2 is first reduced to either

CO or HCO_2H, and then these products are reduced further to formaldehyde (H_2CO).

Finally, H_2CO is reduced via two-electrons or beyond to form methanol or another

chemical fuel. Huff and Sanford have demonstrated tandem catalysis for

hydrogenation of CO_2 to methanol using a homogeneous catalyst;[21] however, this type

of tandem catalysis has not yet been accomplished using electrochemical methods.

Direct conversion: $CO_2 + 6H^+ + 6e^- \longrightarrow CH_3OH + H_2O$

Tandem catalysis:

$CO_2 \xrightarrow[\text{cat. A}]{2H^+, 2e^-} CO \xrightarrow[\text{cat. B}]{2H^+, 2e^-} H_2CO \xrightarrow[\text{cat. C}]{2H^+, 2e^-}$ chemical fuels

$CO_2 \xrightarrow[\text{cat. A}']{2H^+, 2e^-} HCO_2H \xrightarrow[\text{cat. B}']{2H^+, 2e^-} H_2CO \xrightarrow[\text{cat. C}']{2H^+, 2e^-}$ chemical fuels

Via syngas (CO + H$_2$):

$CO_2 \longrightarrow CO$
$+$
$2H^+ \longrightarrow H_2$ $\longrightarrow$ [Fischer-Tröpsch technologies] $\longrightarrow$ chemical fuels

Figure 1.3 Schemes showing the three main strategies for converting CO_2 into chemical fuels by homogenous electrocatalysts: direct conversion to a chemical fuel (such as CH_3OH), tandem catalysis (utilizing a separate catalyst for sequential two-electron reduction steps), and production of chemical fuels via syngas (using existing Fisher-Tröpsch technologies).

The third strategy for producing chemical fuels from CO_2 reduction is via the

production of syngas (i.e. a mixture of CO and H_2). Here, CO_2 is reduced by two-

electrons and two-protons to CO, and protons are reduced to H_2. This syngas mixture

is then incorporated into existing Fisher-Tröpsch technologies, which are capable of

producing a variety of liquid hydrocarbons, primarily alkanes. Fisher-Tröpsch

technologies typically utilize a heterogeneous cobalt- or iron-based catalyst operating

in a temperature range of 150–300 °C and a pressure range of one to several tens of

atm. For cobalt-based catalysts, optimal H_2:CO ratios are in the range of 1.8–2.1;

however, iron-based catalysts tend to promote the water-gas shift reaction[22] and can tolerate lower H_2:CO ratios. Commercial Fisher-Tröpsch plants are currently in operation, including a series of large scale plants operated by Sasol in South Africa.[23] In addition to their South African operations, in 2012, Sasol announced plans to build a 96,000 barrels per day plant in Louisiana.[24] PetroSA and Qatar Petroleum each also have operational Fisher-Tröpsch plants running at 36,000 and 140,000 barrels per day, respectively.[25-26] Fisher-Tröpsch technologies have been the focus of several recent reviews.[10,27-32] In addition to Fisher-Tröpsch, syngas can be used to synthesize a variety of other products, including methanol, ethanol, aldehydes, ammonia, and a variety of other alcohols.[33]

1.3 Carbon Dioxide Reactivity with Organometallic Complexes

Due to kinetic complications dealing with the electrochemical reduction of CO_2, efficient catalysts are required to reduce the overpotentials needed to drive these reactions and enhance the rate of the reactions. Therefore, understanding the interaction between CO_2 and transition metals is of paramount importance. The CO_2 molecule is overall nonpolar, containing two polar, very short C–O bonds. Although CO_2 is considered a relatively inert molecule, it exhibits a wide range of reactivities. CO_2 interacts only weakly with Brønsted and Lewis acids, but is susceptible to attack by nucleophiles (at the weakly electrophilic carbon) and to reduction. CO_2 exhibits two different reaction sites, either at the electrophilic carbon atom or at the

nucleophilic oxygen atoms. Therefore, CO_2 is capable of forming a variety of coordination modes to metal complexes (Figure 1.4a).

Figure 1.4 (a) Selected structural types of metal–CO_2 complexes involving either one or two metal centers. (b) Schematic showing two types of initial insertion of CO_2 into a metal–hydride bond forming metal–OCHO or metal–CO_2H complexes.

For simplification, Figure 1.4 contains only those coordination modes that involve one or two metal centers; however, there exists other coordination modes involving three and four metal centers as well.[13,34-35] Greek letters and numbers are typically used to describe the type of coordination mode. The descriptor η^n signifies the number of bonds between the coordinated CO_2 ligand and the metal center(s), and the descriptor μ_n signifies the number of metal atoms in involved in bonding to the CO_2 ligand. The CO_2 ligand is capable of bonding to a metal center via the following modes: directly through the carbon atom (see η^1), "side on" by a C–O bond (see η^2), or "end on" through one oxygen atom (η^1-O). Since the η^1-O coordination mode has only been characterized in complexes of U, we will not discuss it further here.[36-37] In addition to coordination to a single metal center, CO_2 can also bind between two metal centers. Here, the carbon atom binds to one metal center (M_1 in Figure 1.4a) and either one (μ_2-η^2) or both oxygen atoms (μ_2-η^3) can coordinate to the other metal center (M_2 in Figure 1.4a). All of these coordination modes described in Figure 1.4a have been

considered as intermediates in catalytic reductions of CO_2. The first structurally characterized metal–CO_2 complex was $Ni(\eta^2\text{-}CO_2)(PCy_3)_2$ by Aresta *et al.* in 1975.[38] The η^2 coordination mode is also the most common type of CO_2 coordination to a single metal, with structural examples for complexes of Fe, Ni, Mo, Rh, Pd, W, and Re.[35,39] Additionally, the η^1 coordination mode has been structurally characterized in complexes of Co, Rh, and Ir.[35,39] η^1- and η^2-CO_2 complexes are typically formed by direct reaction of a metal complex with CO_2. For these reactions to occur, the metal center needs to have an open coordination site or have an easily displaced ligand as well as be highly nucleophilic in order to bind the weakly electrophilic carbon of CO_2. The active states for many transition metal catalysts for CO_2 reduction have been modeled after these criteria.[15,19,40-41]

For bimetallic coordination, there are several structural characterizations for the $\mu_2\text{-}\eta^2$ mode).[35,39] The $\mu_2\text{-}\eta^3$, class I coordination mode occurs when there are symmetric M_2–O bond lengths, whereas class II occurs when there are unequal M_2–O bond lengths. The $\mu_2\text{-}\eta^3$, class I mode is typically formed between late and early transition metals,[35,39] and the $\mu_2\text{-}\eta^3$, class II mode has only been structurally characterized in complexes with M_2 = Sn.[42-45] There are numerous routes to form a $\mu_2\text{-}\eta^2$- or $\mu_2\text{-}\eta^3$-CO_2 complexes, but the most common routes include direct CO_2 insertion into a dimeric metal complex, the collapsing of two η^1-bound M–CO_2 complexes, and deprotonation of a M–CO_2H complex to react with another metal complex with weakly coordinating ligands.

In addition to direct CO_2 coordination to a metal center, another type of relevant CO_2 reactivity with organometallic complexes is CO_2 insertion into metal–hydride bonds (M–H). Figure 1.4b shows two ways the initial reaction between CO_2 and a M–H can proceed. Here, the reaction can result in either a metal–formato complex (M–OCHO), where the hydride transfers to the carbon atom of CO_2 and one oxygen atom coordinates to the metal center, or a metal–hydroxycarbonyl complex (M–COOH), where the hydride transfers to an oxygen atom of CO_2 and the carbon atom coordinates to the metal center. A M–COOH complex can also form from the direct protonation of an η^1-coordinated metal–CO_2 complex. Several M–COOH complexes have been structurally characterized, including those for complexes of Ni, Ru, Pd, Re, Ir, and Pt.[35,39,41] Additionally, a wide range of M–OCHO complexes have been structurally characterized, with complexes for well over half of the transition metals.[35,39,41] For many transitional metal complexes that catalyze CO_2 reduction, initial metal–CO_2 coordination products are often short-lived and unstable due to further reaction. In these cases, other techniques are used to trap these intermediates, such as reactions with an organotin compound[13,42] or reactions to form metal–alkyl esters (i.e. M–CO_2CH_3 or M–$CO_2CH_2CH_2$ complexes).[35,46]

1.4 Biological Motivation for Carbon Dioxide Utilization

CO_2 reduction is achieved in nature using the energy from sunlight via photosynthesis. The sun is an inexhaustible energy source available in abundance on our planet. Photosynthetic organisms store the energy from sunlight in chemical bonds

via photosynthesis using both CO_2 reduction and H_2O oxidation. Upon anaerobic fermentation, over the course of millions of years, these solar chemicals (i.e. carbohydrates) were converted into fossil fuels, which are used today for the vast majority of the world's energy needs. Photosynthetic organisms convert approximately 385 Gt of CO_2 into high-energy chemicals annually net (the gross conversion is approximately double).[15,47] Because the process of converting CO_2 into fossil fuels via photosynthesis and anaerobic fermentation takes several millions of years, we must develop new ways to produce chemical fuels in a sustainable manner in order to meet the world's rate of energy consumption. We can use the fundamental ideas from nature to inspire the development of alternative energy sources, such as carbon-based solar fuels (i.e. fuels derived from CO_2 and sunlight).[48]

Photosynthetic plants fixate CO_2 in the Calvin cycle using protons and electrons generated in photosystem I (PSI) and photosystem II (PSII) (Figure 1.5). In PSII, chloroplasts absorb photons from sunlight and use this absorbed energy to oxidize H_2O to O_2 as well as to run a variety of other light-driven redox reactions. In PSI, the electrons harvested from sunlight are used to produce energetically rich reducing agents, nicotinamide adenine dinucleotide phosphate (NADPH) and adenosine triphosphate (ATP). These reducing agents are utilized in the Calvin cycle[49] to reduce atmospheric CO_2 to a variety of carbohydrates.[50]

Figure 1.5 Simplified schematic of the processes involved in photosynthesis in the chloroplast. Figure taken with permission from Ref. 49.

Pathways for CO_2 fixation in nature have evolved over billions of years and use diverse mechanisms and enzymes to process CO_2 into higher order products. The enzymes that carry out these metabolic pathways use readily abundant materials from the environment (i.e. earth-abundant metal centers) to achieve these important energy conversion processes. All of the metabolic pathways dealing with CO_2 fixation involve the storage and utilization of energy in the form of chemical bonds. It is essential that we understand the processes of CO_2 fixation in biological systems in order to carry out similar transformations in a productive manner, independent of these natural systems. There are two main sets of enzymes that catalyze two-electron

conversions of CO_2, carbon monoxide dehydrogenases (CODHs) and formate dehydrogenases (FDHs). These two sets of enzymes catalyze the conversion of CO_2 with CO and formate, respectively. Understanding the structures and mechanisms of these enzymes have aided in developing artificial systems that interconvert CO_2 and CO/formate via two electrons and two protons. The structures of the active sites of both aerobic and anaerobic CODH and Se-dependent FDH enzymes are shown in Figure 1.6. The intricate structures of these enzymes along with the mechanisms that these enzymes use to convert CO_2 to CO/formate have been the focus of many recent studies and reviews.[15]

Figure 1.6 (a) X-ray crystal structure of the [MoSCu] active site in the CODH found in the aerobic bacterium *O. carboxydovorans* (taken with permission from Ref. 51). (b) X-ray crystal structure of CO_2 activation by the [Fe_4S_4Ni] active site of the CODH found in the anaerobic bacterium *C. hydrogenoformans* (taken with permission from Ref. 52). (c) X-ray crystal structure of the formate-reduced state of the Mo(IV) active site found in the FDH enzyme of *E. coli* (taken with permission from Ref. 53).

High catalytic activities and low overpotentials of these enzymes has led research efforts on developing synthetic analogs to the active sites of CODH and FDH enzymes towards the goal of creating an artificial catalytic system for CO_2 reduction (see Figure 1.7). Although mimics of the active sites of these enzymes have been successfully synthesized, most show relatively poor, if any, activity towards CO_2

reduction as compared to the natural-occurring enzymes.[54-58] In these artificial mimics, replicating the crucial interactions and features of the outer and secondary coordination spheres (i.e. hydrophobic/hydrophilic channels, hydrogen-bonding interactions, local proton sources, etc.) is extremely challenging. These outer and secondary coordination environments are essential to the function of these metalloenzymes. These interactions both help lower operating potentials to near thermodynamic potentials and significantly increase the rates of catalysis by stabilizing the active site, facilitating substrate/product transfer to/from the active state, and facilitating the formation/breaking of crucial bonds in the bound substrate. Without these outer and secondary coordination environments, the same bare metal centers with a simplified coordination environment typically do not function well for this reactivity.

Figure 1.7 Selected structural mimics for (a) an Fe_4S_4 cluster, (b) the active site of MoSCu CODH, and (c) the active site of W FDH.

1.5 Methods for Studying Electrocatalytic Processes

Molecular electrocatalysts assist in both transferring electrons between the electrode and reactants and facilitating a chemical transformation. A general schematic of an electrocatalytic process is shown in Figure 1.8. An electrocatalytic process is

dependent on the relationship between the applied potential ($V_{applied}$) and the thermodynamic potential of the catalytic reaction ($E°(S/P)$), which can be used to determine the effective overpotential ($\eta = V_{applied} - E°(S/P)$). Ideal molecular electrocatalysts possess a high heterogeneous electron rate constant (k_h) at $V_{applied}$ as well as a redox couple ($E°(CAT^{m/m-n})$) that is well-matched with $E°(S/P)$, resulting in a minimal η. In addition to these considerations, an ideal electrocatalyst should have a high catalytic rate constant (k_{cat}).

Figure 1.8 General mechanism of an electrocatalytic process, where $V_{applied}$ = applied potential, k_h = heterogeneous electron rate constant, k_{cat} = catalytic rate constant.

    One of the simplest electrochemical processes is known as an EC mechanism, where a molecular species (CAT^m) experiences a reversible heterogeneous electron transfer (E) from the electrode to form a reduced form of the molecular species. This reduced species then undergoes a chemical reaction (C), reacting with a substrate (S) in solution to form a product (P). A variation of this mechanism is shown in E1.8–E1.10, where CAT^m undergoes two reversible heterogeneous electron transfer events

(EE) to form CAT^{m-1} (E1.8) followed by CAT^{m-2} (E1.9). This doubly-reduced species then undergoes a chemical reaction with a substrate to form a product (E1.10).

$$CAT^m + e^- \rightarrow CAT^{m-1} \qquad\qquad \text{(E)} \qquad\qquad \textbf{(E1.8)}$$

$$CAT^{m-1} + e^- \rightarrow CAT^{m-2} \qquad\qquad \text{(E)} \qquad\qquad \textbf{(E1.9)}$$

$$CAT^{m-2} + S \rightarrow P \qquad\qquad \text{(C)} \qquad\qquad \textbf{(E1.10)}$$
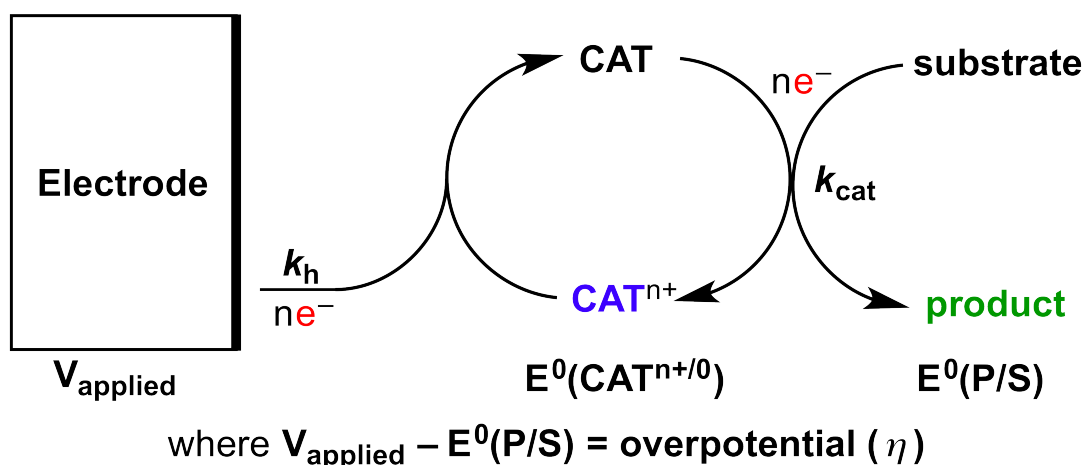
An example of an EEC electrochemical mechanism is shown in the cyclic voltammogram (CV) experiment in Figure 1.9a. Cyclic voltammetry is a type of potentiodynamic electrochemical measurement (Figure 1.9b), where a potential is ramped linearly versus time at the working electrode (potential is controlled by use of a reference electrode). After the set potential is reached in the cyclic voltammetry experiment, the working electrode's potential is ramped in the opposite direction to return to the initial potential. Current, flowing between the working electrode and a counter electrode, is then plotted versus the applied potential to give a CV. During a cyclic voltammetry experiment, the electrochemical solution is left unstirred in order to let diffusional processes control the movement of species near the working electrode surface. For electrocatalytic studies, the working electrode is typically an inert material, such as glassy carbon, and the counter electrode is a highly conductive material, such as platinum or titanium. Typically, Ag/AgCl or $Ag/AgNO_3$ reference electrodes (separated by a porous Vycor tip to prevent leakage) are used.
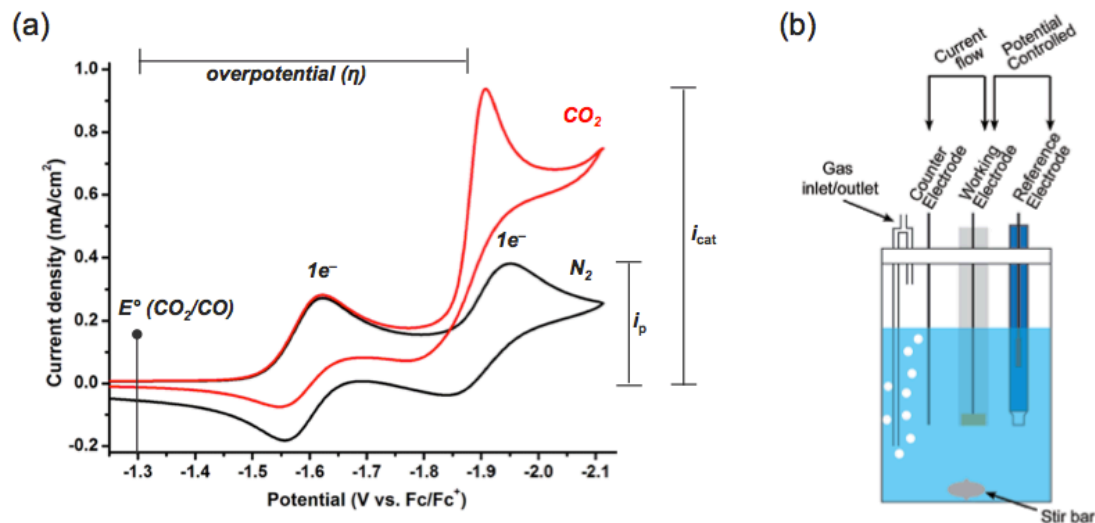
Figure 1.9 (a) Example cyclic voltammograms (CVs) of a molecular catalyst under inert atmosphere (black) and under the presence of CO_2 (red). Each CV shows two one-electron reduction waves of the molecular catalyst. An increase in current is observed at the second reduction under the presence of CO_2 due to electrocatalysis. Figure adapted from Ref. 107. (b) Schematic of a typical electrochemical cell containing a solution of a molecular catalyst in electrolyte. The cell consists of a working electrode, counter electrode, and reference electrode as well as an inlet/outlet port for gas sparging.

When a molecular species that undergoes an EEC-type mechanism is present in the electrochemical solution, a cyclic voltammetry experiment under a dry, inert atmosphere, such as dinitrogen (N_2), produces a CV like the one shown in Figure 1.9a. Here, the molecular species undergoes two reversible one-electron reductions at approximately $E = -1.6$ V and -1.9 V vs. ferrocene/ferrocenium (Fc/Fc^+ or $Fc^{0/+}$). Typically, with organic electrolytes, ferrocene (Fc) is added to the electrochemical solution as an internal reference. The Fc/Fc^+ couple has a known redox potential in a variety of electrolytes and is an example of an ideal, reversible one-electron redox couple. Upon reaching the potential of one of the reductions of the molecular species, a current increase is observed due to the transfer of electrons from the electrode

surface to the molecular species. Once all molecular species in the diffusion layer near the electrode surface is reduced, the current drops off. A reversible redox feature is typically characterized by having a peak cathodic current (i_p) and peak anodic current that are approximately the same value relative to the center of the redox wave. In reality, many molecular species do not display idealized, reversible redox features due to chemical processes such as loss of a ligand, dimerization, and/or changes in geometry.

For electrocatalytic processes, such as CO_2 reduction, exposing the electrochemical solution to the substrate (CO_2) results in an increase in the diffusion-limited current near the potential of the redox wave that generates the active catalyst (Figure 1.9a, at the second one-electron reduction). This increase in current is called "catalytic current," and results from the active catalyst (CAT^{m-2} in our example of an EEC mechanism) chemically reacting with CO_2 and from regeneration of CAT^{m-2} near the electrode surface. The magnitude of the catalytic current observed in CVs is proportional to the catalytic rate constant (described in more detail below). An anodic shift and loss of reversibility of the reduction wave is also typically observed due to the chemical reaction with CO_2.

After screening the redox properties of the molecular catalyst by cyclic voltammetry (as well as other potential sweeping methods), supplemental use of controlled potential electrolysis (CPE), or bulk electrolysis, allows for quantification of the products of the electrocatalytic reaction as well as determination of long-term stability. In CPE, the working electrode is held at a constant potential (typically, a

potential near peak catalytic current in a CV) and current is monitored over time. The current over time can be easily converted to the total amount of Coulombs passed, and thus the amount of electrons passed, over time. In an ideal CPE experiment with a molecular electrocatalyst, current over time should remain constant if catalysis is sustained at a constant rate and if the catalyst does not degrade or become deactivated.

The experimental setup for CPE is typically very similar to that of cyclic voltammetry (Figure 1.9b); however, a few differences are worth noting. (1) The cell must be completely gas tight, especially if gaseous products, such as CO, are produced from CO_2 reduction; (2) the solution is stirred at a constant rate during the experiment to facilitate movement of species from the bulk solution to the electrode surface; (3) a working electrode with large surface area is used to pass a high amount of current over a relatively short amount of time; (4) the counter electrode is enclosed in a porous glass fritted tube in order to separate it from the bulk solution. The latter is important to prevent unwanted oxidation of the molecular species at the counter electrode, which can typically lead to degradation. In order to avoid decomposition of the solvent or electrolyte at the counter electrode (caused by the necessity to balance the current at the working electrode), a large amount of sacrificial oxidant (or reductant for oxidation catalysis), such as Fc or an oxalate salt,[59] is typically added to balance the overall redox reaction. Oxalate salts are useful in this manner, as oxidation of oxalate produces CO_2. For CO_2 reduction studies that produce CO as a product, the headspace (of a constant volume) is sampled during the course of the experiment in order to measure the amount of CO formed by gas chromatography. Typically, formation of H_2

is also measured at this point via gas chromatography to check if any H^+ reduction is occurring. NMR is typically used to identify and quantify the formation of liquid products.

An ideal molecular electrocatalyst must posses a high catalytic rate constant, high selectivity for the desired reaction, high stability, and a good thermodynamic match between its redox potential ($E°(CAT^{m-1/m-2})$ for the EEC mechanism) and the standard potential for the chemical reaction that is being catalyzed (here, CO_2 to CO). This thermodynamic match is calculated as an overpotential ($\eta = E°(CAT) - E°(CO_2/CO)$) for the specific molecular catalyst. The rate of the catalytic reaction, or turnover frequency (TOF), is proportional to the peak current under substrate (i_{cat}) divided by the peak current under inert atmosphere (i_p), or i_{cat}/ i_p (described in more detail in the following chapters). The TOF for the electrocatalytic reaction can also be measured during CPE experiments by quantifying the generated product over time. The selectivity of the electrocatalyst is measured by the Faradaic efficiency, or current efficiency, which is a measure of the amount of the desired product formed divided by the number of electrons passed during a CPE experiment (for the reduction of CO_2 to CO, every two electrons should produce one molecule of CO). Stability of the electrocatalyst is also measured through CPE, by both the turnover number (TON), or the amount of total product formed from the experiment, and by observing how long the electrocatalyst sustains steady current before degrading. These factors characterizing an ideal electrocatalyst can be optimized by both chemical tuning of the

catalyst's metal center via appropriate ligand design and altering the experimental conditions of the electrocatalytic experiment.

Along with cyclic voltammetry and CPE, additional mechanistic details can be revealed about the molecular catalyst and the catalytic process by the isolation and characterization of the precatalyst (parent redox state), any oxidized or reduced species generated before catalytic turnover, potential catalytic intermediates, in addition to product analysis. The isolation and characterization of catalytically relevant species are not only vital to understanding the catalytic mechanism but also vital to determining how the specifics of species' electronic structures can inform further synthetic modifications for the optimization of catalytic activity.

Another means to gain detailed mechanistic information about molecular catalysts and the catalytic reaction is through spectroelectrochemistry (SEC).[60-61] SEC incorporates a spectroscopic technique into the electrochemical cell design, allowing species of interest to be characterized *in situ* during the bulk electrolysis of small amounts of material. This has been shown to work for ultraviolet-visible (UV-Vis) absorbance,[62] nuclear magnetic resonance (NMR),[63] fluorescence,[64] electron paramagnetic/spin resonance (EPR/ESR),[65-66] and infrared (IR) spectroscopies.[67-68]

Our laboratory has been systematically examining electron transfer and catalysis in transition metal compounds with diagnostic v_{CO}, v_{CN}, and pyrazine v_{8a} frequencies.[69-78] Specifically, we have focused on the use of Fourier-Transform Infrared Spectroelectrochemistry (IR-SEC), which has allowed us to simultaneously generate and characterize the IR spectra of molecules at applied potential. The specific

details of the design of our IR-SEC cell has been published,[79] and is shown in Figure 1.10. The cell design consists of a circular working electrode (typically Pt, Au, or glassy carbon) that is polished to a mirror finish within concentric rings of Ag and Pt electrodes that serve as the pseudo-reference and counter electrodes, respectively. The electrode assembly is tightened on top of a thin Teflon spacer (<0.5 mm), which is sandwiched with a calcium fluoride (CaF_2) window, so that solution may be passed through the thin-layer chamber using channels positioned on either side of the electrodes. The electrode platform is fixed on top of a commercially available two-mirror reflectance accessory with mirrors that can attach to a standard IR transmittance stand. In a typical experiment incident light from the spectrometer is directed off a mirror to the working electrode surface, passing through the solution before being reflected back through to the detector (Figure 1.10b). The use of a potentiostat allows stepwise potential changes to be made and immediately characterized by FTIR so that the IR signature can be monitored over the course of an experiment. Since the chamber containing the analyte in electrolyte solution has an extremely small volume and the cell design minimizes the potential gradient, the bulk electrolysis required to identify individual species is often rapid and quantitative. We have used our IR-SEC cell to examine the IR frequencies of many transition metal compounds. This has enabled us to elucidate mechanisms of electron transfer in μ_3-oxo centered ruthenium clusters, the catalytic behavior of Ni isocyanide complexes, and the catalytic behavior of Re(I) and Mn(I) 2,2′-bipyridine (bpy) tricarbonyl complexes (discussed in more detail in the next section).[69-78]
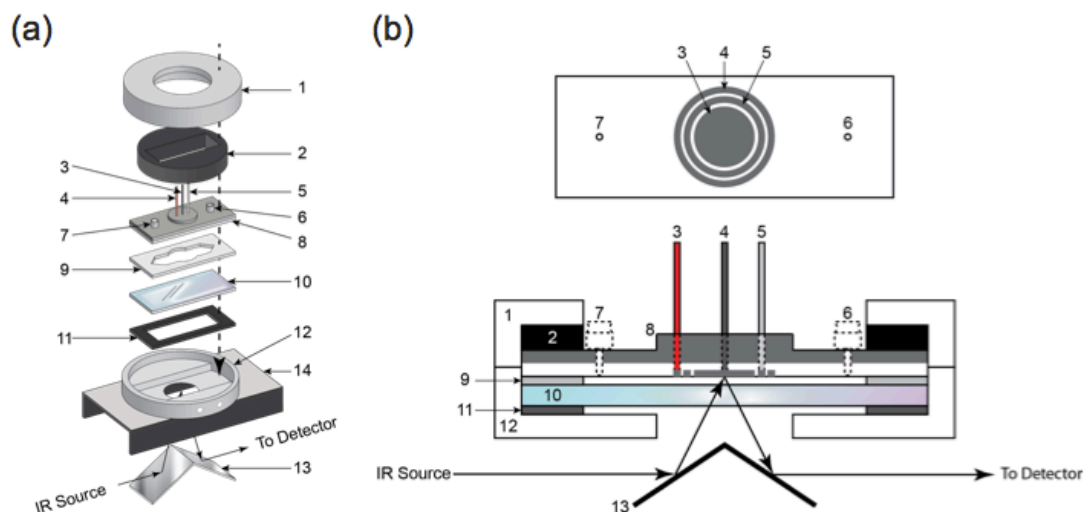
Figure 1.10 (a) Disassembled view and (b) assembled cross-section view of our group's spectroelectrochemical (SEC) cell: (1) tightening brass cap (threaded inside); (2) brass ring required to tighten the cell; (3) working electrode, typically glassy carbon, Pt, or Au; (4) counter electrode, typically Pt; (5) psuedo-reference electrode, Ag/Ag$^+$; (6, 7) injection ports; (8) cell body, top part aluminum, lower part Teflon (all three electrodes and both filling ports are press fitted into the cell body to facilitate replacement); (9) Teflon spacer; (10) CaF$_2$ window; (11) rubber gasket; (12) hollow brass cell body with threaded inlet and outlet ports (Swagelok) for connection to circulating bath; (13) mirrors; (14) two-mirror reflectance accessory (Thermo-SpectraTech FT-30; not shown in cross-section view). Figure taken with permission from Ref. 83.

1.6 Previous Studies on Rhenium and Manganese Bipyridine Tricarbonyl Electrocatalysts for Carbon Dioxide Reduction

Rhenium bipyridine *fac*-tricarbonyl complexes have been known for over seven decades.[80-81] Re(bpy-R)(CO)$_3$Cl, (bpy-R = 4,4′-disubstituted-2,2′-bipyridine, **1-Re**), was first shown to be competent for the electrocatalytic reduction of CO$_2$ to CO by Hawecker *et al.* in 1984.[82] This family of catalysts has also been extensively studied for photochemical CO$_2$ reduction.[83-88] This Re(bpy)-based system is among the most active and selective molecular electrocatalysts for CO$_2$ reduction to date.

In 1985, Meyer and co-workers studied the electrochemical reduction of CO_2 by **1-Re** in further detail.[89] Meyer and co-workers found that there were two reductions for **1-Re** in MeCN. The first reduction is quasireversible and leads to reduction of the π^* molecular orbital on the bpy ligand, and the second reduction leads to reduction of the Re center and loss of Cl^-. They also observed that a Re(0)–Re(0) dimer, $[Re(bpy)(CO)_3]_2$ (**4-Re**), is formed upon bulk electrolysis at the first reduction for **1-Re**. Electrochemical studies suggested that there were in fact two routes by which **1-Re** can reduce CO_2: a slow one-electron pathway and a rapid two-electron pathway (see Figure 1.11). The one-electron pathway proceeds after the first reduction and results in the reductive disproportionation of CO_2 to form CO and carbonate (CO_3^{2-}). Catalysis after the second reduction is much more rapid, as determined by an increased current response in electrochemical studies, and results in high Faradaic efficiency for the production of CO as the primary product. Meyer and co-workers proposed that an oxide acceptor (A) was necessary for the two-electron pathway and suggested that the Re(bpy) catalyst could scavenge protons from the supporting electrolyte (tetrabutylammonium hexafluorophosphate, $TBAPF_6$), based on the observation of NBu_3 in solutions after CPE experiments.

$fac-Re(bpy)(CO)_3Cl$

$-e^-$ ⇅ $+e^-$

$[Re(b\dot{p}y)(CO)_3Cl]^-$

$-Cl^-$

$+e^-$

$CO+CO_3^{2-}$ $Re(bpy)(CO)_3$ CO_2

CO_2+2e^- $Re(bpy)(CO)_3CO_2$

$CO+[AO]^-$ $[Re(bpy)(CO)_3]^-$ CO_2

$A+e^-$ $[Re(bpy)(CO)_3CO_2]^-$
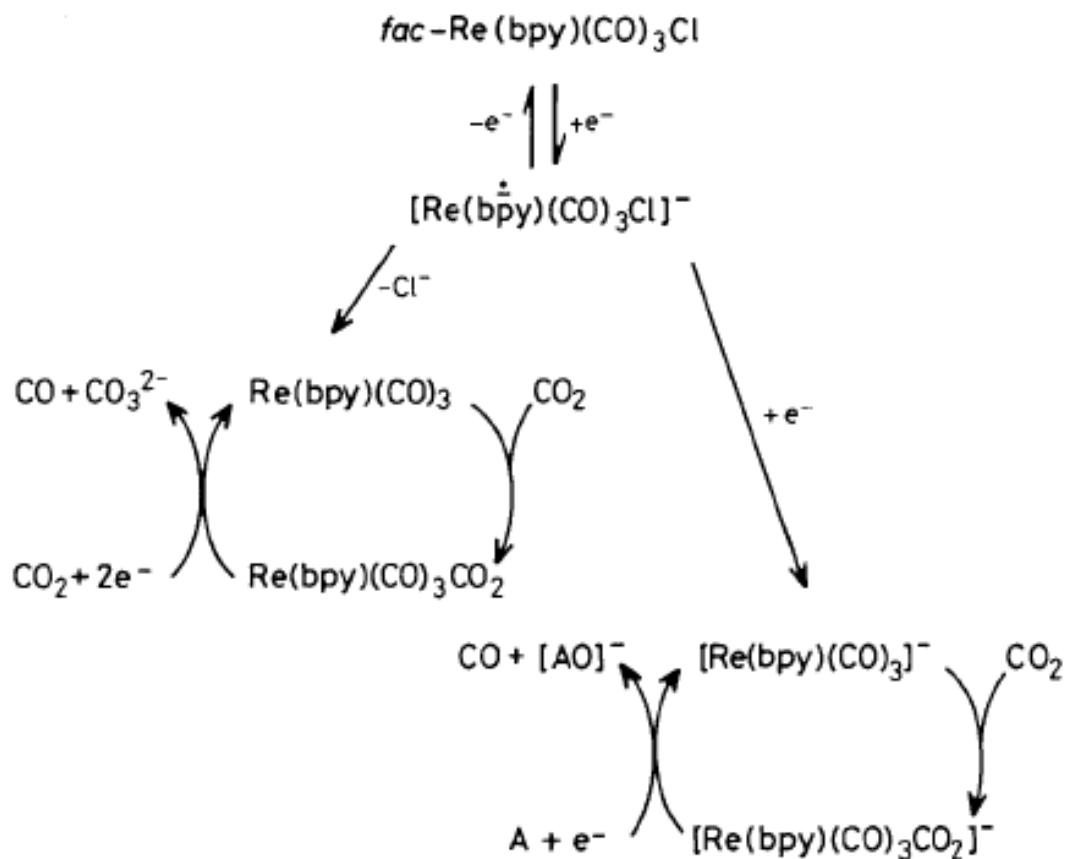
Figure 1.11 One-electron and two-electron mechanisms for CO_2 reduction by Re(bpy-R)(CO)$_3$Cl (**1-Re**), as proposed by Meyer and coworkers. Figure reproduced with permission from Ref. 89.

Other investigations into the reductive mechanism for **1-Re** have focused on UV-Vis and IR studies because of their highly diagnostic MLCT and CO absorbances.[40,87,90-97] In 1992, Christensen *et al.* directly probed the mechanism of reduction for **1-Re** with IR-SEC studies.[98] Consistent with many previous reports, they were able to observe the reduction of **1-Re** and subsequent appearance of anionic, singly-reduced $[Re(bpy-R)^{\cdot-}(CO)_3Cl]^-$ (**2-Re**, Figure 1.12). Complex **2-Re** exists in equilibrium with a Cl⁻-dissociated $[Re(bpy-R)(CO)_3]^0$ complex, **3-Re**, (Figure 1.12) accessed via a ligand-to-metal charge transfer (LMCT). With a stepwise increase in

potential this equilibrium shifts towards the dissociation of Cl⁻ to generate five-coordinate **3-Re**, which also exists in equilibrium with the Re(0)–Re(0) dimer **4-Re** (Figure 1.12).[90] This equilibrium is observed to varying degrees for other Re(bpy)-based complexes and is dependent on the functionalization (R group) of the bpy ligand. The reduction of **3-Re** yields the catalytically active, five-coordinate anionic complex, [Re(bpy-R)(CO)₃]⁻ (**6-Re**, Figure 1.12). Below, I will describe this reductive mechanism in more detail for Re(bpy-*t*Bu)(CO)₃Cl.
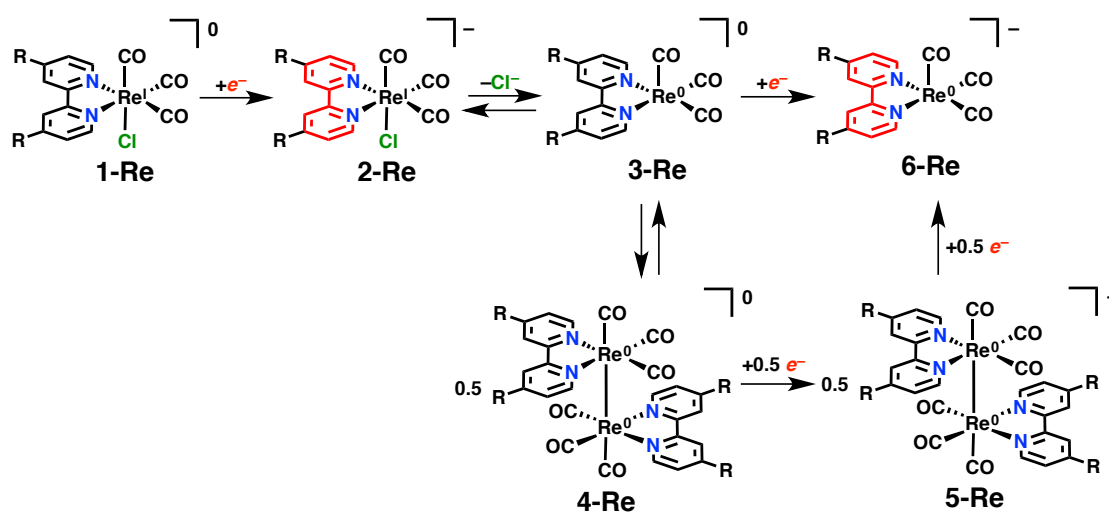
Figure 1.12 Schematic of the reductive mechanism of Re(bpy-R)(CO)₃Cl (**1-Re**), as evidenced by IR-SEC experiments.

Wong *et al.* further studied the electrocatalytic properties of this family of catalysts in the 1990s, and in 1998, they reported that the catalytic activity of [Re(bpy)(CO)₃(py)]⁺ (py = pyridine) was greatly increased in the presence of weak Brønsted acids, such as water (H_2O), methanol (MeOH), 2,2,2-trifluoroethanol (TFE), and phenol.[99] Notably, this catalyst retained 100% Faradaic efficiency for CO production in the presence of these weak acids, even with >1000 equiv of phenol

(surprising, given that the reduction of H^+ to H_2 is thermodynamically preferred). Wong's studies also reported that the reaction order in weak acid is two, consistent with the proton-coupled reduction of CO_2 to CO and H_2O.

These previous reports inspired our group to investigate how to both improve the activity of these Re(bpy)-based electrocatalysts and to better understand the mechanism of catalysis through IR-SEC. In 2010, our group determined that when *tert*-butyl (*t*Bu) groups were appended at the 4,4′-positions of the bpy ligand, a significant increase in catalytic activity could be observed.[73] This improved catalyst, Re(bpy-*t*Bu)(CO)$_3$Cl, was the basis for many mechanistic investigations. CVs of **1-Re** (*t*Bu version) under inert atmosphere revealed a quasi-reversible one-electron reduction at –1.8 V vs. $Fc^{+/0}$ and an irreversible one-electron reduction at –2.1 V vs. $Fc^{+/0}$ (Figure 1.13b), similar to many previous studies of **1-Re**. When the reaction mixture was sparged with CO_2, an increase in current, consistent with a catalytic process, was observed at the second reduction (Figure 1.14a).[73,100] Consistent with previous studies by Wong and co-workers, for **1-Re** with weakly a coordinating py or MeCN ligand instead of Cl^-, peak catalytic currents were increased with the addition of weak Brønsted acids (Figure 1.14b).
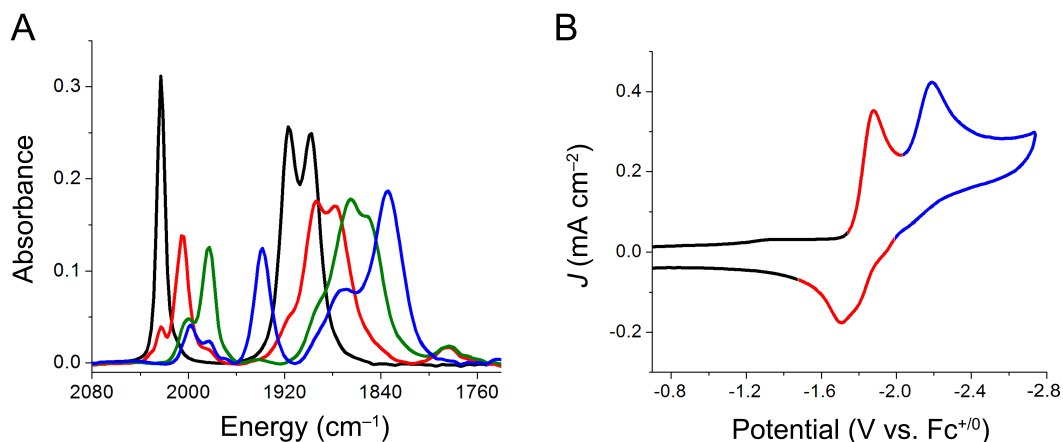
Figure 1.13 (a) IR-SEC experiment of Re(bpy-*t*Bu)(CO)$_3$Cl (**1-Re**, black) under N$_2$ in 0.1 M TBAPF$_6$/MeCN, showing three major species as the potential is increased cathodically: [Re(bpy-*t*Bu)$^{\bullet-}$(CO)$_3$Cl]$^-$ (**2-Re**, red), [Re(bpy-*t*Bu)(CO)$_3$]^0 (**3-Re**, green), and [Re(bpy-*t*Bu)$^{\bullet-}$(CO)$_3$]$^-$ (**6-Re**, blue). (b) CV of Re(bpy-*t*Bu)(CO)$_3$Cl (**1-Re**), under N$_2$ in 0.1 M TBAPF$_6$/MeCN, showing correlation to species seen in IR-SEC. Figures are adapted with permission from Ref. 101 and 79.
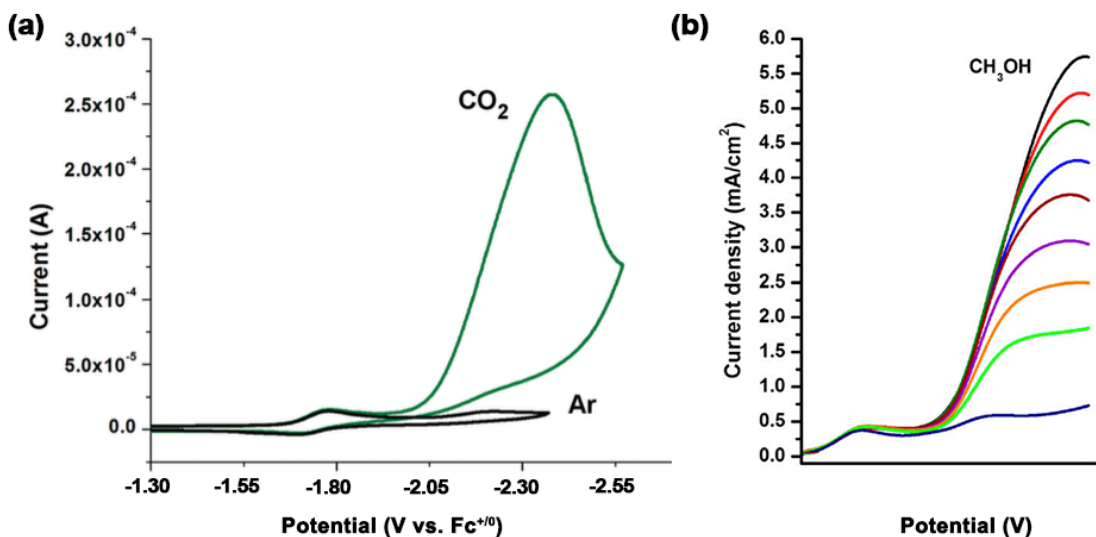
Figure 1.14 (a) CVs of Re(bpy-*t*Bu)(CO)$_3$Cl (**1-Re**) under N$_2$ (black) and under CO$_2$ (green) in 0.1 M TBAPF$_6$/MeCN, showing an increase in current at the second reduction consist with CO$_2$ reduction. (b) Linear voltammograms of Re(bpy-*t*Bu)(CO)$_3$(py)]$^+$ (**1-Re**) under CO$_2$ with increasing amount of methanol (CH$_3$OH) added. Figures are adapted with permission from Ref. 102 and 103.

In the IR-SEC of Re(bpy-*t*Bu)(CO)$_3$Cl under N$_2$, at resting potential (vs. Ag pseudo-reference), complex **1-Re** is the only species observed in solution (Figure

1.13a). IR bands corresponding to the ν_{CO} modes expected for Re *fac*-tricarbonyl systems are observed at 2023, 1916, and 1898 cm^{-1} (consistent with A′ and split E modes, respectively).[73] When the cell potential is increased stepwise to that of the first reduction, these parent stretching modes (**1-Re**) begin to disappear with the concomitant appearance of three new ν_{CO} stretches with a similar intensity pattern, but at lower frequencies (~15-20 cm^{-1}). These new ν_{CO} stretches are consistent with a bpy-based reduction of the parent complex, forming **2-Re**.[98,104] As the cell potential is increased slowly between the first and second reductions, a second shift in these three ν_{CO} stretches (~15-20 cm^{-1}) is observed. This second shift is attributed to the loss of the Cl$^-$ ligand to form a five coordinate Re(0) complex **3-Re** through a LMCT.[73] In previous studies with the bpy and bpy-CH$_3$ versions of **1-Re**, if the electrochemically reduced species **3-Re** were held at potential during these IR-SEC experiments long enough, they formed Re(0)–Re(0) dimers (**4-Re**).[90,93] However, this competing dimerization reaction was not observed in IR-SEC experiments with the bpy-*t*Bu version of **1-Re**. The absence of **4-Re** was confirmed by its direct preparation from Re$_2$(CO)$_{10}$ and 2 equiv of bpy-*t*Bu.[105] Characterization by IR revealed diagnostic ν_{CO} frequencies which were not observed over the course of these IR-SEC experiments.[73,90,92-93] Further experiments on these dimerization products indicated that this competing reaction pathway feeds back into the catalytic cycle (see Figure 1.12).[105] Species of type **4-Re** were isolated and shown to be capable of being reduced by a single electron to form **5-Re**, which could generate the active catalyst **6-Re** upon the addition of a second electron.[104,106]

The dominant pathway for the formation of species **6-Re**, however, is the direct reduction of species **3-Re**. Specifically, in the previously mentioned IR-SEC experiments, when the solution containing **3-Re** was taken to the potential of the second reduction, the ν_{CO} stretches shifted again to lower frequencies (~40 cm^{-1}), indicating the presence of doubly reduced [Re(bpy-tBu)$^{\bullet-}$(CO)$_3$]$^-$ (**6-Re**) with ν_{CO} stretches observed at 1938 and 1834 cm^{-1} (broad). The structural assignment of this compound was confirmed with crystallographic data obtained from complexes isolated by chemical reduction.[104,106-107] Complex **6-Re** is catalytically active for the reduction of CO_2 to CO and H_2O, which was confirmed by bulk electrolysis under CO_2 atmosphere.[73]

Our group has reported the isolation of the active Re(bpy) catalyst, **6-Re**, by chemical means through reduction of **1-Re** by potassium-intercalated graphite (KC$_8$).[6] Our group has isolated the tBu version of the active catalyst, [Re(bpy-tBu)$^{\bullet-}$(CO)$_3$]$^-$, (see Figure 1.15) as well as a variety of other anions with different functionalization at the bpy ligand.[6,104] These anions are stable in an inert atmosphere glovebox, and structural characterizations by X-ray diffraction (XRD) of many of these species have been reported. The XRD structure of **6-Re** shows significant shortening of the C$_{py}$–C$_{py}$ bond distance (as well as bond length alternation in the bpy ring system) as compared to the parent complex **1-Re**, consistent with electron density on the non-innocent bpy ligand. Additionally, shortening of the Re–N bond distances and an increase of the bpy ligand bite angle provides evidence for improved orbital overlap between the bpy ligand and the Re center.
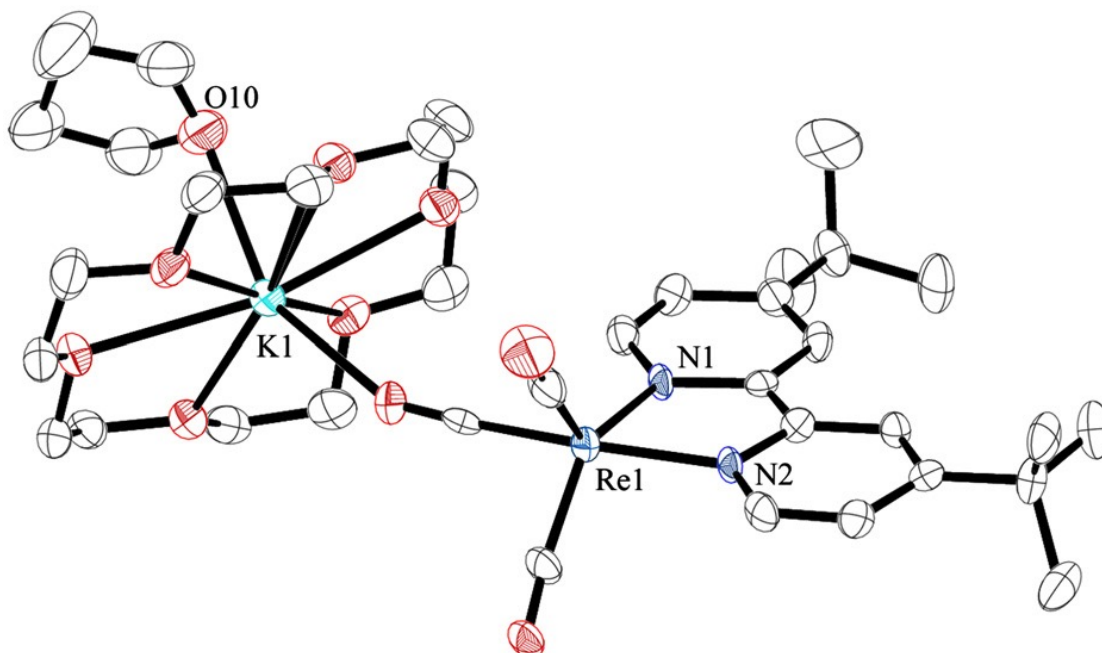
Figure 1.15 X-ray Diffraction (XRD) structure of [Re(bpy-tBu)$^{\bullet-}$(CO)$_3$]$^-$ (**6-Re**), with hydrogen atoms omitted for clarity and ellipsoids shown at 50% probability. Figure taken with permission from Ref. 6.

Chemical isolation of **6-Re** has allowed our group to begin investigating the mechanism of CO_2 reduction by this family of catalysts through stoichiometric means paired with spectroscopy. In 2012, our group studied the direct reaction of [Re(bpy-tBu)$^{\bullet-}$(CO)$_3$]$^-$ (**6-Re**) with CO_2 and weak acids using stopped-flow mixing in tandem with UV-Vis spectroscopy.[6] These studies concluded that anion **6-Re** reacts ~35 times faster with CO_2 than with H_2O, MeOH, or TFE, consistent with the observed high selectivity for electrochemical CO_2 reduction in the presence of high concentrations of weak acids. This study hypothesized that the source for high selectivity was in the inherent preference for the [Re(bpy-R)$^{\bullet-}$(CO)$_3$]$^-$ (**6-Re**) anion to react faster with CO_2 than with H^+.

Since Re is one of the least abundant metals in the Earth's crust,[108] it was important to extend CO_2 reduction studies by Re(bpy)-based complexes to complexes based on Re's earth-abundant first row transition counterpart, Mn.[74] When considering a system for eventual scale-up and industrial use, Mn is much more appealing than Re due to both cost and environmental considerations. Mn(bpy)-based complexes have been known since 1959;[109] however, Johnson *et al.* originally reported that the doubly reduced complex, $[Mn(bpy-R)(CO)_3]^-$ (**4-Mn**), showed no reactivity towards CO_2, and therefore, these complexes were not pursued as catalysts for CO_2 reduction.[110] However, in 2011, Bourrez *et al.* reported that $Mn(bpy)(CO)_3Br$ and $Mn(bpy-CH_3)(CO)_3Br$ complexes (**1-Mn**) were active for the reduction of CO_2 to CO when H_2O was added to the electrochemical cell as a H^+ source.[111] These catalysts showed no activity for CO_2 reduction without added H_2O.[112] Our group expanded on these initial studies and showed that these Mn(bpy)-based catalysts, specifically Mn(bpy-*t*Bu)(CO)$_3$Br, are viable alternatives to the aforementioned Re system in the presence of weak Brønsted acids (i.e. H_2O, MeOH, and TFE).[74] One major advantage of these Mn catalysts in comparison to analogous Re catalysts is that the Mn catalysts operate at considerably lower overpotentials (see Figure 1.16b) without sacrificing significant catalytic activity. Similar to the Re(bpy)-based systems, Mn(bpy)-based complexes maintain 100% Faradaic efficiency for the formation of CO in the presence of high concentrations of these weak Brønsted acids (>6000 equiv), while showing excellent activity (peak TOF for bpy-*t*Bu version = 340 s^{-1} with added TFE).
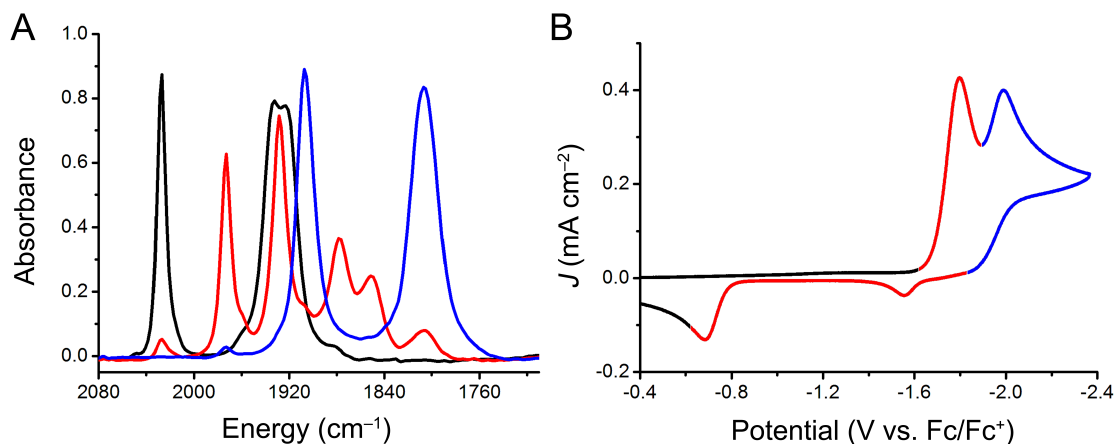
Figure 1.16 (a) IR-SEC experiment of Mn(bpy-*t*Bu)(CO)$_3$Br (**1-Mn**, black) under N$_2$ in 0.1 M TBAPF$_6$/MeCN, showing two major species as the potential is increased cathodically: [Mn(bpy-*t*Bu)(CO)$_3$]$_2$ (**3-Mn**, red) and [Mn(bpy-*t*Bu$^{\bullet-}$)(CO)$_3$]$^-$ (**4-Mn**, blue). (b) CV of Mn(bpy-*t*Bu)(CO)$_3$Br (**1-Mn**), under N$_2$ in 0.1 M TBAPF$_6$/MeCN, showing correlation to species seen in IR-SEC. Figures are adapted with permission from Ref. 113 and 79.

Similar to the mechanistic investigations of the Re(bpy) precatalysts, our group used IR-SEC to observe the sequence of complexes leading up to the catalytically active species for the Mn(bpy)-based system (Figure 1.17). Prior to the discovery that these catalysts are active for the reduction of CO$_2$ to CO, Hartl *et al.* utilized IR-SEC to investigate the reductive behavior of Mn(bpy)(CO)$_3$Cl.[114] The results of a typical IR-SEC experiment from our lab for Mn(bpy)-based complexes under N$_2$ are shown in Figure 1.16a. The spectra in Figure 1.16a were obtained with Mn(bpy-*t*Bu)(CO)$_3$Br (**1-Mn**) as the molecular complex.
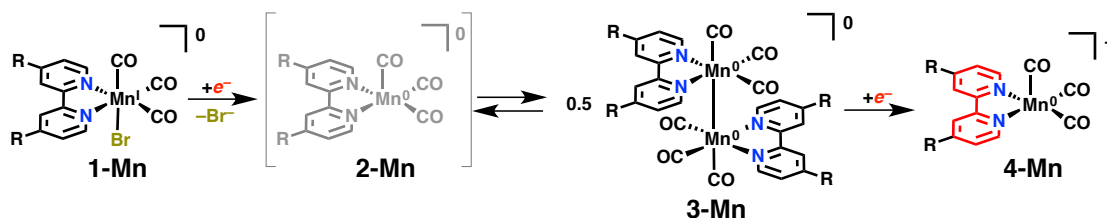
Figure 1.17 Schematic of the reductive mechanism of Mn(bpy-R)(CO)$_3$Br (**1-Mn**), as evidenced by IR-SEC experiments.

At resting potential, **1-Mn** is the only species in solution and a typical ν_{CO} pattern for *fac*-tricarbonyl systems with stretches at 2028, 1933, and 1923 cm^{-1} (A′ and split E modes, respectively) is observed. These ν_{CO} stretches remain constant until the potential of the cell reaches that corresponding to the first reduction of **1-Mn** (see Figure 1.16b). Upon reaching this potential, ν_{CO} stretches matching complex **1-Mn** begin to decay with the concurrent growth of new ν_{CO} stretches at 1973, 1928, 1878, and 1850 cm^{-1} (Figure 1.16a). These new ν_{CO} stretches are consistent with formation of the Mn(0)–Mn(0) dimer **3-Mn**. This species was identified by comparison with previously reported Re(0)–Re(0) dimers[73,87,98,106,115-117] in addition to previous photochemical[118] and IR-SEC identification of Mn(0)(bpy)-based dimers.[114,119] We have also reported the structural characterization of [Mn(bpy)(CO)$_3$]$_2$ with single crystal X-ray crystallography, as further evidence of the formation of **3-Mn** in these IR-SEC experiments.[79] Over the course of the IR-SEC experiments no prior intermediates are observed (one of which would presumably be similar in structure to **2-Mn**) before the formation of the dimer **3-Mn**, indicating that loss of Br$^-$, followed by dimerization, occurs rapidly on this timescale upon the initial reduction of the complex. This result is expected for a first-row transition metal complex (Mn) where the d$_z{}^2$ orbital is lower in energy than the π* orbital of the bpy ligand, causing the first reduction to be metal-based rather than bpy-based, as in the case of Re. Upon reaching the potential of the second reduction in IR-SEC, the ν_{CO} stretches assigned to **3-Mn** disappear with the concomitant growth of two new ν_{CO} stretches at 1907 and 1807 cm^{-1}.[74] These ν_{CO} stretches are consistent with formation of anionic [Mn(bpy-*t*Bu$^{\bullet-}$

)(CO)$_3$]$^-$ (**4-Mn**), which serves as the active catalyst for CO$_2$ reduction. Our group has also structurally characterized this active catalyst using XRD as [Mn(bpy-tBu)$^{\bullet-}$(CO)$_3$][K(18-crown-6)].[74] The IR and XRD characteristics of this Mn(bpy) anion are very similar to those of corresponding [Re(bpy-R$^{\bullet-}$)(CO)$_3$]$^-$ anions.[73,98,104,115-116]

As noted previously, the trends observed in these IR-SEC experiments correlate well to the CVs of these Mn(bpy) complexes. In CVs of **1-Mn**, we see two irreversible one-electron reductions (−1.77 V and −1.95 V vs. Fc$^{+/0}$) and a large oxidation wave (−0.68 V vs. Fc$^{+/0}$) when scanning anodically after the first reduction (Figure 1.16b).[74] These reductions lead to dimer **3-Mn** and anion **4-Mn**, respectively. Additionally, the large oxidation wave is attributed to the oxidative cleavage of dimer **3-Mn**. This is consistent with the reductive sequence of species leading up to the active state **4-Mn** as observed in IR-SEC experiments (Figure 1.7). As previously stated, electrochemical reaction mixtures of **1-Mn** sparged with CO$_2$ display no increase in current in CVs. A current increase at the second reduction, corresponding to the formation of **4-Mn**, is observed when significant concentrations of weak Brønsted acids are added to electrochemical solutions (i.e. H$_2$O, MeOH, TFE, or phenol; see Figure 2.18 for Mn(bpy)(CO)$_3$Br). The peak currents achieved in CVs are directly proportional to the amount of weak acid added (Figure 2.18).
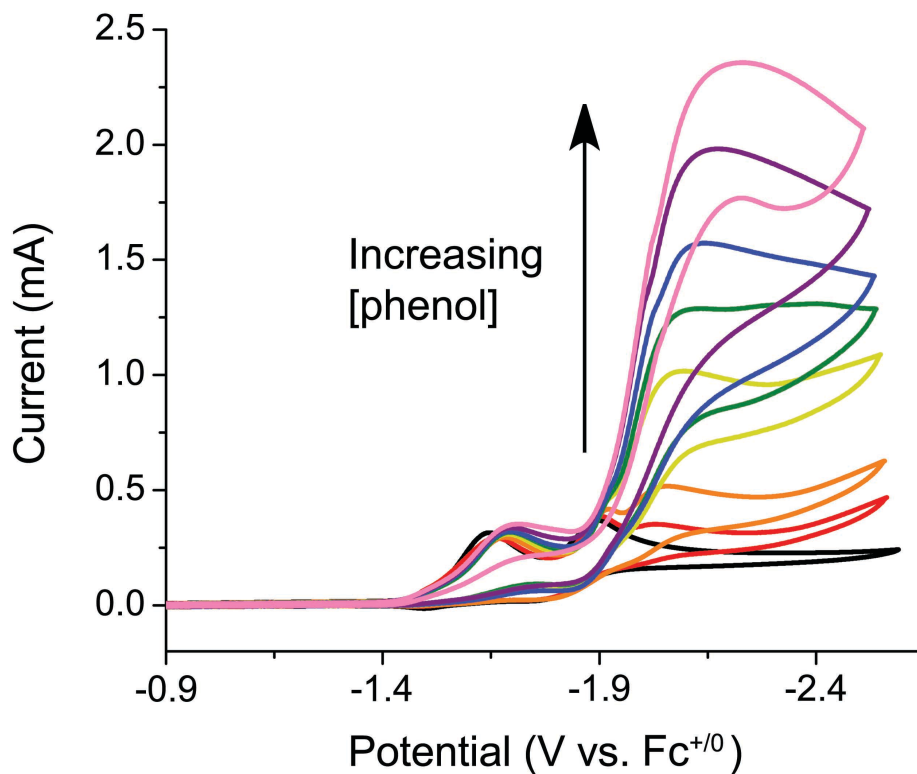
Figure 1.18 CVs of Mn(bpy)(CO)$_3$Br (**1-Mn**) under CO$_2$ with increasing amounts of phenol added as a H$^+$ source. Electrolyte solution is 0.1 M TBAPF$_6$/MeCN. No catalysis is observed in CO$_2$ without an added H$^+$ source. Figure adapted with permission from Ref. 120.

1.7 Conclusions and Future Directions

A dramatic increase in global fuel consumption coupled with unsustainable emissions of CO$_2$ has led to one of the biggest challenges of our modern era – the development of renewable, CO$_2$-neutral fuels. Solar and wind power are promising options for renewable energy; however, the energy sources for these technologies suffer from intermittent availability. Therefore, research in energy storage, particularly storage in chemical bonds, is essential to the sustainability of these technologies. To counteract the intrinsic availability problem of solar and wind energy, the electricity

generated from these sources can be stored in chemical bonds, such as liquid fuels generated from CO_2 reduction. These renewable fuels can be utilized on demand to drive an engine or produce electricity in a fuel cell. By harnessing solar energy, these systems will provide a route to carbon-neutral energy, helping to counteract our unsustainable CO_2 emissions and providing an energy source capable of incorporation into existing infrastructure.

Returning CO_2 to a useful state by activation and reduction is an energetically and kinetically challenging processes. Slow kinetics for CO_2 reduction reactions demands for the use of efficient catalysts in order to decrease the overpotentials needed to drive the reactions. Extensive research effort has been invested in developing molecular catalysts for electrochemical and/or photochemical reduction of CO_2. Of the molecular catalysts that electrochemically reduce CO_2, the Re(bpy-R)(CO)$_3$Cl and Mn(bpy-R)(CO)$_3$Br systems are among the most active and selective catalysts for proton-coupled CO_2 reduction to CO and H_2O.

Since the discovery by Lehn and co-workers that Re(bpy-R)(CO)$_3$Cl is an electrocatalyst for the reduction of CO_2 to CO, this family of catalysts has been the subject of a vast amount of research. Recent studies by our group have shown that the catalyst can be significantly improved through appending *t*Bu groups on the bpy ligand. Our group has also extensively studied the nature of the active state of this catalyst by X-ray crystallography and spectroscopy. Although many *in situ* IR and UV-Vis spectroscopy studies have been reported to elucidate this family of catalyst's reductive chemistry leading up to the active state, little direct evidence has been

provided for the catalytic mechanism. Is it possible to use other spectroscopic methods to directly observe steps in the catalytic mechanism? Stopped-flow UV-Vis spectroscopy studies have revealed that the active state of the Re(bpy) catalyst shows high selectivity for engaging CO_2 over weak acid. What is the origin for this observed high selectivity? Although this catalyst family has been extensively studied since the 1980s, clearly, there is still room for exploration and important discovery.

The recent finding by Deronzier and co-workers that Mn can be substituted for Re and function as a competent molecular electrocatalyst for CO_2 reduction has opened up many new opportunities to study and develop this earth-abundant system. This Mn(bpy) system is attractive, not only due to its earth-abundance, but also for its ability to operate at significantly lower overpotentials than its Re counterpart. Similarly to our studies with Re, our group was able to significantly enhance rates of electrocatalysis by this family of catalysts by placing *t*Bu groups on the backbone of the bpy ligand. How can this Mn(bpy) catalytic system be further improved? Can we use synthetic modification of the bpy ligand to further enhance catalytic activities and lower overpotentials? Can we directly probe the catalytic mechanism for Mn(bpy-R)(CO)$_3$Br and unravel key differences between the Mn and Re systems? In the past several years, our group has focused a great deal of effort attempting to probe these questions.

A deployable device for CO_2 reduction will likely need to use a heterogeneous catalyst, and therefore, methods for attaching these catalysts to a solid electrode need to be explored. It should be noted that the Re(bpy) catalyst has been attached to

surfaces by polymerization; however, this leads to amorphous films in which the orientation and environment around the metal center is not controlled.[121-122] Work towards understanding how Re(bpy)-type species behave when attached to a surface in a controlled fashion is beginning to appear in the literature. For example, Lian, Batista, and co-workers have appended Re(bpy) catalysts to TiO_2, [123-124] and similar catalysts have also been attached to tin-doped indium oxide (ITO) through alkoxy groups[125] and been chemisorbed on gold.[126] Ideally, the surface environment for these heterogeneous catalysts should be controlled and designed to enhance catalysis. Positioning functional groups (such as proton relays, hydrogen bonding groups, or electrostatic effects) on a surface to interact favorably with the molecular catalyst may be troublesome on a flat electrode surface, but, for example, may be possible in a highly-functional and robust metal-organic framework (MOF). Continued work in these areas will be critical to the development of a device for reducing CO_2 to valuable products. Finally, when considering the development of a homogeneous or heterogeneous device for CO_2 reduction using solar energy, care will need to be taken to match the incoming power and the limiting current densities of the catalyst.[127] Research into all of the areas described in this section is underway in our laboratory as well as others.

Steven A. Chabolla, Tram Dang, and Clifford P. Kubiak, which has been published in

Organometallics, **2014**, 33, 4550–4559. http://dx.doi.org/10.1021/om500044a. The

dissertation author is a co-author of this manuscript. The rest of the material in this

chapter is unpublished work.

1.8 References

(1) Cook, T. R.; Dogutan, D. K.; Reece, S. Y.; Surendranath, Y.; Teets, T. S.; Nocera, D. G. *Chem. Rev.* **2010**, 110, 6474-6502.

(2) Concepcion, J. J.; House, R. L.; Papanikolas, J. M.; Meyer, T. J. *Proc. Natl. Acad. Sci. U. S. A.* **2012**, 109, 15560-15564.

(3) Wright, R. T.; Boorse, D., F. *Environmental Science: Toward a Sustainable Future*; 11th ed.; Benjamin Cummings, **2010**.

(4) IPCC In *Climate Change 2014: Impacts, Adaptation, and Vulnerability. Part A: Global and Sectoral Aspects. Contribution of Working Group II to the Fifth Assessment Report of the Intergovernmental Panel on Climate Change*; Field, C. B., Barros, V. R., Dokken, D. J., Mach, K. J., Mastrandrea, M. D., Bilir, T. E., Chatterjee, M., Ebi, K. L., Estrada, Y. O., Genova, R. C., Girma, B., Kissel, E. S., Levy, A. N., MacCracken, S., Mastrandrea, P. R., White, L. L., Eds.; Cambridge University Press: Cambridge, United Kingdom, and New York, NY, USA, **2014**, p 1-32.

(5) "A Glimpse at Our Possible Future Climate, Best to Worst Case Scenarios," *Skeptical Science,* **2013,** skepticalscience.com.

(6) Smieja, J. M.; Benson, E. E.; Kumar, B.; Grice, K. A.; Seu, C. S.; Miller, A. J. M.; Mayer, J. M.; Kubiak, C. P. *Proc. Natl. Acad. Sci. U. S. A.* **2012**, 109, 15646–15650.

(7) Kumar, B.; Llorente, M.; Froehlich, J.; Dang, T.; Sathrum, A.; Kubiak, C. P. *Annu. Rev. Phys. Chem.* **2012**, 63, 541-569.

(8) Kumar, B.; Smieja, J. M.; Kubiak, C. P. *J. Phys. Chem. C* **2010**, 114, 14220-14223.

(9) Kumar, B.; Smieja, J. M.; Sasayama, A. F.; Kubiak, C. P. *Chem. Commun.* **2012**, 48, 272-274.

(10) Dorner, R. W.; Hardy, D. R.; Williams, F. W.; Willauer, H. D. *Energ. Environ. Sci.* **2010**, 3, 884-890.

(11) Costentin, C.; Robert, M.; Saveant, J.-M. *Chem. Soc. Rev.* **2013**, 42, 2423-2436.

(12) Whipple, D. T.; Kenis, P. J. A. *J. Phys. Chem. Lett.* **2010**, 1, 3451-3458.

(13) Mikkelsen, M.; Jorgensen, M.; Krebs, F. C. *Energ. Environ. Sci.* **2010**, 3, 43-81.

(14) Wang, W.; Wang, S.; Ma, X.; Gong, J. *Chem. Soc. Rev.* **2011**, 40, 3703-3727.

(15) Appel, A. M.; Bercaw, J. E.; Bocarsly, A. B.; Dobbek, H.; DuBois, D. L.; Dupuis, M.; Ferry, J. G.; Fujita, E.; Hille, R.; Kenis, P. J. A.; Kerfeld, C. A.; Morris, R. H.; Peden, C. H. F.; Portis, A. R.; Ragsdale, S. W.; Rauchfuss, T. B.; Reek, J. N. H.; Seefeldt, L. C.; Thauer, R. K.; Waldrop, G. L. *Chem. Rev.* **2013**, 113, 6621-6658.

(16) Federsel, C.; Jackstell, R.; Beller, M. *Angew. Chem., Int. Ed.* **2010**, 49, 6254-6257.

(17) Morris, A. J.; Meyer, G. J.; Fujita, E. *Acc. Chem. Res.* **2009**, 42, 1983-1994.

(18) Sutin, N.; Creutz, C.; Fujita, E. *Comments Inorg. Chem.* **1997**, 19, 67-92.

(19) Benson, E. E.; Kubiak, C. P.; Sathrum, A. J.; Smieja, J. M. *Chem. Soc. Rev.* **2009**, 38, 89-99.

(20) Halmann, M. M.; Steinberg, M. *Greenhouse Gas Carbon Dioxide Mitigation Science and Technology*; Lewis Publishers, **1999**.

(21) Huff, C. A.; Sanford, M. S. *J. Am. Chem. Soc.* **2011**, 133, 18122-18125.

(22) Smith R J, B.; Loganathan, M.; Shekhar Shantha, M. *Int. J. Chem. React. Eng.* **2010**, 8, 1542-6580.

(23) "Sasol," *Sasol,* **2015,** sasol.com.

(24) Krauss, C. "South African Company to Build U.S. Plant to Convert Gas to Liquid Fuels," *The New York Times,* **December 4, 2012,** B8.

(25) "PetroSA – South Africa's National Oil Company," *Sasol,* petrosa.co.za.

(26) Davis, J. "Sasol set to open Qatar taps," *Upstream – The International Oil & Gas Newspaper,* **10/30/2007**.

(27) Schulz, H. *Appl. Catal. A.* **1999**, 186, 3-12.

(28) Geerlings, J. J. C.; Wilson, J. H.; Kramer, G. J.; Kuipers, H. P. C. E.; Hoek, A.; Huisman, H. M. *Appl. Catal. A.* **1999**, 186, 27-40.

(29) Dry, M. E. *J. Chem. Technol. Biotechnol.* **2002**, 77, 43-50.

(30) Dry, M. E. *Catal. Today* **2002**, 71, 227-241.

(31) Leckel, D. *Energy Fuels* **2009**, 23, 2342-2358.

(32) van Vliet, O. P. R.; Faaij, A. P. C.; Turkenburg, W. C. *Energy Conversion and Management* **2009**, 50, 855-876.

(33) Spath, P. L.; Dayton, D. C. *Preliminary Screening – Technical and Economic Assessment of Synthesis Gas to Fuels and Chemicals with Emphasis on the Potential for Biomass-Derived Syngas*, NREL/TP-510-34929, National Renewable Energy Laboratory: Golden, CO, **2003**.

(34) Gibson, D. H. *Coord. Chem. Rev.* **1999**, 185–186, 335-355.

(35) Gibson, D. H. *Chem. Rev.* **1996**, 96, 2063-2096.

(36) Castro-Rodriguez, I.; Meyer, K. *J. Am. Chem. Soc.* **2005**, 127, 11242-11243.

(37) Castro-Rodriguez, I.; Nakai, H.; Zakharov, L. N.; Rheingold, A. L.; Meyer, K. *Science* **2004**, 305, 1757-1759.

(38) Aresta, M.; Nobile, C. F.; Albano, V. G.; Forni, E.; Manassero, M. *J. Chem. Soc., Chem. Commun.* **1975**, 636-637.

(39) Palmer, D. A.; Van Eldik, R. *Chem. Rev.* **1983**, 83, 651-731.

(40) Grice, K. A.; Kubiak, C. P. In *Adv. Inorg. Chem.*; Michele, A., Rudi van, E., Eds.; Academic Press: **2014**; Vol. Volume 66, p 163-188.

(41) Kolomnikov, I. S.; Lysyak, T. V. *Russ. Chem. Rev.* **1990**, 59, 344.

(42) Gibson, D. H.; Ye, M.; Sleadd, B. A.; Mehta, J. M.; Mbadike, O. P.; Richardson, J. F.; Mashuta, M. S. *Organometallics* **1995**, 14, 1242-1255.

(43) Gibson, D. H.; Richardson, J. F.; Ong, T. S. *Acta Crystallogr., Sect. C: Cryst. Struct. Commun.* **1991**, 47, 259-261.

(44) Hirano, M.; Akita, M.; Tani, K.; Kumagai, K.; Kasuga, N. C.; Fukuoka, A.; Komiya, S. *Organometallics* **1997**, 16, 4206-4213.

(45) Senn, D. R.; Emerson, K.; Larsen, R. D.; Gladysz, J. A. *Inorg. Chem.* **1987**, 26, 2737-2739.

(46) Gibson, D.; Sleadd, B.; Vij, A. *J. Chem. Crystallogr.* **1999**, 29, 619-622.

(47) Field, C. B.; Behrenfeld, M. J.; Randerson, J. T.; Falkowski, P. *Science* **1998**, 281, 237-240.

(48) Jajesniak, P.; Ali, H. E. M. O.; Wong, T. S. *J. Bioprocess. Biotech.* **2014**, 4, 1–15.

(49) Minagawa, J. *Frontiers in Plant Science* **2013**, 4.

(50) Berardi, S.; Drouet, S.; Francas, L.; Gimbert-Surinach, C.; Guttentag, M.; Richmond, C.; Stoll, T.; Llobet, A. *Chem. Soc. Rev.* **2014**, 43, 7501-7519.

(51) Jeoung, J.-H.; Fesseler, J.; Goetzl, S.; Dobbek, H. In *The Metal-Driven Biogeochemistry of Gaseous Compounds in the Environment*; Kroneck, P. M. H., Torres, M. E. S., Eds.; Springer Netherlands: **2014**; Vol. 14, p 37-69.

(52) Jeoung, J.-H.; Dobbek, H. *Science* **2007**, 318, 1461-1464.

(53) Romao, M. J. *Dalton Trans.* **2009**, 4053-4068.

(54) Averill, B. A.; Herskovitz, T.; Holm, R. H.; Ibers, J. A. *J. Am. Chem. Soc.* **1973**, 95, 3523-3534.

(55) Tezuka, M.; Yajima, T.; Tsuchiya, A.; Matsumoto, Y.; Uchida, Y.; Hidai, M. *J. Am. Chem. Soc.* **1982**, 104, 6834-6836.

(56) Takuma, M.; Ohki, Y.; Tatsumi, K. *Inorg. Chem.* **2005**, 44, 6034-6043.

(57) Gourlay, C.; Nielsen, D. J.; White, J. M.; Knottenbelt, S. Z.; Kirk, M. L.; Young, C. G. *J. Am. Chem. Soc.* **2006**, 128, 2164-2165.

(58) Enemark, J. H.; Cooney, J. J. A.; Wang, J.-J.; Holm, R. H. *Chem. Rev.* **2004**, 104, 1175-1200.

(59) Costentin, C.; Drouet, S.; Robert, M.; Saveant, J. M. *J. Am. Chem. Soc.* **2012**, 134, 11235-11242.

(60) Kaim, W.; Fiedler, J. *Chem. Soc. Rev.* **2009**, 38, 3373–3382.

(61) *Spectroelectrochemistry*; Royal Society of Chemistry: Cambridge, England, **2008**.

(62) Geskes, C.; Heinze, J. *J. Electroanal. Chem.* **1996**, 418, 167–173.

(63) Zhang, X.; Zwanziger, J. W. *J. Magn. Reson.* **2011**, 208, 136–147.

(64) Dias, M.; Hudhomme, P.; Levillain, E.; Perrin, L.; Sahin, Y.; Sauvage, F.-X.; Wartelle, C. *Electrochem. Commun.* **2004**, 6, 325–330.

(65) Murray, P. R.; Collison, D.; Daff, S.; Austin, N.; Edge, R.; Flynn, B. W.; Jack, L.; Leroux, F.; McInnes, E. J. L.; Murray, A. F.; Sells, D.; Stevenson, T.; Wolowska, J.; Yellowlees, L. J. *J. Magn. Reson.* **2011**, 213, 206–209.

(66) Webster, R. D.; Bond, A. M.; Coles, B. A.; Compton, R. G. *J. Electroanal. Chem.* **1996**, 404, 303–308.

(67) Ashley, K.; Pons, S. *Chem. Rev.* **1988**, 88, 673–695.

(68) Holze, R. *J. Solid State Electreochem.* **2004**, 8, 982–997.

(69) Benson, E. E.; Kubiak, C. P.; Sathrum, A. J.; Smieja, J. M. *Chem. Soc. Rev.* **2009**, 38, 89–99.

(70) Kubiak, C. P. *Inorg. Chem.* **2013**, 52, 5663–5676.

(71) Ito, T.; Hamaguchi, T.; Nagino, H.; Yamaguchi, T.; Washington, J.; Kubiak, C. P. *Science* **1997**, 277, 660-663.

(72) Glover, S. D.; Goeltz, J. C.; Lear, B. J.; Kubiak, C. P. *Coord. Chem. Rev.* **2010**, 254, 331–345.

(73) Smieja, J. M.; Kubiak, C. P. *Inorg. Chem.* **2010**, 49, 9283–9289.

(74) Smieja, J. M.; Sampson, M. D.; Grice, K. A.; Benson, E. E.; Froehlich, J. D.; Kubiak, C. P. *Inorg. Chem.* **2013**, 52, 2484–2491.

(75) Smieja, J. M.; Benson, E. E.; Kumar, B.; Grice, K. A.; Seu, C. S.; Miller, A. J. M.; Mayer, J. M.; Kubiak, C. P. *PNAS USA* **2012**, 109, 15646–15650.

(76) Ito, T.; Ota, K.; Matsui, T.; Yamaguchi, T.; Zavarine, I. S.; Kubiak, C. P. *Inorg. Chem.* **2000**, 39, 2696–2698.

(77) Londergan, C. H.; Salsman, J. C.; Ronco, S.; Kubiak, C. P. *Inorg. Chem.* **2003**, 42, 926–928.

(78) Wittrig, R. E.; Ferrence, G. M.; Washington, J.; Kubiak, C. P. *Inorg. Chim. Acta* **1998**, 270, 111–117.

(79) Machan, C. W.; Sampson, M. D.; Chabolla, S. A.; Dang, T.; Kubiak, C. P. *Organometallics* **2014**, 33, 4550-4559.

(80) Hieber, W.; Fuchs, H. *Z. Anorg. Allg. Chem.* **1941**, 248, 269-275.

(81) Fisher, E. O. *Chem. Ber.* **1979**, 112, XXI-XXXIX.

(82) Hawecker, J.; Lehn, J.-M.; Ziessel, R. *J. Chem. Soc., Chem. Comm.* **1984**, 328–330.

(83) Hawecker, J.; Lehn, J. M.; Ziessel, R. *J. Chem. Soc., Chem. Commun.* **1983**, 536-538.

(84) Agarwal, J.; Fujita, E.; Schaefer, H. F.; Muckerman, J. T. *J. Am. Chem. Soc.* **2012**, 134, 5180-5186.

(85) Fujita, E.; Hayashi, Y.; Kita, S.; Brunschwig, B. S. In *Stud. Surf. Sci. Catal.*; Sang-Eon Park, J.-S. C., Kyu-Wan, L., Eds.; Elsevier: **2004**; Vol. Volume 153, p 271-276.

(86) Fujita, E.; Muckerman, J. T. *Inorg. Chem.* **2004**, 43, 7636-7647.

(87) Hayashi, Y.; Kita, S.; Brunschwig, B. S.; Fujita, E. *J. Am. Chem. Soc.* **2003**, 125, 11976-11987.

(88) Shinozaki, K.; Hayashi, Y.; Brunschwig, B.; Fujita, E. *Res. Chem. Intermediat.* **2007**, 33, 27-36.

(89) Sullivan, B. P.; Bolinger, C. M.; Conrad, D.; Vining, W. J.; Meyer, T. J. *J. Chem. Soc., Chem. Commun.* **1985**, 1414-1416.

(90) Breikss, A. I.; Abruna, H. D. *J. Electroanal. Chem.* **1986**, 201, 347–358.

(91) George, M. W.; Johnson, F. P. A.; Westwell, J. R.; Hodges, P. M.; Turner, J. J. *J. Chem. Soc., Dalton Trans.* **1993**, 2977–2979.

(92) Sullivan, B. P.; Bolinger, C. M.; Conrad, D.; Vining, W. J.; Meyer, T. J. *J. Chem. Soc., Chem. Comm.* **1985**, 1414–1416.

(93) Cosnier, S.; Deronzier, A.; Moutet, J.-C. *New J. Chem.* **1990**, 14, 831–839.

(94) Berger, S.; Klein, A.; Kaim, W.; Fiedler, J. *Inorg. Chem.* **1998**, 37, 5664–5671.

(95) Kaim, W.; Kramer, H. E. A.; Vogler, C.; Rieker, J. *J. Organomet. Chem.* **1989**, 367, 107–115.

(96) Klein, A.; Vogler, C.; Kaim, W. *Organometallics* **1996**, 15, 236–244.

(97) Shu, C. F.; Wrighton, M. S. *Inorg. Chem.* **1988**, 27, 4326–4329.

(98) Christensen, P.; Hamnett, A.; Muir, A. V. G.; Timney, J. A. *J. Chem. Soc., Dalton Trans.* **1992**, 1455–1463.

(99) Wong, K.-Y.; Chung, W.-H.; Lau, C.-P. *J. Electroanal. Chem.* **1998**, 453, 161-169.

(100) Hawecker, J.; Lehn, J. M.; Ziessel, R. *Helv. Chim. Acta* **1986**, 69, 1990-2012.

(101) Smieja, J. M.; Sampson, M. D.; Grice, K. A.; Benson, E. E.; Froehlich, J. D.; Kubiak, C. P. *Inorg. Chem.* **2013**, 52, 2484-2491.

(102) Smieja, J. M.; Kubiak, C. P. *Inorg. Chem.* **2010**, 49, 9283-9289.

(103) Smieja, J. M.; Benson, E. E.; Kumar, B.; Grice, K. A.; Seu, C. S.; Miller, A. J. M.; Mayer, J. M.; Kubiak, C. P. *Proc. Natl. Acad. Sci. U. S. A.* **2012**, 109, 15646–15650.

(104) Benson, E. E.; Grice, K. A.; Smieja, J. M.; Kubiak, C. P. *Polyhedron* **2013**, 58, 229–234.

(105) Benson, E. E.; Kubiak, C. P. *Chem. Commun.* **2012**, 48, 7374-7376.

(106) Benson, E. E.; Kubiak, C. P. *Chem. Commun.* **2012**, 48, 7374–7376.

(107) Benson, E. E.; Sampson, M. D.; Grice, K. A.; Smieja, J. M.; Froehlich, J. D.; Friebel, D.; Keith, J. A.; Carter, E. A.; Nilsson, A.; Kubiak, C. P. *Angew. Chem. Int. Ed.* **2013**, 52, 4841–4844.

(108) *CRC Handbook of Chemistry and Physics*; 92nd ed.; Haynes, W. M., Ed.; CRC Press: Boca Raton, FL, **2011-2012**.

(109) Abel, E. W.; Wilkinson, G. *J. Chem. Soc.* **1959**, 1501–1505.

(110) Johnson, F. P. A.; George, M. W.; Hartl, F.; Turner, J. J. *Organometallics* **1996**, 15, 3374–3387.

(111) Bourrez, M.; Molton, F.; Chardon-Noblat, S.; Deronzier, A. *Angew. Chem. Int. Ed.* **2011**, 50, 9903–9906.

(112) Hartl, F.; Rosa, P.; Ricard, L.; Le Floch, P.; Záliš, S. *Coord. Chem. Rev.* **2007**, 251, 557–576.

(113) Smieja, J. M.; Sampson, M. D.; Grice, K. A.; Benson, E. E.; Froehlich, J. D.; Kubiak, C. P. *Inorg. Chem.* **2013**, 52, 2484-2491.

(114) Hartl, F.; Rossenaar, B. D.; Stor, G. J.; Stufkens, D. J. *Recl. Trav. Chim. Pays-Bas* **1995**, 114, 565–570.

(115) Johnson, F. P. A.; George, M. W.; Hartl, F.; Turner, J. J. *Organometallics* **1996**, 15, 3374-3387.

(116) Stor, G. J.; Hartl, F.; van Outersterp, J. W. M.; Stufkens, D. J. *Organometallics* **1995**, 14, 1115-1131.

(117) Fujita, E.; Muckerman, J. T. *Inorg. Chem.* **2004**, 43, 7636–7647.

(118) Stor, G. J.; Morrison, S. L.; Stufkens, D. J.; Oskam, A. *Organometallics* **1994**, 13, 2641-2650.

(119) Hartl, F.; Rossenaar, B. D.; Stor, G. J.; Stufkens, D. J. *Recueil des Travaux Chimiques des Pays-Bas* **1995**, 114, 565-570.

(120) Riplinger, C.; Sampson, M. D.; Ritzmann, A. M.; Kubiak, C. P.; Carter, E. A. *J. Am. Chem. Soc.* **2014**, 136, 16285-16298.

(121) Cecchet, F.; Alebbi, M.; Bignozzi, C. A.; Paolucci, F. *Inorg. Chim. Acta* **2006**, 359, 3871-3874.

(122) Cheung, K.-C.; Guo, P.; So, M.-H.; Lee, L. Y. S.; Ho, K.-P.; Wong, W.-L.; Lee, K.-H.; Wong, W.-T.; Zhou, Z.-Y.; Wong, K.-Y. *J. Organomet. Chem.* **2009**, 694, 2842-2845.

(123) Anfuso, C. L.; Snoeberger, R. C.; Ricks, A. M.; Liu, W.; Xiao, D.; Batista, V. S.; Lian, T. *J. Am. Chem. Soc.* **2011**, 133, 6922-6925.

(124) Anfuso, C. L.; Xiao, D.; Ricks, A. M.; Negre, C. F. A.; Batista, V. S.; Lian, T. *J. Phys. Chem. C* **2012**, 116, 24107-24114.

(125) Paoprasert, P.; Kandala, S.; Sweat, D. P.; Ruther, R.; Gopalan, P. *J. Mater. Chem.* **2012**, 22, 1046-1053.

(126) Anfuso, C. L.; Ricks, A. M.; Rodríguez-Córdoba, W.; Lian, T. *J. Phys. Chem. C* **2012**, 116, 26377-26384.

(127) Sathrum, A. J.; Kubiak, C. P. *J. Phys. Chem. Lett.* **2011**, 2, 2372-2379.

Chapter 2

Electronic states of rhenium bipyridine tricarbonyl electrocatalysts for carbon dioxide reduction as revealed by X-ray absorption spectroscopy.

2.1 Introduction

Of the systems that electrocatalytically reduce CO_2, the $Re(bpy-R)(CO)_3Cl$ family of compounds (bpy-R = 4,4′-disubstituted-2,2′-bipyridine) is one of the most robust and well-characterized systems known to date.[1-5] This system converts CO_2 into carbon monoxide (CO) with high rates and efficiencies; it suffers, however, from large overpotentials believed to arise from accessing the highly reduced, formally Re(–I) state in $[Re(bpy-R)(CO)_3]^-$. This state has long been proposed as the active state of the electrocatalyst.[1-2,5] Apart from this assumption, there is little known about the

electronic structure of the catalyst in its reduced (active) state and its subsequent interaction with CO_2.

Our group recently reported stopped-flow kinetics studies showing the relative selectivities of the [Re(bpy-tBu)(CO)$_3$]$^-$ anion reacting with CO_2 and proton sources. These studies revealed that reaction rates of the anion were ~35 times faster with CO_2 than with weak acid.[2] The bpy ligand was proposed to play a non-innocent role by storing charge and preventing a doubly occupied d_z^2 orbital at the Re center, which would be needed to form a metal hydride. Indeed, X-ray diffraction (XRD) studies of both [Re(bpy)(CO)$_3$]$^-$ and [Re(bpy-tBu)(CO)$_3$]$^-$ show the bpy ligands exhibit bond length alternation and short C_{py}–C_{py} bond distances (1.370(15) Å, for bpy-tBu), indicating significant electron density on these ligands. The short inter-ring bonds suggest a doubly-reduced bpy ligand,[6] more representative of a Re(I)bpy(–2) state rather than a Re(0)bpy(–1) or Re(–I)bpy(0) state. The redox activities of bpys[6-7] as well as other non-innocent ligands have been extensively studied.[8-11]

To fully confirm that the non-innocence of bpy contributes to this unique catalysis, we employ experimental spectroscopy and theoretical quantum chemistry to characterize this catalyst family. We compare the halide starting materials, Re(bpy)(CO)$_3$Cl (**1**) and Re(bpy-tBu)(CO)$_3$Cl (**2**); the one-electron reduced dimer, [Re(bpy)(CO)$_3$]$_2$ (**3**); the two-electron reduced anions, [Re(bpy)(CO)$_3$][K(18-crown-6)] (**4**) and [Re(bpy-tBu)(CO)$_3$][K(18-crown-6)] (**5**); the commercially available standards, Re(CO)$_5$Cl (**6**) and Re$_2$(CO)$_{10}$ (**7**); and a synthesized Re(–I) standard, [Re(CO)$_5$][K(18-crown-6)] (**8**). Infrared (IR) spectroscopy of the stretching

frequencies of the carbonyl ligands characterizes the electronic states of these complexes. X-ray absorption spectroscopy (XAS) at the Re L_3 absorption edge using the strong "white-line" resonance arising from 2p → 5d transitions probes the Re $5d$ unoccupied states. Kohn-Sham density functional theory (KS-DFT) calculations provide a first-principles description of electronic structures. Lastly, Extended X-ray Absorption Fine Structure (EXAFS) studies of frozen THF solutions of **1**, **2**, **4,** and **5** confirm the monomeric nature of the catalysts and rule out solvent coordination to the Re centers in solution.

2.2 Results and Discussion

Synthesis. Compounds **1–5** were prepared according to literature procedures.[1-2,5] [Re(CO)$_5$][K(18-crown-6)] (**8**) was prepared by the reduction of Re$_2$(CO)$_{10}$ (**7**) in tetrahydrofuran (THF) by excess KC$_8$ (potassium intercalated graphite) in the presence of 18-crown-6 (see Experimental section).

Infrared Spectroscopy. The IR stretching frequencies of complexes **1–7** have been reported previously;[1-2,5,12] however, we obtained frequencies for complexes **1–7** and the newly synthesized complex **8** under the same conditions for fair comparison (Table 2.1). The one-electron reduction of the formally Re(I) chloride species **2** results in formation of the one-electron reduced monomer, [Re(bpy)(CO)$_3$Cl]$^-$, which has been previously characterized spectroscopically (Table 1).[5,13] This reduction results in a shift of ~21 cm^{-1} in the high-energy band and has been previously attributed to formation of a bpy radical.[5,13] This species has not been isolated and quickly converts

to the [Re(bpy)(CO)$_3$]$_2$ dimer (**3**). The two-electron reduction of the formally Re(I) chloride species (**1** and **2**) to the anionic species (**4** and **5**) results in a shift of ~75 cm^{-1} in the high-energy band. This has been previously attributed to the formation of a Re(0)bpy(−1) state.[2] In contrast, the two-electron reduction of standard **6** to its anionic state **8** results in a shift of 134 cm^{-1}. This larger shift in the carbonyl stretching frequencies can be attributed to the formation of a Re(−I) formal oxidation state since the [Re(CO)$_5$]$^-$ anion lacks a redox-active ligand to store additional charge.

Table 2.1 IR stretching frequencies for selected compounds.

Compound	ν(CO) (cm^{-1})
Re(bpy)(CO)$_3$Cl (**1**)[a]	2019, 1918, 1894
Re(bpy-tBu)(CO)$_3$Cl (**2**)[a]	2018, 1915, 1890
[Re(bpy)(CO)$_3$Cl]$^-$ [b]	1998, 1880, 1866
[Re(bpy)(CO)$_3$]$_2$ (**3**)[a]	1991, 1951, 1885, 1862
[Re(bpy)(CO)$_3$]$^-$ (**4**)[a]	1945, 1839 (br)
[Re(bpy-tBu)(CO)$_3$]$^-$ (**5**)[a]	1940, 1835 (br)
Re(CO)$_5$Cl (**6**)[a]	2041, 1980 (br)
Re$_2$(CO)$_{10}$ (**7**)[a]	2070, 2010, 1966
[Re(CO)$_5$]$^-$ (**8**)[a]	1907, 1861 (br)

[a]IR stretching frequencies for these compounds were obtained for this study (THF).
[b]IR stretching frequencies were taken from Ref. 8 (CH$_3$CN).

X-ray Crystallography. Compounds **1**–**5** have been crystallized previously.[1-2,14] Table 3 lists relevant bond lengths for compounds **1**, **2**, **4**, and **5** (*vide infra*). Reduction of the dimer **7** using KC$_8$ results in the formation of the five-coordinate rhenium anion [Re(CO)$_5$][K(18-crown-6)] (**8**). XRD quality crystals of complex **8** were grown from the vapor diffusion of *n*-hexane into a solution of the complex in THF (Figure 2.5). Crystal data and structure refinement information for complex **8** are listed in Table 2.3.

X-ray Absorption Spectroscopy (XAS). XAS at the Re L_3 edge were collected at SSRL beam line 4–1 for compounds **1–8**. XAS of low-valence Re complexes containing carbonyl ligands exhibit extraordinarily strong white lines that resemble Re oxides much more than metallic Re(0).[15-16] This is attributed to metal d orbitals coupling to empty π* orbitals of the carbonyl ligands; this generates additional unoccupied states with partial Re 5d character that would not exist in purely σ-bonded compounds or in Re metal.

Figure 2.1 shows a comparison of the XAS white-line region for the standards **6–8**. The white-line intensity expectedly decreases with decreasing formal oxidation state of the Re center. In contrast, when considering a series of Re bipyridyl complexes formally charged as Re(I), Re(0) and Re(–I), we observe a marked decrease of the white-line intensity for the first reduction step from **1** $\rightarrow$ **3** (Figure 2.2a), but not for the second reduction step from **3** $\rightarrow$ **4** (Figure 2.2b). The two-electron reduction of the bpy-*t*Bu complex **2** $\rightarrow$ **5** likewise has a similar spectral change as that for **1** $\rightarrow$ **4** (Figure 2.7 and 2.6 respectively). This indicates the metal center in the anionic rhenium complexes possess similar electronic states as the Re(0) dimer **3** (Figure 2.2b).
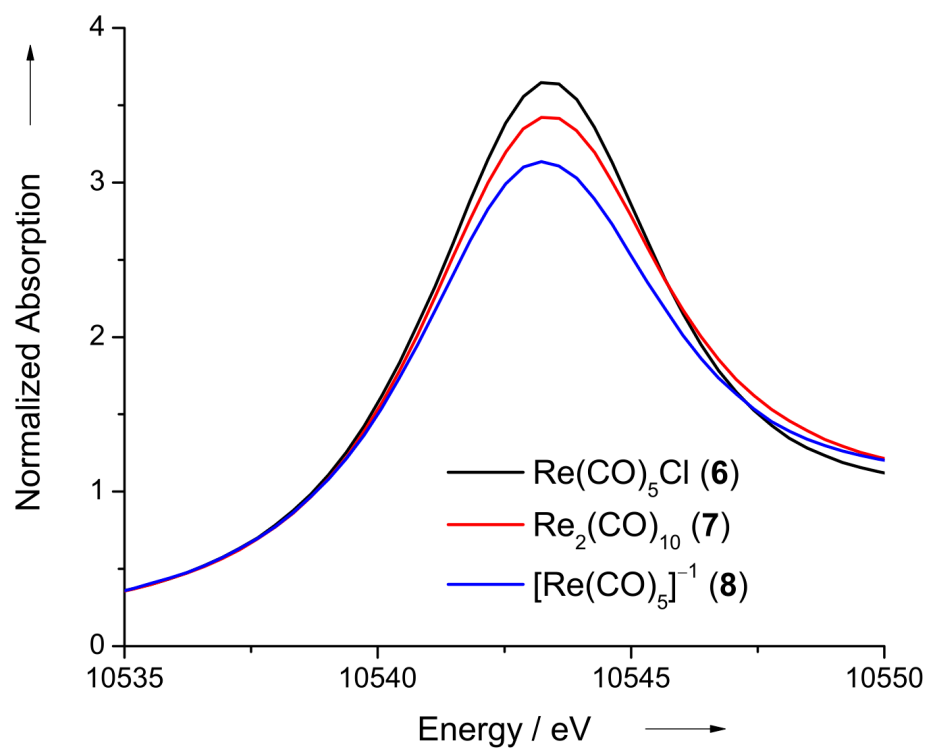
Figure 2.1 Comparison of the XAS white line regions for standards **6**–**8**.
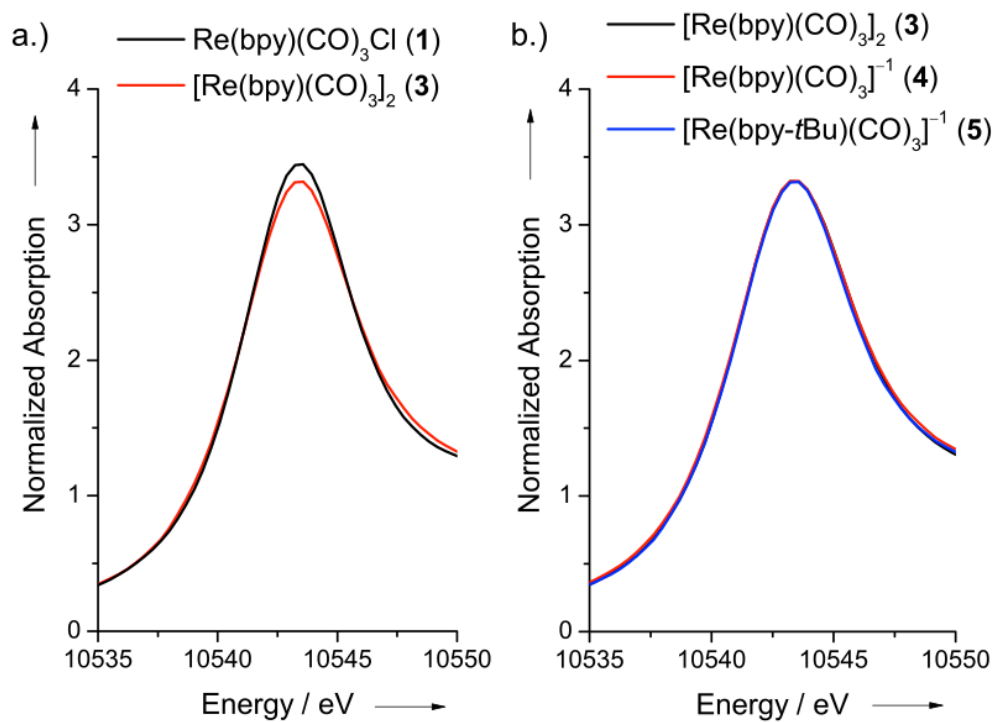
Figure 2.2 (a) XAS white line regions for complexes **1** and **3**. (b) XAS white line regions for complexes **3**, **4**, and **5**, showing no change in features.

Figure 2.3 shows reduction-induced white-line intensity changes in more detail. We compare the white line intensity decrease for reduction of standard **6 → 7**, and the two-electron reductions of the chloride compounds **1** and **2** to the anions **4** and **5**, respectively. The difference spectra $\mu(\mathbf{6})–\mu(\mathbf{7})$ and $\mu(\mathbf{6})–\mu(\mathbf{8})$ (where μ is a normalized absorption coefficient) represent the Re(I) → Re(0) and Re(I) → Re(–I) reductions, respectively. Note, however, that changes in the Re 5d – CO π^* coupling will inevitably accompany the oxidation state and symmetry changes and in turn will contribute additional small changes to the white-line and overlapping multiple-scattering resonances. The latter complication limits the accuracy of counting 5d vacancies by integrating $\Delta\mu$. However, Figure 2.2 and 2.9 clearly show that the Re electronic structure differences between the anions (**4** and **5**) and dimer **3** are negligible. Therefore, a very similar amount of electron density lies on the metal center in the anions as in the dimer. Charge density difference plots (obtained from restricted gas phase DFT-B3LYP[17-18] calculations using the LANL2DZ effective core potential and basis set with 15 explicit electrons on the Re,[19] the 6-31+G**[20] basis set on all other atoms, and calculated with GAMESS-US[21-22]) show this result as well (Figure 2.4). Here, the red (dark) regions of the density difference show the unique orbital space of the HOMO of the $[Re(bpy)(CO)_3]^-$ anion is clearly delocalized across both the Re center and the bpy ligand. The purple (light) regions depict polarization of the complex after adding two electrons to the $[Re(bpy)(CO)_3]^+$ cation. These features are robust with respect to whether the anion state is calculated as a closed-shell singlet or as an open-shell singlet (see Experimental section).
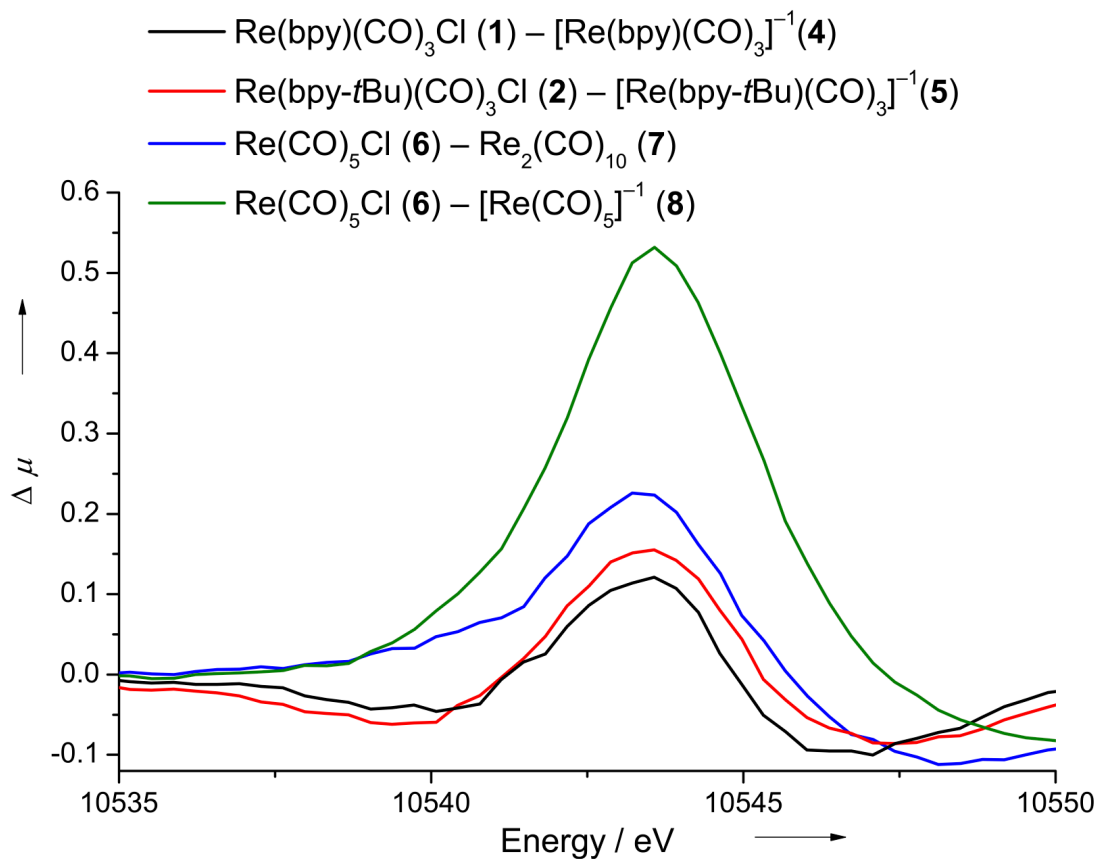
Figure 2.3 XANES difference spectra for the Re(I) complexes **1** and **2** and their corresponding anionic complexes **4** and **5** ($\Delta\mu$ is the change in normalized absorption). The Re(bpy)(CO)$_3$ pair (**1**, **4**) is shown in (black), and the Re(bpy-tBu)(CO)$_3$ pair (**2**, **5**) is shown in (red). For reference, the difference in XANES spectra for Re(CO)$_5$Cl (**6**) and Re$_2$(CO)$_{10}$ (**7**) is shown in (blue), and the difference spectra for Re(CO)$_5$Cl (**6**) and [Re(CO)$_5$]$^-$ (**8**) is shown in (green).
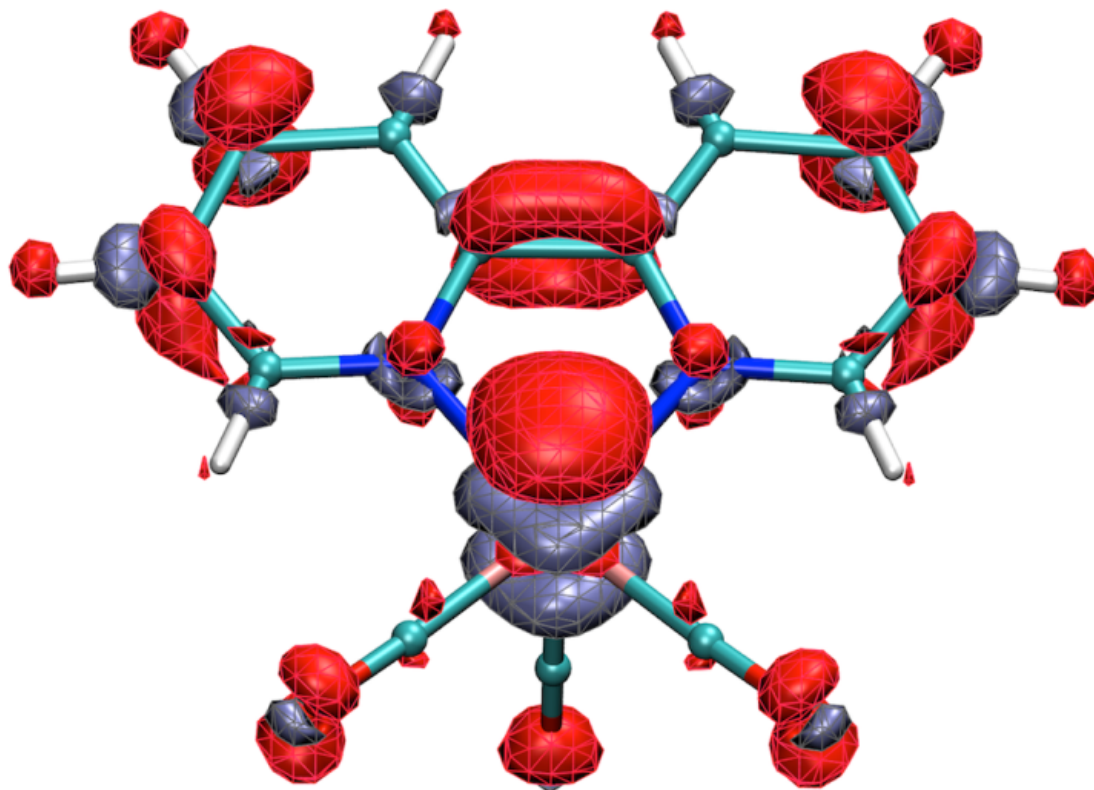
Figure 2.4 Density difference plots showing the polarization that occurs upon adding two electrons to the LUMO of the [Re(bpy)(CO)$_3$]$^+$ cation to form the HOMO of the [Re(bpy)(CO)$_3$]$^-$ anion. Isosurface depicts contour values of 0.005; red = increased charge density; purple = decreased charge density.

Figure 2.3 shows the area of the peak is smaller (~50%) for $\mu(\mathbf{1})$–$\mu(\mathbf{4})$ than for the transfer of a single electron into Re 5d states ($\mu(\mathbf{6})$–$\mu(\mathbf{7})$). The same observation can also be made for the reduction of the Re(I) species **1** to dimer **3**. Therefore, the first reduction step from **1** → **3** involves a portion of the electronic charge stored in a bpy π^* orbital that weakly overlaps with Re 5d orbitals. In a simplified view, the ground states of the anionic species (**4** and **5**) are best described formally as Re(0)bpy(–1), rather than Re(I)bpy(–2) or Re(–I)bpy(0). This formally places one electron in a Re d$_z^2$ orbital and one in the bpy π^* orbital. These catalysts have been

shown to react ~20 times faster with CO_2 than with H^+.[2] The Re(0)bpy(−1) ground state appears to be an electronic configuration which is favorable for engaging CO_2 preferentially over H^+ because engaging CO_2 involves transferring two electronic charges through both σ and π-interactions, whereas engaging H^+ involves only a σ (Re d_z^2 + H 1s) interaction. This ground state is, by all appearances, a closed-shell singlet, showing no evidence of paramagnetism in room temperature NMR spectra or from spin-polarized quantum mechanics calculations (where the closed-shell singlet state is favored over the triplet state by 0.79 eV in gas phase and 0.65 eV in acetonitrile solution, see Experimental section). The singlet nature of this ground state implies some long range coupling of the Re and bpy orbitals (overlapping tails of the wavefunctions would favor the singlet).

We previously characterized the structures of **1**, **2**, **4** and **5** using XRD, but these results may not necessarily be valid for *in situ* catalysis. For instance, under ambient conditions, the catalyst could become coordinated with solvent molecules. However, EXAFS at the Re L_3 edge of complexes **1**, **2**, **4**, and **5** in frozen THF confirms that the XRD results accurately represent the coordination of the active catalyst. The solubility of the dimer **3** was too low to collect reliable data with the available experimental time. Table 2.5 lists quantitative results of EXAFS analysis for complexes **1**, **2**, **4**, and **5**.

Bond lengths and coordination around the metal centers obtained from the frozen solution EXAFS agree with XRD structures previously reported,[2,14] as well as the structures obtained in our and Fujita and Muckerman's DFT calculations.[13] Table

2.2 compares data from EXAFS, XRD, and gas phase DFT calculations showing coordination numbers and bond lengths. Individual scattering paths that contribute to the Fourier transformed EXAFS data for complex **1** are shown in Figure 2.9. Fourier transformed EXAFS data and fittings for complexes **1**, **2**, **4**, and **5** are shown in Figure 2.10–2.11. EXAFS data and fittings displayed in k-space are shown in Figures 2.12–2.13. From the EXAFS data we can conclude that the anions **4** and **5** remain five-coordinate in solution with no detectable coordination of solvent and no dimer formation.

Table 2.2 Coordination numbers (C. N.) and bond distances (in Å) for compounds **1**, **2**, **4**, and **5**.

Compound		EXAFS	XRD[a]	Reference
Re(bpy)(CO)₃Cl (**1**)	C. N.	6.1(2)	6	14
	Re – C	1.93(2)	1.930(8)	
	Re – N	2.18(5)	2.175(6)	
	Re – Cl	2.49(2)	2.460(2)	
Re(bpy-tBu)(CO)₃Cl (**2**)	C. N.	6.2(2)	6	23
	Re – C	1.92(1)	1.911(4)	
	Re – N	2.17(4)	2.176(3)	
	Re – Cl	2.49(2)	2.463(1)	
[Re(bpy)(CO)₃]⁻ (**4**)	C. N.	4.9(2)	5	1
	Re – C	1.91(2)	1.892(5)	
	Re – N	2.14(2)	2.082(4)	
[Re(bpy-tBu)(CO)₃]⁻ (**5**)	C. N.	5.1(2)	5	24
	Re – C	1.91(2)	1.917(10)	
	Re – N	2.14 (2)	2.093(7)	

[a]Averages of values found in the unit cell.

2.3 Conclusions

In summary, we have applied experimental spectroscopy (XANES and EXAFS) and computational quantum chemistry (KS-DFT) to study the electronic structures and local coordination environments of catalytically relevant Re complexes

and their reactive anions. XANES spectra of standards $Re(CO)_5Cl$ (**6**) and $Re_2(CO)_{10}$ (**7**) as well as a synthesized Re(–I) anion, [$Re(CO)_5$][K(18-crown-6)] (**8**), have given us three distinct Re oxidation states for comparison with these catalytically relevant Re complexes. In terms of simplified formal charges, the anions [$Re(bpy)(CO)_3$]⁻ (**4**) and [$Re(bpy-tBu)(CO)_3$]⁻ (**5**) are best described as possessing formally Re(0)bpy(–1) ground states. The anions **4** and **5** are five-coordinate in solution with no coordination of solvent or dimer formation, which is consistent with XRD structures obtained in previous experiments.[2,14]

The findings reported here, together with recently reported stopped-flow kinetics studies of the anion, [$Re(bpy-tBu)(CO)_3$]⁻ (**5**), with CO_2 and weak acids[2], explain the high selectivity of the $Re(bpy)(CO)_3Cl$ family of catalysts for the reduction of CO_2 in the presence of significant concentrations of H^+ sources. In general, the reduction of H^+ to H_2 is favored thermodynamically by 0.1 V over the reduction of CO_2 to CO, and so any catalyst that reduces CO_2 selectively in the presence of H^+ must do so on a kinetic basis with origins in the particular electronic structure of the catalyst. The formally Re(0)bpy(–1) state found for these anions places one electron in a Re d_z^2 orbital, and one in the bpy π^* orbital. It appears that this is an electronic configuration which is favorable for engaging CO_2 preferentially over H^+, and one that provides a lower reorganization energy for transferring two electronic charges to CO_2 through both σ and π-interactions, compared to H^+, which could only involve σ (Re d_z^2 + H 1s) interaction. These findings may provide principles useful in the design of future catalysts for both carbon dioxide and proton reduction. Mechanistic

investigations are underway to understand the complete CO_2 reduction process with these catalysts.

2.4 Experimental

General Considerations. Syntheses and manipulations were carried out under an inert atmosphere using standard glovebox techniques. Complexes **1–5** were synthesized by previously reported methods.[1-2] Complexes 6 and 7 were obtained from Acros Organics and used without further purification. All other chemicals were purchased from commercial sources and used as received. THF was sparged with argon and dried over basic alumina with a custom dry solvent system. *n*-Hexane was distilled over NaH over the course of five hours. THF and *n*-hexane were then stored over activated 3 Å molecular sieves. KC_8 was prepared by literature methods.[25] All glassware was dried overnight in an oven prior to use. Infrared spectra were collected on a Thermo Scientific Nicolet 6700. Sample solutions (*ca.* 3 mM in THF) were placed in a Specac Advanced Liquid Transmission cell and sealed in the glovebox for analysis. Spectra were acquired by averaging 16 scans at 1.0 cm^{-1} resolution. Elemental analysis was performed by Midwest MicroLab, LLC for C. H, and N.

Synthesis of [Re(CO)$_5$][K(18-crown-6)]. $Re_2(CO)_{10}$ (50 mg, 0.08 mmol) was dissolved in 20 mL THF. The solution was allowed to cool to −35 °C. 18-crown-6 (79 mg, 0.30 mmol) and KC_8 (41 mg, 0.30 mmol) were added to the cooled solution, and the solution was allowed to warm to room temperature over a period of 30 min. The solution was filtered, affording a bright red solution of [Re(CO)$_5$]$^-$. Solvent was

removed under vacuum to yield a dark red solid (typical yield of 70%). X-ray quality crystals were grown from the vapor diffusion of *n*-hexane into a THF solution of the complex. IR(THF) ν(CO): 1907 cm^{-1} and 1861 cm^{-1} (broad). Analysis Calculated, $C_{17}H_{24}KO_{11}Re$: C, 32.43; H, 3.84; N, 0.00. Found: C, 32.65; H, 3.84; N, 0.00.

X-ray Crystallography. Complex **8** crystallized in the space group P2(1)/c, where the rhenium atom lies on an inversion center. The pentacarbonyl anion exists in the solid state as an almost ideal trigonal bipyramid where $\tau_5 = 0.96$. For comparison, a perfect trigonal bipyramid has a $\tau_5 = 1$.[26] The potassium cation is encapsulated by the crown ether with the axial positions coordinated by two solvent molecules of THF.[27]

While the $[Re(CO)_5]^-$ anion has been synthesized previously,[28-29] it has not been isolated as the crown ether encapsulated potassium salt. The pentacarbonyl anion is very similar to that previously reported by Roesky and Stalke,[29] which crystallized with a bulky $[L_3Re(CO)_3]^+$ silylene cation and has a $t_5 = 0.94$. The anion **8** has an average equatorial Re–C bond length of 1.953(5) Å and an average axial Re–C bond length of 1.976(4) Å, whereas Roesky and Stalke's anion has an average equatorial Re–C bond length of 1.937(7) Å and an average axial Re–C bond length of 1.946(8) Å.

In comparison to the previously reported crystal structures of the standards **6** and **7**,[30-31] the average equatorial Re–C bond length decreases as the oxidation state on the metal decreases from $Re(CO)_5Cl$ (**6**) to $Re_2(CO)_{10}$ (**7**) to $[Re(CO)_5]^-$ (**8**) (average Re–C$_{eq.}$ = 2.019(7) Å, 1.987(6) Å, 1.953(5) Å respectively). In contrast, the average

C–O bond length increases as the oxidation state on the metal decreases from standard **6** to **7** to **8** (average C–O = 1.128(11) Å, 1.132(8) Å, 1.150(6) Å respectively). Both of these crystallographic features are attributed to increased π back-bonding to the carbonyls. The average axial Re–C bond length increases as the oxidation state on the metal decreases from standard **6** to **7** to **8** (average Re–C$_{ax.}$ = 1.91(1) Å, 1.929(7) Å, 1.976(4) Å respectively) due to the increased occupation of the metal $d_{x^2-y^2}$ and d_{xy} orbitals upon reduction.

The single crystal X-ray diffraction studies were carried out on a PHOTON 100 CMOS diffractometer equipped with Mo Kα radiation (λ = 0.71073 Å). The crystals were mounted on a Cryoloop with Paratone oil, and data was collected under a nitrogen gas stream at 100(2) K using w and f scans. Data was integrated using the Bruker SAINT software program and scaled using the SADABS software program. Solution by direct methods (SHELXS) produced a complete phasing model consistent with the proposed structure. All non-hydrogen atoms were refined anisotropically by full-matrix least-squares (SHELXL-97).[32] All hydrogen atoms were placed using a riding model. Their positions were constrained relative to their parent atom using the appropriate HFIX command in SHELXL-97. Crystallographic data are summarized in Table 2.3.

X-ray Absorption Spectroscopy (XAS) Details. Re *L$_3$* edge (~10.5 keV) EXAFS and XANES measurements were carried out at the Stanford Synchrotron Radiation Lightsource (SSRL) on Beamline 4–1 equipped with a Si (220) (phi = 0°) double-crystal monochromator calibrated to the first inflection point of Re(0) foil

(10535 eV). Samples were prepared under an inert atmosphere in a nitrogen filled glovebox. 3 mM solutions of the complexes were injected into a custom aluminum cell for use in a liquid He cryostat. The cell and sample holder were removed from the box and immediately submerged in liquid nitrogen for transfer to the beam station. The sample was then transferred to a continuous flow liquid He cryostat (Oxford Instruments CF1208) where the temperature was maintained at or below 50 K. EXAFS and XANES measurements were simultaneously carried out in transmission as well as fluorescence mode.

X-ray Absorption Near Edge Structure (XANES). XANES data were collected as fluorescence using a Canberra 13-element solid-state Ge detector. The effect of dead time on the counting efficiency was carefully measured for each detector element and the fluorescence intensities were corrected accordingly. Data acquisition was performed with XAS-Collect.[25] All XANES data presented result from averages of at least three spectra. All spectra were normalized to a unit step edge using the SIXPack software suite.[33]

Extended X-ray Absorption Fine Structure (EXAFS) Spectroscopy. EXAFS data were collected as fluorescence using a Lytle detector with Soller slits. Data acquisition was performed with XAS-Collect.[25] All EXAFS data presented result from averages of six spectra. The SIXPack software suite was used for background subtraction, spline fitting and least-square fitting of the Fourier-transformed EXAFS signal. Backscattering phase and amplitude functions required for fitting of spectra were obtained from FEFF 6.[34] Fitting was performed in *k*-space prior to Fourier

transformation. During least-squares fitting, the Debye-Waller factors for multiple scattering paths were fixed at values consistent with other experiments,[35-37] while the coordination number and bond distances were allowed to refine. The *k*-range and *r*-range used in fitting were 3–13 and 1–4, respectively. For the EXAFS fittings of the anions (**4** and **5**), the same scattering paths as the starting chloride complexes (**1** and **2**) were kept, except for the single scattering path for Re–Cl. The loss of the chloride scattering path can be seen as a significant decrease in the peak in the Fourier transformed EXAFS data at $r^2 = 2.21$ Å for the anions **4** and **5** (Figure 2.9 and 2.10).

Quantum Chemical Calculations. Electron density differences were obtained from electronic structure calculations using GAMESS-US.[21-22] Geometries were optimized using spin-restricted DFT-B3LYP[17-18] and the Hay-Wadt effective core potential (replacing the nucleus and core electrons) and its corresponding double-zeta basis set for the remaining 15 outer-core/valence electrons of Re.[19] The 6-31+G** basis set was used on all other atoms.[20] See Tables 2.6 and 2.7 in the Appendix for optimized coordinates.

Beyond the calculations described in the main text, we were concerned that the [Re(bpy)(CO)₃]⁻ anion might actually be an open-shell singlet state instead of the closed shell singlet initially assumed. To test this hypothesis, we attempted to obtain a spin-polarized (open-shell) singlet density for the [Re(bpy)(CO)₃]⁻ anion by first calculating the Kohn-Sham orbitals of the spin-polarized triplet and quintet states at the geometry of the restricted closed shell singlet. Those orbitals served as different initial guesses for the spin-polarized (open-shell) singlet. However, the spin-polarized

singlet states optimized to the same total energy as the restricted closed shell singlet and had an S^2 expectation value of exactly zero, thereby proving that the original spin-restricted DFT calculations introduced no artifact via spin-restriction and in fact that closed-shell singlet is the variational ground state within DFT. (The closed-shell singlet density of the $[Re(bpy)(CO)_3]^+$ cation was obtained at the geometry of the anion so that the density differences between the cation and anion could be clearly assigned to the addition of two electrons without the convolution of structural relaxation.)

As a final test of the potential open-shell character of this unusual electronic state, a proper open-shell singlet eigenfunction was computed from a restricted open-shell Hartree-Fock (ROHF) calculation for the anion (while the cation's density was obtained from a restricted HF calculation). Density differences for the DFT-B3LYP calculations were qualitatively similar to density differences obtained from HF calculations, as shown in Figure 2.14, namely the added electrons are quite delocalized over the anion and are most definitely not confined to a Re d_z^2 orbital. The ROHF density differences show greater polarization to the carbonyls, which is not surprising, since HF theory overemphasizes ionic character due to its lack of electron correlation.

To evaluate the relative energy of the triplet anion with respect to the singlet anion, we optimized the geometry of the triplet species in gas phase and a Hessian calculation confirmed these coordinates as a stable minimum energy structure. A comparison between single point energies calculated as above but with the aug-cc-pVDZ basis set[38] on non-Re atoms found the triplet state to be 0.79 eV higher in

energy in gas phase (involving SCF + zero point vibrational energy contributions) and 0.65 eV higher in energy in acetonitrile solvent. Acetonitrile single point solvation calculations were run using the CPCM program[39] with SUAHF radii as implemented in GAMESS-US, using the following solvent parameters for acetonitrile: probe radius = 2.18Å; dielectric constant = 35.69. The latter energies included thermal contribution (enthalpic and entropic) at 298 K as calculated using the ideal gas, rigid rotor, harmonic oscillator approximations.[40]

Much of the material for this chapter comes directly from a manuscript entitled: "The Electronic States of Rhenium Bipyridyl Electrocatalysts for CO_2 Reduction as Revealed by X-ray Absorption Spectroscopy and Computational

Quantum Chemistry" by Eric E. Benson, Matthew D. Sampson, Kyle A. Grice, Jonathan M. Smieja, Jesse D. Froehlich, Daniel Friebel, John A. Keith, Emily A. Carter, Anders Nilsson, and Clifford P. Kubiak, which has been published in *Angew. Chem. Int. Ed.*, **2013**, 52, 4841–4844. http://dx.doi.org/10.1002/anie.201209911. The dissertation author is the primary co-author of this manuscript.

2.5 References

(1) Benson, E. E.; Kubiak, C. P. *Chem. Commun.* **2012**, 48, 7374-7376.

(2) Smieja, J. M.; Benson, E. E.; Kumar, B.; Grice, K. A.; Seu, C. S.; Miller, A. J. M.; Mayer, J. M.; Kubiak, C. P. *Proc. Natl. Acad. Sci. U. S. A*. **2012**, 109, 15646–15650.

(3) Savéant, J.-M. *Chem. Rev.* **2008**, 108, 2348-2378.

(4) Morris, A. J.; Meyer, G. J.; Fujita, E. *Acc. Chem. Res.* **2009**, 42, 1983-1994.

(5) Smieja, J. M.; Kubiak, C. P. *Inorg. Chem.* **2010**, 49, 9283-9289.

(6) Gore-Randall, E.; Irwin, M.; Denning, M. S.; Goicoechea, J. M. *Inorg. Chem.* **2009**, 48, 8304-8316.

(7) Scarborough, C. C.; Sproules, S.; Weyhermüller, T.; DeBeer, S.; Wieghardt, K. *Inorg. Chem.* **2011**, 50, 12446-12462.

(8) Lippert, C. A.; Riener, K.; Soper, J. D. *Eur. J. Inorg. Chem.* **2012**, 2012, 554-561.

(9) Kaim, W. *Eur. J. Inorg. Chem.* **2012**, 2012, 343-348.

(10) de Bruin, B.; Bill, E.; Bothe, E.; Weyhermüller, T.; Wieghardt, K. *Inorg. Chem.* **2000**, 39, 2936-2947.

(11) Spikes, G. H.; Milsmann, C.; Bill, E.; Weyhermüller, T.; Wieghardt, K. *Inorg. Chem.* **2008**, 47, 11745-11754.

(12) Hartl, F.; Rossenaar, B. D.; Stor, G. J.; Stufkens, D. J. *Recueil des Travaux Chimiques des Pays-Bas* **1995**, 114, 565-570.

(13) Fujita, E.; Muckerman, J. T. *Inorg. Chem.* **2004**, 43, 7636-7647.

(14) Kurz, P.; Probst, B.; Spingler, B.; Alberto, R. *Eur. J. Inorg. Chem.* **2006**, 2006, 2966-2974.

(15) Fröba, M.; Lochte, K.; Metz, W. *J. Phys. Chem. Solids* **1996**, 57, 635-641.

(16) Tougerti, A.; Cristol, S.; Berrier, E.; Briois, V.; La Fontaine, C.; Villain, F.; Joly, Y. *Phys. Rev. B* **2012**, 85, 125136.

(17) Lee, C.; Yang, W.; Parr, R. G. *Phys. Rev. B* **1988**, 37, 785-789.

(18) Becke, A. D. *Phys. Rev. A* **1988**, 38, 3098-3100.

(19) Hay, P. J.; Wadt, W. R. *J. Chem. Phys.* **1985**, 82, 299-310.

(20) Hariharan, P. C.; Pople, J. A. *Theor. Chim. Acta.* **1973**, 28, 213–222.

(21) Schmidt, M. W.; Baldridge, K. K.; Boatz, J. A.; Elbert, S. T.; Gordon, M. S.; Jensen, J. H.; Koseki, S.; Matsunaga, N.; Nguyen, K. A.; Su, S.; Windus, T. L.; Dupuis, M.; Montgomery, J. A. *J. Comput. Chem.* **1993**, 14, 1347-1363.

(22) Gordon, M. W.; Schmidt, M. W. *Theory and Applications of Computational Chemistry: The First Forty Years*; Elsevier Science: Amsterdam, **2005**.

(23) Yam, V. W. W.; Lau, V. C. Y.; Cheung, K. K. *Organometallics* **1995**, 14, 2749-2753.

(24) Smieja, J. M.; Benson, E. E.; Kumar, B.; Grice, K. A.; Seu, C. S.; Miller, A. J. M.; Mayer, J. M.; Kubiak, C. P. *Proc. Natl. Acad. Sci. U. S. A.* **2012**, 109, 15646–15650.

(25) George, M. *Journal of Synchrotron Radiation* **2000**, 7, 283-286.

(26) Addison, A. W.; Rao, T. N.; Reedijk, J.; van Rijn, J.; Verschoor, G. C. *Coord. Chem. Rev.* **1984**, 251, 1349-1356.

(27) Sutin, N.; Creutz, C.; Fujita, E. *Comments Inorg. Chem.* **1997**, 19, 67-92.

(28) Poplaukhin, P. V.; Chen, X.; Meyers, E. A.; Shore, S. G. *Inorg. Chem.* **2006**, 45, 10115-10125.

(29) Azhakar, R.; Sarish, S. P.; Roesky, H. W.; Hey, J.; Stalke, D. *Inorg. Chem.* **2011**, 50, 5039-5043.

(30) Cotton, F. A.; Daniels, L. M. *Acta Crystallogr., Sect. C: Cryst. Struct. Commun.* **1983**, 39, 1495-1496.

(31) Churchill, M. R.; Amoh, K. N.; Wasserman, H. J. *Inorg. Chem.* **1981**, 20, 1609-1611.

(32) Sheldrick, G. *Acta Crystallogr., Sect. A: Found. Crystallogr.* **2008**, 64, 112-122.

(33) Webb, S. M. *Phys. Scr.* **2005**, T115, 1011-1014.

(34) Rehr, J. J.; Albers, R. C.; Zabinsky, S. I. *Phys. Rev. Lett.* **1992**, 69, 3397-3400.

(35) Vila, F. D.; Rehr, J. J.; Rossner, H. H.; Krappe, H. J. *Phys. Rev. B* **2007**, 76, 014301.

(36) Sapelkin, A. V.; Bayliss, S. C. *Phys. Rev. B* **2002**, 65, 172104.

(37) Dalba, G.; Fornasini, P. *Journal of Synchrotron Radiation* **1997**, 4, 243-255.

(38) Dunning, J. T. H. *J. Chem. Phys.* **1989**, 90, 1007-1023.

(39) Barone, V.; Cossi, M. *J. Phys. Chem. A* **1998**, 102, 1995-2001.

(40) Cramer, C. J. *Essentials of Computational Chemistry: Theories and Models, 2nd ed.*; John Wiley & Sons, Inc.: Hoboken, NJ, **2004**.

2.6   Appendix
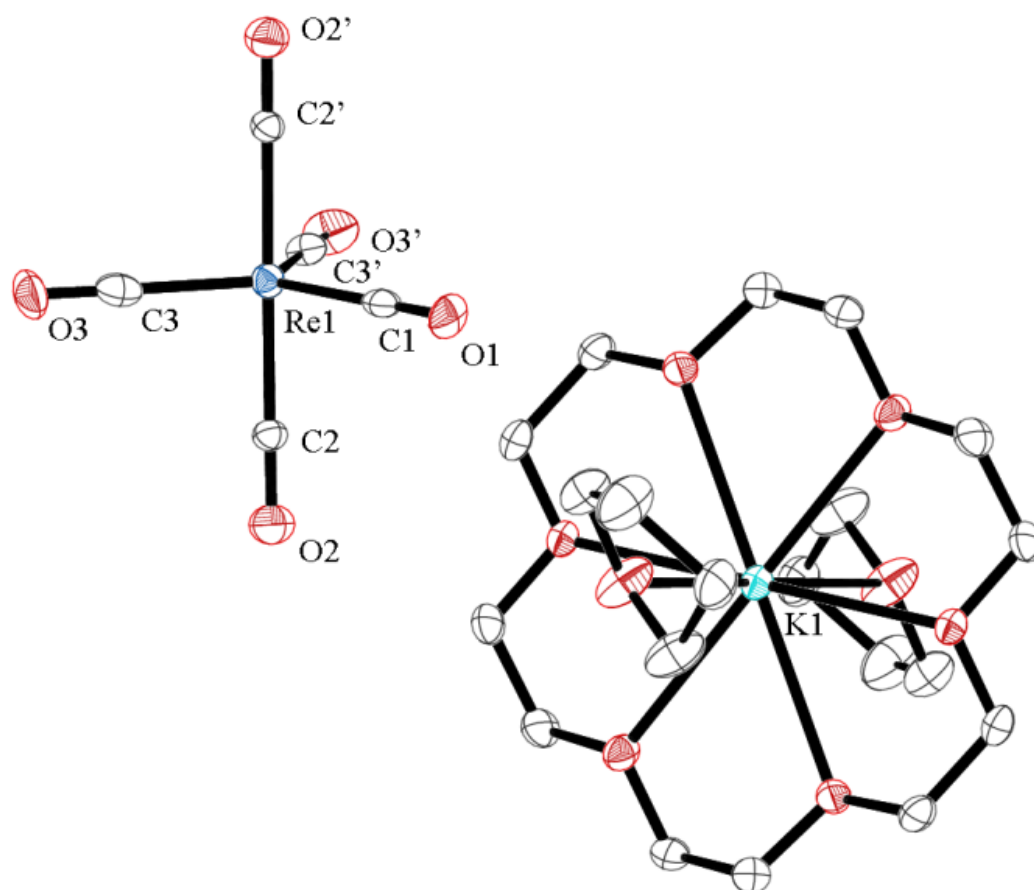
Figure 2.5 Molecular structure of [Re(CO)$_5$][K(18-crown-6)(THF)$_2$] (**8**), with hydrogen atoms excluded for clarity and ellipsoids set at the 50% probability level. Relevant distances (Å) and bond angles (°): Re1–C1, 1.955(6); Re1–C2, 1.976(4); Re1–C3, 1.952(4); O1–C1, 1.138(8); O2–C2, 1.141(5); O3–C3, 1.165(6); K1–O7, 2.678(3); C1–Re1–C2, 89.6(2); C1–Re1–C3, 119.2(2); C2–Re1–C3, 91.0(2); C2–Re1–C2´, 179.3(2); C3–Re1–C3´, 121.6(2); C2´–Re1–C3, 89.3(2).

Table 2.3 Crystal data and structure refinement for [Re(CO)$_5$][K(18-crown-6)(THF)$_2$] (**8**).

Parameter	Value	
Identification code	120607_ms_reco5anion_0m	
Empirical formula	C25 H40 K O13 Re	
Formula weight	773.87	
Temperature (K)	100 (15)	
Wavelength (Å)	0.71073	
Crystal system	Monoclinic	
Space group	P2(1)/c	
Unit cell dimensions	a = 8.6551(11) Å	$\alpha = 90.00°$
	b = 9.0682(11) Å	$\beta = 90.095(5)°$
	c = 19.443(3) Å	$\gamma = 90.00°$
Volume (Å^3)	1526.0(3)	
Z	2	
Density (calculated) (Mg m^{-3})	1.684	
Absorption coefficient (mm^{-1})	4.179	
F(000)	776	
Crystal size (mm^3)	0.1 x 0.1 x 0.03	
Theta range for data collection	3.072 to 25.428°	
Index ranges	−10<=h<=10, −10<=k<=10, −23<=l<=23	
Reflections collected	109291	
Independent reflections	2819 [R(int) = 0.1540]	
Completeness to theta = 50.00°	74.5 %	
Absorption correction	Semi-empirical from equivalents	
Max. and min. transmission	0.7452 and 0.4902	
Refinement method	Full-matrix least-squares on F^2	
Data / restraints / parameters	2819 / 0 / 184	
Goodness-of-fit on F^2	1.161	
Final R indices [I > 2sigma(I)]	R1 = 0.0300, wR2 = 0.0750	
R indices (all data)	R1 = 0.0315, wR2 = 0.0763	
Largest diff. peak and hole	2.615 and −1.329 e.Å^{-3}	
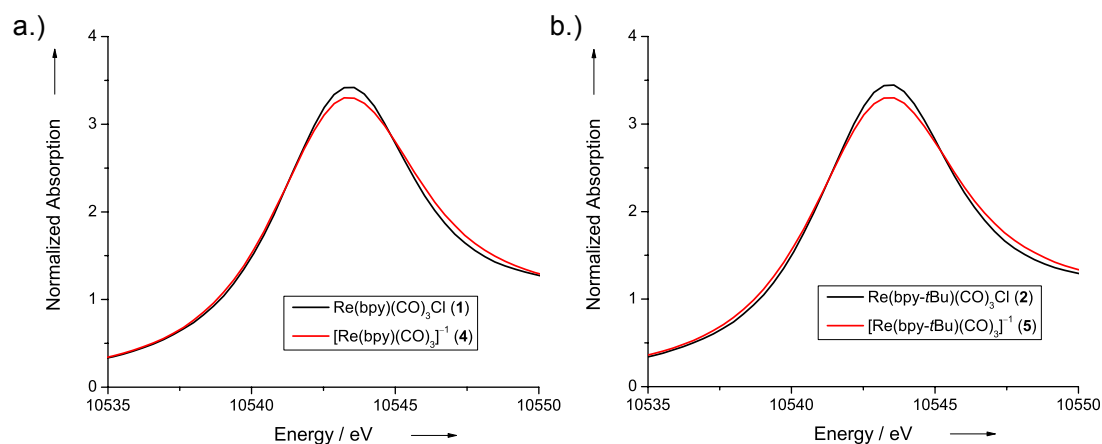
Figure 2.6 Comparison of the XAS white line regions (a) for complexes **1** and **4** and (b) for complexes **2** and **5**.
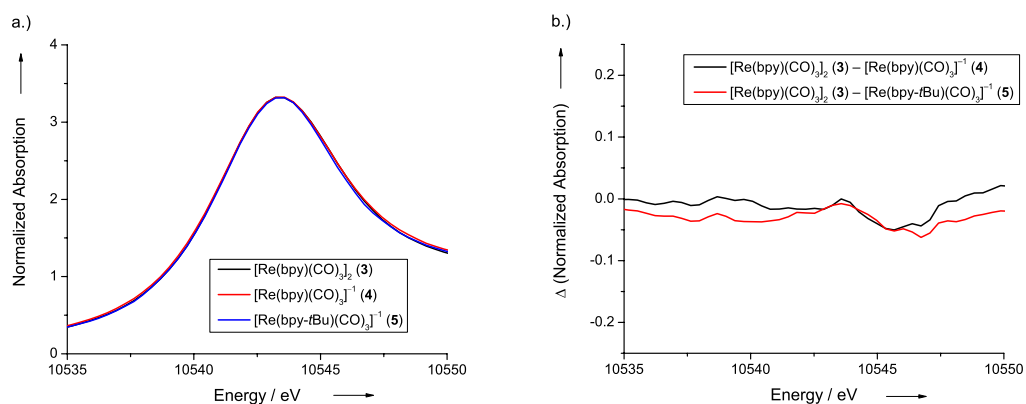
Figure 2.7 (a) Normalized XANES spectra of compounds **3**, **4** and **5**. (b) Difference XANES spectra between the dimer **3** and the anions **4** and **5**.

Table 2.4 XANES white line intensities and widths at half-maximum for complexes **1**–**8**.

Complex	Height (a. u.)	FWHM (eV)
Re(bpy)(CO)$_3$Cl (**1**)	3.42	6.82
Re(bpy-tBu)(CO)$_3$Cl (**2**)	3.44	6.86
[Re(bpy)(CO)$_3$]$_2$ (**3**)	3.32	7.51
[Re(bpy)(CO)$_3$]$^-$ (**4**)	3.30	7.52
[Re(bpy-tBu)(CO)$_3$]$^-$ (**5**)	3.30	7.70
Re(CO)$_5$Cl (**6**)	3.65	6.23
Re$_2$(CO)$_{10}$ (**7**)	3.42	6.82
[Re(CO)$_5$]$^-$ (**8**)	3.13	7.18

Table 2.5 Quantitative results of EXAFS analysis for compounds **1**, **2**, **4**, and **5**.

Compound	N	r (Å)	σ^2 (Å^2)	S_0^2	E_0 (eV)
Re(bpy)(CO)$_3$Cl (**1**)	3 C 2 N 1 Cl	1.93(2) 2.18(5) 2.49(2)	0.0019 0.0015 0.001	0.98	12.97 (2.69)
Re(bpy-tBu)(CO)3Cl (**2**)	3 C 2 N 1 Cl	1.92(1) 2.17(4) 2.49(2)	0.0019 0.0015 0.001	0.98	12.53 (2.56)
[Re(bpy)(CO)$_3$]$^-$ (**4**)	3 C 2 N	1.91(2) 2.14(2)	0.004 0.0012	0.98	9.75 (2.63)
[Re(bpy-tBu)(CO)$_3$]$^-$ (**5**)	3 C 2 N	1.91(2) 2.14(2)	0.0045 0.0012	0.98	9.64 (2.46)

Figure 2.8 Fourier transformed EXAFS data, fit and individual scattering paths for Re(bpy)(CO)$_3$Cl (**1**) (MS = multiple scattering).
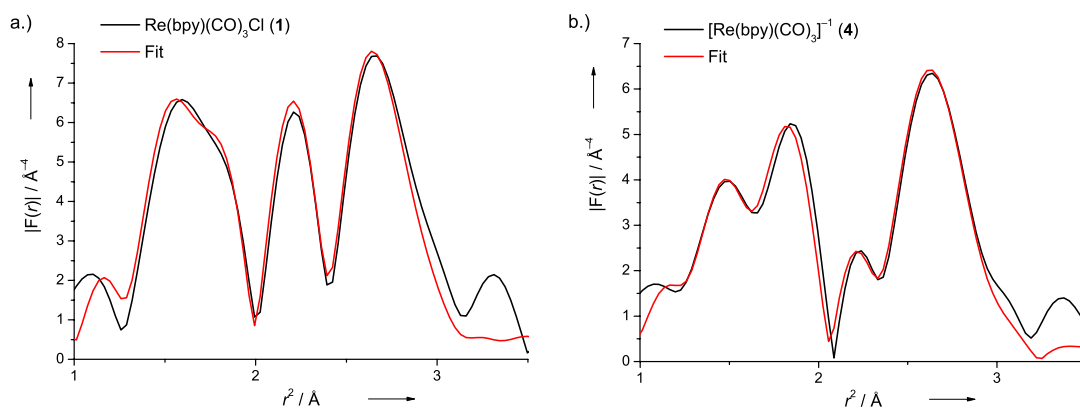
Figure 2.9 (a) Fourier transformed EXAFS data and fitting (displayed in *r*-space) in for complex **1**. (b) Fourier transformed EXAFS data and fitting (displayed in *r*-space) in for complex **4**.
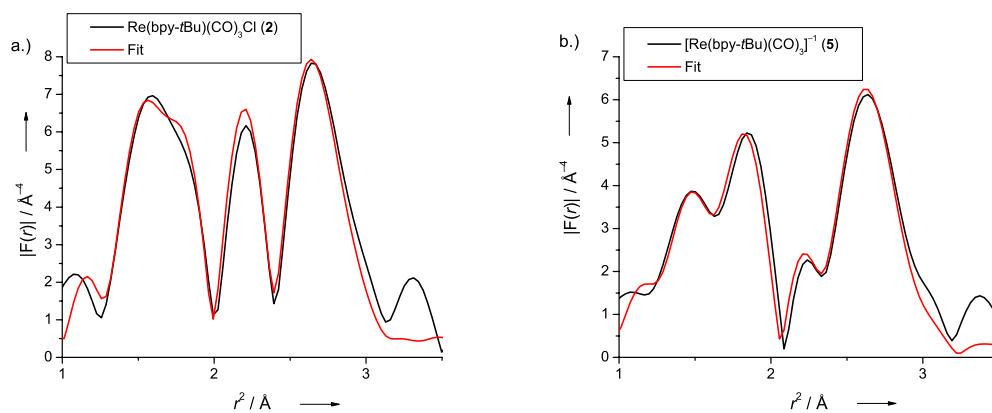
Figure 2.10 (a) Fourier transformed EXAFS data and fitting (displayed in *r*-space) for complex **2**. (b) Fourier transformed EXAFS data and fitting (displayed in *r*-space) for complex **5**.
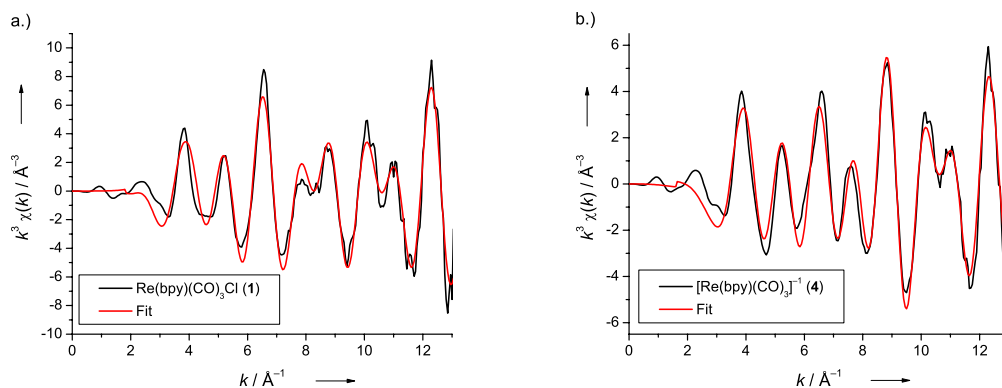
Figure 2.11 (a) Fourier transformed EXAFS data and fitting in *k*-space for complex **1**. (b) Fourier transformed EXAFS data and fitting in *k*-space for complex **4**.
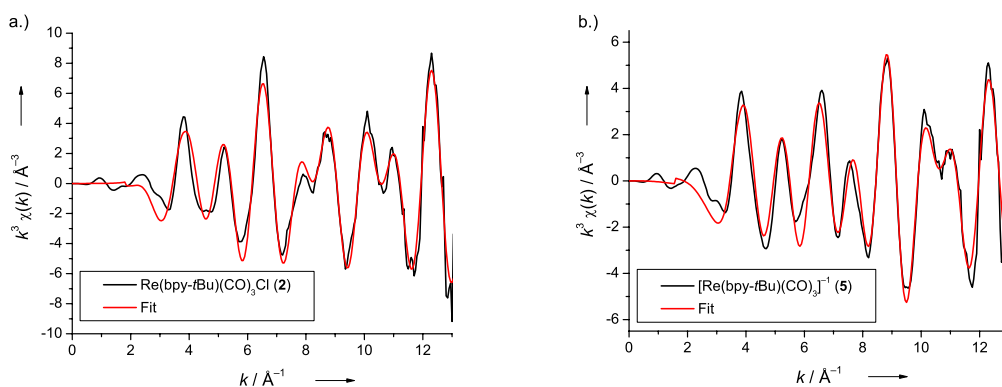
Figure 2.12 (a) Fourier transformed EXAFS data and fitting in *k*-space for complex **2**. (b) Fourier transformed EXAFS data and fitting in *k*-space for complex **5**.
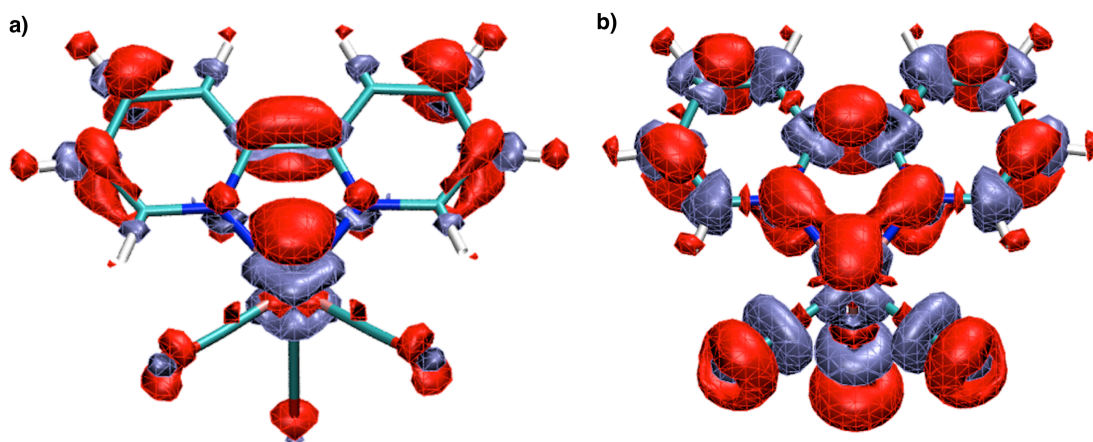
Figure 2.13 Density differences with the anion calculated as (a) the singlet state within unrestricted DFT-B3LYP and (b) an open-shell singlet eigenfunction within ROHF. Isosurface depicts contour values of 0.005; red = increased charge density; purple = decreased charge density. Figures made using VMD.

Table 2.6 Optimized Cartesian coordinates for singlet [Re(bpy)(CO)$_3$]$^-$ (**4**).

Atom	X	Y	Z
Re	-0.2226826703	0.4347675117	0.0000000000
N	1.4330421837	0.1526980111	1.2929674459
N	1.4330421837	0.1526980111	-1.2929674459
C	1.3797439761	0.1509458254	2.6692274033
C	1.3797439761	0.1509458254	-2.6692274033
C	2.4712052230	0.0155464870	3.4843935085
C	2.4712052230	0.0155464870	-3.4843935085
C	3.7680701299	-0.1290330073	2.8946116002
C	3.7680701299	-0.1290330073	-2.8946116002
C	3.8617821112	-0.1250513476	1.5263743943
C	3.8617821112	-0.1250513476	-1.5263743943
C	2.7061652177	0.0137329869	0.7036660302
C	2.7061652177	0.0137329869	-0.7036660302
H	0.3880166301	0.2686547475	3.0911184620
H	0.3880166301	0.2686547475	-3.0911184620
H	2.3369543100	0.0213473299	4.5617929352
H	2.3369543100	0.0213473299	-4.5617929352
H	4.6542952412	-0.2353743984	3.5142647626
H	4.6542952412	-0.2353743984	-3.5142647626
H	4.8319671622	-0.2273818146	1.0501772037
H	4.8319671622	-0.2273818146	-1.0501772037
C	-0.6527858667	2.2785438587	0.0000000000
O	-0.9127823425	3.4266927652	0.0000000000
C	-1.5329972448	0.0548875973	1.3612862823
C	-1.5329972448	0.0548875973	-1.3612862823
O	-2.3012851004	-0.2033072350	2.2139511002
O	-2.3012851004	-0.2033072350	-2.2139511002

Table 2.7 Optimized Cartesian coordinates for triplet [Re(bpy)(CO)₃]⁻.

Atom	X	Y	Z
Re	-0.2995710157	0.3326425460	0.0000000000
N	1.4414976349	0.1598185503	1.3481894758
N	1.4414976349	0.1598185503	-1.3481894758
C	1.3946071570	0.1723715724	2.6881580384
C	1.3946071570	0.1723715724	-2.6881580384
C	2.5125947399	0.0451181649	3.5129860457
C	2.5125947399	0.0451181649	-3.5129860457
C	3.7719851644	-0.1118560802	2.8893057408
C	3.7719851644	-0.1118560802	-2.8893057408
C	3.8515976010	-0.1293058519	1.5128726187
C	3.8515976010	-0.1293058519	-1.5128726187
C	2.6754354990	0.0121101487	0.7122783814
C	2.6754354990	0.0121101487	-0.7122783814
H	0.4051389697	0.2905616980	3.1180864156
H	0.4051389697	0.2905616980	-3.1180864156
H	2.3999318284	0.0689404856	4.5912476587
H	2.3999318284	0.0689404856	-4.5912476587
H	4.6750018692	-0.2187188104	3.4864423119
H	4.6750018692	-0.2187188104	-3.4864423119
H	4.8153877214	-0.2507464748	1.0314385246
H	4.8153877214	-0.2507464748	-1.0314385246
C	-0.5178833860	2.2275938854	0.0000000000
O	-0.8217562773	3.3677240732	0.0000000000
C	-1.6194660862	0.0147339606	1.3545906290
C	-1.6194660862	0.0147339606	-1.3545906290
O	-2.4012723591	-0.1893403656	2.2127988738
O	-2.4012723591	-0.1893403656	-2.2127988738

Chapter 3

Direct observation of the reduction of carbon dioxide by rhenium bipyridine tricarbonyl catalysts utilizing stopped-flow IR spectroscopy.

3.1 Introduction

In order to optimize carbon dioxide (CO_2) reduction catalysts for eventual scale up and industrial use, efforts must be made to understand the mechanism of CO_2 reduction. Of the systems that electrocatalytically reduce CO_2, the Re(bpy-R)(CO)$_3$Cl (bpy-R = 4,4′-disubstituted-2,2′-bipyridine) catalyst family, first introduced by Lehn in coworkers, in the 1980s, is one of the most robust and well-characterized systems known to date.[1-13] This system converts CO_2 to carbon monoxide (CO) with high rates and selectivities; it suffers, however, from large overpotentials.

A proposed catalytic mechanism for the reaction of $Re(bpy-R)(CO)_3X$ with CO_2 is shown in Figure 3.1. Here, two sequential one-electron reductions lead to the catalytically-active state, $[Re(bpy-R)(CO)_3]^-$, which then can interact with CO_2 to form an η^1-bound CO_2 adduct at the Re center. Upon protonation of this proposed CO_2 adduct, a $Re–CO_2H$ species can form, followed by loss of H_2O and formation of a Re tetracarbonyl complex. Release of CO can occur upon further reduction,[14] regenerating the catalytically-active state. The steps leading up to the catalytically-active state are supported by many reports;[2,5,7-8,15-19] however, none of the aforementioned catalytic intermediates have ever been observed. Multiple studies on the effect of weak Brønsted acids on catalysis indicate that protons (H^+) are involved in the rate-determining step.[10,15] Hamnett suggested a $Re–CO_2H$ species as an intermediate in the electrocatalytic reduction of CO_2 by $Re(dmbpy)(CO)_3Cl$ (dmbpy = 4,4′-dimethyl-2,2′-bipyridine), but IR spectral data showed multiple bands in the carboxyl region. Therefore, identification of the intermediate was not demonstrated.[19] Both $[Re(bpy-R)(CO)_4](OTf)$ and $Re(bpy-R)(CO)_3(CO_2H)$ have been synthesized previously in relation to CO_2 reduction catalysis.[14,20-22] However, *in situ* identification of these species in catalytic context has never been achieved.
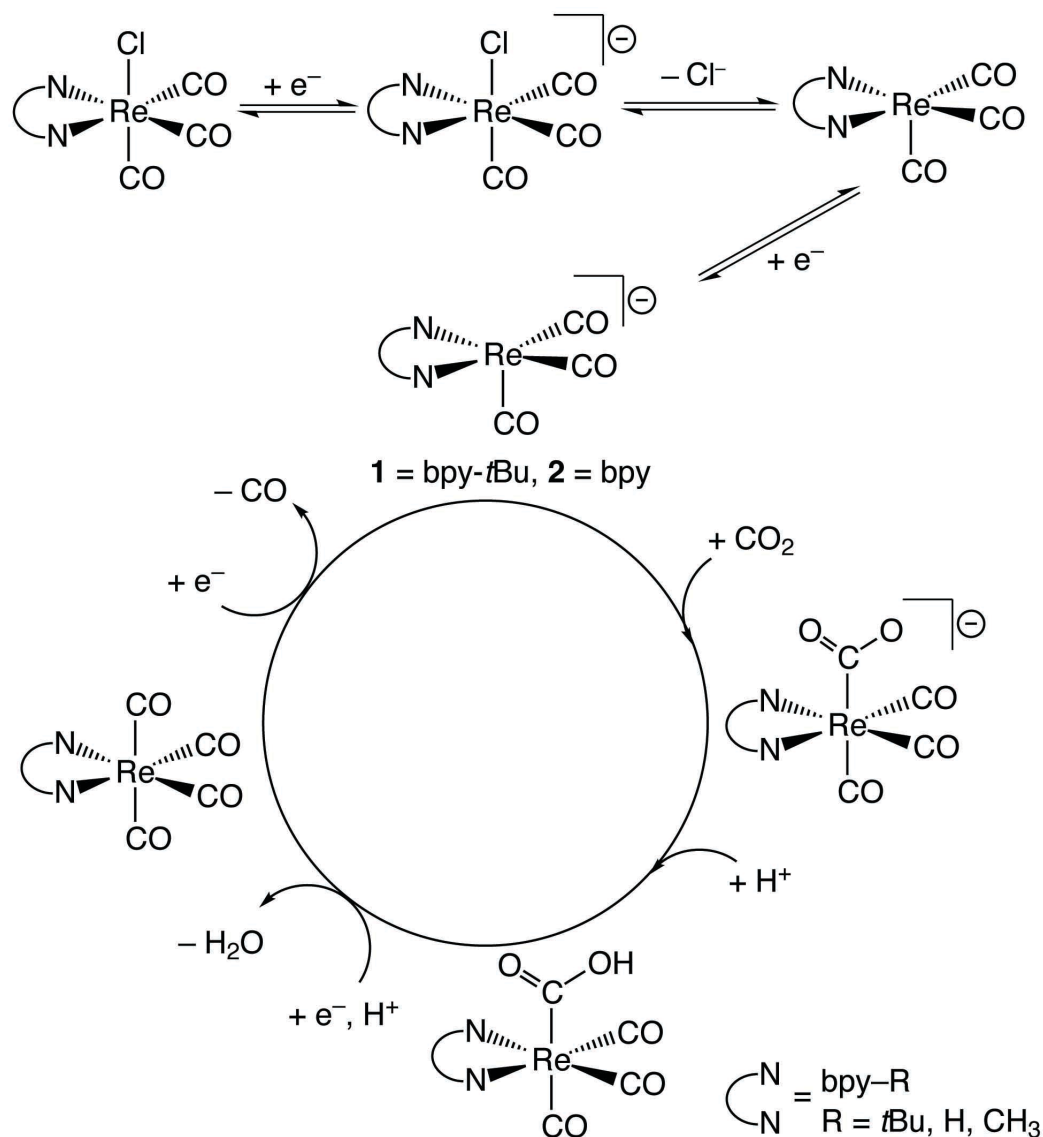
Figure 3.1 Proposed electrocatalytic mechanism for Re(bpy–R)(CO)$_3$Cl with CO$_2$.

Insights into the mechanism of this catalyst family are essential to provide a route to directed modification of the catalytic framework in order to improve activity and stability. Many approaches have been used to understand the kinetics and mechanism of these rhenium catalysts in regards to their reactions with CO$_2$, including electrochemical studies,[1-4,8,10,16,23-24] X-ray crystallographic studies,[6,15,17] X-ray

Absorption Spectroscopy studies,[18] and theory.[25-26] One approach that has not been explored significantly is the direct observation of the reaction of these catalytically-active complexes with CO_2 by stopped-flow mixing.[15]

Stopped-flow mixing is a technique used for studying fast chemical reactions in solution over timescales from one millisecond up to hundreds of seconds. In general, two reagents are rapidly mixed and steady state flow is then 'stopped' in an observation cell. Reagent concentrations and formation of products are monitored as a function of time, usually as a fluorescence signal[27] or by the change in the absorbance at a specific wavelength.[28-32] Analysis of the resulting kinetic data can determine reaction rate constants, complexity of the reaction mechanisms, and information on short-lived reaction intermediates. In addition, a series of stopped-flow experiments can be used to show the effect of parameters such as temperature,[33] pH,[34] and reagent concentration[35] on the kinetics of reactions. The application of stopped-flow mixing in studying the reaction kinetics of active catalyst species and their substrates is not well developed. We recently reported stopped-flow UV-Vis spectroscopy studies on the catalytically-active species **1**. These studies concluded that the rate of reaction of **1** is ~35 times faster with CO_2 than with weak acids.[15]

The catalytically-active species **1** and **2** can be isolated by chemical reduction of $Re(bpy-R)(CO)_3Cl$ with potassium intercalated graphite (KC_8) in tetrahydrofuran (THF),[15,17,36] making this catalyst ideal for study by stopped-flow spectroscopy. The strongly infrared-absorbing carbonyl groups on rhenium, with vibrational energies that are sensitive to local charge density make stopped-flow IR spectroscopy an

informative method for studying kinetics and intermediates formed in reactions with CO_2.

Herein we report the stopped-flow IR spectroscopy studies on the reactions between CO_2 and the two catalytically-active species, **1** and **2**, which provides the first *in situ* observation of the CO_2 reduction product, gives insight into the catalytic mechanism, and allows us to measure the kinetics of these reactions. Evidence for this CO_2 reduction product includes isotopic labeling studies, stopped-flow experiments of the kinetics of its formation in the presence of proton sources, comparison with genuine $Re(bpy)(CO)_3(CO_2H)$ (**2-CO₂H**), and DFT calculations. Kinetic analyses were performed by tracking the absorbance of $\nu(CO)$ stretches over time in these reactions. This work represents a new use for stopped-flow mixing that enables product and intermediate identification and kinetic comparison of the reaction between catalysts and CO_2 at various concentrations. Furthering mechanistic understanding of catalysts will help further efforts in synthesis and catalysis, with the goal of attaining a catalytic system capable of implementation on an industrial scale.

3.2   Results and Discussion

The solution-phase IR stretching frequencies from the carbonyl ligands of **1** (in THF) consist of two strong ν_{CO} stretches at 1940 and 1832 cm^{-1}. Complex **2** has a very similar IR spectrum, with ν_{CO} stretches at 1940 and 1840 cm^{-1} (see Experimental section). Catalytically-active species **1** reacts with CO_2, yielding an IR spectrum that resembles that of a Re(I) product (Figure 3.2). The spectrum of this octahedral Re(I)

product (pseudo C_{3v} symmetry) has one high energy ν_{CO} stretch at 2001 cm^{-1} and one stretch at 1901 cm^{-1}. For comparison, the IR spectrum of the Re(I) starting material, Re(bpy-tBu)(CO)$_3$Cl, is shown in Figure 3.10. Complex **2** reacts with CO_2 in a similar fashion as **1**, aside from formation of the Re(0) dimer, [Re(bpy)(CO)$_3$]$_2$, a known degradation pathway for the Re(bpy)(CO)$_3$Cl family of catalysts (see Experimental section, Figure 3.11).[5,17] Dimer formation is not observed as a product for the reactions of **1** with CO_2, indicating that the tBu groups at the 4,4'-positions of the bpy ligand provide sufficient steric hindrances and/or electronic differences to eliminate this degradation pathway. The presence of this degradation pathway, as well as other factors, helps explain the observed reduce rates of electrocatalysis for **2** as compared to **1**.[16] In each reaction, no additional species between the starting anionic complexes and the oxidized products are observed. Therefore, we classify these reactions as fast, net two-electron oxidative additions of CO_2 to the metal centers.

In addition to the ν_{CO} stretches associated with the fully oxidized species, reactions with CO_2 result in the emergence of two weaker IR stretches at 1662 cm^{-1} and 1616 cm^{-1} (Figure 3.2). These ν_{OCO} stretches indicate an η^1-bound CO_2 adduct at the Re center and are consistent with previously reported M–CO$_2$H complexes (M = Re, Ir, Ru, Pt).[21,37-42] We did not detect free CO in solution from these reactions, indicating that these reactions stop at a Re–CO$_2^-$ or Re–CO$_2$H intermediate in the catalytic cycle. In order to confirm that the stretches at 1662 cm^{-1} and 1616 cm^{-1} for **1** are features resulting from the CO_2 substrate, we repeated the stopped-flow reactions using $^{13}CO_2$. The reaction of **1** with $^{13}CO_2$ resulted in a shift in energy of the two ν_{OCO}

stretches from 1662 and 1616 cm^{-1} to 1608 and 1577 cm^{-1}, corresponding to a shift of ~54 cm^{-1} and ~39 cm^{-1}, respectively (Figure 3.3). The shifts in energy for these two weak stretches indicate that these features in the IR develop directly from the starting CO_2 substrate. The shift in the free CO_2 peak at 2333 to 2272 cm^{-1} is shown in Figure 3.12.
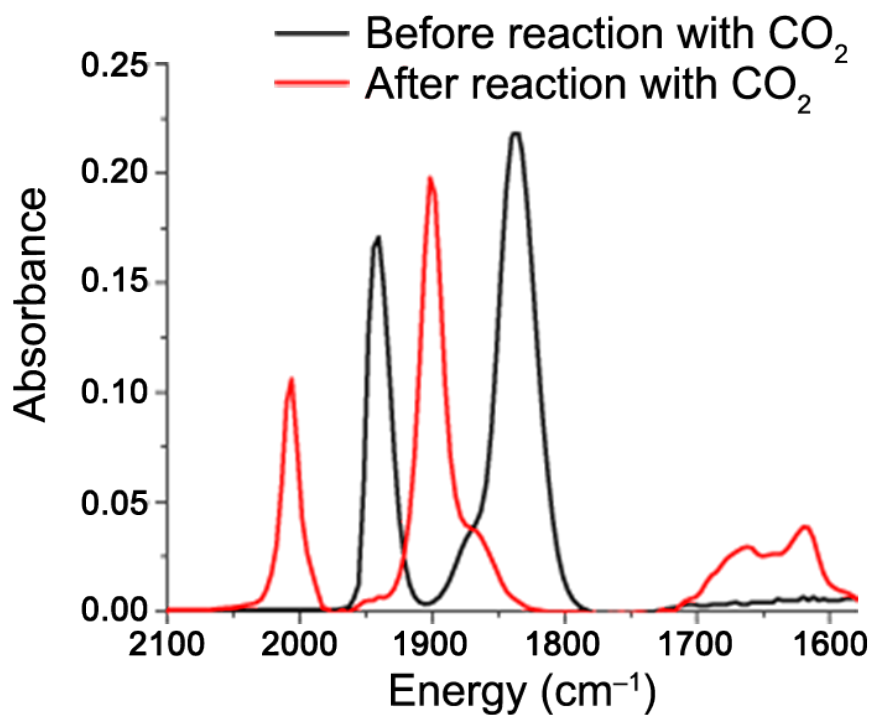
Figure 3.2 IR spectra of **1** before reaction with CO_2 (black) and after reaction with CO_2 (red).
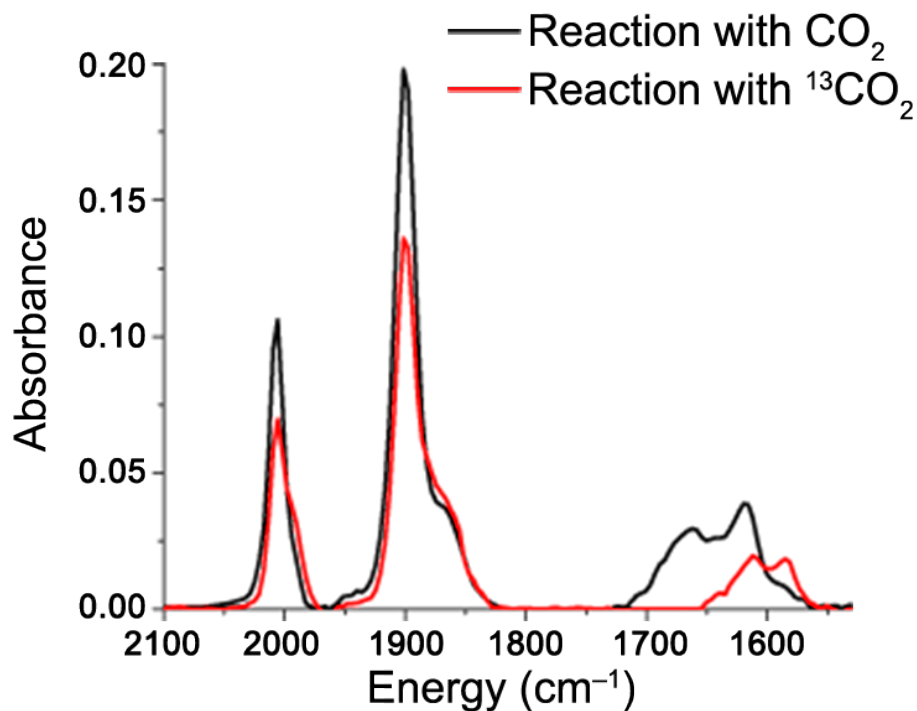
Figure 3.3 IR spectra of **1** after reaction with CO_2 (black) and after reaction with $^{13}CO_2$ (red), showing a shift of the two weaker ν_{OCO} stretches from 1662 and 1616 cm^{-1} to 1608 and 1577 cm^{-1}, respectively.

Stopped-flow experiments with added methanol (MeOH) were required to prove the formation of a Re–CO_2H complex, rather than a Re–CO_2^- complex. Reactions with 2.5 mM **1**, 25 mM CO_2, and *ca.* 0–200 mM MeOH show increased growth of the stretches at 1662 and 1616 cm^{-1} with increasing [MeOH], as shown by kinetic traces of the 1616 cm^{-1} mode in Figure 3.4. Providing an increased concentration of H^+ source (i.e. MeOH) results in more rapid formation of ν_{OCO} stretches, indicating that formation of the final product is H^+ dependent. Additionally, protonation of this Re–CO_2 adduct is observed to be facile, even in the absence of added MeOH. Since protons are involved in the rate-determining step of catalysis,[10,15] a second protonation step in the catalytic cycle is the rate-determining step. We also

performed experiments with added H_2O (see Experimental section, Figure 3.13) and plan to use other proton sources in future studies to probe the dependence of the formation of the Re–CO_2H species at a range of pH values.
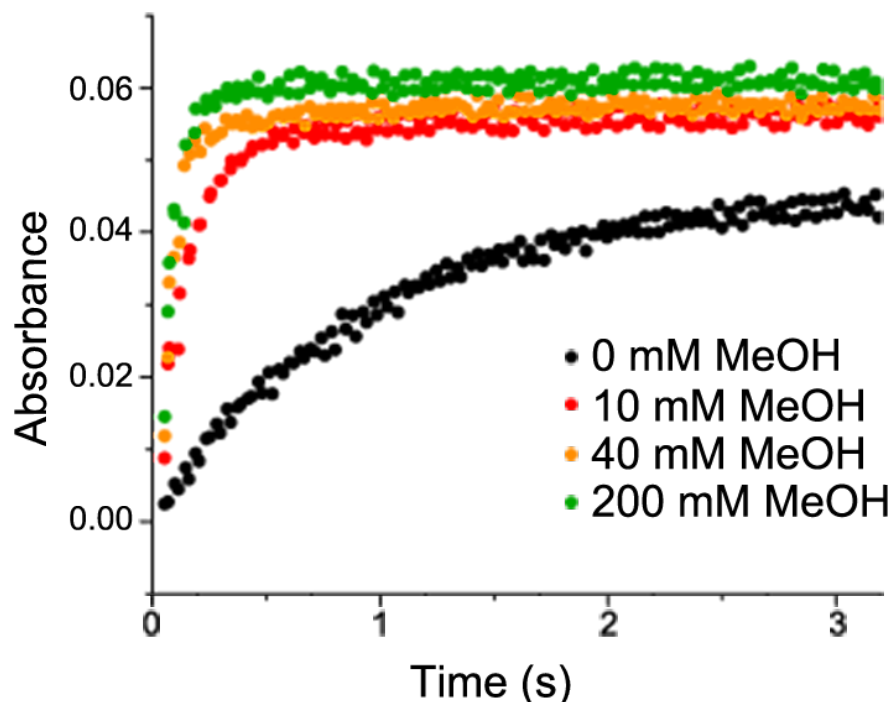
Figure 3.4 Growth of the ν_{OCO} stretch at 1616 cm^{-1} as a function of time for the reaction of 2.5 mM **1** with 25 mM CO_2 with the addition of various concentrations of MeOH.

To gain further validation of this Re(I)–CO_2H product, we synthesized **2-CO₂H** in analogous fashion to Gibson's Re(dmbpy)(CO)₃(CO_2H), by reaction of [Re(bpy)(CO)₄](OTf) with aqueous KOH.[21] **2-CO₂H** was characterized by ^1H NMR spectroscopy, IR spectroscopy, and elemental analysis. The IR spectrum of **2-CO₂H** in THF is very similar to the IR spectra of the products of the reactions of **1** and **2** with CO_2, with IR stretches at 2008, 1902, 1617, and a weaker, broad feature at ~1650 cm^{-1} (Figure 3.14–3.15). In order to more closely mimic the conditions in the stopped-flow

reactions, we added potassium hexafluorophosphate (KPF$_6$) to a THF solution of **2-CO$_2$H**. KPF$_6$ was added to mimic the K$^+$ present from the chemical reductions to form **1** and **2**. The IR spectrum of **2-CO$_2$H** with KPF$_6$ more closely resembles the products in the stopped-flow reactions, with a distinct feature at ~1643 cm^{-1}, in addition to the IR stretches at 2008, 1902, and 1617 cm^{-1} (Figure 3.5). We believe that K$^+$ ions can interact and partially coordinate to the Re–CO$_2$H adduct, causing equilibrium between two or more ν_{OCO} stretches. K$^+$ ions present from the chemical reduction to form **1** and **2** likely interact with the stopped-flow product in this fashion (Figure 3.30). Due to the stability of **2-CO$_2$H**, the rate-determining step in the catalytic mechanism (the second protonation step) likely occurs after further electron transfer.
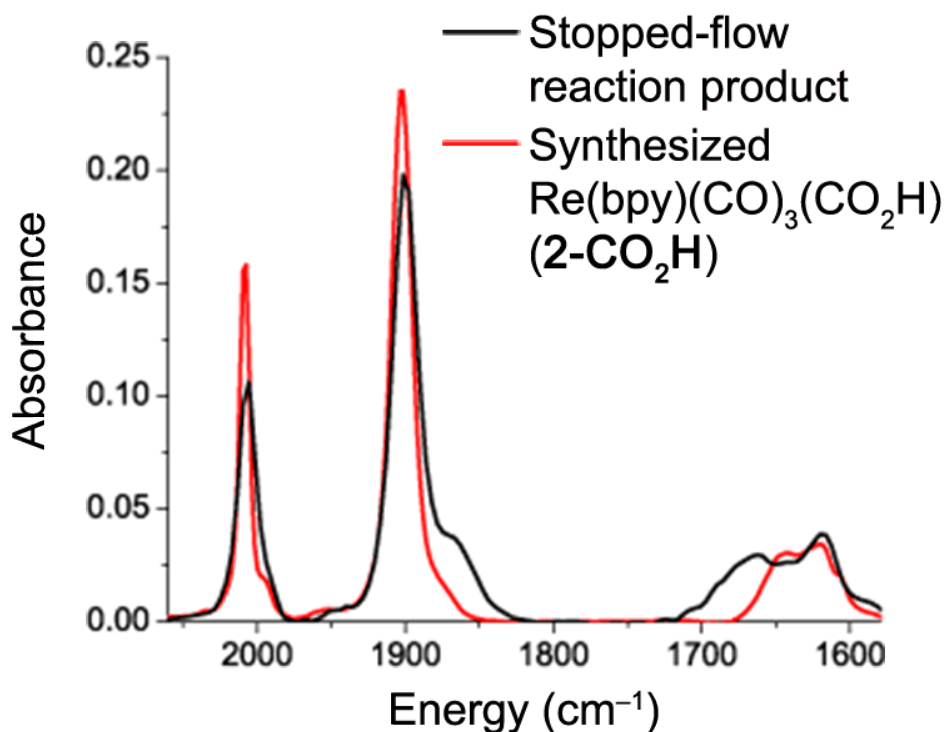
Figure 3.5 Comparison of the IR spectrum of **1** after reaction with CO_2 in stopped-flow experiments (black) and of the IR spectrum of synthesized **2-CO$_2$H** with KPF_6 in THF (red).

^{13}C NMR experiments of the product of the reaction between **1** and $^{13}CO_2$ are consistent with a Re–CO$_2$H species (Figure 3.31). We have identified the ^{13}C NMR chemical shift for the –CO$_2$H group as 161.61 ppm. The other chemical shifts in the ^{13}C NMR spectrum of this reaction product agree very well with the ^{13}C NMR spectra of **2-CO$_2$H** and of Gibson's Re(dmbpy)(CO)$_3$(CO$_2$H).[21]

DFT-calculated IR frequencies of gas-phase Re(bpy-tBu)(CO)$_3$(CO$_2$H) (**1-CO$_2$H**) and **2-CO$_2$H** closely match those of the products of these stopped-flow reactions (Tables 1 and S1). DFT-calculated **1-CO$_2$H** has two v_{CO} stretches at 1992 and 1920 cm^{-1}, as well as a v_{OCO} stretch at 1617 cm^{-1}. DFT-calculated **2-CO$_2$H** has similar IR stretches in this region at 1997, 1926, 1616 cm^{-1} (Table S1). DFT was used

to calculate gas-phase $[Re(bpy-R)(CO)_3(CO_2)]^-$ and $[Re(bpy-R)(CO)_3(CO_2)][K]$ (where R = tBu or H); however, these species have ν_{OCO} stretches that do not agree with stretches seen in our stopped-flow reactions, further supporting the identity of our Re–CO$_2$H product (see Experimental section). Isotopic shifts seen in stopped-flow reactions match with DFT-calculated shifts as well. DFT-calculated Re(bpy-tBu)(CO)$_3$(^{13}CO$_2$H) results in a 40 cm^{-1} shift of the ν_{OCO} stretch from 1619 to 1579 cm^{-1}. This closely matches the shift seen in the stopped-flow reactions, where the low energy ν_{OCO} stretch shifts by 39 cm^{-1}, from 1616 to 1577 cm^{-1}.

Table 3.1 IR stretching frequencies of the stopped-flow reaction product **1-CO₂H**, of synthesized **2-CO₂H**, and of DFT-calculated gas-phase **1-CO₂H**.

Complex	IR stretching frequencies (cm^{-1})
Stopped-flow **1-CO₂H**	2001, 1901, 1662, 1616
Synthesized **2-CO₂H**	2008, 1902, 1643, 1617
DFT-calculated **1-CO₂H**	1992, 1920, 1617

3D plots of the stopped-flow reactions with CO$_2$ are shown in Figure 3.6 and 3.15 for **1** and **2**, respectively. The decay of the ν_{CO} stretches at 1832 cm^{-1} for **1** and 1840 cm^{-1} for **2** were used for kinetic analysis. The increase in reaction rate as a function of [CO$_2$] can be determined by monitoring the decay of the ν_{CO} stretch. Figure 3.7 shows kinetic traces of the decay of the low energy ν_{CO} stretch for each reaction. The decays of the peaks at 1940 cm^{-1}, as well as the growths of the peaks at 1901 cm^{-1} and 2001/2009 cm^{-1}, are shown in Figure 3.17–3.19 for both **1** and **2**. The growths of the ν_{OCO} stretches at 1608 and 1662 cm^{-1} for **1** are shown in Figure 3.20. The ν_{CO} stretches at 1940 and 1832 cm^{-1} decay with very similar rates to the growths

of the ν_{CO} stretches at 2001 and 1901 cm^{-1} and to the growths of the ν_{OCO} stretches at

1662 and 1616 cm^{-1} (Figure 3.21).
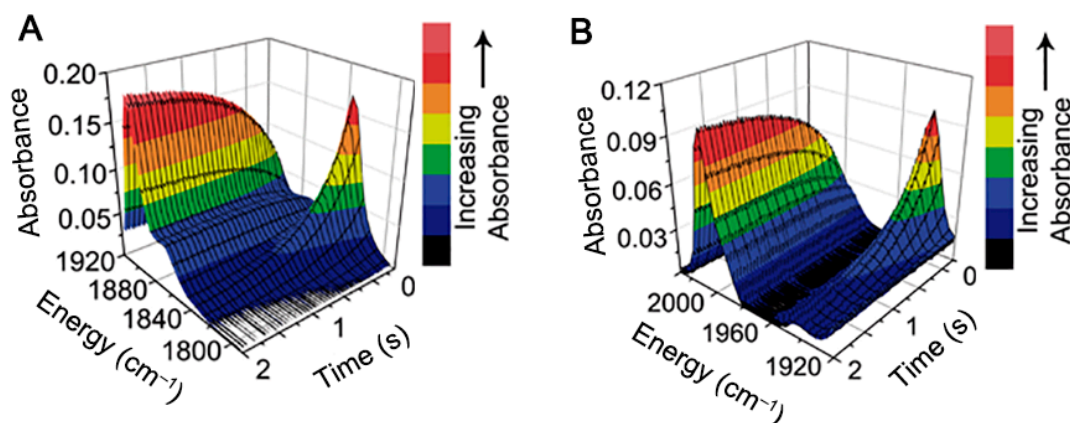
Figure 3.6 Reaction of 2.5 mM **1** with 32 mM CO_2: (a) 3D plot of the reaction showing the decay of the ν_{CO} stretch at 1832 cm^{-1} and the growth of the ν_{CO} stretch at 1901 cm^{-1}; (b) 3D plot of the reaction showing the decay of the ν_{CO} stretch at 1940 cm^{-1} and the growth of the ν_{CO} stretch at 2001 cm^{-1}.
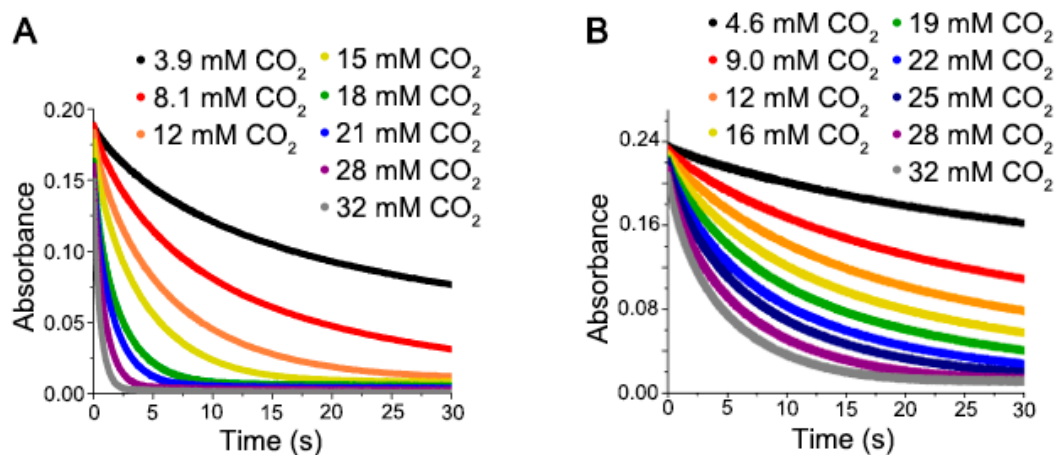
Figure 3.7 Reaction of 2.5 mM 1 or 2 with various concentrations of CO_2: (a) decays of the ν_{CO} stretch at 1832 cm^{-1} as a function of time for the reaction of **1** with CO_2; (b) decays of the ν_{CO} stretch at 1840 cm^{-1} as a function of time for the reaction of **2** with CO_2.

Pseudo-first order kinetic analysis was performed for both complexes at

various CO_2 concentrations in order to compare the reaction rate constants (Figure

3.22–3.23, Table 3.3). Pseudo-first order kinetic curves were fit through a minimum of two half-lives for each run. Plots of k_{obs} vs. $[CO_2]$ (for $[CO_2] \geq 15$ mM) were used to calculate second order rate constants for each complex (Figure 3.24). In electrochemical experiments, $[CO_2]$ is typically in greater than 40-fold excess to [Re]. Since we are most interested in stopped-flow reaction conditions that correlate to these electrochemical experiments, we have included only reactions that correspond to pseudo-first order reaction conditions for kinetic analysis. We note that the kinetics of these stopped-flow reactions are more complicated than assumed here. However, we feel this simplified analysis is justified for comparison purposes between complexes **1** and **2** and between stopped-flow reactions and electrochemical experiments. More complex reaction kinetics result from various side reactions, such as dimer formation, reaction of **1** or **2** with oxidized species, and/or reaction of **1** or **2** with protons.

At equal concentrations of anions **1** and **2** (2.5 mM), **1** reacts 10 times faster than **2**, with rate constants (k_{CO2}) of 120 ± 20 $M^{-1}s^{-1}$ and 12 ± 1.5 $M^{-1}s^{-1}$, respectively. This relative difference is comparable to previously observed differences between rate constants in electrocatalysis of the two catalysts (10,000 $M^{-1}s^{-1}$ for **1** compared to 1,000 $M^{-1}s^{-1}$ for **2**).[16,43] We note that the rate constants in these stopped-flow experiments are significantly slower than the rate constants determined from electrocatalysis (80 $M^{-1}s^{-1}$ vs. 10,000 $M^{-1}s^{-1}$ for **1**). A possible reason for this discrepancy is the presence of 18-crown-6 from the reduction reaction to form complexes **1** and **2**. 18-crown-6 is added in order to encapsulate the potassium ion and inhibit its coordination to the carbonyls of the anions.[15,17] In the X-ray crystal structure

of **1** and **2**,[15,17] the 18-crown-6 resides near the rhenium center, and if the same is true in solution, the 18-crown-6 could act as a steric shield to the incoming CO_2 substrate.

Removing 18-crown-6 from solution in the reductions to form complexes **1** and **2** (IR spectra in Figure 3.25) and repeating stopped-flow reactions results in significantly increased reaction rates. The decay of the ν_{CO} stretches at 1832 and 1840 cm^{-1} for **1** and **2**, respectively, are shown in Figure 3.26. Pseudo-first order kinetic analysis was performed for complex **2** without 18-crown-6 at the two lowest CO_2 concentrations (0.75 mM and 1.4 mM) to obtain reaction rate constants (Figure 3.27, Table 3.4). At 2.5 mM **2** without 18-crown-6 an average k_{CO2} of 1,500 $M^{-1}s^{-1}$ was obtained (compared to 8 $M^{-1}s^{-1}$ for **2** with 18-crown-6), i.e. over 120 times faster than for **2** with 18-crown-6. This result is in much better agreement with the rate constant for **2** determined via electrocatalysis (1,000 $M^{-1}s^{-1}$). The reaction of **2** with CO_2 without 18-crown-6 in solution is first order in $[CO_2]$, in agreement with both electrochemical experiments and reactions with added 18-crown-6. Increasing $[CO_2]$ by 2-fold results in approximately a 2-fold increase in the observed rate constant (k_{obs}) (Figure 3.27). For complex **1**, removal of 18-crown-6 increased reaction rates to such an extent that the decays of the starting material ν_{CO} stretches were difficult to observe (Figure 3.26a). We have estimated the rate constant for the reaction of **1** without 18-crown-6 to be 15,000 $M^{-1}s^{-1}$ (see Experimental section), which is in good agreement with the rate constant in electrocatalysis for **1** (k_{CO2} = 10,000 $M^{-1}s^{-1}$).

3.3   Conclusions

Through the use of rapid scan FTIR spectroscopy and stopped-flow mixing, we were able to observe the CO_2 reduction product, further elucidate the mechanism, and measure the kinetics of the reactions between catalytically-active species, [Re(bpy-*t*Bu)(CO)$_3$]$^-$ (**1**) or [Re(bpy)(CO)$_3$]$^-$ (**2**), and CO_2. With 18-crown-6 in solution, anion **1** reacts ten times faster than anion **2** (k_{CO2} = 120 M^{-1}s^{-1} and k_{CO2} = 12 M^{-1}s^{-1}, respectively). Removing 18-crown-6 from solution increases reaction rate constants by over 120-fold, leading to a rate constant of 1,500 M^{-1}s^{-1} for the reaction of **2** with CO_2, which is in good agreement with rates derived from electrocatalysis experiments.

We observe a higher rate constant for the reaction **1** with CO_2 as compared to the reaction **2** with CO_2 due to several differences in these two catalysts. In both stopped-flow reactions and electrochemical experiments, we see no evidence of dimerization with **1**; whereas with the reaction of **2** with CO_2 in stopped-flow reactions, we see formation of Re(0) dimer concurrent with formation of **2-CO$_2$H**. The absence of this degradation pathway helps explain the observed higher rates of electrocatalysis for **1** as compared to **2**.[16] Additionally, the *t*Bu groups on catalytically-active complex **1** cause this catalyst to operate at a more negative potential than **2**, which provides more driving force for catalysis.

Both reactions result in the formation of Re(I) products, with no observable, additional species forming between the anionic Re starting materials and the Re(I) products. The growth of ν_{OCO} stretches at 1662 and 1616 cm^{-1} is characteristic of a Re–CO$_2$H species. Stopped-flow reaction kinetics, isotopic labeling with $^{13}CO_2$,

proton dependence of the ν_{OCO} stretches at 1616 and 1662 cm^{-1}, and agreement between the stopped-flow reaction product and independently, chemically synthesized Re(bpy)(CO)$_3$(CO$_2$H) (**2-CO$_2$H**) have confirmed the product of the stopped-flow reactions as Re(bpy-R)(CO)$_3$(CO$_2$H). These data also lead to the following mechanism: CO$_2$ binds to the catalytically-active complex in a two-electron oxidative addition of CO$_2$ to the Re center, and this Re–CO$_2$ adduct is immediately protonated to form a Re–CO$_2$H species. Further experiments are planned to understand this Re–CO$_2$H species in more detail, including its reactivity.

Previous electrochemical studies indicate that protons are involved in the rate-limiting step of catalysis. These stopped-flow reactions prove that protonation of a Re–CO$_2$ adduct is facile and occurs rapidly even in reactions without added proton sources. Therefore, a second step involving protons, after formation of Re–CO$_2$H, is the rate-limiting step, likely protonation to release H$_2$O and form a tetracarbonyl species. This step likely occurs after further electron transfer due to the stability of the Re–CO$_2$H species, which explains why formation of a tetracarbonyl species and/or release of CO is not observed in the stopped-flow reactions.

This study provides the first *in situ* observation of the CO$_2$ reduction product between catalytically-active Re bpy complexes and CO$_2$. This use of stopped-flow IR spectroscopy is an exciting example of analyzing catalytically-relevant reactions to gain insight into their reaction mechanisms and kinetics. Understanding the mechanisms of these catalysts will help further efforts in synthesis and catalysis, with

the goal of attaining a catalytic system capable of implementation on an industrial scale.

3.4   Experimental

General Considerations. Complex **1** and **2**, as well as the Re(I) starting materials, Re(bpy)(CO)$_3$Cl and Re(bpy-tBu)(CO)$_3$Cl, were prepared by previously reported methods.[15-17] KC$_8$ was prepared by literature procedures.[44] THF was sparged with argon and dried over basic alumina with a custom dry solvent system before storing over activated 3 Å molecular sieves. All other chemicals were purchased from commercial sources and used as received. CO$_2$ solutions of THF were prepared by sparging THF with dry CO$_2$ for 15 minutes, followed by 1:1 dilution of the saturated solution (*ca.* 0.2 M) with THF to prevent cavitation within the stopped-flow unit. ^{13}CO$_2$ solutions of THF were prepared by evacuating a Schlenk flask, filling the Schlenk flask with ^{13}CO$_2$, and then adding THF to this ^{13}CO$_2$-filled flask. NMR spectra were recorded on either a Jeol or Varian 500 MHz spectrometer at 298 K. ^{1}H and ^{13}C chemical shifts are reported relative to TMS ($\delta = 0$) and referenced against solvent residual peaks. Microanalyses were performed by Midwest Microlab, LLC (Indianapolis, IN) for C, H, N.

Stopped-flow IR Spectroscopy. A Biologic SFM-400 stopped-flow apparatus with four syringes and multiple mixing capabilities was used for rapid mixing with a Biologic IR observation head (mixing schematic in Figure 3.8). The stopped-flow apparatus and IR observation head were flushed with nitrogen for 10 minutes prior to

running a group of experiments. In a typical experiment, syringe 4 was filled with a solution of 5 mM **1** or **2** in THF, syringe 2 and 3 were filled with THF, and syringe 1 was filled with a solution of *ca*. 0.1 M CO_2 in THF. For experiments with MeOH, syringe 2 was filled with *ca.* 0.2–0.8 M MeOH in THF.

In order to control the final concentration of CO_2 in the FT-IR observation head, the CO_2-containing solution was mixed with THF (at mixer 1 or 2) before final mixing with solutions of **1** or **2** (at mixer 3). This pre-mixing of the CO_2 solution allowed for control of the final CO_2 concentration from *ca.* 1–50 mM. Since the original concentration of CO_2 was not known precisely, the absorbance of the CO_2 peak after each mixing injection of the stopped-flow apparatus, along with the extinction coefficient for CO_2 in the IR (1300 $M^{-1}cm^{-1}$ at 2342 cm^{-1}),[45] was used to calculate the concentration of CO_2 in each run.

The observation head and stopped-flow apparatus were separated by an umbilical of approximately 18 inches that allowed for conformational flexibility. The final mixing event between the Re anions (**1** and **2**) and the CO_2 solution, however, occurred at the observation head after the solutions had traveled through the umbilical. The observation head contains two ports, an inlet and outlet, allowing for flow of substrates through the small-volume mixing chamber created by a 0.2 mm PTFE spacer between two calcium fluoride windows. A schematic of the observation head can be found in Figure 3.9. No hard stop was used in these experiments, but a 50 mL syringe was attached to the waste port on the observation head to provide some

resistance for improved stopping characteristics. The temperature of mixing was recorded to be 27 °C and was constant throughout all experiments.

FT-IR Spectra Collection. Rapid scan infrared transmission spectra were collected in double-sided forward-backward mode using a Bruker Vertex 80v equipped with a liquid nitrogen-cooled MCT detector and a 4000 cm^{-1} low-pass filter. During measurement, the interferometer compartment was evacuated and the sample compartment was purged with dry nitrogen. In order to obtain quantitative kinetic data, stopped-flow mixing was synchronized with the forward motion of the traveling mirror of the interferometer. The output trigger of the Bruker spectrometer, which signals the start of the forward mirror motion, was input to a BNC Model 575 pulse delay generator that was programmed to account for the delayed response of the Biologic Stopped-Flow mixing unit, the total time of the pushing phase, and the period of oscillation of the traveling mirror of the interferometer. The shot-to-shot jitter was determined to be approximately ±2 ms by monitoring all synchronization pulses with a Tektronix DPO 4054 Digital Phosphor Oscilloscope. After splitting interferograms, this method provided a full spectrum approximately every 11.4 ms at 8 cm^{-1} resolution. Background solvent spectra were obtained by flushing the IR observation head with THF from syringe 2 or 3 immediately prior to stopped-flow kinetic measurements. All data were converted to absolute absorbance from percent transmission for the purposes of plotting and fitting kinetics. Data were collected and manipulated using OPUS 6.5. For IR data without stopped-flow mixing, IR spectra were collected on a Thermo Scientific Nicolet 6700 spectrometer.

Reaction of [Re(bpy)(CO)$_3$]$^-$ (2) with CO$_2$. A comparison of the IR spectrum of Re(bpy-tBu)(CO)$_3$Cl and the product of the stopped-flow reaction between **1** and CO$_2$ is shown in Figure 3.10. Complex **2** reacts with CO$_2$, yielding an IR spectrum that indicates the presence of two products (Figure 3.11). The ν_{CO} stretches at 2009 and 1901 cm^{-1} are consistent with a Re(I) product which is similar to that observed in the reaction of **1** with CO$_2$. The ν_{CO} stretches at 1986, 1948, 1886, and 1867 cm^{-1} match precisely with those reported for the [Re(bpy)(CO)$_3$]$_2$ dimer.[5,17] For complex **2**, no appreciable formation of intermediates before formation of the fully oxidized species and the Re(0) dimer was observed. This Re(0) dimer has been proposed as a degradation pathway for the Re(bpy)(CO)$_3$Cl family of catalysts.[17] Additionally, the [Re(bpy)(CO)$_3$]$_2$ dimer could form upon oxidation of anion **2** by the Re(I) product. Dimer formation is not observed as a product of the reactions of **1** with CO$_2$, suggesting that the tBu groups at the 4,4'-positions of the bpy ligand provide sufficient steric hindrances and/or electronic differences to eliminate this degradation pathway. The presence of this degradation pathway, as well as other factors, helps explain the observed reduced rates of electrocatalysis for **2** as compared to **1**.[16]

In both these reactions of **2** and in reactions of **1**, no additional species between the starting anionic complexes and the oxidized products are observed. Therefore, we classify these reactions as fast, net two-electron oxidative additions of CO$_2$ to the metal centers. It is possible that intermediate species do form, but are fleeting and only accumulate in very small concentrations due to fast conversion to the final state.

However, this assignment is supported by experiments with higher concentrations of starting material (15 mM **1** or **2**), which also show no intermediate species.

Isotopic Labeling Experiments. Reactions with $^{13}CO_2$ were performed nearly identically to the reactions with unlabeled CO_2, and the stopped-flow mixing schematic was the same as shown in Figure 3.8. However, due to a limited supply of $^{13}CO_2$, it was not possible to sparge THF for a significant amount of time. Nevertheless, we were successful in dissolving *ca.* 80 mM $^{13}CO_2$ in solution (as calculated from the extinction coefficient for CO_2 in the IR, 1300 $M^{-1}cm^{-1}$) (Figure 3.12). Here, the $^{13}CO_2$ peak can be seen at 2272 cm^{-1}, as compared to 2333 cm^{-1} for unlabeled CO_2 (a shift of ~61 cm^{-1}).

Experiments with Added H^+. In addition to reactions with added MeOH, we also performed stopped-flow experiments with added H_2O. These experiments were performed in the same manner as experiments with added MeOH, with 2.5 mM **1**, 25 mM CO_2, and *ca.* 0-200 mM H_2O. Very similar reaction kinetics are observed with added H_2O, very much like the experiments with added MeOH. As shown in Figure 3.13, with added H_2O, the rate of formation of the stopped-flow reaction product increases significantly. Due to this drastic increase, it is very difficult to distinguish differences in the dependence of these IR frequencies with small differences in pK_as of various weak Brønsted acids. In this study, we are limited to weak Brønsted acids with a narrow pK_a range because acids with too high of pK_as will cause Re anions to favor engaging protons over CO_2.

Synthesis of Re(bpy)(CO)₃(CO₂H) (2-CO₂H). Re(bpy)(CO)$_3$(CO$_2$H) was synthesized in analogous fashion to Gibson's Re(dmbpy)(CO)$_3$(CO$_2$H) complex (dmbpy = 4,4'-dimethyl-2,2'-bipyridine), by reaction of [Re(bpy)(CO)$_4$](OTf) with aqueous KOH.[21] [Re(bpy)(CO)$_4$](OTf) was synthesized as previously reported, by reaction of Re(CO)$_5$Cl, silver triflate (AgOTf), and 2,2'-bipyridine in methylene chloride.[20] [Re(bpy)(CO)$_4$](OTf) (100 mg, 0.17 mmol) and KOH (9.3 mg, 0.17 mmol) were stirred at room temperature in water (30 mL), and the mixture became yellow almost immediately. After stirring for 1 h, the yellow precipitate was collected by filtration, washed with water (100 mL), and dried under vacuum overnight to give complex **2-CO₂H**. The reaction was shielded from light during synthesis and isolation. The yield of **2-CO₂H** was 35 mg (43%). ^{1}H NMR (DMSO-d_6): δ 7.72 – 7.62 (m, 2H), 8.26 (t, J = 7.8 Hz, 2H), 8.73 (d, J = 8.1 Hz, 2H), 8.98 (d, J = 5.3 Hz, 2H), 9.10 (s, 1H). ^{13}C NMR (THF-d_8): δ 210.48 (CO), 202.13 (CO), 190.21 (CO), 158.82 (2,2'-bpy), 155.14 (6,6'-bpy), 140.22 (4,4'-bpy), 128.43 (3,3'-bpy), 125.41 (5,5'-bpy). IR (THF) ν_{CO}: 2008 cm^{-1}, 1902 cm^{-1}; ν_{OCO}: 1643 cm^{-1} (m), 1617 cm^{-1} (m). IR (MeCN) ν_{CO}: 2010 cm^{-1}, 1901 cm^{-1}; ν_{OCO}: 1621 cm^{-1} (m), 1162 cm^{-1} (w). Anal. Calcd for **3**, C$_{14}$H$_9$N$_2$O$_5$Re: C, 35.67; H, 1.92; N, 5.94. Found: C, 35.61; H, 1.93; N, 5.84.

Density Functional Theory (DFT) Calculations. DFT calculations were performed with the Amsterdam Density Functional (ADF) program suite (version 2012.01).[46-48] The triple-ζ Slater-type orbital TZ2P basis set was utilized without frozen cores for all atoms. Relativistic effects were included via the zeroth-order regular approximation (ZORA).[49-50] The BP86 functional and the local density

approximation (LDA) of Vosko, Wilk and Nusair (VWN)[51] was coupled with the generalized gradient approximation (GGA) corrections described by Becke[52] and Perdew[53-54] for electron exchange and correlation, respectively. Frequency calculations were performed to verify that the optimized geometries were at minima. Geometry optimized xyz coordinates and a sample input file are included below.

Kinetic Analysis. 3D plots of the stopped-flow reaction of **2** with CO_2 are shown in Figure 3.16. Decays of the ν_{CO} stretches at 1940 cm^{-1} for **1** and **2** are shown in Figure 3.17. Growths of the ν_{CO} stretches at 1901 cm^{-1} for **1** and **2** are shown in Figure 3.18. Growths of the ν_{CO} stretches at 2001 and 2009 cm^{-1} for **1** and **2**, respectively, are shown in Figure 3.19. Growths of the ν_{OCO} stretches at 1616 and 1662 cm^{-1} for **1** are shown in Figure 3.20. The starting ν_{CO} stretches at 1940 and 1832 cm^{-1} decay with very similar rates to the growths of the ν_{CO} stretches at 2001 and 1901 cm^{-1} and to the growths of the ν_{OCO} stretches at 1616 and 1662 cm^{-1} (Figure 3.21).

Pseudo-first order kinetics were fit by plotting the decay of the lowest energy ν_{CO} stretch at 1832 cm^{-1} for **1** and 1840 cm^{-1} for **2** vs. time (Figure 3.22 and 3.23). Pseudo-first order kinetic curves were fit through a minimum of two half-lives for each run at all concentrations of CO_2 studied. Plotting $\ln(A/A_0)$ vs. time gave linear plots through the first two half-lives of the reaction and the slope of the plots gave observed rates in units of s^{-1} for each complex at each CO_2 concentration (Table S1).[55]

Plots of $\ln(A/A_0)$ vs. time gave better fits than plotting either $1/[Re]$ or $[Re]^{1/2}$ vs. time. Second order kinetic analysis was also performed for both complexes at all concentrations of CO_2 studied. This analysis gave the same rates within error as the

pseudo-first order fits, but the agreement between the data and the second order kinetic fits was not as suitable as pseudo-first order kinetic fits. As expected, lower concentrations of CO_2 fit second order kinetics slightly better due to a larger change in $[CO_2]$ over the course of the reaction, while higher concentrations of CO_2 fit pseudo-first order kinetics better. Pseudo-first order kinetic analysis was also completed for the growths of ν_{CO} stretches at 1901 cm^{-1} for complexes **1** and **2**. Rates and half-lives for the growth of these peaks were the same as the decays of ν_{CO} stretches at 1832 and 1840 cm^{-1} (for **1** and **2**, respectively), within experimental error.

We attempted to calculate separate rate constants for the reaction of **2** with CO_2 for the formation of the Re(I) product and for the formation of the dimer, $[Re(bpy)(CO)_3]_2$. For the formation of the Re(I) product, we attempted to fit kinetic data for the growth of the ν_{CO} stretches at 2009 and 1901 cm^{-1}. For the formation of the dimer, we attempted to fit kinetic data for the growth of the ν_{CO} stretches at 1986, 1948, 1886, and 1867 cm^{-1}. However, because most of these ν_{CO} stretches overlap with one another and/or overlap with starting material ν_{CO} stretches, we were unsuccessful in calculating separate rate constants using this analysis.

Plotting pseudo-first order rates (k_{obs}) vs. $[CO_2]$ (for $[CO_2] \geq 15$ mM) gives rise to fairly linear plots and second order rate constants (k_{CO2}) of 120 ± 20 M^{-1}s^{-1} for **1** and 12 ± 1.5 M^{-1}s^{-1} for **2** (Figure 3.24). We believe that including only $[CO_2] \geq 15$ mM is justified because we are most interested in comparing the kinetics and mechanisms of these stopped-flow reactions with electrochemical experiments. In electrochemical experiments, we usually have greater than 40-fold excess of CO_2 to

the catalyst. Electrochemical reactions are also first order in $[CO_2]$;[10] therefore, the kinetics of these stopped-flow reactions (at high $[CO_2]$ to [Re] ratios) tend to agree well with electrochemical experiments.

Experiments Without 18-Crown-6. Stopped-flow IR spectroscopy experiments were repeated after removing 18-crown-6 that was in solution to form anions **1** and **2**. The IR spectra of **1** and **2** without 18-crown-6 in solution are shown in Figure 3.25. The decay of the ν_{CO} stretch at 1832 cm^{-1} for the reaction of **1** with CO_2 without 18-crown-6 in solution is shown in Figure 3.26a. Here, this ν_{CO} stretch had almost entirely decayed at the time of the first data point collection, making it impossible to perform detailed kinetic analysis on these reactions. Although we cannot calculate a rate constant directly through kinetic analysis for the reaction of **1** without 18-crown-6, we can estimate this rate constant at 15,000 M^{-1}s^{-1} by employing both the calculated rate constant for the reaction of **2** without 18-crown-6 (k_{CO2} = 1,500 M^{-1}s^{-1}) and the difference in rate constants for the reactions of **1** and **2** with 18-crown-6 in solution (10-fold). This estimation is valid if the reaction of **1** without 18-crown-6 is approximately 10 times faster than the reaction of **2** without 18-crown-6 (as was true for reactions with 18-crown-6 in solution). This estimate of the rate constant is in good agreement with the rate constant in electrocatalysis for **1** (k_{CO2} = 10,000 M^{-1}s^{-1}).

For the reaction of **2** without 18-crown-6, decay of the ν_{CO} stretch at 1840 cm^{-1} is observable at low $[CO_2]$ (Figure 3.26b), allowing for kinetic analysis. Experiments without 18-crown-6 in solution indicate that reactions are first order in $[CO_2]$. Figure 3.27 shows that a 2-fold increase in $[CO_2]$ results in approximately a 2-fold increase in

the observed rate constant (k_{obs}), which is consistent with a first order [CO_2] dependence. Because of this, we are confident that reactions with 18-crown-6 in solution are also first order in [CO_2] at high concentrations of CO_2. Calculated rate constants for reactions of **2** without 18-crown-6 in solution are shown in Table S2.

^{13}**C NMR of the Reaction of [Re(bpy-*t*Bu)(CO)$_3$]$^-$ (1) with ^{13}CO$_2$.** In order to further prove the existence of a Re–CO_2H species as a product in the reaction of **1** with CO_2, we utilized ^{13}C NMR spectroscopy. The reaction of anion **1** with ^{13}CO$_2$ in THF-d$_8$ results in a ^{13}C NMR spectrum with peaks at 161.61 and 168.25 ppm, in addition to peaks for the bipyridine carbons and carbonyl ligands (Figure 3.31). We believe that the peak at 161.61 ppm corresponds to the –CO_2H group in the reaction product. The peak at 168.25 ppm could result from either bicarbonate (HCO_3^-) or degradation of the Re–CO_2H species into a μ_2-η^2-CO_2-bridged complex, fac, fac-Re(bpy-*t*Bu)(CO)$_3$(CO_2)Re(bpy-*t*Bu)(CO)$_3$ (as seen in similar studies by Gibson).[21] Bicarbonate could be formed in a variety of degradation reactions, such as by degradation of the Re–CO_2H species to [Re(bpy-*t*Bu)(CO)$_4$]$^+$ and OH$^-$ which can rapidly react with the excess CO_2. For comparison, Figure 3.31 shows the ^{13}C NMR spectrum of KHCO$_3$ in a mixture of THF-d$_8$/H$_2$O, and a similar peak at 168.91 ppm is observed.

Much of the material for this chapter comes directly from a manuscript entitled: "Direct Observation of the Reduction of Carbon Dioxide by Rhenium Bipyridine Catalysts" by Matthew D. Sampson, Jesse D. Froehlich, Jonathan M. Smieja, Eric E. Benson, Ian D. Sharp, and Clifford P. Kubiak, which has been published in *Energy Environ. Sci.*, **2013**, 6, 3748–3755. http://dx.doi.org/10.1039/C3EE42186D. The dissertation author is the primary author of this manuscript.

3.5   References

(1) Cosnier, S.; Deronzier, A.; Moutet, J.-C. *J. Mol. Catal.* **1988**, 45, 381-391.

(2) Hawecker, J.; Lehn, J. M.; Ziessel, R. *J. Chem. Soc., Chem. Commun.* **1984**, 328-330.

(3) Hawecker, J.; Lehn, J. M.; Ziessel, R. *Helv. Chim. Acta* **1986**, 69, 1990-2012.

(4) Hawecker, J.; Lehn, J.-M.; Ziessel, R. *J. Chem. Soc., Chem. Commun.* **1983**, 536-538.

(5) Johnson, F. P. A.; George, M. W.; Hartl, F.; Turner, J. J. *Organometallics* **1996**, 15, 3374-3387.

(6) Kurz, P.; Probst, B.; Spingler, B.; Alberto, R. *Eur. J. Inorg. Chem.* **2006**, 2006, 2966-2974.

(7) Stor, G. J.; Hartl, F.; van Outersterp, J. W. M.; Stufkens, D. J. *Organometallics* **1995**, 14, 1115-1131.

(8) Sullivan, B. P.; Bolinger, C. M.; Conrad, D.; Vining, W. J.; Meyer, T. J. *J. Chem. Soc., Chem. Commun.* **1985**, 1414-1416.

(9) Sung-Suh, H. M.; Kim, D. S.; Lee, C. W.; Park, S.-E. *Appl. Organomet. Chem.* **2000**, 14, 826-830.

(10) Wong, K.-Y.; Chung, W.-H.; Lau, C.-P. *J. Electroanal. Chem.* **1998**, 453, 161-169.

(11) Worl, L. A.; Duesing, R.; Chen, P.; Ciana, L. D.; Meyer, T. J. *J. Chem. Soc., Dalton Trans.* **1991**, 849-858.

(12) Yam, V. W. W.; Lau, V. C. Y.; Cheung, K. K. *Organometallics* **1995**, 14, 2749-2753.

(13) Yoon, K. B. *Chem. Rev.* **1993**, 93, 321-339.

(14) Grice, K. A.; Gu, N. X.; Sampson, M. D.; Kubiak, C. P. *Dalton Trans.* **2013**, 42, 8498–8503.

(15) Smieja, J. M.; Benson, E. E.; Kumar, B.; Grice, K. A.; Seu, C. S.; Miller, A. J. M.; Mayer, J. M.; Kubiak, C. P. *Proc. Natl. Acad. Sci. U. S. A.* **2012**, 109, 15646–15650.

(16) Smieja, J. M.; Kubiak, C. P. *Inorg. Chem.* **2010**, 49, 9283-9289.

(17) Benson, E. E.; Kubiak, C. P. *Chem. Commun.* **2012**, 48, 7374-7376.

(18) Benson, E. E.; Sampson, M. D.; Grice, K. A.; Smieja, J. M.; Froehlich, J. D.; Friebel, D.; Keith, J. A.; Carter, E. A.; Nilsson, A.; Kubiak, C. P. *Angew. Chem., Int. Ed.* **2013**, 52, 4841–4844.

(19) Christensen, P.; Hamnett, A.; Muir, A. V. G.; Timney, J. A. *J. Chem. Soc., Dalton Trans.* **1992**, 0, 1455-1463.

(20) Shaver, R. J.; Rillema, D. P. *Inorg. Chem.* **1992**, 31, 4101-4107.

(21) Gibson, D. H.; Yin, X. *J. Am. Chem. Soc.* **1998**, 120, 11200-11201.

(22) Scheiring, T.; Kaim, W.; Fiedler, J. *J. Organomet. Chem.* **2000**, 598, 136-141.

(23) Kumar, B.; Smieja, J. M.; Kubiak, C. P. *J. Phys. Chem. C* **2010**, 114, 14220-14223.

(24) Kumar, B.; Smieja, J. M.; Sasayama, A. F.; Kubiak, C. P. *Chem. Commun.* **2012**, 48, 272-274.

(25) Fujita, E.; Muckerman, J. T. *Inorg. Chem.* **2004**, 43, 7636-7647.

(26) Keith, J. A.; Grice, K. A.; Kubiak, C. P.; Carter, E. A. *J. Am. Chem. Soc.* **2013**, 135, 15823–15829.

(27) Johnson, J. D.; Charlton, S. C.; Potter, J. D. *J. Biol. Chem.* **1979**, 254, 3497-3502.

(28) Christian, G. D.; Růžička, J. *Anal. Chim. Acta* **1992**, 261, 11-21.

(29) Corraine, M. S.; Atwood, J. D. *Inorg. Chem.* **1989**, 28, 3781-3782.

(30) Fabian, H.; Naumann, D. *Methods* **2004**, 34, 28-40.

(31) George, S. J.; Kurkin, S.; Thorneley, R. N. F.; Albracht, S. P. J. *Biochemistry* **2004**, 43, 6808-6819.

(32) Groves, J. T.; Lee, J.; Marla, S. S. *J. Am. Chem. Soc.* **1997**, 119, 6269-6273.

(33) Nichols, P. J.; Ducommun, Y.; Merbach, A. E. *Inorg. Chem.* **1983**, 22, 3993-3995.

(34) Janda, K. D.; Lo, C. H.; Li, T.; Barbas, C. F.; Wirsching, P.; Lerner, R. A. *Proc. Natl. Acad. Sci. U. S. A.* **1994**, 91, 2532-2536.

(35) Navas Diaz, A.; Garcia, J. A. G. *Anal. Chem.* **1994**, 66, 988-993.

(36) Benson, E. E.; Grice, K. A.; Smieja, J. M.; Kubiak, C. P. *Polyhedron* **2013**, 58, 229–234.

(37) Lee, D. W.; Jensen, C. M.; Morales-Morales, D. *Organometallics* **2003**, 22, 4744-4749.

(38) Ke Chan, P.; Kee Leong, W. *Organometallics* **2008**, 27, 1247-1253.

(39) Gibson, D. H.; Ding, Y.; Andino, J. G.; Mashuta, M. S.; Richardson, J. F. *Organometallics* **1998**, 17, 5178-5183.

(40) Gibson, D. H.; Sleadd, B. A.; Mashuta, M. S.; Richardson, J. F. *Acta Crystallogr. Sect. C: Cryst. Struct. Commun.* **1998**, 54, 1584-1586.

(41) Bennett, M. A.; Jin, H.; Willis, A. C. *J. Organomet. Chem.* **1993**, 451, 249-256.

(42) Bennett, M. A.; Robertson, G. B.; Rokicki, A.; Wickramasinghe, W. A. *J. Am. Chem. Soc.* **1988**, 110, 7098-7105.

(43) Costentin, C.; Drouet, S.; Robert, M.; Savéant, J.-M. *Science* **2012**, 338, 90-94.

(44) Schwindt, M. A.; Lejon, T.; Hegedus, L. S. *Organometallics* **1990**, 9, 2814-2819.

(45) Wittrig, R. E. Dissertation, Purdue University, **1994**.

(46) Fonseca Guerra, C.; Snijders, J. G.; te Velde, G.; Baerends, E. J. *Theor. Chem. Acc.* **1998**, 99, 391-403.

(47) te Velde, G.; Bickelhaupt, F. M.; Baerends, E. J.; Fonseca Guerra, C.; van Gisbergen, S. J. A.; Snijders, J. G.; Ziegler, T. *J. Comput. Chem.* **2001**, 22, 931-967.

(48) SCM In *Theoretical Chemistry* Vrije Universiteit: Amsterdam, The Netherlands.

(49) van Lenthe, E.; Baerends, E. J.; Snijders, J. G. *J. Chem. Phys.* **1993**, 99, 4597-4610.

(50) Lenthe, E. v.; Snijders, J. G.; Baerends, E. J. *J. Chem. Phys.* **1996**, 105, 6505-6516.

(51) Vosko, S. H.; Wilk, L.; Nusair, M. *Can. J. Phys.* **1980**, 58, 1200-1211.

(52) Becke, A. D. *Phys. Rev. B* **1988**, 38, 3098.

(53) Perdew, J. P. *Phys. Rev. B* **1986**, 33, 8822-8824.

(54) Perdew, J. P. *Phys. Rev. B* **1986**, 34, 7406-7406.

(55) Connors, K. A. *Chemical kinetics, the study of reaction rates in solution*; Wiley-VCH Publishers: Weinheim, Germany, **1991**.

3.6 Appendix
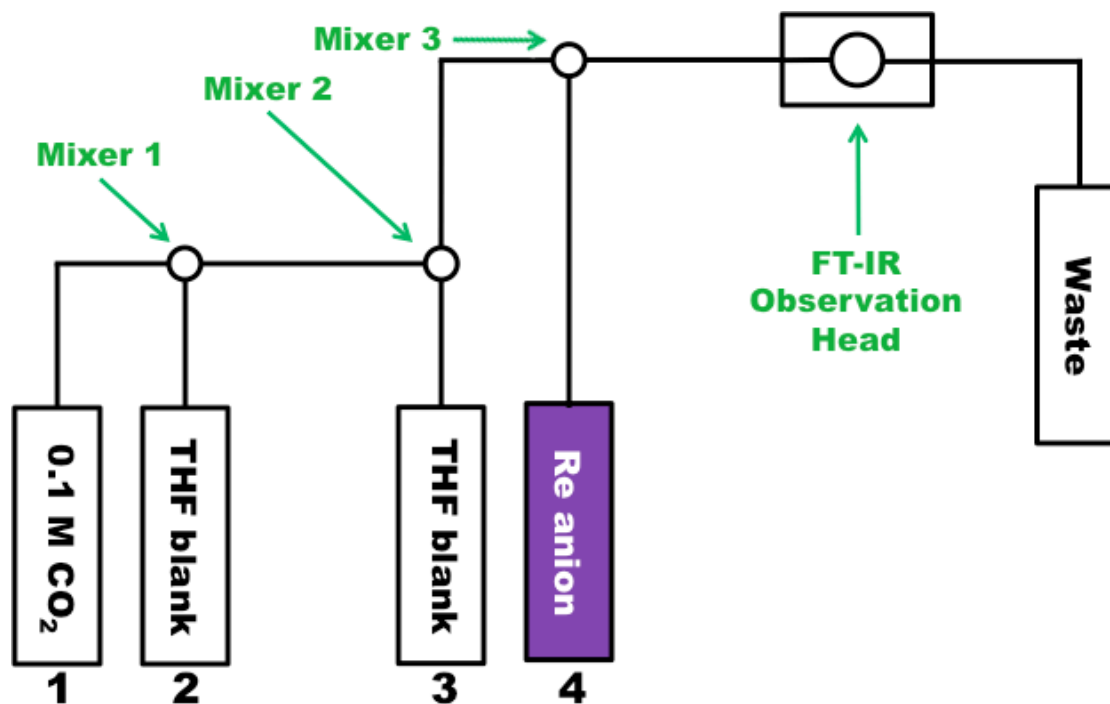
Figure 3.8 Mixing schematic for a typical stopped-flow IR spectroscopy experiment.
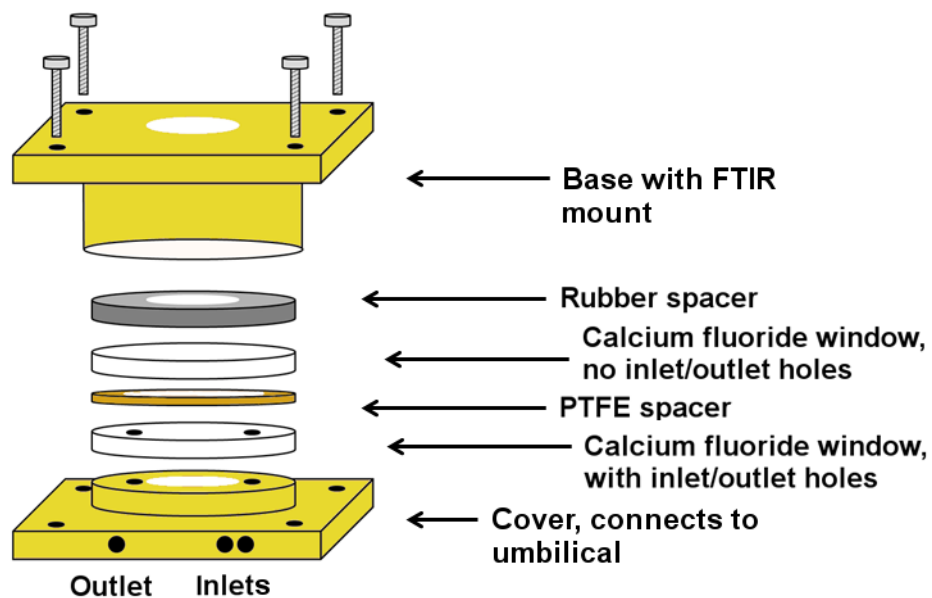
Figure 3.9 Schematic of the flow through FTIR observation head for the Biologic SFM 400 stopped flow instrument. The observation head contains two inlet ports, and the final mixing event (mixer 3 in Figure 3.8) occurs immediately prior to introduction of solution to the transmission cell.
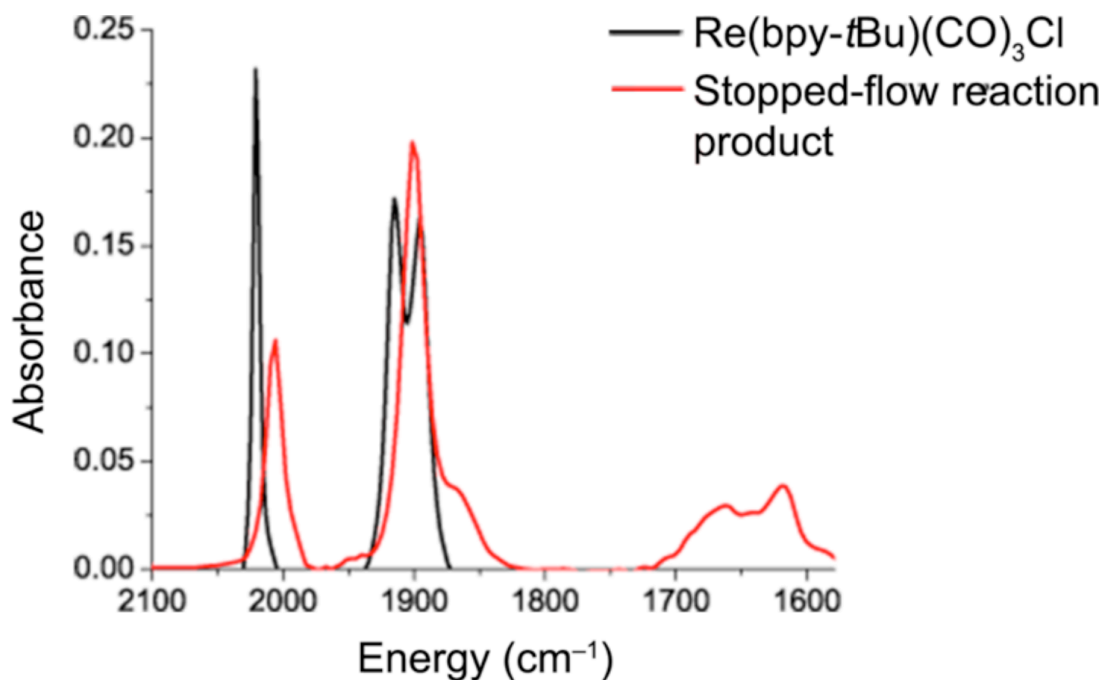
Figure 3.10 Comparison of the IR spectra of Re(bpy-*t*Bu)(CO)$_3$Cl (black) and the product from stopped-flow reactions involving 1 and CO$_2$ (red).
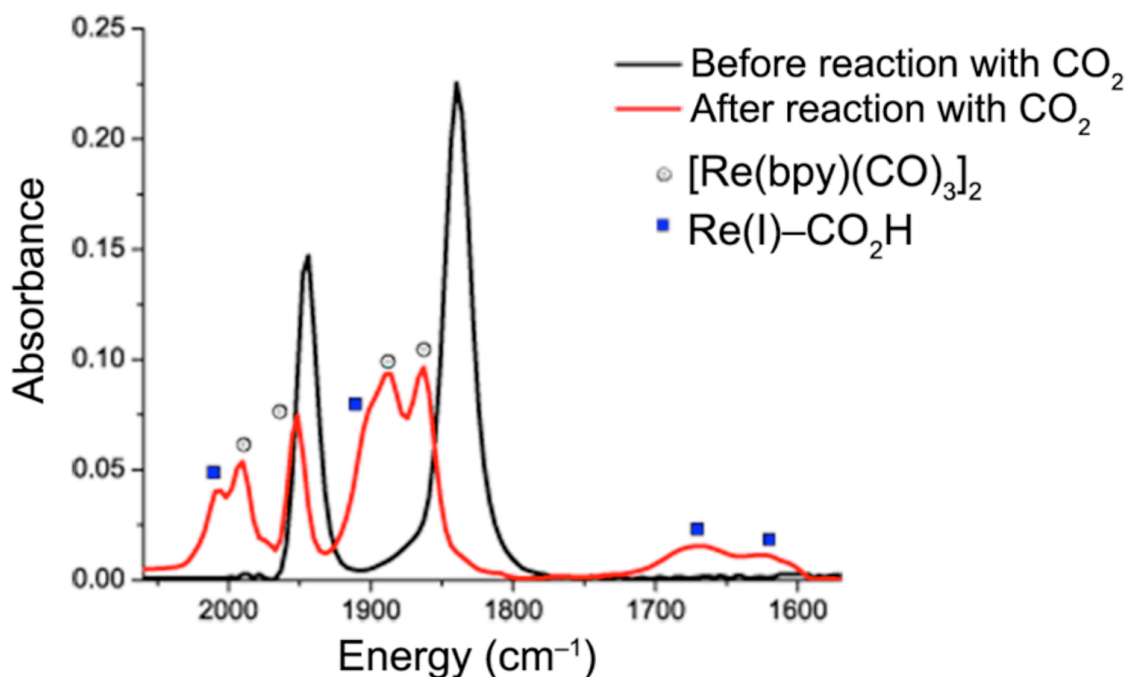
Figure 3.11 IR spectra of **2** before reaction with CO$_2$ (black) and after reaction with CO$_2$ (red). Grey circles indicate ν_{CO} stretches that correspond to the dimer, [Re(bpy)(CO)$_3$]$_2$, and blue squares indicate ν_{CO} stretches that correspond to the Re(I)–CO$_2$H product.
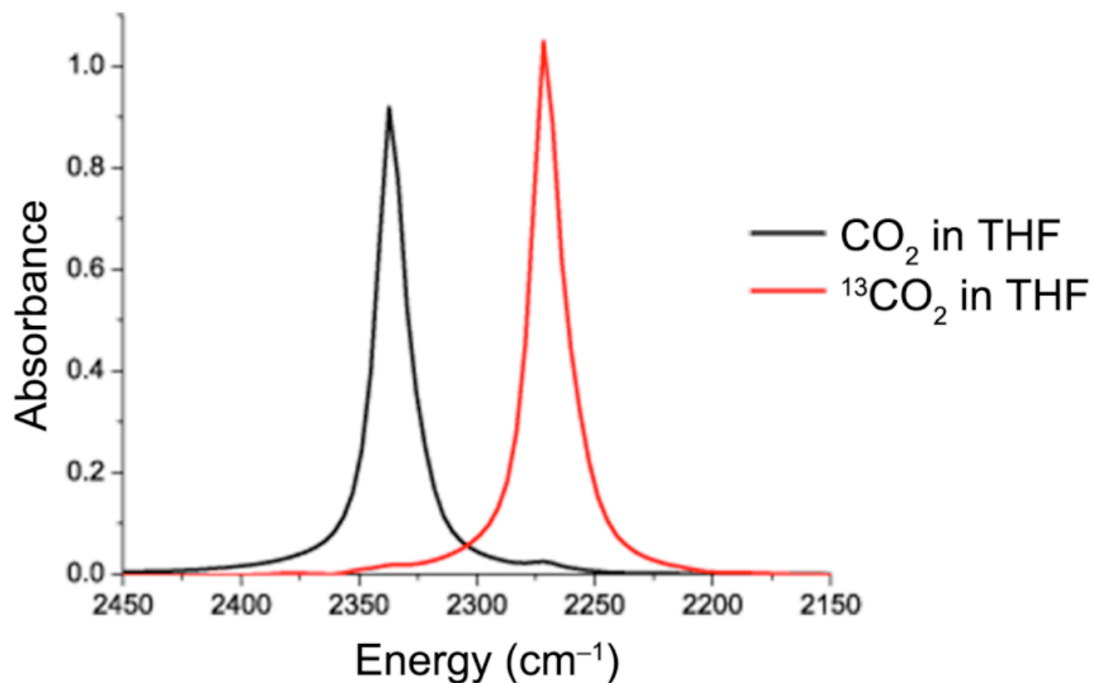
Figure 3.12 IR spectra of pure CO_2 in THF (black) and pure $^{13}CO_2$ in THF (red), showing the shift of the CO_2 peak from 2333 cm^{-1} to 2268 cm^{-1}.
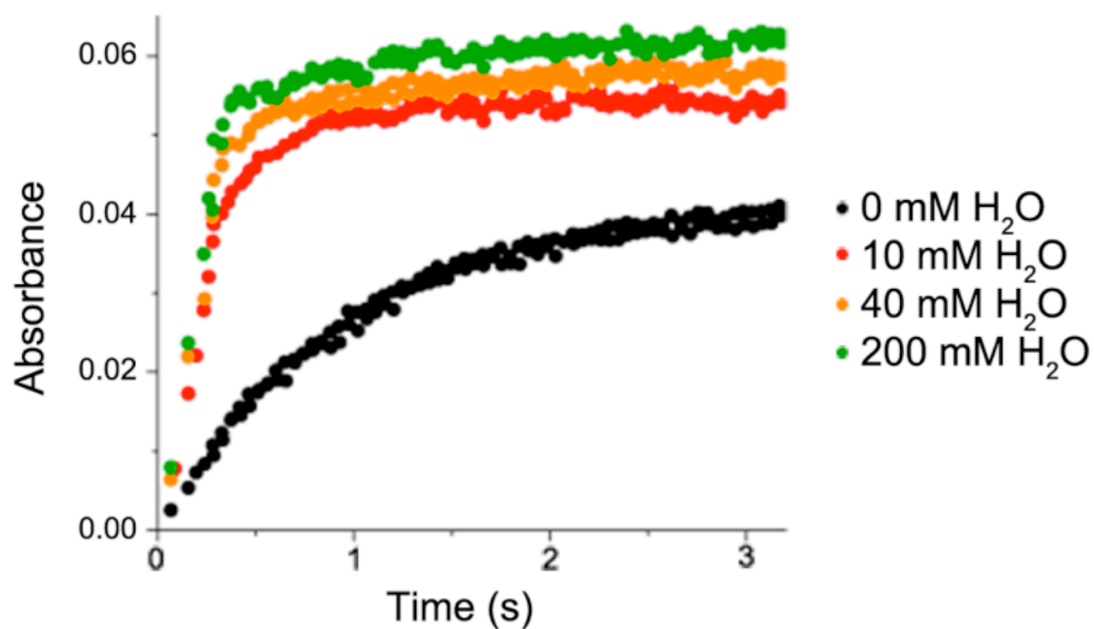
Figure 3.13 Growth of the ν_{OCO} stretch at 1616 cm^{-1} as a function of time for the reaction of 2.5 mM **1** with 25 mM CO_2 with the addition of various concentrations of H_2O.
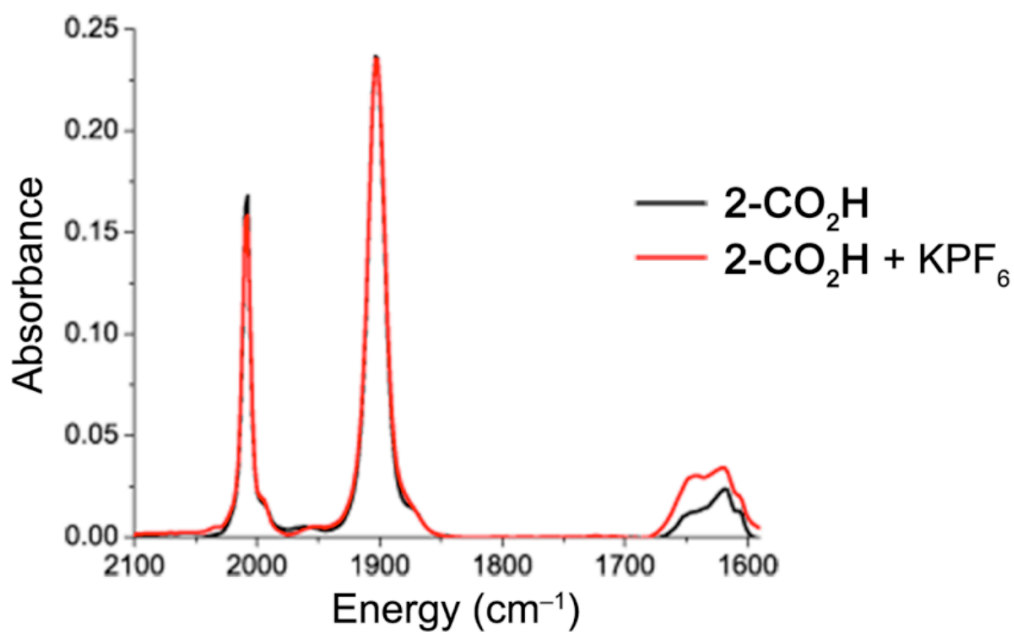
Figure 3.14 Comparison of the IR spectra of **2-CO₂H** without KPF₆ (black) and with KPF₆ (red). Spectra are normalized relative to each other.
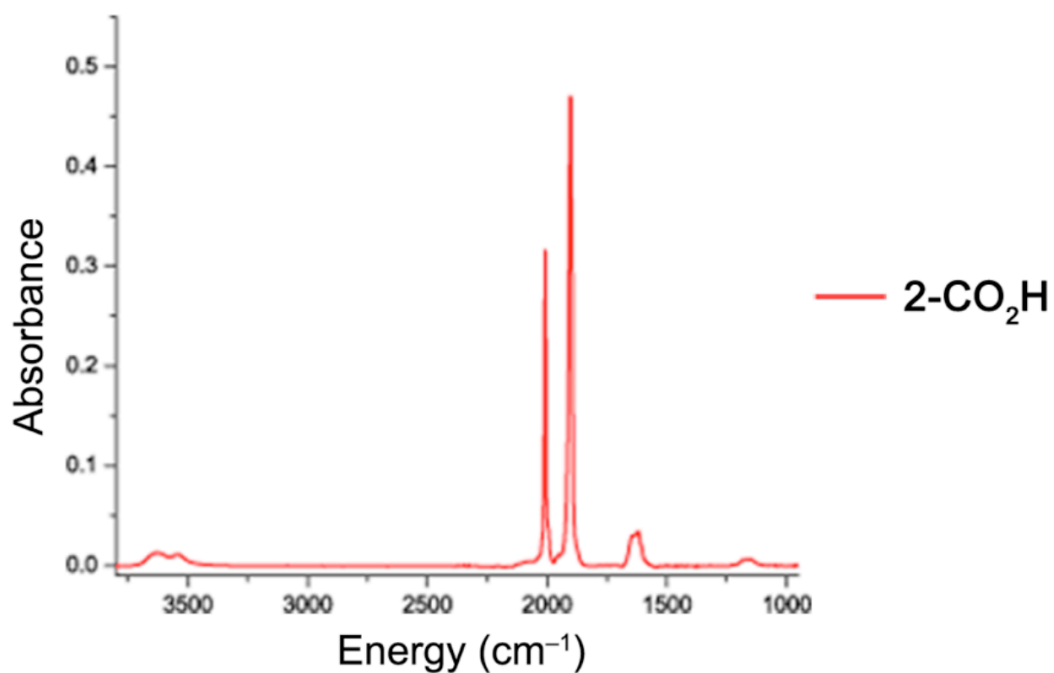
Figure 3.15 Full IR spectrum of **2-CO₂H** in MeCN from 4000 cm^{-1} to 1000 cm^{-1}.

Table 3.2 IR stretching frequencies of **1-CO$_2$H** and **2-CO$_2$H** in stopped-flow reactions, synthesized solutions, and gas-phase DFT calculations.

	IR stretching frequencies (cm^{-1})		
Complex	Stopped-flow reaction	Synthesized	DFT-calculated
1-CO$_2$H	2001, 1901, 1662, 1616	–	1992, 1920, 1619
2-CO$_2$H	2009, 1901, 1662, 1616	2008, 1902, 1643, 1617	1997, 1926, 1616
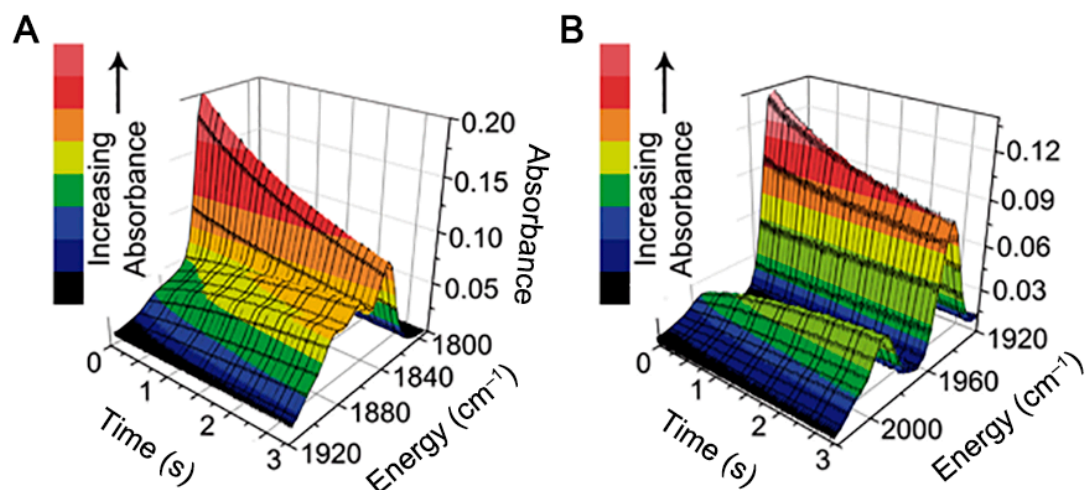
Figure 3.16 Reaction of 2.5 mM **2** with 32 mM CO$_2$: (a) 3D plot of the reaction showing the decay of the ν_{CO} stretch at 1840 cm^{-1} and the growth of the ν_{CO} stretch at 1901 cm^{-1}; (b) 3D plot of the reaction showing the decay of the ν_{CO} stretch at 1940 cm^{-1} and the growth of the ν_{CO} stretch at 2009 cm^{-1}.
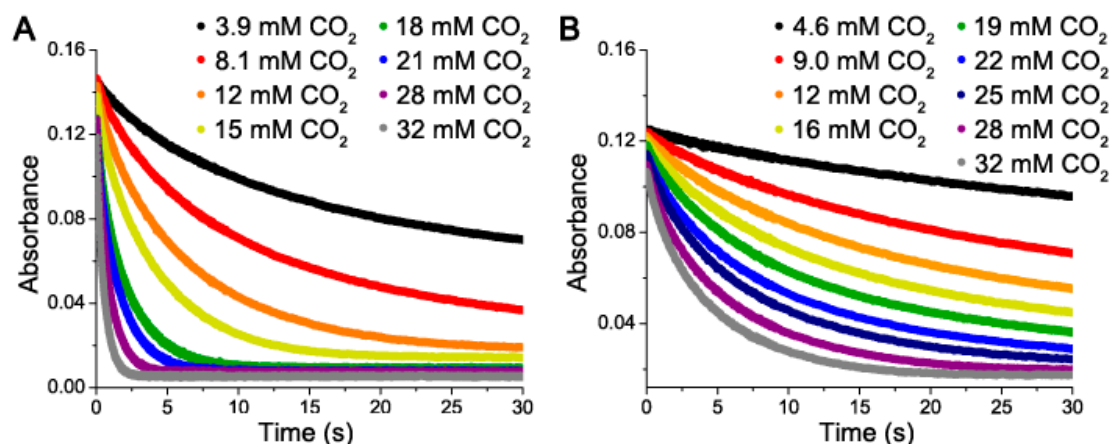
Figure 3.17 (a) Decays of the ν_{CO} stretch at 1940 cm^{-1} as a function of time for the reaction of 2.5 mM **1** with various concentrations of CO$_2$. (b) Decays of the ν_{CO} stretch at 1940 cm^{-1} as a function of time for the reaction of 2.5 mM **2** with various concentrations of CO$_2$.
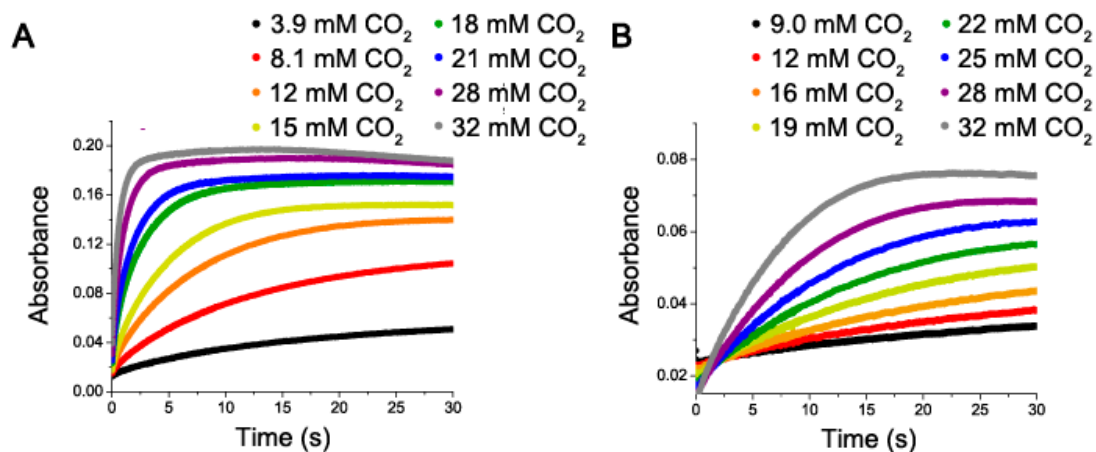
Figure 3.18 (a) Growths of the v_{CO} stretch at 1901 cm^{-1} as a function of time for the reaction of 2.5 mM **1** with various concentrations of CO_2. (b) Growths of the v_{CO} stretch at 1901 cm^{-1} as a function of time for the reaction of 2.5 mM **2** with various concentrations of CO_2.
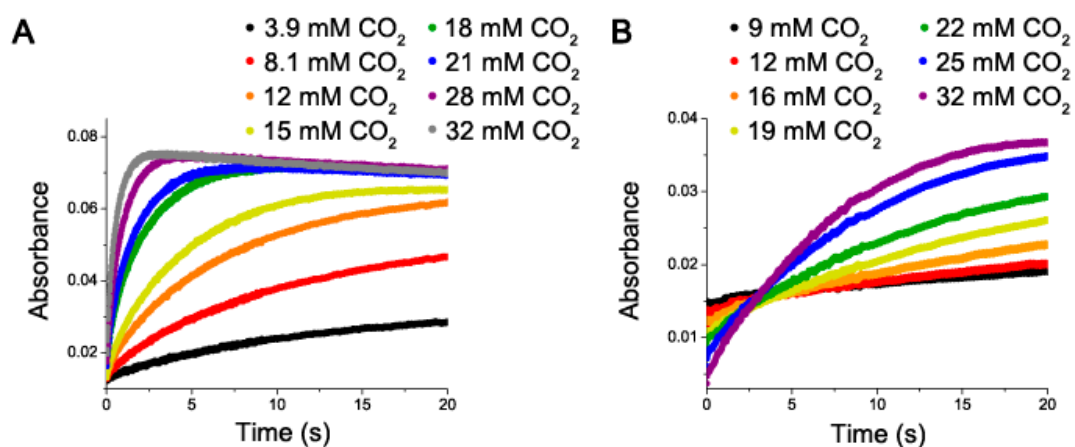
Figure 3.19 (a) Growths of the v_{CO} stretch at 2001 cm^{-1} as a function of time for the reaction of 2.5 mM **1** with various concentrations of CO_2. (b) Growths of the v_{CO} stretch at 2009 cm^{-1} as a function of time for the reaction of 2.5 mM **2** with various concentrations of CO_2.
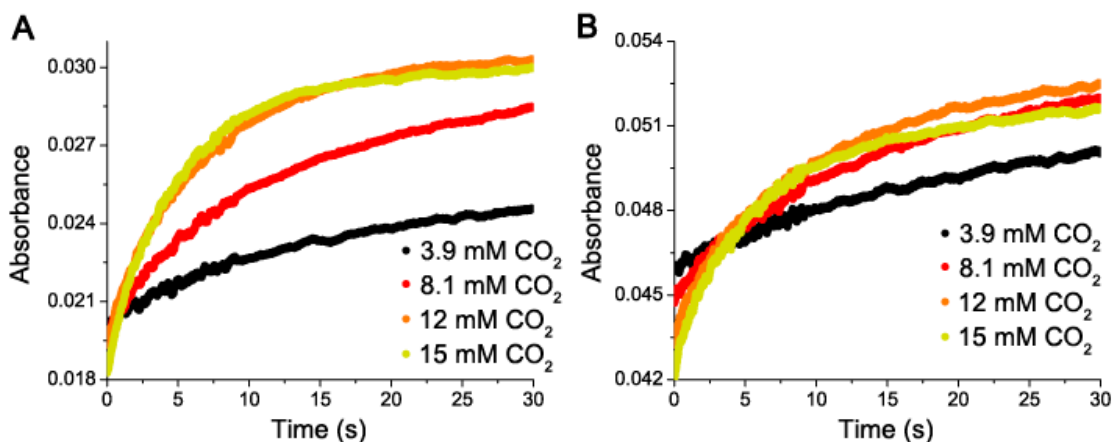
Figure 3.20 (a) Growths of the ν_{OCO} stretch at 1616 cm^{-1} as a function of time for the reaction of 2.5 mM **1** with various concentrations of CO_2. (b) Growths of the ν_{OCO} stretch at 1662 cm^{-1} as a function of time for the reaction of 2.5 mM **1** with various concentrations of CO_2. The growths of these ν_{OCO} stretches saturate around 12 mM CO_2 due to the limited supply of H$^+$ in solution.
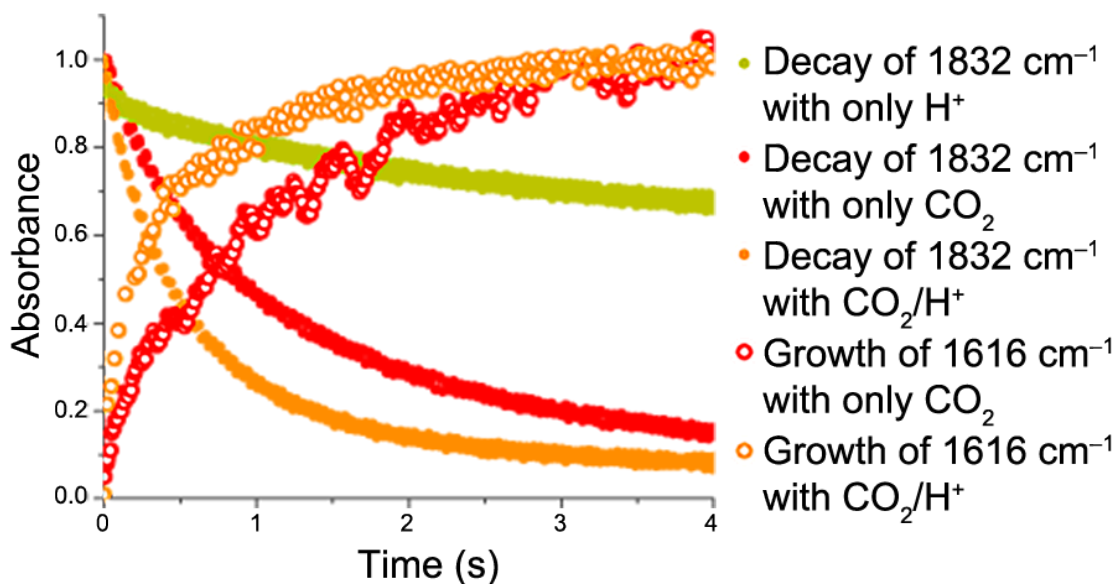
Figure 3.21 Comparison of the decay rates of the ν_{CO} stretch at 1832 cm^{-1} and the growth rates of the ν_{OCO} stretch at 1616 cm^{-1} for the reaction of 2.5 mM **1** with various substrates. Data in yellow correspond to reactions with only H$^+$ added (3 mM MeOH), data in red correspond to reactions with only CO_2 added (25 mM), and data in orange correspond to reactions with both CO_2 and H$^+$ added (25 mM and 3 mM, respectively). Initial absorbance values for the decays of 1832 cm–1 are normalized to 1 by multiplying each data set by 7.5. Saturated absorbance values for the growths of 1616 cm–1 are normalized to 1 by multiplying each data set by 25.
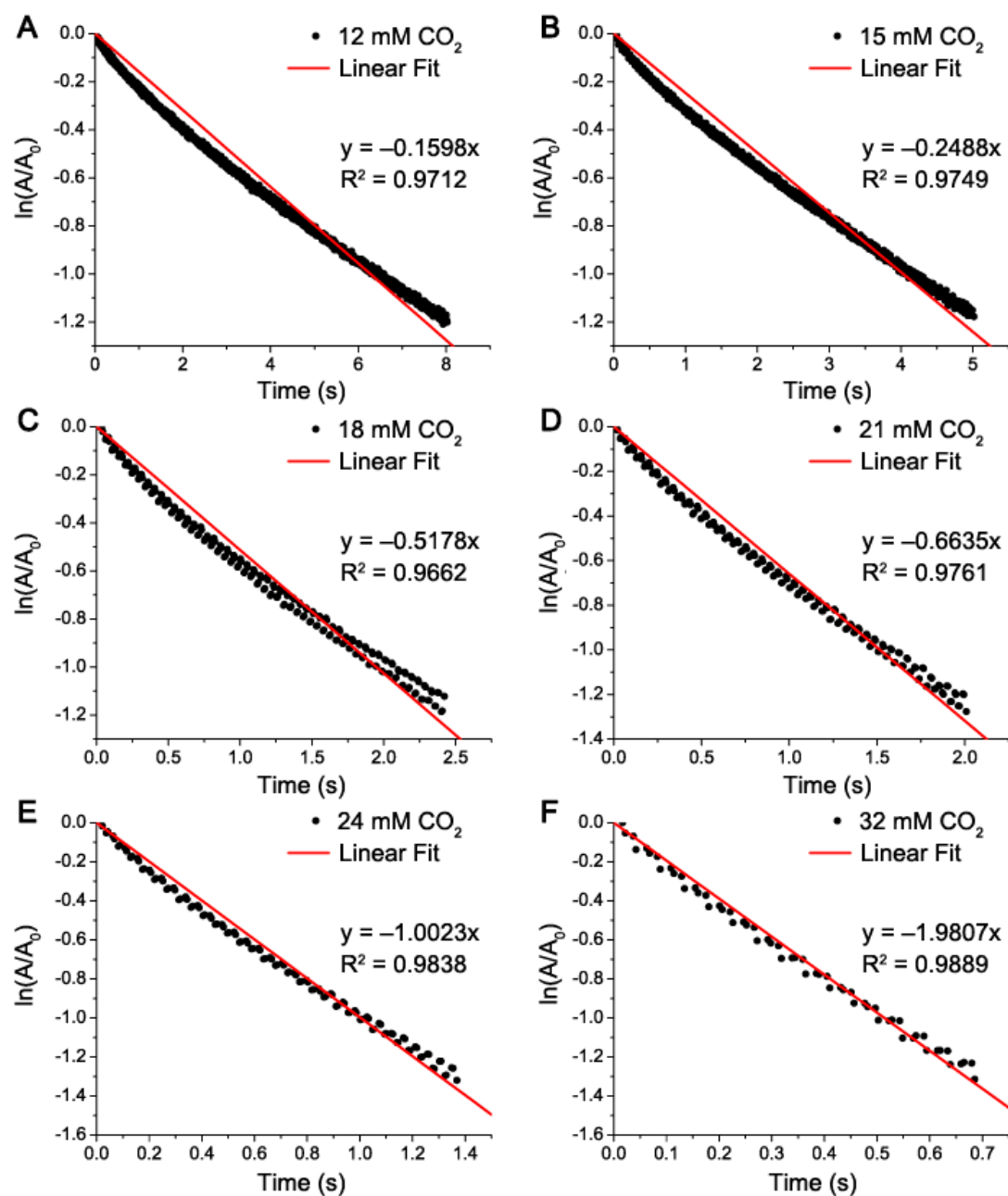
Figure 3.22 Plot of $\ln(A/A_0)$ vs. time for the ν_{CO} stretch at 1832 cm^{-1} for the reaction of 2.5 mM **1** with (a) 12 mM CO_2, (b) 15 mM CO_2, (c) 18 mM CO_2, (d) 21 mM CO_2, (e) 24 mM CO_2, and (f) 32 mM CO_2. For each plot, kinetic data is shown in black and a linear fit of the data is shown in red. Similar plots and fits were obtained for the reactions of **1** with 3.9, 8.1, and 28 mM CO_2.
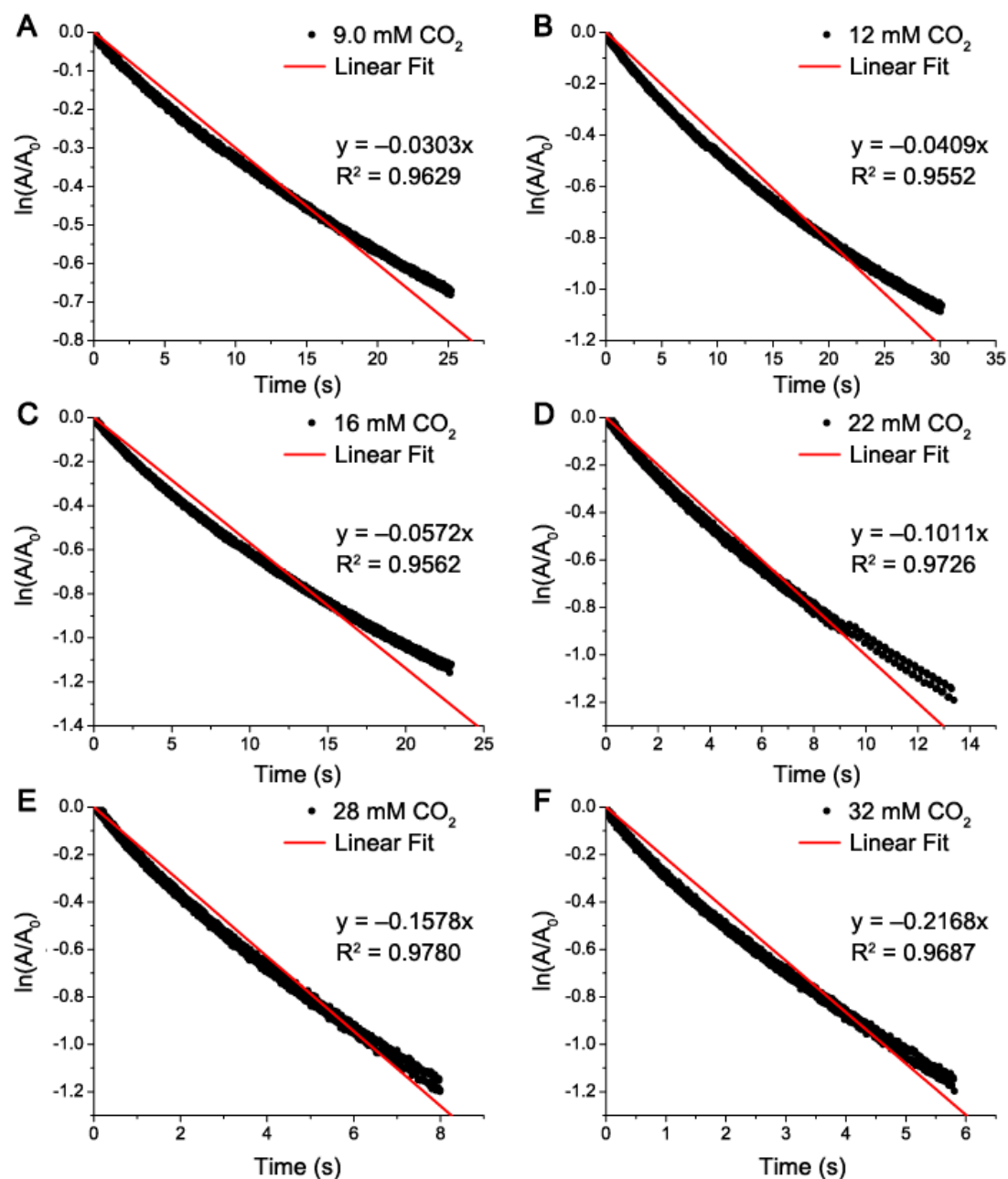
Figure 3.23 Plot of $\ln(A/A_0)$ vs. time for the ν_{CO} stretch at 1840 cm^{-1} for the reaction of 2.5 mM **2** with (a) 9.0 mM CO_2, (b) 12 mM CO_2, (c) 16 mM CO_2, (d) 22 mM CO_2, (e) 28 mM CO_2, and (f) 32 mM CO_2. For each plot, kinetic data are shown in black and a linear fit of the data is shown in red. Similar plots and fits were obtained for the reactions of **2** with 4.6, 19, 25, and 31 mM CO_2.

Table 3.3 Pseudo-first order rates for the reaction of 2.5 mM **1** and **2** with various concentrations of CO_2 with 18-crown-6 in solution. Rates were obtained by following the decay of the ν_{CO} stretch at 1832 and 1840 cm^{-1} in stopped-flow IR spectroscopy experiments.

[CO_2] (mM)	Rate of **1** (s^{-1})	[CO_2] (mM)	Rate of **2** (s^{-1})
15	0.25	16	0.057
18	0.52	19	0.079
21	0.66	22	0.10
24	1.0	25	0.13
28	2.0	28	0.16
32	2.0	31	0.21
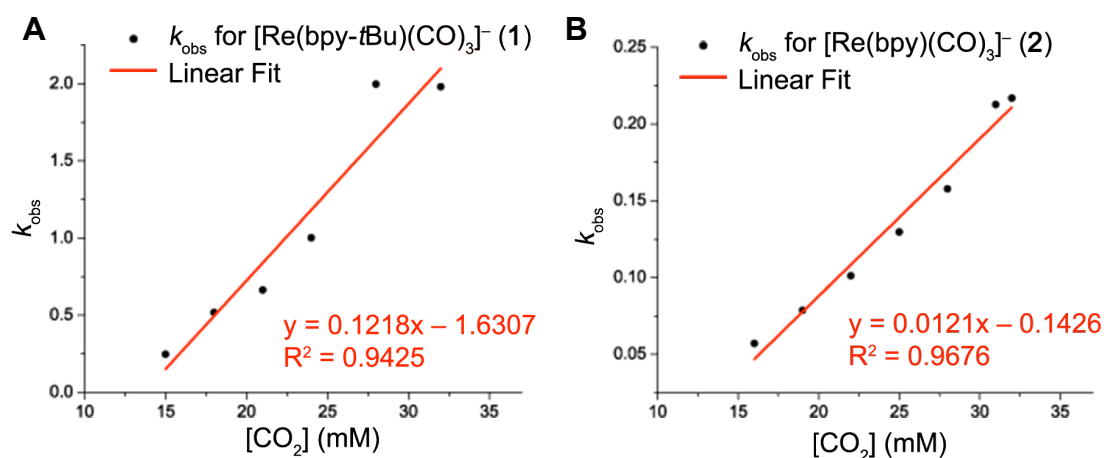
Figure 3.24 (a) Plot of k_{obs} vs. [CO_2] for the reaction of (a) 2.5 mM **1** with CO_2 and (b) 2.5 mM **2** with CO_2. A linear fit of the kinetic data for each is shown in red (y = 0.1218x − 1.6307 and y = 0.0121x − 0.1426, respectively). Pseudo-first order rate constants (k_{CO2}) of 120 ± 20 $M^{-1}s^{-1}$ and 12 ± 1.5 $M^{-1}s^{-1}$ were obtained from these linear fits, respectively.
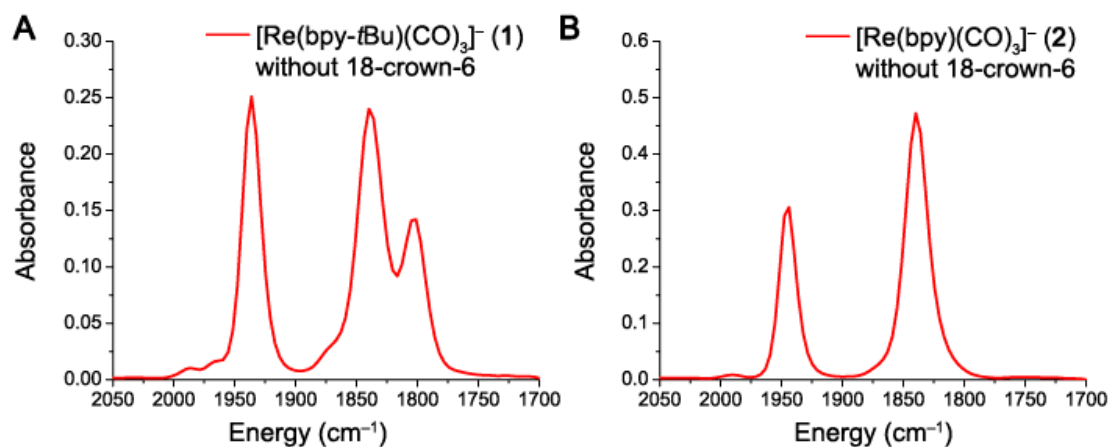
Figure 3.25 (a) IR spectrum of **1** without 18-crown-6 in solution. (b) IR spectrum of **2** without 18-crown-6 in solution. Three ν_{CO} stretches are observed in the spectrum of **1** without 18-crown-6 due to potassium coordination to the carbonyl ligands.
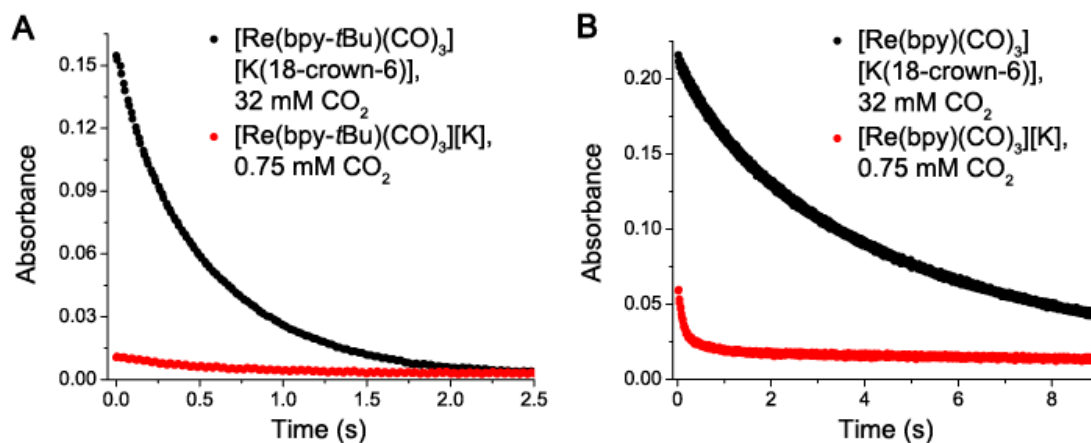
Figure 3.26 (a) Decay of the ν_{CO} stretch at 1832 cm^{-1} for the reaction of **1** with CO_2 with 18-crown-6 in solution (black, 32 mM CO_2) and without 18-crown-6 in solution (red, 0.75 mM CO_2). (b) Decay of the ν_{CO} stretch at 1840 cm^{-1} for the reaction of **2** with CO_2 with 18-crown-6 in solution (black, 32 mM CO_2) and without 18-crown-6 in solution (red, 0.75 mM CO_2).
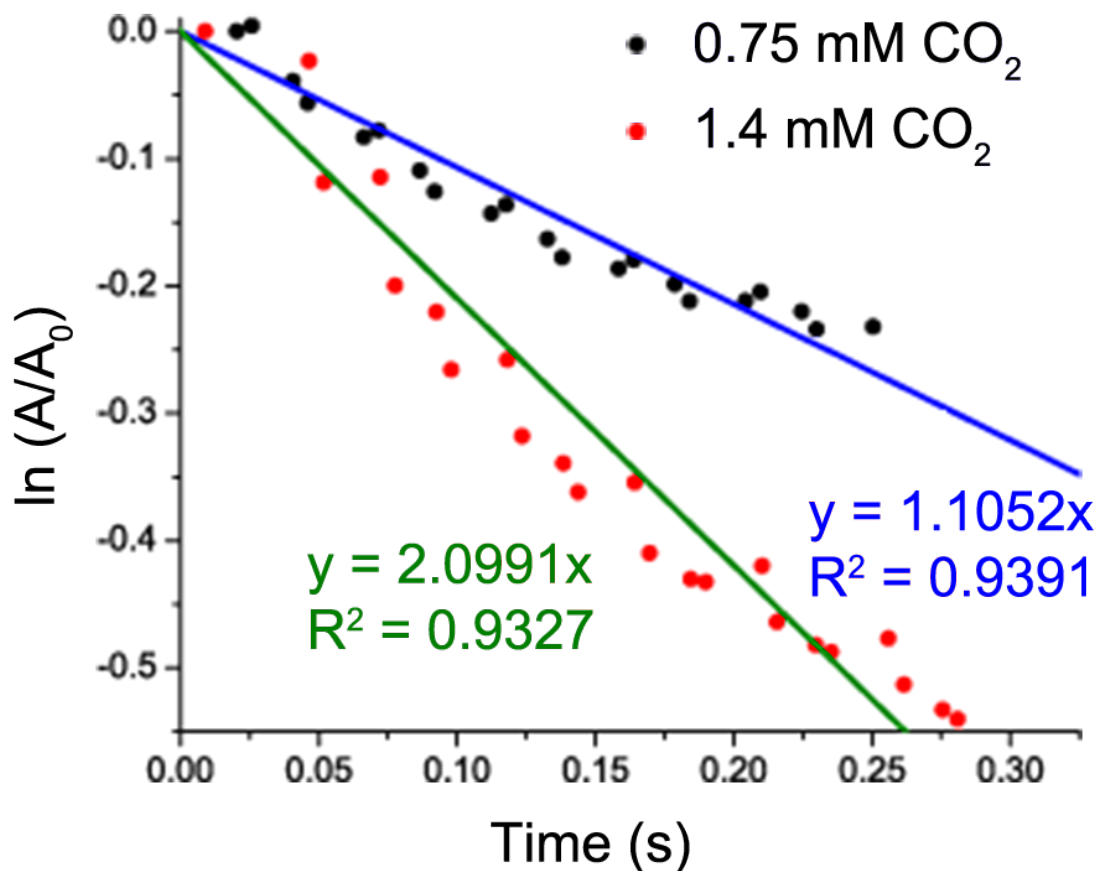
Figure 3.27 Plot of $\ln(A/A_0)$ vs. time ($\nu_{CO} = 1832$ cm^{-1}) for the reaction of 2.5 mM **1** with CO_2 without 18-crown-6 in solution. The reaction with 0.75 mM CO_2 is shown in black, with a linear fit of the kinetic data shown in blue. The reaction with 1.4 mM CO_2 is shown in red, with a linear fit of the kinetic data shown in green.

Table 3.4 Pseudo-first order rates for the reaction of 2.5 mM **2** with various concentrations of CO_2 without 18-crown-6 in solution. Rates were obtained by following the decay of the ν_{CO} stretch at 1840 cm^{-1} in stopped-flow IR spectroscopy experiments.

[CO$_2$] (mM)	Rate of **2**, no 18-crown-6 (s^{-1})
0.75	1.1
1.4	2.1
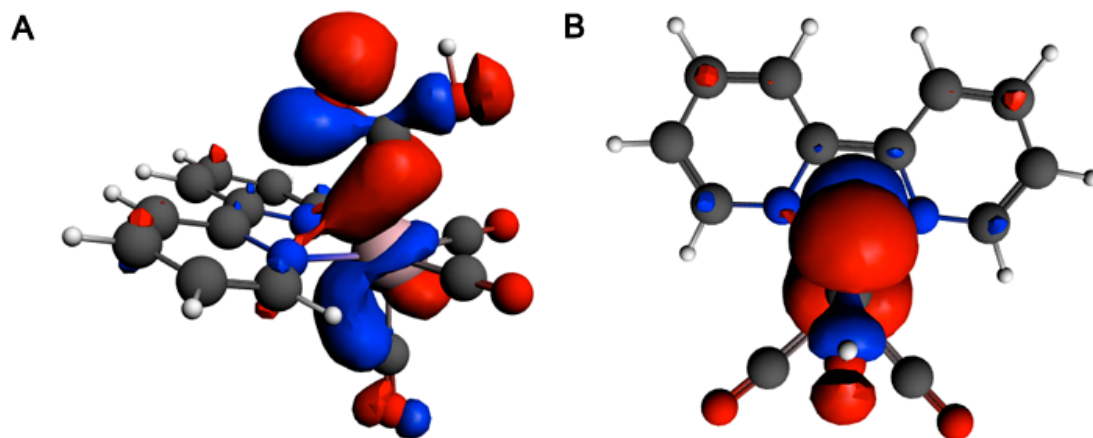
Figure 3.28 Side and top view of highest occupied molecular orbital (HOMO) of Re(bpy)(CO)$_3$(CO$_2$H) (**2-CO$_2$H**) calculated with ADF 2012.1.
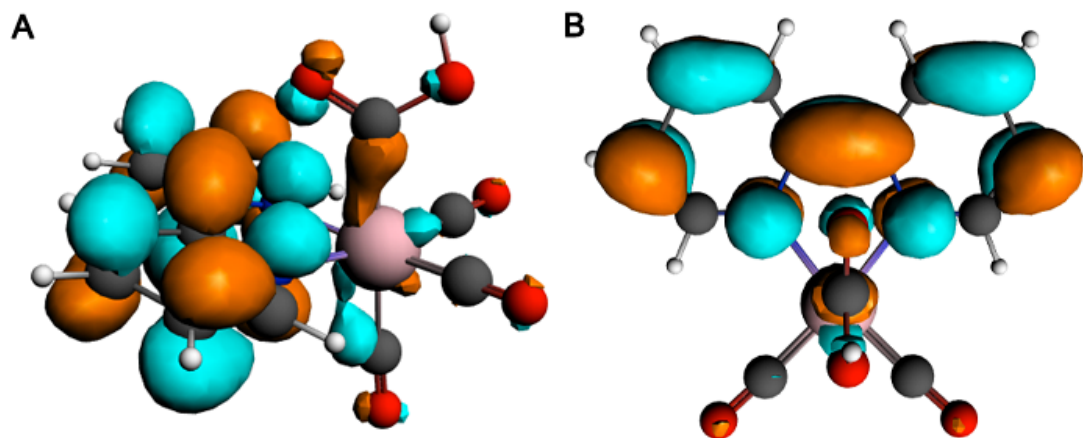
Figure 3.29 Side and top view of the lowest unoccupied molecular orbital (LUMO) of Re(bpy)(CO)$_3$(CO$_2$H) (**2-CO$_2$H**) calculated with ADF 2012.1.
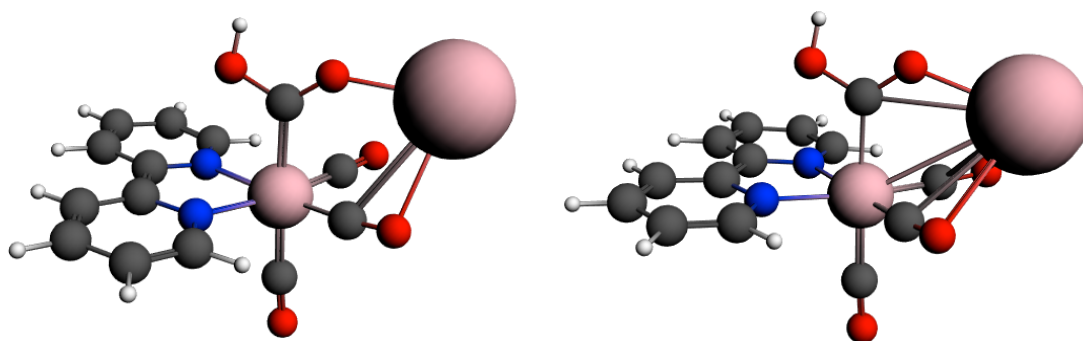
Figure 3.30 DFT-calculated structure of [Re(bpy)(CO)$_3$(CO$_2$H)][K] showing two different converged structures, calculated with ADF 2012.1.

Table 3.5 Geometry Optimized xyz Coordinates for Re(bpy)(CO)$_3$(CO$_2$H) (**2-CO$_2$H**).

Atom	X	Y	Z
Re	3.026371	1.968157	15.694743
O	5.214482	3.937542	16.664230
O	5.120679	0.162458	14.294824
O	2.720793	3.648001	13.064137
O	2.335121	0.357960	18.243248
O	4.549107	0.492364	17.942706
N	1.386362	2.878925	16.798065
N	1.325443	0.643089	15.396700
C	1.452844	4.071453	17.431245
H	2.366593	4.637977	17.275613
C	0.433364	4.555302	18.235119
H	0.546228	5.521929	18.721678
C	-0.718159	3.780410	18.403438
C	-0.801662	2.560651	17.748780
H	-1.689960	1.944479	17.857742
C	0.261255	2.121637	16.947918
C	0.229933	0.878978	16.175349
C	-0.861738	0.000346	16.169113
H	-1.725116	0.202249	16.797351
C	-0.836882	-1.129368	15.365047
C	0.283730	-1.356465	14.560313
H	0.350610	-2.224485	13.907762
C	1.333648	-0.453699	14.606530
H	2.226289	-0.594446	14.003576
C	4.412462	3.182822	16.284229
C	4.353632	0.861745	14.823473
C	2.790084	3.022446	14.042276
C	3.257121	0.778282	17.551521
H	4.456204	-0.035051	18.768603
H	-1.537354	4.126197	19.032043
H	-1.678002	-1.820802	15.359661
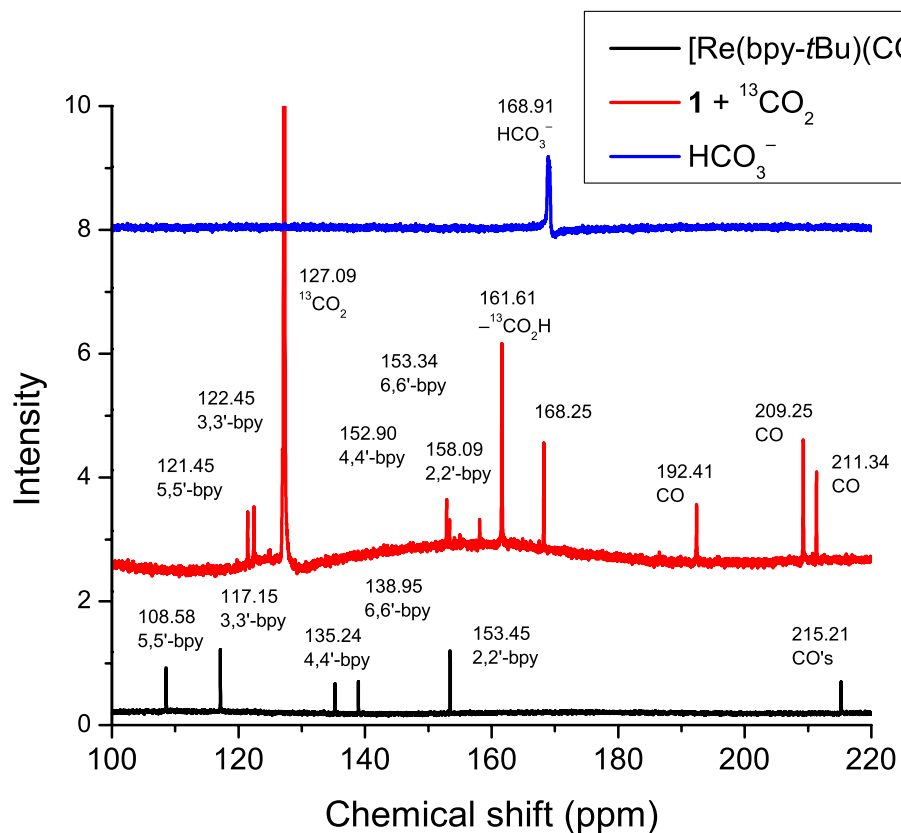
Figure 3.31 ^{13}C NMR spectra (from 100–220 ppm) for the reaction between [Re(bpy-*t*Bu)(CO)$_3$]$^-$ (**1**) and ^{13}CO$_2$ in THF-d$_8$, mimicking stopped-flow reactions. The starting anionic complex **1** is shown in black and the reaction product between **1** and ^{13}CO$_2$ is shown in red. The ^{13}C NMR spectrum of bicarbonate (HCO$_3^-$) in a THF-d$_8$/H$_2$O mixture is shown in blue for comparison purposes. The assignments for the ^{13}C NMR chemical shifts are shown in the figure.

Chapter 4

Manganese catalysts with bulky bipyridine ligands: Eliminating dimerization and altering catalysis for the reduction of carbon dioxide.

4.1 Introduction

Of the systems that electrochemically reduce CO_2 to CO, Re and Mn bpy complexes (bpy = 2,2′-bipyridine) are superior to most others in terms of rates, selectivities, and lifetimes.[1-5] Since Mn is ~1.3 million times more abundant in the Earth's crust than Re,[6] we have recently shifted our focus on CO_2 reduction chemistry to these Mn complexes.[7] When considering a system for eventual scale-up and industrial use, Mn is much more appealing than Re due to cost and environmental ramifications. The Mn(bpy-R)(CO)$_3$X (bpy-R = 4,4′-disubstituted-2,2′-bipyridine, X

= Br or solvent molecule with counter anion) complexes, first reported by Bourrez *et al.* in 2011 to be active catalysts,[8] have been shown to be viable alternatives to the aforementioned Re system in the presence of weak Brønsted acids (namely H_2O, methanol (MeOH), and 2,2,2-trifluoroethanol (TFE)). Specifically, Mn(bpy-R)(CO)$_3$X complexes are comparable in activity at similar conditions, but offer the advantage of considerably lower overpotentials than the corresponding Re catalysts.[7-8] Mn(bpy-*t*Bu)(CO)$_3$X maintains high activity in the presence of high concentrations of Brønsted acid (greater than 6000 equivalents), while showing 100% Faradaic efficiency for the formation of CO.

One distinct difference between these Mn catalysts and their Re counterparts is the tendency for dimerization after the first reduction.[7-8] In the electrochemistry of Mn(bpy-R)(CO)$_3$X, two irreversible, one-electron reductions are observed, separated by 200–300 mV. A large oxidation peak occurs at more positive potentials after scanning through the first reduction. This indicates that a Mn–Mn dimer forms after rapid, irreversible loss of X. The two sequential one-electron reductions of typical Mn(bpy-R)(CO)$_3$X complexes are summarized in E4.1–E4.2. In contrast, for Re(bpy-R)(CO)$_3$X, the first one-electron reduction is reversible and loss of X^- is usually not observed until the second reduction. This tendency for dimerization is thought to contribute to an overpotential for two-electron reduction, as well as to limiting the activity of these Mn catalysts.[7]

$$Mn^I(\text{bpy-R})(CO)_3Br + e^- \rightarrow {}^1/_2\,[Mn^0(\text{bpy-R})(CO)_3]_2 + Br^- \qquad \textbf{(E4.1)}$$

$$^1/_2\,[Mn^0(\text{bpy-R})(CO)_3]_2 + e^- \rightarrow [Mn(\text{bpy-R})(CO)_3]^- \qquad \textbf{(E4.2)}$$
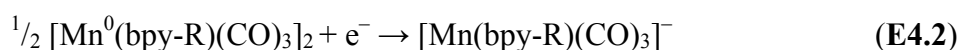
In the studies described here, we sought to eliminate this dimerization pathway (E4.1) for the Mn(bpy-R)(CO)$_3$X catalysts and study the effects this has on catalytic overpotential and activity. We use a bulky bipyridine ligand, 6,6′-dimesityl-2,2′-bipyridine (mesbpy), to synthesize Mn(mesbpy)(CO)$_3$X. The mesbpy ligand was previously synthesized by Schmittel *et al.* and studied in regards to its Cu(I) coordination.[9] We have previously utilized a similar bulky ligand, 6,6′-(2,4,6-triisopropylphenyl)-2,2′-bipyridine (tripbpy), to enforce tetrahedral geometries in late first row transition metal chlorides,[10] as well as to isolate intermediates leading up to the catalytically-active state in Re(bpy-R)(CO)$_3$X complexes.[11] We report the synthesis, electrochemistry, infrared spectroelectrochemistry (IR-SEC), and X-ray crystallography of Mn(mesbpy)(CO)$_3$Br (**1**) and [Mn(mesbpy)(CO)$_3$(MeCN)](OTf) (**2**, MeCN = acetonitrile, OTf = trifluoromethanesulfonate). In the cyclic voltammograms (CVs), these complexes exhibit a single, reversible, two-electron reduction wave, with no evidence for dimerization. This behavior is distinctly different than the electrochemistry of typical Mn(bpy-R)(CO)$_3$X complexes, where two irreversible one-electron reductions are observed. For **1** and **2**, the usual second reduction has been shifted positive by ~300 mV and incorporated into a two-electron couple near the potential of the typical first reduction. A notable finding in this work is that complexes **1** and **2** show high activity for CO$_2$ reduction to CO, but at ~400 mV more negative than the two electron redox couple that generates the anionic, CO$_2$-binding state, [Mn(mesbpy)(CO)$_3$]$^-$ (**4**). IR-SEC experiments under CO$_2$ and H$^+$ indicate that reduction of a Mn(I)–CO$_2$H catalytic intermediate may be the source of this "over

reduction" process required to initiate catalysis. By "over reduction," we mean that while **1** or **2** can be reduced by two electrons to form **4**, and while **4** shows clear evidence for binding and reducing CO_2/H^+, catalysis is not initiated until a third electron is introduced at *ca.* –2.0 V vs. Fc^+/Fc. The studies and findings reported here provide new mechanistic and synthetic insights for improving catalysts in the future, with the ultimate goal of attaining a catalytic system capable of implementation on a large scale.

4.2 Results and Discussion

Synthesis and Characterization. Synthesis of 6,6′-dimesityl-2,2′-bipyridine (mesbpy) was performed by the Suzuki coupling of 6,6′-dibromo-2,2′-bipyridine with mesityl boronic acid, as previously reported.[9] Syntheses of $Mn(mesbpy)(CO)_3Br$ (**1**) and $[Mn(mesbpy)(CO)_3(MeCN)](OTf)$ (**2**) were performed analogously to previously reported procedures for $Mn(bpy-R)(CO)_3X$ species.[7-8,12] Complexes **1** and **2** were characterized by NMR, FTIR, and elemental analysis. Complex **1** was also characterized by X-ray crystallography. Singly-reduced $[Mn(mesbpy)(CO)_3]^0$ (**3**) and doubly-reduced $[Mn(mesbpy)(CO)_3][K(18-crown-6)]$ (**4**) were prepared by reduction of **1** in tetrahydrofuran (THF) by potassium-intercalated graphite (KC_8) (1.3 and 2.3 equiv., respectively), and anion **4** was characterized by NMR, FTIR, and X-ray crystallography. Paramagnetic **3** was characterized by IR spectroscopy; however, further characterization was not possible due to air sensitivity and short lifetime in solution.

Electrochemistry Under N$_2$. Electrochemical experiments were performed to determine how the bulky bipyridine ligand affects the electrocatalytic properties of Mn(bpy-R)(CO)$_3$X complexes. The cyclic voltammograms of **1** (Figure 4.13, 4.2) and **2** (Figure 4.1) in dry MeCN with 0.1 M tetrabutylammonium hexafluorophosphate (TBAPF$_6$) as the supporting electrolyte under an atmosphere of nitrogen (N$_2$) are distinctively different than previously reported electrochemistry of Mn(bpy)(CO)$_3$X, Mn(dmbpy)(CO)$_3$X (dmbpy = 4,4'-dimethyl-2,2'-bipyridine), and Mn(bpy-tBu)(CO)$_3$X.[7-8] The CV of **2** consists of one reversible reduction wave at −1.55 V vs. Fc$^+$/Fc. Peak-to-peak separation of this reversible couple is 39 mV, as compared to a peak-to-peak separation of 68 mV for Fc/Fc$^+$ in the same CV. This redox couple is best described as either an EEC or ECE mechanism, where two one-electron reductions occur combined with loss of a MeCN ligand. The second of the two one-electron reductions occurs either at the same or at a lower potential than the first reduction.[13] This overall two-electron reduction leads to the anionic state, [Mn(mesbpy)(CO)$_3$]$^−$ (**4**), as evidenced by chemical reductions and IR-SEC experiments (*vide infra*). For **2** in MeCN, digital simulations best support an EEC mechanism (Figure 4.19), where two one-electron reductions occur followed by loss of a MeCN ligand. Additionally, CVs of **2** feature an additional reduction at −2.25 V vs. Fc$^+$/Fc (Figure 4.21), likely corresponding to a bpy ligand-based reduction.
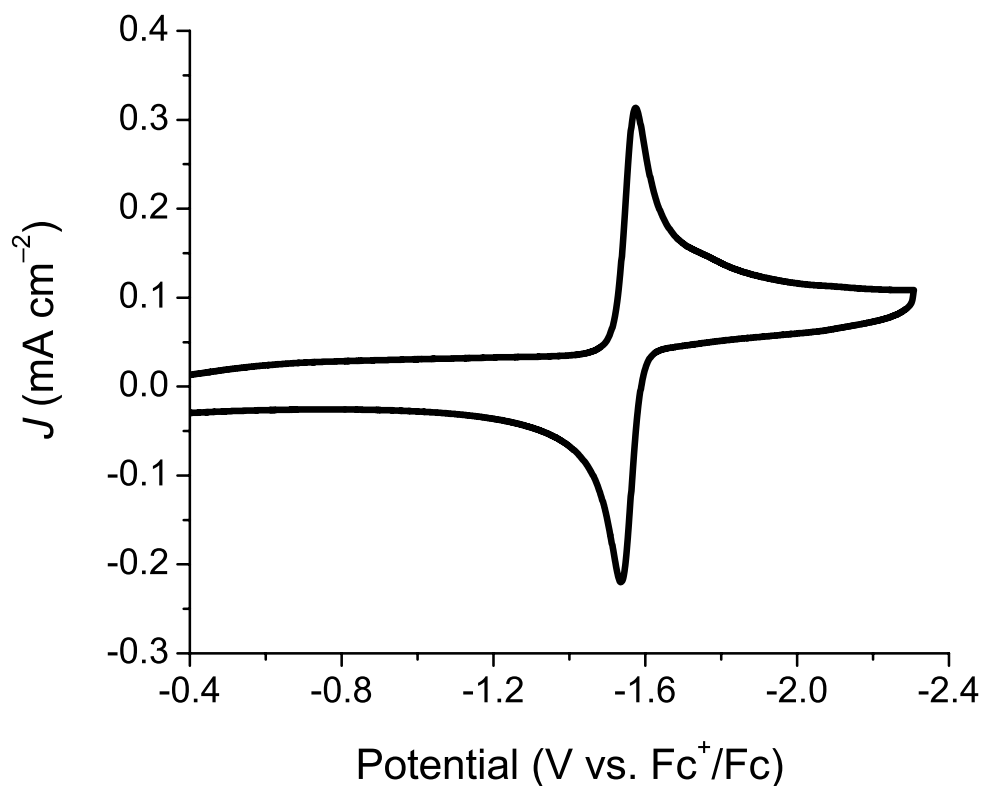
Figure 4.1 Cyclic voltammogram of 0.7 mM [Mn(mesbpy)(CO)$_3$(MeCN)](OTf) (**2**) in MeCN with 0.1 M TBAPF$_6$ as the supporting electrolyte under an atmosphere of N$_2$, showing one reversible, two-electron reduction of the complex. Scan rate is 0.1 V/s.

The corresponding two-electron reduction in CVs of **1** (peak-to-peak separation = 79 mV) is slightly less reversible than in CVs of **2** due to loss of Br$^-$ to form the anionic state (Figure 4.12, 4.2). The difference in peak-to-peak separation between **1** and **2** is likely due to the Br$^-$ ligand causing a larger change of the total charge of the complex upon dissociation, as well as the difference in binding affinity of MeCN versus Br$^-$. The scan rate dependence of the peak-to-peak separation in CVs of **1** and **2** is shown in Figure 4.18. IR-SEC experiments best support an ECE mechanism for complex **1** (*vide infra*), where loss of Br$^-$ occurs directly after the first one-electron reduction.

Typically, CVs of Mn(bpy-R)(CO)$_3$X complexes exhibit two irreversible, one-electron reduction waves, separated by 200–300 mV (depending on bpy substitution).[7-8] The first reduction of Mn(bpy)(CO)$_3$Br (–1.6 V vs. Fc$^+$/Fc)[8] is near the same potential as the reversible, two-electron couples of complexes **1** and **2** (–1.55 V vs. Fc$^+$/Fc). Incorporation of the bulky mesbpy ligand shifts the typical one- electron second reduction positive by ~300 mV, so that this reduction is now merged with the first reduction as an overall two-electron couple. This represents a 300 mV decrease in the potential required to form the anionic state. For comparison, CVs of complex **1** and of Mn(bpy)(CO)$_3$Br, under identical conditions, are overlaid in Figure 4.2.

The electrochemistry of Mn(bpy-R)(CO)$_3$X complexes typically show a large oxidation wave at approximately –0.63 V vs. Fc$^+$/Fc after scanning through the first one-electron reduction (Figure 4.2).[7-8] Lack of this oxidation peak and complete reversibility of the two-electron couple in the CVs of **1** and **2** suggests dimerization has been completely eliminated by the bulky mesbpy ligand. Experiments with slower scan rates also show no evidence for dimerization (Figure 4.14–4.15). Complexes **1** and **2** are freely diffusing in solution according to Randles–Sevcik analysis (Figure 4.16–4.17).[14]
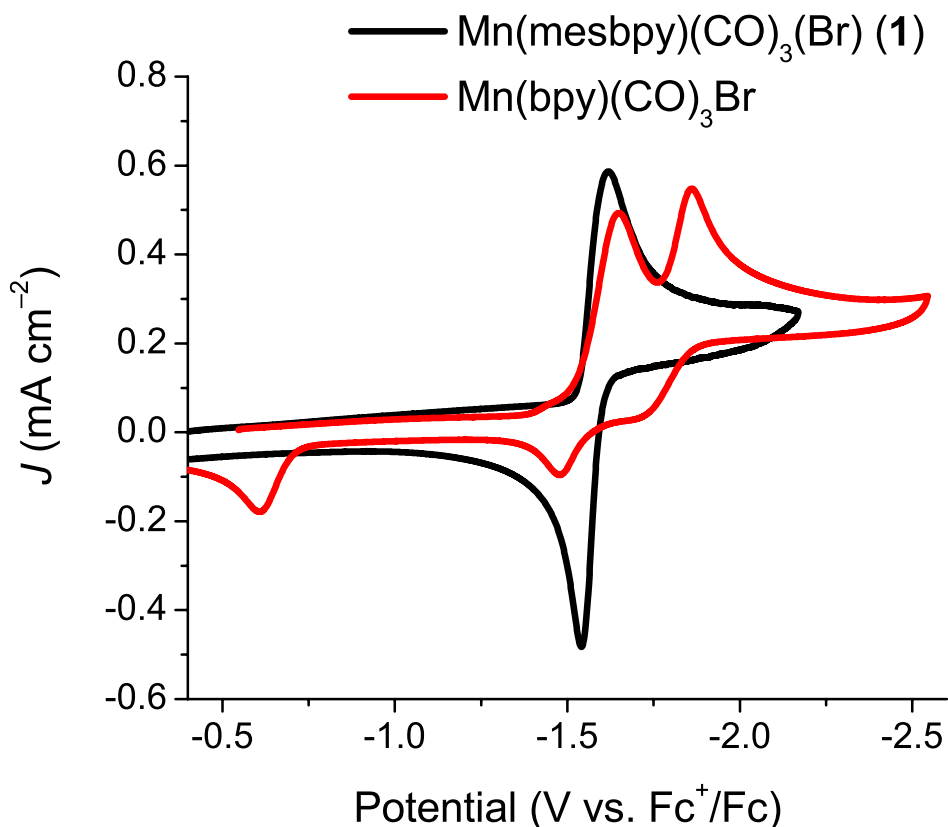
Figure 4.2 Comparison of the cyclic voltammograms of Mn(mesbpy)(CO)$_3$Br (**1**) and Mn(bpy)(CO)$_3$Br under identical conditions (1 mM complex). Each experiment is performed in MeCN with 0.1 M TBAPF$_6$ as the supporting electrolyte, under an atmosphere of N$_2$, at a scan rate of 0.1 V/s.

Infrared Spectroelectrochemistry (IR-SEC) Under N$_2$. IR-SEC of complex

1 under N$_2$ was performed to observe changes in accumulating species as the potential

is scanned cathodically (Figure 4.3). At its resting state, **1** has three characteristic v_{CO}

stretches for facially coordinated- tricarbonyl complexes at 2023, 1936, and 1913 cm$^-$

^{1}. When voltage is applied at the potential of the two-electron reduction seen in CVs

(*ca.* −1.6 V vs. Fc$^+$/Fc), we see growth of v_{CO} stretches at 1973, 1883, 1866, and 1808

cm^{-1}, decay of v_{CO} stretches at 2023 and 1936 cm^{-1}, and a shift of the v_{CO} stretch at

1913 cm^{-1} to slightly lower energy.

The ν_{CO} stretches at 1973, 1883, and 1866 cm^{-1} are indicative of a singly-reduced Mn complex, assigned as [Mn(mesbpy)(CO)$_3$]^0 (**3**). A shift of the high-energy ν_{CO} stretch from 2023 to 1973 cm^{-1} (~50 cm^{-1} shift to lower energy) is observed between **1** and this singly-reduced complex. This shift is very similar to the shift observed in five-coordinate [Re(bpy-R)(CO)$_3$] complexes, with no bound X,[1] and agrees well with our chemical reductions with KC$_8$ (*vide infra*). The ν_{CO} stretches at 1909 and 1808 cm^{-1} in the IR-SEC are indicative of a doubly-reduced [Mn(mesbpy)(CO)$_3$]$^-$ species (**4**), which binds CO$_2$ in electrocatalysis studies (*vide infra*). A shift of the high-energy ν_{CO} stretch from 2021 to 1917 cm^{-1} (~100 cm^{-1} shift to lower energy) is observed between **1** and **4**. The ν_{CO} stretches of this species match well with those for the anionic [Mn(mesbpy)(CO)$_3$]$^-$ complex produced by the chemical reduction of **1** with KC$_8$ (1917 and 1815 cm^{-1}, *vide infra*) and also match well with previously reported anionic [Mn(bpy-R)(CO)$_3$]$^-$ complexes.[7,15]

Both species **3** and **4** grow in at the same potential, and there is very small accumulation of the ν_{CO} stretches corresponding to singly-reduced **3**. When voltage is held at *ca.* −1.6 V vs. Fc$^+$/Fc for more than one minute, all singly-reduced species is converted to doubly-reduced species, **4**. Because a singly-reduced species is observed in these IR-SEC experiments, we believe that the reversible couple seen in CVs is the result of two one-electron reductions that occur at the same potential, instead of a direct two-electron reduction. Chemical reduction experiments (*vide infra*) and computer simulations (Figure 4.19) also support two one-electron reductions. These observations in IR-SEC are consistent with an ECE mechanism for **1**, where a single-

electron reduction and loss of Br$^-$ occurs followed by a second one-electron reduction resulting in the formation of complex **4**.
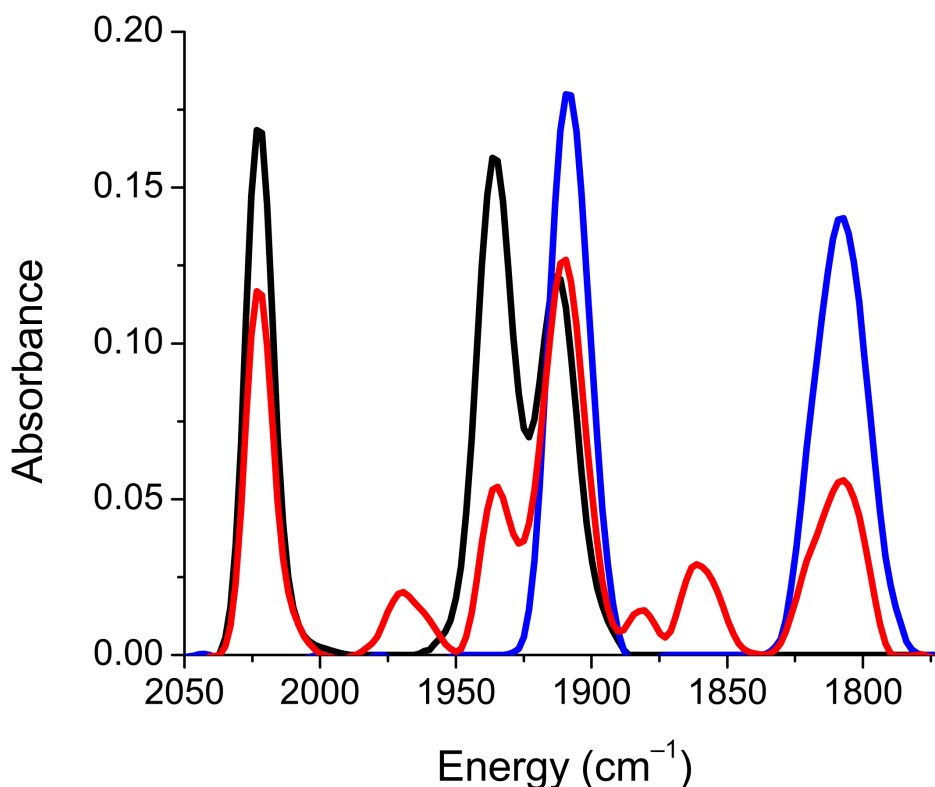
Figure 4.3 IR-SEC of 3mM **1** in MeCN with 0.1 M TBAPF$_6$ electrolyte under an atmosphere of N$_2$. The resting species (black, **1**) has three ν_{CO} stretches at 2023, 1936, and 1913 cm^{-1}. Upon initial reduction at *ca.* −1.6 V (red), singly-reduced species **3** (1973, 1883, 1866 cm^{-1}) and doubly-reduced species **4** (1909 and 1808 cm^{-1}) form. When the voltage of the cell is held at *ca.* −1.6 V for more than one min., all species are converted to **4** (blue).

Chemical Reductions. In addition to IR-SEC studies providing insights into the species leading up to the catalytically-active state, complexes **3** and **4** can be prepared via chemical reduction with KC$_8$. Reduction of **1** with ~1 equiv. of KC$_8$ in THF produces singly-reduced **3**. For this one-electron reduction, from **1** to **3**, the high-energy ν_{CO} stretch shifts by ~44 cm^{-1} to lower energy (2021 to 1984 cm^{-1}). This shift is very similar to the shift observed in the IR-SEC of Re(bpy-R)(CO)$_3$X complexes,

where the high energy v_{CO} stretch shifts ~40 cm^{-1} lower in energy to form the neutral five-coordinate Re(0)bpy(0) species with no bound X.[1] Likewise, the average of the two low-energy v_{CO} stretches shifts by ~36 cm^{-1} to lower energy. Due to the similar IR features between this complex and our singly-reduced Mn complex, we are assigning our singly-reduced species as [Mn(mesbpy)(CO)$_3$]^0 (**3**) with no bound Br$^-$ or solvent molecule. This one-electron reduction is in agreement with one-electron reductions of other Mn complexes, where loss of halide occurs rapidly,[7] except that the mesbpy ligand inhibits dimerization at the sixth coordination position. DFT-calculated v_{CO} stretches of **3** agree very well with the experimental v_{CO} stretches (see Experimental section). Complex **3** has a relatively short lifetime in THF solution. Although we were able to get an IR spectrum of **3**, this complex disproportionates into various species, including a Mn(I) complex and complex **4**, over the course of hours. Unreduced **1** and doubly-reduced **4** are much more stable than singly-reduced **3**, giving rise to a net two-electron reduction in CVs of **1** and **2**.

Additionally, the two-electron reduction in CVs of **1** and **2** in THF solution show much larger peak-to-peak separations than the corresponding reductions in MeCN solution (Figure 4.20). Specifically, a peak-to-peak separation of ~300 mV is observed for this reduction in the CV of **1** in THF. This peak-to-peak separation further supports the assignment of complex **3** as five-coordinate [Mn(mesbpy)(CO)$_3$]^0. In MeCN, species **3** is likely very unstable, as evidenced by the peak-to-peak separations in CVs of **1** and **2** in MeCN (39 mV and 79 mV, respectively). However, in THF solution, this species is stable long enough to obtain spectroscopic analysis.

Reduction of **1** with >2 equiv. of KC_8 in THF produces anion **4** and results in a shift of the high-energy ν_{CO} stretch from 2021 to 1917 cm^{-1} (~100 cm^{-1} shift to lower energy). Additionally, the average of the two low-energy ν_{CO} stretches of **3** shifts to the low-energy broad ν_{CO} stretch of **4**, a ~72 cm^{-1} shift to lower energy, from ~1887 cm^{-1} to 1815 cm^{-1}. These ν_{CO} stretches match those observed in our IR-SEC studies (1909 and 1808 cm^{-1}) and are indicative of a doubly-reduced [Mn(mesbpy)(CO)$_3$]$^-$ complex (**4**). The ν_{CO} stretches for **4** match well with previously reported anionic [Mn(bpy-R)(CO)$_3$]$^-$ complexes;[7,15] however, these ν_{CO} stretches are shifted to lower energy when compared to [Re(bpy-R)(CO)$_3$]$^-$ complexes.[2,16] Bond length alternation in the bpy ring in the crystal structure of **4** (*vide infra*) and DFT calculations (see Experimental section) indicate that significant electron density resides on the bpy ring. Although, the low-energy ν_{CO} stretches indicate that M–CO back bonding is notably increased in these Mn anions as compared to the analogous Re anions. The FTIR spectra of **1**, **3**, and **4** are shown in Figure 4.4.
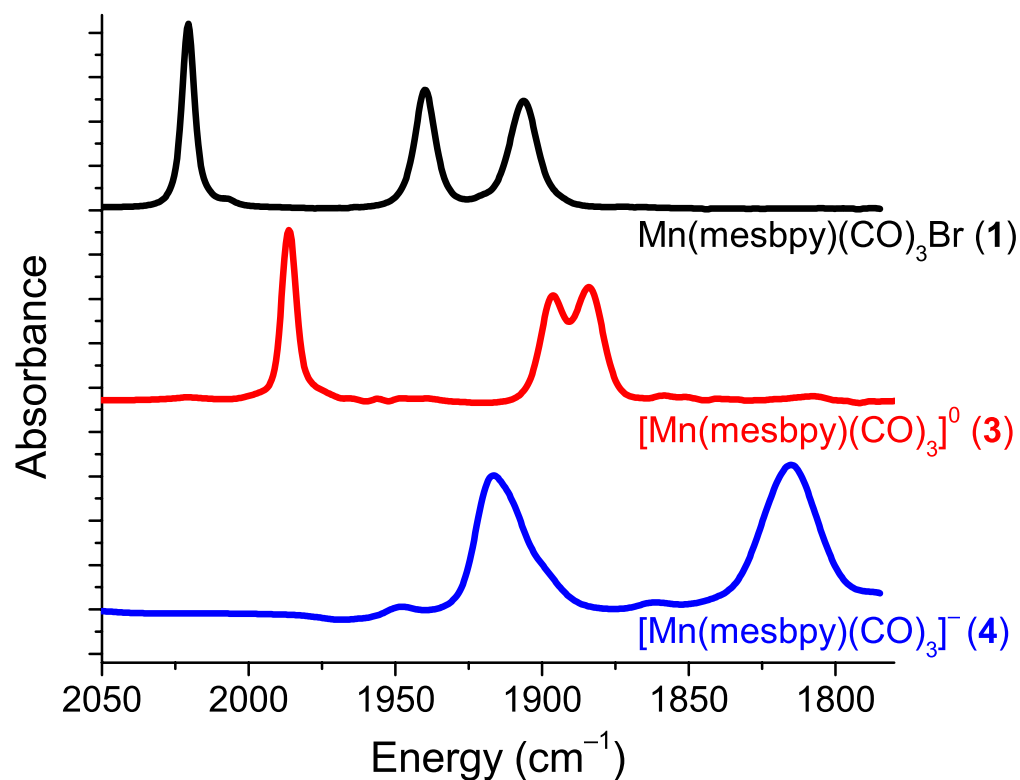
Figure 4.4 FTIR spectra of Mn(mesbpy)(CO)₃Br (black, **1**), [Mn(mesbpy)(CO)₃]^0 (red, **3**), and [Mn(mesbpy)(CO)₃][K(18-crown-6)] (blue, **4**) in THF, showing high correlation to species observed in IR-SEC studies.

X-ray Crystallography. We have had success growing crystals of the parent and anionic species of both Re(bpy-R)(CO)₃X and Mn(bpy-R)(CO)₃X complexes.[2,7,16] X-ray quality crystals of complex **1** were grown by vapor diffusion of pentane into a THF solution of the complex (Figure 4.5). Complex **1** crystallized in the space group C_2/c with 8 independent molecules in the unit cell. Attempts to crystallize singly-reduced **3** were not successful, as this species is not long-lived in solution. Specifically, any attempts at growing crystals of **3** resulted in a mixture of crystals of a Mn(I) complex and complex **4**. DFT calculations on **3** show a five-coordinate, unsaturated monomer with a HOMO delocalized across the bpy ligand and the Mn

center (Figure 4.40). Reduction of **1** by >2 equiv. of KC_8 in the presence of 18-crown-6 results in loss of bromide, forming the anionic complex **4**. 18-crown-6 was added during reduction to inhibit potassium coordination to the carbonyl ligands of **4**. The crystal structure of **4** was obtained from the vapor diffusion of pentane into a THF solution of the complex (Figure 4.6). Complex **4** is a five-coordinate, unsaturated anion with a $[K^+(18\text{-crown-6})]$ counter cation. In this structure, the $[K^+(18\text{-crown-6})(THF)]$ fragment has positional disorder over two positions (Figure 4.6, 4.20); however, the Mn anion fragment, the pertinent fragment for this study, is modeled without disorder. The geometry of anion **4** is square pyramidal (slightly skewed from a perfect square pyramid) with a $\tau_5 = 0$ ($\tau_5 = 0$ for a perfect square pyramid and $\tau_5 = 1$ for a perfect trigonal bipyramid).[17] X-ray diffraction structures of most other Re and Mn bipyridine anions are intermediate between square pyramidal and trigonal bipyramidal[2,7,16]. Specifically, [Re(bpy-*t*Bu)(CO)$_3$][K(18-crown-6)] and [Mn(bpy-*t*Bu)(CO)$_3$][K(18-crown-6)] are five coordinate and have a $\tau_5 = 0.46$ and $\tau_5 = 0.53$, respectively.[2,7] The bulky mesbpy ligand on **4** seems to prevent the carbonyls from rearranging towards trigonal bipyramidal, resulting in an almost ideal square pyramid. The X-ray crystal structure of **4** is nearly identical to that of its DFT-calculated structure (Figure 4.41).
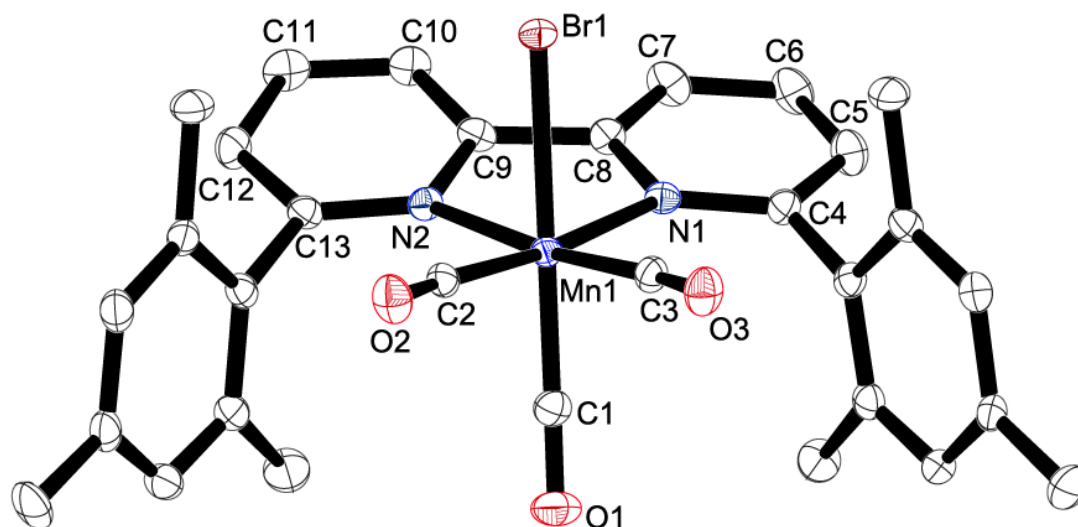
Figure 4.5 Molecular structure of Mn(mesbpy)(CO)$_3$Br (**1**), with hydrogen atoms omitted for clarity. Ellipsoids are set at the 50% probability level. Platon's SQUEEZE was used to remove a disordered THF solvent molecule from the asymmetric unit in the crystal structure. Relevant distances (Å) and bond angles (°): Mn1–Br1, 2.5298(6); Mn1–N1, 2.090(2); Mn1–N2, 2.084(2); Mn1–C1, 1.795(3); Mn1–C2, 1.809(3); Mn1–C3, 1.816(3); C1–O1, 1.147(3); C2–O2, 1.150(3); C3–O3, 1.142(3); N1–C4, 1.351(3); C4–C5, 1.393(4); C5–C6, 1.379(4); C6–C7, 1.380(4); C7–C8, 1.378(3); N1–C8, 1.366(3); C8–C9, 1.473(4); N2–C9, 1.364(3); C9–C10, 1.387(4); C10–C11, 1.375(4); C11–C12, 1.378(4); C12–C13, 1.387(4); N2–C13, 1.358(3); Br1–Mn1–N1, 84.90(6); Br1–Mn1–N2, 86.16(6); Br1–Mn1–C1, 176.71(9); Br1–Mn1–C2, 88.06(8); Br1–Mn1–C3, 87.54(8); N1–Mn1–N2, 79.35(8); N1–Mn1–C1, 97.63(10); N1–Mn1–C2, 172.96(10); N1–Mn1–C3, 99.25(10); N2–Mn1–C1, 96.35(10); N2–Mn1–C2, 100.28(10); N2–Mn1–C3, 173.64(10); C1–Mn1–C2, 89.39(12); C1–Mn1–C3, 89.98(12); C2–Mn1–C3, 80.34(11).

X-ray crystallography of **1** and **4** provide insight into the amount of electron density stored on the non-innocent bpy ligand. In the crystal structure of **4**, bond length alternation and the short inter-ring C_{py}–C_{py} bond in the bpy ligand are indicative of significant electron density on this non-innocent ligand (Figure 4.6).[18-19] The inter-ring C_{py}–C_{py} bond shortens from 1.473 Å in the crystal structure of **1** to 1.424 Å in **4**. This inter-ring C_{py}–C_{py} bond of **4** agrees well with previously reported crystal structures of [Mn(bpy-*t*Bu)(CO)$_3$]$^-$ and [Mn(bpy-*t*Bu)(CO)$_3$]$^-$ (1.413 and 1.418 Å,

respectively).[7,15] Our recent XAS and computational studies on similar [Re(bpy-R)(CO)$_3$]$^-$ complexes have determined that these anions possess formally Re(0)bpy(−1) ground states.[20] The crystal structure of **4** shows high similarity to that of many [Re(bpy-R)(CO)$_3$]$^-$ complexes. Recent DFT calculations by Scarborough *et al.*[21] and Hartl *et al.*[15] have characterized the [Mn(bpy)(CO)$_3$]$^-$ anion as a singlet diradical Mn(I)bpy(−2) complex with significant π-donation of the electron density from a bpy(−2) dianion to a Mn(I) ion. Scarborough *et al.* explains that this π-donation results in a crystal structure with C_{py}–C_{py} distances that resemble a bpy(−1) radical anion, which would imply a Mn(0) center. Both this computational and our experimental analyses are consist with a significant amount of electron density on the bpy-R ligand. In contrary to the aforementioned calculations, the increased Mn–CO back bonding observed by IR spectroscopy could indicate that less electron density lies on the bpy ligand in **4** and other [Mn(bpy-R)(CO)$_3$]$^-$ anions as compared to similar Re anions (which have Re(0)bpy(−1) formal ground states). The non-innocence of the bpy ligand helps explain the high selectivity of M(bpy-R)(CO)$_3$X (M = Mn or Re) catalysts for the reduction of CO_2 in the presence of significant concentrations of H$^+$, where electron density on the bpy ligand favors transferring two electronic charges to CO_2 through both σ and π interactions.[20]
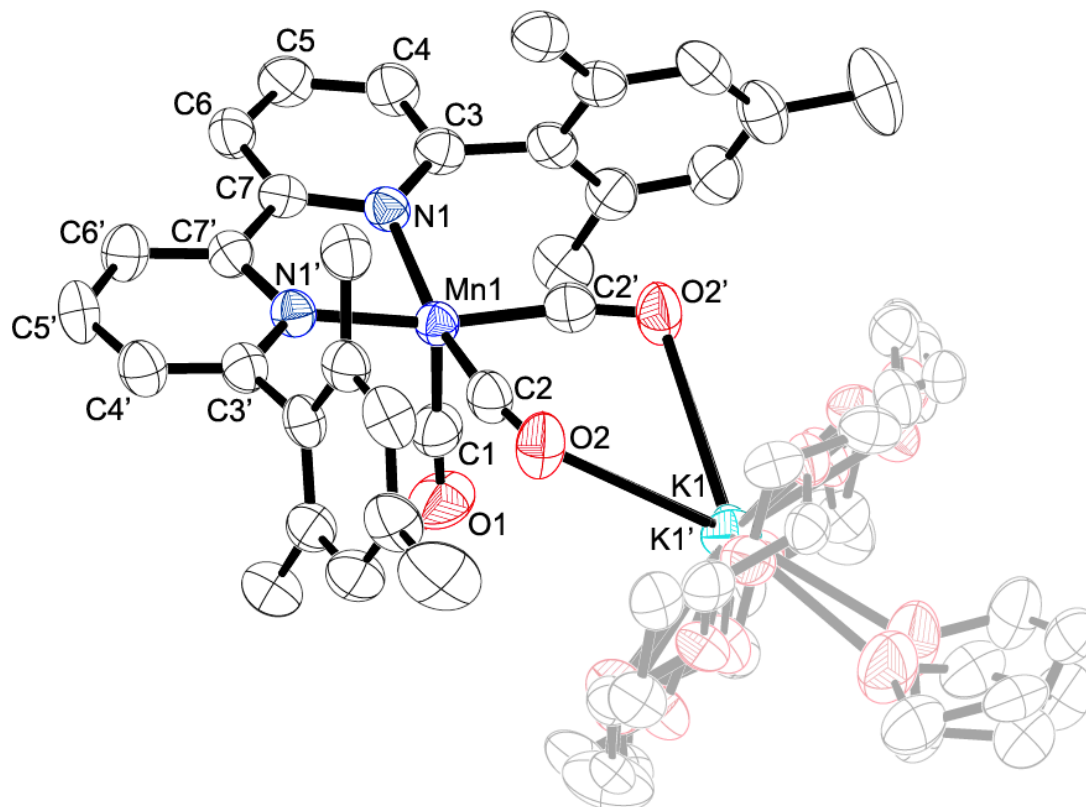
Figure 4.6 Molecular structure of [Mn(mesbpy)(CO)$_3$][K(18-crown-6)(THF)] (**4**), with hydrogen atoms omitted for clarity. The counter cation, [K$^+$(18-crown-6)] and THF solvent molecules are shown as partially transparent in order to emphasize the [Mn(mesbpy)(CO)$_3$]$^-$ anion. The [K$^+$(18-crown-6)(THF)] fragment has positional disorder over two positions (Figure 4.20). Ellipsoids are set at the 50% probability level. Relevant distances (Å) and bond angles (°): Mn1–N1, 2.005(4); Mn1–C1, 1.770(9); Mn1–C2, 1.783(6); C1–O1, 1.162(10); C2–O2, 1.178(7); N1–C3, 1.386(7); N1–C7, 1.389(6); C3–C4, 1.355(8); C4–C5, 1.417(8); C5–C6, 1.367(8); C6–C7, 1.399(7); C7–C7′, 1.424(10); N1–Mn1–N1′, 79.7(2); C1–Mn1–N1, 104.6(2); C1–Mn1–C2, 91.4(3); N1–Mn1–C2, 99.7(2); N1–Mn1–C2′, 163.7(2); C2–Mn1–C2′, 76.2(3).

Electrocatalysis. The electrocatalytic properties of **1** and **2** were studied in a custom-made, single-compartment, airtight cell with a glassy carbon working electrode, Pt wire counter electrode, and a Ag/AgCl wire pseudo-reference electrode separated from the main compartment by a Vycor tip. The electrochemical solution was sparged with CO$_2$ until gas-saturation (*ca.* 0.28 M).[22] CVs of complexes **1** and **2**

did not change under CO_2 in dry MeCN (Figure 4.7, 4.23–4.25). However, addition of weak Brønsted acid (H_2O, MeOH, or TFE) to **2** resulted in an increase in current at approximately –2.0 V vs. Fc^+/Fc, i.e. ~400 mV after the two-electron reduction that generates anionic species **4** (Figure 4.7, 4.23–4.26). This current increase corresponds to the electrocatalytic reduction of CO_2 to CO, as verified by controlled potential electrolysis (CPE) (*vide infra*). No current increase was observed in the CV of **2** under N_2 with added weak acid, indicating that the current increase is not due to proton reduction (Figure 4.7, 4.25). Higher concentrations of weak Brønsted acid in CO_2 reduction electrocatalysis experiments resulted in increased current densities, before reaching a peak current density and leveling off or dropping with addition of more H^+ (Figure 4.8, 4.24, 4.26 for MeOH, H_2O, and TFE, respectively). Addition of weak acid to **1** resulted in very similar trends in CVs (Figure 4.23).
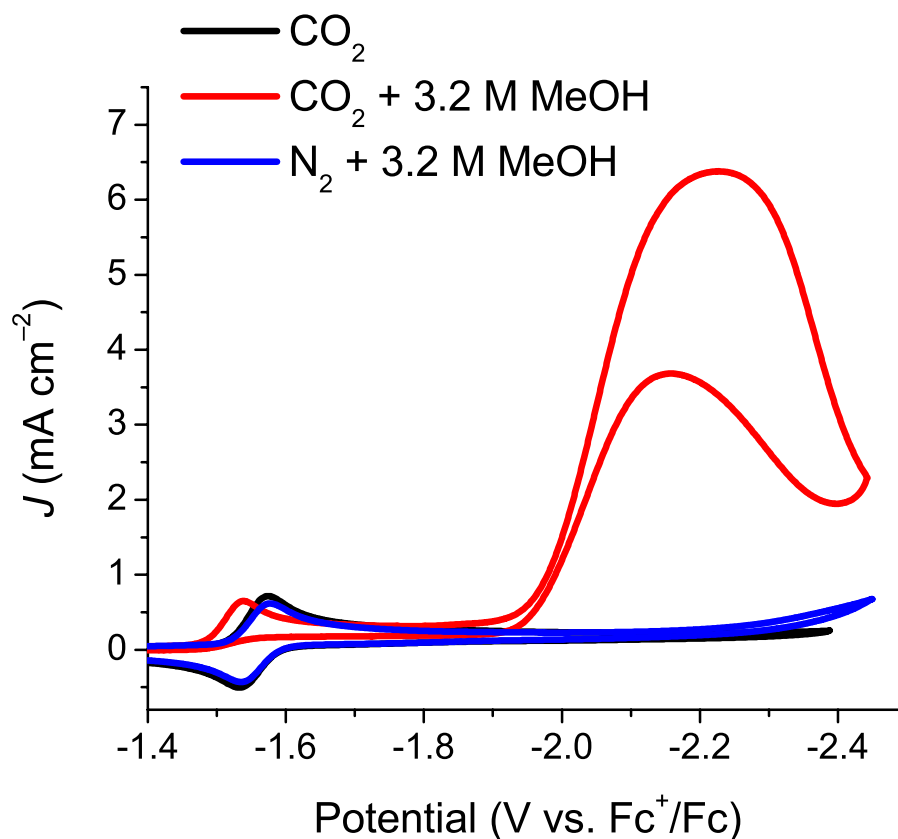
Figure 4.7 Cyclic voltammograms (CVs) showing catalytic current for 1 mM [Mn(mesbpy)(CO)₃(MeCN)](OTf) (**2**) under CO_2 with added MeOH (red). This current increase is due solely to the electrocatalytic reduction of CO_2 to CO. Under N_2 with added MeOH, no current increase is observed (blue), which is similar to the CV under CO_2 with no added MeOH (black). CVs were taken in 0.1 M TBAPF₆/MeCN with a scan rate of 0.1 V/s.
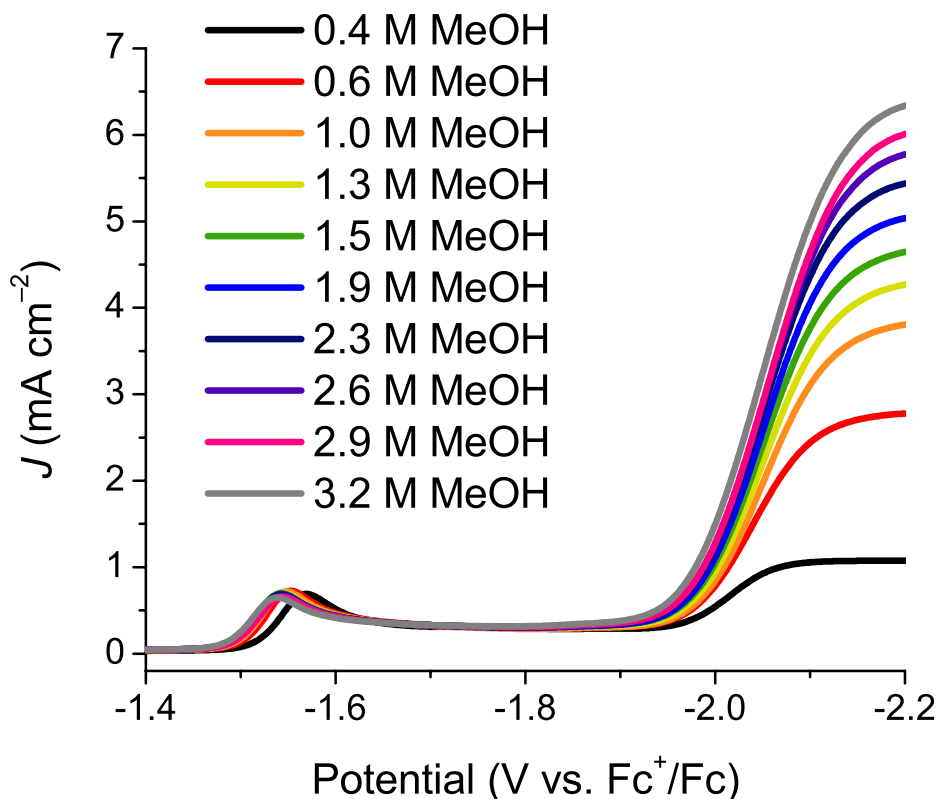
Figure 4.8 Linear scan voltammograms showing the electrocatalytic reduction of CO_2 to CO by 1 mM [Mn(mesbpy)(CO)$_3$(MeCN)](OTf) (**2**) in 0.1 M TBAPF$_6$/MeCN with addition of MeOH. The solution is under an atmosphere of, and saturated with (ca. 0.28 M), CO_2. Voltammograms are taken at a scan rate of 0.1 V/s.

For a reversible electron-transfer reaction followed by a fast catalytic reaction ($E_R C_{cat}$ scheme), the peak catalytic current (i_{cat}) is given by E4.3.[23] The derivation of E4.3 assumes that pseudo-first order kinetics apply, i.e. the reaction is first order in catalyst and that the concentrations of the substrates, Q, are large in comparison to the concentration of catalyst. In E4.3, n_{cat} is the number of electrons required for the catalytic reaction ($n_{cat} = 2$ for the reduction of CO_2 to CO), F is Faraday's constant, A is the surface area of the electrode, [cat] is the catalyst concentration, D is the diffusion constant of the catalytically-active species, k_{cat} is the rate constant of the catalytic reaction, and [Q] is the substrate concentrations. Plotting i_{cat} versus the square

root of [CO$_2$] shows a linear relationship, indicating that the catalytic reaction is first order in [CO$_2$] (Figure 4.33). Additionally, plots of i_{cat} versus [H$^+$] show second order dependence on [H$^+$] at low [H$^+$] (Figure 4.34). At high [H$^+$], i_{cat} reaches a limiting value independent of [H$^+$] (Figure 4.34), which is typical of saturation kinetics expected for catalytic reactions.[24] Electrocatalytic reactions are also first order in [cat], as evidenced by plotting i_{cat} vs. [cat] (Figure 4.35–4.36). The initial catalytic current plateaus are relatively scan rate independent for all CVs with added H$_2$O, MeOH, and TFE (Figure 4.29, 4.30, and 4.32). In summary, at high [H$^+$], the electrocatalytic reduction of CO$_2$ is first order in catalyst, first order in CO$_2$, independent of acid concentration, and at steady state conditions.

$$i_{cat} = n_{cat}FA[cat]\left(Dk_{cat}[Q]^y\right)^{1/2} \tag{E4.3}$$

The equation below (E4.4) describes the peak current of a complex with a reversible electron transfer and with no following reaction.[25] In E4.4, R is the universal gas constant, T is temperature, n_p is the number of electrons in the reversible, non-catalytic reaction, and v is scan rate (0.1 V/s). Dividing E4.3 by E4.4 allows for the determination of i_{cat}/i_p and allows to further calculate the catalytic rate constant (k_{cat}) and the turnover frequency (TOF), as shown in E4.5. In this equation, A cancels out because the same electrode was used for the experiments under CO$_2$ and N$_2$. D also cancels out because we are assuming that the diffusion constant of the catalytically-active species does not change significantly under CO$_2$ or N$_2$.

$$i_p = 0.4463n_p^{3/2}FA[cat]\left(\frac{F}{RT}\right)^{1/2}v^{1/2}D^{1/2} \tag{E4.4}$$

$$\text{TOF} = k_{cat}[Q] = \frac{F \upsilon n_p^3}{RT} \left(\frac{0.4463}{n_{cat}} \right)^2 \left(\frac{i_{cat}}{i_p} \right)^2 \qquad \textbf{(E4.5)}$$

Using E4.3–E4.5, we can calculate peak i_{cat}/i_p and TOF values for catalyst **2** with added H_2O, MeOH, or TFE. For these calculations, i_p is determined as the peak current under N_2 with an amount of weak Brønsted acid corresponding to peak i_{cat} conditions. Addition of H_2O (pK_a = 31.4 in DMSO)[26] to a 1 mM solution of **2** under CO_2 resulted in a peak i_{cat}/i_p = 20 (4.8 mA/cm^2 peak current density) and a TOF = 700 s^{-1} at 3.5 M H_2O. Addition of MeOH or TFE (pK_a = 29.0[26] and 23.5,[27] respectively, in DMSO) leads to higher peak current densities under CO_2. (Note: literature values for pK_as of H_2O, MeOH, and TFE in MeCN are not reported; however, these values can be estimated accordingly from pK_a values in DMSO.) Specifically, addition of MeOH resulted in a peak i_{cat}/i_p = 30 (7.6 mA/cm^2 peak current density) and a TOF = 2000 s^{-1} at 3.2 M MeOH. Addition of TFE resulted in a peak i_{cat}/i_p = 50 (13 mA/cm^2 peak current density) and a TOF = 5000 s^{-1} at 1.4 M TFE. Calculated i_{cat}/i_p and TOF values for **2** and previously reported Mn(bpy-tBu)(CO)$_3$Br are listed in Table 4.1. Catalyst **2** is more active than the most active Mn bpy catalyst previously reported, Mn(bpy-^{t}Bu)(CO)$_3$Br,[15] under all weak Brønsted acids studied. Under similar concentrations of TFE, catalyst **2** is over 10 times more active than Mn(bpy-^{t}Bu)(CO)$_3$Br.

Table 4.1 Comparison of peak i_{cat}/i_p and TOF values for both [Mn(mesbpy)(CO)$_3$(MeCN)](OTf) (2) and [Mn(bpy-tBu)(CO)$_3$Br in MeCN (1 mM each catalyst). Solutions are saturated with (ca. 0.19–0.28 M)^a and under an atmosphere of CO$_2$ with added weak Brønsted acids. Data are taken from voltammograms at a scan rate of 0.1 V/s.

Brønsted acid	[Mn(mesbpy)(CO)$_3$(MeCN)](OTf) (2)			Mn(bpy-tBu)(CO)$_3$Br		
	[acid]^b (M)	$i_{cat}/i_p{}^c$	TOF (s^{-1})	[acid]^d (M)	$i_{cat}/i_p{}^e$	TOF (s^{-1})
H$_2$O	3.5	20	700	3.1	25	120
MeOH	3.2	30	2000	5.8	26	130
TFE	1.4	50	5000	1.4	42	340

^{a}[CO$_2$] is ca. 0.28 M in dry MeCN, 0.26 M in 3.5 M H$_2$O, 0.27 M in 3.2 M MeOH, and 0.27 M in 1.4 M TFE.[14] ^{b}[acid] at highest i_{cat}/i_p for **2**. ^{c}i_{cat}/i_p values are calculated at equal [acid]. ^{d}[acid] at highest i_{cat}/i_p for Mn(bpy-tBu)(CO)$_3$Br. ^{e}Values taken from Ref. 7.

A notable feature of the catalytic CVs of **1** and **2** is the pronounced deviation from a steady state "S-shaped" wave (Figure 4.7, 4.25). The peak maximum at *ca.* −2.2 V vs. Fc$^+$/Fc and especially the peak in the return oxidation (*ca.* −2.1 V vs. Fc$^+$/Fc) are quite unusual and deserve comment. These unusual characteristics likely arise from multiple factors. The main factor contributing to this odd current response is an overlapping bpy-based reduction at *ca.* −2.3 V vs. Fc$^+$/Fc (Figure 4.21, 4.27, 4.31). At a scan rate of 100 mV/s, this additional reduction feature cannot be distinguished from the catalytic current response (Figures 4.7, 4.25, 4.27, 4.31). However, at higher scan rates, this reduction feature becomes apparent (Figures 4.27, 4.28, 4.31). The catalytic current plateaus, directly before the bpy-based reduction (Figure 4.27–4.32), are fairly scan rate independent. The scan rate dependences of the catalytic current plateaus are shown in Figures 4.29, 4.30, and 4.32 (for added H$_2$O, MeOH, and TFE, respectively). Additionally, diffusional characteristics (peaks) in catalytic CVs under slow scan rates can be ascribed to side phenomena.[28-29] These side phenomena are generally side

reactions that are generated by the catalytic reaction, but that compete with this catalytic reaction.[29] The fact that the catalytic wave occurs at a potential beyond the formally Mn(I/–I) prewave, where no electrochemical process is observed in the absence of CO_2/H^+, indicates that this catalytic wave involves the reduction of a species that does not exist without CO_2/H^+. In view of the formally Mn(I/–I) prewave dependence of CO_2 concentration (*vide infra*), this species is likely the hydroxycarbonyl complex, Mn(mesbpy)(CO)$_3$(CO$_2$H) (*vide infra*). This 18-e$^-$ complex appears to be stable until it is reduced by a third e$^-$, in a likely bpy-based reduction. This reduction presumably labilizes the CO$_2$H$^-$ group to form CO and $^-$OH, the latter of which rapidly reacts with H$^+$ in solution. This has the effect of raising the pH in the reaction diffusion layer. The subsequent reduction of a Mn(I) complex and reaction with CO_2/H^+ to form another Mn–CO$_2$H species further raises the local pH and depletes CO_2. In addition, since the source of the H$^+$ is a weak acid, the conjugate base RO$^-$ should be capable of binding a second equivalent of CO_2 to give the alkyl carbonate ROCO$_2^-$, further depleting the CO_2 concentration. These side reactions compete with catalysis for the same substrates and have the effect of decreasing overall rates of catalysis. Lastly, if catalysis can occur only upon bpy-based reduction of Mn(mesbpy)(CO)$_3$(CO$_2$H), then this reduction process should show diffusional characteristics, as should the return oxidation of the radical anion. These side reactions along with the overlapping bpy-based reduction at *ca*. –2.3 V vs. Fc$^+$/Fc are likely the origins of the unusual catalytic wave shape. A more detailed relation between the

catalytic mechanism and appearance of the catalytic wave in this system is beyond the scope of this article, and will be the subject of ongoing investigation.

CPE was performed on **2** at –2.2 V vs. Fc^+/Fc to measure the efficiency at which CO is produced and to gain insights into the lifetime of the catalyst. Gas chromatography indicates that no hydrogen is formed during these experiments, and catalyst **2** operates with a Faradaic efficiency of $98 \pm 6\%$ for the formation of CO from CO_2, measured for the first ~4 turnovers of the catalyst (first ~70 minutes of catalysis, based on total catalyst concentration in cell) (Figure 4.9). These CPE experiments were performed with 0.5 mM **2** and 0.3 M TFE with a carbon rod working electrode (surface area = 7.4 cm^2). Although Faradaic efficiency was only recorded for the first 70 minutes of catalysis, the lifetime of catalyst **2** is much great than this, as evidence by the CPE trace in Figure 4.37. The catalyst sustained current densities of approximately 3.5 mA/cm^2 during the first hour of electrolysis (Figure 4.37), corresponding to a TOF = 480 s^{-1} (see Experimental section). This calculated TOF is significantly higher than the TOF calculated for $Mn(bpy-tBu)(CO)_3Br$ during CPE with 1.4 M TFE (270 s^{-1}).[7] Current density fluctuated between 3.4 – 2.9 mA/cm^2 over the next ~6 hours and gradually declined throughout the remainder of the experiment (total time of CPE was ~25 hours). Faradaic efficiencies for CO production gradually dropped after the first few hours of electrolysis; however, no hydrogen production was observed throughout the entire experiment.
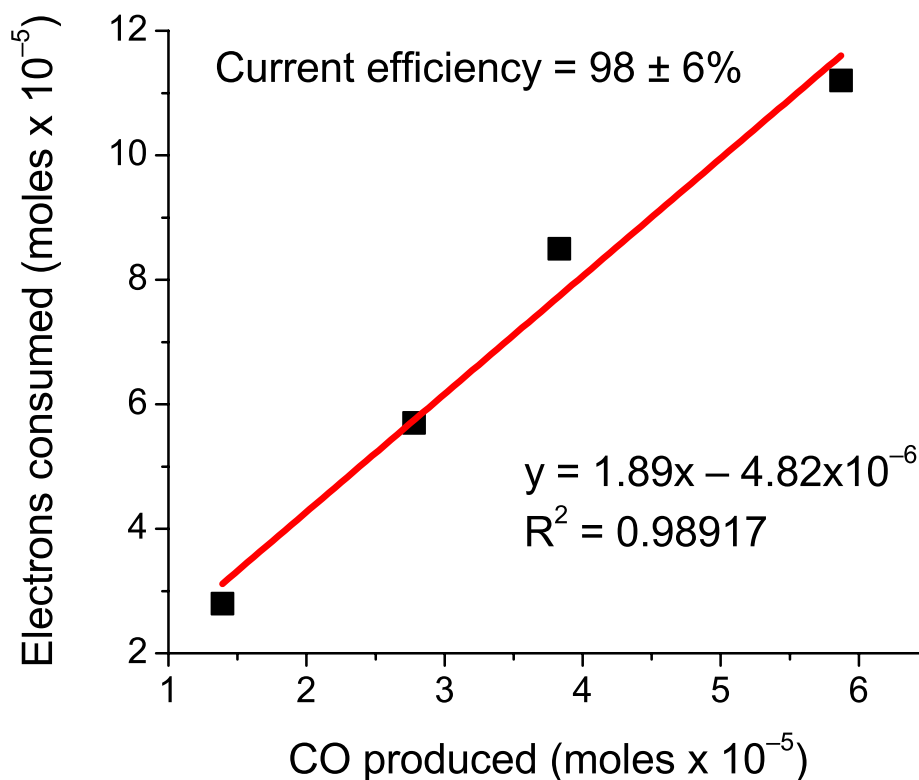
Figure 4.9 Production of CO from CO_2 by 0.5 mM [Mn(mesbpy)(CO)$_3$(MeCN)](OTf) (**2**) during controlled potential electrolysis at -2.2 V vs. Fc$^+$/Fc with 0.3 M TFE. The slope of ca. 2 represents a Faradaic efficiency of $98 \pm 6\%$. After reaching a steady state current, bulk electrolysis of this solution showed no significant current degradation over the course of several hours.

CPE under N_2 with 0.3 M TFE was performed in order to prove that the observed CO did not result from degradation of catalyst **2** (Figure 4.37). The results of this CPE show that only a minuscule amount of CO (Faradaic efficiency = ~2%), and no H_2 was observed over the course of ~24 hrs. Therefore, within error, all observed CO in our CPE experiment under CO_2 resulted from the reduction of CO_2, rather than degradation of the catalyst. After ~1.15×10^{-4} moles of electrons were consumed, 5.87 $\times 10^{-5}$ moles of CO were produced for CPE under CO_2 and only 1.87×10^{-6} moles of CO were produced for CPE under N_2. Additionally, this experiment proves that the

catalyst is extremely stable under the conditions of this CPE experiment over the course of ~24 hrs.

CO$_2$ Binding. In addition to catalytic current enhancement, CVs of **2** under CO$_2$ with added Brønsted acid show loss of reversibility at the two-electron reduction (Figure 4.7) and a shift of the reduction wave to more positive potentials (Figure 4.10, Table 4.2). Both of these characteristics are indicative of CO$_2$ binding to the Mn catalyst.[30-31] Gagne *et al.* and Fujita *et al.* have utilized E4.6 to calculate substrate binding constants (K_Q) for various copper, cobalt, and nickel macrocycles.[30-32] This equation describes an $E_R C_{cat}$ mechanism, where electron transfer and forward and backward reactions are sufficiently rapid and K_Q is relatively large. For complex **2**, we see no change in the two-electron reduction between CVs under N$_2$ or under CO$_2$ (without added H$^+$), indicating that CO$_2$ binding occurs only with the addition of an external proton source (Figure 4.10, 4.39). CVs in Figure 4.10 and 4.39 do not show the reversal potentials in order to more clearly show the shift of the cathodic peak. CVs show the same behavior whether the cathodic scan is reversed before or after the potential of the catalytic wave (see Figure 4.7). In CVs of **2**, we see irreversible behavior under CO$_2$/H$^+$, *i.e.* only the cathodic component of the voltammograms was observed. This feature is likely due to a Mn(I)–CO$_2$H species forming as a result of a two-electron oxidative addition of CO$_2$/H$^+$ to the Mn center of **4**. This Mn(I)–CO$_2$H species appears to be stable at these potentials once it is formed, which explains the irreversible behavior observed in CVs. Because of these characteristics, our CVs are a limiting case of an $E_R C_{cat}$ scheme, where electron transfer and forward reactions are

sufficiently rapid, but the reverse reaction is slow. Although E4.6 applies to reversible

kinetics, this analysis is sufficient to estimate a binding constant for CO_2/H^+. The

observed shift in potential (ΔE) of the cathodic peak is not a linear function of

$\ln[CO_2]$, consistent with a binding constant ($K_{CO2/H+}$) ≤ 100 M^{-1} (Figure 4.38).[31] An

average $K_{CO2/H+} = 46 \pm 10$ M^{-1} was calculated for **2** using E4.6.

$$E = E^\circ + (RT/nF)\ln\{1+[CO_2]K_Q\} \qquad \textbf{(E4.6)}$$
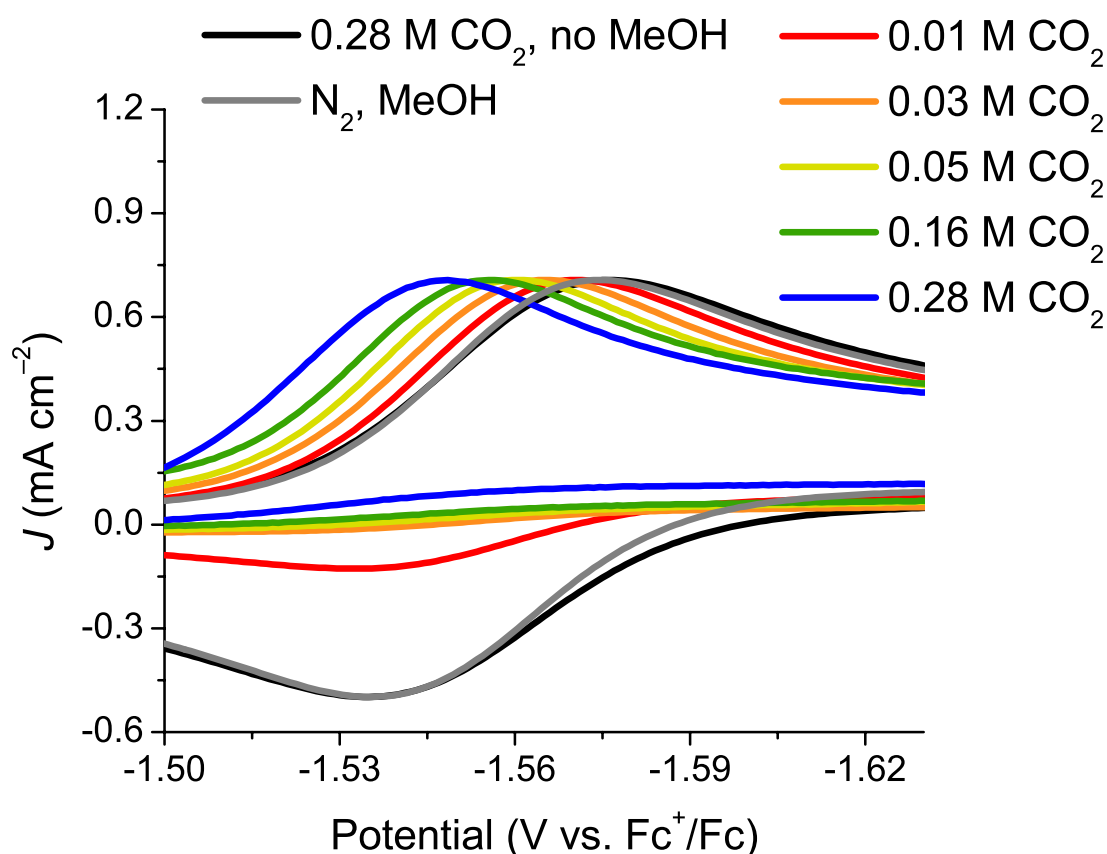
Figure 4.10 Cyclic voltammograms (CVs) of 1 mM
[Mn(mesbpy)(CO)$_3$(MeCN)](OTf) (**2**) showing evidence for CO_2 binding with 0.8 M
MeOH. As the [CO_2] increases from ca. 0 to 0.28 M, the cathodic peak potential of the
two-electron reduction shifts to more positive potentials. In these CVs, the reverse
oxidation scans are not shown in order to more clearly show the shift of the cathodic
peak. CVs are taken at a scan rate of 0.1 V/s.

Table 4.2 Cathodic peak potentials (E) in CVs[b] of [Mn(mesbpy)(CO)$_3$(MeCN)](OTf) (2)[c] under various [CO$_2$] and 0.8 M MeOH.

[CO$_2$][a] (M)	E (V vs. Fc$^+$/Fc)
0.00	− 1.576
0.01	− 1.571
0.03	− 1.565
0.05	− 1.561
0.16	− 1.550
0.26	− 1.546

[a][CO$_2$] in MeOH taken from reference 14. [b]CVs were taken in 0.1 M TBAPF$_6$/MeCN with a scan rate of 0.1 V/s. [c][**2**] = 1 mM.

Infrared Spectroelectrochemistry (IR-SEC) Under CO$_2$/H$^+$. We utilized IR-SEC with added CO$_2$ and MeOH in order to elucidate why catalysis occurs at a potential ~400 mV more negative than the potential at which the two-electron reduced, anionic CO$_2$-binding state is formed. The results of this IR-SEC experiment on complex **1** with 0.14 M CO$_2$ (half-saturated) and *ca.* 80 mM MeOH are shown in Figure 4.11. At *ca.* −1.4 V, complex **1** is the only species in solution with ν_{CO} stretches at 2023, 1936, and 1904 cm^{-1}. Upon reaching the potential of the two-electron reduction seen in CVs (*ca.* −1.6 V), we see complete conversion of complex **1** to two new species that, based on the ν_{CO} spectrum, must be a Mn(I) complex and anion **4**. Specifically, we see growth of ν_{CO} stretches at 2006, 1907, and 1806 cm^{-1}. Since the ν_{CO} band at 1907 cm^{-1} has a much greater intensity than either of the other bands, we believe two ν_{CO} stretches contribute to this lineshape. The ν_{CO} stretches at 1907 and 1806 cm^{-1} match anion **4**. The other ν_{CO} stretches at 2006 and 1907 cm^{-1} are consistent with a Mn(I) tricarbonyl complex, likely a *fac*-Mn(I) tricarbonyl species. Upon reaching the potential of catalysis (*ca.* −2.1 V), the ν_{CO} stretches corresponding to this Mn(I) tricarbonyl species disappear, and the only species that persists is anion

4. The ν_{CO} stretches of this Mn(I) tricarbonyl species (2006 and 1907 cm^{-1}) agree well with previously reported *fac*-Mn tricarbonyl complexes with bound ester groups and chelating diphosphine ligands,[33] as well as with previously reported *fac*-Re(bpy-R)(CO)$_3$(CO$_2$H) complexes.[34-35] Bourrez *et al.* recently reported the characterization of a *mer*-Mn(II)(dmbpy)(CO)$_3$(CO$_2$H) intermediate in the electrocatalytic CO$_2$ reduction studies of a [Mn(0)(dmbpy)(CO)$_3$]$_2$ dimer.[36] A *mer*-Mn(I) tricarbonyl species would likely have at least one ν_{CO} stretch higher in energy than complex **1**.[37-38] Therefore, we are assigning the Mn(I) tricarbonyl species formed under two-electron reduction conditions in the presence of CO$_2$/H$^+$ as *fac*- Mn(mesbpy)(CO)$_3$(CO$_2$H). Complexes of this type usually have a weak ν_{OCO} stretch between 1700–1500 cm^{-1}, but this stretch was not observed in our experiments likely due to the small accumulation of this Mn–CO$_2$H complex or due to overlapping ν_{OH} bends from added MeOH in this region. In addition to these IR-SEC experiments, reacting chemically-reduced anion **4** with CO$_2$, followed by the addition of a small concentration of MeOH, results in a color change of the solution from dark blue to yellow-orange. This color change is consistent with the formation of a Mn(I) complex. Experiments are ongoing in our laboratory to independently synthesize, isolate, and fully characterize this Mn(I)–CO$_2$H species.
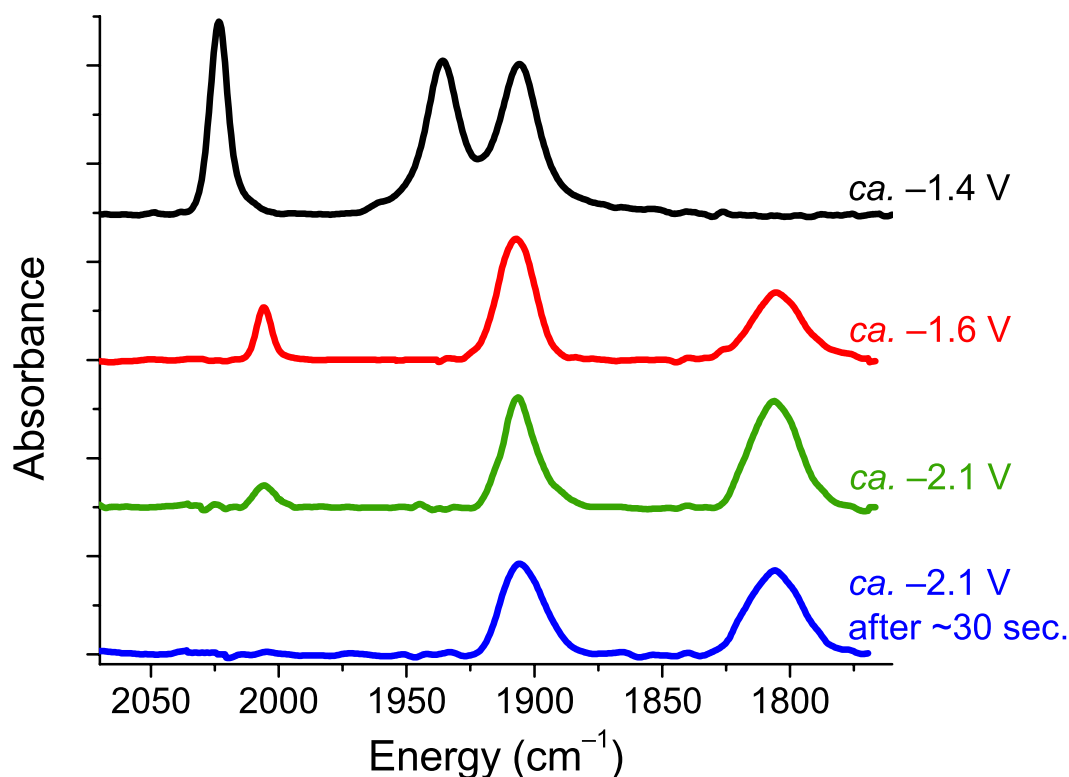
Figure 4.11 IR-SEC of 3 mM **1** in MeCN with 0.1 M TBAPF$_6$ electrolyte, *ca.* 0.14 M CO$_2$ (half-saturation), and *ca.* 80 mM MeOH. At *ca.* −1.4 V (black), **1** is the only species in solution (ν_{CO} = 2023, 1936, and 1913 cm^{-1}). At the potential of the two-electron reduction (red), **1** fully converts into two new species form, a Mn(I)–CO$_2$H tricarbonyl complex and anion **4**. The Mn(I)–CO$_2$H complex persists until the potential of catalysis (green), and this species fully disappears upon holding the cell at this potential (blue).

Since a Mn(I)–CO$_2$H species appears to be observed between the potentials of *ca.* −1.6 V and −2.1 V, we have concluded that this species is responsible for the unusual "over reduction" required to initiate catalysis. Again, by "over reduction," we mean that while **1** or **2** can be reduced by two electrons to form **4**, and while **4** shows clear evidence for binding and reducing CO$_2$/H$^+$, catalysis is not initiated until a third electron is introduced at ca. −2.0 V vs. Fc$^+$/Fc. Other possible intermediates that might have contributed to the high added potential could either be a formally Mn(I) or Mn(0)

tetracarbonyl species. We see no evidence for the characteristic ν_{CO} pattern for tetracarbonyl species in our IR-SEC spectra, which further supports the identification of a Mn(I)–CO$_2$H species. We propose a simplified catalytic mechanism in Figure 4.12 that is consistent with all of our experimental observations. Here, after **1** is reduced to **4** at −1.6 V vs. Fc$^+$/Fc, anion **4** binds CO$_2$ with H$^+$ forming the hydroxycarbonyl complex, Mn(I)(mesbpy)(CO)$_3$(CO$_2$H). This 18-e$^-$ Mn(I)–CO$_2$H species is reduced at −2.0 V vs. Fc$^+$/Fc, likely through a bpy-based reduction, which is the source of the additional potential required for catalysis. After being reduced, this species is a formally 19-e$^-$ species, and thus, decomposition to CO and OH$^-$, the latter of which rapidly reacts with H$^+$, is believed to be extremely fast. This presumption is also supported by not observing any species other than anion **4** and the Mn–CO$_2$H species at the potential of catalysis in our IR-SEC experiments. Further reduction regenerates the catalytically-active state **4**. This proposed mechanism is very similar to the mechanism of [Re(bpy-R)(CO)$_3$]$^-$ complexes, reported recently by our group.[34,39] For these Re complexes, CO$_2$ and H$^+$ bind rapidly to Re, and the resulting Re(I)–CO$_2$H complex must be reduced to continue the catalytic cycle.
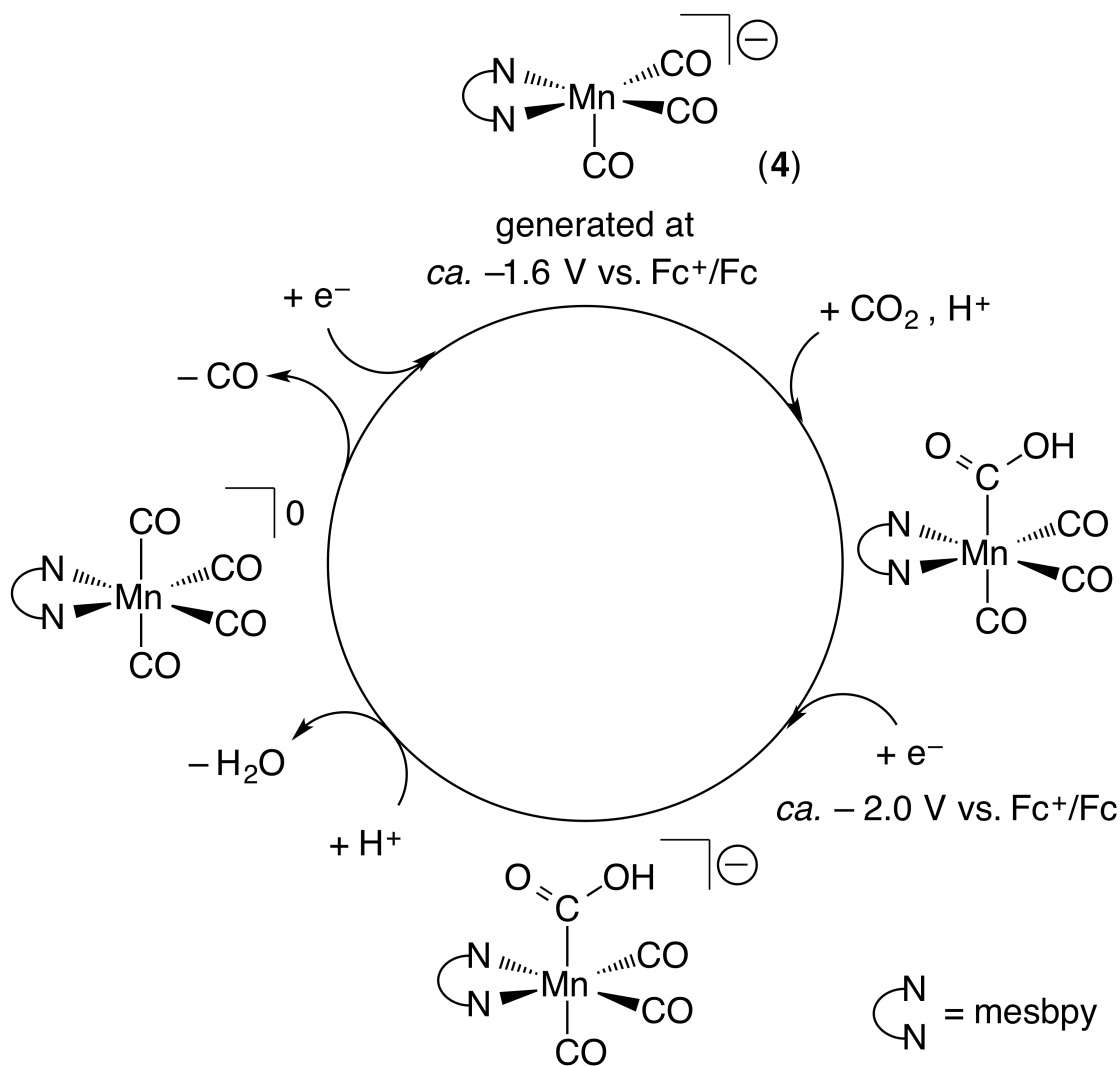
Figure 4.12 Proposed catalytic mechanism of [Mn(mesbpy)(CO)$_3$]$^-$ (**4**) with CO$_2$ and H$^+$, showing how reduction of a Mn(I)–CO$_2$H species can determine the overpotential for catalysis.

4.3 Conclusions

We have described earth-abundant metal catalyst precursors, Mn(mesbpy)(CO)$_3$Br (**1**) and [Mn(mesbpy)(CO)$_3$(MeCN)](OTf) (**2**), which show increased catalytic activity for the reduction of CO$_2$ to CO when compared to previously reported Mn(bpy-R)(CO)$_3$X complexes. In the electrochemistry of

complexes **1** and **2**, we see no evidence for dimerization, indicating that the bulky mesbpy ligand possesses sufficient steric hindrance to eliminate dimerization at the Mn center. Eliminating dimerization results in atypical electrochemistry compared to standard Mn(bpy-R)(CO)$_3$X complexes. Typically, CVs of Mn bpy complexes show two one-electron reductions separated by ~300 mV. For complexes **1** and **2**, a single, reversible two-electron reduction wave is observed under N$_2$ at *ca.* −1.6 V vs. Fc$^+$/Fc. This two-electron reduction generates the anionic state, [Mn(mesbpy)(CO)$_3$]$^-$ (**4**), at a potential of 300 mV more positive than in typical Mn bpy catalysts. We have characterized both complex **1** and **4** by X-ray crystallography. IR-SEC of **1** under N$_2$ shows that both a singly-reduced, [Mn(mesbpy)(CO)$_3$]^0 (**3**), and anionic complex **4** form at the same potential. Since a singly-reduced species is observed in IR-SEC experiments, we believe that the two-electron reversible reduction seen in CVs of **1** and **2** is the result of two one-electron reductions, rather than a direct two-electron reduction. This conclusion is consistent with chemical reductions with KC$_8$ and with DFT results.

Although anion **4** is generated at −1.6 V vs. Fc$^+$/Fc, catalysis does not occur until ~400 mV more negative, at *ca.* −2.0 V vs. Fc$^+$/Fc. CVs of **1** and **2** under CO$_2$ with added Brønsted acid show loss of reversibility at the two-electron reduction and a shift of this reduction wave to more positive potentials, indicative of CO$_2$ binding with H$^+$ to complex **4**. IR-SEC experiments under CO$_2$ with added Brønsted acid indicate that reduction of a Mn(I)–CO$_2$H intermediate in the catalytic cycle may determine the unusual overpotential. A TOF of 5000 s^{-1} (i_{cat}/i_p = 50) was calculated for catalyst **2**

with 1.4 M TFE. A Faradaic efficiency of $98 \pm 6\%$ was observed for the formation of CO from CO_2 with 0.3 M TFE, with no observable production of H_2. At these activities, complexes **1** and **2** are more active than the best previously reported Mn bpy catalyst, Mn(bpy-tBu)(CO)$_3$Br. Although no decrease in catalytic overpotential was observed from previously reported Mn(bpy)(CO)$_3$X, many synthetic strategies can be utilized to move the catalytic potential to a similar potential as substrate binding, including placing local proton sources or local hydrogen bonding interactions in the vicinity of the Mn center. The findings reported in this study provide new mechanistic and synthetic insights for improving catalysts in the future, with the ultimate goal of attaining a catalytic system capable of implementation on a large scale.

4.4   Experimental

General Considerations. NMR spectra were recorded on a Varian 300 MHz spectrometer at 298 K, and data were manipulated using Bruker TopSpin software. ^{1}H chemical shifts are reported relative to TMS ($\delta = 0$) and referenced against solvent residual peaks. Infrared spectra were collected on a Thermo Scientific Nicolet 6700 or a Bruker Equinox 55 spectrometer. Microanalyses were performed by Midwest Microlab, LLC (Indianapolis, IN) for C, H, and N. Solvents were sparged with argon, dried on a custom dry solvent system over alumina columns, and stored over molecular sieves before use. Manipulations of Mn complexes were covered from light. Potassium graphite (KC$_8$) was prepared by literature methods and stored at -30 °C under dry nitrogen in a glovebox.[40] Tetrabutylammonium hexafluorophosphate

(TBAPF$_6$, Aldrich, 98%) was twice recrystallized from methanol (MeOH) and dried under a vacuum at 90 °C overnight before use. 18-crown-6 (Sigma Aldrich, 99%) was recrystallized from acetonitrile (MeCN) and dried under a vacuum at 90 °C overnight before use. Other reagents were used as received from the following: 6,6′-di-dibromo-2,2′-bipyridine (TCI America, >95%), 2,4,6-trimethylphenylboronic acid (Frontier Scientific), sodium bicarbonate (Na$_2$CO$_3$, Macron Chemicals), tetrakis(triphenylphosphine)palladium(0) (Pd(PPh$_3$)$_4$, Alfa Aesar, 99.8%), manganesepentacarbonylbromide (Mn(CO)$_5$Br, Alfa Aesar, 98%), and silver trifluoromethanesulfonate (AgOTf, Oakwood Products, 99%).

Synthesis of 6,6′-dimesityl-2,2′-bipyridine (mesbpy). This ligand was synthesized in an analogous fashion to a previous report.[9] To a toluene (250 mL) solution of 6,6′-dibromo-2,2′-bipyridine (4.00 g, 12.7 mmol) an excess of 2,4,6-trimethylphenylboronic acid (5.44 g, 33.1 mmol) suspended in 30 mL of MeOH was added. A 60 mL sample of 2 M Na$_2$CO$_3$ and Pd(PPh$_3$)$_4$ (2.3% mol. cat.) were added to the reaction flask, and the mixture was refluxed for 72 h in air. After cooling, the layers were separated. The organic layer was washed with brine (3 x 100 mL), and the aqueous layer was washed with chloroform (3 x 100 mL). The organic fractions were combined and dried under rotary evaporation. The resulting crude solid was dissolved in a minimal amount of hot chloroform and filtered. Methanol was added until a white precipitate crashed out from the filtrate. The white precipitate was filtered and dried overnight under vacuum at 80 ˚C. The yield of pure product was 3.56 g (71%). All

characterization matched previous reports[9] and were consistent with the structure of the ligand.

Synthesis of Mn(mesbpy)(CO)₃Br (1). $Mn(CO)_5Br$ (200 mg, 0.73 mmol) was added to 50 mL diethyl ether (Et_2O) in ambient air. Mesbpy (280 mg, 0.71 mmol) was added to the mixture and heated to reflux. The solution turned orange within 30 min, and the product crashed out of solution. The mixture was cooled to room temperature, and the precipitate was filtered off and cleaned with Et_2O. The orange solid was dried overnight under vacuum. The yield of Mn(mesbpy)(CO)₃Br was 308 mg (69%). X-ray quality crystals were grown from the vapor diffusion of pentane into a THF solution of the complex (Table 4.3). ^{1}H NMR (CD_3CN): δ =2.08 (s, 12H, CH_3's), 2.34 (s, 6H, CH_3's), 7.02 (s, 4H, phenyl H's), 7.41 (d, 2 H, 5,5′ H's, J = 7 Hz), 8.14 (t, 2H, 4,4′ H's, J = 7 Hz), 8.41 (d, 2H, 3,3′ H's, J = 8 Hz). IR (THF) v_{CO}: 2021, 1940, 1906 cm^{-1}. Anal. Calcd for **1**, $C_{31}H_{28}BrMnN_2O_3$: C, 60.90; H, 4.62; N, 4.58. Found: C, 60.58; H, 4.58; N, 4.53.

Synthesis of [Mn(mesbpy)(CO)₃(MeCN)](OTf) (2). Complex **1** (500 mg, 0.82 mmol) was added to 80 mL MeCN in a Schlenk flask in a nitrogen-filled, dry glovebox. AgOTf (233 mg, 0.90 mmol) was suspended in 20 mL MeCN, and this solution was added in the flask. The reaction flask was brought out of the box, covered with foil (to avoid exposure to light), and heated to reflux overnight under a stream of N_2. The reaction mixture was yellow/orange during reflux and had a black/brown solid at the bottom. After 18 h of reflux, the heat was removed, and the black/brown solid was removed by vacuum filtration. The filtrate was dried by rotary evaporation,

yielding yellow/orange powder. The product was purified by flash chromatography with a Teledyne CombiFlash Rf by passing the mixture through a basic alumina column with MeCN as the eluent. The fractions were combined, and the solvent was removed by rotary evaporation, yielding a bright yellow/orange solid. The final yield of pure product was 405 mg (69%). ^{1}H NMR (CD$_3$CN): δ = 2.05 (s, 12H, CH$_3$'s), 2.19 (s, 6H, CH$_3$'s), 2.35 (s, 3H, bound MeCN), 7.06 (s, 4H, phenyl H's), 7.55 (d, 2 H, 5,5′ H's, J = 8 Hz), 8.27 (t, 2H, 4,4′ H's, J = 8 Hz), 8.50 (d, 2H, 3,3′ H's, J = 8 Hz). IR (THF) ν_{CO}: 2038, 1956, 1926 cm^{-1}. Anal. Calcd for **2**, C$_{34}$H$_{31}$F$_3$MnN$_3$O$_6$S: C, 56.59; H, 4.33; N, 5.82. Found: C, 56.52; H, 4.24; N, 5.93.

Chemical Reductions of Mn(mesbpy)(CO)$_3$Br. One to ten millimolar solutions of Mn(mesbpy)(CO)$_3$Br were prepared in THF in a nitrogen-filled, dry glovebox and cooled to −35 °C. For one-electron reductions, KC$_8$ (1.3 equiv) was added to the solution, and the solution was allowed to warm to room temperature over a period of 30 min. The solution was filtered over silica to remove any over-reduced, charged complex. Filtration afforded a dark red solution of the neutral, Mn(0) complex, [Mn(mesbpy)(CO)$_3$]^0 (**3**). For two-electron reductions, 18-crown-6 (2.5 equiv) and KC$_8$ (2.3 equiv) were added to the solution, and the solution was allowed to warm to room temperature over a period of 30 min. The solution was filtered, affording a dark blue solution of the anion, [Mn(mesbpy)(CO)$_3$][K(18-crown-6)] (**4**). NMR samples were prepared by repeating the described chemical reductions in THF-d_8.

Characterization for complex **3**: The instability of this complex did not allow for isolation as a solid. Additionally, **3** was not long-lasting in solution, and any attempts to isolate this species for characterization beyond IR spectroscopy (i.e. XRD) were unsuccessful. IR (THF) v_{CO}: 1984, 1894, 1880 cm^{-1}.

Characterization of complex **4**: X-ray quality crystals were grown from the vapor diffusion of pentane into a THF solution of the complex (Table 4.3). ^{1}H NMR (THF-d_8): δ = 2.16 (s, 12H, CH$_3$'s), 2.32 (s, 6H, CH$_3$'s), 3.57 (br s, 24H, K[18-crown-6]), 7.02 (s, 4H, phenyl H's), 7.31 (d, 2 H, 5,5′ H's, J = 7 Hz), 7.93 (t, 2H, 4,4′ H's, J = 8 Hz), 8.33 (d, 2H, 3,3′ H's, J = 8 Hz). IR (THF) v_{CO}: 1917, 1815 cm^{-1}.

Electrochemistry. Electrochemical experiments were performed using a BASi Epsilon potentiostat. A single-compartment cell was used for all cyclic voltammetry experiments with a glassy carbon working electrode (3 mm in diameter from BASi), a Pt wire counter electrode, and a Ag/AgCl pseudo-reference. Ferrocene (Fc) was added as an internal reference. All electrochemical experiments were performed with 0.1 M TBAPF$_6$ as the supporting electrolyte. Electrochemical cells were shielded from light during experiments. All solutions were purged with N$_2$ or CO$_2$ before CVs were taken. "Bone dry" CO$_2$ run through a Drierite column was used for all electrochemistry experiments. Mn complex concentrations ranged from 0.5−5.0 mM, and experiments with CO$_2$ were performed at gas saturation (~0.28 M) in MeCN. For experiments with varying [CO$_2$], a solution of saturated CO$_2$ in MeCN was diluted to afford the appropriate [CO$_2$]. All potentials were referenced vs. Fc/Fc$^+$.

Bulk Electrolysis. Bulk electrolysis experiments (at *ca.* −2.2 V vs. Fc$^+$/Fc) were carried out in a 60 mL single-compartment cell with a custom Teflon top designed in our laboratory. The setup included a carbon rod working electrode (7.4 cm^2 surface area), a Pt wire counter electrode separated from the solution by a porous glass frit, and an Ag/AgCl pseudo-reference separated from the solution by a Vycor tip. A BASi Epsilon potentiostat was used to apply potential and record current. The bulk reductions were carried out in MeCN with various amounts of added Brønsted acid and 0.1 M TBAPF$_6$. Bulk electrolysis solutions were purged with CO_2 for 10 min prior to electrolysis. Solutions were constantly stirred and shielded from light throughout bulk electrolysis experiments. Gas analysis for bulk electrolysis experiments were performed using 1 mL sample injections on a Hewlett-Packard 7890A Series gas chromatograph with two molsieve columns (30 m × 0.53 mm ID × 25 μm film). The 1 mL injection was split between two columns, one with N_2 as the carrier gas and one with He carrier gas, in order to quantify both CO and H_2 simultaneously in each run. Gas chromatography calibration curves were made by sampling known volumes of CO and H_2 gas.

TOF Calculations from CPE. We have calculated TOF from CPE data in an analogous fashion to Costentin and Savéant[28,41] using E4.7–E4.9. We have used this analysis previously with Mn(bpy-*t*Bu)(CO)$_3$Br.[7] Here, *i* is the stable current transferred during CPE, *F* is Faraday's constant, *A* is the surface area of the working electrode, k_{cat} is the overall rate constant of the catalytic reaction, *D* is the diffusion coefficient, [cat] is the concentration of the catalyst without substrate, *R* is the

universal gas constant, T is temperature, $E_{applied}$ is the applied potential during CPE (–

1.8 V vs. SCE), E^0_{cat} is the standard potential of the catalyst (– 1.17 V vs. SCE)[41], and

TOF is the turnover frequency. This leads to a calculated TOF of 480 s^{-1} for catalyst **2**

with 0.3 M TFE. The following values were used in these TOF calculations: [cat] = 5

x 10^{-7} mol cm^{-3}, D = 1.1 x 10^{-5} cm^2 s^{-1} (from Ref. 7), A = 7.4 cm^2, i = 0.026 C s^{-1}, F

= 96845 C mol^{-1}, F/RT = 38.92 V^{-1}, $E_{applied}$ = –2.2 V vs. Fc$^+$/Fc, E^0_{cat} = –1.55 V vs.

Fc$^+$/Fc.

$$\frac{i}{F\,A} = \frac{\sqrt{k_{cat}D}\,[\text{cat}]}{1+\exp\left[\dfrac{F}{RT}\left(E_{applied}-E^0_{cat}\right)\right]} \tag{E4.7}$$

$$k_{cat} = \frac{i^2\left(1+\exp\left[\dfrac{F}{RT}\left(E_{applied}-E^0_{cat}\right)\right]\right)^2}{F^2A^2D[\text{cat}]^2} \tag{E4.8}$$

$$\text{TOF} = \frac{k_{cat}}{1+\exp\left[\dfrac{F}{RT}\left(E_{applied}-E^0_{cat}\right)\right]} \tag{E4.9}$$

Infrared Spectroelectrochemistry (IR-SEC). The design of the IR

spectroelectrochemical cell used for these studies has been reported previously by our

group.[42] This cell was used for these experiments with one modification. Here, a cell

with a 4.5 mm glassy carbon disk working electrode was used in place of the polished

platinum working electrode. This modification ensures that IR-SEC conditions mimic

those of CVs as closely as possible and ensures that CO_2 reduction on the Pt working

electrode is eliminated. A more detailed design of this cell will be published in a

future manuscript. All spectroelectrochemical experiments were carried out in a 0.1 M

TBAPF$_6$ solution in MeCN, and all solutions were prepared under an atmosphere of

dry nitrogen in a glovebox. Blank MeCN solutions with 0.1 M TBAPF$_6$ were used for the FTIR solvent subtractions. For experiments under CO_2, a solution of catalyst in TBAPF$_6$/MeCN was saturated with CO_2 (*ca.* 0.28 M) and diluted in half by an N$_2$-sparged solution of TBAPF$_6$/MeCN, affording a solution of *ca.* 0.14 M CO_2. A Pine Instrument Company model AFCBP1 bipotentiostat or a Gamry Reference 600 series three electrode potentiostat was used to affect and monitor thin layer bulk electrolysis.

X-ray Crystallography. The single crystal X-ray diffraction studies were carried out on a Bruker Kappa APEX-II CCD diffractometer equipped with Mo Kα radiation (λ = 0.71073 Å) or a Bruker Kappa APEX CCD diffractometer equipped with Cu Kα radiation (λ = 1.54184 Å). The crystals were mounted on a Cryoloop with Paratone oil and data were collected under a nitrogen gas stream at 100(2) K using ω and φ scans. Data were integrated using the Bruker SAINT software program and scaled using the software program. Solution by direct methods (SHELXS) produced a complete phasing model consistent with the proposed structure. All non-hydrogen atoms were refined anisotropically by full-matrix least- squares (SHELXL-97).[43] All hydrogen atoms were placed using a riding model. Their positions were constrained relative to their parent atom using the appropriate HFIX command in SHELXL-97. Crystallographic data and structure refinement parameters are summarized in Table 4.3

Table 4.3 Crystallographic Data for Mn(mesbpy)(CO)$_3$Br (**1**) and
[Mn(mesbpy)(CO)$_3$][K(18-crown-6)] (**4**).

	Mn(mesbpy)(CO)$_3$Br (**1**)	[Mn(mesbpy)(CO)$_3$][K(18-crown-6)] (**4**)
Empirical formula	C$_{33}$H$_{32}$BrMnN$_2$O$_{3.5}$	C$_{47}$H$_{60}$KMnN$_2$O$_{10}$
Formula weight	647.45	907.01
Temperature (K)	100(2)	100(2)
Wavelength (Å)	0.71073	1.54178
Space group	C$_2$/c (No. 15)	Cmca (No. 64)
a (Å)	35.078(5)	21.4105(15)
b (Å)	8.2392(11)	13.7151(8)
c (Å)	22.640(3)	31.255(2)
α (°)	90.00	90.00
β (°)	115.873(9)	90.00
γ (°)	90.00	90.00
Volume (Å^3)	5887.3(15)	9177.9(10)
Z	8	8
Density$_{calcd}$ (Mg/m^3)	1.461	1.313
μ (mm^{-1})	1.844	3.630
R	0.0363	0.0873
R$_w$	0.0855	0.1724

Density Function Theory (DFT) Calculations. DFT calculations were performed with the Amsterdam Density Functional (ADF) program suite (version 2012.01).[44-46] The triple-ζ Slater-type orbital TZ2P basis set was utilized without frozen cores for all atoms. Relativistic effects were included via the zeroth-order regular approximation (ZORA).[47-48] The BP86 functional and the local density approximation (LDA) of Vosko, Wilk and Nusair (VWN)[49] was coupled with the generalized gradient approximation (GGA) corrections described by Becke[50] and Perdew[51-52] for electron exchange and correlation, respectively. Frequency calculations were performed to verify that the optimized geometries were at minima. Geometry optimized xyz coordinates and a sample input file are included in the Appendix.

Much of the material for this chapter comes directly from a manuscript entitled: "Manganese Catalysts with Bulky Bipyridine Ligands for the Electrocatalytic Reduction of Carbon Dioxide: Eliminating Dimerization and Altering Catalysis" by Matthew D. Sampson, An D. Nguyen, Kyle A. Grice, Curtis E. Moore, Arnold L. Rheingold, and Clifford P. Kubiak, which has been published in *J. Am. Chem. Soc.*, **2014**, 136, 5460–5471. http://dx.doi.org/10.1021/ja501252f. The dissertation author is the primary author of this manuscript.

4.5   References

(1) Smieja, J. M.; Kubiak, C. P. *Inorg. Chem.* **2010**, 49, 9283-9289.

(2) Smieja, J. M.; Benson, E. E.; Kumar, B.; Grice, K. A.; Seu, C. S.; Miller, A. J. M.; Mayer, J. M.; Kubiak, C. P. *Proc. Natl. Acad. Sci. U. S. A.* **2012**, 109, 15646–15650.

(3) Johnson, F. P. A.; George, M. W.; Hartl, F.; Turner, J. J. *Organometallics* **1996**, 15, 3374-3387.

(4) Wong, K.-Y.; Chung, W.-H.; Lau, C.-P. *J. Electroanal. Chem.* **1998**, 453, 161-169.

(5) Hawecker, J.; Lehn, J. M.; Ziessel, R. *J. Chem. Soc., Chem. Commun.* **1984**, 328-330.

(6) *CRC Handbook of Chemistry and Physics*; 92nd ed.; Haynes, W. M., Ed.; CRC Press: Boca Raton, FL, **2011-2012**.

(7) Smieja, J. M.; Sampson, M. D.; Grice, K. A.; Benson, E. E.; Froehlich, J. D.; Kubiak, C. P. *Inorg. Chem.* **2013**, 52, 2484-2491.

(8) Bourrez, M.; Molton, F.; Chardon-Noblat, S.; Deronzier, A. *Angew. Chem., Int. Ed.* **2011**, 50, 9903-9906.

(9) Schmittel, M.; Ganz, A.; Schenk, W. A.; Hagel, M. *Z. Naturforsch.* **1999**, 54b, 559–564.

(10) Benson, E. E.; Rheingold, A. L.; Kubiak, C. P. *Inorg. Chem.* **2010**, 49, 1458-1464.

(11) Benson, E. E., University of California, San Diego, **2012**.

(12) Staal, L. H.; Oskam, A.; Vrieze, K. *J. Organomet. Chem.* **1979**, 170, 235-245.

(13) Tulyathan, B.; Geiger, W. E. *J. Am. Chem. Soc.* **1985**, 107, 5960-5967.

(14) Wang, J. *Analytical Electrochemistry*; Third ed.; John Wiley & Sons, Inc.: Hoboken, New Jersey, **2006**.

(15) Hartl, F.; Rosa, P.; Ricard, L.; Le Floch, P.; Záliš, S. *Coord. Chem. Rev.* **2007**, 251, 557-576.

(16) Benson, E. E.; Grice, K. A.; Smieja, J. M.; Kubiak, C. P. *Polyhedron* **2013**, 58, 229–234.

(17) Addison, A. W.; Rao, T. N.; Reedijk, J.; van Rijn, J.; Verschoor, G. C. *J. Chem. Soc., Dalton Trans.* **1984**, 1349-1356.

(18) Gore-Randall, E.; Irwin, M.; Denning, M. S.; Goicoechea, J. M. *Inorg. Chem.* **2009**, 48, 8304-8316.

(19) Scarborough, C. C.; Sproules, S.; Weyhermüller, T.; DeBeer, S.; Wieghardt, K. *Inorg. Chem.* **2011**, 50, 12446-12462.

(20) Benson, E. E.; Sampson, M. D.; Grice, K. A.; Smieja, J. M.; Froehlich, J. D.; Friebel, D.; Keith, J. A.; Carter, E. A.; Nilsson, A.; Kubiak, C. P. *Angew. Chem., Int. Ed.* **2013**, 52, 4841–4844.

(21) Scarborough, C. C.; Wieghardt, K. *Inorg. Chem.* **2011**, 50, 9773-9793.

(22) Gennaro, A.; Isse, A. A.; Vianello, E. *J. Electroanal. Chem.* **1990**, 289, 203-215.

(23) Savéant, J.-M.; Vianello, E. *Electrochim. Acta* **1962**, 8, 905-923.

(24) Espension, J. H. *Chemical Kinetics and Reaction Mechanisms*; McGraw–Hill: New York, **1981**.

(25) Bard, A. J.; Faulkner, L. R. *Electrochemical Methods*; Wiley: New York, **1980**.

(26) Olmstead, W. N.; Margolin, Z.; Bordwell, F. G. *J. Org. Chem.* **1980**, 45, 3295-3299.

(27) Bordwell, F. G. *Acc. Chem. Res.* **1988**, 21, 456-463.

(28) Costentin, C.; Robert, M.; Saveant, J.-M. *Chem. Soc. Rev.* **2013**, 42, 2423-2436.

(29) Costentin, C.; Savéant, J.-M. *ChemElectroChem* **2014**, 1, 1226-1236.

(30) Gagne, R. R.; Allison, J. L.; Ingle, D. M. *Inorg. Chem.* **1979**, 18, 2767-2774.

(31) Fujita, E.; Creutz, C.; Sutin, N.; Szalda, D. J. *J. Am. Chem. Soc.* **1991**, 113, 343-353.

(32) Gagne, R. R.; Ingle, D. M. *J. Am. Chem. Soc.* **1980**, 102, 1444-1446.

(33) Mandal, S. K.; Ho, D. M.; Orchin, M. *Polyhedron* **1992**, 11, 2055-2063.

(34) Sampson, M. D.; Froehlich, J. D.; Smieja, J. M.; Benson, E. E.; Sharp, I. D.; Kubiak, C. P. *Energ. Environ. Sci.* **2013**, 6, 3748-3755.

(35) Gibson, D. H.; Yin, X. *J. Am. Chem. Soc.* **1998**, 120, 11200-11201.

(36) Bourrez, M.; Orio, M.; Molton, F.; Vezin, H.; Duboc, C.; Deronzier, A.; Chardon-Noblat, S. *Angew. Chem., Int. Ed.* **2014**, 53, 240-243.

(37) Stor, G. J.; Stufkens, D. J.; Vernooijs, P.; Baerends, E. J.; Fraanje, J.; Goubitz, K. *Inorg. Chem.* **1995**, 34, 1588-1594.

(38) Uson, R.; Riera, V.; Gimeno, J.; Laguna, M.; Gamasa, M. P. *J. Chem. Soc., Dalton Trans.* **1979**, 996-1002.

(39) Keith, J. A.; Grice, K. A.; Kubiak, C. P.; Carter, E. A. *J. Am. Chem. Soc.* **2013**, 135, 15823–15829.

(40) Schwindt, M. A.; Lejon, T.; Hegedus, L. S. *Organometallics* **1990**, 9, 2814-2819.

(41) Costentin, C.; Drouet, S.; Robert, M.; Savéant, J.-M. *Science* **2012**, 338, 90-94.

(42) Zavarine, I. S.; Kubiak, C. P. *J. Electroanal. Chem.* **2001**, 495, 106-109.

(43) Sheldrick, G. *Acta Crystallogr., Sect. A: Found. Crystallogr.* **2008**, 64, 112-122.

(44) Fonseca Guerra, C.; Snijders, J. G.; te Velde, G.; Baerends, E. J. *Theor. Chem. Acc.* **1998**, 99, 391-403.

(45) te Velde, G.; Bickelhaupt, F. M.; Baerends, E. J.; Fonseca Guerra, C.; van Gisbergen, S. J. A.; Snijders, J. G.; Ziegler, T. *J. Comput. Chem.* **2001**, 22, 931-967.

(46) SCM In *Theoretical Chemistry* Vrije Universiteit: Amsterdam, The Netherlands.

(47) van Lenthe, E.; Baerends, E. J.; Snijders, J. G. *J. Chem. Phys.* **1993**, 99, 4597-4610.

(48) Lenthe, E. v.; Snijders, J. G.; Baerends, E. J. *J. Chem. Phys.* **1996**, 105, 6505-6516.

(49) Vosko, S. H.; Wilk, L.; Nusair, M. *Can. J. Phys.* **1980**, 58, 1200-1211.

(50) Becke, A. D. *Phys. Rev. B* **1988**, 38, 3098.

(51) Perdew, J. P. *Phys. Rev. B* **1986**, 33, 8822-8824.

(52) Perdew, J. P. *Phys. Rev. B* **1986**, 34, 7406-7406.

(53) Mocak, J.; Feldberg, S. W. *J. Electroanal. Chem.* **1994**, 378, 31-37.

(54) Feldberg, S. W.; Goldstein, C. I. *J. Electroanal. Chem.* **1995**, 397, 1-10.

4.6   Appendix
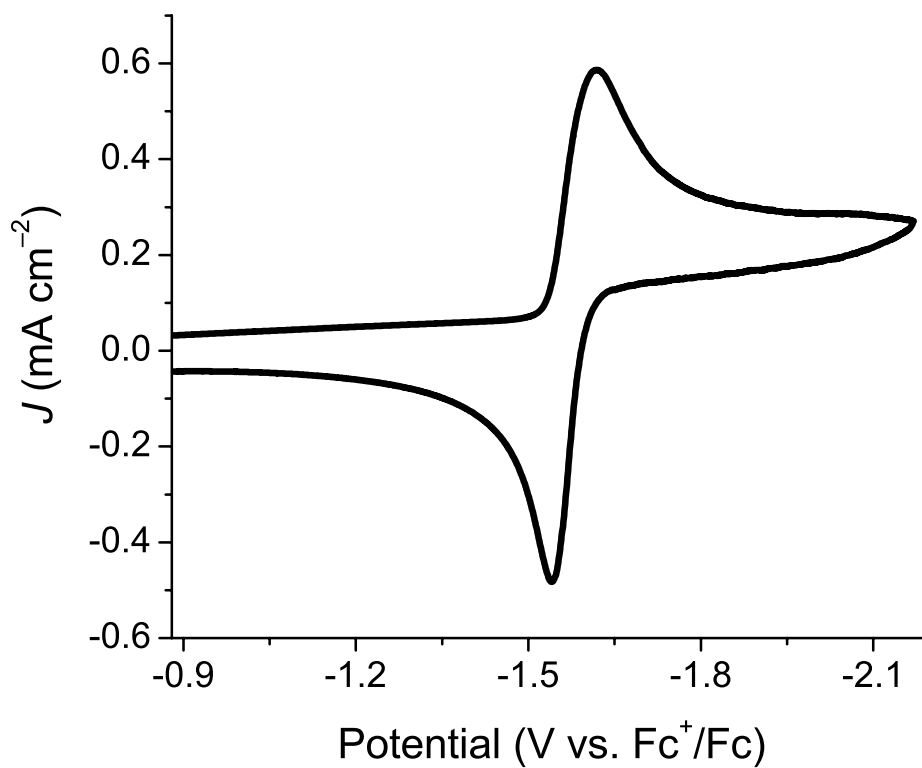
Figure 4.13 Cyclic voltammogram of 1 mM Mn(mesbpy)(CO)$_3$Br (**1**) in 0.1 M TBAPF$_6$/MeCN under N$_2$. Scan rate is 0.1 V/s.
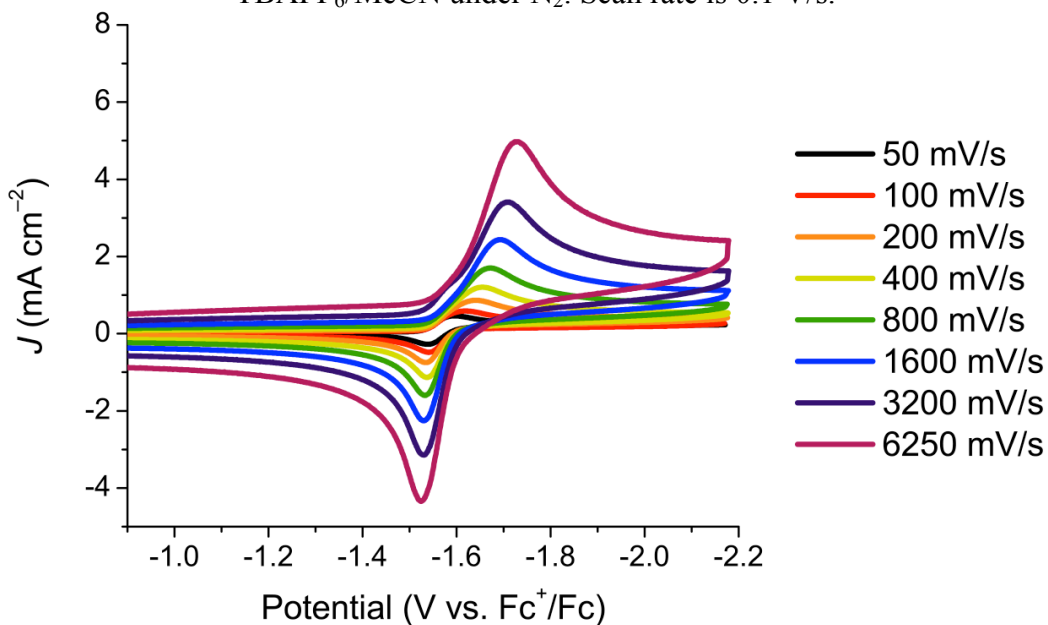
Figure 4.14 Cyclic voltammogram scan rate dependence of 1 mM Mn(mesbpy)(CO)$_3$Br (**1**) under N$_2$ in 0.1 M TBAPF$_6$/MeCN.
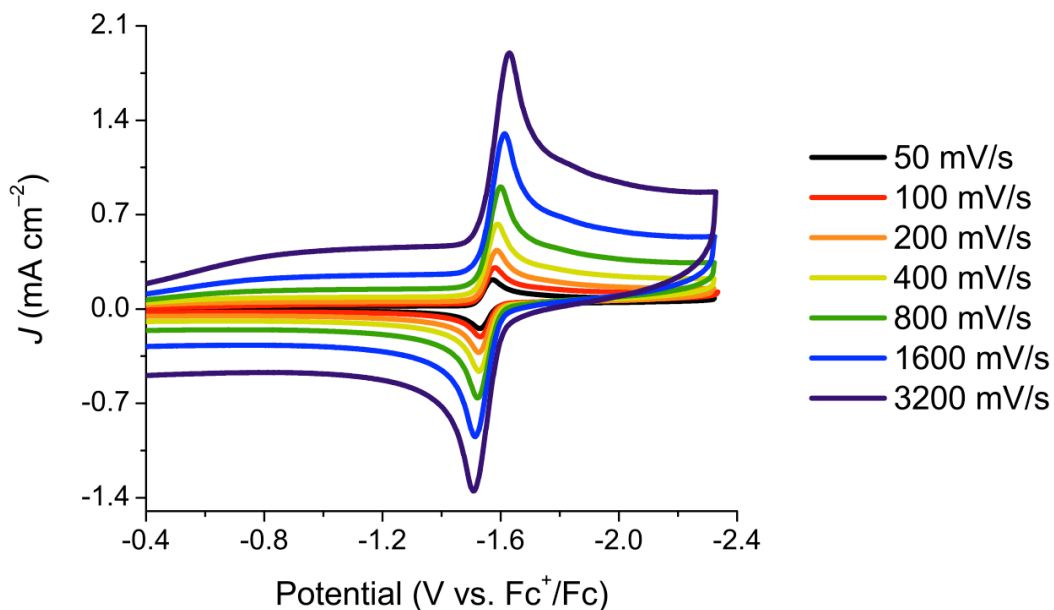
Figure 4.15 Cyclic voltammogram scan rate dependence of 1 mM [Mn(mesbpy)(CO)$_3$(MeCN)](OTf) (**2**) under N$_2$ in 0.1 M TBAPF$_6$/MeCN.
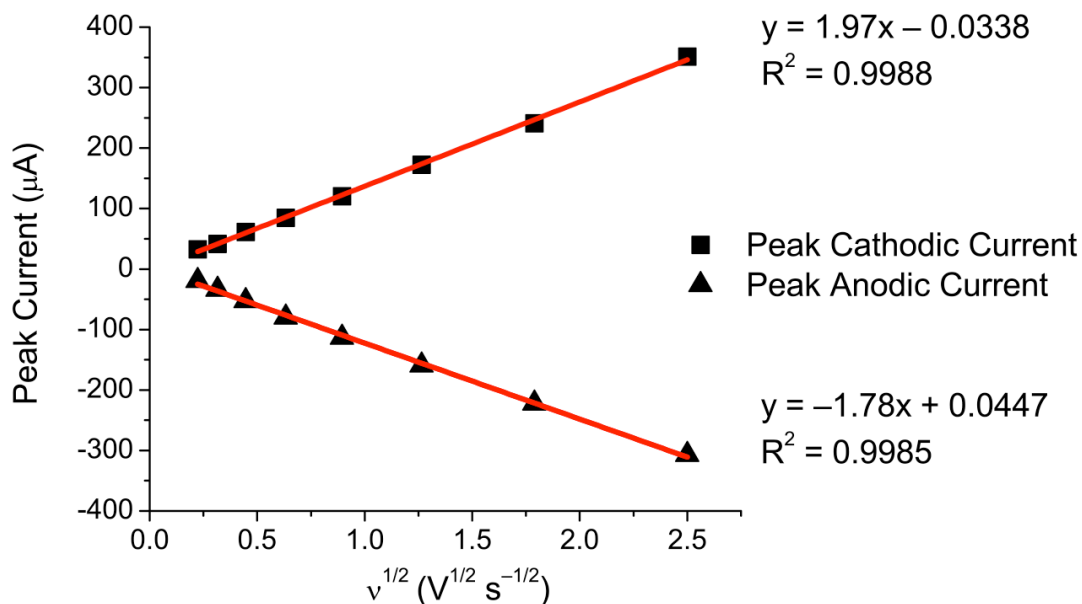
Figure 4.16 Plot showing that the peak current, both cathodic and anodic, in the cyclic voltammograms (CVs) of 1 mM Mn(mesbpy)(CO)$_3$Br (**1**) increases linearly with the square root of the scan rate. Data points from Figure 4.14.

$y = 0.759x - 0.02873$
$R^2 = 0.9994$

$y = -0.54868x + 0.02461$
$R^2 = 0.9998$

■ Peak Cathodic Current
▲ Peak Anodic Current
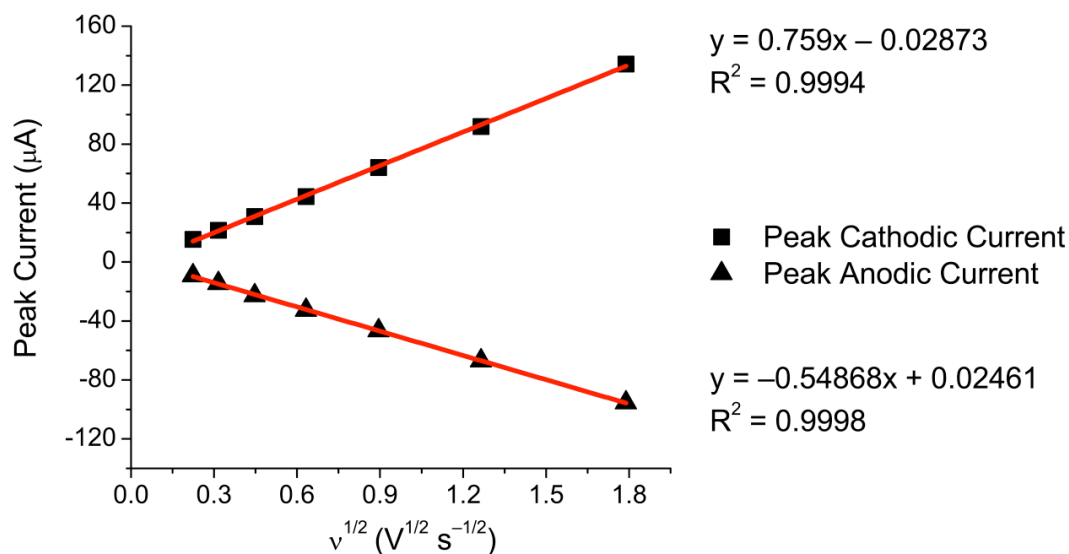
Figure 4.17 Plot showing that the peak current, both cathodic and anodic, in the cyclic voltammograms (CVs) of 1 mM $[Mn(mesbpy)(CO)_3(MeCN)](OTf)$ (**2**) increases linearly with the square root of the scan rate. Data taken from Figure 4.15.

● $Mn(mesbpy)(CO)_3Br$ (**1**)
● $[Mn(mesbpy)(CO)_3(MeCN)](OTf)$ (**2**)
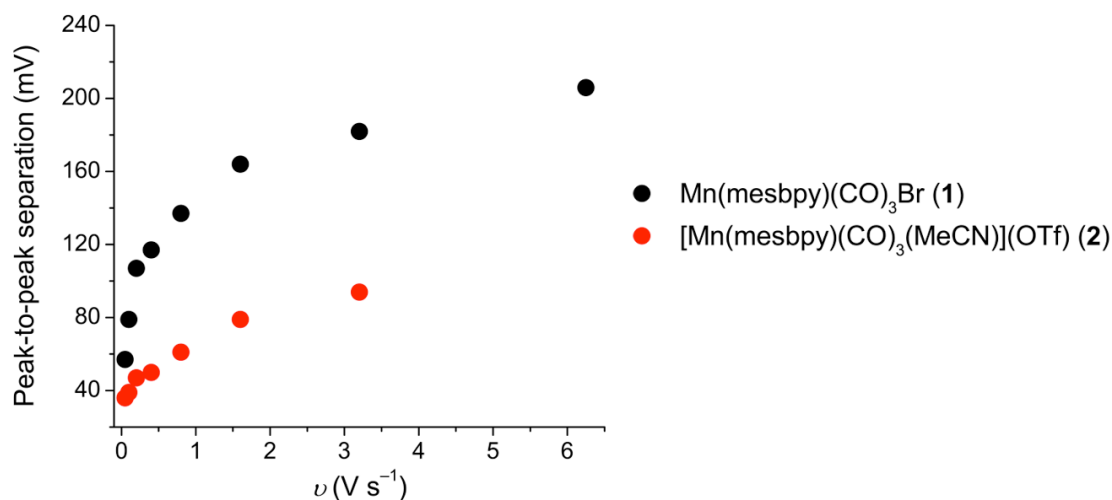
Figure 4.18 Plot showing the scan rate dependence of the peak-to-peak separation in the cyclic voltammograms (CVs) of 1 mM **1** and **2**. CVs are taken under an atmosphere of N_2 in 0.1 M TBAPF$_6$/MeCN with a glassy carbon (3 mm) working electrode, a platinum wire counter electrode, and a Ag/AgCl wire psuedoreference with ferrocene (Fc) added as an internal reference.
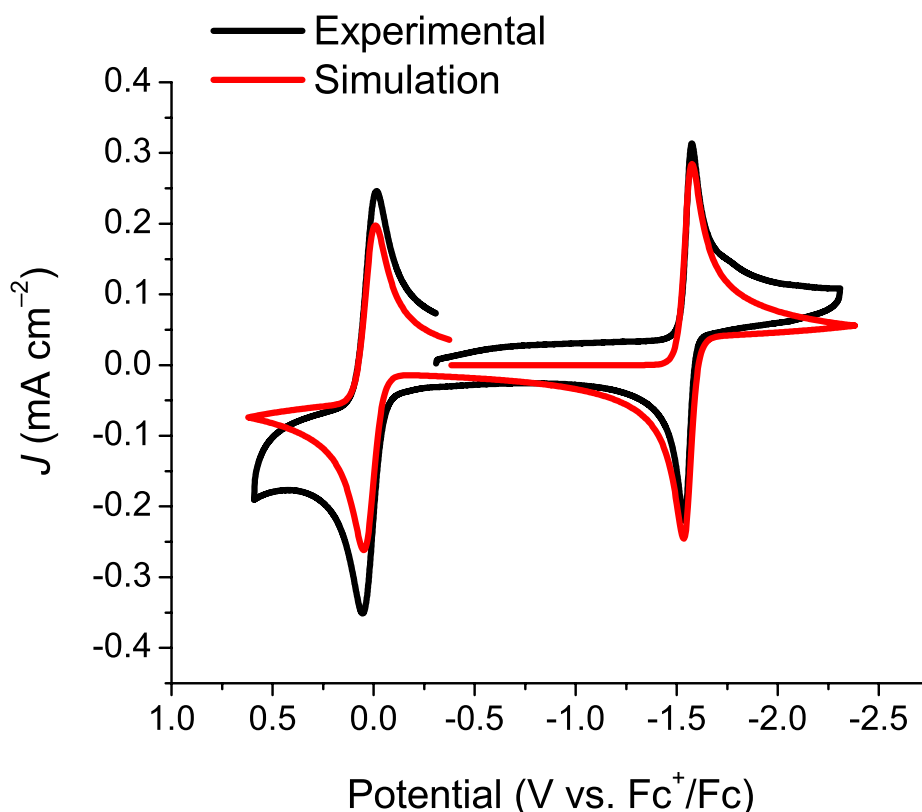
Figure 4.19 Comparison of experimental and simulated cyclic voltammograms (CVs) of 1 mM [Mn(mesbpy)(CO)$_3$(MeCN)](OTf) (**2**) in MeCN with 0.1 M TBAPF$_6$ as the supporting electrolyte under an atmosphere of N$_2$ at scan rates of 0.1 V/s. Peak-to-peak separation for the reduction at -1.55 V vs. Fc$^+$/Fc is 39 mV for the experimental CV and 42 mV for the simulated CV. Experimental conditions are the same as described in Figure 1 of the manuscript. Simulated CV is obtained with BASi DigiSim Simulation Software by modeling the following EEC mechanism, which provided a better fit than an ECE mechanism: Mn(I)S + e$^-$ = Mn(0)S [E^0 = -1.55 V]; Mn(0)S + e$^-$ = Mn(–I)S [E^0 = -1.55 V]; Mn(–I)S = Mn(–I) + S. "DigiSim is based on a fully implicit finite difference (IFD) method suggested by Manfred Rudolph. Rudolph's work expanded upon ideas originally put forth by Newman. Subsequent modifications by Feldberg[53-54] and Rudolph led to the current algorithm which is robust as well as computationally efficient." http://www.basinc.com/products/ec/digisim/.
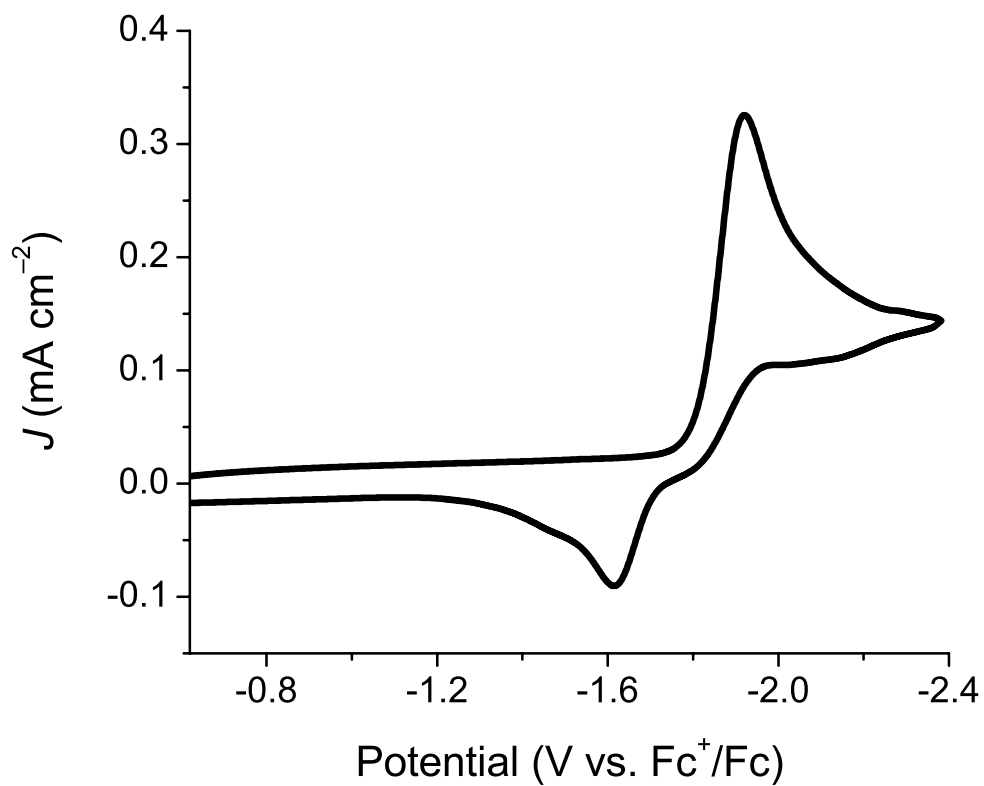
Figure 4.20 Cyclic voltammogram of 1 mM [Mn(mesbpy)(CO)$_3$(MeCN)](OTf) (**2**) in THF with 0.1 M TBAPF$_6$ under N$_2$. Scan rate is 0.1 V/s.
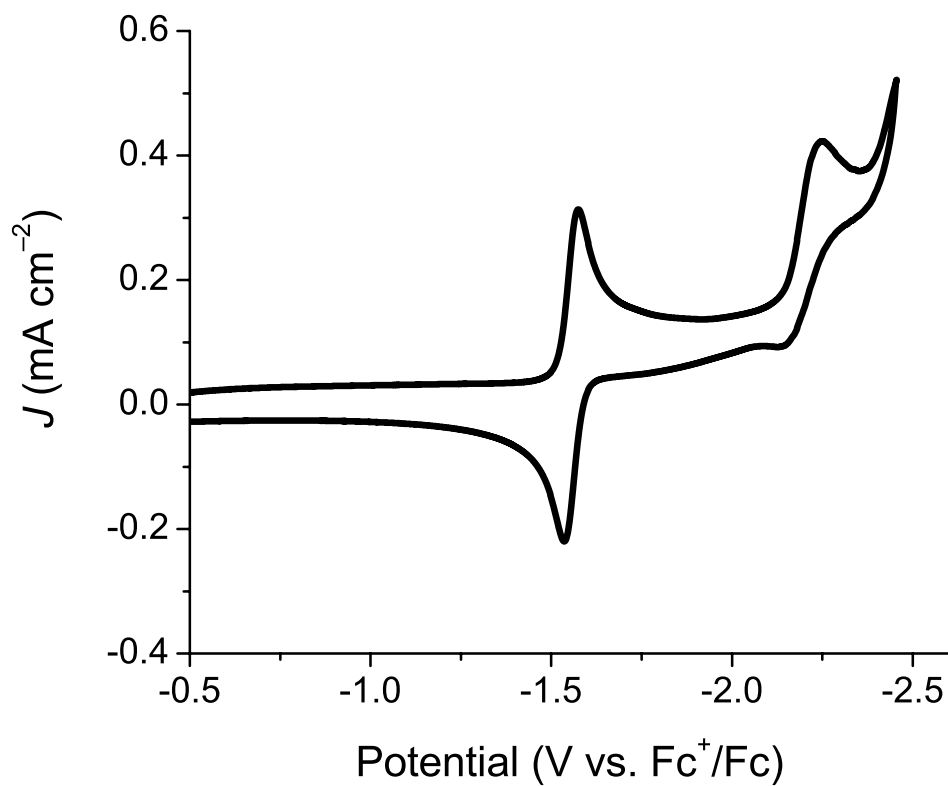
Figure 4.21 Cyclic voltammogram of 1 mM [Mn(mesbpy)(CO)$_3$(MeCN)](OTf) (**2**) in MeCN with 0.1 M TBAPF$_6$ under N$_2$, showing a second reduction feature at -2.25 V vs. Fc$^+$/Fc. This feature likely corresponds to a bpy ligand-based reduction. Scan rate is 0.1 V/s.
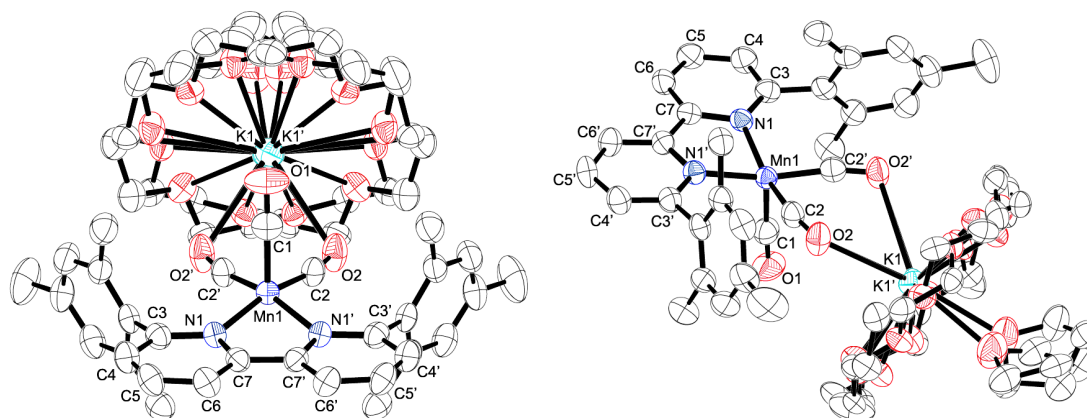
Figure 4.22 Molecular structure of [Mn(mesbpy)(CO)$_3$][K(18-crown-6)(THF)] (**4**) at two orientations, showing the disordered [K$^+$(18-crown-6)(THF)] fragment. Hydrogen atoms have been omitted for clarity, and ellipsoids are set at the 50% probability level.
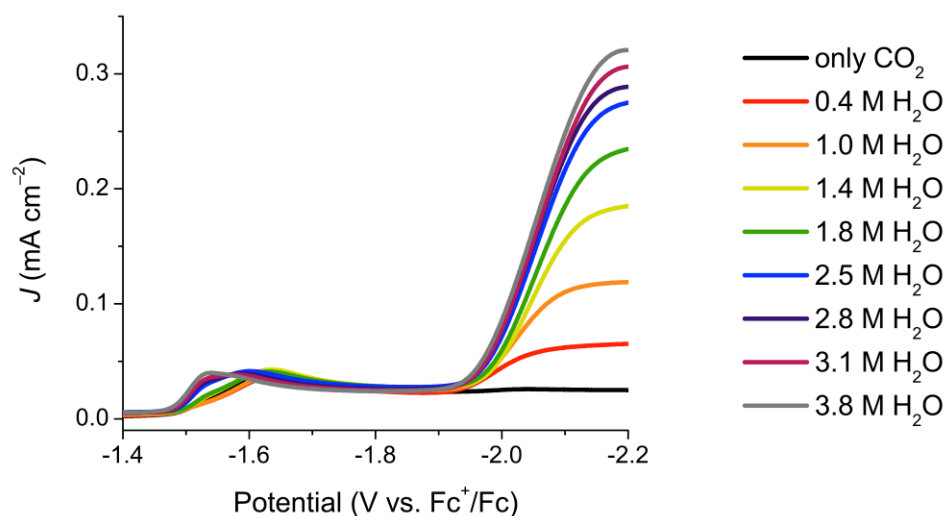
Figure 4.23 Linear scan voltammograms showing the electrocatalytic reduction of CO$_2$ to CO by 1 mM Mn(mesbpy)(CO)$_3$Br (**1**) in 0.1 M TBAPF$_6$/MeCN with addition of H$_2$O. The solution is under an atmosphere of, and saturated with (ca. 0.28 M), CO$_2$. Scan rates are 0.1 V/s.
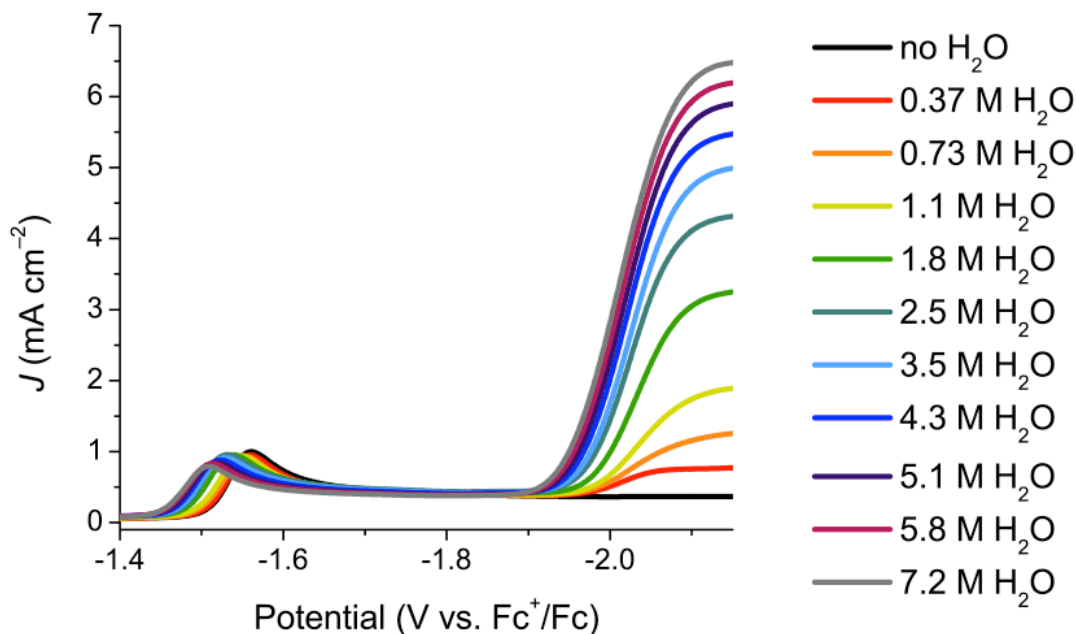
Figure 4.24 Linear scan voltammograms showing the electrocatalytic reduction of CO_2 to CO by 1 mM [Mn(mesbpy)(CO)$_3$(MeCN)](OTf) (**2**) in 0.1 M TBAPF$_6$/MeCN with addition of H_2O. The solution is under an atmosphere of, and saturated with (ca. 0.28 M), CO_2. Scan rates are 0.1 V/s.
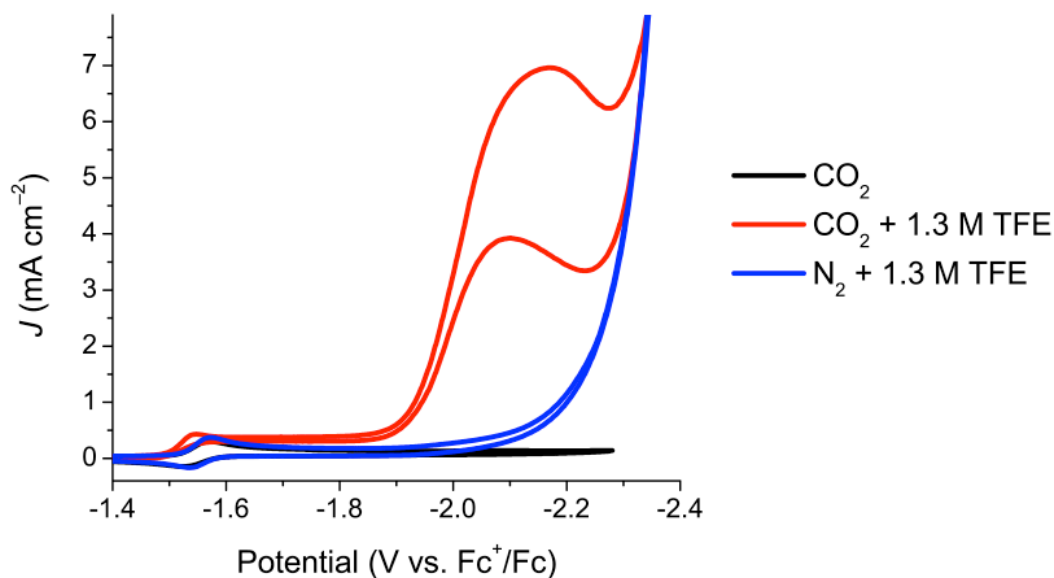
Figure 4.25 Cyclic voltammograms (CVs) showing catalytic current for 1 mM [Mn(mesbpy)(CO)$_3$(MeCN)](OTf) (**2**) under CO_2 with added TFE (red). This current increase is due solely to the electrocatalytic reduction of CO_2 to CO. Under N_2 with added TFE, no current increase is observed, until a much more negative potential (blue). CV under CO_2 with no added TFE is also shown (black). CVs were taken in 0.1 M TBAPF$_6$/MeCN at a scan rate of 0.1 V/s.
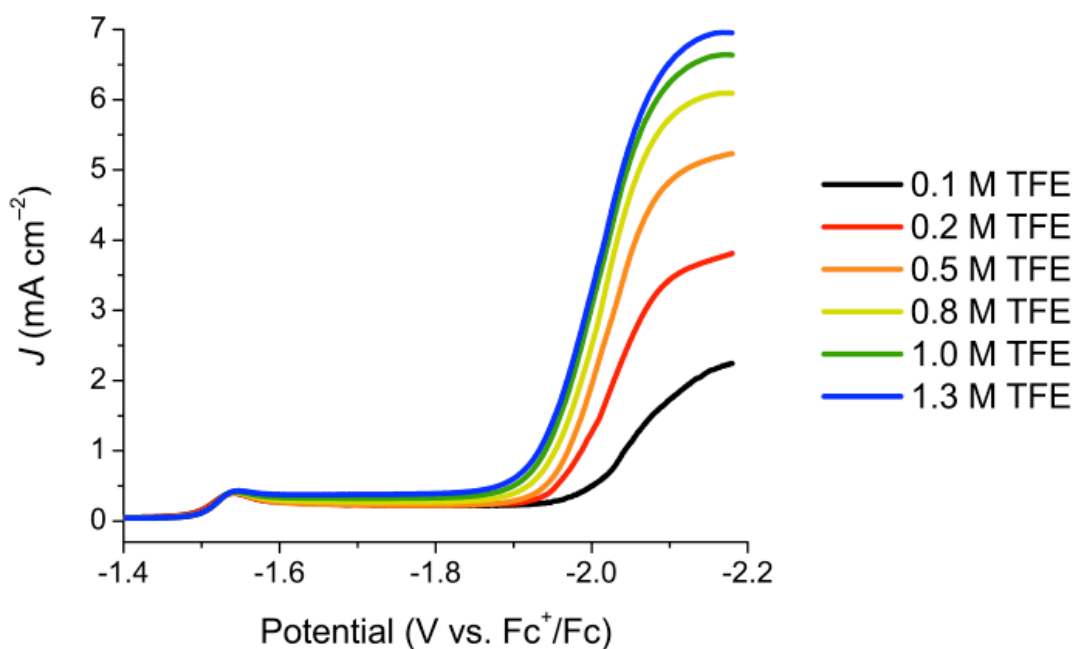
Figure 4.26 Linear scan voltammograms showing the electrocatalytic reduction of CO_2 to CO by 1 mM $[Mn(mesbpy)(CO)_3(MeCN)](OTf)$ (**2**) in 0.1 M $TBAPF_6$/MeCN with addition of TFE. The solution is under an atmosphere of, and saturated with (ca. 0.28 M), CO_2. Scan rates are 0.1 V/s.
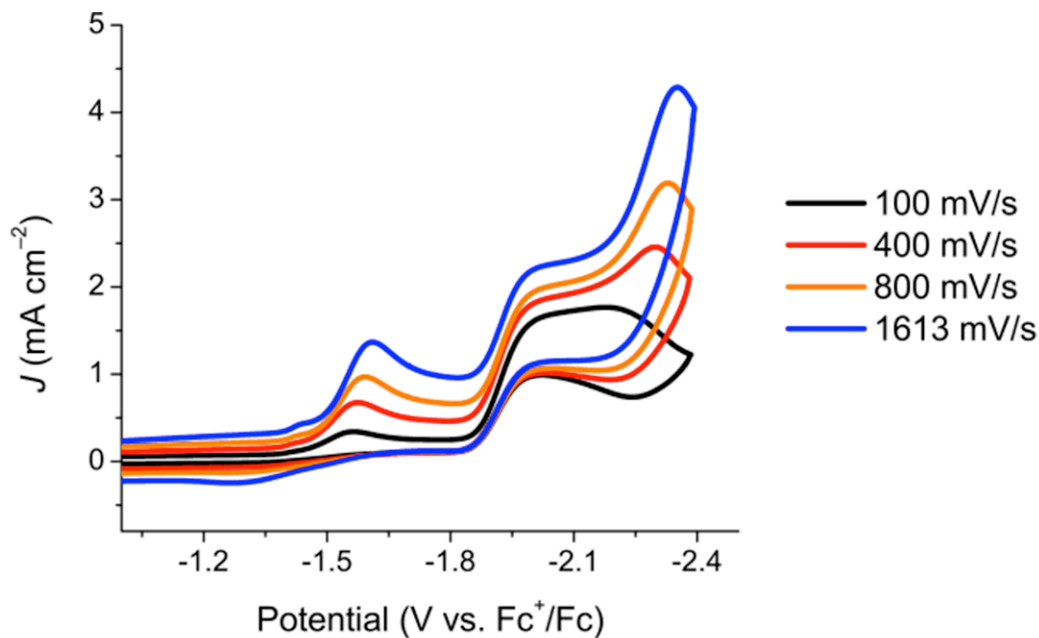
Figure 4.27 Cyclic voltammogram scan rate dependence of 1 mM $[Mn(mesbpy)(CO)_3(MeCN)](OTf)$ (**2**) under an atmosphere of CO_2 with 2.6 M H_2O, showing the scan rate dependence of the peak at *ca.* −2.3 V vs. Fc⁺/Fc. Scans are in 0.1 M $TBAPF_6$/MeCN.
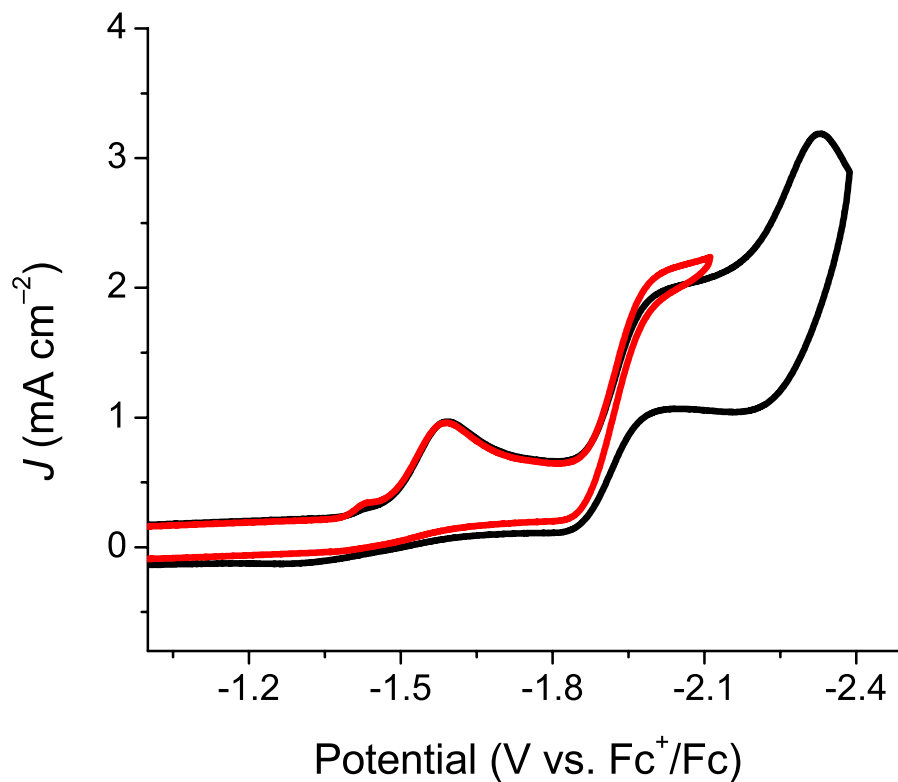
Figure 4.28 Cyclic voltammograms of 1 mM [Mn(mesbpy)(CO)$_3$(MeCN)](OTf) (**2**) under an atmosphere of CO$_2$ with 2.6 M H$_2$O. If scanning is reversed after *ca.* –2.3 V vs. Fc$^+$/Fc, a large scan rate dependent peak is observed (black). If scanning is reversed before this scan rate dependent peak (red), then the catalytic current response is well behaved. Scans are taken at 0.8 V/s in 0.1 M TBAPF$_6$/MeCN.
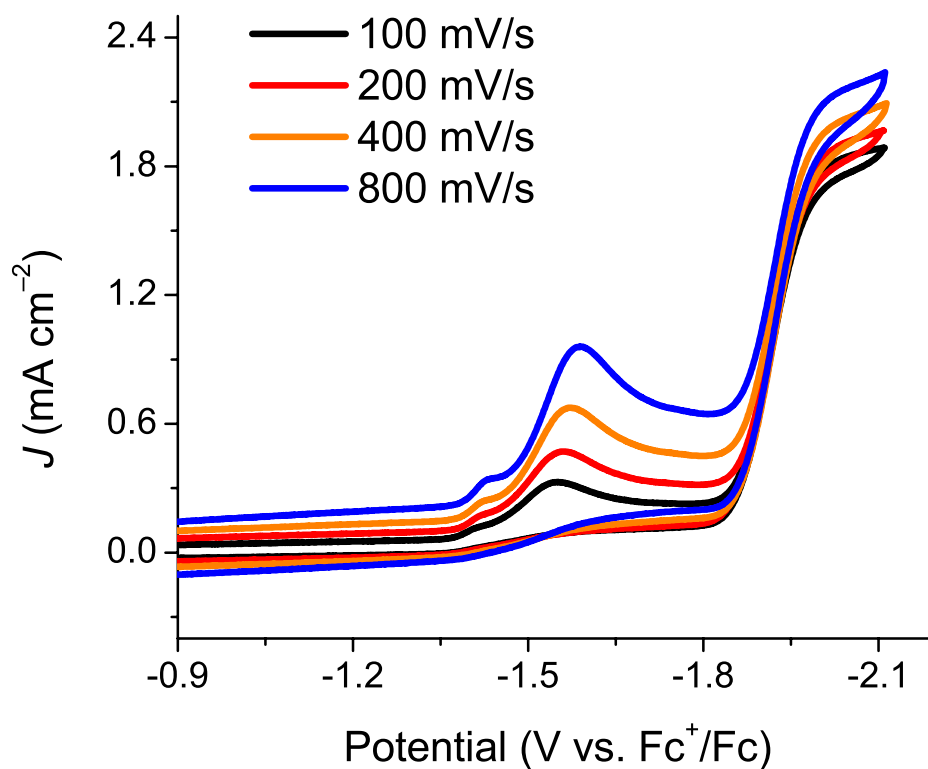
Figure 4.29 Cyclic voltammogram scan rate dependence of 1 mM [Mn(mesbpy)(CO)$_3$(MeCN)](OTf) (**2**) under an atmosphere of CO$_2$ with 2.6 M H$_2$O, reversing the scan before the scan rate dependent peak at *ca*. –2.3 V vs. Fc$^+$/Fc. The initial plateau of the catalytic current is fairly scan rate independent. Scans are in 0.1 M TBAPF$_6$/MeCN.
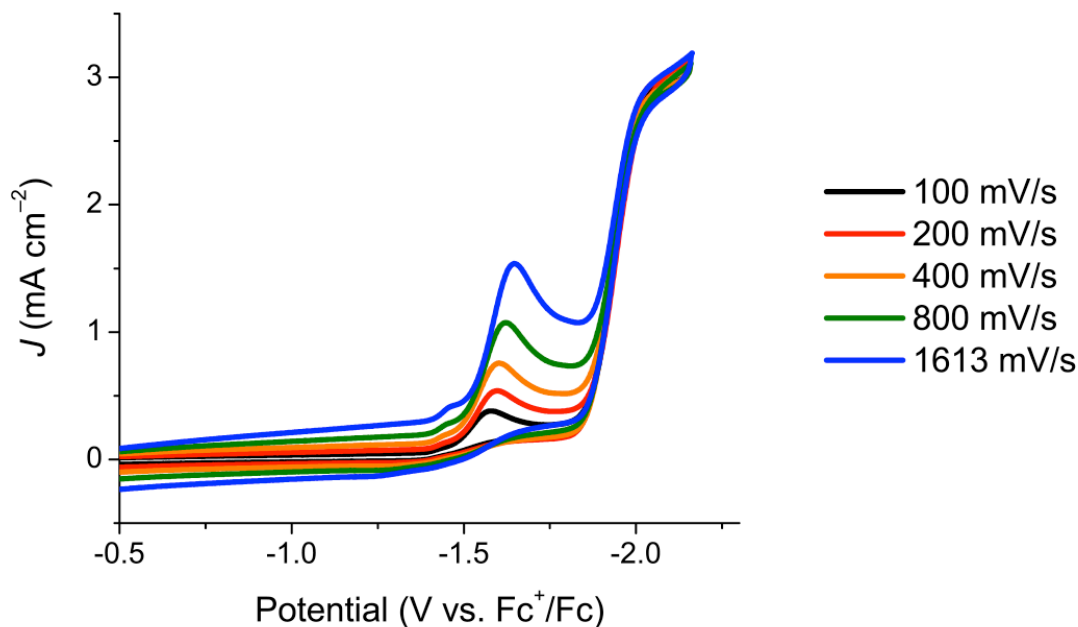
Figure 4.30 Cyclic voltammogram scan rate dependence of 1 mM [Mn(mesbpy)(CO)$_3$(MeCN)](OTf) (**2**) under an atmosphere of CO_2 with 1.4 M MeOH. The initial plateau of the catalytic current is scan rate independent. Scans are in 0.1 M TBAPF$_6$/MeCN.
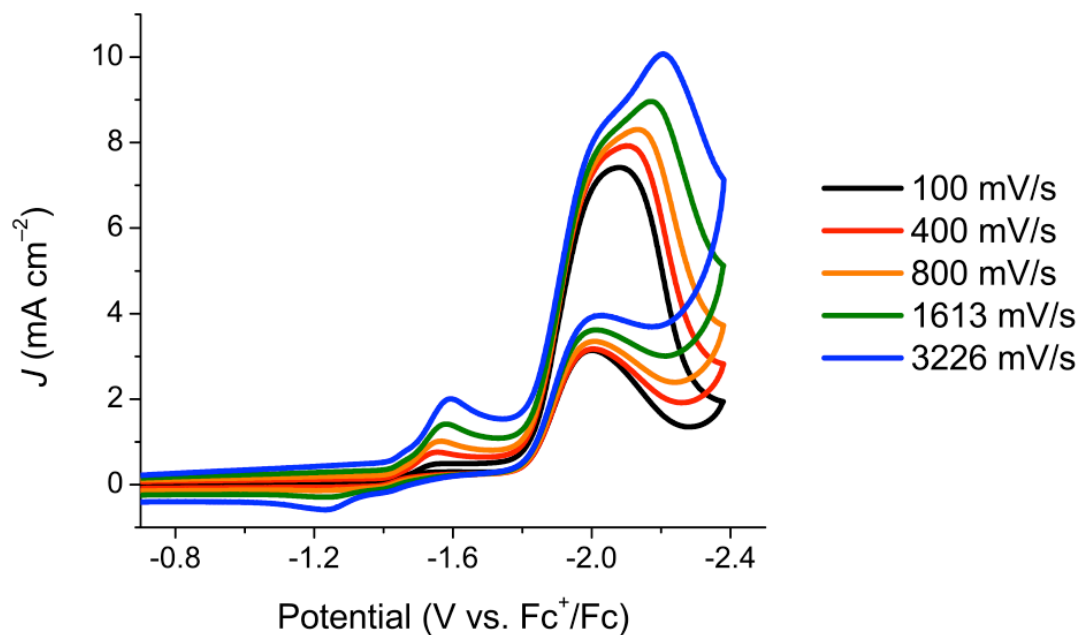
Figure 4.31 Cyclic voltammogram scan rate dependence of 1 mM [Mn(mesbpy)(CO)$_3$(MeCN)](OTf) (**2**) under an atmosphere of CO_2 with 1.5 M TFE, showing the scan rate dependence of the peak at *ca.* –2.3 V vs. Fc$^+$/Fc. Scans are in 0.1 M TBAPF$_6$/MeCN.
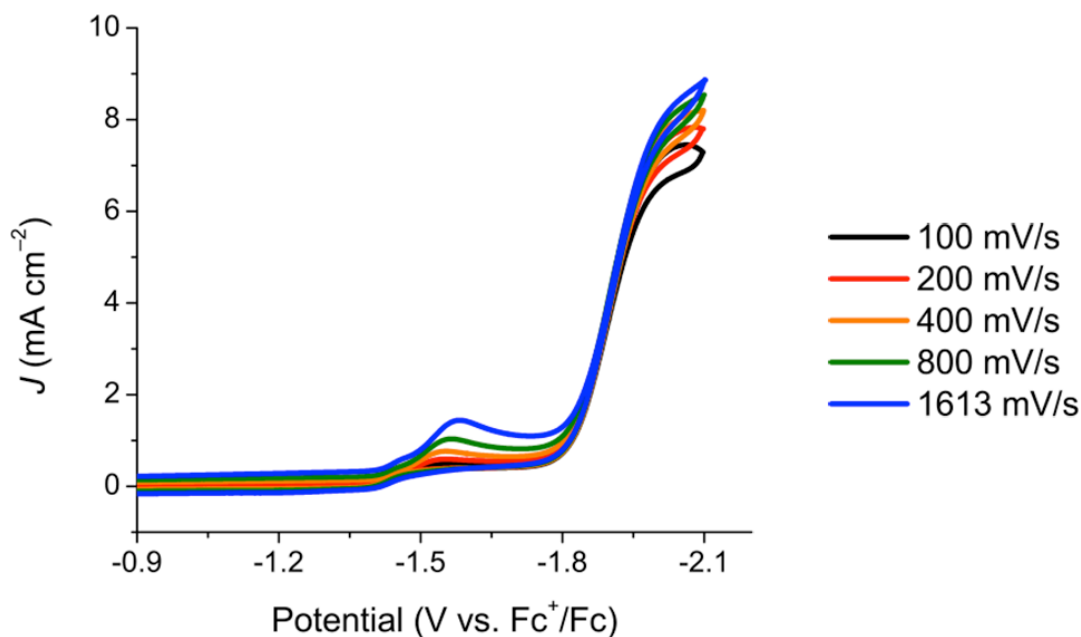
Figure 4.32 Cyclic voltammogram scan rate dependence of 1 mM [Mn(mesbpy)(CO)₃(MeCN)](OTf) (**2**) under an atmosphere of CO_2 with 1.5 M TFE. The initial plateau of the catalytic current is fairly scan rate independent. Scans are in 0.1 M TBAPF₆/MeCN.
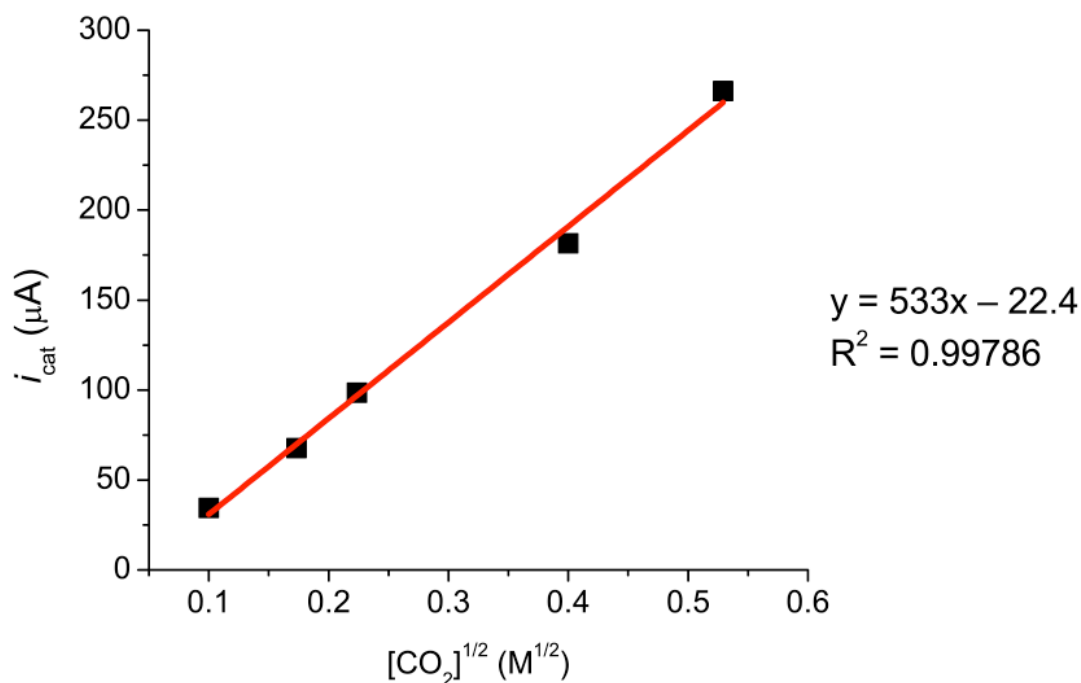
Figure 4.33 Plot of i_{cat} vs. $[CO_2]^{1/2}$ for CVs of [Mn(mesbpy)(CO)₃(MeCN)](OTf) (**2**) under CO_2 and 0.8 M MeOH, showing a linear dependence on $[CO_2]^{1/2}$. This trend is consistent with a catalytic reaction that is first order in $[CO_2]$.
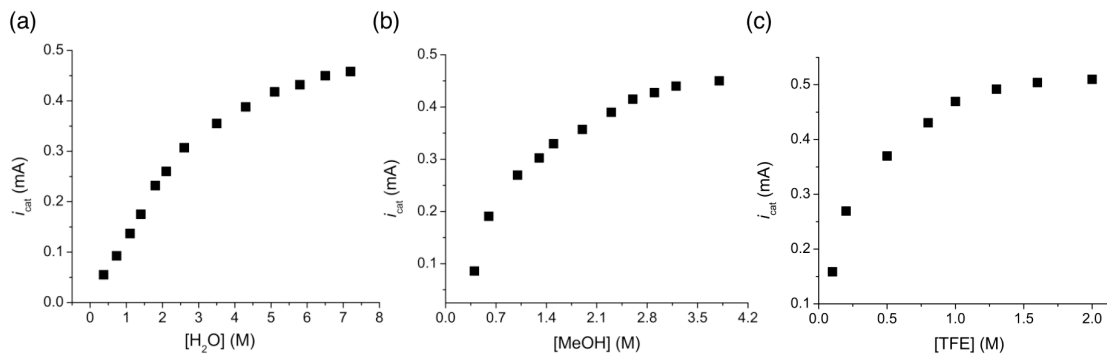
Figure 4.34 (a) Plot of i_{cat} vs. [H$_2$O], (b) plot of i_{cat} vs. [MeOH], and (c) Plot of i_{cat} vs. [TFE] for CVs of [Mn(mesbpy)(CO)$_3$(MeCN)](OTf) (**2**) under CO$_2$ and added weak acid. At low [weak acid], i_{cat} follows a linear trend, indicating that the catalytic reaction is second order in [weak acid]. At high [weak acid], i_{cat} reaches a limiting value independent of [weak acid], which is typical of saturation kinetics expected for catalytic reactions.
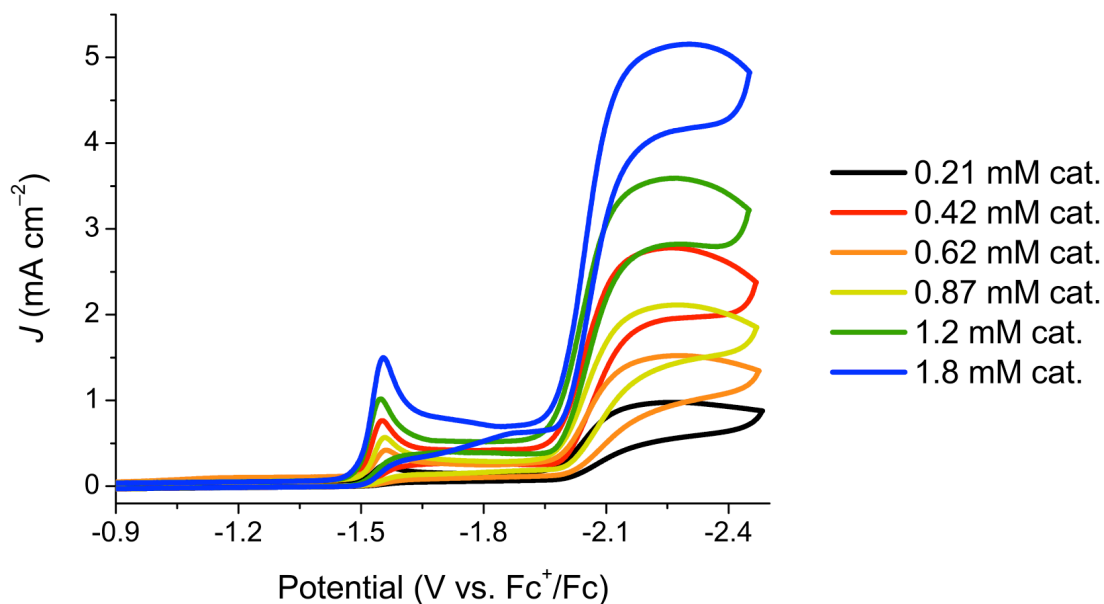
Figure 4.35 Cyclic voltammograms (CVs) showing catalytic current for 1 mM [Mn(mesbpy)(CO)$_3$(MeCN)](OTf) (**2**) under CO$_2$ with 1.8 M MeOH as [**2**] is changed from 0.21 mM to 1.8 mM. CVs are taken at a scan rate of 0.1 V/s.
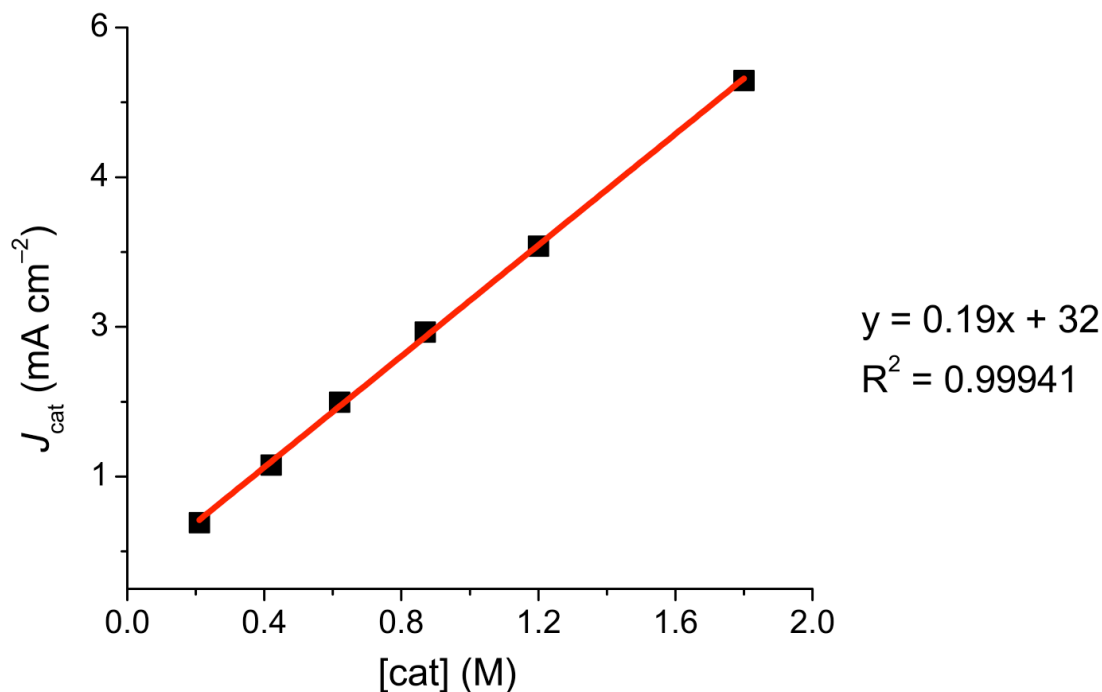
Figure 4.36 Plot of J_{cat} vs. [cat] for CVs of [Mn(mesbpy)(CO)$_3$(MeCN)](OTf) (**2**) under CO_2 and 0.8 M MeOH, showing a linear dependence on [cat]. This trend is consistent with a catalytic reaction that is first order in catalyst.
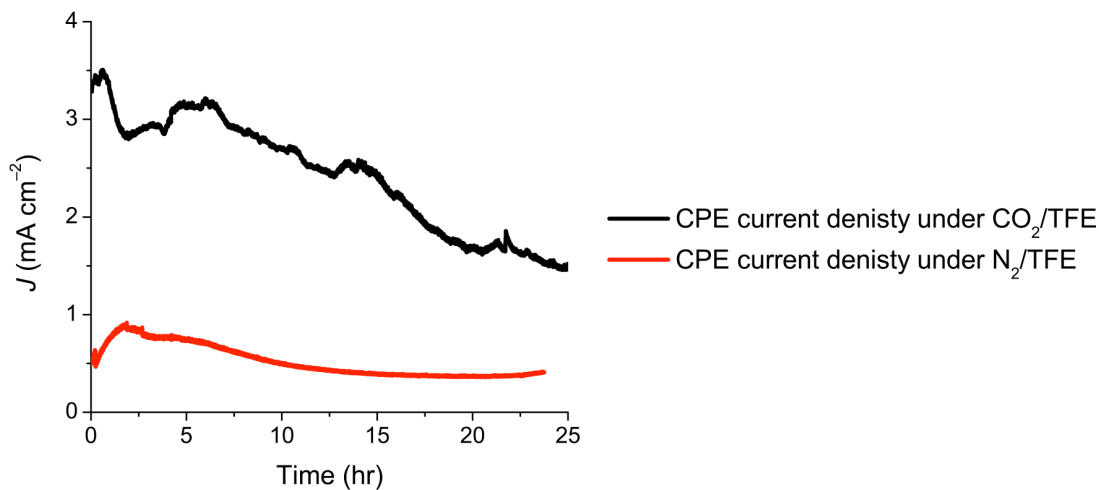
Figure 4.37 Current density trace for controlled potential electrolysis (CPE) experiment over ca. 25 hours for [Mn(mesbpy)(CO)$_3$(MeCN)](OTf) (**2**) at −2.2 V vs. Fc$^+$/Fc under CO_2 (black) or N_2 (red) with 0.3 M TFE. Current density under CO_2 remains fairly stable over the course of ca. 7 hours before steadily declining throughout the remainder of the experiment. For CPE under N_2, an average current efficiency of only 2% was observed for the formation of CO, and no H_2 was observed.
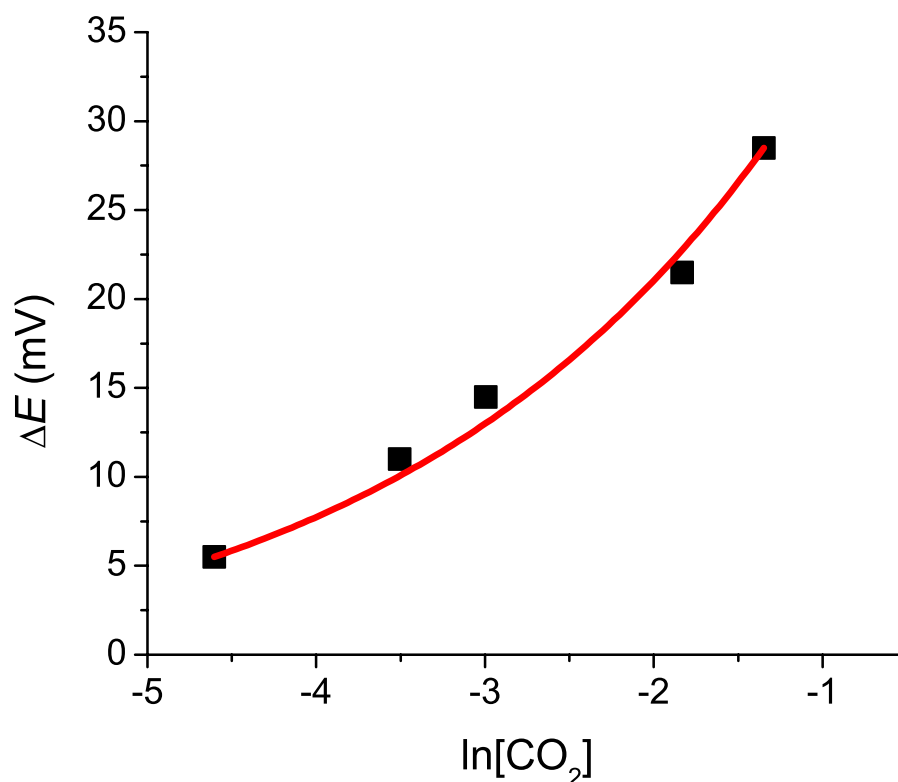
Figure 4.38 Plot of ΔE vs. $\ln[CO_2]$ for CVs of 1 mM [Mn(mesbpy)(CO)$_3$(MeCN)](OTf) (**2**) under CO_2 and 0.8 M MeOH, showing a non-linear relationship consistent with a $K_{CO2} \leq 100$ M^{-1}.
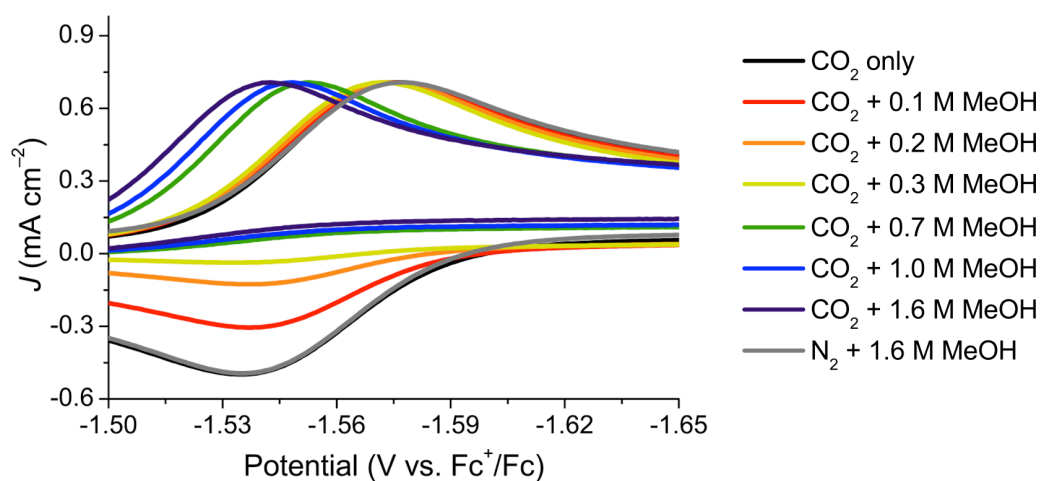
Figure 4.39 Cyclic voltammograms (CVs) of 1 mM [Mn(mesbpy)(CO)$_3$(MeCN)](OTf) (**2**) showing evidence for CO_2 binding with varying concentrations of MeOH. CVs were taken in 0.1 M TBAPF$_6$/MeCN at a scan rate of 0.1 V/s
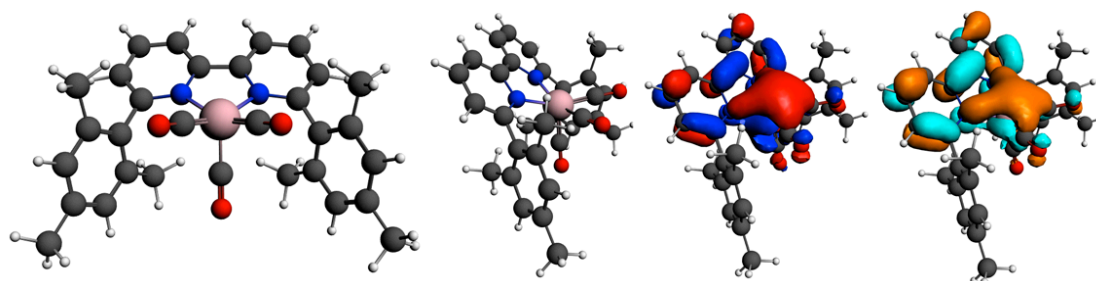
Figure 4.40 Representations of DFT-calculated [Mn(mesbpy)(CO)$_3$] (**3**), showing the HOMO (red/blue electron density) and LUMO(orange/aqua electron density), using ADF 2012.01. DFT-calculated ν_{CO} = 1969, 1902 (broad) cm^{-1}.
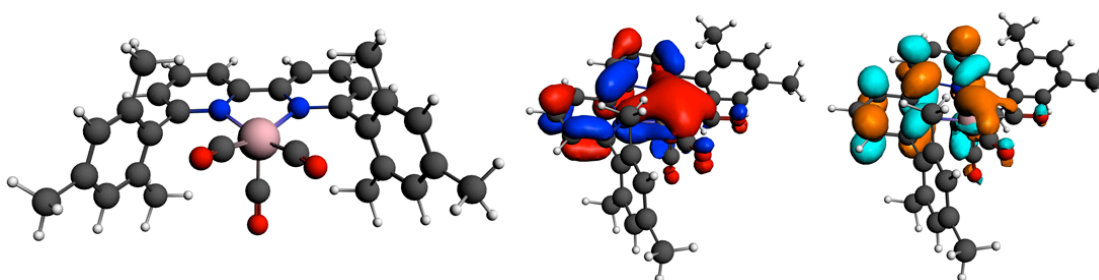
Figure 4.41 Representations of DFT-calculated [Mn(mesbpy)(CO)$_3$]$^-$ (**4**), showing the HOMO (red/blue electron density) and LUMO(orange/aqua electron density), using ADF 2012.01. DFT-calculated ν_{CO} = 1915, 1837 cm^{-1}.

Table 4.4 Sample Input File for DFT-calculated [Mn(mesbpy)(CO)$_3$]$^-$ (**4**).

```
$ADFBIN/adf -n8 \
 <<< "
TITLE Mnmesbpy_anion

MAXMEMORYUSAGE 23000

RELATIVISTIC ZORA

UNRESTRICTED

CHARGE -1 0

SCF
DIIS
END

XC
 LDA VWN
 GGA Becke Perdew
END

SYMMETRY NOSYM
ATOMS
Mn    5.299692   6.518705   11.112638
N     4.002447   7.997814   10.725297
N     6.567712   8.012554   10.716142
O     3.681521   4.395849   12.373807
C     1.901696   6.925551   11.578065
C     6.413504   5.420031   11.993122
C     8.684059   7.005468   11.553755
C     8.773569   7.163028   12.942319
C     5.967253   9.130927   10.139068
C     2.623559   7.978294   10.789448
C     9.414223   5.993244   10.918968
C     1.826994   7.046139   12.986628
C     4.208341   5.346620   11.873445
O     5.466701   4.823077    8.721569
C     1.837616   8.956764   10.257526
H     0.913207   8.897066   10.340144
C     6.730843  10.176396    9.553933
H     6.301936  10.901061    9.159218
C     1.212524   5.905999   10.941716
```

Table 4.4 Sample Input File for DFT-calculated [Mn(mesbpy)(CO)$_3$]$^-$ (**4**), continued.

C	4.554255	9.121091	10.123851
C	8.071590	10.117575	9.571150
H	8.580749	10.787514	9.175154
C	2.404274	10.057096	9.584524
H	1.870568	10.702570	9.180278
C	7.944369	8.161703	13.660568
H	7.910392	8.974942	13.151551
H	8.330782	8.338839	14.521335
H	7.055332	7.817570	13.773620
C	7.942097	8.014321	10.754982
C	8.699444	9.008517	10.208125
H	9.627297	8.962257	10.251183
C	3.770098	10.140274	9.548089
H	4.180660	10.869869	9.143094
C	2.642560	8.094649	13.712501
H	3.575539	7.879665	13.642101
H	2.387664	8.114320	14.637825
H	2.481741	8.954901	13.317911
C	5.384122	5.526043	9.656549
C	0.419291	5.039870	11.682400
H	-0.071438	4.382369	11.244470
C	10.278087	5.188225	11.671713
H	10.762409	4.515998	11.249282
C	1.300271	5.723863	9.427006
H	0.806157	6.422323	8.991576
H	0.930398	4.871625	9.185215
H	2.219411	5.763247	9.152687
C	1.036974	6.150079	13.695846
H	0.972920	6.235434	14.619701
C	9.301433	5.765726	9.438318
H	8.375107	5.748452	9.186871
H	9.710299	4.927350	9.211338
H	9.746780	6.475993	8.970578
C	9.655915	6.350460	13.663693
H	9.727636	6.467226	14.583517
C	0.345928	5.138307	13.065871
C	10.423228	5.380154	13.048997
C	-0.506311	4.173207	13.864050
H	-1.313666	4.612751	14.140806
H	-0.019423	3.881196	14.638169
H	-0.725935	3.414091	13.318973
C	11.420991	4.590587	13.833521

Table 4.4 Sample Input File for DFT-calculated [Mn(mesbpy)(CO)$_3$]$^-$ (**4**), continued.

```
H     11.173647   3.663047   13.824303
H     12.290860   4.693723   13.440744
O      6.934387   4.543423   12.548448
END

GEOMETRY
 GO
 Iterations 500
END

AnalyticalFreq
END

BASIS
 type TZ2P
END

END INPUT
```

Table 4.5 Geometry optimized xyz coordinates of DFT-calculated
[Mn(mesbpy)(CO)₃] (**3**).

Atom	X (Å)	Y (Å)	Z (Å)
Mn	2.848285	2.013372	2.726051
O	3.943874	2.230770	5.464823
O	1.810434	4.790590	2.842323
O	5.063215	3.656508	1.632409
N	3.387087	0.211646	1.894305
N	1.039181	1.036883	2.742962
C	3.504712	2.119402	4.390586
C	2.147743	3.675472	2.842671
C	4.249351	2.942511	2.062761
C	4.643555	-0.283640	1.636709
C	4.829946	-1.391630	0.817416
H	5.846743	-1.736339	0.638293
C	3.733202	-2.059524	0.258206
H	3.874982	-2.920525	-0.392580
C	2.464169	-1.621750	0.591207
H	1.589784	-2.146025	0.215154
C	2.305494	-0.507405	1.426530
C	1.008943	-0.049891	1.892380
C	-0.193132	-0.679209	1.540219
H	-0.185571	-1.509671	0.839437
C	-1.384977	-0.249184	2.095052
H	-2.328483	-0.723217	1.830626
C	-1.338757	0.781305	3.042743
H	-2.239525	1.107757	3.559427
C	-0.133538	1.395122	3.365369
C	5.847075	0.316847	2.285545
C	6.103338	0.037016	3.649296
C	7.268370	0.536810	4.232193
H	7.452958	0.330745	5.288907
C	8.200760	1.286645	3.505909
C	7.944307	1.514135	2.154110
H	8.655311	2.099242	1.566763
C	6.790993	1.032130	1.523045
C	5.189410	-0.847633	4.462733
H	4.134389	-0.574845	4.342621
H	5.438780	-0.785080	5.528217
H	5.292109	-1.899396	4.153631
C	9.453104	1.810982	4.166605

Table 4.5 Geometry optimized xyz coordinates of DFT-calculated
[Mn(mesbpy)(CO)$_3$] (**3**), continued.

Atom	X (Å)	Y (Å)	Z (Å)
H	9.228436	2.267814	5.139605
H	9.949994	2.563141	3.542269
H	10.173762	0.999393	4.348257
C	6.601992	1.301155	0.047834
H	7.071955	0.513842	-0.561646
H	7.068007	2.253998	-0.229861
H	5.544732	1.347631	-0.235993
C	-0.132337	2.411387	4.459223
C	0.366951	2.050427	5.732587
C	0.296445	2.979816	6.772496
H	0.693967	2.699712	7.750343
C	-0.272090	4.245975	6.600949
C	-0.799344	4.560354	5.347389
H	-1.254623	5.540523	5.189515
C	-0.751080	3.664828	4.273836
C	0.894400	0.664401	6.016346
H	0.068040	-0.061214	6.068805
H	1.423009	0.641027	6.976151
H	1.584052	0.316537	5.238647
C	-0.289183	5.248993	7.729459
H	0.630945	5.852885	7.726635
H	-0.350709	4.753536	8.706746
H	-1.135432	5.941731	7.640040
C	-1.361702	4.076351	2.953635
H	-0.838374	3.635489	2.097663
H	-1.330882	5.166623	2.842423
H	-2.416370	3.767168	2.888197

Table 4.6 Geometry optimized xyz coordinates of DFT-calculated
[Mn(mesbpy)(CO)$_3$]$^-$ (**4**).

Atom	X	Y	Z (Å)
Mn	5.326834	6.631417	11.423627
N	3.980042	8.023394	10.779785
N	6.600464	8.073412	10.779357
O	3.747229	5.059794	13.383937
C	1.844615	6.862945	11.438388
C	6.491167	5.650978	12.399500
C	8.783506	7.015330	11.445800
C	9.202516	7.169419	12.782595
C	5.976997	9.157207	10.130657
C	2.597057	7.987170	10.791743
C	9.259451	5.930815	10.681615
C	1.426321	6.984221	12.780161
C	4.253623	5.743152	12.573514
O	5.222068	4.554759	9.327082
C	1.810599	8.971422	10.223074
H	0.727889	8.866453	10.287796
C	6.721423	10.187748	9.514200
H	6.190972	10.992912	9.010320
C	1.402223	5.772795	10.663232
C	4.558413	9.131366	10.136093
C	8.095184	10.186808	9.540172
H	8.674553	10.980298	9.070117
C	2.398129	10.083130	9.571466
H	1.785095	10.859393	9.115094
C	8.710659	8.326527	13.618424
H	9.135118	9.281100	13.273004
H	8.984123	8.189500	14.672735
H	7.617613	8.417799	13.550105
C	7.986174	8.099330	10.787792
C	8.728728	9.108520	10.206915
H	9.815042	9.050214	10.272113
C	3.769987	10.140744	9.537763
H	4.264810	10.975550	9.046332
C	1.878271	8.150043	13.625557
H	2.973672	8.241856	13.603132
H	1.561489	8.022432	14.668568
H	1.470493	9.100581	13.251017
C	5.254065	5.395304	10.153253

Table 4.6 Geometry optimized xyz coordinates of DFT-calculated
[Mn(mesbpy)(CO)$_3$]$^-$ (**4**), continued

Atom	X	Y	Z (Å)
C	0.592754	4.798053	11.260307
H	0.272321	3.942804	10.659192
C	10.122221	5.005487	11.278520
H	10.473555	4.157584	10.684572
C	1.764154	5.651960	9.202909
H	1.306992	6.461508	8.614685
H	1.419339	4.693061	8.794587
H	2.848746	5.718523	9.053509
C	0.606592	5.997428	13.332350
H	0.306916	6.089685	14.379827
C	8.861804	5.765215	9.234884
H	7.774015	5.845580	9.113319
H	9.181000	4.787107	8.852331
H	9.316399	6.545705	8.606259
C	10.071954	6.226092	13.338350
H	10.378231	6.343296	14.381116
C	0.187312	4.887110	12.593060
C	10.538559	5.131433	12.606214
H	-1.551376	4.223132	13.713591
H	-0.089108	3.267843	14.002852
H	-0.985541	3.068928	12.485111
C	11.425980	4.088124	13.245220
H	10.822468	3.294588	13.712808
H	12.058840	4.523003	14.030715
H	12.080250	3.607628	12.505193
O	7.051827	4.884819	13.090668

Chapter 5

Manganese catalysts with bulky bipyridine ligands:
Electrocatalytic dihydrogen production.

5.1 Introduction

In recent years, efforts have been made to develop technologies for solar and wind power; however, the energy sources for these technologies suffer from intermittent availability. Therefore, research in energy storage, particularly storage in chemical bonds, is essential to the sustainability of these technologies. To counteract the intrinsic availability problem of solar and wind energy, electricity generated from these sources can be stored in chemical fuels, such as those produced from proton (H^+) reduction (i.e. dihydrogen, H_2) or from CO_2 reduction.[1-2] Molecular complexes

containing earth-abundant metals are promising options as H^+ or CO_2 reduction catalysts.[3-5]

Recently, our group reported electrocatalytic CO_2 reduction by a Mn complex with a bulky bpy ligand, [Mn(mesbpy)(CO)$_3$(MeCN)](OTf) (**1**; mesbpy = 6,6′-dimesityl-2,2′-bipyridine; MeCN = acetonitrile; OTf = trifluoromethanesulfonate; structure in Figure 5.1 and 5.4).[6] In contrast to typical Mn(bpy)(CO)$_3$X complexes, **1** does not dimerize after one-electron reduction, which significantly lowers the potential necessary for two-electron reduction (by 0.30 V). Although the doubly-reduced state of **1** binds CO_2 with added weak Brønsted acid, high catalytic rates are not observed until a ~400 mV more negative potential. This unusual "over reduction" is required to reduce the Mn(I)–COOH intermediate in the catalytic cycle. One strategy to achieve significant catalytic rates at the same potential as substrate binding (i.e. approximately –1.6 V vs. Fc$^{+/0}$) is to utilize stronger Brønsted acids, such as acetic acid, trifluoroacetic acid (TFA), or dimethylformamidium ([(DMF)H]$^+$) to promote C–O bond cleavage in the bound CO_2 ligand, essentially bypassing the need to reduce the Mn(I)–COOH intermediate. A resulting Mn(I) tetracarbonyl complex would be more easily reduced at these potentials,[7] and hence, catalysis could occur.

Upon initially surveying stronger Brønsted acids to promote CO_2 reduction at these low overpotentials, we failed to find any Brønsted acid (stronger than phenol) that would preferentially engage CO_2 over a proton (H$^+$). Even in the presence of CO_2, all acids surveyed resulted in surprisingly high activity for electrocatalytic H$^+$ reduction by **1** at –1.6 V vs. Fc$^{+/0}$, displaying no evidence for CO_2 reduction (*vide*

infra). Although Mn and Re bpy complexes have been extensively studied for CO_2 reduction, they have not been investigated as H^+ reduction catalysts, mainly due to the high overpotentials necessary to access their doubly-reduced states.[8] Because **1** possesses a relatively moderate reduction potential (resulting from bypassing dimerization), we further investigate the catalytic properties for **1** in regards to the H_2 evolution reaction (HER).

Of the homogeneous catalysts studied for HER, including numerous examples of those based on earth-abundant metals Ni, Fe, and Co, few catalysts have been developed based on Mn. Sparse research on homogeneous Mn HER catalysts is surprising, especially considering that the $Mn(I)(CO)_3$ fragment is isolobal with the $Fe(II)(CO)(CN)_2$ fragment found in the active site of [NiFe]-hydrogenases.[9] The majority of Mn HER catalysts studied to date are binuclear complexes ([NiMn]- and $Mn_2(CO)_6$-type complexes).[10-11] To our knowledge, there have only been two reports of mononuclear Mn catalysts,[12-13] and they both suffer from very low activity. Here, we report the ability of **1**, an earth-abundant, mononuclear Mn complex, to function as a competent HER electrocatalyst, displaying high activity for HER with rates as high as 5500 s^{-1}.

5.2   Results and Discussion

Cyclic Voltammetry. The cyclic voltammogram (CV) of **1** in dry MeCN with 0.1 M tetrabutylammonium hexafluorophosphate (TBAPF$_6$) as the supporting electrolyte under inert atmosphere is shown in Figure 5.1 and has been previously

described.[6] The CV of **1** displays a single reversible, two-electron reduction wave at −1.55 V vs. Fc$^{+/0}$. Addition of TFA (pK_a = 12.7 in MeCN)[14] to electrochemical solutions of **1** resulted in an increase in current near this two-electron reduction, as shown in Figure 5.2. This current increase corresponds to the electrocatalytic reduction of H$^+$ from TFA to H$_2$, as verified by controlled potential electrolysis (CPE) experiments, with 100% Faradaic efficiency (Figures 5.8–5.10). Higher concentrations of TFA resulted in further increased current densities in electrocatalysis experiments (Figure 5.2 and S3). For reference, a CV of TFA in the electrolyte solution (without added catalyst) is shown in Figure 5.5.
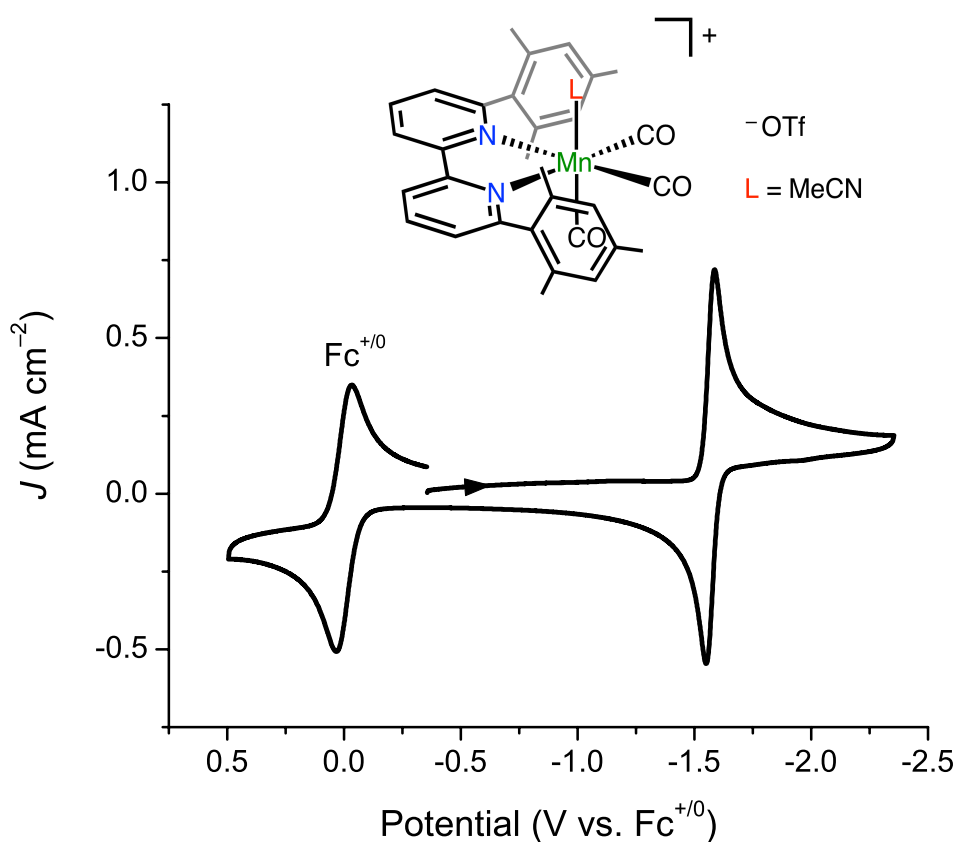
Figure 5.1 Cyclic voltammogram (CV) of 1 mM complex **1** in MeCN (0.1 M TBAPF$_6$) under N$_2$ atmosphere (scan rate = 0.1 V s^{-1}).

For HER, the overpotential (η) is defined as the difference between the thermodynamic potential for the reduction of H^+ (E_{H+}) and the potential at half of the catalytic current ($E_{cat/2}$).[15] For many acids, such as TFA, homoconjugation of acid/base pairs is a known problem, which lowers the accuracy of calculating E_{H+} and lowers the *effective* pK_a of the acid in MeCN.[15-16] Artero has accurately measured E_{H+} for TFA, taking into account homoconjugation of the acid at various concentrations.[17] At 0.1 M TFA, E_{H+} = –0.65 V vs. Fc$^{+/0}$,[17] and thus, η = 0.90 V using $E_{cat/2}$ = –1.55 V vs. Fc$^{+/0}$ (see Supporting Information, Figure 5.11). The η for **1**, although far from ideal, is comparable to many previously reported HER electrocatalysts.[9,18-23]
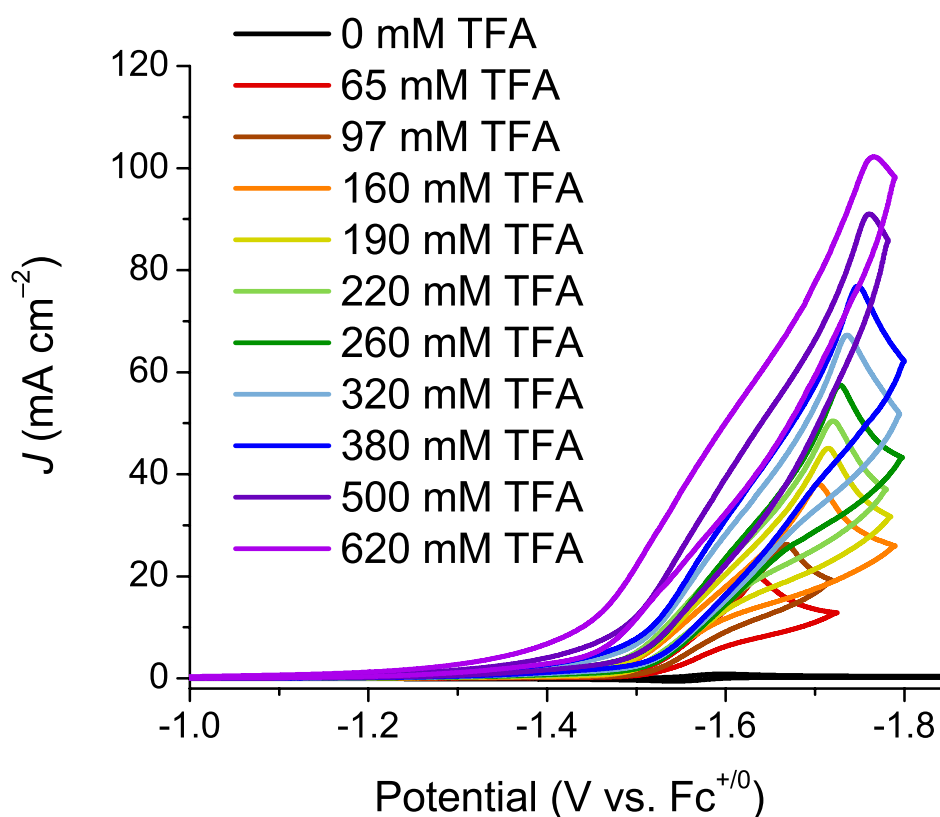
Figure 5.2 Cyclic voltammograms (CVs) of 1 mM complex **1** with varying [TFA]. Conditions: 0.1 M TBAPF$_6$/MeCN; under N$_2$; scan rate = 0.1 V s^{-1}.

The peak-shaped current response in our catalytic CVs can be attributed to a variety of "side-phenomena," which cause local perturbations in the diffusion layer and have been previously discussed.[24-25] Additionally, peak-shaped current responses are typical for electrocatalysis involving TFA due to issues involving homoconjugation.[17,26-27] At high concentrations of TFA, the catalytic current response splits into two features. The first feature shifts to more positive potentials as the concentration of TFA is increased, whereas the second feature shifts to more negative potentials. Artero has previously described this phenomenon as follows: the wave at more positive potentials corresponds to the reduction of TFA to H_2 by **1**, resulting in the formation of the homoconjugate adduct of TFA, and the wave at more negative potentials corresponds to the reduction of the homoconjugate adduct, [TFA-H-TFA], by **1** (into H_2 and TFA$^-$).[17]

The turnover frequency (TOF) of **1**-catalyzed TFA reduction can be estimated from CVs by comparing the peak catalytic current (i_{cat}) to the peak current of the reversible redox wave under inert atmosphere (i_p), as described in the Supporting Information. Due to the complications of homoconjugation, i_{cat} values were determined from catalytic current values at $E_{cat/2} = -1.55$ V vs. Fc$^{+/0}$. In order to make this analysis, the catalytic reaction must be at steady state. Scan rate studies indicate that the catalytic current response is at steady state despite the peak-shaped current responses (Figure 5.7). Addition of 620 mM TFA results in a peak $i_{cat}/i_p = 59.3$ and a TOF = 5,500 s^{-1} (Figure 5.2). This calculated TOF is likely an underestimation in overall catalyst activity due to **1**-catalyzed reduction of [TFA-H-TFA] at higher

overpotentials (described above). However, a small amount of current at $E_{cat/2}$ results from TFA reduction by the glassy carbon electrode, further complicating the true activity of **1**. The TOF of **1** is comparable to the widely studied Ni bis(diphosphine) complexes bearing pendant amines, arguably the most active family of HER electrocatalysts to date (see Supporting Information).[22,28-29]

Controlled Potential Electrolysis. CPE was performed on **1** at −1.5 V vs. $Fc^{+/0}$ to measure the efficiency at which H_2 is produced and to measure the lifetime of the catalyst. Gas chromatography indicated that catalyst **1** operates with a Faradaic efficiency of 105 ± 5% for the formation of H_2 from H^+ (0.2 M TFA), measured for over 21 hours of electrolysis (Figure 5.8). Catalyst **1** sustained current densities of approximately 25 mA/cm^2 during the first 12 hours of electrolysis (Figure 5.9), and the catalyst reached a turnover number (TON) of approximately 75 after 21 hours of electrolysis (Figure 5.10). The current density gradually decreased after the first 12 hours of electrolysis throughout the remainder of the experiment. However, little decrease in Faradaic efficiency was observed throughout this time indicating that the true lifetime of the catalyst is much higher than 21 hours. Very little CO (1.53 µmol, Faradaic efficiency = 1 ± 3%) was detected during electrolysis, indicating that little catalyst degradation occurred throughout the experiment. In order to confirm that H_2 production was not simply the result of direct TFA reduction on the glassy carbon working electrode, CPE experiments were repeated in the absence of catalyst **1** (Figure 5.9). Over the course of 22 hours, only 33 µmol of H_2 were produced (equivalent TON

= 4.4, see Figure 5.10), as compared to 560 μmol of H_2 produced over 21 hours with catalyst **1**.

Tafel Plots. Catalytic Tafel plots, along with a determination of η at $E_{cat/2}$, provide a cohesive method for comparing electrocatalysts at different experimental conditions.[30] A "good" electrocatalyst is defined to have a high TOF, low η, and high stability. Catalytic Tafel plots assess the later two of these parameters in a single plot, allowing for catalyst benchmarking independent of variable experimental conditions. For this analysis, we assume an in Figure 5.3 (see Supporting Information, Figure 5.12–5.13). Recently, Artero and Savéant have compared the Tafel plots of widely-studied HER electrocatalysts.[30] With a $\log\text{TOF}_{max} = \sim4.0$, **1** displays similar maximum activity to $Co(dmgH)_2$. Catalyst **1** has a lower TOF_0 (TOF at $\eta = 0$) than $Co(dmgH)_2(py)$, $[Ni(P^{Ph}_2N^{Ph})_2]^{2+}$, and $Fe(TPP)$.[30]
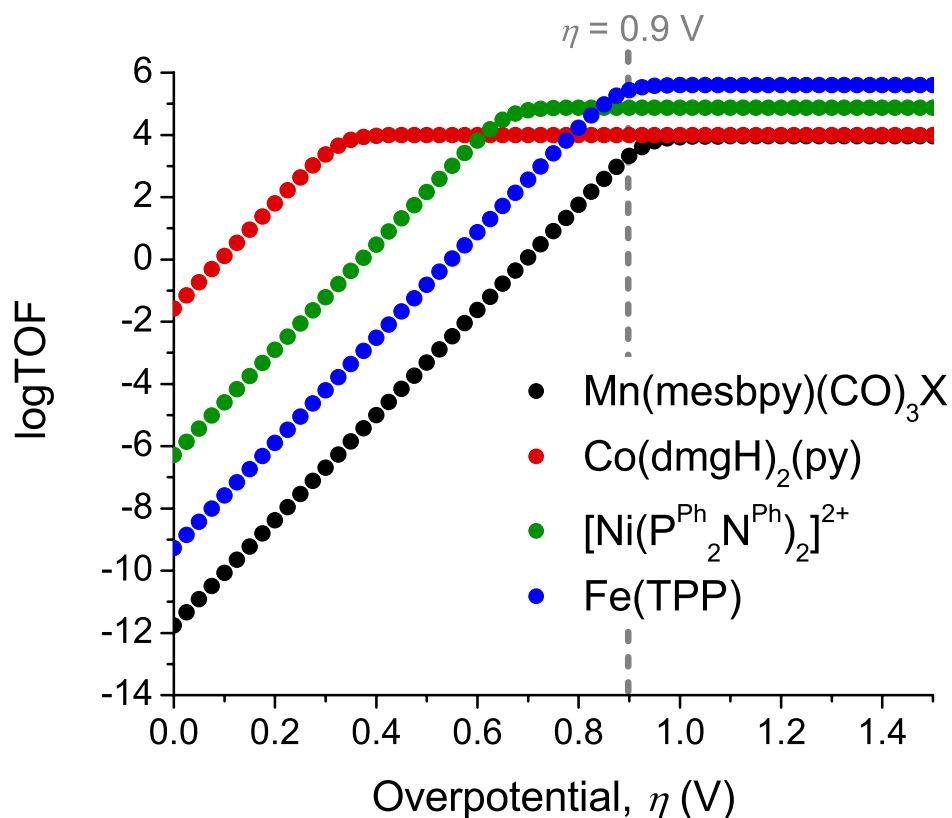
Figure 5.3 Catalytic Tafel plots for **1**, Co(dmgH)$_2$(py), [Ni(P$^{Ph}_2$N^{Ph})$_2$]$^{2+}$, and Fe(TPP) with 1.0 M H$^+$.

5.3   Conclusions

We have investigated the ability for the earth-abundant Mn complex **1** to perform HER using TFA as a H$^+$ source. Upon two-electron reduction, **1** displays remarkably high activity for HER, reaching a TOF of 5,500 s^{-1}. We utilize two complementary methods to benchmark catalyst **1** with other HER catalysts in the literature. These findings provide a new example of catalytic small molecule reduction by these well-studied Mn bpy catalysts, which to this date have been primarily investigated in regards to CO_2 reduction. Future studies will include exploring the

ability for catalyst **1** to produce a tunable syngas ratio using acids under CO_2 atmosphere.

5.4   Experimental

General Considerations. Solvents were sparged with argon, dried on a custom dry solvent system over alumina columns, and stored over molecular sieves before use. Synthesis of 6,6'-dimesityl-2,2'-bipyridine (mesbpy) was performed by the Suzuki coupling of 6,6′-dibromo-2,2′-bipyridine with trimethylphenylboronic acid, as previously reported.[31] Synthesis of [Mn(mesbpy)(CO)3(MeCN)](OTf) (**1**) was performed as previously reported.[6,31] Manipulations of Mn complexes were covered from light. Tetrabutylammonium hexafluorophosphate (TBAPF6, Aldrich, 98%) was twice recrystallized from methanol (MeOH) and dried under a vacuum at 90 °C overnight before use. Trifluoroacetic acid (TFA, Acros, Extra pure, 99%) was used as received. All other chemicals were purchased from commercial sources and used as received.

Electrochemistry. Electrochemical experiments were performed using a BASi Epsilon potentiostat. A single-compartment cell was used for all cyclic voltammetry experiments with a glassy carbon working electrode (3 mm in diameter from BASi), a Pt wire counter electrode (flame annealed with a butane torch and separated from the bulk solution by a Vycor tip), and a Ag/AgCl pseudo-reference (separated from the bulk solution by a Vycor tip). Ferrocene (Fc) was added as an internal reference. All electrochemical experiments were performed with 0.1 M TBAPF$_6$ as the supporting

electrolyte. Electrochemical cells were shielded from light during experiments. All solutions were purged with N_2 (run through a custom Drierite/activated 3Å molecular sieves drying column) before CVs were taken. Mn complex concentrations ranged from 0.25−1.0 mM in MeCN. All potentials were referenced vs. $Fc^{+/0}$. A current increase is observed without the addition of catalyst **1**, with only TFA in the electrolyte solution, at −1.8 V vs. $Fc^{+/0}$, indicating that H^+ reduction from TFA can occur on the glassy carbon working electrode without the assistance of catalyst (Figure 5.5).[32] However, this current increase in the absence of catalyst **1** occurs at a significantly slower rate (i.e. lower peak current density).

Bulk Electrolysis. Bulk electrolysis experiments (at ca. − 1.5 V vs. $Fc^{+/0}$) were carried out in a 60 mL Gamry 5-neck cell equipped with 3 Ace-Thred ports to hold each electrode and two joints capable of being sealed with septa for gas sparging. This setup included a glassy carbon working electrode (3 mm diameter), a Pt wire counter electrode (flame annealed with a butane torch before use and separated from the solution by a Vycor tip), and a Ag/AgCl pseudo-reference (separated from the solution by a Vycor tip). A BASi Epsilon potentiostat was used to apply potential and record current. These bulk electrolysis experiments were carried out in 30 mL MeCN with 0.1 M $TBAPF_6$ and added TFA. Bulk electrolysis solutions were purged with dry N_2 for 10 min prior to electrolysis. Solutions were constantly stirred and shielded from light throughout bulk electrolysis experiments. Gas analysis for bulk electrolysis experiments were performed using 1 mL sample injections on a Hewlett-Packard 7890A Series gas chromatograph with two molsieve columns (30 m × 0.53 mm ID ×

25 μm film). The 1 mL injection was split between two columns, one with N_2 as the carrier gas and one with He as the carrier gas, in order to quantify both H_2 and CO (to test for catalysis degradation) simultaneously in each run. Gas chromatography calibration curves were made by sampling known volumes of CO and H_2 gas.

Overpotential Determination. An accurate determination of the overpotential, or "the additional potential (beyond the thermodynamic requirement) needed to drive a reaction at a certain rate,"[33] is required in order to properly compare various catalytic systems. In laboratory research, the reaction conditions used to measure the performance of catalysts vary considerably from standard state conditions, and therefore, the process for determining the overpotential for many catalytic reactions is far from straightforward. When performing catalytic studies in nonaqueous solvent, one needs to calculate the thermodynamic potential for the reduction of H^+ (E_{H+}), correcting for the strength of the acid used. For many acids, homoconjugation of acid/base pairs is a known problem, which significantly lowers the accuracy of calculating E_{H+}.[15] As described in the main text, TFA has a relatively large homoconjugation constant in MeCN (7.6 x 103 M^{-1}).[16] E_{H+} has been accurately measured by Artero and coworkers by taking into account homoconjugation of the acid at various concentrations.[17] For 1, 10, and 100 mM TFA, E_{H+} = −0.71 V, −0.68 V, and −0.65 V vs. $Fc^{+/0}$, respectively.[17]

Now that we have determined a value for E_{H+}, we can calculate the overpotential (η) for the reduction of H^+ to H_2 via E5.1, where the catalytic potential is defined as the potential at half of the catalytic current ($E_{cat/2}$), as recommended by

Appel and Helm.[15] For non-ideal catalytic waves, the use of Ecat/2 results in a smaller variance in potential for varying values of i_{cat}.[15] The overpotential determination for catalyst **1** is shown in Figure 5.10. Here, we define E_{cat} to be near the potential of the first of two features observed in our catalytic CVs (see Figure 5.10), as this wave corresponds to the catalytic reduction of TFA to H_2. The second of these two features corresponds to the reduction of the homoconjugate adduct of TFA, as described in the main text. From these catalytic CVs, we have determined $E_{cat/2}$ to be −1.55 V vs. $Fc^{+/0}$ at ~100 mM TFA (Figure 5.2 and 5.11). Utilizing E5.1, we calculate η = 0.90 V for catalyst **1** with ~100 mM TFA.

$$\eta = \left| E_{H^+} - E_{cat/2} \right|$$

(**E5.1**)

Turnover Frequency Calculations. For a reversible electron-transfer reaction followed by a fast catalytic reaction ($E_R C_{cat}$ scheme), the peak catalytic current (i_{cat}) is given by E5.2.[34] The derivation of E5.2 assumes that pseudo- first order kinetics apply, i.e. the reaction is first order in catalyst and that the concentrations of the substrates, Q, are large in comparison to the concentration of catalyst. In E5.2, ncat is the number of electrons required for the catalytic reaction (n = 2 for the reduction of H^+ to H_2), F is Faraday's constant, A is the surface area of the electrode, [cat] is the catalyst concentration, D is the diffusion constant of the catalytically-active species, k_{cat} is the rate constant of the catalytic reaction, and [Q] is the substrate concentrations. Plotting icat versus [TFA] shows a linear relationship at low and moderate [TFA], indicating that the catalytic reaction is second order in [TFA] (Figure 5.6). At high

[TFA], i_{cat} begins to reach a limiting value (Figure 5.6), which is typical of saturation kinetics expected for catalytic reactions.[35]

$$i_{cat} = n_{cat}FA[cat]\left(Dk_{cat}[Q]^{y}\right)^{1/2}$$

(E5.2)

The first equation below (E5.3) describes the peak current of a complex with a reversible electron transfer and with no following reaction.[36] In E5.3, R is the universal gas constant, T is temperature, n_p is the number of electrons in the reversible, non-catalytic reaction ($n_p = 2$ for the reduction of complex 1), and v is scan rate (0.1 V/s). For these calculations, i_p is determined as the peak current under N_2 without added TFA. A comparison of E5.2 and E5.3 allows for the determination of i_{cat}/i_p and allows to further calculate the catalytic rate constant (k_{cat}) and the turnover frequency (TOF), as shown in E5.4. In this equation, A cancels out because the same electrode was used for the experiments with and without added H^+. D also cancels out because we are assuming that the diffusion constant of the catalytically-active species does not change significantly with or without added H^+.

$$i_p = 0.4463 n_p^{3/2} FA[cat]\left(\frac{F}{RT}\right)^{1/2} v^{1/2} D^{1/2}$$

(E5.3)

$$TOF = k_{cat}[Q] = \frac{Fvn_p^3}{RT}\left(\frac{0.4463}{n_{cat}}\right)^2\left(\frac{i_{cat}}{i_p}\right)^2$$

(E5.4)

Due to the complications of homoconjugation (described in the main text), i_{cat} values were determined from catalytic current values at $E_p = -1.6$ V vs. $Fc^{+/0}$. Addition of 620 mM TFA to an electrochemical solution of 1 resulted in a peak $i_{cat}/i_p = 59.3$ (51.3 mA/cm^2 peak current density) and a TOF = 5,500 s^{-1} (Figure 5.2). The TOF of catalyst 1 is comparable to the extensively studied Ni bis(diphosphine) complexes

bearing pendant amines, arguably the most active family of HER electrocatalysts to date. $[Ni(P^R_2N^{R'}_2)_2]^{2+}$ complexes $(P^R_2N^{R'}_2$ = 1,5-diaza-3,7-diphosphacyclooctane ligand) have TOFs ranging from approximately 500–7,000 s^{-1} using TFA or $[(DMF)H]^+/H_2O$ as the H$^+$ source,[28-29,37-38] depending on the R, R' functional groups on the phosphorus and nitrogen atoms in the $P^R_2N^{R'}_2$ ligand.[23,28-29,39] However, these $[Ni(P^R_2N^{R'}_2)_2]^{2+}$ complexes typically operate at much lower overpotentials than catalyst **1** (vide infra). Similar Ni complexes bearing two seven-membered cyclic diphosphine ligands with only a single pendant amine on each ligand, i.e. $[Ni(P^R_2N^{R'})_2]^{2+}$ complexes $(P^R_2N^{R'}$ = 1-aza-3,6-diphosphacycloheptane), are among the most active HER catalysts reported. These complexes display TOFs as high as 33,000 s^{-1} and 106,000 s^{-1} with $[(DMF)H]^+$ and $[(DMF)H]^+/H_2O$, respectively, out-competing Mn catalyst **1**.[22,40]

Catalytic Tafel Plots. In order to accurately construct catalytic Tafel plots, our catalytic CVs must be at steady state conditions, and we must know the catalytic mechanism for HER. In this regard, we acknowledge that the peak-shaped current responses in catalytic CVs suggest that the catalytic reaction is not at steady state; however, this would likely lead to an underestimation of the TOF based on i_{cat}/i_p. As such, we have continued to analyze the Tafel behavior of **1** with the knowledge that these Tafel plots will be an underestimation of performance of catalyst **1**. Additionally, we have assumed an EECC-type catalytic mechanism of the following:

$$Mn(I) + 2\ e– = Mn(–I) \qquad (EE)$$

$$Mn(–I) + H^+ = Mn(I)–H \qquad (C)$$

$$Mn(I)\text{–}H + H^+ = Mn(I) + H_2 \quad (C)$$
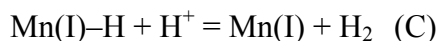
Although we do not have direct experimental evidence for an EECC-type mechanism, we have used literature precedent to confidently propose this mechanism. From our previous studies with [Mn(mesbpy)(CO)$_3$(MeCN)](OTf),[6] we know that the starting Mn(I) complex undergoes a two-electron reduction to form [Mn(mesbpy)(CO)$_3$]$^-$. Computational studies have shown that [Mn(bpy)(CO)$_3$]$^-$ complexes can be protonated by strong acid.[7] Additional computational studies have suggested that the reduction potential of a Mn(bpy)(CO)$_3$H complex occurs at approximately –2.1 V vs. Fc$^{+/0}$,[41] i.e. at least 400 mV more negative than the reduction of Mn(bpy)(CO)$_3$Br. This suggests that, after forming a Mn(I)–H complex, further protonation should occur rather than reduction (i.e. an ECEC-type mechanism is unlikely). These two reaction schemes are the most plausible mechanisms, and therefore, we are confident in our assignment of EECC.

We have followed Artero and Savéant's procedures for constructing Tafel plots from an EECC-type HER mechanism.[30,42] We have also assumed that $k_2 \gg k_1$ (the respective rate constants for the chemical reactions listed above), as digital simulations of the catalytic CVs using this stipulation provided better fits than other values for k_1 and k_2. Therefore, the equations needed to calculate k_1, TOF$_{max}$, and TOF (and therefore, construct Tafel plots) are provided below (E5.5–E5.8). Relevant values used in E5.5–E5.8 are as follows: $F/RT = 38.92$ V^{-1}, $v = 0.1$ V/s, $n_p = 2$, and $E_{1/2} = -1.55$ V vs. Fc$^{+/0}$. In order to calculate TOF values from TOF$_{max}$, values for E_{H+} must be determined for each [TFA] studied. We have extrapolated the data from Ref. 25 to

determine the following E_{H+} values for 97 mM, 220 mM, 380 mM, and 1 M TFA: E_{H+} for 97 mM TFA = –0.651 V vs. $Fc^{+/0}$, E_{H+} for 620 mM TFA = –0.626 V vs. $Fc^{+/0}$, and E_{H+} for 1.0 M TFA = –0.620 V vs. $Fc^{+/0}$.

$$\frac{i_{cat}}{i_p} = 4.484\sqrt{k_1[\text{TFA}]}\sqrt{\frac{RT}{Fvn_p^3}} \tag{E5.5}$$

$$k_1 = \frac{\left(0.223\frac{i_{cat}}{i_p}\sqrt{\frac{Fvn_p^3}{RT}}\right)^2}{[\text{TFA}]} \tag{E5.6}$$

$$\text{TOF}_{max} = k_1[\text{TFA}] \tag{E5.7}$$

$$\text{TOF} = \frac{\text{TOF}_{max}}{1+\exp\left[\frac{F}{RT}\left(E_{H+} - E_{1/2}\right)\right]\exp\left[\frac{F}{RT}\eta\right]} \tag{E5.8}$$

An accurate value of k_1 was determined by fitting the plot in Figure 5.6 to E5.5 (see Figure 5.12). Here, we calculate k_1 = 9.0 x 103 M^{-1} s^{-1}. We have used DigiSim simulation software to confirm our calculated value of k_1 (see Figure 5.13). TOF_{max} values can then be calculated from E5.7 for each [TFA] studied. For fair comparison with reported Tafel plots for the HER electrocatalysts in Ref. 38, we extrapolated the equation obtained in Figure 5.12 to 1.0 M TFA. For 1.0 M TFA, we calculate TOF_{max} = 9.0 x 103 s^{-1}. Plotting logTOF (from E5.8) vs. overpotential (η) leads to the catalytic Tafel plot shown in Figure 5.3. Comparison between the Tafel plots of catalyst **1**, Co(dmgH)$_2$(py), $[\text{Ni(II)}(P^{Ph}_2N^{Ph})_2]^{2+}$, and Fe(TPP) was made in Figure 5.3. Tafel plots for Co(dmgH)$_2$(py), $[\text{Ni(II)}(P^{Ph}_2N^{Ph})_2]^{2+}$, and Fe(TPP) were constructed using TOF_{max}, E^0_{cat}, and E_{H+} values from Ref. 38.

5.5   References

(1) Berardi, S.; Drouet, S.; Francas, L.; Gimbert-Surinach, C.; Guttentag, M.; Richmond, C.; Stoll, T.; Llobet, A. *Chem. Soc. Rev.* **2014**, 43, 7501-7519.

(2) Lewis, N. S.; Nocera, D. G. *Proc. Natl. Acad. Sci. U. S. A.* **2006**, 103, 15729-15735.

(3) Wang, M.; Chen, L.; Sun, L. *Energ. Environ. Sci.* **2012**, 5, 6763-6778.

(4) Du, P.; Eisenberg, R. *Energ. Environ. Sci.* **2012**, 5, 6012-6021.

(5) DuBois, D. L. *Inorg. Chem.* **2014**, 53, 3935-3960.

(6) Sampson, M. D.; Nguyen, A. D.; Grice, K. A.; Moore, C. E.; Rheingold, A. L.; Kubiak, C. P. *J. Am. Chem. Soc.* **2014**, 136, 5460-5471.

(7) Riplinger, C.; Sampson, M. D.; Ritzmann, A. M.; Kubiak, C. P.; Carter, E. A. *J. Am. Chem. Soc.* **2014**, 136, 16285-16298.

(8) Grice, K. A.; Kubiak, C. P. *Adv. Inorg. Chem.* **2014**, 66, 163-188.

(9) Gloaguen, F.; Rauchfuss, T. B. *Chem. Soc. Rev.* **2009**, 38, 100-108.

(10) Hou, K.; Poh, H. T.; Fan, W. Y. *Chem. Commun.* **2014**, 50, 6630-6632.

(11) Hou, K.; Fan, W. Y. *Dalton Trans.* **2014**, 43, 16977-16980.

(12) Valyaev, D. A.; Peterleitner, M. G.; Semeikin, O. V.; Utegenov, K. I.; Ustynyuk, N. A.; Sournia-Saquet, A.; Lugan, N.; Lavigne, G. *J. Organomet. Chem.* **2007**, 692, 3207-3211.

(13) Mukhopadhyay, T. K.; MacLean, N. L.; Gan, L.; Ashley, D. C.; Groy, T. L.; Baik, M.-H.; Jones, A. K.; Trovitch, R. J. *Inorg. Chem.* **2015**, 54, 4475-4482.

(14) Eckert, F.; Leito, I.; Kaljurand, I.; Kütt, A.; Klamt, A.; Diedenhofen, M. *J. Comput. Chem.* **2009**, 30, 799-810.

(15) Appel, A. M.; Helm, M. L. *ACS Catal.* **2013**, 4, 630-633.

(16) Izutsu, K. *Acid-Base Dissocation Constants in Dipolar Aprotic Solvents*; Blackwell Scientific Publications: Oxford, Boston, **1990**.

(17) Fourmond, V.; Jacques, P.-A.; Fontecave, M.; Artero, V. *Inorg. Chem.* **2010**, 49, 10338-10347.

(18) Laga, S. M.; Blakemore, J. D.; Henling, L. M.; Brunschwig, B. S.; Gray, H. B. *Inorg. Chem.* **2014**.

(19) McKone, J. R.; Marinescu, S. C.; Brunschwig, B. S.; Winkler, J. R.; Gray, H. B. *Chem. Sci.* **2014**, 5, 865-878.

(20) Fourmond, V.; Canaguier, S.; Golly, B.; Field, M. J.; Fontecave, M.; Artero, V. *Energ. Environ. Sci.* **2011**, 4, 2417-2427.

(21) Bhugun, I.; Lexa, D.; Savéant, J.-M. *J. Am. Chem. Soc.* **1996**, 118, 3982-3983.

(22) Helm, M. L.; Stewart, M. P.; Bullock, R. M.; DuBois, M. R.; DuBois, D. L. *Science* **2011**, 333, 863-866.

(23) Wiese, S.; Kilgore, U. J.; Ho, M.-H.; Raugei, S.; DuBois, D. L.; Bullock, R. M.; Helm, M. L. *ACS Catal.* **2013**, 3, 2527-2535.

(24) Costentin, C.; Robert, M.; Saveant, J.-M. *Chem. Soc. Rev.* **2013**, 42, 2423-2436.

(25) Costentin, C.; Dridi, H.; Savéant, J.-M. *J. Am. Chem. Soc.* **2014**, 136, 13727-13734.

(26) McNamara, W. R.; Han, Z.; Alperin, P. J.; Brennessel, W. W.; Holland, P. L.; Eisenberg, R. *J. Am. Chem. Soc.* **2011**, 133, 15368-15371.

(27) McNamara, W. R.; Han, Z.; Yin, C.-J.; Brennessel, W. W.; Holland, P. L.; Eisenberg, R. *Proc. Natl. Acad. Sci. U. S. A.* **2012**, 109, 15594-15599.

(28) Kilgore, U. J.; Roberts, J. A. S.; Pool, D. H.; Appel, A. M.; Stewart, M. P.; DuBois, M. R.; Dougherty, W. G.; Kassel, W. S.; Bullock, R. M.; DuBois, D. L. *J. Am. Chem. Soc.* **2011**, 133, 5861-5872.

(29) Kilgore, U. J.; Stewart, M. P.; Helm, M. L.; Dougherty, W. G.; Kassel, W. S.; DuBois, M. R.; DuBois, D. L.; Bullock, R. M. *Inorg. Chem.* **2011**, 50, 10908-10918.

(30) Artero, V.; Saveant, J.-M. *Energ. Environ. Sci.* **2014**, 7, 3808-3814.

(31) Schmittel, M.; Ganz, A.; Schenk, W. A.; Hagel, M. *Z. Naturforsch.* **1999**, 54b, 559–564.

(32) McCarthy, B. D.; Martin, D. J.; Rountree, E. S.; Ullman, A. C.; Dempsey, J. L. *Inorg. Chem.* **2014**, 53, 8350-8361.

(33) Bard, A. J.; Faulkner, L. R. *Electrochemical Methods: Fundamentals and Applications*; 2nd ed.; Wiley Global Education: New York, **2001**.

(34) Savéant, J. M.; Vianello, E. *Electrochim. Acta* **1962**, 8, 905-923.

(35) Espension, J. H. *Chemical Kinetics and Reaction Mechanisms*; McGraw–Hill: New York, **1981**.

(36) Bard, A. J.; Faulkner, L. R. *Electrochemical Methods*; Wiley: New York, **1980**.

(37) Wiedner, E. S.; Helm, M. L. *Organometallics* **2014**, 33, 4617-4620.

(38) Wiese, S.; Kilgore, U. J.; DuBois, D. L.; Bullock, R. M. *ACS Catal.* **2012**, 2, 720-727.

(39) Dutta, A.; Lense, S.; Hou, J.; Engelhard, M. H.; Roberts, J. A. S.; Shaw, W. J. *J. Am. Chem. Soc.* **2013**, 135, 18490-18496.

(40) Stewart, M. P.; Ho, M.-H.; Wiese, S.; Lindstrom, M. L.; Thogerson, C. E.; Raugei, S.; Bullock, R. M.; Helm, M. L. *J. Am. Chem. Soc.* **2013**, 135, 6033-6046.

(41) Lam, Y. C.; Nielsen, R. J.; Gray, H. B.; Goddard, W. A. *ACS Catal.* **2015**, 5, 2521-2528.

(42) Costentin, C.; Savéant, J.-M. *ChemElectroChem* **2014**, 1, 1226-1236.

5.6   Appendix
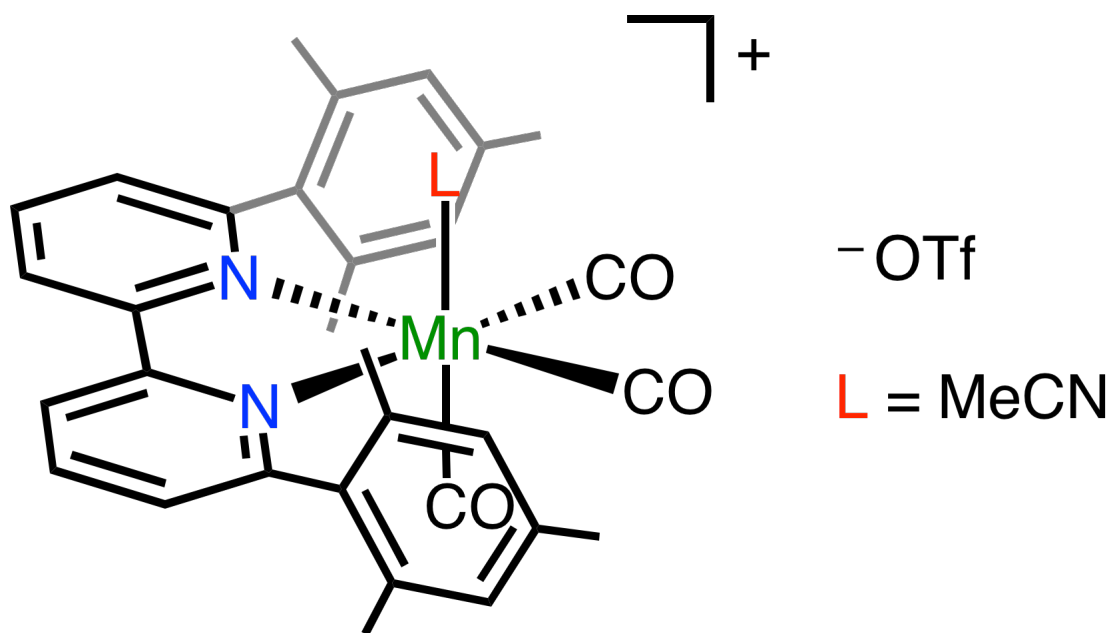
Figure 5.4 Schematic of the molecular structure of complex **1**.
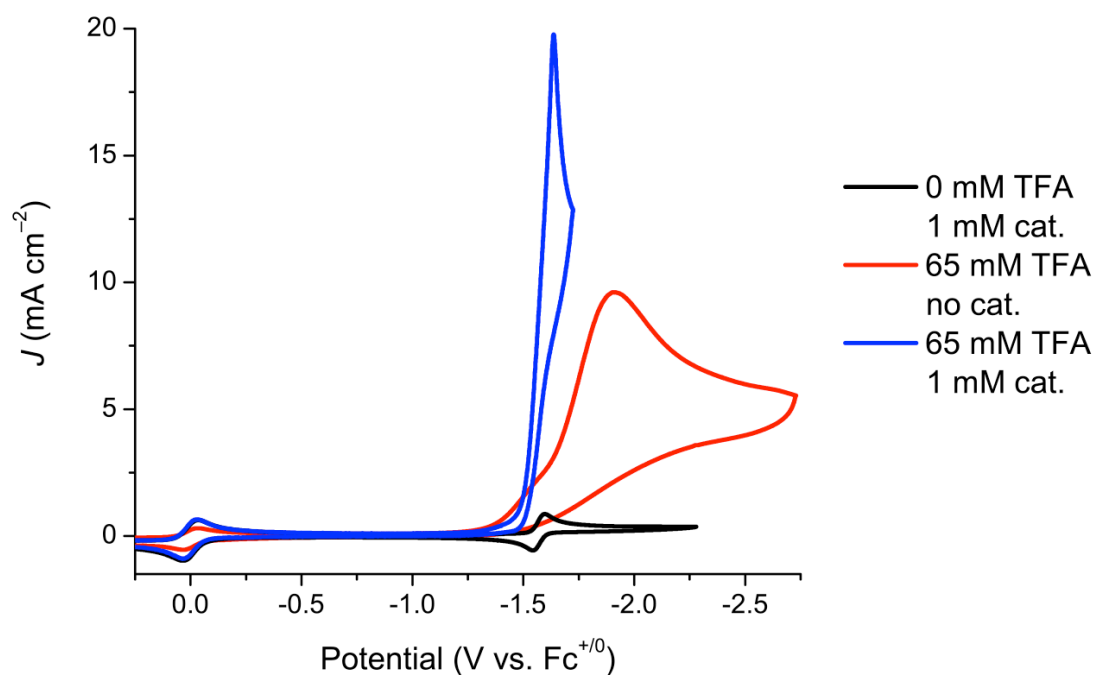
Figure 5.5 Cyclic voltammograms of 1 mM [Mn(mesbpy)(CO)$_3$(MeCN)](OTf) (**1**) in the absence of TFA (black) and in the presence of 65 mM TFA (blue). Cyclic voltammogram of 65 mM TFA without complex **1** is shown in red. Conditions: 0.1 M TBAPF$_6$ in MeCN, inert atmosphere (N$_2$), scan rate = 0.1 V s^{-1}.
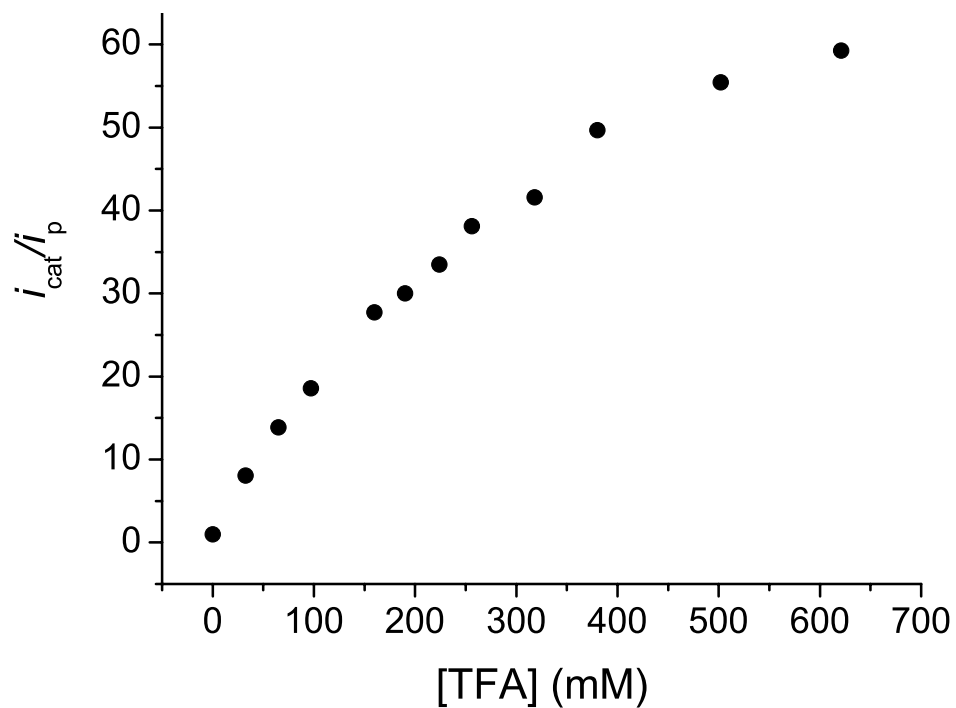
Figure 5.6 Plot of i_{cat}/i_p versus concentration of TFA. Data is taken from cyclic voltammograms shown in Figure 5.2.
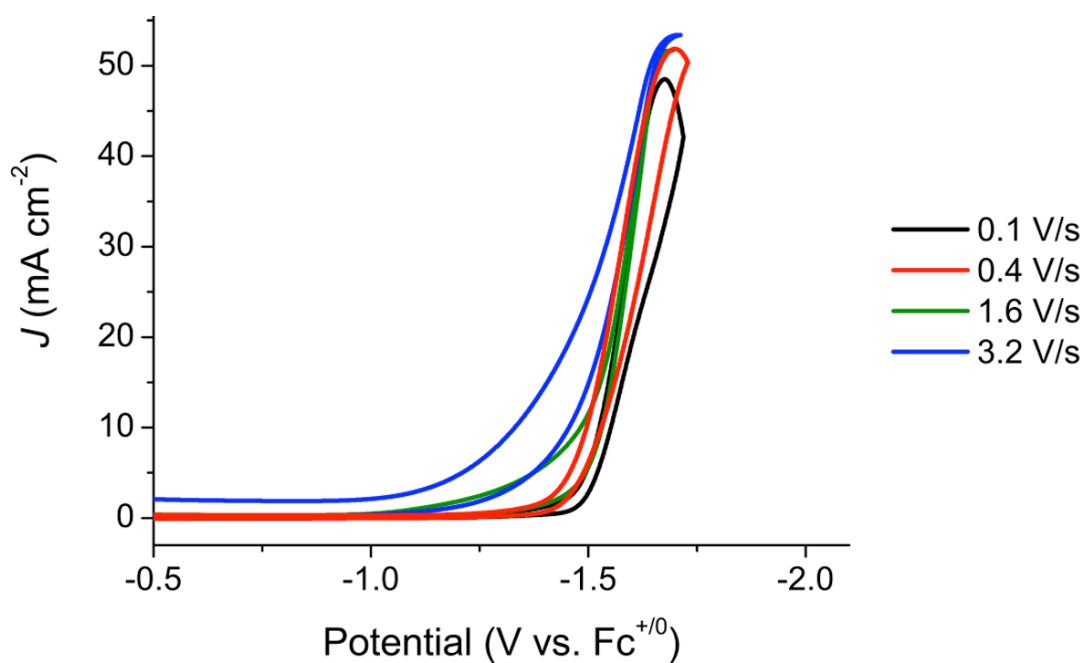
Figure 5.7 Cyclic voltammograms of 1 mM [Mn(mesbpy)(CO)$_3$(MeCN)](OTf) (**1**) in the presence of 200 mM TFA at varying scan rates. Conditions: 0.1 M TBAPF$_6$ in MeCN, inert atmosphere (N$_2$).
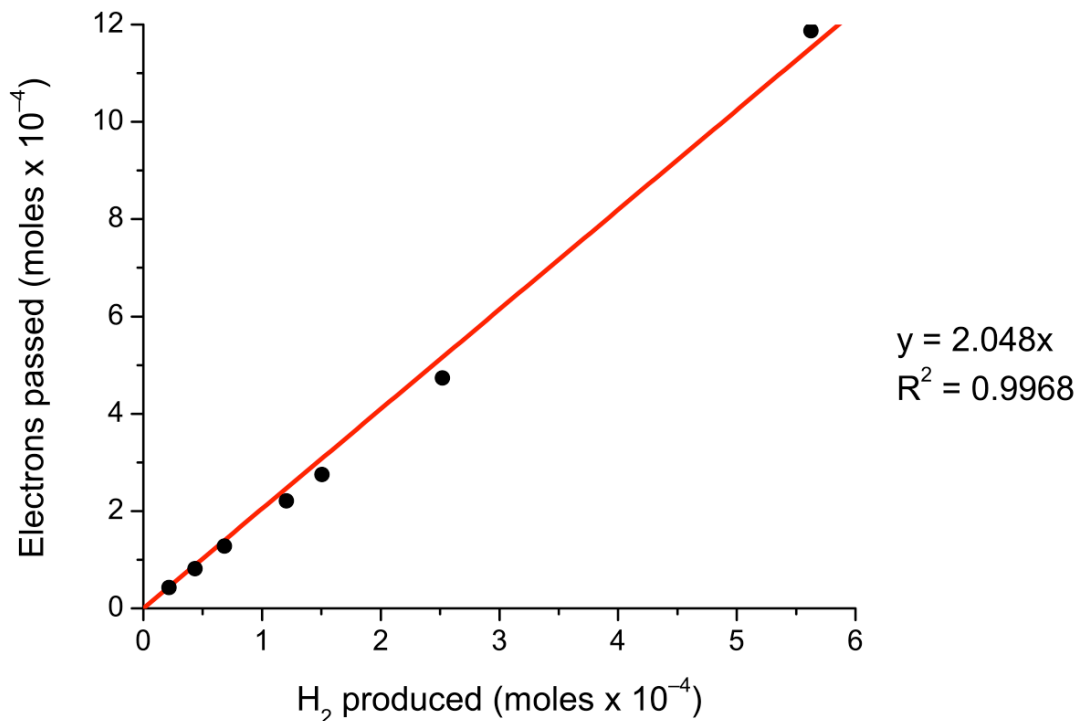
Figure 5.8 Plot of electrons passed versus H_2 produced during controlled potential electrolysis. The slope of ~2 represents a Faradaic efficiency of 105 ± 5 %.
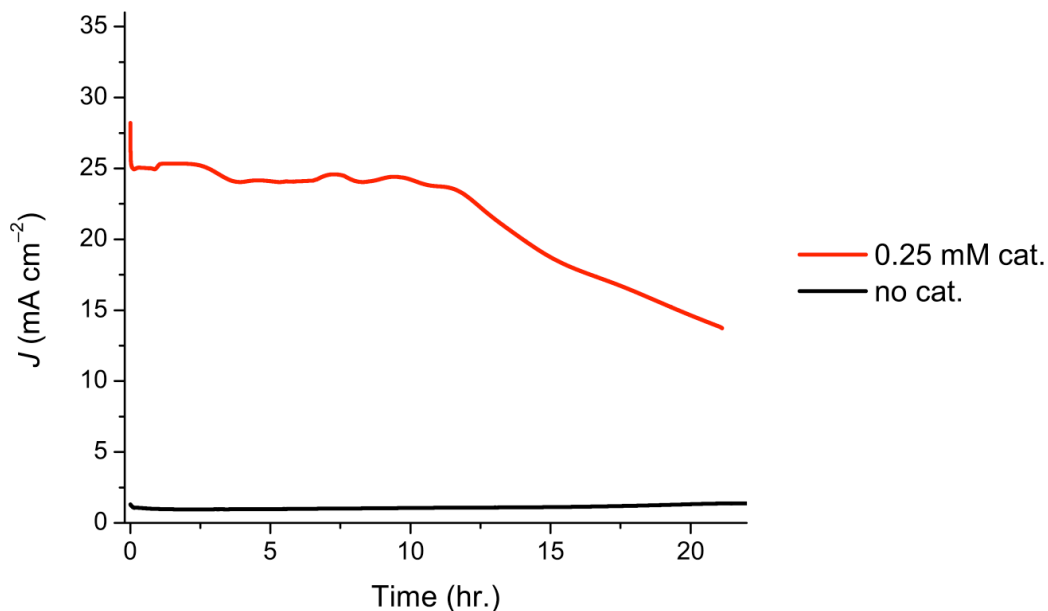
Figure 5.9 Controlled potential electrolysis (CPE) current versus time traces for 0.25 mM catalyst **1** (red) and no added catalyst (black), both with added 0.2 M TFA. Conditions: 0.1 M TBAPF$_6$ in MeCN, inert atmosphere (N$_2$), potential $= -1.5$ V vs. Fc$^{+/0}$.
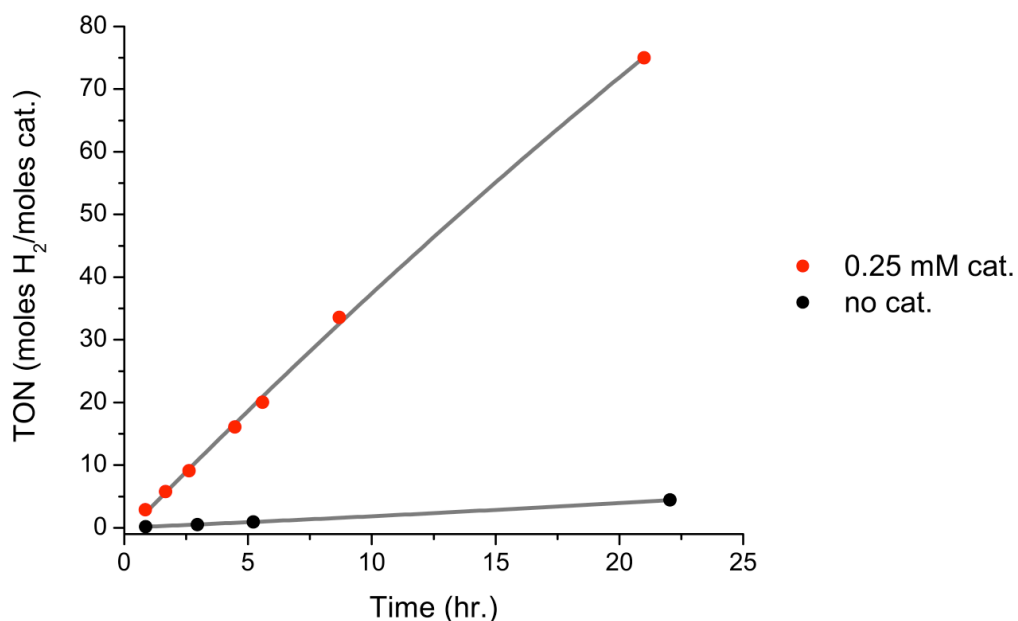
Figure 5.10 Plot of turnover number (TON, moles H$_2$/moles catalyst) versus time during CPE. Conditions: 0.25 mM complex **1**, 0.2 M TFA, 0.1 M TBAPF$_6$ in MeCN, N$_2$ atmosphere, glassy carbon working electrode (surface area = ~7 mm^2, potential = –1.5 V vs. Fc$^{+/0}$.
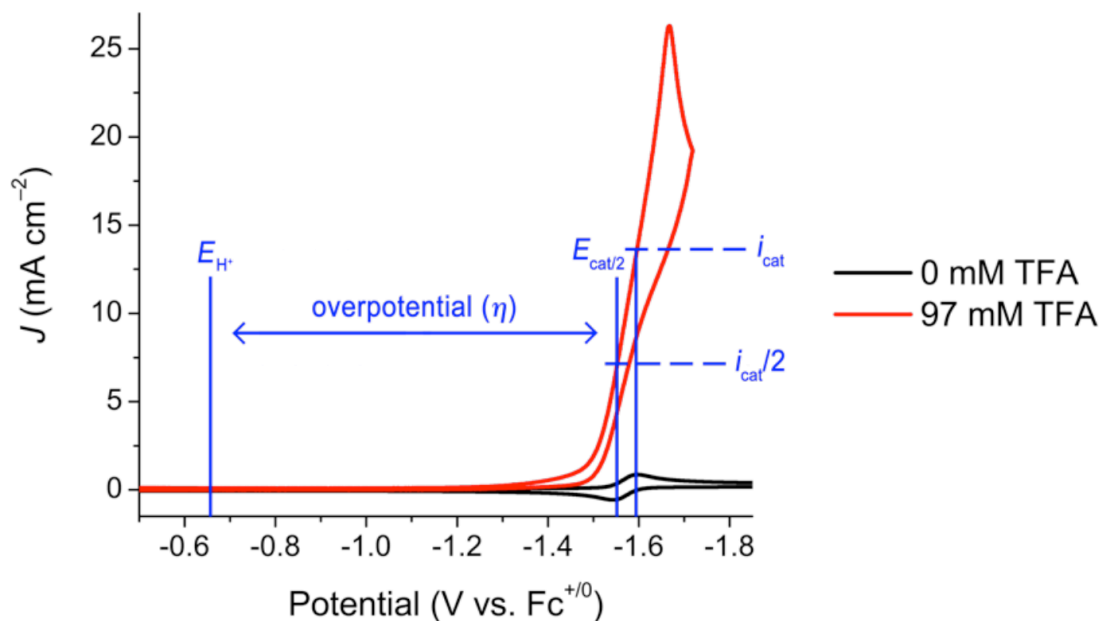
Figure 5.11 Determination of overpotential, following method from Appel and Helm.[15] Conditions: 1 mM complex 1, 0.1 M TBAPF$_6$ in MeCN, inert atmosphere (N$_2$), glassy carbon working electrode (3 mm diameter), scan rate = 100 mV s^{-1}.
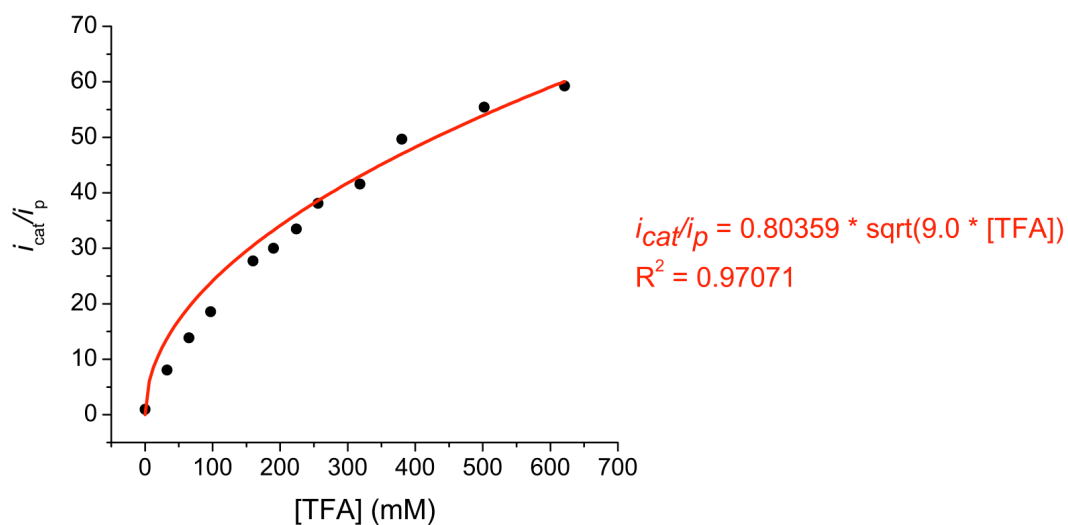
Figure 5.12 Fit of i_{cat}/i_p vs. [TFA] plot with E5.5: i_{cat}/i_p = 0.80359 * sqrt(9.0 * [TFA]). A k_1 value of 9.0 x 10^3 M^{-1} s^{-1} was determined through this analysis.
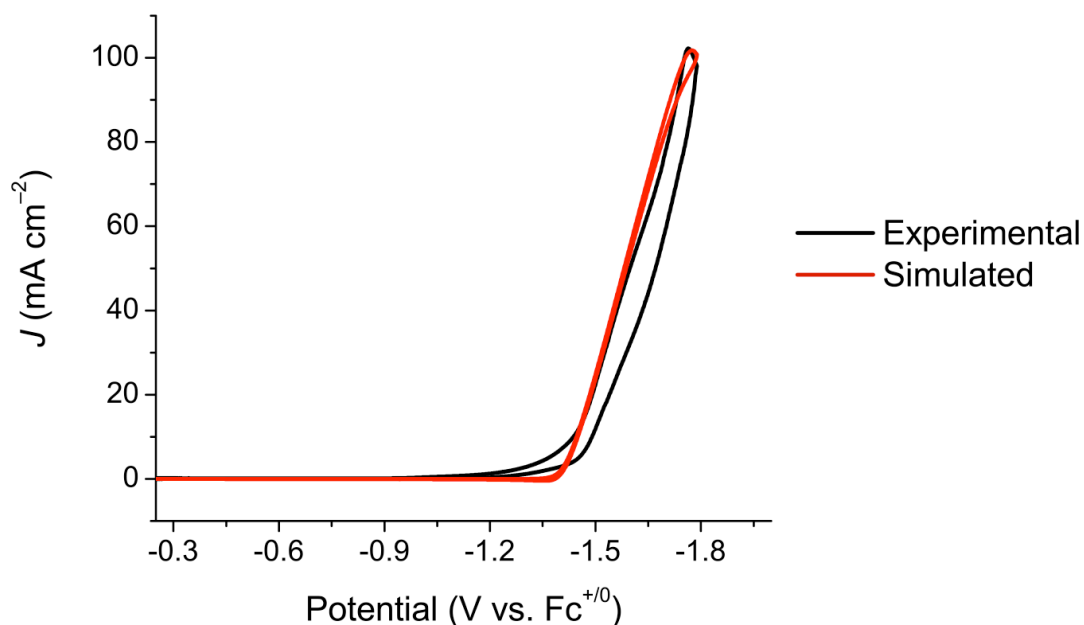
Figure 5.13 Simulated (red) and experimental (black) cyclic voltammograms of 1 mM [Mn(mesbpy)(CO)$_3$(MeCN)](OTf) (**1**) with 620 mM TFA. Experimental conditions are the same as described in Figure 2 of the manuscript. Simulated CV is obtained with BASi DigiSim Simulation Software using an EECC mechanism (described in the SI) and rate constants of k_1 = ~ –9.0 x 10^{-3} M^{-1} s^{-1} and $k_2 \gg k_1$.

Chapter 6

Manganese catalysts with bulky bipyridine ligands: Utilizing Lewis acids to promote electrochemical carbon dioxide reduction at low overpotentials.

6.1 Introduction

Re and Mn bpy (bpy = 2,2′-bipyridine) complexes have garnered significant interest in recent years as CO_2 reduction catalysts.[1-6] These catalysts are among the most active and selective molecular electrocatalysts for proton-coupled CO_2 reduction to carbon monoxide (CO). However, these catalysts suffer from high overpotentials, which originate from the potentials required to access their active, doubly reduced states.[3,6-7] Mn bpy catalysts are desirable, in comparison with their Re analogs, due to the earth-abundance (and thus low cost) of Mn and the ability for these catalysts to

operate at lower overpotentials (i.e. less energy is needed to drive their catalytic reactions).

Previously, our group reported electrocatalytic CO_2 reduction by a pair of Mn complexes with bulky bpy ligands, Mn(mesbpy)(CO)$_3$Br (**1**; mesbpy = 6,6′-dimesityl-2,2′-bipyridine) and [Mn(mesbpy)(CO)$_3$(MeCN)](OTf) (**2**, MeCN = acetonitrile; OTf = trifluoromethanesulfonate).[8] The structures of complexes **1** and **2** are shown in Figure 6.1. In contrast to typical Mn(bpy-R)(CO)$_3$X (X = Br or MeCN) complexes, **1** and **2** do not dimerize after one-electron reduction (E5.1), which significantly lowers the potential necessary to access their doubly-reduced, anionic states (by ~300 mV).[9] Moreover, **1** and **2** undergo a single, two-electron reduction (E5.3) rather than two separate one-electron reductions (E5.1 and E5.2) to access their doubly-reduced states. The doubly-reduced state for complexes **1** and **2** bind CO_2 in the presence of weak Brønsted acids (Figure 6.2) to form a Mn(I)–COOH complex.[8] Upon forming this Mn(I)–COOH complex, catalysis does not proceed with significant rates until a ~400 mV more negative potential (Figure 6.2). Infrared spectroelectrochemistry (IR-SEC) experiments suggest that this unusual "over reduction" is necessary to reduce the Mn(I)–COOH complex, which is needed to drive catalysis. At these more negative potentials, **1** and **2** are highly active for CO_2 reduction, reaching rates of ~5,000 s^{-1} with trifluoroethanol (TFE) as a proton source.[8]

$$Mn^I(bpy)(CO)_3Br + e^- \rightarrow {}^1/_2\,[Mn^0(bpy)(CO)_3]_2 + Br^- \qquad \textbf{(E5.1)}$$

$$^1/_2\,[Mn^0(bpy)(CO)_3]_2 + e^- \rightarrow [Mn(bpy)(CO)_3]^- \qquad \textbf{(E5.2)}$$

$$Mn^I(mesbpy)(CO)_3Br + 2e^- \rightarrow [Mn(mesbpy)(CO)_3]^- + Br^- \qquad \textbf{(E5.3)}$$
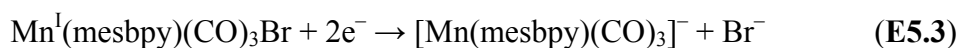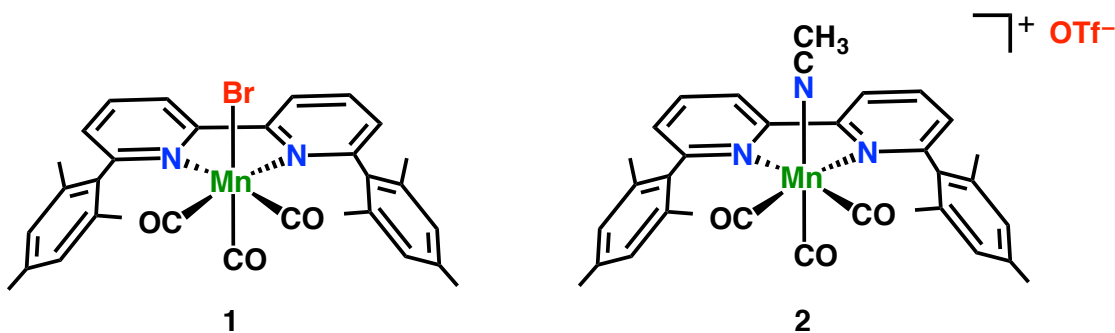
Figure 6.1 Schematic of the molecular structures of **1** and **2**.
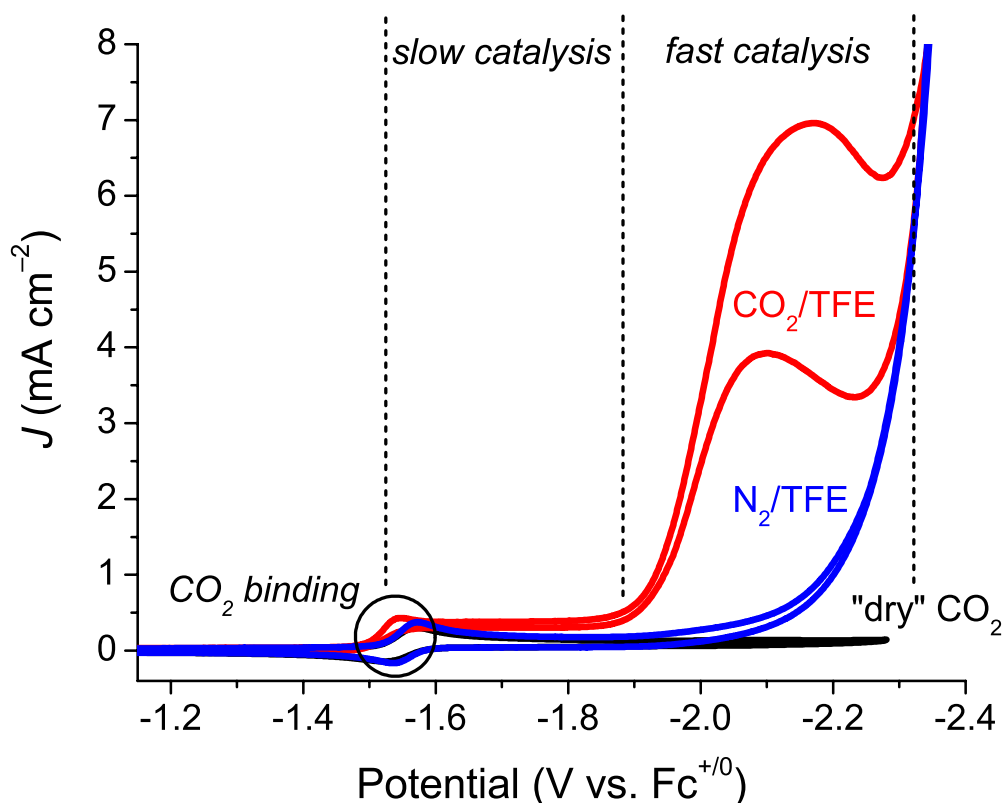
Figure 6.2 CVs of [Mn(mesbpy)(CO)$_3$(MeCN)](OTf) (**2**) under CO_2 without added weak acid (black) and under CO_2 with added 1.3 M TFE (red). Two regions are depicted in the figure. Under N_2 with added TFE, no current increase is observed until much more negative potential (blue). Conditions: 0.1 M TBAPF$_6$/MeCN; ν = 0.1 V/s.

At potentials between CO_2 binding and "fast catalysis" (see the large catalytic wave in Figure 6.2), it is likely that "slow catalysis" occurs via an alternate mechanism. After forming a Mn(I)–COOH complex from CO_2 binding by

$[Mn(mesbpy)(CO)_3]^-$ followed by protonation, this species can be further protonated to cleave one C–O bond and form a cationic $[Mn^I(mesbpy)(CO)_4]^-$ complex. This tetracarbonyl complex can be easily reduced at these potentials to release CO and regenerate $[Mn(mesbpy)(CO)_3]^-$. Previous computational studies have shown that Mn bpy complexes can operate via these two pathways.[7]

Since reporting the electrocatalytic CO_2 reduction activity of **1** and **2**, we have explored a few strategies to increase the rate of catalysis in this "slow catalysis" regime (near –1.6 V vs. $Fc^{+/0}$, see Figure 6.2). One strategy was to utilize stronger Brønsted acids than H_2O, methanol, TFE, or phenol to promote faster C–O bond cleavage in the Mn(I)–COOH complex. All acids that we surveyed (stronger than phenol) resulted in H^+ reduction catalysis rather than CO_2 reduction catalysis. Specifically, with a strong acid, such as trifluoroacetic acid (TFA), complex **2** is highly active for H^+ reduction at –1.6 V vs. $Fc^{+/0}$, reaching rates of 5,500 s^{-1} (see Chapter 5 for details on this study).[10]

In the early 1990s, Savéant and coworkers utilized Mg^{2+} cations as well as other Lewis acids to increase the rate of CO_2 reduction and greatly improve the stability of catalysis for Fe tetraphenylporphyrins (FeTPP).[11] These Lewis acids facilitate the breaking of one C–O bond of a bound CO_2 ligand to produce CO and both increase the stability and activity of catalysis. Herein, we report a similar technique – the use of Lewis acids in place of Brønsted acids – to increase the rate of catalysis in the "slow catalysis" regime for catalysts **1** and **2**. First, we demonstrate that slow catalysis occurs at –1.6 V vs. $Fc^{+/0}$ with added TFE has a H^+ source. We

further employ Mg^{2+} to alter the mechanism for CO_2 reduction by **1** and **2** and increase the rate of catalysis at these low overpotentials. Specifically, use of Mg^{2+} increases the maximum catalytic turnover frequency (TOF) by greater than 10-fold. We utilize IR-SEC under CO_2 to gain insight into the mechanism for catalysis with Mg^{2+}. Since this catalysis generates insoluble $MgCO_3$ during the reaction course, we employed a sacrificial Mg anode during bulk electrolysis experiments to stabilize catalysis over several hours. Finally, foot-of-the-wave (FOTW) analysis is used to compare the Tafel behavior (logTOF vs. overpotential relationship) of catalyst **2** with those of other commonly studied CO_2 reduction catalysts.

6.2 Results and Discussion

Synthesis and Characterization. Synthesis of mesbpy and complexes **1** and **2** were performed as previously reported.[8,12] Spectroscopic characterization by NMR and FTIR were consistent with previous reports of complexes **1** and **2**.[8] The electrochemical behaviors of complexes **1** and **2** have been described previously.[8] Notably, under inert atmosphere, complexes **1** and **2** undergo a single, two-electron reduction near -1.6 V vs. $Fc^{+/0}$. This overall two-electron reduction generates the anionic complex $[Mn(mesbpy)(CO)_3]^-$. This doubly-reduced, anionic complex binds CO_2 in the presence of H^+ to form a Mn(I)–COOH complex; however, further reduction of this hydroxycarbonyl complex (at approximately -2.0 V vs. $Fc^{+/0}$) is required to achieve fast catalytic rates to produce CO.

Controlled Potential Electrolysis at Low Overpotential. To confirm that "slow catalysis" occurs at the potential of CO_2 binding (i.e. -1.6 V vs. $Fc^{+/0}$), controlled potential electrolysis (CPE) was performed on complex **2** with 1.3 M TFE using a glassy carbon working electrode with large surface area ($\sim$80 cm^2). Indeed, under CO_2, slightly higher current densities were achieved with TFE than with "dry" CO_2 (Figure 6.3). Additionally, formation of CO in the headspace of the CPE cell was confirmed by gas chromatography (GC). Complex **2** operated with $96 \pm 3\%$ Faradaic efficiency for CO production from CO_2 (Figure 6.11). The turnover number (TON) of CO reached $\sim$30 after 24 h of electrolysis (Figure 6.12), further confirming the slow rate of catalysis. In previous CPE experiments, **2** sustained over 10-fold higher current densities at -2.2 V vs. $Fc^{+/0}$ over a similar time range with only 0.3 M TFE.[8] Minimal H_2 formation was observed over 24 h of electrolysis (TON of $H_2 = \sim0.06$). CPE experiments at -1.6 V vs. $Fc^{+/0}$ with "dry" CO_2 resulted in little CO formation.
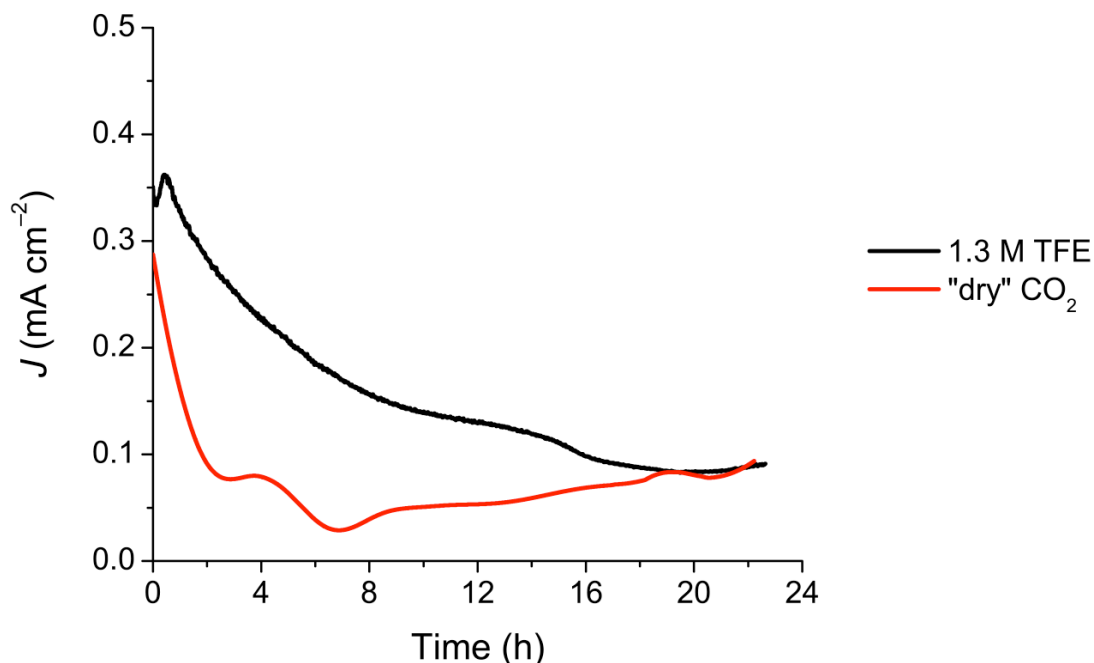
Figure 6.3 CPE current density over time for 0.5 mM [Mn(mesbpy)(CO)$_3$(MeCN)](OTf) (**2**) under CO$_2$ with added 1.3 M TFE (black) and without added TFE (red). CPE is run at -1.6 V vs. Fc$^{+/0}$, showing that slow catalysis does occur at this potential. Conditions: 0.1 M TBAPF$_6$/MeCN.

Cyclic Voltammograms with Added Mg^{2+}. In order to investigate the ability

of Lewis acids to increase rates of catalysis at the potential of CO$_2$ binding (i.e. -1.6 V

vs. Fc$^{+/0}$), CVs were recorded in the presence of Mg(OTf)$_2$. Electrocatalytic properties

were studied in a custom-made, single-compartment, airtight cell with a glassy carbon

working electrode, Pt wire counter electrode, and a Ag/AgCl leakless reference

electrode (see Experimental section for more details). As previously described, CVs of

complex **2** do not change under CO$_2$ atmosphere in dry MeCN. Upon addition of

Mg^{2+}, a current increase is observed near -1.6 V vs. Fc$^{+/0}$ in CVs of **2** under CO$_2$

(Figure 6.4). This current increase corresponds to the electrocatalytic reduction of

CO$_2$, as verified by CPE (*vide infra*). Under either inert atmosphere or CO$_2$, CVs of

Mg^{2+} without added Mn catalyst show no reductive reactivity in the window we are

probing. Additionally, under N_2 atmosphere, no current increase is observed in CVs of **2** with added Mg^{2+} (Figure 6.4). Higher concentrations of Mg^{2+} in CVs resulted in increased current densities, up to a peak current density of approximately 2.7 mA cm^{-2} (Figure 6.5). Under N_2 atmosphere, two interesting features are apparent in CVs of **2** with added Mg^{2+}: (1) a pre-wave exists prior to the two-electron reduction of **2**, which increases as $[Mg^{2+}]$ increases; (2) loss of reversibility of the two-electron reduction is observed (Figure 6.4–6.5, 6.13). These features are consistent with interaction between the singly- or doubly-reduced Mn complex and Mg^{2+} (*vide infra*).
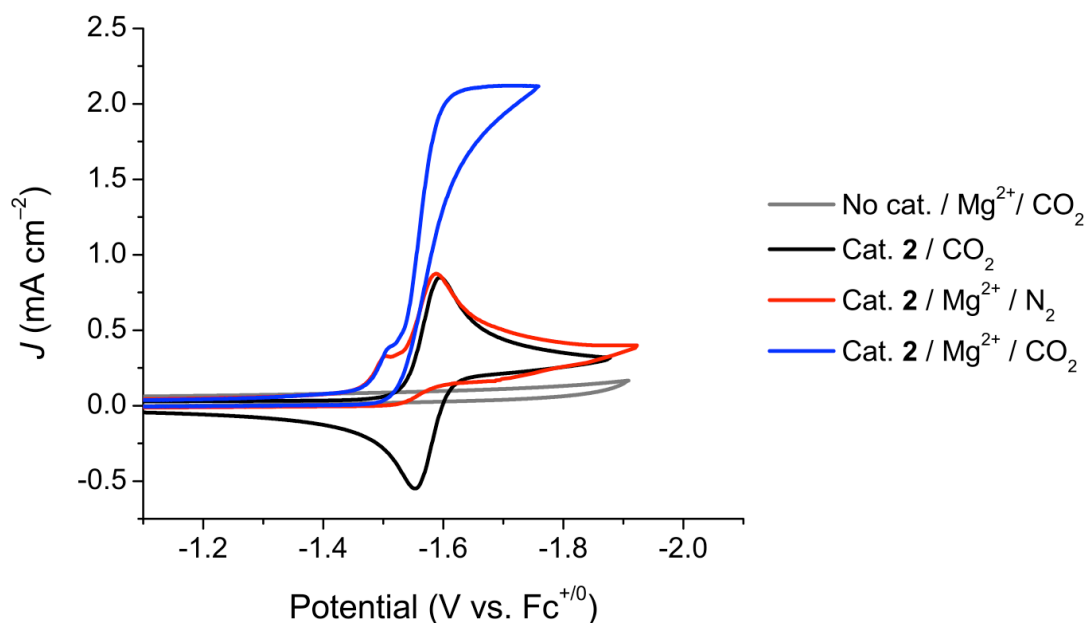
Figure 6.4 CVs of 1 mM [Mn(mesbpy)(CO)$_3$(MeCN)](OTf) (**2**) under CO_2 without Mg^{2+} (black), under N_2 with 20 mM Mg^{2+} (red), and under CO_2 with 20 mM Mg^{2+} (blue). For reference, a CV without complex **2**, only with 20 mM Mg^{2+} under CO_2 is shown in grey. Catalytic current is only observed with all of the following: complex **2**, Mg^{2+}, and CO_2. Conditions: 0.1 M TBAPF$_6$/MeCN; $v = 0.1$ V/s.
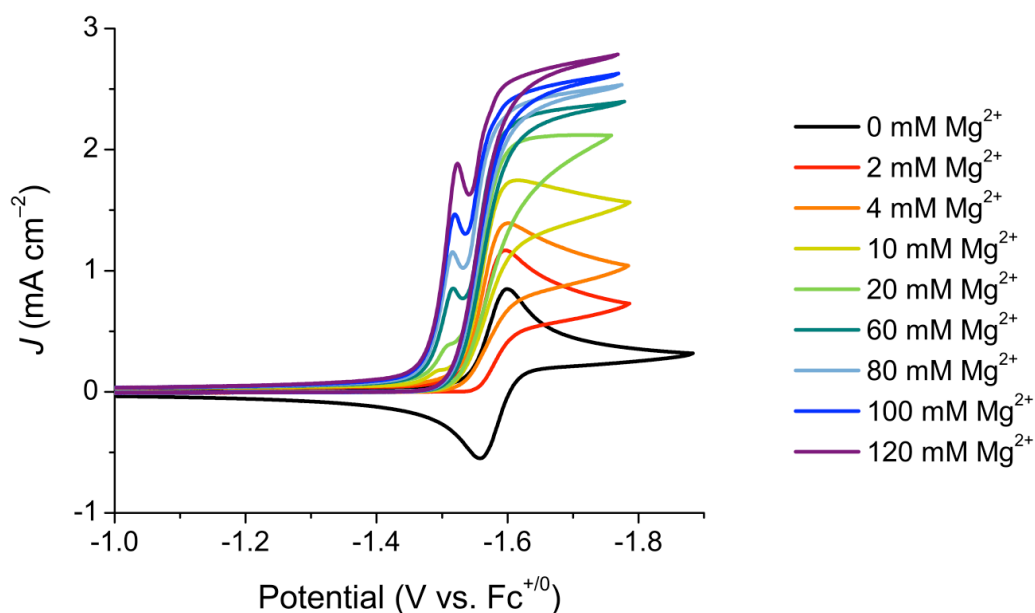
Figure 6.5 CVs of 1 mM [Mn(mesbpy)(CO)$_3$(MeCN)](OTf) (**2**) under CO$_2$ with varying concentrations of Mg^{2+}, showing electrocatalytic reduction of CO$_2$. Conditions: 0.1 M TBAPF$_6$/MeCN; v = 0.1 V/s.

The normalized peak catalytic current (i_{cat}/i_p) is related to the turnover frequency (TOF) of the catalytic reaction, as described in more detail in the Supporting Information. Using this relationship, we can estimate TOF values for catalyst **2** with added Mg^{2+}. Addition of 120 mM Mg^{2+} to a 1 mM solution of **2** under CO$_2$ resulted in a peak i_{cat}/i_p = 3.5 and TOF = 20 s^{-1}. Using peak i_{cat}/i_p values as a metric for TOF, at peak activity, catalyst **2** operates with greater than 200-fold less activity at approximately −1.6 V vs. Fc$^{+/0}$ with added Mg^{2+} than in the "fast catalysis" regime with added TFE (−2.1 V vs. Fc$^{+/0}$, see Figure 6.2). However, catalyst **2** does operate with approximately 10-fold greater activity in the "slow catalysis" regime with added Mg^{2+} than with added TFE (with TFE at −1.6 V vs. Fc$^{+/0}$, $i_{cat}/i_p \approx 1$, TOF ≈ 2). In order to gain further details about the catalytic mechanism, variable concentration

CV studies were performed to obtain the rate of the catalytic reaction in [2], [CO_2], and [Mg^{2+}]. Plotting i_{cat} versus [2] shows a linear relationship, indicating that the catalytic reaction is first order in [2] (Figure 6.14). The electrocatalytic reaction is second order in [CO_2], as evidenced by plotting i_{cat} versus [CO_2] (Figure 6.15, see Supporting Information for relationship between i_{cat} and [substrate]). A plot of i_{cat} versus [Mg^{2+}] shows a first-order dependence on [Mg^{2+}] at low [Mg^{2+}] (Figure 6.16). At higher [Mg^{2+}], i_{cat} reaches a limiting value independent of [Mg^{2+}], which is typical of saturation kinetics expected for catalytic reactions.[13] The catalytic current plateaus in catalytic CVs with added Mg^{2+} are also scan rate independent (Figure 6.17), indicating that the catalytic reaction is at steady state. In summary, at high concentrations of [Mg^{2+}], the catalytic reaction is first order in 2, second order in CO_2, and independent of Mg^{2+}.

Although rates of electrocatalysis with Mg^{2+} are not up to par with rates typically observed for Mn bpy catalysts at further negative potentials, any significant rate for catalysis at −1.6 V vs. $Fc^{+/0}$ is noteworthy. Costentin et al. have calculated the standard reduction potential for the reaction $2CO_2 + 2H_2O + 2e^- \rightarrow CO + H_2O + HCO_3^-$, where one CO_2 molecule serves as the weak acid.[14] The mechanism for CO_2 reduction by 2 with Mg^{2+} is: $2CO_2 + 2e^- \rightarrow CO + CO_3^{2-}$, as evidenced by IR-SEC and CPE experiments (*vide infra*). It is likely that our electrochemical solutions have small amounts of H_2O, and therefore, the thermodynamic reaction described by Costentin et al. is a very good approximation for our catalytic reaction. To the best of our knowledge, the standard reduction potential for $2CO_2 + 2e^- \rightarrow CO + CO_3^{2-}$ has not

been determined in MeCN due to unavailable free energy thermodynamic values for CO_3^{2-} in MeCN. For an estimation of the overpotential for our catalytic reaction, substitution of the CO_3^{2-} product with HCO_3^- using the thermodynamic reaction described by Costentin et al. is adequate. In MeCN, the standard reduction potential for $2CO_2 + 2H_2O + 2e^- \rightarrow CO + H_2O + HCO_3^-$ is $E° = -0.65$ V vs. NHE (or approximately -1.3 vs. $Fc^{+/0}$).[14] Using this estimated standard potential, at -1.6 V vs. $Fc^{+/0}$, **2** operates with an overpotential $\eta = 0.3$ V. At this overpotential, **2** displays one of the lowest overpotentials for CO_2 reduction to CO for a homogeneous electrocatalyst. Other electrocatalysts that exhibit relatively low overpotentials are $[Ni(cyclam)]^{2+}$,[15] $[Co^{III}(N_4H)(Br)_2]^+$,[16] and $Re(bpy)(CO)_3Cl$ operating in neat 1-ethyl-3-methylimidazolium tetracyanoborate ionic liquid (each operating at approximately $\eta = 0.5$ V).[17] Table 6.1 lists the overpotentials of a variety of other commonly studied CO_2 reduction electrocatalysts. Catalyst **2** operates with a 0.2 V lower overpotential than the lowest operating homogeneous CO_2 reduction electrocatalyst previously reported.

Infrared Spectroelectrochemistry with Added Mg^{2+}. IR-SEC of complex **1** under N_2 with added Mg^{2+} was performed to observe how the reductive chemistry of **1** is altered by the presence of Mg^{2+} (Figure 6.6). At its resting state, **1** has three characteristic ν_{CO} bands associated with a facially coordinated tricarbonyl complex at 2023, 1936, and 1913 cm^{-1}. Before reaching the potential of the two-electron reduction seen in CVs, solvolysis of the Mn–Br bond occurs, resulting in the formation of a cationic Mn–MeCN complex ($\nu_{CO} = 2039$, 1949 cm^{-1}). When the

potential of the cell reaches approximately -1.45 V vs. $Fc^{+/0}$, we see growth of ν_{CO} bands at 1984 and 1883 cm^{-1}, along with decay of the ν_{CO} bands associated with the cationic Mn–MeCN complex. These new ν_{CO} bands are consistent with the formation of the singly-reduced Mn(0) complex, $[Mn(mesbpy)(CO)_3]^0$. In previous IR-SEC experiments in the absence of Mg^{2+}, complete formation of this singly-reduced Mn(0) complex was not observed.[8] Instead, only a small amount of singly-reduced complex was observed along with concomitant formation of the doubly-reduced complex, $[Mn(mesbpy)(CO)_3]^-$. In these IR-SEC studies, with added Mg^{2+}, we see complete and stable formation of $[Mn(mesbpy)(CO)_3]^0$ (Figure 6.6). Not until the potential of the cell is shifted slightly further negative (approximately -1.5 V vs. $Fc^{+/0}$) is reduction of $[Mn(mesbpy)(CO)_3]^0$ to $[Mn(mesbpy)(CO)_3]^-$ observed ($\nu_{CO} = 1907, 1805$ cm^{-1}). The fact that complete formation of $[Mn(mesbpy)(CO)_3]^0$ is observed prior to conversion to $[Mn(mesbpy)(CO)_3]^-$ indicates that Mg^{2+} is stabilizing the singly-reduced Mn(0) complex. This helps explain the pre-wave observed in CVs with added Mg^{2+} (Figure 6.4 and 6.5), where Mg^{2+} likely splits the two-electron reduction of **1** and **2** into two closely-spaced one-electron reductions. The specific interaction between the singly-reduced Mn(0) complex and Mg^{2+} is currently under investigation.
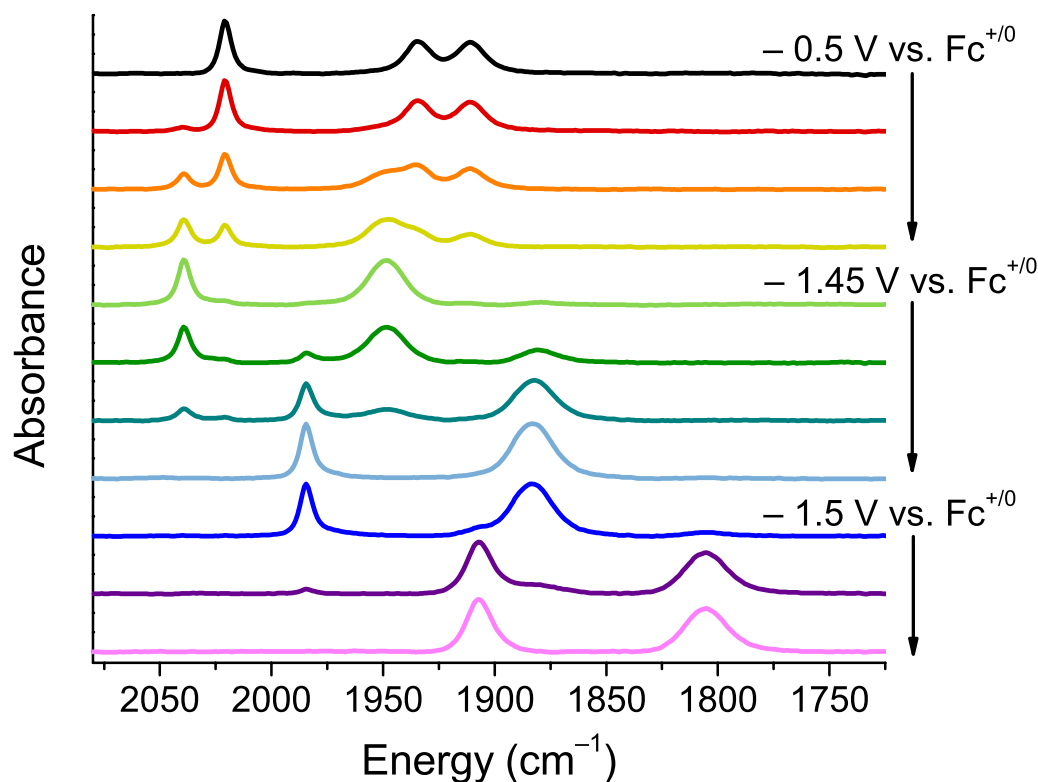
Figure 6.6 IR-SEC of 3 mM complex **1** in MeCN with 0.1 M TBAPF$_6$ electrolyte and 0.1 M Mg(OTf)$_2$ under an atmosphere of N$_2$. Solvolysis of the Mn–Br bond in resting species **1** (pink) occurs over time in solution to form [Mn(mesbpy)(CO)$_3$(MeCN)]$^+$ (teal). At –1.45 V, the Mn(I) complex is reduced to the radical species, [Mn(mesbpy)(CO)$_3$]^0 (yellow). At slightly more negative potentials (–1.5 V), this Mn radical species is reduced to the anionic complex, [Mn(mesbpy)(CO)$_3$]$^-$ (black).

We further utilized IR-SEC under CO$_2$ with added Mg^{2+} in order to gain insight into electrocatalysis in the presence of Mg^{2+}. The results of an IR-SEC experiment on complex **1** with added ~0.14 M CO$_2$ (half-saturated) and 0.1 M Mg^{2+} are shown in Figure 6.7. Initially, prior to reaching the reduction potential of complex **1**, partial solvolysis of the Mn–Br bond is observed to form a cationic Mn–MeCN complex, similarly to what was observed in IR-SEC experiments under N$_2$ (Figure 6.6). Additionally, at these potentials formation of IR bands at 1713 and 1632 cm^{-1} is observed. The IR band at 1632 cm^{-1} is consistent with HCO$_3^-$, formed from the

reaction of Mg^{2+} with CO_2 in the presence of trace H_2O.[18] We tentatively assign the IR band at 1713 cm^{-1} to soluble $MgCO_3$, which reaches a maximum concentration due to poor solubility and remains unchanged during the course of the reaction. The exact identity of this band is still under investigation; however, oxalate and other reduced CO_2 species[19-20] have been ruled out due to comparative IR experiments (Figure 6.20) and quantitative CO production observed in CPE experiments (*vide infra*). The species at 1713 and 1632 cm^{-1} are also observed upon stirring a solution of Mg^{2+} with CO_2 in 0.1 M TBAPF$_6$/MeCN overnight (Figure 6.20). These IR bands remain unchanged upon pulling vacuum on the reaction mixture, indicating that these products are the result of an irreversible reaction with Mg^{2+} and CO_2, which rules out the presence of a type of activated/coordinated CO_2 species.[44-45] The IR band at 1713 cm^{-1} remains unchanged upon addition of H_2O to the reaction mixture (Figure 6.28), consistent with the formation of a soluble $MgCO_3$-type species, which is present at a constant concentration due to an equilibrium with excess Mg^{2+} and CO_2 available in solution. Holding the IR-SEC cell at -0.5 V vs. $Fc^{+/0}$ for over 5 min (and upon moving the potential of the cell to -1.4 V vs. $Fc^{+/0}$) results in these species reaching equilibrium (Figure 6.7b).
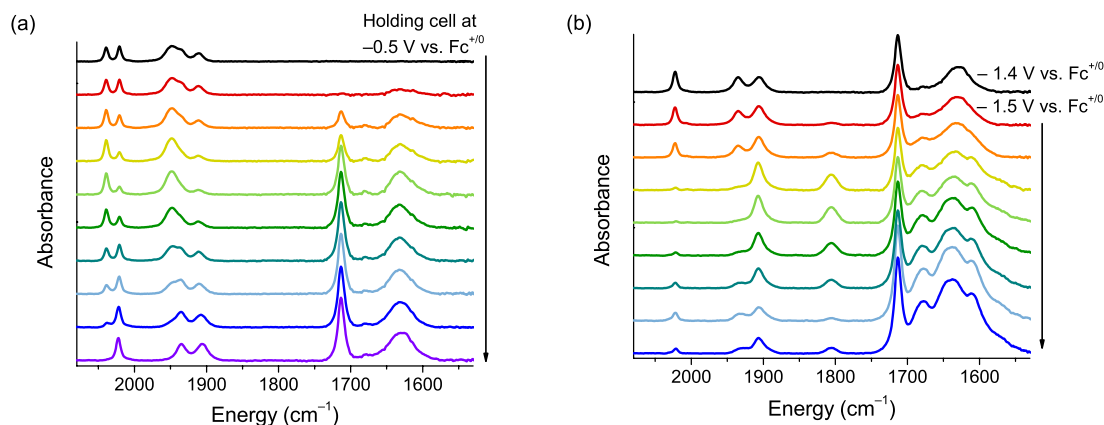
Figure 6.7 IR-SEC of 3 mM complex **1** in MeCN with 0.1 M TBAPF$_6$ electrolyte, 0.1 M Mg(OTf)$_2$, and *ca.* 0.14 M CO$_2$ (half-saturation). (a) At –0.5 V, a mixture of **1** and [Mn(mesbpy)(CO)$_3$(MeCN)]$^+$ exists. Holding the cell at this potential results in the formation of CO$_3^{2-}$/HCO$_3^{2-}$ species. (b) Holding the cell at –1.5 V, catalytic formation of CO$_3^{2-}$/HCO$_3^{2-}$ species are observed consistent with reductive disproportionation of 2CO$_2$ to CO and CO$_3^{2-}$.

Upon reaching the reduction potential of **1** at approximately –1.5 V vs. Fc$^{+/0}$, we see complete conversion of the complex **1** to two new species that, based on the ν_{CO} spectrum, must be a new Mn(I) complex and doubly-reduced [Mn(mesbpy)(CO)$_3$]$^-$ (Figure 6.7b). These two complexes are evidenced by the ν_{CO} bands at 2022, 1933, 1907, and 1805 cm^{-1}. This new Mn(I) complex is very similar to the Mn(I)–COOH complex formed in electrocatalysis with CO$_2$ and weak Brønsted acids (ν_{CO} = 2006, 1907 cm^{-1}). We have tentatively assigned this Mn(I) complex as [Mn(I)–CO$_2$Mg]$^+$, since C–O bond cleavage in the bound CO$_2$ ligand is likely the rate determining step in the catalytic reaction.[7-8] Along with the formation of these two ν_{CO} bands, we see catalytic growth of IR bands at 1679, 1632, and 1611 cm^{-1}, which is consistent with the formation of CO$_3^{2-}$ and HCO$_3^-$ species. Catalytic formation of CO$_3^{2-}$-type species and a catalytic reaction that has a second order dependence on [CO$_2$] are consistent with an overall reductive disproportionation of 2CO$_2$ + 2e$^-$ → CO

+ CO_3^{2-}. Repeating IR-SEC experiments with $^{13}CO_2$ indicates that the CO_3^{2-} and HCO_3^- species originate from the starting $^{13}CO_2$ substrate (Figure 6.18–6.19).

Controlled Potential Electrolysis with Added Mg^{2+}. CPE was performed on **2** at -1.6 V vs. Fc$^{+/0}$ to confirm that the electrocatalytic reaction was indeed producing CO and to measure the efficiency at which CO is produced. First attempts at CPE resulted in very short-lived catalysis due to the formation of insoluble MgCO$_3$. In order to circumvent this issue, a sacrificial Mg rod, in conjunction with added Mg(OTf)$_2$, was used as the counter electrode in place of the Pt wire typically used (schematic in Figure 6.21). CPE experiments with this sacrificial Mg anode showed fairly stable current densities up to six hours of electrolysis (Figure 6.8).
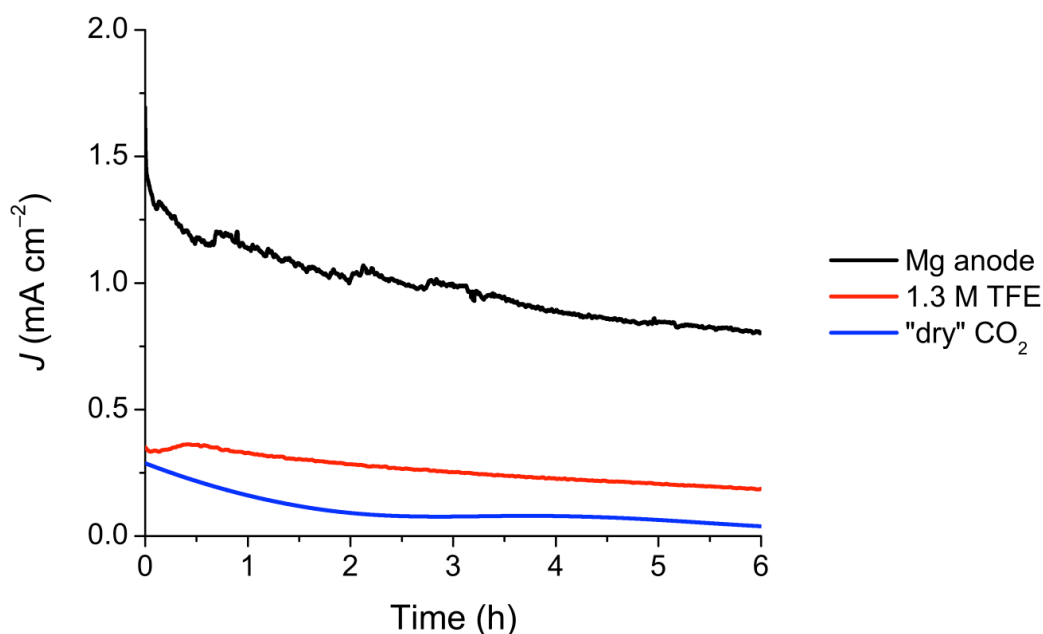
Figure 6.8 CPE current density over time for 0.5 mM [Mn(mesbpy)(CO)$_3$(MeCN)](OTf) (**2**) under CO$_2$ with a sacrificial Mg anode and 0.2 M Mg^{2+} (black), added TFE (red), and without added TFE (blue). Conditions: Potential $= -1.6$ V vs. Fc$^{+/0}$; 0.1 M TBAPF$_6$/MeCN; working electrode = glassy carbon; counter = Mg anode (black) or Pt (red and blue); reference = Ag/AgCl.

Gas chromatography indicates that little hydrogen is formed during these experiments (Faradaic efficiency = 1%, TON for H_2 = 0.35). Catalyst **2** operates with a Faradaic efficiency of 98 ± 3% for the formation of CO from CO_2, measured through approximately 6 h of electrolysis (Figure 6.22). The catalyst sustained current densities greater than 1 mA/cm^2 throughout the first few hours of electrolysis (Figure 6.8). With the sacrificial Mg anode, TON for CO production reached ~36 after 6 h of electrolysis, significantly out-performing CPE experiments at −1.6 V vs. $Fc^{+/0}$ with added TFE (TON = ~14 after 6 h, Figure 6.23). CPE experiments under N_2 with added $Mg(OTf)_2$ and the sacrificial Mg anode showed minimal CO formation over 6 h of electrolysis (Figure 6.23), indicating that degradation of the $Mn(CO)_3$ moiety does not occur in these experiments. FTIR analysis of the post-electrolysis solution and particulates formed during CPE confirms the formation of CO_3^{2-} and HCO_3^- salts (Figure 6.24), displaying similar IR bands as those observed in IR-SEC experiments.

Foot-of-the-Wave Analysis. The low overpotential exhibited by catalyst **2** in the presence of Mg^{2+}, led us to perform Costentin and Savéant's foot-of-the-wave (FOTW) analysis[14,21-23] in order to benchmark this catalyst with other commonly studied catalysts in terms of TOF and η without taking into account side phenomena that interfere with catalysis at high current densities. FOTW analysis allows for determination of the relationship between TOF and η, or the Tafel behavior (logTOF– η relationship), for a catalyst under a given set of conditions. In this manner, catalysts can be benchmarked based on their TOF at zero overpotential (TOF$_0$). FOTW analysis can be performed on the CVs shown in Figure 6.5, as described in more detail in the

Supporting Information (Figures 6.25–6.26), leading to the Tafel plots shown in Figure 6.9 and 6.27. The low overpotential for catalyst **2** with added Mg^{2+} is obvious when comparing its Tafel behavior with other catalysts' Tafel behaviors,[24] as shown in Figure 6.9. Under these conditions, catalyst **2** possesses a $logTOF_0 = -2.3$ and $logTOF_{max} = 2.8$. The $logTOF_0$ and $logTOF_{max}$ values of the other catalysts shown in Figure 6.9 are listed in Table 6.2.
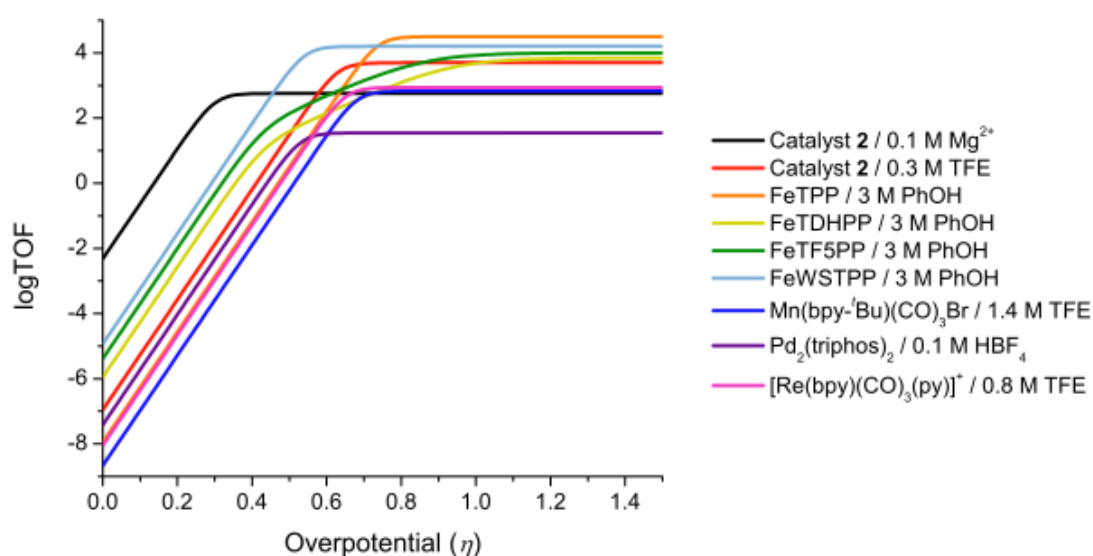
Figure 6.9 Catalytic Tafel plots derived from foot-of-the-wave (FOTW) analysis for **2** with added Mg^{2+} and other commonly studied homogeneous CO_2 reduction electrocatalysts.[24] TPP = tetraphenylporphyrin, TDHPP = 5,10,15,20-tetrakis(2´,6´-dihydroxylphenyl)porphyrin, TF5PP = 5,15-bis(2´,6´-dihydroxyphenyl)-10,20-bis(pentrafluorophenyl)porphyrin, WSTPP = 5,10,15,20-tetra(4´-*N,N,N*-trimethylanilinium)porhyrin, bpy-*t*Bu = 4,4´-*tert*-butyl-2,2´-bipyridine, triphos = $C_6H_4(P[CH_2CH_2P(C_6H_{11})_2])_2$.

6.3   Conclusions

We have described the use of a Lewis acid, $Mg(OTf)_2$, to significantly increase the catalytic rate for CO_2 reduction for $Mn(mesbpy)(CO)_3Br$ (**1**) and $[Mn(mesbpy)(CO)_3(MeCN)](OTf)$ (**2**) at low overpotentials. In previous studies, with

weak Brønsted acids, catalysts **1** and **2** showed little to no reactivity for CO_2 reduction upon CO_2 binding at -1.6 V vs. $Fc^{+/0}$. With the use of a glassy carbon working electrode with high surface area, we demonstrated using CPE that "slow catalysis" occurs upon CO_2 binding with added TFE. The rate of this catalysis is increased by over 10-fold by utilizing Mg^{2+} cations in place of TFE. At an operating potential of -1.6 V vs. $Fc^{+/0}$, these Mn catalysts operate with the lowest overpotential ($\eta = 0.3$ V) for homogeneous electrocatalysts for CO_2 reduction. Variable concentration CV studies, IR-SEC experiments, and CPE have allowed us to conclude that electrocatalysis with added Mg^{2+} proceeds via a reductive disproportionation mechanism of $2CO_2 + 2e^- \rightarrow CO + CO_3^{2-}$, as shown in the mechanism in Figure 6.8. Here, CO_2 binds to the active $[Mn(mesbpy)(CO)_3]^-$ catalyst and is capped by a Mg^{2+} cation. At this point, the Mg^{2+} cation has already aided in weakening a C–O bond of the bound CO_2 molecule. The addition of a second CO_2 molecule completes the breaking of a C–O bond, resulting in CO_3^{2-} formation in the form of $MgCO_3$. The resulting cationic Mn(I) tetracarbonyl complex is easily reduced at the operating potentials, releasing the CO product and regenerating the active catalyst.
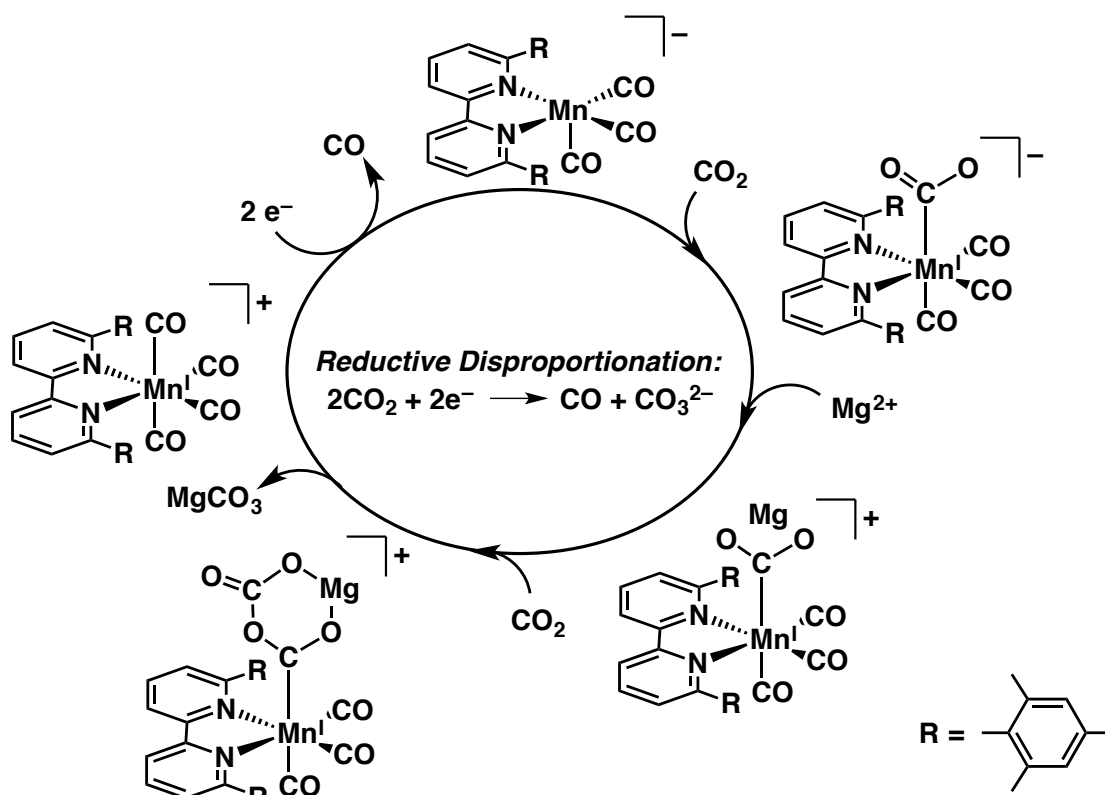
Figure 6.10 Proposed catalytic mechanism of $[Mn(mesbpy)(CO)_3]^-$ with CO_2 and Mg^{2+} at -1.5 V vs. $Fc^{+/0}$, showing an overall reaction of $2CO_2 + 2e^- \rightarrow CO + CO_3^{2-}$.

The role played by Mg^{2+} cations in this catalytic reaction is a rare example of heterobimetallic chemical catalysis of an electrochemical reaction, where in an electron-rich center (Mn bpy framework) initiates the reduction process, and an electron-deficient center (Mg^{2+}) aids in bond transformation (cleavage of a C–O bond). In this reaction, Mg^{2+} plays the role of a cosubstrate rather than that of a cocatalyst. The findings in this work will allow for the exploration of Lewis acids to facilitate and enhance catalysis that requires the assistance of an oxide acceptor (in our case, weak Brønsted acids). We believe this strategy can be applied to a wide variety of catalytic systems, not only for CO_2 reduction. These studies and findings provide strategies and mechanistic insights for improving catalysts for eventual scale-up and

use on an industrial scale. Future work will focus on investigating softer Lewis acids, which will not bind carbonate salts as strongly as Mg^{2+} as well as applying this cosubtrate strategy to other CO_2 reduction systems.

6.4 Experimental

General Considerations. Solvents were sparged with argon, dried on a custom dry solvent system over alumina columns, and stored over molecular sieves before use. Synthesis of 6,6'-dimesityl-2,2'-bipyridine (mesbpy) was performed by the Suzuki coupling of 6,6′-dibromo-2,2′-bipyridine with trimethylphenylboronic acid, as previously reported.[12] Syntheses of Mn(mesbpy)(CO)$_3$Br (**1**) and [Mn(mesbpy)(CO)$_3$(MeCN)](OTf) (**2**) were performed as previously reported.[8,12] Manipulations of Mn complexes were covered from light. Tetrabutylammonium hexafluorophosphate (TBAPF$_6$, Aldrich, 98%) was twice recrystallized from methanol (MeOH) and dried under a vacuum at 90 °C overnight before use. Magnesium triflate (Mg(OTf)$_2$, Aldrich, 97%) was dried in a vacuum oven at 100 °C overnight before use. All other chemicals were purchased from commercial sources and used as received. Infrared spectra were collected on a Thermo Scientific Nicolet 6700.

Electrochemistry. Electrochemical experiments were performed using a BASi Epsilon potentiostat. A single-compartment cell was used for all cyclic voltammetry experiments with a glassy carbon working electrode (3 mm in diameter disc from BASi), a Pt wire counter electrode (flame annealed with a butane torch and separated from the bulk solution by a Vycor tip), and a Ag/AgCl leakless reference electrode

(eDAQ, Inc.). Ferrocene (Fc) was added as an internal reference. All electrochemical experiments were performed with 0.1 M TBAPF$_6$ as the supporting electrolyte. Electrochemical cells were shielded from light during experiments. All solutions were purged with N$_2$ or "bone dry" CO$_2$ (each run through a custom Drierite/activated 3Å molecular sieves drying column) before CVs were taken. All potentials were referenced vs. Fc$^{+/0}$.

Bulk Electrolysis. Bulk electrolysis experiments (at *ca.* $- 1.6$ V vs. Fc$^{+/0}$) were carried out in a 60 mL Gamry 5-neck cell equipped with 3 Ace-Thred ports to hold each electrode and two joints capable of being sealed with septa for gas sparging. This setup included a glassy carbon working electrode (surface area = ~80mm), either a Pt wire counter electrode (flame annealed with a butane torch before use and separated from the bulk solution by porous frit) or a sacrificial Mg rod, and a Ag/AgCl leakless reference electrode (eDAQ, Inc.). A BASi Epsilon potentiostat was used to apply potential and record current. These bulk electrolysis experiments were carried out in 30 mL MeCN with 0.1 M TBAPF$_6$ with the appropriate amount of either TFE or Mg(OTf)$_2$. Bulk electrolysis solutions were purged with either dry N$_2$ or dry CO$_2$ for 10 min prior to electrolysis. Solutions were constantly stirred and shielded from light throughout bulk electrolysis experiments. Gas analysis for bulk electrolysis experiments were performed using 1 mL sample injections on a Hewlett-Packard 7890A Series gas chromatograph with two molsieve columns (30 m $\times$ 0.53 mm ID $\times$ 25 μm film). The 1 mL injection was split between two columns, one with N$_2$ as the carrier gas and one with He as the carrier gas, in order to quantify both H$_2$ and CO

simultaneously in each run. Gas chromatography calibration curves were made by sampling known volumes of CO and H_2 gas.

Infrared Spectroelectrochemistry. The design of the IR spectroelectrochemical cell used for these studies has been reported previously by our group.[25] The working electrode for the cell was a 4.5 mm glassy carbon disk. All spectroelectrochemical experiments were carried out in a 0.1 M TBAPF$_6$ solution in MeCN with 0.1 M Mg(OTf)$_2$, and all solutions were prepared under an atmosphere of dry nitrogen in a glovebox. Blank MeCN solutions with 0.1 M TBAPF$_6$ and 0.1 M Mg(OTf)$_2$ were used for the FTIR solvent subtractions. For experiments under CO_2, a solution of catalyst in TBAPF$_6$/Mg(OTf)$_2$/MeCN was saturated with CO_2 (*ca.* 0.28 M) and diluted in half by an N$_2$-sparged solution of TBAPF$_6$/Mg(OTf)$_2$/MeCN, affording a solution of *ca.* 0.14 M CO_2. A Gamry Reference 600 series three electrode potentiostat was used to affect and monitor thin layer bulk electrolysis.

TOF Calculations. The three equations below (E6.1–E6.3) were used to calculate experimental i_{cat}/i_p and TOF values from catalytic CVs. For a reversible electron-transfer reaction followed by a fast catalytic reaction (E$_R$C$_{cat}$ scheme), the peak catalytic current (i_{cat}) is given by E6.1.[26] The derivation of E6.1 assumes that pseudo-first-order kinetics apply, i.e., the reaction is first order in catalyst and that the concentrations of the substrates, Q, are large in comparison to the concentration of catalyst. In E6.1, n_{cat} is the number of electrons required for the catalytic reaction (n_{cat} = 2 for the reduction of CO_2 to CO), F is Faraday's constant, A is the surface area of the electrode, [cat] is the catalyst concentration, D is the diffusion constant of the

catalytically-active species, k_{cat} is the rate constant of the catalytic reaction, and $[Q]$ is the substrate concentration.

The second equation below (E6.2) describes the peak current of a reversible electron transfer and with no following reaction.[27] In E6.2, R is the universal gas constant, T is temperature, n_p is the number of electrons in the reversible, non-catalytic reaction, and v is scan rate (0.1 V/s). Dividing E6.1 by E6.2 allows for determination of i_{cat}/i_p and allows one to further calculate the catalytic rate constant (k_{cat}) and the turnover frequency (TOF), as shown in E6.3. In this equation, A cancels out because the same electrode was used for the experiments under CO_2 and N_2. D also cancels out because we are assuming that the diffusion constant of the catalytically-active species does not change significantly under CO_2 or N_2. Using E6.1–E6.3, we can calculate peak i_{cat}/i_p and TOF values for $[Mn(mesbpy)(CO)_3(MeCN)](OTf)$ (**2**). For these calculations, i_p is determined as the peak current under N_2 with an equivalent amount of added weak Brønsted acid or Lewis acid corresponding to peak i_{cat} conditions.

$$i_{cat} = n_{cat}FA[cat]\left(Dk_{cat}[Q]^y\right)^{1/2} \tag{E6.1}$$

$$i_p = 0.4463 n_p^{3/2} FA[cat]\left(\frac{F}{RT}\right)^{1/2} v^{1/2} D^{1/2} \tag{E6.2}$$

$$TOF = k_{cat}[Q] = \frac{Fvn_p^3}{RT}\left(\frac{0.4463}{n_{cat}}\right)^2\left(\frac{i_{cat}}{i_p}\right)^2 \tag{E6.3}$$

Foot-of-the-Wave Analysis. Costentin and Savéant's foot-of-the-wave (FOTW) analysis[14,21-23] is a means of benchmarking catalysts in terms of TOF and overpotential (η) without taking into account side phenomena that interfere with catalysis at high current densities. FOTW analysis allows for determination of the

relationship between TOF and η, or the Tafel behavior (logTOF–η relationship), for a catalyst under a given set of conditions. In this manner, catalysts can be benchmarked based on their TOF at zero overpotential (TOF_0). We performed FOTW analysis on the CVs shown in Figure 6.5, using E6.4 (Figures 6.25–6.26). In E6.4, k is the observed rate constant for the catalytic reaction, and E^0_{cat} is the standard potential of the catalyst under inert atmosphere (for **2**, –1.6 V vs. $Fc^{+/0}$). Plotting i/i_p versus $(1+\exp[(F/RT)(E–E^0_{cat})])^{-1}$ gives rise to the FOTW analysis plot. The slope of the linear fit of this plot allows for calculation of k, where slope $=$ $2.24((RT/Fvn_p^3)(2k)[CO_2])^{1/2}$. FOTW analysis plots without the pre-waves observed in catalytic CVs (Figure 6.27b) gives very similar results (within the same order of magnitude for k) as FOTW analysis plots with the pre-waves included (Figure 6.27a).

$$\frac{i}{i_p} = \frac{2.24\sqrt{\dfrac{RT}{Fvn_p^3}2k[CO_2]}}{1+\exp\left[\dfrac{F}{RT}\left(E-E^0_{cat}\right)\right]} \tag{E6.4}$$

Calculation of k gives access to TOF and TOF_0, and thus the Tafel behavior, using E6.5, as shown in Figure 6.27. In E6.5, E^0_{CO2} is the standard potential for the reduction of CO_2 to CO under the specific conditions of catalysis (–1.39 V vs. $Fc^{+/0}$).[14] With 0.1 M Mg^{2+}, catalyst **2** possesses a $logTOF_0 = -0.8$ and $logTOF_{max} = 2.8$. This Tafel behavior is compared with those of other commonly studied molecular CO_2 reduction catalysts in Figure 6.9.[24] Derivations of E6.4 and E6.5 and the Tafel behavior of the other catalysts shown in Figure 6.9 have been previously described.[21-22,24]

$$\text{TOF} = \frac{2k}{1 + \exp\left[\frac{F}{RT}\left(E^0_{CO2} - E^0_{cat}\right)\right]\exp\left(-\frac{F}{RT}\eta\right)} \qquad \textbf{(E6.5)}$$

Much of the material for this chapter comes directly from a manuscript entitled: "Manganese Electrocatalysts with Bulky Bipyridine Ligands: Utilizing Lewis Acids to Promote Carbon Dioxide Reduction at Low Overpotentials" by Matthew D. Sampson and Clifford P. Kubiak, which has been submitted for publication. The dissertation author is the primary author of this manuscript.

6.5 References

(1) Hawecker, J.; Lehn, J. M.; Ziessel, R. *J. Chem. Soc., Chem. Commun.* **1984**, 328-330.

(2) Wong, K.-Y.; Chung, W.-H.; Lau, C.-P. *J. Electroanal. Chem.* **1998**, 453, 161-169.

(3) Smieja, J. M.; Kubiak, C. P. *Inorg. Chem.* **2010**, 49, 9283-9289.

(4) Smieja, J. M.; Benson, E. E.; Kumar, B.; Grice, K. A.; Seu, C. S.; Miller, A. J. M.; Mayer, J. M.; Kubiak, C. P. *Proc. Natl. Acad. Sci. U. S. A.* **2012**, 109, 15646–15650.

(5) Bourrez, M.; Molton, F.; Chardon-Noblat, S.; Deronzier, A. *Angew. Chem., Int. Ed.* **2011**, 50, 9903-9906.

(6) Smieja, J. M.; Sampson, M. D.; Grice, K. A.; Benson, E. E.; Froehlich, J. D.; Kubiak, C. P. *Inorg. Chem.* **2013**, 52, 2484-2491.

(7) Riplinger, C.; Sampson, M. D.; Ritzmann, A. M.; Kubiak, C. P.; Carter, E. A. *J. Am. Chem. Soc.* **2014**, 136, 16285-16298.

(8) Sampson, M. D.; Nguyen, A. D.; Grice, K. A.; Moore, C. E.; Rheingold, A. L.; Kubiak, C. P. *J. Am. Chem. Soc.* **2014**, 136, 5460-5471.

(9) Hartl, F.; Rosa, P.; Ricard, L.; Le Floch, P.; Záliš, S. *Coord. Chem. Rev.* **2007**, 251, 557-576.

(10) Sampson, M. D.; Kubiak, C. P. *Inorg. Chem.* **2015**, 54, 6674-6676.

(11) Hammouche, M.; Lexa, D.; Momenteau, M.; Saveant, J. M. *J. Am. Chem. Soc.* **1991**, 113, 8455-8466.

(12) Schmittel, M.; Ganz, A.; Schenk, W. A.; Hagel, M. *Z. Naturforsch.* **1999**, 54b, 559–564.

(13) Espension, J. H. *Chemical Kinetics and Reaction Mechanisms*; McGraw–Hill: New York, **1981**.

(14) Costentin, C.; Drouet, S.; Robert, M.; Savéant, J.-M. *Science* **2012**, 338, 90-94.

(15) Froehlich, J. D.; Kubiak, C. P. *Inorg. Chem.* **2012**, 51, 3932-3934.

(16) Lacy, D. C.; McCrory, C. C. L.; Peters, J. C. *Inorg. Chem.* **2014**, 53, 4980-4988.

(17) Grills, D. C.; Matsubara, Y.; Kuwahara, Y.; Golisz, S. R.; Kurtz, D. A.; Mello, B. A. *J. Phys. Chem. Lett.* **2014**, 5, 2033-2038.

(18) Ferrini, V.; De Vito, C.; Mignardi, S. *J. Hazard. Mater.* **2009**, 168, 832-837.

(19) Dossmann , H.; Afonso, C.; Lesage, D.; Tabet, J.-C.; Uggerud, E. *Angew. Chem., Int. Ed.* **2012**, 51, 6938-6941.

(20) Miller, G. B. S.; Esser, T. K.; Knorke, H.; Gewinner, S.; Schöllkopf, W.; Heine, N.; Asmis, K. R.; Uggerud, E. *Angew. Chem., Int. Ed.* **2014**, 53, 14407-14410.

(21) Costentin, C.; Drouet, S.; Robert, M.; Savéant, J.-M. *J. Am. Chem. Soc.* **2012**, 134, 11235-11242.

(22) Costentin, C.; Robert, M.; Saveant, J.-M. *Chem. Soc. Rev.* **2013**, 42, 2423-2436.

(23) Costentin, C.; Savéant, J.-M. *ChemElectroChem* **2014**, 1, 1226-1236.

(24) Costentin, C.; Robert, M.; Savéant, J.-M.; Tatin, A. *Proc. Natl. Acad. Sci. U. S. A.* **2015**, 112, 6882-6886.

(25) Machan, C. W.; Sampson, M. D.; Chabolla, S. A.; Dang, T.; Kubiak, C. P. *Organometallics* **2014**, *33*, 4550-4559.

(26) Savéant, J.-M.; Vianello, E. *Electrochim. Acta* **1962**, *8*, 905-923.

(27) Bard, A. J.; Faulkner, L. R. *Electrochemical Methods*; Wiley: New York, **1980**.

(28) Froehlich, J. D.; Kubiak, C. P. *J. Am. Chem. Soc.* **2015**, *137*, 3565-3573.

(29) Raebiger, J. W.; Turner, J. W.; Noll, B. C.; Curtis, C. J.; Miedaner, A.; Cox, B.; DuBois, D. L. *Organometallics* **2006**, *25*, 3345-3351.

(30) Chen, Z.; Chen, C.; Weinberg, D. R.; Kang, P.; Concepcion, J. J.; Harrison, D. P.; Brookhart, M. S.; Meyer, T. J. *Chem. Commun.* **2011**, *47*, 12607-12609.

(31) Kang, P.; Meyer, T. J.; Brookhart, M. *Chem. Sci.* **2013**, *4*, 3497-3502.

(32) *CRC Handbook of Chemistry and Physics*; 92nd ed.; Haynes, W. M., Ed.; CRC Press: Boca Raton, FL, **2011-2012**.

6.6   Appendix
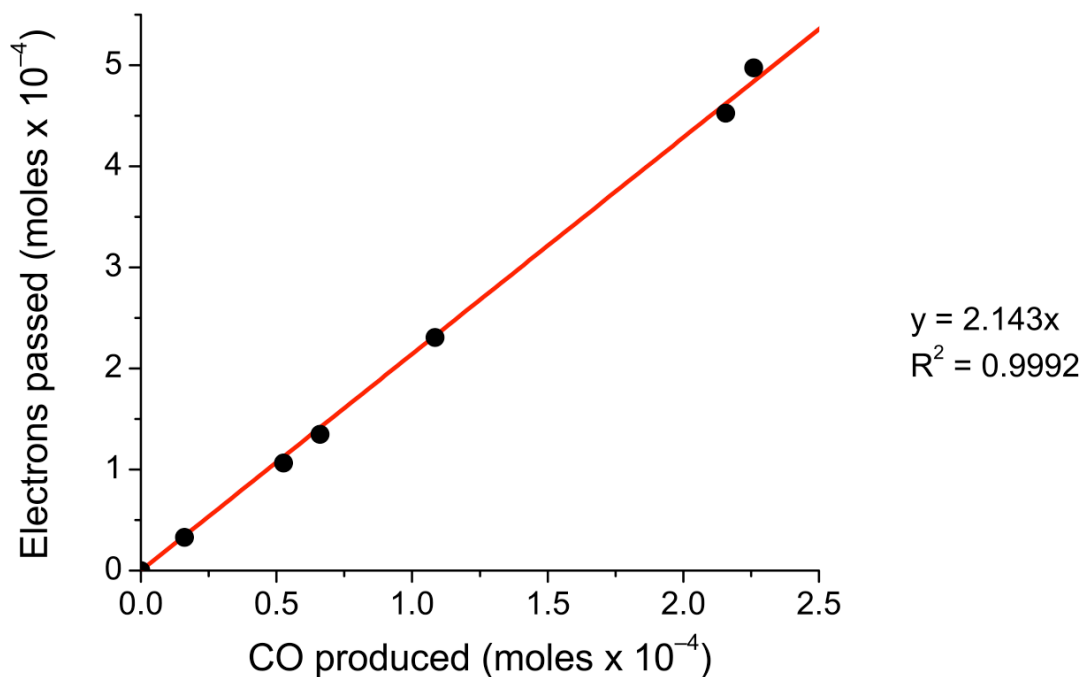
Figure 6.11 Production of CO from CO_2 by 0.5 mM
[Mn(mesbpy)(CO)$_3$(MeCN)](OTf) (**2**) during CPE at -1.6 V vs. Fc$^{+/0}$ with 1.3 M TFE.
The slope of ca. 2 represents a Faradaic efficiency of $96 \pm 3\%$.
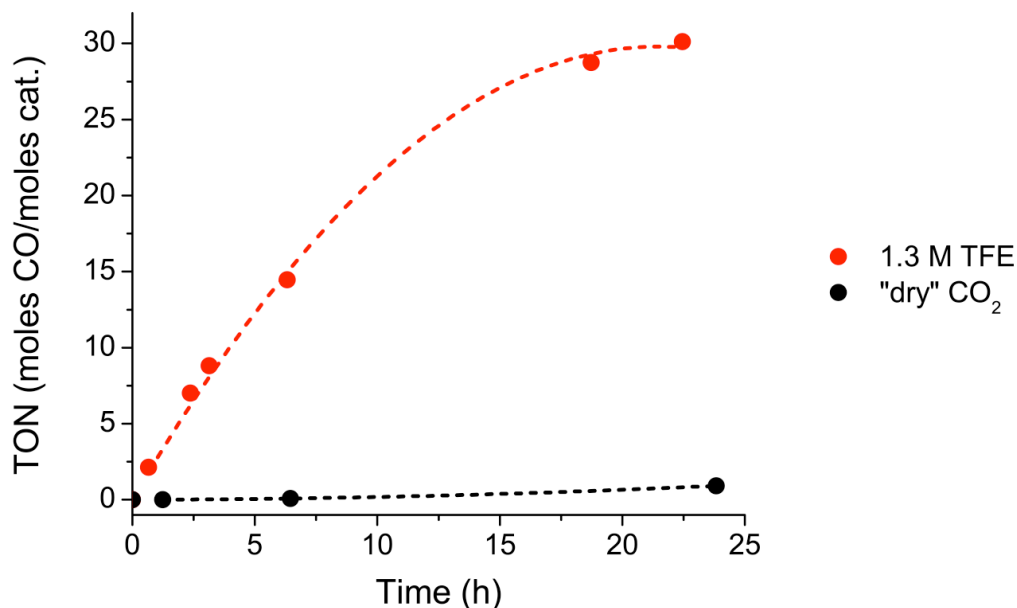
Figure 6.12 Turnover number (TON) of CO (moles CO/moles **2**) over time by 0.5
mM [Mn(mesbpy)(CO)$_3$(MeCN)](OTf) (**2**) during CPE at -1.6 V vs. Fc$^{+/0}$ with 1.3 M
TFE (red) and with no added TFE (black). Solutions of 0.1 M TBAPF$_6$/MeCN were
under an atmosphere of and saturated with CO_2.
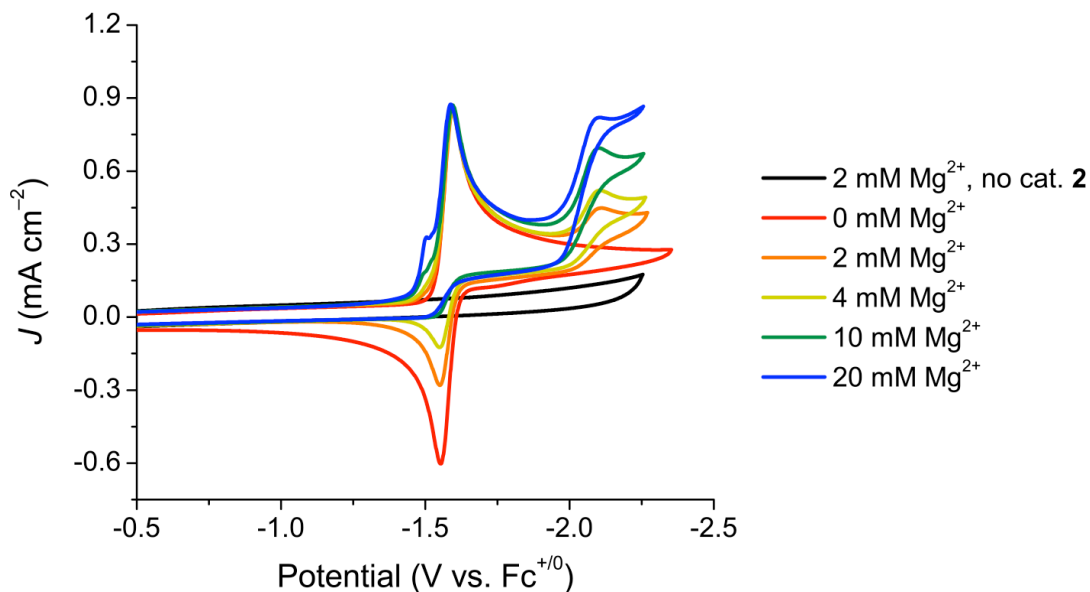
Figure 6.13 CVs of 1 mM [Mn(mesbpy)(CO)$_3$(MeCN)](OTf) (**2**) under N$_2$ with varying concentrations of Mg^{2+}. Conditions: 0.1 M TBAPF$_6$/MeCN; $\nu = 0.1$ V/s.

y = 0.1285x + 0.09546
R^2 = 0.99917
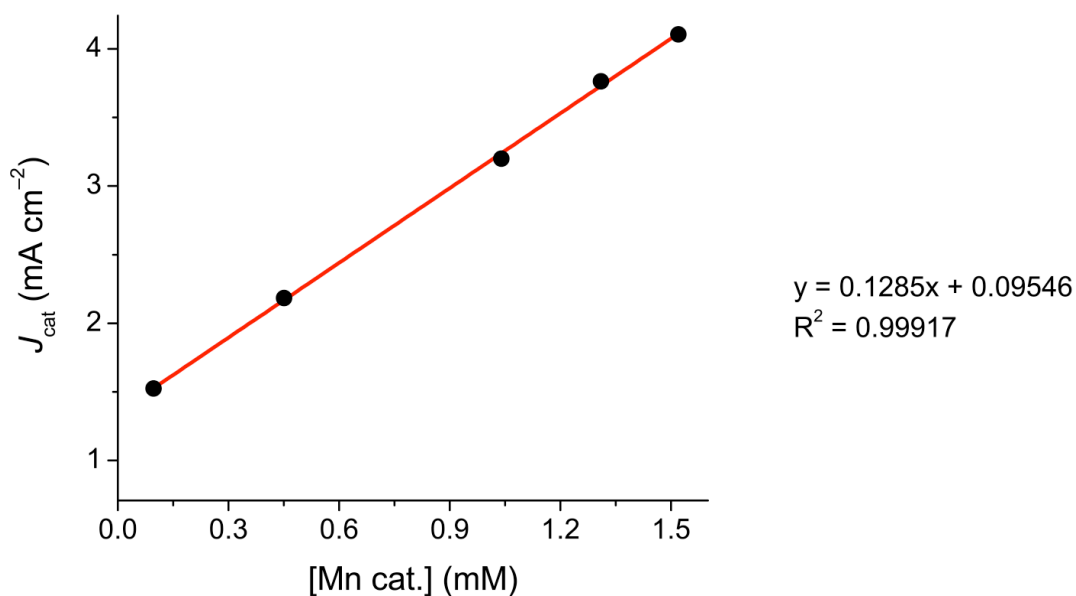
Figure 6.14 Plot of J_{cat} vs. [**2**] for CVs of [Mn(mesbpy)(CO)$_3$(MeCN)](OTf) (**2**) under CO$_2$ and 0.2 M Mg^{2+}, showing a linear dependence on [**2**]. This trend is consistent with a catalytic reaction that is first order in [**2**].
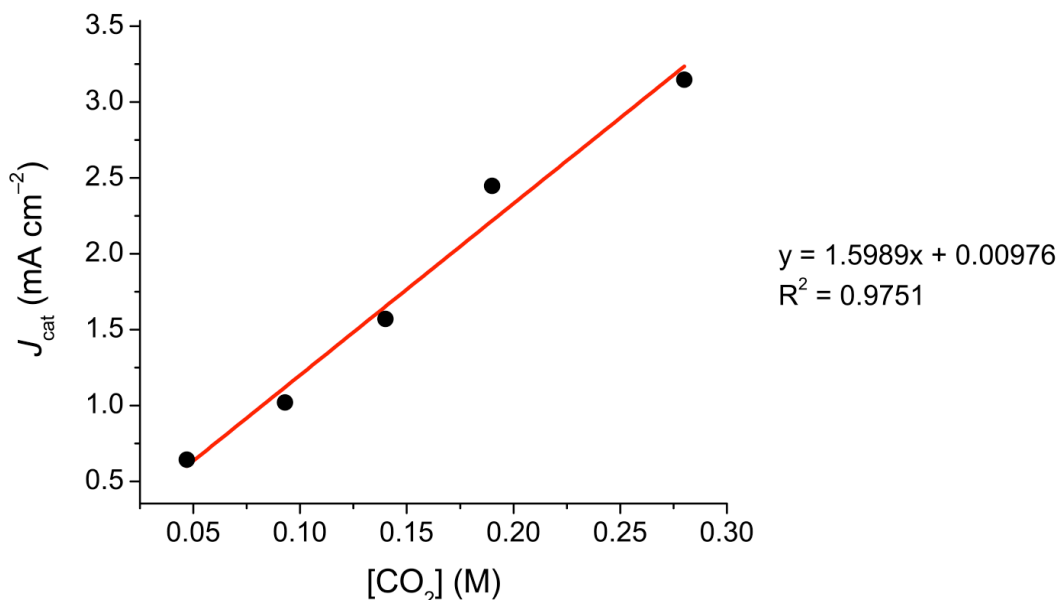
Figure 6.15 Plot of J_{cat} vs. $[CO_2]$ for CVs of 1 mM $[Mn(mesbpy)(CO)_3(MeCN)](OTf)$ (**2**) with 0.2 M Mg^{2+}, showing a linear dependence on $[CO_2]$. This trend is consistent with a catalytic reaction that is second order in $[CO_2]$.
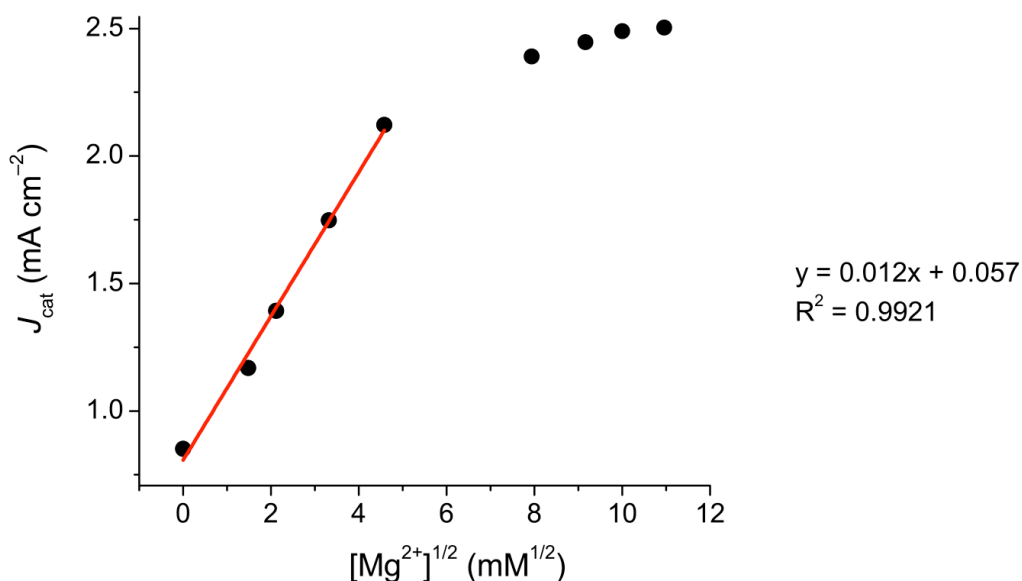
Figure 6.16 Plot of J_{cat} vs. $[Mg^{2+}]^{1/2}$ for CVs of 1 mM $[Mn(mesbpy)(CO)_3(MeCN)](OTf)$ (**2**) under CO_2, showing a linear dependence on $[Mg^{2+}]$ at low Mg^{2+} concentrations. This trend is consistent with a catalytic reaction that is first order in $[Mg^{2+}]$. At low $[Mg^{2+}]$, J_{cat} follows a linear trend with $[Mg^{2+}]^{1/2}$, indicating that the catalytic reaction is first order in $[Mg^{2+}]$. At higher $[Mg^{2+}]$, J_{cat} begins to reach a limiting value independent of $[Mg^{2+}]^{1/2}$, which is typical of saturation kinetics expected for catalytic reactions.
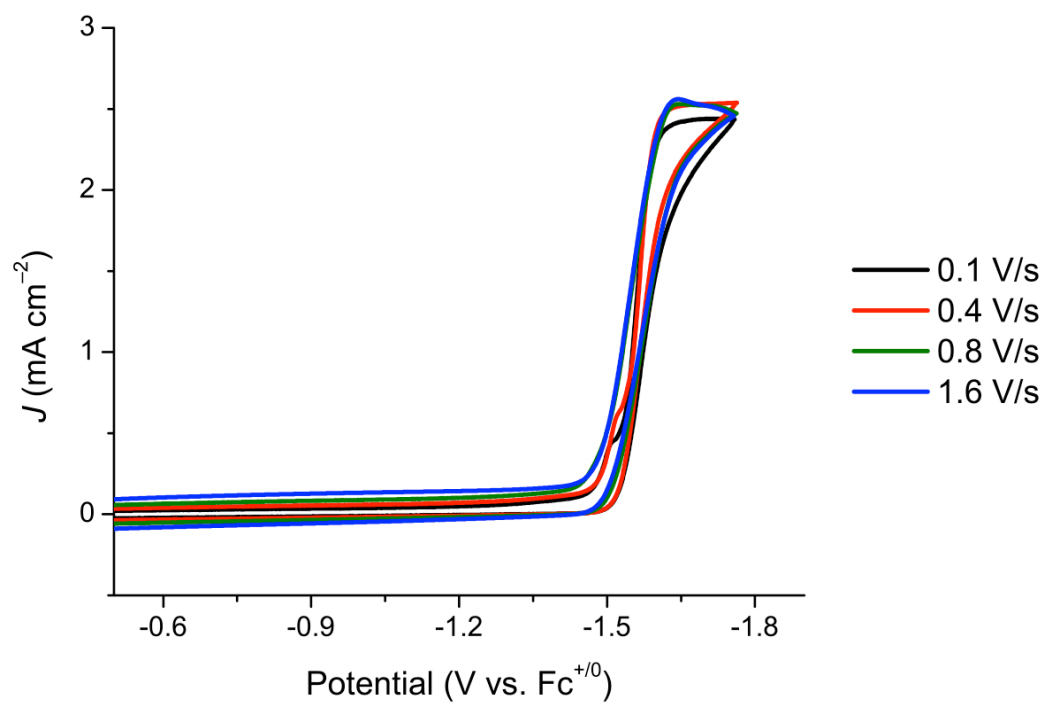
Figure 6.17 CV scan rate dependence of 1 mM [Mn(mesbpy)(CO)$_3$(MeCN)](OTf) (**2**) under CO$_2$ with added 0.2 M Mg^{2+} at varying scan rates. Conditions: 0.1 M TBAPF$_6$/MeCN.
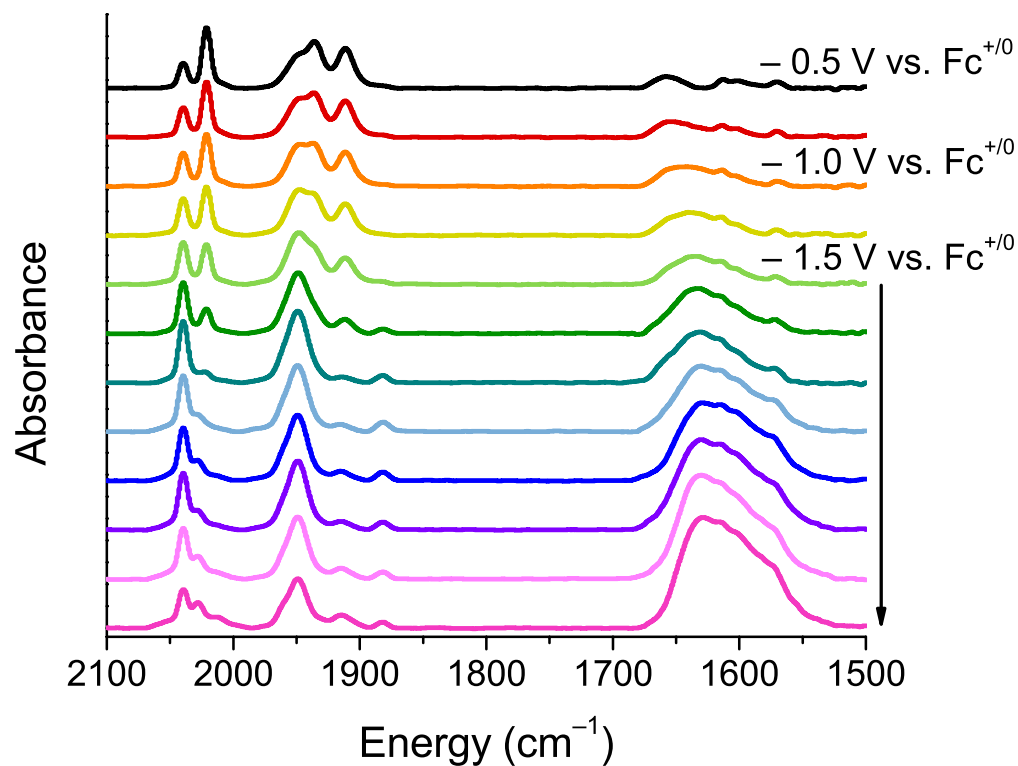
Figure 6.18 IR-SEC of 3 mM complex **1** in MeCN with 0.1 M TBAPF$_6$ electrolyte, 0.1 M Mg(OTf)$_2$, and $^{13}CO_2$. At potentials between -0.5 and -1.0 V vs. Fc$^{+/0}$ (black, red, orange, yellow), species consistent with [Mg–$^{13}CO_2$]$^{2+}$ and $^{13}CO_3^{2-}$/H$^{13}CO_3^-$ are observed. At -1.5 V vs. Fc$^{+/0}$ (light green and below), catalytic formation of $^{13}CO_3^{2-}$ /H$^{13}CO_3^-$ are observed, along with scrabbling of the CO ligands on the Mn complex with produced ^{13}CO.
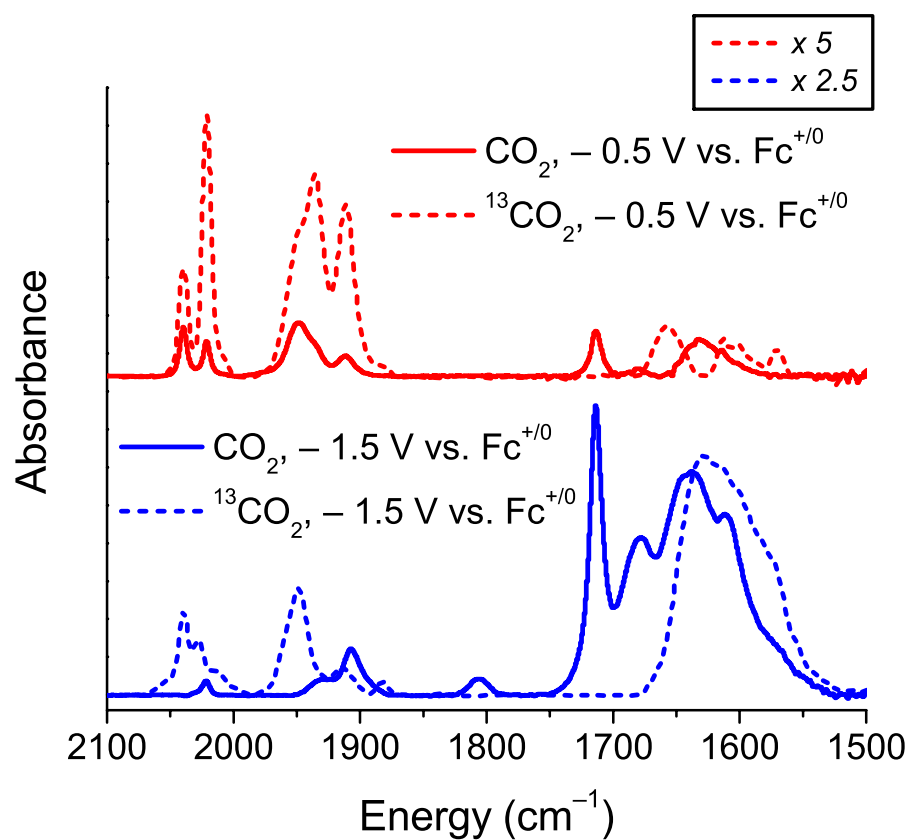
Figure 6.19 Comparison of FTIR spectra during IR-SEC experiments of complex **1** with CO_2 and $^{13}CO_2$. Comparison of FTIR spectra at -0.5 V vs. $Fc^{+/0}$ is shown in red, and comparison of FTIR spectra at -1.5 V vs. $Fc^{+/0}$ is shown in blue (solid lines = CO_2, dashed lines = $^{13}CO_2$). Conditions: 0.1 M TBAPF$_6$/MeCN and 0.1 M Mg(OTf)$_2$. The FTIR spectra for $^{13}CO_2$ have been enhanced by 5- and 2.5-fold for -0.5 V and -1.5 V vs. $Fc^{+/0}$, respectively, for better comparison.
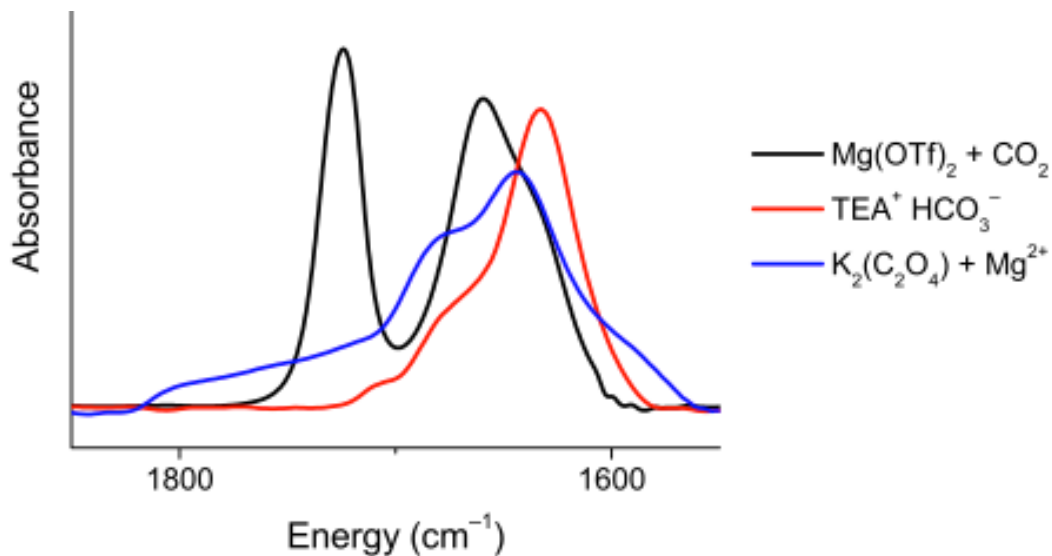
Figure 6.20 FTIR spectrum of the reaction product between $Mg(OTf)_2$ and CO_2 in 0.1 M TBAPF$_6$/MeCN (reaction stirred overnight under CO_2), showing formation of $MgCO_3$ and additional CO_3^{2-}/HCO_3^- species (black). FTIR spectra of TEA$^+$ HCO$_3^-$ (red) and $K_2(C_2O_4)$ (blue) in MeCN are shown for comparison.
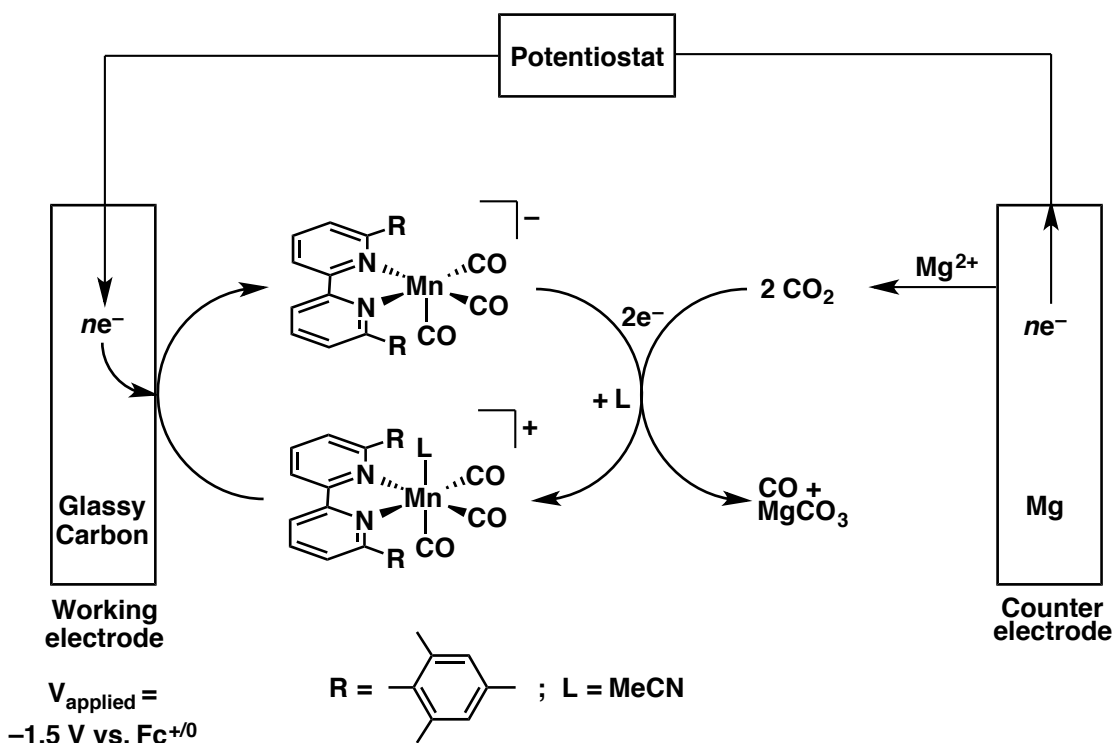
Figure 6.21 Schematic for CPE with sacrificial Mg anode, catalyst **2**, CO_2 in 0.1 M TBAPF$_6$/MeCN, showing release of Mg^{2+} cations as a negative voltage is applied at the working electrode.
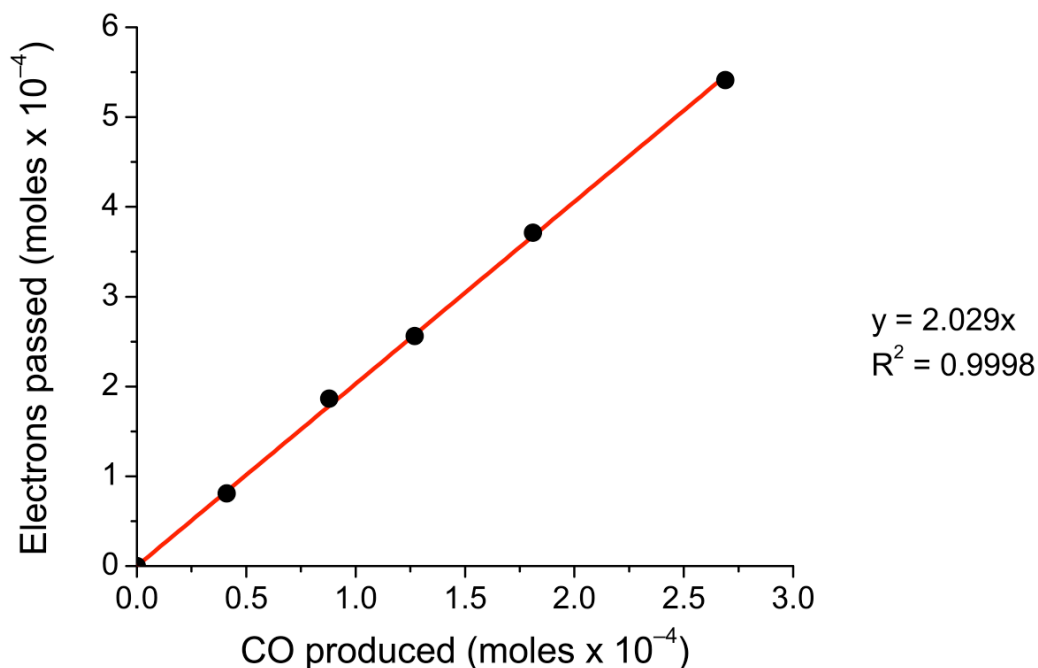
Figure 6.22 Production of CO from CO_2 by 0.5 mM [Mn(mesbpy)(CO)$_3$(MeCN)](OTf) (**2**) during CPE at -1.6 V vs. Fc$^{+/0}$ with a sacrificial Mg anode and 0.2 M Mg^{2+}. Slope of ca. 2 represents a Faradaic efficiency of 98 ± 3%.
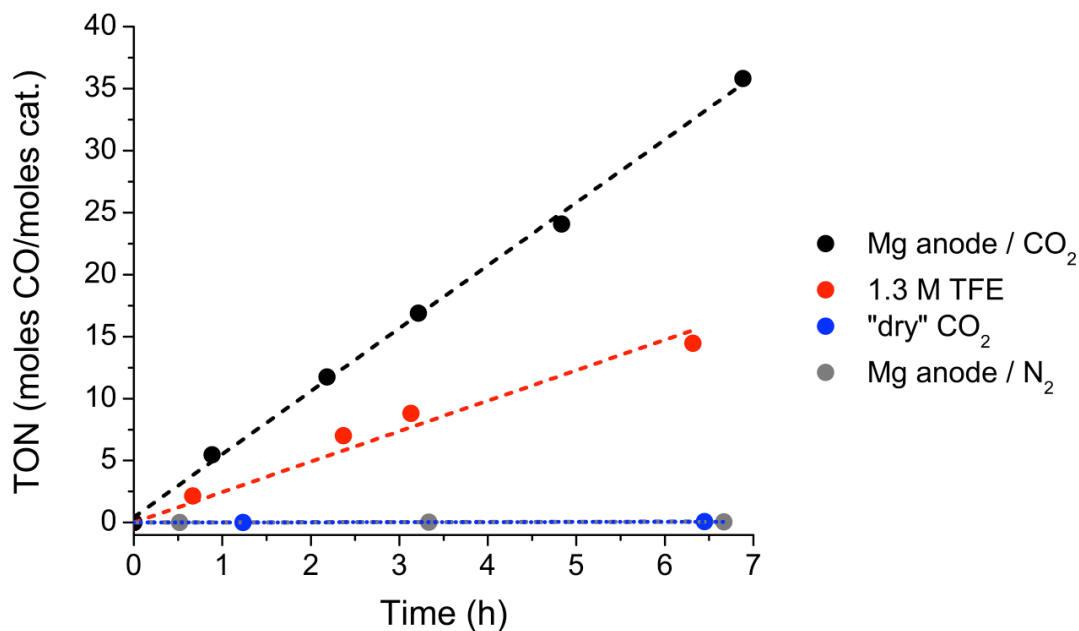
Figure 6.23 Turnover number (TON) of CO (moles CO/moles **2**) over time by 0.5 mM [Mn(mesbpy)(CO)$_3$(MeCN)](OTf) (**2**) during CPE at -1.6 V vs. Fc$^{+/0}$ with a sacrificial Mg anode and 0.2 M Mg^{2+} (black). For comparison TON over time for CPE experiments with 1.3 M TFE (red), with no added TFE (blue), and with a sacrificial Mg anode and 0.2 M Mg^{2+}under N_2 (grey) are also shown.
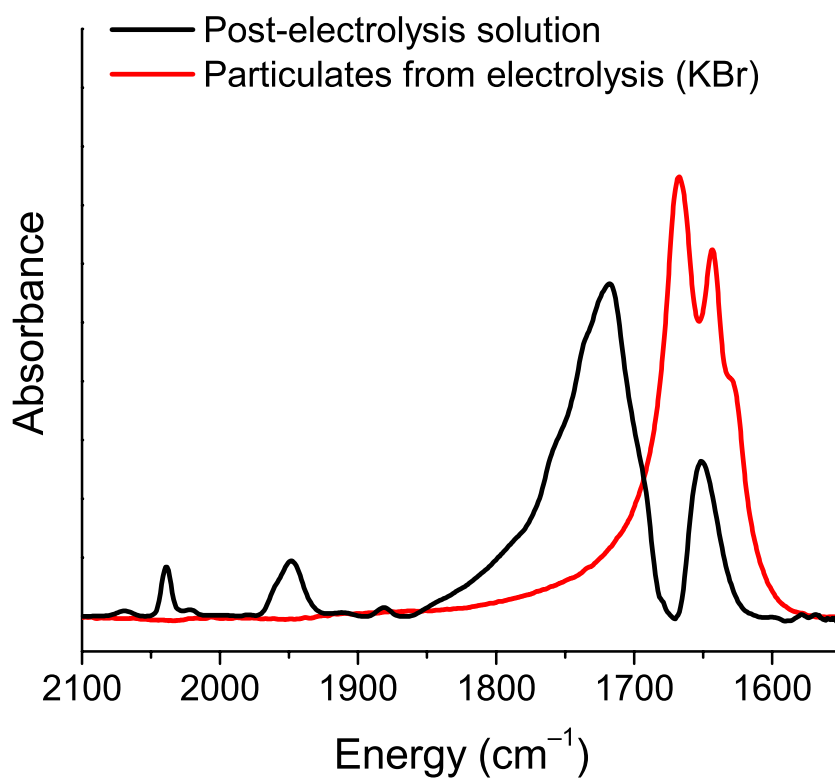
Figure 6.24 FTIR spectra of post-electrolysis samples containing Mg^{2+}. FTIR spectrum of the post-electrolysis solution is shown in black. This 6 h electrolysis solution, contained 0.5 mM **2**, 0.1 M $TBAPF_6$, 0.1 M $Mg(OTf)_2$, and CO_2 (at saturation) in MeCN. FTIR spectrum of the particulates formed during electrolysis (by KBr pellet) is shown in red. These FTIR spectra are consistent with the formation of CO_3^{2-}/HCO_3^- during catalysis.

Table 6.1 Overpotentials (η)[a] and operating conditions of selected homogeneous CO_2 reduction electrocatalysts.

Catalyst precursor	Operating Conditions	E_{cat} (V vs. $Fc^{+/0}$)	η (V)	Ref.
Mn(mesbpy)(CO)$_3$Br	MeCN + 120 mM Mg^{2+}	−1.60	0.3	This work
	MeCN + 3.2 M MeOH	−2.00	0.7	8
Mn(bpy)(CO)$_3$Br	MeCN + 5% H_2O (or + 0.2 M phenol)	−2.00	0.7	5,7
Re(bpy)(CO)$_3$Cl	MeCN	−2.20	0.9	3
	1-ethyl-3-methylimidazolium tetracyanoborate	−1.75	0.5[b]	17
[Re(bpy)(CO)$_3$(py)]$^+$	MeCN + 0.48 M MeOH	−1.90	0.6	2
Fe^{II}(TDHPP)	DMF + 2 M H_2O	−1.93	0.5	14
[Ni(cyclam)]$^{2+}$	MeCN + 25% H_2O	−1.75	0.5	15
	MeCN + 25% H_2O with CO scavenger	−1.87	0.56	28
[Pd$_2$(triphos)$_2$(MeCN)$_2$]$^{4+}$	DMF + 0.1 M HBF$_4$	−1.49	0.5	29
[Ru(tpy)(bpy)(MeCN)]$^{2+}$	MeCN	−1.83	0.5	30
[Co^{III}(N$_4$H)(Br)$_2$]$^+$	MeCN + 10 M H_2O	−1.75	0.5	16
[Ir(POCOP)(MeCN)$_2$(H)]$^{2+}$	H_2O	−1.85	0.7	31

[a]$\eta = E_{cat} − E°_{CO2}$. $E°_{CO2}$ for $2CO_2 + 2e^− \rightarrow CO + CO_3^{2−}$ estimated at −1.30 V vs. $Fc^{+/0}$ (Ref. 32). Standard potential for CO_2/CO couple in MeCN: $E°_{CO2} = −1.40$ V vs. $Fc^{+/0}$ (Ref. 14). Standard potential for CO_2/CO couple in DMF: $E°_{CO2} = −1.32$ V vs. $Fc^{+/0}$, and the standard potential for CO_2/CO couple in DMF with 0.1 M HBF$_4$: $E°_{CO2} = −0.98$ V vs. $Fc^{+/0}$ (Ref. 14). Standard potential for CO_2/HCOOH couple in H_2O (pH 7): $E°_{CO2} = −1.12$ V vs. $Fc^{+/0}$ (Ref. 31). [b]$E°_{CO2}$ assumed to be similar to value in MeCN; 0.45 V lower overpotential than same catalyst in MeCN (Ref. 17).
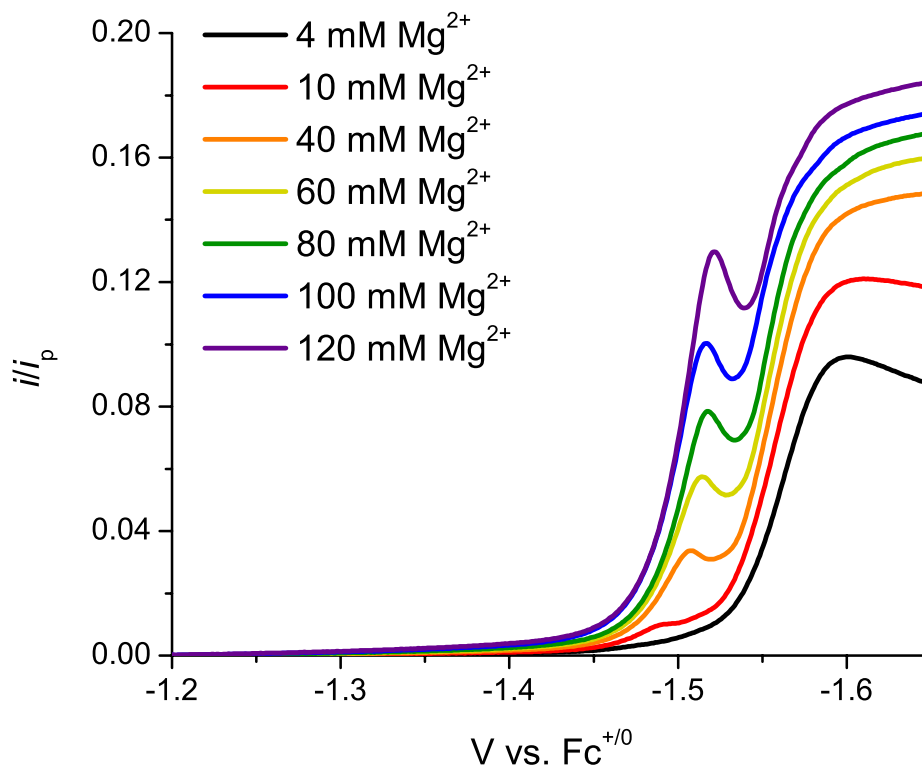
Figure 6.25 Voltammograms from Figure 6.5 normalized to i_p (the peak current of the two-electron reduction of **2** under N_2).
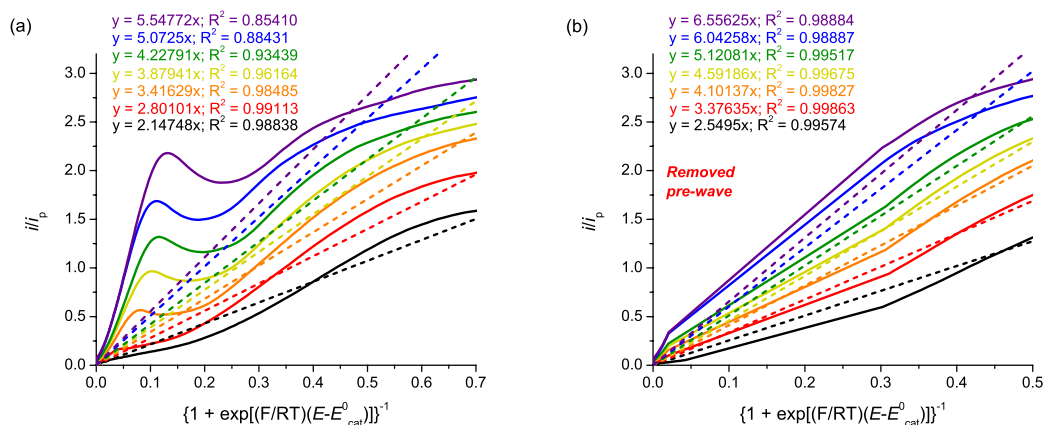
Figure 6.26 (a) Foot-of-the-wave (FOTW) analyses of the voltammograms in Figure S15, with linear fits shown. (b) FOTW analyses after removal of the prewave feature, with linear fits shown.
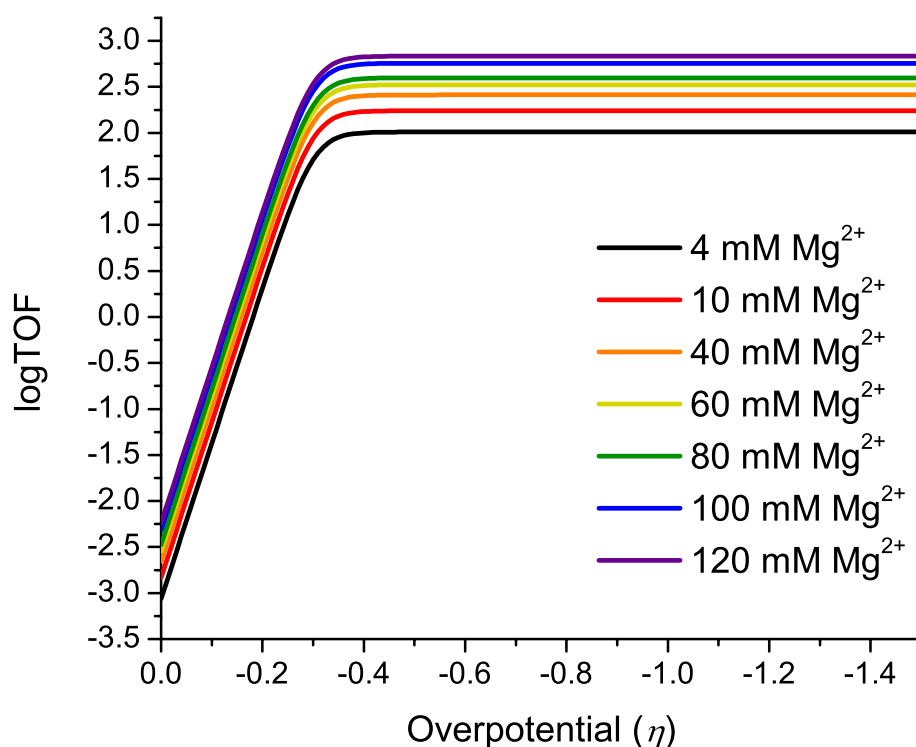
Figure 6.27 Catalytic Tafel plots for catalyst **2** in MeCN with varying concentrations of Mg^{2+}. Tafel plots are derived from FOTW analysis.

Table 6.2 Comparison of $logTOF_{max}$ and logTOF at zero overpotential (TOF_0), derived from Tafel plots shown in Figure 6.9, for selected homogeneous CO_2 reduction electrocatalysts.[24]

Catalyst precursor	Operating Conditions	TOF_{max}	TOF_0
[Mn(mesbpy)(CO)$_3$(MeCN)](OTf) (**2**)	MeCN + 0.1 M Mg^{2+}	2.8	−2.3
	MeCN + 0.3 M TFE	3.7	−7.0
FeTPP	DMF + 3 M PhOH	4.5	−7.9
FeTDHPP[a]	DMF + 3 M PhOH	3.8	−6.0
FeTF5PP[b]	DMF + 3 M PhOH	4.0	−5.5
FeWSTPP[c]	DMF + 3 M PhOH	4.2	−4.3
Mn(bpy-^{t}Bu)(CO)$_3$Br[d]	MeCN + 1.4 M TFE	2.8	−7.5
[Pd$_2$(triphos)$_2$(MeCN)$_2$]$^{4+}$[e]	DMF + 0.1 M HBF$_4$	1.5	−7.4
[Re(bpy)(CO)$_3$(py)]$^+$	MeCN + 0.8 M TFE	2.9	−8.0

[a]TDHPP = 5,10,15,20-tetrakis(2′,6′-dihydroxylphenyl)porphyrin. [b]TF5PP = 5,15-bis(2′,6′-dihydroxyphenyl)-10,20-bis(pentrafluorophenyl)porphyrin. [c]WSTPP = 5,10,15,20-tetra(4′-N,N,N-trimethylanilinium)porhyrin. [d]bpy-tBu = 4,4′-*tert*-butyl-2,2′-bipyridine. [e]triphos = C$_6$H$_4$(P[CH$_2$CH$_2$P(C$_6$H$_{11}$)$_2$])$_2$.
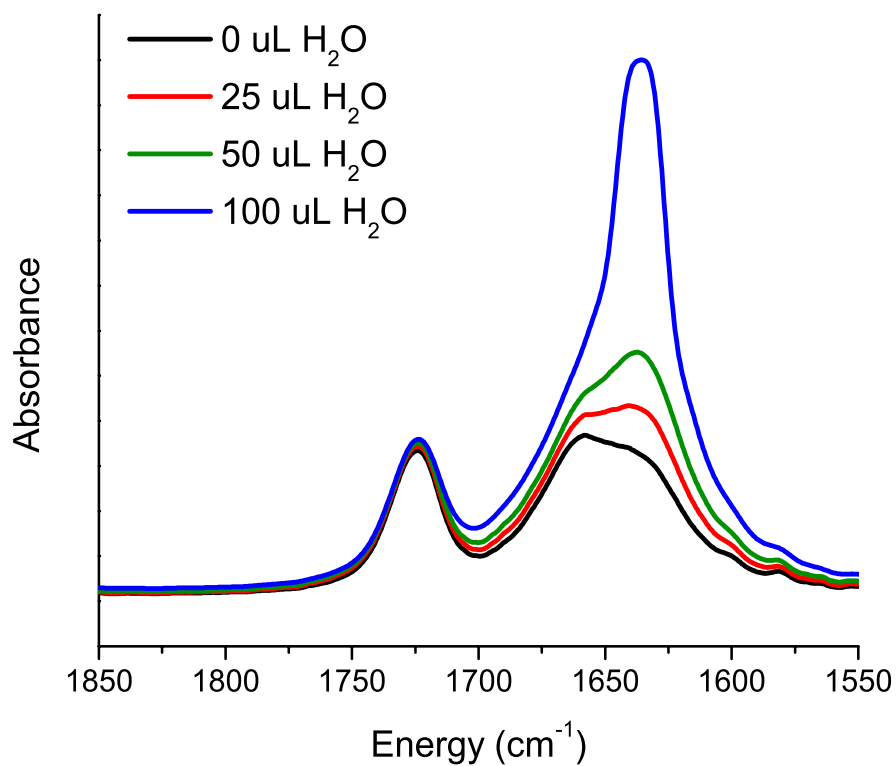
Figure 6.28 Resulting FTIR spectra upon H_2O additions to the reaction mixture of $Mg(OTf)_2$ and CO_2 in 0.1 M $TBAPF_6$/MeCN (reaction stirred overnight under CO_2). Upon addition of H_2O, CO_3^{2-} species at ~1660 cm^{-1} are converted to HCO_3^- species at ~1640 cm^{-1}. The peak at ~1720 cm^{-1} remains unchanged upon H_2O addition, consistent with an assignment as soluble $MgCO_3$ (present at a maximum concentration due to poor solubility).

Chapter 7

Photocatalytic carbon dioxide reduction to formate by a manganese bipyridine molecular catalyst supported on a robust metal-organic framework.

7.1 Introduction

Along with electrochemical methods, mimicking a natural photosynthetic system using a photosensitizer, catalytic site, and sacrificial reducing agent is one viable approach to utilizing solar energy to activate and reduce CO_2.[1-2] Among artificial photosynthetic systems for CO_2 reduction, molecular complexes incorporating second and third row transition metals, such as Ru and Re, are considered to be benchmarks and generally exhibit the best performance.[3-6] However, the use of earth-abundant, first-row transition metal catalysts rather than precious

metals is more attractive for an economically viable, sustainable technology.[7] Increasing the robustness of these artificial photocatalytic systems is important as well, as they often exhibit limited stability; thus, it is desirable to incorporate these systems into a heterogeneous matrix to achieve isolated active sites.[8-9]

Metal-organic frameworks (MOFs) have emerged as an intriguing class of crystalline and microporous materials with a vast array of topologies[10] and applications in gas absorption,[11-12] catalysis,[13-14] molecular separation,[15] chemical sensing,[16] and drug delivery.[17] The ability to design and tune the functional components of the organic linkers, along with inherently high porosity, allows MOFs to be a versatile platform for artificial photosynthesis.[18-19] A number of MOFs have been used as photocatalysts for both of the half reactions in water splitting (i.e. proton reduction[20-26] and water oxidation[27-29]). Site-isolation of molecular catalysts residing in MOFs allows for significantly enhanced stability of the catalytic complexes, thus, improving long-term performance of these systems.[18]

The first example of photocatalytic MOFs for CO_2 reduction was demonstrated by Lin and co-workers, who doped *fac*-Re(bpydc)(CO)$_3$Cl (bpydc = 5,5′-dicarboxylate-2,2′-bipyridine) into a UiO-67 (UiO = University of Oslo) framework to reduce CO_2 to carbon monoxide (CO) with a turnover number (TON) of 10.9 in 6 h.[27] In this system, Re site incorporation was limited (4.2 wt.%), and the recovered MOFs were found to be inactive for additional photocatalytic cycles due to the detachment of the Re(CO)$_3$ moiety. Another strategy to achieve photocatalytic MOFs for CO_2 reduction involved the introduction of amino groups onto the organic dicarboxylate

ligands of MIL-125(Ti) (MIL = Materials of the Institute Lavoisier) or UiO-66(Zr) solids.[30-31]   Here, the functionalized MOFs reduced CO_2 to formate, and the photocatalytic performance was ascribed to visible light absorption by the amino-functionalized ligands and catalytically active Ti^{3+} or Zr^{3+} centers in the metal-oxo clusters. However, both of these examples showed low TONs (0.03 per catalytic site). Lee et al. employed postsynthetic exchange to introduce Ti into UiO-66(Zr) as well as a mixed-ligand strategy to achieve photocatalytic CO_2 reduction to formic acid with a TON ~6.3.[32] Recently, Wang et al. reported efficient proton and CO_2 reduction using Co-ZIF-9 (ZIF = zeolitic imidazolate framework) in conjunction with $[Ru(bpy)_3]^{2+}$ (bpy = 2,2′-bipyridine) as a photosensitizer and TEOA as a sacrificial reductant, reaching a TON for CO as high as 89.6 within 30 min.[33] However, the mechanism for this high activity was not discussed, and the selectivity for CO_2 reduction against proton reduction was low (CO:H_2 ratio = ~1.4:1).

The earth-abundant Mn complex, Mn(bpy)(CO)$_3$Br, has been shown to be an efficient electrocatalyst for CO_2 reduction to CO.[34-40] Recently, Takeda et al. reported on a photochemical system that incorporates this Mn catalyst for highly selective CO_2 reduction to formic acid.[41] The thermal instability of the Mn(CO)$_3$-moiety has proven difficult for incorporation of this Mn complex into MOFs via a conventional solvothermal manner.[27] Herein, we report the postsynthetic metalation of a robust Zr(IV)-based MOF with open bpy metal-chelating linkers to achieve isolated Mn(bpy)(CO)$_3$Br moieties in the MOF. More importantly, in conjunction with $[Ru(dmb)_3]^{2+}$ (dmb = 4,4′-dimethyl-2,2′-bipyridine) as a redox photosensitizer and 1-

benzyl-1,4-dihydronicotinamide (BNAH) as a sacrificial reducing agent, the resulting UiO-67-Mn(bpy)(CO)$_3$Br was found to be highly active and selective for the photocatalytic reduction of CO$_2$ to formate with a TON of 110 through 18 h of catalysis. UiO-67 materials exhibited catalytic activities exceeding those of the Mn(bpy)(CO)$_3$Br and Mn(bpydc)(CO)$_3$Br homogeneous analogs, as well as many precious-metal-based MOF photocatalysts. The external UiO-67 matrix enhanced stability of the Mn active sites, allowing them to be reused up to three cycles without significant loss of performance.

7.2 Results and Discussion

Synthesis of UiO-67-Mn(bpy)(CO)$_3$Br. The UiO series of MOFs were first discovered by Lillerud and co-workers, and are constructed from Zr$_6$O$_4$(OH)$_3$(CO$_2$)$_{12}$ secondary building units and dicarboxylate bridging ligands.[42] The UiO-67 framework with open bpy chelating groups (UiO-67-bpydc) was synthesized using a direct solvothermal synthesis according to our previous report.[43] Heating a DMF solution containing 1:1 molar ratio of H$_2$bpydc and 4,4´-biphenyldicarboxylic acid (H$_2$bpdc) with ZrCl$_4$ and acetic acid (as a modulator) at 120 °C for 24 h afforded highly crystalline UiO-67-bpydc containing 50±4% bpydc (Figure 7.1). After washing with MeOH and activation under dynamic vacuum, the high crystallinity and phase purity of UiO-67-bpydc was confirmed by powder X-ray diffraction (PXRD, Figure 7.2a). Field-emission scanning electron microscopy (FE-SEM) showed an

octahedral morphology of the resultant materials with a crystal size ranging from 0.7~1 μm.
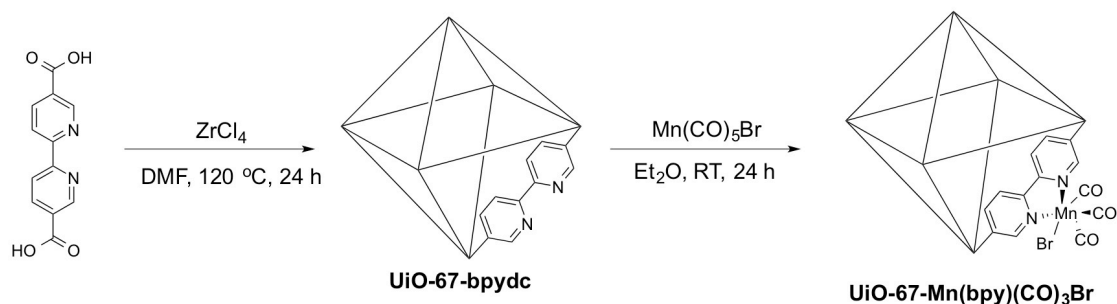
Figure 7.1 Schematic for the synthesis of UiO-67-Mn(bpy)(CO)$_3$Br.

Attempts to directly include Mn(bpydc)(CO)$_3$Br into MOFs during solvothermal synthesis (100-120 °C) resulted in decomposition of the Mn complex, presumably due to the labile Mn–CO bonds. Taking advantage of mild postsynthetic modification (PSM) conditions,[44] we successfully introduced the targeted Mn complex onto the struts of UiO-67-bpydc framework. The activated UiO-67-bpydc was incubated in a diethyl ether (Et$_2$O) solution containing Mn(CO)$_5$Br at room temperature for 24 h. The metalated material, UiO-67-Mn(bpy)(CO)$_3$Br, was isolated as a red microcrystalline powder, after washing thoroughly with fresh Et$_2$O and activation under vacuum. PXRD and FE-SEM confirmed the retention of the UiO-67 topology after metalation (Figure 7.2a and 7.5). Dinitrogen (N$_2$) absorption/desorption isotherms (77 K) of UiO-67-bpydc and UiO-67-Mn(bpy)(CO)$_3$Br indicate a decrease in porosity upon metalation (Figure 7.2c), with Brunauer-Emmett-Teller (BET) surface areas determined to be 2340±134 m^2/g and 1430±133 m^2/g for UiO-67-bpydc and UiO-67-Mn(bpy)(CO)$_3$Br, respectively. The lower BET surface area is consistent with the increased wt.% and steric bulk of the Mn complexes residing in the metalated

MOF, and the specific surface area is actually higher than other MOFs possessing metalated bpy sites.[45-47]
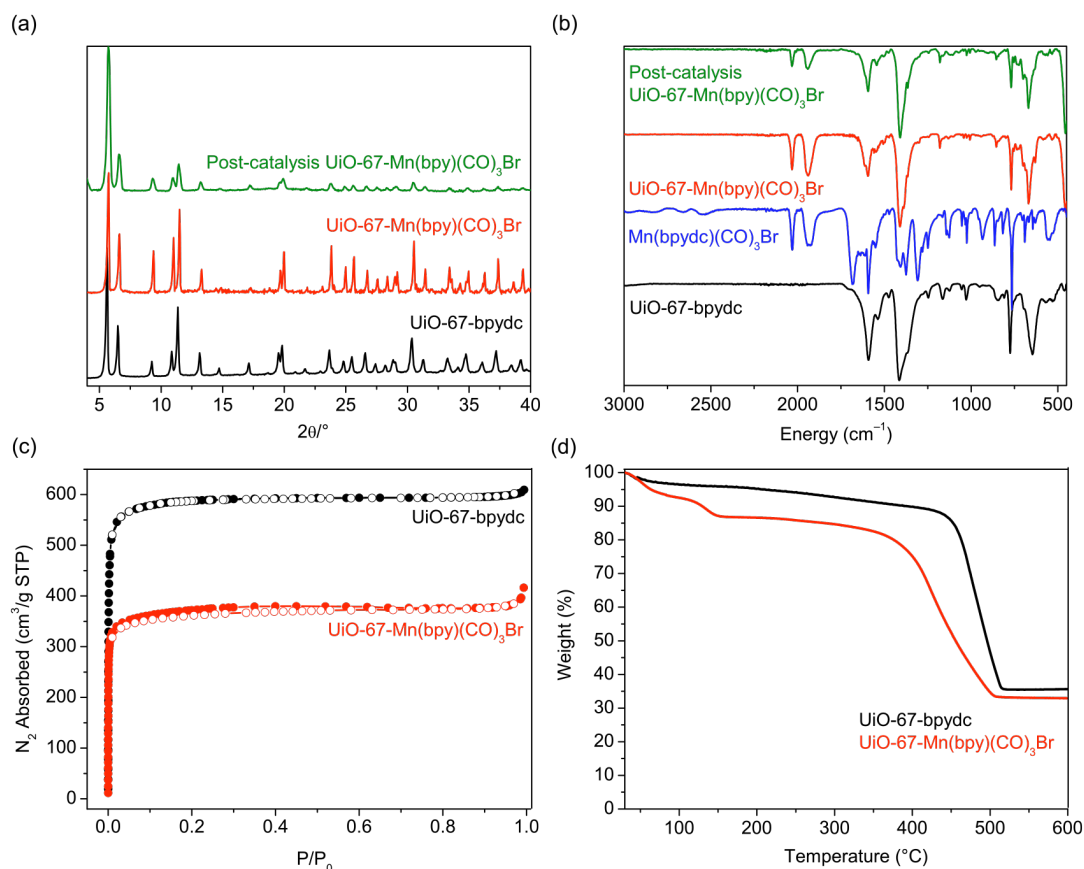
Figure 7.2 (a) PXRD of UiO-67-bpydc (black), UiO-67-Mn(bpy)(CO)$_3$Br (red), and UiO-67-Mn(bpy)(CO)$_3$Br after one 4 h photocatalysis experiment. (b) FTIR of UiO-67-bpydc (black), Mn(bpydc)(CO)$_3$Br (blue), UiO-67-Mn(bpy)(CO)$_3$Br (red), and UiO-67-Mn(bpy)(CO)$_3$Br (green) after 1 cycle of catalysis. (c) N$_2$ isotherm of UiO-67-bpydc (black) and UiO-67-Mn(bpy)(CO)$_3$Br (red). (d) TGA of UiO-67-bpydc (black) and UiO-67-Mn(bpy)(CO)$_3$Br (red).

The degree of Mn(bpydc)(CO)$_3$Br functionalization was characterized by inductively coupled plasma-optical emission spectroscopy (ICP-OES), energy-dispersed X-ray spectroscopy (EDX), and thermogravimetric analysis (TGA). The ratio of heavy elements in UiO-67-Mn(bpy)(CO)$_3$Br was determined to be 1:0.376 (Zr:Mn) via ICP-OES and 1:0.39:0.37 (Zr:Mn:Br) via EDX, which suggests that

~76% of bpy sites were metalated, achieving an overall formula of $Zr_6O_4(OH)_4(Mn(bpydc)(CO)_3Br)_{2.3}(bpydc)_{0.7}(bpdc)_3$. It was found that increasing the bpy functionalization to 75~100% for parent UiO-67-bpydc followed by Mn metalation did not significantly enhance the incorporation of $Mn(bpy)(CO)_3Br$ moieties, perhaps due to steric hindrance by the Mn complexes in the MOF cavities. The TGA trace of UiO-67-$Mn(bpy)(CO)_3Br$ exhibited two decomposition steps at ~70-150 °C and ~370-500 °C, unlike pristine UiO-67-bpydc, which displayed only one major decomposition step at ~450-500 °C (Figure 7.2d). The first decomposition step for UiO-67-$Mn(bpy)(CO)_3Br$ is likely due to thermal liberation of the carbonyl ligands bound to the Mn centers (obs: 7.2%, calcd: 7.3%). The remaining organic ligands decompose at ~370 °C, leading to mixed ZrO_2 and Mn_2O phases (obs: 33.4%, calcd: 33.7%, percent weight residual mass). In addition, we employed Fourier-transform infrared spectroscopy (FTIR) to demonstrate the incorporation of the targeted $Mn(bpy)(CO)_3Br$ complex into the MOF. FTIR of UiO-67-$Mn(bpy)(CO)_3Br$ exhibited two prominent CO stretching frequencies at 2031 cm^{-1} and 1940 cm^{-1}, while no such CO bands were observed between 2200–1800 cm^{-1} for the parent UiO-67-bpydc material (Figure 7.2b). Moreover, the position and relative intensity of these characteristic CO stretching frequencies was identical to the free $Mn(bpydc)(CO)_3Br$ complex, suggesting successful formation of the targeted catalytic site on the strut of the MOFs. Indeed, the color change (colorless to red) during metalation is due to the coordination of Mn(I) to the nitrogen atoms of the bpydc ligand, and ascribed to the metal-to-ligand ($Mn^I \rightarrow$ bipyridine π^*) charge transfer (MLCT) band.

Photocatalytic CO$_2$ Reduction. Having observed successful incorporation of the Mn complex into a robust MOF, we explored the efficiency of this material as a catalyst in photochemical CO$_2$ reduction. In tandem with [Ru(dmb)$_3$]$^{2+}$ (0.5 mM) as a redox photosensitizer and BNAH (0.2 M) as a sacrificial reductant, visible light irradiation (470 nm) of a mixed solution of DMF and TEOA (4:1 v/v) containing UiO-67-Mn(bpy)(CO)$_3$Br (0.5 mM Mn sites) and saturated with CO$_2$ afforded highly selective production (~96%) of formate (see a simplified scheme of the photocatalysis apparatus in Figure 7.6). UiO-67-Mn(bpy)(CO)$_3$Br catalyzed formate production reaches TONs of 50±7.8 and 110±13 over 4 and 18 h, respectively (Figure 7.3 and Table 7.1). Production of formate was determined by ^{1}H NMR spectroscopy after a basic workup and comparison with both an internal standard (ferrocene) and formate standard solutions (see Supporting Information, Figure 7.7). With a light intensity of 2.51×10^{-7} einstein s^{-1}, the Mn-functionalized MOF produced formate with a quantum yield ($\Phi_{formate}$) of 13.8% over the course of 4 h. Additionally, these photocatalysis experiments produced low yields of CO and dihydrogen (H$_2$), as determined by gas chromatography (CO TON = 1.5 and 4.5; H$_2$ TON = 0.41 and 1.0 for 4 and 18 h, respectively). To directly compare the CO$_2$ reduction ability of UiO-67-Mn(bpy)(CO)$_3$Br to the homogeneous catalytic system, we synthesized both Mn(bpy)(CO)$_3$Br and Mn(bpydc)(CO)$_3$Br and studied these complexes as photosensitized catalysts. UiO-67-Mn(bpy)(CO)$_3$Br out-performed each homogeneous Mn complex in formate production over 4 and 18 h experiments (Figure 7.3, Table 7.1). Specifically, Mn(bpy)(CO)$_3$Br and Mn(bpydc)(CO)$_3$Br reached TONs

for formate of 70±7.6 and 57±7.8 after 18 h (Table 7.1, entries 7, 9). UiO-67-Mn(bpy)(CO)$_3$Br out-performed a mixture of the homogeneous Mn(bpy)(CO)$_3$Br complex in combination with UiO-67 (Table 7.1, entry 14). It is important to note that, although photocatalytic reactions were run for a total of 18 h, this likely does not represent the lifetime of the catalyst under these photocatalytic conditions (see details on recyclability studies below). These 18 h photocatalytic experiments are reported to demonstrate the maximum TONs for each catalyst in one run.

The framework of UiO-67-Mn(bpy)(CO)$_3$Br clearly aids in catalysis, likely by both stabilizing the Mn(CO)$_3$ moiety and inhibiting dimerization in the singly-reduced Mn complex (see below). Additionally, UiO-67 could serve as a reservoir of CO$_2$ for supplying CO$_2$ to the Mn active sites. UiO-67 displays a CO$_2$ adsorption capacity of ~25 cc/g at room temperature and 1 bar of CO$_2$ (~2.4 CO$_2$/UiO-67 unit cell).[48-49] Hence, UiO-67 may sequester CO$_2$ at the Mn active sites when compared to the homogeneous Mn complexes, which have no ability to sequester or concentrate CO$_2$. However, in the presence of solvents, it is unlikely that UiO-67 functions as an additional CO$_2$ reservoir to aid in catalysis. The photocatalytic ability of UiO-67-Mn(bpy)(CO)$_3$Br compares very favorably with other MOFs that have been investigated for photocatalytic CO$_2$ reduction (Table 7.2).

Table 7.1 Turnover Numbers (TONs) for Formate (HCOO⁻), CO, and H₂ From Photocatalytic Experiments.[a]

Entry	System	Irradiation time (h)	HCOO⁻ TON	HCOO⁻ Φ	CO TON	H₂ TON
1	UiO-67-Mn(bpy)(CO)$_3$Br [b]	4	50 ± 7.8	13.8 %	1.5 ± 2.0	0.41 ± 0.54
2	UiO-67-Mn(bpy)(CO)$_3$Br [b]	18	110 ± 13	6.74 %	4.5 ± 0.73	1.0 ± 0.11
3	UiO-67-Mn(bpy)(CO)$_3$Br (reused 1) [c]	4	24 ± 6.4	6.64 %	0.73	0.46
4	UiO-67-Mn(bpy)(CO)$_3$Br (reused 2) [c]	4	19 ± 2.3	5.25 %	0.64	0.48
5	UiO-67-Mn(bpy)(CO)$_3$Br (reused 3) [c]	4	17 ± 2.0	4.70 %	0.51	0.49
6	Mn(bpy)(CO)$_3$Br	4	35 ± 4.6	9.64 %	2.1	0.01
7	Mn(bpy)(CO)$_3$Br	18	70 ± 7.6	4.27 %	5.1	0.14
8	Mn(bpydc)(CO)$_3$Br	4	32 ± 3.6	8.89 %	2.3	0.03
9	Mn(bpydc)(CO)$_3$Br	18	57 ± 7.8	3.49 %	5.2	0.06
10	UiO-67-bpydc	18	38 ± 3.4	2.31 %	0.40	0.42
11	Only [Ru(dmb)$_3$]$^{2+}$ [d]	18	33 ± 4.2	2.02 %	0.30	0.29
12	UiO-67-Mn(bpy)(CO)$_3$Br, no [Ru(dmb)$_3$]$^{2+}$ [e]	18	4.9 ± 1.0	0.30 %	0.02	0.0
13	UiO-67-Mn(bpy)(CO)$_3$Br, under N$_2$ [f]	18	2.1 ± 1.4	0.13 %	1.0	8.3
14	UiO-67 and Mn(bpy)(CO)$_3$Br [g]	18	73 ± 3.6	4.46 %	4.3	0.02

[a] All photocatalytic experiments were performed in a DMF/TEOA (4:1 v/v, 20 mL total) solution with 0.5 mM catalyst, 0.5 mM [Ru(dmb)$_3$]$^{2+}$, and 0.2 M BNAH with CO$_2$ saturation (unless otherwise noted). All experiments were irradiated with 470 nm monochromatic light (intensity = 2.51 × 10^{-7} einstein s^{-1}). [b] Experiments with UiO-67-Mn(bpy)(CO)$_3$Br were performed at [Mn] = 0.5 mM using the formula Zr$_6$O$_4$(OH)$_4$(Mn(bpydc)(CO)$_3$Br)$_{2.3}$(bpydc)$_{0.7}$(bpdc)$_3$. [c] The MOF solids were recovered from the previous 4 h photocatalysis experiment by decanting the solution, washing with acetone, and drying under vacuum before being reused in a new catalytic run. [d] Experiment did not contain any Mn catalyst or UiO-67 MOF. [e] Experiment did not contain any [Ru(dmb)$_3$]$^{2+}$ photosensitizer. [f] Experiment was performed under N$_2$ atmosphere. [g] Experiment performed with 0.5 mM UiO-67 and 0.5 mM Mn(bpy)(CO)$_3$Br.

In Figure 7.4, we present a proposed mechanism for the photocatalytic reaction. In these reactions, BNAH serves as the sacrificial reductant, reducing the excited Ru(II) photosensitizer and initiating the photocatalytic reaction. The reduced photosensitizer transfers an electron to the Mn catalyst, forming a Mn(0) complex that can then engage in catalysis. The large pores of UiO-67 (pore diameter = 1~2.3 nm)[48,50] are sufficient to allow electron transfer between the Ru(II) photosensitizer (longest molecular dimension = ~1.5 nm) and the Mn complex within the MOF, as the Ru(II) photosensitizer is capable of accessing the interior of UiO-67. To further support this claim, soaking UiO-67 in a solution of the Ru(II) photosensitizer resulted in a color change to the MOF (persisting after multiple washes with acetone), suggestive of encapsulation of the Ru(II) complex within the MOF. TEOA likely facilitates the reaction by donating a sacrificial proton and electron (i.e. a hydrogen atom) during catalysis via a Hofmann-type degradation process (see our proposed mechanism in Figure 7.4).[51] It is unknown whether or not TEOA coordinates to the Mn center during this process; however, previous studies with Re bipyridine photocatalysts have shown that CO_2 can bind to the metal center with the aid of TEOA, forming an O-bound $Re–OC(O)OCH_2CH_2NR_2$ complex.[52] Additionally, these studies have shown that the aforementioned Re–OC(O)R complex can convert into a Re–OC(O)H complex under similar photocatalytic conditions (i.e. TEOA donates a hydrogen atom to the Re complex). In any case, we invoke TEOA donating one proton and one electron to the catalytic reaction, forming a Mn(I)–H complex. CO_2 can insert into the Mn–H bond, forming a Mn(I)–OC(O)H complex. Formate (or

formic acid after further protonation) can then dissociate from the Mn center regenerating the starting Mn(I) complex. These conclusions are drawn from a large body of previous work published by others on photosensitized catalysis driven by sacrificial reducing agents.[53-58]

It is important to note that photocatalysis experiments without UiO-67-Mn(bpy)(CO)$_3$Br or a homogeneous Mn catalyst (i.e., with only the Ru^{2+} photosensitizer and BNAH) still catalyzed the production of formate, with a TON of 33±4.2 over 18 h (Table 7.1, entry 11). Photocatalysis experiments with unmetalated UiO-67-bpydc showed similar yields of formate, with a TON of 38±3.4 over 18 h (Table 7.1, entry 10). These TONs without Mn complex are not surprising given that in 1985 Hawecker et al. reported that [Ru(bpy)$_3$]$^{2+}$ is a homogeneous catalyst for the photochemical reduction of CO$_2$ to formate.[59] In the original report of the photocatalytic ability of Mn(bpy)(CO)$_3$Br by Takeda et al. in 2014, the authors report slightly lower TONs for formate by only the Ru^{2+} photosensitizer (TON = 25 after 12 h).[41] Although the [Ru(dmb)$_3$]$^{2+}$ photosensitizer also serves as a catalyst for CO$_2$ reduction, it is clear that the Mn complex enhances CO$_2$ reduction to formate by at least a factor of ~2 in the homogeneous system and a factor of ~3 in the heterogeneous UiO-67-Mn(bpy)(CO)$_3$Br system. Photocatalysis experiments under dinitrogen (N$_2$) atmosphere or without added Ru^{2+} photosensitizer resulted in minimal formation of formate over 18 h (Table 7.1, entries 12–13).
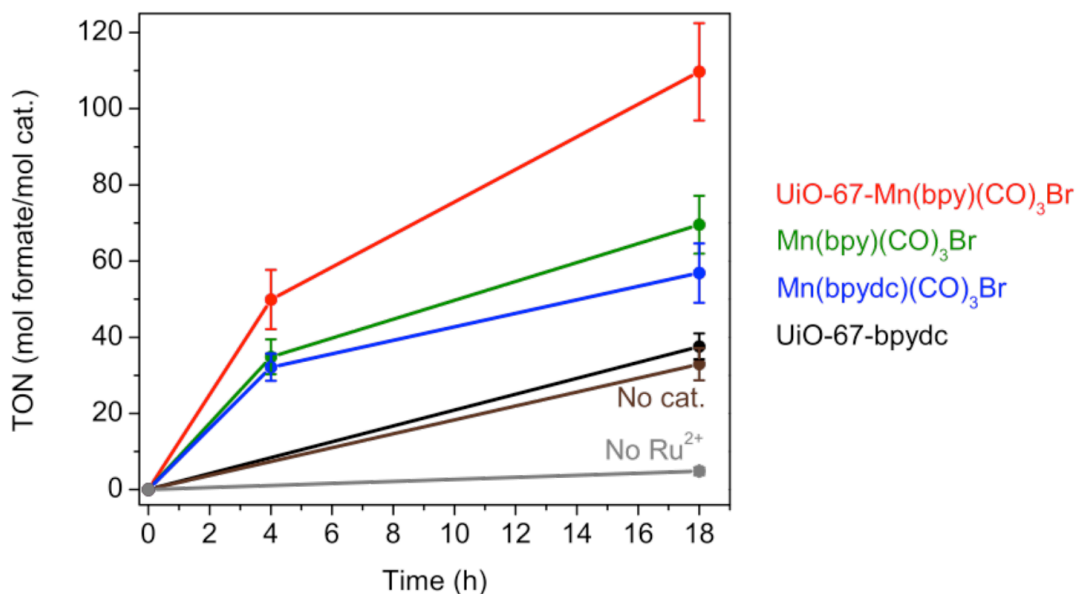
Figure 7.3 Plot of formate turnover number (TON, mol of formate/mol of catalyst) during photocatalysis experiments for the following systems: UiO-67-Mn(bpy)(CO)₃Br (red), Mn(bpy)(CO)₃Br (green), Mn(bpydc)(CO)₃Br (blue), UiO-67-bpydc (black), no added Mn complex or MOF (only Ru^{2+}, brown), and UiO-67-Mn(bpy)(CO)₃Br without added Ru^{2+} (grey). All photocatalytic experiments were performed in a DMF/TEOA (4:1 v/v, 20 mL total) solution with 0.5 mM catalyst, 0.5 mM [Ru(dmb)₃]²⁺, 0.2 M BNAH with CO_2 saturation, and irradiated with 470 nm light (unless otherwise noted).
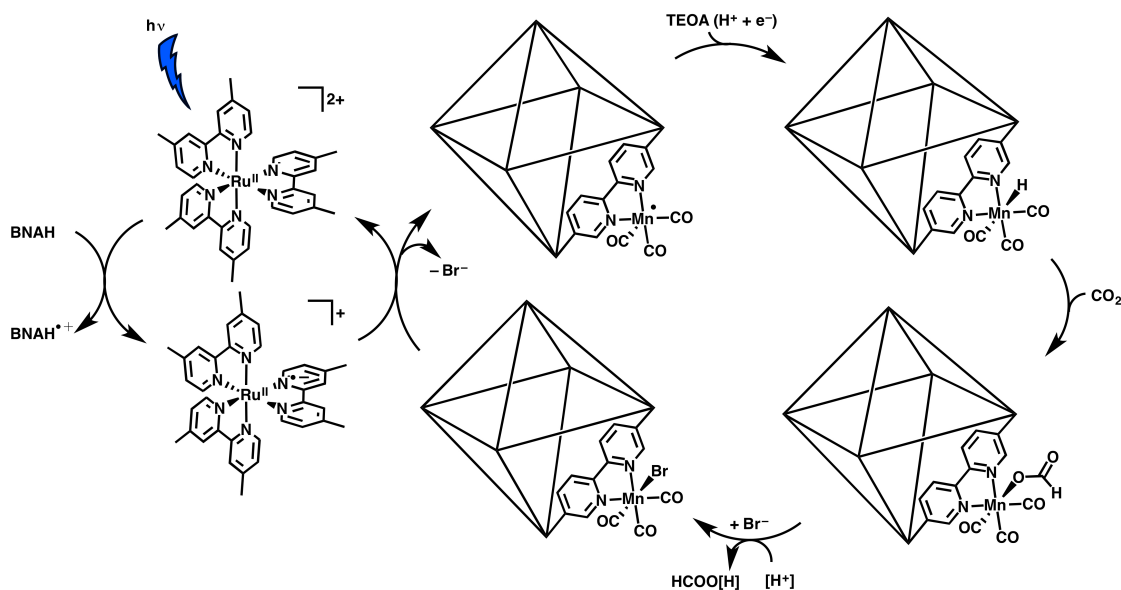
Figure 7.4 Proposed mechanism for the formation of formate from the photocatalytic reaction with UiO-67-Mn(bpy)(CO)₃Br.

With respect to the mechanism of photocatalysis, upon a photo-induced one-electron reduction of $Mn(bpy)(CO)_3Br$, the Mn–Mn dimer, $[Mn(bpy)(CO)_3]_2$, is rapidly formed.[34-36] Bourrez et al. have identified this Mn–Mn dimer as an active catalyst for electrocatalytic CO_2 reduction to CO.[40] During visible-light irradiation, the Ru photosensitizer is selectively photoexcited, and the excited state of $[Ru(dmb)_3]^{2+}$ is reductively quenched by BNAH to give $[Ru(dmb)_2(dmb^-)]^+$. This reduced Ru complex has sufficient reducing power to transfer one electron to $Mn(bpy)(CO)_3Br$,[41] which immediately forms the Mn–Mn dimer upon reduction. Takeda et al. suggested that the active catalyst for photochemical CO_2 reduction was a monomeric Mn radical species, citing evidence from UV-Vis, FTIR, and ^1H NMR experiments.[41] Additionally, photoexcitation of similar Mn–Mn dimers, such as $[(CO)_2(bpy)Mn–Mn(CO)_5]$, efficiently induced cleavage of the Mn–Mn bond to the corresponding Mn radical species.[60-62] Indeed, if a monomeric Mn radical species is the active catalyst for photochemical CO_2 reduction to formate, then the framework of UiO-67-$Mn(bpy)(CO)_3Br$ sufficiently eliminates dimerization prior to formation of the active catalyst, which as a result significantly enhances the efficiency for photochemical CO_2 reduction. Because the Mn sites in UiO-67-$Mn(bpy)(CO)_3Br$ cannot dimerize upon one-electron reduction and UiO-67-$Mn(bpy)(CO)_3Br$ operates as an efficient photocatalyst, the active catalyst for CO_2 reduction to formate is likely a monomeric species.

In order to further gauge the ability of the external UiO-67 framework to enhance the stability of the Mn catalyst, catalyst recyclability studies were performed

using UiO-67-Mn(bpy)(CO)$_3$Br (Table 7.1, entries 3–5). In these studies, the MOF was recovered by decanting off the reaction mixture, washing the MOF with acetone, and drying the MOF under vacuum before being used in a new photocatalytic experiment. Significant TONs for formate were detected after three consecutive 4 h photocatalytic runs. More specifically, UiO-67-Mn(bpy)(CO)$_3$Br retained ~48%, ~38%, and ~34% activity after one, two, and three 4 h experiments, respectively. Post-catalysis FTIR of MOFs after one catalytic cycle indicates that a significant loss of the Mn(CO)$_3$ complex residing in the framework, with only ~37% of Mn complexes remaining (Figure 7.2b). Post-catalysis PXRD indicates that crystallinity is largely retained after the first 4 h run (Figure 7.2a). The persistence of some Mn active sites residing in UiO-67-Mn(bpy)(CO)$_3$Br was also confirmed using ICP-OES, with the atomic ratio of Zr:Mn decreasing only from 1:0.376 to 1:0.361 after one 4 h experiment. Therefore, the reduced photochemical performance over a few catalytic cycles is likely due to loss of the Mn(CO)$_3$ moiety in the framework, resulting from both prolonged irradiation by visible light and prolonged exposure to the alkaline photochemical solution. This is also confirmed by the post-catalysis characterization of UiO-67-Mn(bpy)(CO)$_3$Br after four catalytic cycles. After these four cycles, a large portion of the MOF solid was degraded and dissolved in the alkaline photocatalytic solution. At this time, FTIR indicated the negligible survival of the Mn(CO)$_3$ moiety in the MOF framework (Figure 7.8), and ICP-OES gave a Zr:Mn ratio of 1:0.324. This data indicates that the main sources for loss of catalytic activity

for each consecutive photocatalytic cycle are both the loss of CO ligands from the Mn catalytic sites and degradation of the MOF framework.

7.3 Conclusions

We employed PSM as a mild functionalization technique to incorporate an earth-abundant, but thermally unstable molecular photocatalyst for CO_2 reduction into a robust MOF platform. The resulting UiO-67-Mn(bpy)(CO)$_3$Br combines the efficient photochemical performance of Mn active sites with the enhanced stability of the solid-state MOF host. This Mn-incorporated MOF functions as a highly efficient CO_2 reduction catalyst under visible-light irradiation. The overall TON and selectivity of CO_2 reduction to formate for this Mn-incorporated MOF exceeds not only the homogeneous reference systems, but also many precious-metal-based MOF photocatalysts (Table 7.2). Using UiO-67-Mn(bpy)(CO)$_3$Br, TONs for formate reached 50 and 110 over 4 and 18 h, respectively, displaying a selectivity of 96% over 4 h. The robust nature of the Zr(IV)-based MOFs and hence isolation of the molecular catalytic sites inhibits dimerization of the singly-reduced Mn catalyst, enabling some (albeit, low) degree of reusability over three catalytic cycles. Due to the low degree of recyclability achieved in this Mn-functionalized MOF, future studies will be focused on exploring other, more stable MOFs and other porous materials as supports for these Mn catalysts. Additionally, future studies will include varying photocatalytic conditions to increase the stability of the Mn–MOF and investigating the use of different photosensitizers in order to isolate the catalytic activity of only the Mn–

MOF. We will also explore developing thin films of these Mn–MOFs in order to utilize this heterogeneous Mn catalyst for electrochemical CO_2 reduction. These findings open up new opportunities for artificial photosynthesis by immobilizing and protecting molecular catalysts in MOFs, thus enhancing their performance for photocatalysis.

7.4   Experimental

General Methods. Starting materials and solvents were purchased and used without further purification from commercial suppliers (Sigma-Aldrich, Alfa Aesar, EMD, TCI, Cambridge Isotope Laboratories, Inc., and others). DMF and TEOA were dried over 3 Å molecular sieves and stored under dry N_2 prior to use. Proton nuclear magnetic resonance spectra (^{1}H NMR) were recorded on a Varian FT-NMR spectrometer (400 MHz). Chemical shifts were quoted in parts per million (ppm) referenced to the appropriate solvent peak or 0 ppm for TMS. NMR spectra for photocatalysis product analysis were recorded on a Varian 300 MHz spectrometer at 198 K, and data were processed using Bruker TopSpin software. ESI-MS was performed using a ThermoFinnigan LCQ-DECA mass spectrometer, and the data was analyzed using the Xcalibur software suite. Inductively-coupled plasma-optical emission spectroscopy (ICP-OES) was performed by Intertek USA, Inc. (Whitehouse, NJ). Mn(bpy)(CO)$_3$Br[63-64] and [Ru(dmb)$_3$](PF$_6$)$_2$ were prepared as previously reported.[65]

Synthesis of UiO-67-bpydc. ZrCl$_4$ (24.5 mg, 0.105 mmol), glacial acetic acid (189 mg, 3.15 mmol), biphenyl-4,4′-dicarboxylic acid (H$_2$bpdc, 13 mg, 0.053 mmol), and 2,2′-bipyridine-5,5′-dicarboxylic acid (H$_2$bpydc, 13 mg, 0.053 mmol) were placed in a scintillation vial with 4 mL *N,N′*-dimethylformamide (DMF). The solids were dispersed via sonication for ~10 min, followed by incubation at 120 °C for 24 h. After cooling, the solids were isolated via centrifugation at 6,000 rpm for 15 min using a fixed angle rotor, and the solvent was decanted. The solids were washed with DMF (2×10 mL), followed by soaking in methanol (MeOH) for 3 d, and the solution was exchanged with fresh MeOH (10 mL) every 24 h. After 3 d of soaking, the solids were collected via centrifugation and dried under vacuum. Yield: 33 mg (88% based on Zr).

Synthesis of UiO-67-Mn(bpy)(CO)$_3$Br. Bromopentacarbonylmanganese(I) (Mn(CO)$_5$Br, 14.1 mg, 0.05 mmol) was dissolved in 6 mL diethyl ether (Et$_2$O). UiO-66-bpydc (30 mg, 0.042 mmol equiv. bpydc) was added to this Mn solution. The solids were dispersed via sonication for ~10 min, then incubated at room temperature for 24 h. After 24 h, the solids were isolated via centrifugation and the red solids were washed profusely with Et$_2$O (3×10 mL), until the supernatant was colorless. The solids were left to soak in MeOH for 3 d, and the solution was exchanged with fresh MeOH (10 mL) every 24 h. After 3 d of soaking, the solids were collected via centrifugation and dried under vacuum (yield: *ca.* 99%). Due to light-sensitive nature of Mn complex, the MOF incubation, washing, and drying steps were performed with minimal exposure to ambient light.

Synthesis of Mn(bpydc)(CO)$_3$Br.   The synthesis of Mn(bpydc)(CO)$_3$Br was performed with a slight modification to literature procedures.[66]   Mn(CO)$_5$Br (200 mg, 2.17 mmol) was added to a N$_2$ sparged round-bottom flask containing 20 mL Et$_2$O. The flask was covered in foil to shield it from ambient light.   The H$_2$bpydc ligand (212 mg, 2.17 mmol) was added to the mixture, and the reaction was heated to reflux. After 3 h, the reaction mixture was allowed to cool to room temperature, and then the reaction flask was placed in a freezer for 2 h.   After this time, a dark red solid was collected via vacuum filtration and dried under vacuum overnight.   All spectroscopic characterization matched previous reports[66] and was consistent with the structure of the complex.   Yield: 483 mg (48%).

Photocatalysis.   Photochemical reactions were performed in 36-mL quartz cell (NSG Precision Cell, Inc.; pathlength = 2 cm) equipped with a rubber septum (Figure 7.6).   All experiments were performed in a DMF/TEOA solvent mixture (4:1 v/v, 20 mL total) containing 0.5 mM Mn catalyst, 0.5 mM [Ru(dmb)$_3$](PF$_6$)$_2$ as a photosensitizer, 0.2 M BNAH as a sacrificial reductant.   Each photochemical solution was sparged with dry N$_2$ for 5 min followed by dry CO$_2$ for 15 min prior to irradiation. N$_2$ and CO$_2$ gases were run through custom Drierite/molecular sieves (3 Å) drying columns before use.   The photochemical cell was irradiated with a 470 nm LED (ThorLabs, Inc.), and the photochemical solutions were constantly stirred throughout each experiment.   The light intensity was calculated to be 2.51×10^{-7} einstein/s, as determined by actinometry.[67]   For recyclability studies, the photocatalytic solution was decanted, washed with acetone five times (decanted after each wash), and then dried

under vacuum overnight to yield the post-catalysis UiO-67-Mn(bpy)(CO)$_3$Br solid. This retained solid was recycled for additional photocatalytic experiments.

Product Analysis from Photocatalysis. The headspace of the photochemical cell was analyzed for CO and H$_2$ products after each experiment. Gas analyses were performed using a 1-mL sample injection on a Hewlett-Packard 7890A Series gas chromatograph with two molsieve columns (30 m×0.53 mm ID×25 μm film). Each 1-mL injection was split between two columns, one with N$_2$ and one with He as the carrier gas, in order to quantify both CO and H$_2$ simultaneously in each run. Gas chromatography calibration curves were made by sampling known volumes of CO and H$_2$ gas. All photochemical solutions were analyzed for organic products via ^{1}H NMR after the following workup: a known concentration of ferrocene (typically ~5–8 mg), used as an internal standard, was added to a 5-mL aliquot of the irradiated solution, and the solution was sonicated for 10 min. A 0.8-mL aliquot of the resulting solution was added to a 2-mL volumetric flask containing 0.1 mmol of Verkade's base (2,8,9-triisobutyl-2,5,8,9-tetraaza-1-phosphabicyclo[3.3.3]undecane). The solution was diluted to 2 mL with CD$_3$CN, and the resulting solution was sonicated for 10 min. Three NMR samples were made from this solution, and each NMR sample was run for 128 scans on a Varian 300 MHz spectrometer at 198 K. The formate chemical shift (δ = ~8.50 ppm) was integrated against the ferrocene chemical shift (δ = ~4.14 ppm). Standard formate samples were prepared using the same procedure, starting with a non-irradiated, 20-mL sample of the following: a known concentration of formic acid, 0.5 mM Mn(bpy)(CO)$_3$Br, 0.5 mM [Ru(dmb)$_3$](PF$_6$)$_2$, 0.2 M BNAH, 4:1 DMF:TEOA

(v/v). Upon basic work-up with Verkade's base and addition of a known concentration of ferrocene, ^{1}H NMR samples were used to create a calibration curve. The integration values for the formate chemical shift and the ferrocene chemical shift were used to calculate the [formate] in the NMR samples and, after back calculating, the [formate] in the photochemical solution. Blank NMR samples of non-irradiated, CO_2-saturated photochemical solutions showed no detectable production of formate, indicating that the Verkade's base does not produce formate in a solution of CO_2. Representative ^{1}H NMR spectra for formate production are shown in Figure 7.7.

Powder X-ray Diffraction Analysis. ~20-30 mg of UiO-67 samples were dried under vacuum prior to PXRD analysis. PXRD data were collected at ambient temperature on a Bruker D8 Advance diffractometer at 40 kV, 40 mA for Cu Kα (λ= 1.5418 Å), with a scan speed of 1 sec/step, a step size of 0.02° in 2θ, and a 2θ range of ~5 to 40° (sample dependent). The experimental backgrounds were corrected using Jade 5.0 software package.

Digestion and Analysis by ^{1}H NMR. ~10 mg of UiO-67 material was dried under vacuum and digested with sonication in 595 µL DMSO-d_6 and 5 µL of 40% HF.

BET Surface Area Analysis. ~50 mg of UiO-67 sample was evacuated on a vacuum line overnight at room temperature. The sample was then transferred to a pre-weighed sample tube and degassed at 30 °C on an Micromeritics ASAP 2020 Adsorption Analyzer for a minimum of 12 h or until the outgas rate was <5 mm Hg. The sample tube was re-weighed to obtain a consistent mass for the degassed exchanged MOF. BET surface area (m^2/g) measurements were collected at 77 K by

N_2 on a Micromeritics ASAP 2020 Adsorption Analyzer using the volumetric technique. The sample was then manually degassed on the analysis port at 30 °C for approximately 6 h. N_2 sorption isotherms were collected at 77 K.

Thermogravimetric Analysis. ~10-15 mg of UiO-67 sample was used for TGA measurements, after BET analysis (activated samples). Samples were analyzed under a stream of N_2 using a TA Instrument Q600 SDT running from room temperature to 800 °C with a scan rate of 5 °C/min.

Scanning Electron Microscopy-Energy Dispersed X-ray Spectroscopy. ~2-5 mg of activated UiO-67 materials was transferred to conductive carbon tape on a sample holder disk, and coated using a Cr-sputter coating for 8 sec. A Philips XL ESEM instrument was used for acquiring images using a 10 kV energy source under vacuum. Oxford EDX and Inca software are attached to determine elemental mapping of particle surfaces at a working distance at 10 mm. ~19000× magnification images were collected.

Fourier-transformed Infrared Spectroscopy. ~5 mg of UiO-67 samples were dried under vacuum prior to FTIR analysis. FTIR data were collected at ambient temperature on a Bruker ALPHA FTIR Spectrometer from 4000 cm^{-1} and 450 cm^{-1}. The experimental backgrounds were corrected using OPUS software package.

0572). I would like to thank Dr. Honghan Fei, Dr. Yeob Lee, and Professor Seth M. Cohen for a highly productive collaboration on this work.

Much of the material for this chapter comes directly from a manuscript entitled: "Photocatalytic CO_2 Reduction to Formate Using a Mn(I) Molecular Catalyst in a Robust Metal-Organic Framework" by Honghan Fei, Matthew D. Sampson, Yeob Lee, Clifford P. Kubiak, and Seth M. Cohen, which has been published in *Inorg. Chem.*, **2015**, 54, 6821–6828. http://dx.doi.org/10.1021/acs.inorgchem.5b00752. The dissertation author is a primary co-author of this manuscript.

7.5   References

(1) Devens, G.; Moore, T. A.; Moore, A. L. *Acc. Chem. Res.* **2009**, 42, 1890-1898.

(2) Morris, A. J.; Meyer, G. J.; Fujita, E. *Acc. Chem. Res.* **2009**, 42, 1983-1994.

(3) Morimoto, T.; Nishiura, C.; Tanaka, M.; Rohacova, J.; Nakagawa, Y.; Funada, Y.; Koike, K.; Yamamoto, Y.; Shishido, S.; Kojima, T.; Saeki, T.; Ozeki, T.; Ishitani, O. *J. Am. Chem. Soc.* **2013**, 135, 13266-13269.

(4) Tanaka, K.; Ooyama, D. *Coord. Chem. Rev.* **2002**, 226, 211-218.

(5) Benson, E. E.; Kubiak, C. P.; Sathrum, A. J.; Smieja, J. M. *Chem. Soc. Rev.* **2009**, 38, 89-99.

(6) Sato, S.; Morikawa, T.; Saeki, S.; Kajino, T.; Motohiro, T. *Angew. Chem., Int. Ed.* **2010**, 49, 5101-5105.

(7) Thoi, V. S.; Chang, C. J. *Chem. Commun.* **2011**, 47, 6578-6580.

(8) Kudo, A.; Miseki, Y. *Chem. Soc. Rev.* **2009**, 38, 253-278.

(9) Qu, Y.; Duan, X. *Chem. Soc. Rev.* **2013**, 42, 2568-2580.

(10) Eddaoudi, M.; Sava, D. F.; Eubank, J. F.; Adil, K.; Guillerm, V. *Chem. Soc. Rev.* **2015**, 44, 228-249.

(11) Sumida, K.; Rogow, D. L.; Mason, J. A.; McDonald, T. M.; Bloch, E. D.; Herm, Z. R.; Bae, T.-H.; Long, J. R. *Chem. Rev.* **2012**, 112, 724-781.

(12) Suh, M. P.; Park, K. S.; Prasad, T. K.; Lim, D. *Chem. Rev.* **2012**, 112, 782-835.

(13) Liu, J.; Chen, L.; Cui, H.; Zhang, J.; Zhang, L.; Su, C.-Y. *Chem. Soc. Rev.* **2014**, 43, 6011-6061.

(14) Yoon, M.; Srirambalaji, R.; Kim, K. *Chem. Rev.* **2012**, 112, 1196-1231.

(15) Van de Voorde, B.; Bueken, B.; Denayer, J.; De Vos, D. *Chem. Soc. Rev.* **2014**, 43, 5766-5788.

(16) Kreno, L. E.; Leong, K.; Farha, O. K.; Allendorf, M.; Van Duyne, R. P.; Hupp, J. T. *Chem. Rev.* **2012**, 112, 1105-1125.

(17) Horcajada, P.; Gref, R.; Baati, T.; Allan, P. K.; Maurin, G.; Couvreur, P.; Ferey, G.; Morris, R. E.; Serre, C. *Chem. Rev.* **2012**, 112, 1232-1268.

(18) Zhang, T.; Lin, W. *Chem. Soc. Rev.* **2014**, 43, 5982-5993.

(19) Wang, J.-L.; Wang, C.; Lin, W. *ACS Catal.* **2012**, 2, 2630-2640.

(20) Kataoka, Y.; Sato, K.; Miyazaki, Y.; Masuda, K.; Tanaka, H.; Naito, S.; Mori, W. *Energy Environ. Sci.* **2009**, 2, 397-400.

(21) Fateeva, A.; Chater, P. A.; Ireland, C. P.; Tahir, A. A.; Khimyak, Y. Z.; Wiper, P. V.; Darwent, J. R.; Rosseinsky, M. J. *Angew. Chem., Int. Ed.* **2012**, 51, 7440-7444.

(22) Pullen, S.; Fei, H.; Orthaber, A.; Cohen, S. M.; Ott, S. *J. Am. Chem. Soc.* **2013**, 135, 16997-17003.

(23) Wang, C.; deKrafft, K. E.; Lin, W. *J. Am. Chem. Soc.* **2012**, 134, 7211-7214.

(24) Sasan, K.; Lin, Q.; Mao, C.; Feng, P. *Chem. Commun.* **2014**, 50, 10390-10393.

(25) Nasalevich, M. A.; Becker, R.; Ramos-Fernandez, E. V.; Castellanos, S.; Veber, S. L.; Fedin, M. V.; Kapteijn, F.; Reek, J. N. H.; van de Vlugt, J. I.; Gascon, J. *Energy Environ. Sci.* **2015**, 8, 364-375.

(26) Zhou, T.; Du, Y.; Borgna, A.; Hong, J.; Wang, Y.; Han, J.; Zhang, W.; Xu, R. *Energy Environ. Sci.* **2013**, 6, 3229-3234.

(27) Wang, C.; Xie, Z.; deKrafft, K. E.; Lin, W. *J. Am. Chem. Soc.* **2011**, 133, 13445-13454.

(28) Wang, C.; Wang, J.-L.; Lin, W. *J. Am. Chem. Soc.* **2012**, 134, 19895-19908.

(29) Nepal, B.; Das, S. *Angew. Chem., Int. Ed.* **2013**, 52, 7224-7227.

(30) Fu, Y.; Sun, D.; Chen, Y.; Huang, R.; Ding, Z.; Fu, X.; Li, Z. *Angew. Chem., Int. Ed.* **2012**, 51, 3364-3367.

(31) Sun, D.; Fu, Y.; Liu, W.; Ye, L.; Wang, D.; Yang, L.; Fu, X.; Li, Z. *Chem. Eur. J.* **2013**, 19, 14279-14285.

(32) Lee, Y.; Kim, S.; Kang, J. K.; Cohen, S. M. *Chem. Commun.* **2015**, 51, 16549-16552.

(33) Wang, S.; Yao, W.; Lin, J.; Ding, Z.; Wang, X. *Angew. Chem., Int. Ed.* **2014**, 53, 1034-1038.

(34) Sampson, M. D.; Nguyen, A. D.; Grice, K. A.; Moore, C. E.; Rheingold, A. L.; Kubiak, C. P. *J. Am. Chem. Soc.* **2014**, 136, 5460-5471.

(35) Smieja, J. M.; Sampson, M. D.; Grice, K. A.; Benson, E. E.; Froehlich, J. D.; Kubiak, C. P. *Inorg. Chem.* **2013**, 52, 2484-2491.

(36) Bourrez, M.; Molton, F.; Chardon-Noblat, S.; Deronzier, A. *Angew. Chem., Int. Ed.* **2011**, 123, 10077-10080.

(37) Grice, K. A.; Kubiak, C. P. In *Adv. Inorg. Chem.*; Michele, A., Rudi van, E., Eds.; Academic Press: **2014**; Vol. Volume 66, p 163-188.

(38) Franco, F.; Cometto, C.; Ferrero Vallana, F.; Sordello, F.; Priola, E.; Minero, C.; Nervi, C.; Gobetto, R. *Chem. Commun.* **2014**, 50, 14670-14673.

(39) Walsh, J. J.; Neri, G.; Smith, C. L.; Cowan, A. J. *Chem. Commun.* **2014**, 50, 12698-12701.

(40) Bourrez, M.; Orio, M.; Molton, F.; Vezin, H.; Duboc, C.; Deronzier, A.; Chardon-Noblat, S. *Angew. Chem., Int. Ed.* **2014**, 53, 240-243.

(41) Takeda, H.; Koizumi, H.; Okamoto, K.; Ishitani, O. *Chem. Commun.* **2014**, 50, 1491-1493.

(42) Cavka, J. H.; Jakobsen, S.; Olsbye, U.; Guillou, N.; Lamberti, C.; Bordiga, S.; Lillerud, K. P. *J. Am. Chem. Soc.* **2008**, 130, 13850-13851.

(43) Fei, H.; Cohen, S. M. *Chem. Commun.* **2014**, 50, 4810-4812.

(44) Cohen, S. M. *Chem. Rev.* **2012**, 112, 970-1000.

(45) Bloch, E. D.; Britt, D.; Lee, C.; Doonan, C. J.; Uribe-Romo, F. J.; Furukwa, H.; Long, J. R.; Yaghi, O. M. *J. Am. Chem. Soc.* **2010**, 132, 14382-14384.

(46) Carson, F.; Agrawal, S.; Gustafsson, M.; Bartoszewicz, A.; Moraga, F.; Zou, X.; Martin-Matute, B. *Chem. Eur. J.* **2012**, 18, 15337-15344.

(47) Manna, K.; Zhang, T.; Lin, W. *J. Am. Chem. Soc.* **2014**, 136, 6566-6569.

(48) Wang, B.; Huang, H.; Lv, X.-L.; Xie, Y.; Li, M.; Li, J.-R. *Inorg. Chem.* **2014**, 53, 9254-9259.

(49) Ko, N.; Hong, J.; Sung, S.; Cordova, K. E.; Park, H. J.; Yang, J. K.; Kim, J. *Dalton Trans.* **2015**, 44, 2047-2051.

(50) Katz, M. J.; Brown, Z. J.; Colon, Y. J.; Siu, P. W.; Scheidt, K. A.; Snurr, R. Q.; Hupp, J. T.; Farha, O. K. *Chem. Commun.* **2013**, 49, 9449-9451.

(51) Georgopoulos, M.; Hoffman, M. Z. *J. Phys. Chem.* **1991**, 95, 7717-7721.

(52) Morimoto, T.; Nakajima, T.; Sawa, S.; Nakanishi, R.; Imori, D.; Ishitani, O. *J. Am. Chem. Soc.* **2013**, 135, 16825-16828.

(53) Hawecker, J.; Lehn, J.-M.; Ziessel, R. *J. Chem. Soc., Chem. Commun.* **1983**, 536-538.

(54) Hori, H.; Takano, Y.; Koike, K.; Sasaki, Y. *Inorg. Chem. Commun.* **2003**, 6, 300-303.

(55) Shinozaki, K.; Hayashi, Y.; Brunschwig, B.; Fujita, E. *Res. Chem. Intermediat.* **2007**, 33, 27-36.

(56) Fujita, E.; Hayashi, Y.; Kita, S.; Brunschwig, B. S. *Stud. Surf. Sci. Catal.* **2004**, 153, 271-276.

(57) Agarwal, J.; Johnson, R. P.; Li, G. *J. Phys. Chem. A* **2011**, 115, 2877-2881.

(58) Hayashi, Y.; Kita, S.; Brunschwig, B. S.; Fujita, E. *J. Am. Chem. Soc.* **2003**, 125, 11976-11987.

(59) Hawecker, J.; Lehn, J.-M.; Ziessel, R. *Chem. Commun.* **1985**, 56-58.

(60) Meyer, T. J.; Caspar, J. V. *Chem. Rev.* **1985**, 85, 187-218.

(61) Allen, D. M.; Cox, A.; Kemp, T. J.; Sultana, Q.; Pitts, R. B. *J. Chem. Soc. Dalton Trans.* **1976**, 1189-1193.

(62) Van de Graaf, T.; Hofstra, R. M. J.; Schilder, P. G. M.; Rijkhoff, M.; Stufkens, D. J.; Van de Linden, J. G. M. *Organometallics* **1991**, 10, 3668-3679.

(63) Bourrez, M.; Molton, F.; Chardon-Noblat, S.; Deronzier, A. *Angew. Chem., Int. Ed.* **2011**, 50, 9903-9906.

(64) Staal, L. H.; Oskam, A.; Vrieze, K. *J. Organomet. Chem.* **1979**, 170, 235-245.

(65) Sullivan, B. P.; Salmon, D. J.; Meyer, T. J. *Inorg. Chem.* **1978**, 17, 3334-3341.

(66) Blake, A. J.; Champness, N. R.; Easun, T. L.; Allan, D. R.; Nowell, H.; George, M. W.; Jia, J.; Sun, X.-Z. *Nat Chem* **2010**, 2, 688-694.

(67) Hatchard, C. G.; Parker, C. A. *Proc. R. Soc. Lond., Ser. A* **1956**, 235, 518-536.

(68) Li, L.; Zhang, S.; Xu, L.; Wang, J.; Shi, L.-X.; Chen, Z.-N.; Hong, M.; Luo, J. *Chem. Sci.* **2014**, 5, 3808-3813.

(69) Sun, D.; Gao, Y.; Fu, J.; Zeng, X.; Chen, Z.; Li, Z. *Chem. Commun.* **2015**, 51, 2645-2648.

7.6   Appendix
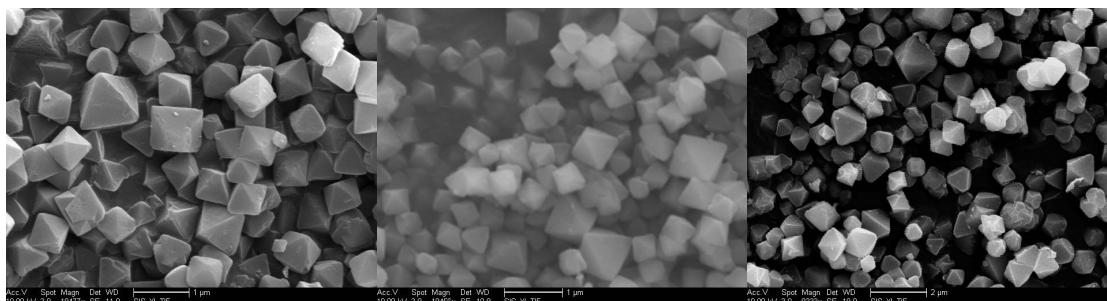
Figure 7.5 FE-SEM of UiO-67-bpydc (left), UiO-67-Mn(bpy)(CO)$_3$Br (middle), and UiO-67-Mn(bpy)(CO)$_3$Br after one catalytic run (right).
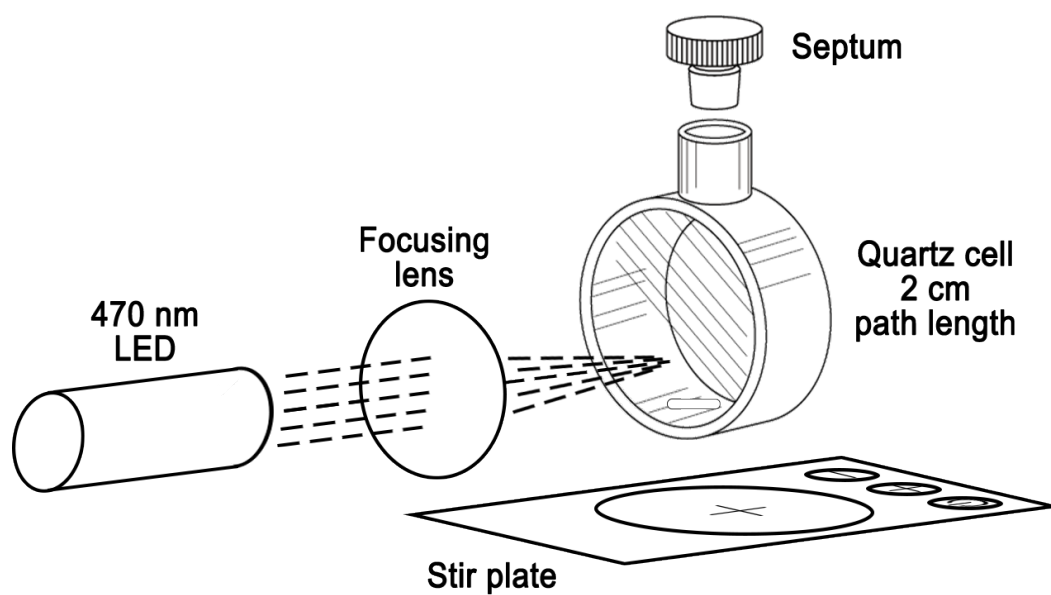
Figure 7.6 Simplified schematic of the photocatalysis setup for all reactions.
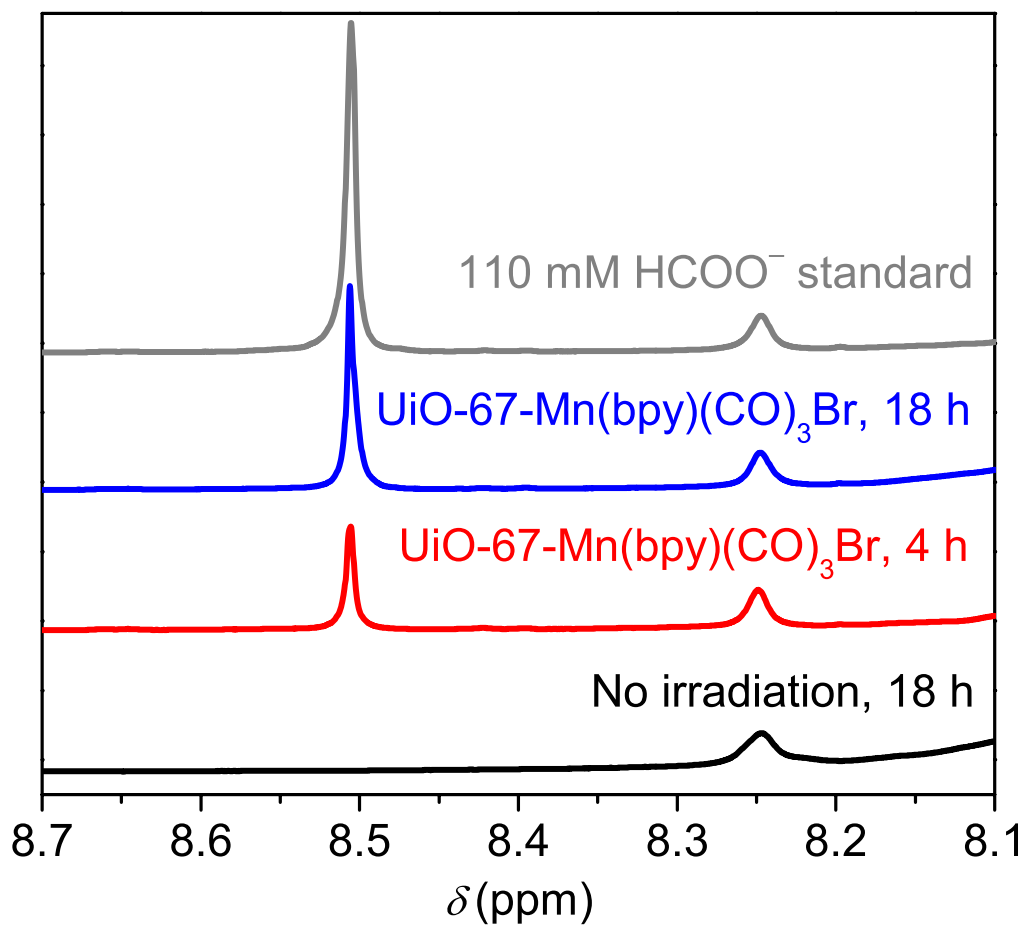
Figure 7.7 Example ^{1}H NMR spectra for formate production analysis after workup for the following photocatalysis samples: UiO-67-Mn(bpy)(CO)$_3$Br after 18 h without irradiation (black), UiO-67-Mn(bpy)(CO)$_3$Br after 4 h of irradiation (red), UiO-67-Mn(bpy)(CO)$_3$Br after 18 h of irradiation (blue), and UiO-67-Mn(bpy)(CO)$_3$Br with 110 mM formic acid added before basic workup (grey).
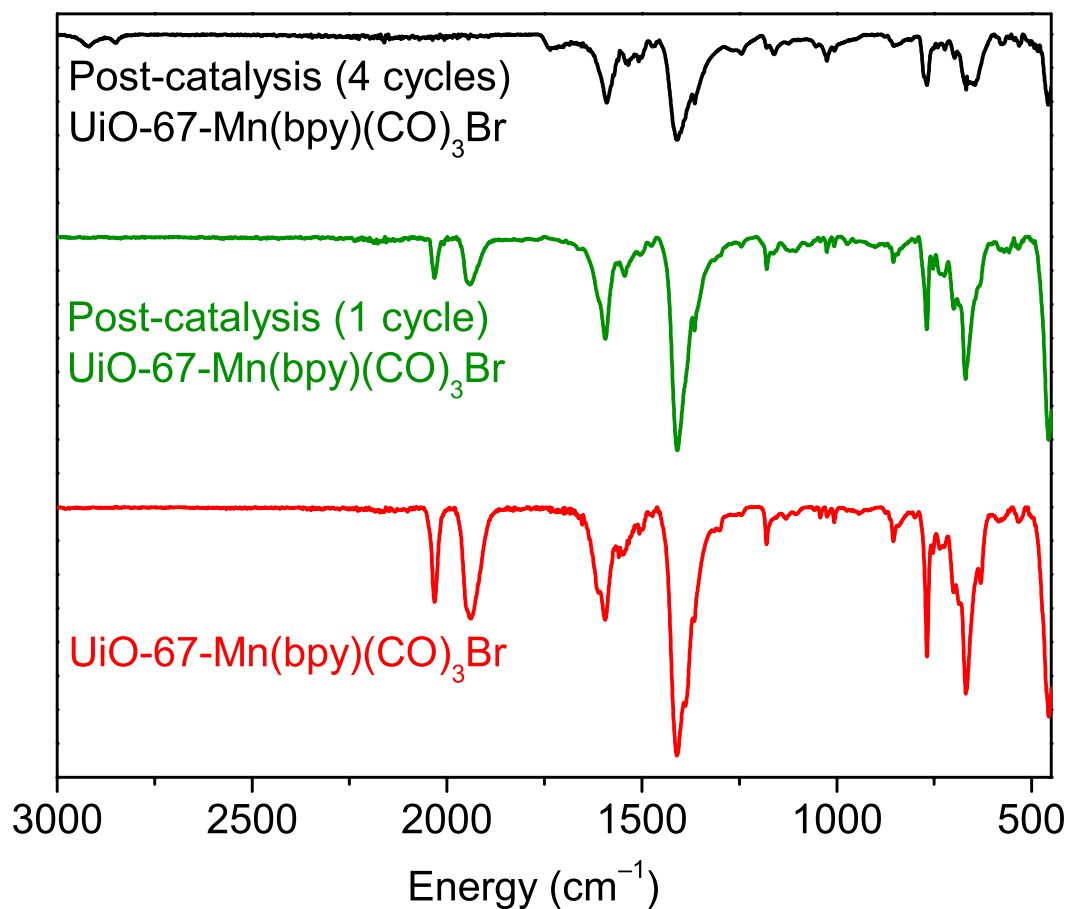
Figure 7.8 Post-catalysis FTIR characterization of Mn-MOF samples before catalysis (red), after one 4 h catalytic cycle (green), and after four 4 h catalytic cycles (black). After four recycled catalytic runs, there is no detectable CO bands in the MOF framework, indicating that the Mn catalytic sites had lost all of their CO ligands at this time.

Table 7.2 List of MOFs used for photocatalytic CO_2 reduction.

Catalyst	Photo-sensitizer	Reductant	Product	TON	Selectivity	Recyclablity	TOF (h^{-1})	Reference
UiO-67-Re(bpydc)(CO)₃Cl	None	TEA	CO	5.0 (6 h) 11 (20 h)	91%	Decompose after two 6-h runs	0.8	27
MIL-125-NH₂(Ti)	None	TEOA	Formate	<1 (10 h)	N/A	N/A	0.04	30
UiO-66-NH₂(Zr)	None	TEOA	Formate	<1 (10 h)	N/A	N/A	0.01	31
Y[Ir(ppy)₂(dcbpy)]₂[OH]	Ir(ppy)₂(dcbpy)	TEOA	Formate	<1 (10 h)	N/A	Active for five 6-h runs	0.1	68
MOF-253-Ru(CO)₂Cl₂	Ru(bpy)₂Cl₂	TEOA	Formate	36 (8 h)	65%	N/A	9.0	69
Co-ZIF-9	[Ru(bpy)₃]Cl₂	TEOA	CO	33 (0.5 h)	58%	Active for five 0.5-h runs	67	33
UiO-67-Mn(bpy)(CO)₃Br	[Ru(dmb)₃](PF₆)₂	BNAH	Formate	50 (4 h) 110 (18 h)	96%	Active for three 4-h runs	13	This work

Chapter 8

Towards competent, heterogenized molecular catalysts for electrochemical carbon dioxide reduction: Fe-porphyrin-based metal-organic framework films.

8.1 Introduction

For electrochemical CO_2 reduction, systems based on molecular catalysts in homogeneous solutions are mainly attractive for two reasons: (1) reaction intermediates are comparatively easy to spectroscopically characterize, thereby facilitating elucidation of the mechanistic details of the catalytic reaction, and (2) modulation of the catalyst structure to suit the appropriate catalytic process is

achievable in a straightforward manner through synthetic means. However, homogenous catalysts are only electro-activate at or near the surface of a conductive electrode. Heterogeneous electrocatalysis offers the possibility of overcoming this and other drawbacks often associated with homogenous electrocatalysis. Thus, the use of catalysts in heterogeneous form has the potential to eliminate deactivation processes such as dimerization or aggregation of the highly active catalyst species[1] (thereby increasing the lifetime of the catalytic system), provide better control of the chemical surroundings of the catalyst's active-site for improved performance,[2] and permit the use of solvents which otherwise could not be employed due to the catalyst's poor solubility.[3] Heterogenization additionally eliminates the possible problem, in a complete catalytic cell, of keeping the reduction catalyst away from the electrode where the corresponding oxidation half-reaction (for example, water to O_2) is occurring. (Contact with the anode holds the possibility of catalyst interference with the oxidation reaction, as well as oxidative degradation of the catalyst.)

Several examples of heterogeneous electrocatalytic CO_2 reduction systems, based, on immobilization of molecular catalysts on electrode surfaces, are known. The means of immobilization include covalent bonding of molecular monolayers,[4-5] non-covalent molecular attachment,[6-7] and surface polymerization of permeable, molecular catalyst multilayers.[8-12] In part due to the fact that planar electrode geometries are most often used, the amount (*i.e.* areal concentration) of heterogenized molecular catalysts has thus far been limited to *ca.* 10^{-12} mol/cm^2 (sub-monolayers) to 10^{-8} mol/cm^2 (multilayers, albeit of limited molecular-scale porosity or permeability). [4-8,13]

In an EC′ type of catalytic mechanism,[14] the first step is electron transfer (E) from the electrode to the catalyst, reducing it to its active form, which in turn chemically reacts (C′) with a substrate to form the reaction products. The magnitude of the steady state current density (and thus overall catalytic rate) for a given EC′ system (whether homogenous or heterogeneous), is governed by both the rate of the reaction of the substrate with the individual molecular catalyst and the active-catalyst concentration.[14-15] A key difference between catalytic heterogeneous (i.e., electrode-immobilized) and homogenous (i.e., solution dissolved) molecular systems is that the overall reaction kinetics for heterogeneous systems are not limited by the rate of diffusion of the catalyst toward the electrode; nor are overall rates in the heterogeneous case limited by catalyst solubility. Thus, for heterogeneous systems, enhancement of either the molecular-scale reaction rate or the active-catalyst areal concentration, may, in principle, lead to higher overall rates (greater catalytic current densities) at a given applied potential. (Note: Once a monolayer of molecular catalyst has been immobilized, further catalyst immobilization increases the areal concentration (2D concentration), but not the volumetric (i.e. molar) concentration.) It is clear, then, that a significant leap in catalytic performance may be anticipated if one can drastically increase the amount of stable, surface-bound catalyst.

With this notion in mind, we have realized the potential in employing metal-organic framework (MOF) thin films[16] as a high surface area platform to substantially boost the areal concentration of a molecular CO_2 reduction catalyst. In contrast to a densely packed polymerized film, a MOF creates an ordered, porous heterogeneous

network, which allows for free permeation of electrolyte counter ions and dissolved CO_2 into the interior of the film. [17-19] In order to realize our hypothesis, first the MOF should possess the ability to transport electrons from the current collector toward the electrocatalyst to drive the reaction. Several recent studies have established that charge transport can occur within MOF films, following the mechanism of either linker-to-linker[20-23] or shuttle-to-shuttle[24] electron/hole redox hopping. Consequently, a MOF having a redox-active molecular catalyst as a linker could constitute a candidate heterogeneous electrocatalytic system (An especially germane example is the recent work of Arhenholtz, *et al.*[20] involving the electrocatalytic degradation of carbon tetrachloride by the metallo-porphyrinic MOF, cobalt-PIZA-1[25]).

Here, we have used the well-known Fe-porphyrin CO_2 reduction catalyst as a test system, incorporating the porphyrin into a MOF as both a structural and functional element, with the MOF being deployed in a thin-film electrode-immobilized form. Iron porphyrin complexes have been extensively studied for electrocatalytic reduction of CO_2 to CO by Savéant and coworkers.[26-29] When dissolved in nominally non-aqueous solutions under inert atmosphere, three distinct reduction waves are observed in cyclic voltammetry (CV) measurements, corresponding to the Fe(III/II), Fe(II/I) and Fe(I/0) couples. Previous studies have shown that in CO_2-saturated solutions, the Fe(I/0) wave becomes enhanced and irreversible, typical of a catalytic process, indicating that the Fe(0)-porphyrin species is the active catalyst for CO_2 reduction. As shown in Figure 8.1, similar behavior was readily observed in our labs.
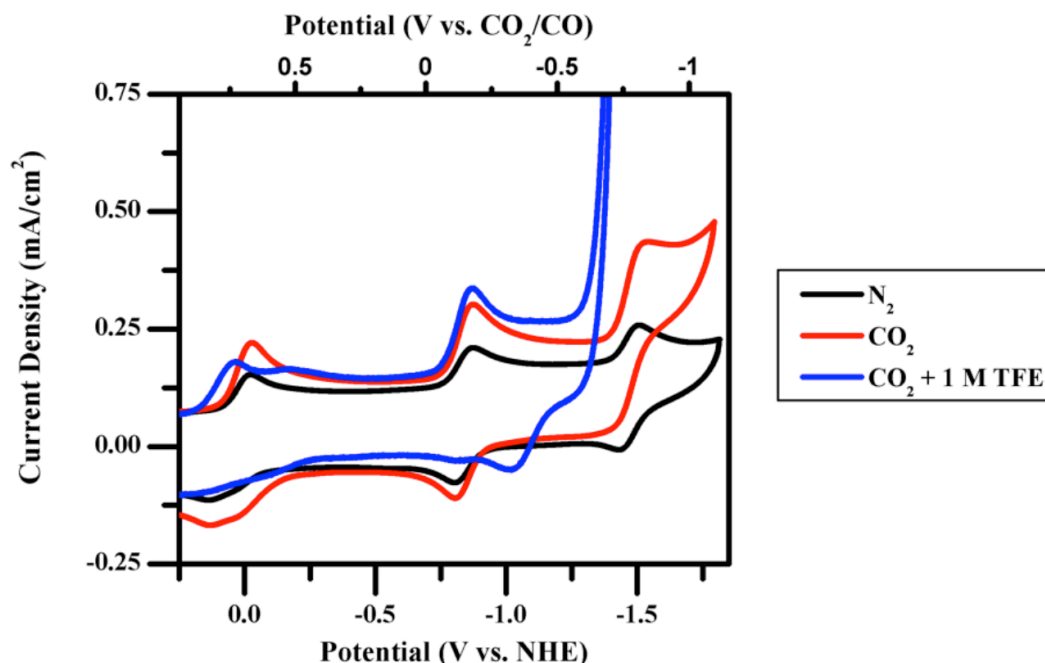
Figure 8.1 Cyclic voltammograms of homogeneous Fe-TPP (1 mM) in DMF (scan rate = 0.1 V/s). Comparison between N_2 (black) and CO_2 atmosphere, with no added proton source (red) and with 1 M added trifluoroethanol (TFE) proton source (blue).

Herein, we demonstrate the use of a thin film of Fe-porphyrin-based MOF-525[30-31] (Fe_MOF-525; Figure 8.2) as a platform for anchoring an unprecedented quantity of electro-active molecular catalyst on an electrode for electrochemical reduction of CO_2. We chose MOF-525 as the catalyst-immobilizer, in part because of its good molecular-scale porosity, but also because of its excellent chemical stability, an important requirement for an electrocatalytic assembly. (Superior chemical stability is a consequence of the use of hexa-zirconium(IV) nodes, together with carboxylate-based linker binding.[32-35]) Reductive potential step analysis of the Fe_MOF-525 film revealed an effective catalyst surface concentration three orders of magnitude higher than catalyst monolayer coverage and close to one order of magnitude higher than any previously reported loading for a heterogenized molecular CO_2 reduction catalyst. CV

measurements, under N_2 and CO_2, confirmed that the Fe-porphyrin linker of Fe_MOF-525 is responsible for electrocatalysis, with a catalytic wave evident at the potential of the Fe(I/0) couple. In addition, bulk electrolysis experiments showed sizable current densities, with mixtures of CO and H_2 as products.
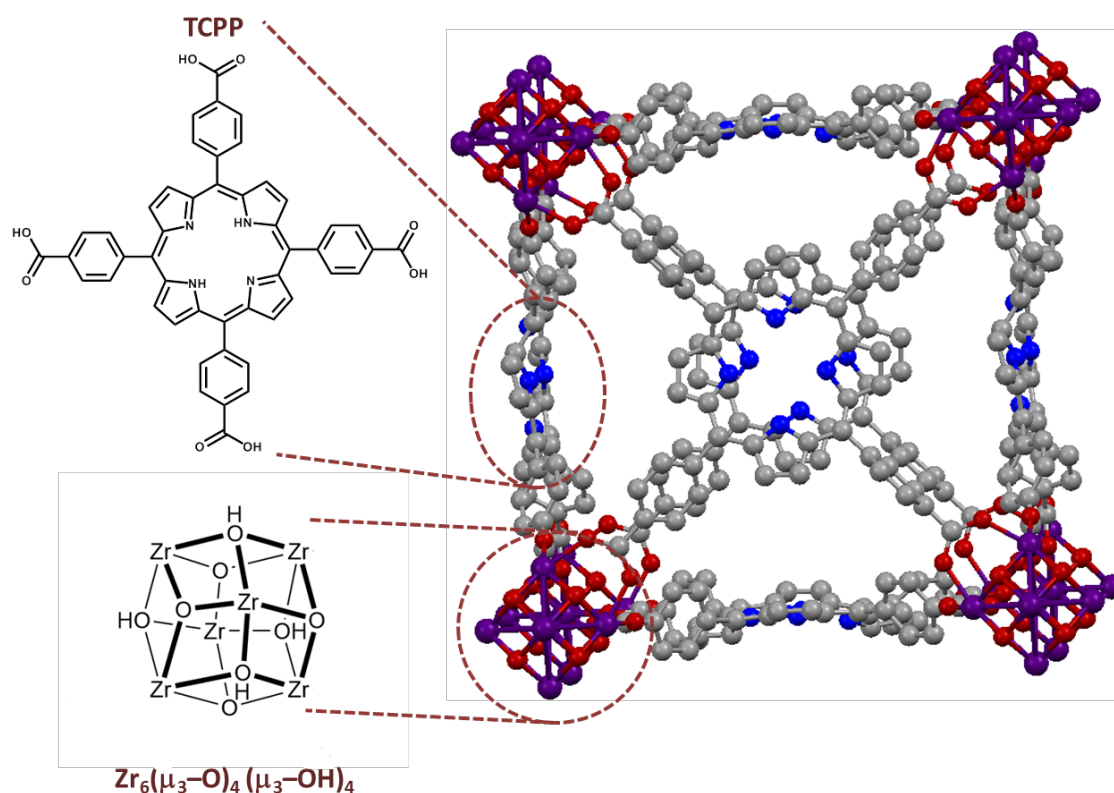
Figure 8.2 Illustration of the crystal structure of MOF-525 in porphyrin free-base form, including the chemical structure of the TCPP linker and the Zr_6-based node.

8.2   Results and Discussion

MOF Film Formation and Characterization. Microcrystalline MOF-525 particles were synthesized via a solvothermal route according to a previously reported procedure[31] (see Experimental section). The MOF contains TCPP (meso-tetra(4-carboxyphenyl)porphyrin) linkers and hexa-zirconium nodes, assembled to form

interconnected boxes (cubes; see Figure 8.2). Thin films of MOF-525 on FTO were then obtained from a toluene suspension of microcrystalline MOF powder via electrophoretic deposition (EPD).[21] The films were infiltrated with $FeCl_3$ solution, and the free-base porphyrin linkers reacted to give the desired Fe_MOF-525 films (see Figure 8.7). SEM images (Figure 8.3a) show that EPD-formed films consist of cubic particles of 300–500 nm size. PXRD measurements (Figure 8.3b) confirm that the films are composed of MOF-525. Energy dispersive X-ray spectroscopy (EDS) yielded a Zr_6 to Fe ratio of 1:2.8, which is equivalent to 93% metalation (see Figure 8.7b). EDS mapping measured across a single Fe_MOF-525 crystallite, revealed a uniform distribution of Fe (Figure 8.8).
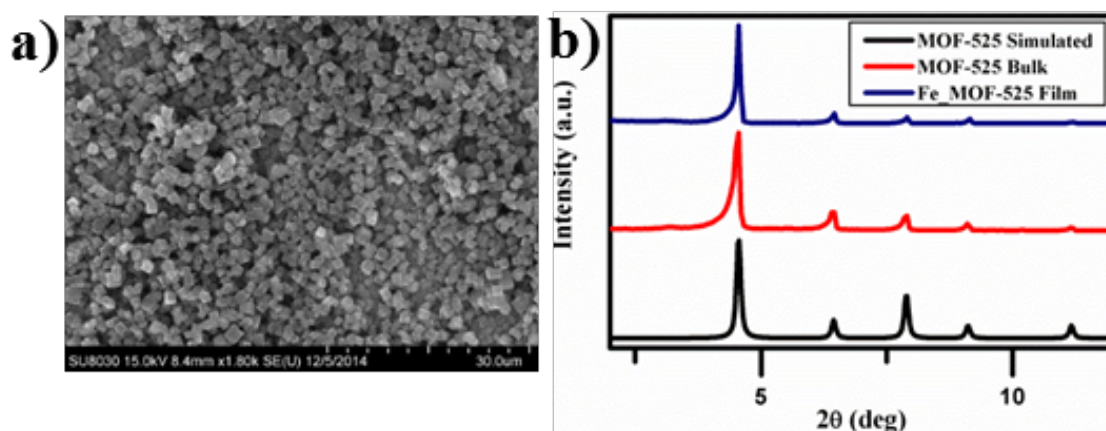
Figure 8.3 (a) Scanning electron microscopy image of a Fe_MOF-525 thin film, exhibiting the typical cubic morphology of MOF-525 (b) PXRD comparison between simulated, bulk powder, and thin film diffraction patterns. Upon film fabrication, the Fe_MOF-525 particles retain their crystal structure.

To assess the electroactivity of the prepared Fe_MOF-525 films, CV measurements were conducted in a 1 M $TBAPF_6$ acetonitrile solution under an N_2 atmosphere, with a standard 3-electrode configuration containing the Fe_MOF-525

film, Ag/AgCl (saturated KCl) electrode, and a Pt mesh as the working, reference, and counter electrodes respectively (Figure 8.4a). Scanning the electrochemical potential in the reductive direction, three distinct redox waves were observed, attributable to Fe(III/II) (E_f = –0.32 V vs. NHE), Fe(II/I) (E_f = –0.87 V vs. NHE) and Fe(I/0) (E_f = *ca.* –1.4 V vs. NHE).[36] These electrochemical features demonstrate the ability of the Fe_MOF-525 film to transfer charge by redox hopping between neighboring Fe-TCPP sites.
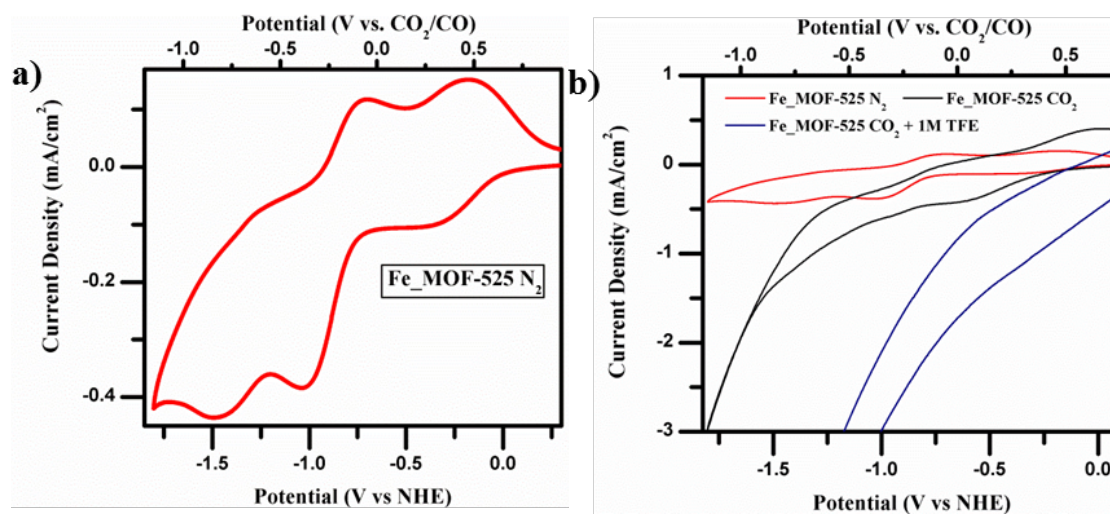
Figure 8.4 Cyclic voltammograms of Fe_MOF-525 films in 1 M TBAPF$_6$ acetonitrile solution: (a) under N$_2$ atmosphere, demonstrating the redox hopping ability of the Fe_MOF-525 film; (b) comparing behavior in N$_2$- vs. CO$_2$-saturated solutions, with and without addition of 1 M TFE proton source, showing electrocatalytic CO$_2$ reduction behavior.

The amount of electroactive catalyst was measured by chrono-amperommetry. Upon potential stepping from 0.2 to –0.5 V vs. NHE (reducing the Fe(III) to Fe(II)) the current decay over time was recorded (Figure 8.9). From the charge passed, an electrocatalyst surface-concentration of 6.2 x 10^{-8} mol/cm^2 was obtained. Visible-region spectroelectrochemistry measurements show that 77% of the

electrophoretically deposited porphyrin sites are electrochemically addressable in the region of the Fe(III/II) couple (Figure 8.10). In contrast, estimation of the surface concentration of a monolayer of TCPP molecules on a flat electrode (TCPP area is 2.5 nm^2), assuming full packing, gives only 7×10^{-11} mol/cm^2. In other words, the use of Fe_MOF-525 on a FTO electrode raised the amount of active catalyst by about 3 orders of magnitude, as compared to a monolayer of catalyst immobilized on the same flat electrode. To our knowledge, no previously heterogenized molecular CO_2 reduction catalysts have been installed at surface concentrations (areal concentrations) higher than 1×10^{-8} mol/cm^2, emphasizing the advantage of using the MOF as a strategy to boost the catalyst quantity and catalytic performance.

MOF Film Electrocatalysis. We assessed the MOF film's performance as an electrocatalyst for CO_2 reduction. As can be seen in Figures 8.4b and 8.11, compared to N_2 atmosphere, upon saturating a 1 M $TBAPF_6$ acetonitrile electrolyte solution with CO_2, the Fe(I/0) redox wave shows catalytic behavior and exhibits an increase in current density, suggesting CO_2 reduction at this potential.

In order to confirm that the current increase is due to catalytic CO_2 reduction, we subjected a Fe_MOF-525-containing cell to controlled potential electrolysis (CPE) at a constant working-electrode potential of -1.30 V vs. NHE. Figure 8.5 summarizes the CPE behavior over time. The Fe_MOF-525 system reached current densities of up to 2.3 mA/cm^2 after 30 minutes of electrolysis. The remainder of the experiment showed a slow decline in current density attributed to catalyst degradation (Figure 8.3a). Gas chromatographic analysis after over 4 hours of CPE indicated that the

Fe_MOF-525 generated two products: CO and H_2 (15.3 µmol/cm^2 and 14.9 µmol/cm^2 of CO and H_2, respectively). Taking into account the amount of electroactive catalyst in the film (6.2 x 10^{-8} mol/cm^2), these values correspond to a CO TON of 272 and an average turnover frequency (TOF) of 0.018 s^{-1} (Figure 8.5b). (Note: TOF that corresponds to the CPE peak current density is 5.6 hr^{-1}.)
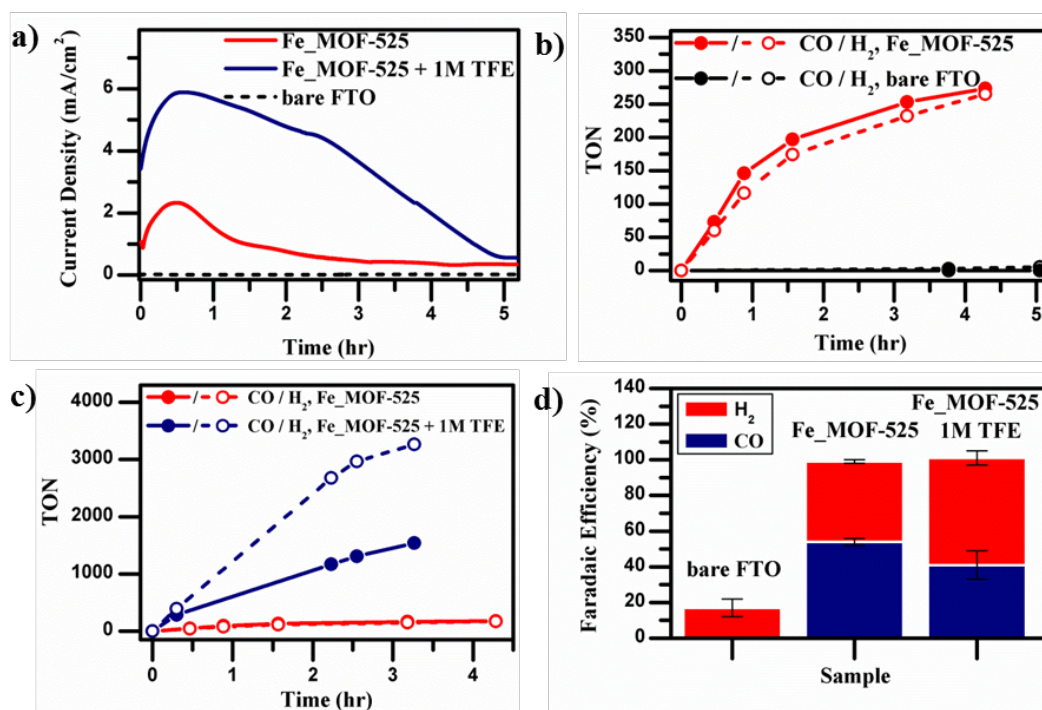
Figure 8.5 Controlled potential electrolysis of Fe_MOF-525 in 1 M TBAPF$_6$ acetonitrile solutions: (a) Current density vs. time for Fe_MOF-525 without added TFE (red), Fe_MOF-525 with added TFE (blue), and a bare FTO blank (black). (b) TON vs. time for Fe_MOF-525 without added TFE (red) and a bare FTO blank (black). (c) TON vs. time for Fe_MOF-525 without added TFE (red) and Fe_MOF-525 with added TFE (blue). (d) Faradaic efficiency over approximately 4 hours of electrolysis.

Even without an intentionally added proton source, the amount of H_2 evolved during the CPE experiments is nontrivial. Dihydrogen presumably derives from electrochemical reduction of residual water in the organic solvent (acetonitrile), or

from abstracting a proton from the $TBAPF_6$ electrolyte via Hofmann-type degradation. A second role for trace water may be to consume the dianionic oxygen atom lost upon conversion of CO_2 to CO. The produced mixtures of CO and H_2 (Faradaic efficiencies = 54 ± 2% and 45 ± 1% for CO and H_2 formation, respectively) could be directly converted to useful hydrocarbons by the Fischer-Tropsch (FT) process. (The optimal CO/H_2 ratio for FT reactions varies depending on the type of catalyst, the operating temperature, and the hydrocarbon products desired.)[37] As expected, the bare FTO electrode showed no catalytic activity for CO_2 reduction to CO, and produced only trace amounts of H_2 (Figure 8.5b).

In electrocatalysis studies with homogenous Fe-TPP in (nominally) nonhydroxylic solvent, it has been shown that the addition of weak Brönsted acids, such as 2,2,2-trifluoroethanol (TFE), elicit significant improvement in both catalytic current densities and system stability.[27,38] The improvements are a result of the ready protonation of the Fe–CO_2 adduct, which facilitates C–O bond cleavage and release of the CO product.[39-40] The added acid also provides a way of stabilizing the released oxygen anion (as water). As can be seen in Figure 8.5a, upon addition of 1 M TFE, the Fe_MOF-525 system exhibited significantly increased current densities, up to 5.9 mA/cm^2, as well as increased catalyst stability. CPE experiments with added TFE, at E = −1.3 V, resulted in a 7-fold increase in CO production, with the CO TON reaching 1520 (average TOF = 0.13 s^{-1}) after 3.2 hours of electrolysis (Figure 8.5c). As shown in Figure 8.5d, Faradaic efficiencies are 41 ± 8 and 60 ± 4% for CO and H_2 formation, respectively, meaning that the total Faradaic efficiency (CO + H_2) of the Fe_MOF-525

system is *ca.* 100%, both with and without TFE. At -1.3 V vs. NHE, CV experiments (Figures 8.4b and 8.11) return a catalytic current similar to the average current in the CPE experiment, *i.e.* 4 mA/cm^2. Notable in the CV measurements is the presence of significant catalytic current well positive of the formal potential for the film-based Fe(I/0) couple, *ca.* -1.4 V.

Comparisons to Homogeneous Catalysis. Figures 8.1 and 8.12 show electrochemical CV responses for a 1 mM solution of Fe-TPP in 30 mL of CO_2-saturated DMF (230 mM CO_2),[41] with and without 1 M TFE. (Thus, the total number of moles of catalyst is 3 x 10^{-5}) Figures 8.6 and 8.13a show the behavior of the homogeneous catalyst during constant potential electrolysis (-1.3 V vs. NHE). Over a six-hour period, in 30 mL of stirred CO_2-saturated acetonitrile containing 1 M TFE, the 1 mM catalyst solution yields an nearly constant catalytic current of ~12 mA/cm^2.
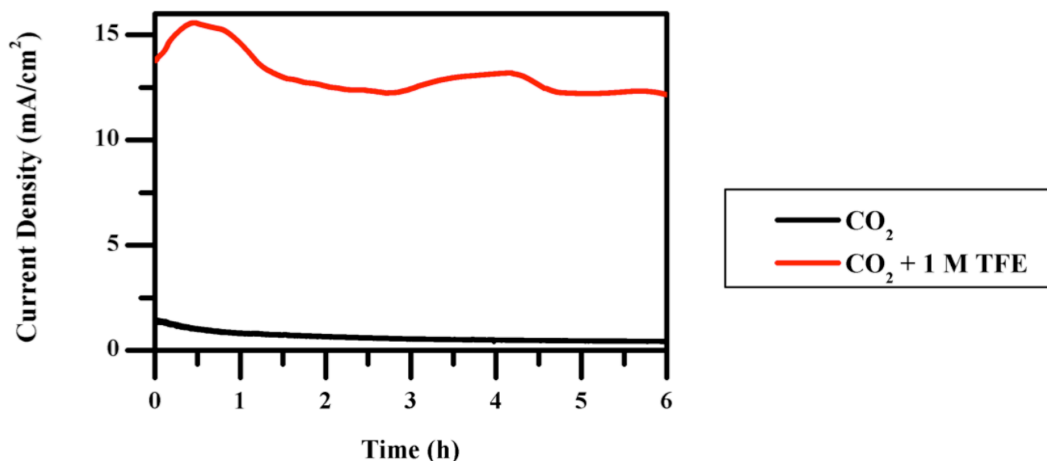
Figure 8.6 Controlled potential electrolysis of homogeneous Fe-TPP in 1 M TBAPF$_6$ DMF solution. Current density vs. time for Fe-TPP without added TFE (black) and with added TFE (red).

From Figure 8.1 (homogeneous Fe-TPP), the catalytic current is strongly potential dependent—much more strongly dependent than for the heterogenized MOF-

based catalyst (Figure 8.4). The fact that catalytic current is easily observable at potentials positive of E(I/0) implies that Fe(0)-TPP is strongly catalytic for CO_2 reduction, a point previously emphasized by Savéant and co-workers for this catalyst system.[27-29] Since only a tiny fraction of the dissolved homogeneous catalyst is present at any given time within the reaction zone of the electrode, it is comparatively uninformative to calculate TOF (or TON) values based on the total amount of catalyst in solution. Instead, we have used Savéant's foot-of-the-wave analysis.[41] From the analysis (see Experimental section for details), the second-order rate constant for Fe-TPP reduction of CO_2 to CO is 2400 M^{-1} s^{-1}. The TOF at $E = -1.3$ V versus NHE is 2.1 s^{-1}. These values, while larger than for many molecular electrocatalysts, are consistent with Savéant's observations.

A plot of E vs. logTOF yields a slope of about -53 mV/decade-TOF (see Figure 8.14), close to the value of -59 mV/decade-TOF expected if the Nernst equation, rather than the kinetics of interfacial electron-transfer, describes the fraction of metalloporphyrin present at the solution–electrode interface in the catalytically active Fe(0) form. By plot extrapolation, the TOF at $E = -1.25$ V is 0.3 s^{-1} while at $E = -1.2$ V it is 0.043 s^{-1}.

With respect to the result obtained at -1.3 V versus NHE, the homogeneous catalyst (Fe-TPP) displays a TOF that is 16 times higher than that of the heterogeneous version (Fe_MOF-525). This observation raises intriguing questions. First, why are the catalytic activities between the immobilized catalyst and the homogeneous catalysts so different? Second, how can the TOF for the immobilized

catalyst be so small relative to the homogeneous catalyst yet support catalytic currents that are within a factor of 2 or 3 of that of the homogeneous catalyst? Third, why is the catalytic current with Fe_MOF-525 so much less dependent on the applied potential than is the catalytic current produced with the homogeneous species?

Catalyst heterogenization via porous MOF formation occurs beyond the perimeter of the catalyst, at carboxylate linkages on pendant phenyl groups. As such, it seems unlikely that the intrinsic activity of the catalyst—as influenced, for example, by substituent or environmental electronic effects—is affected significantly by MOF formation. If electronic attenuation is unimportant, then other factors must be limiting the TOF. Figure 8.4a offers a hint: the voltammetric wave for the Fe(I/0) couple is distorted in a way that suggests slow diffusion, presumably of either electrons hopping from site-to-site (iron to iron) or ions moving in charge-compensating fashion (the porphyrin sites themselves, of course, are spatially fixed).

The notion of rate-limiting charge diffusion is supported by variable scan-rate CV studies which show that the voltammetric peak current increases as the square-root of the voltammetric scan rate, rather than linearly (as expected if diffusive limitations are unimportant); see Figure 8.15. Chrono-amperommetry measurements (see Figure 8.16) permit the charge-diffusion coefficient, D, to be quantified, and yield a value of 5×10^{-13} cm^2 s^{-1}. While the value is tiny in comparison to diffusion coefficients for small molecules in conventional solutions, it is not grossly out of line with the few values reported for MOF-based charge transport.[20] It is important to recognize as well that the relevant transport distances are comparatively small, as the thickness of the

MOF-525 film is only on the order of several hundreds of nanometers; thus, complete charge diffusion and concomitant film reduction from Fe(I) to Fe(0), requires on the order of only a few to several seconds. Nevertheless, these times are about an order of magnitude greater than the time required for turnover of a single Fe-TPP catalyst outside the MOF environment (*i.e.* 0.5 s at −1.3V). We conclude, therefore, that at E = −1.3 V the rate of catalytic reduction of CO_2 by the MOF film is largely limited by the rate of charge diffusion.

The ability of the MOF to provide catalytic currents that are within a factor of two or three of those obtained with the homogeneous catalyst, despite the 16-fold difference in effective TOF values, is a consequence of the MOF-based concentration and immobilization of Fe-TPP catalysts at or near the electrode surface. Thus, 1 cm^2 of densely packed (but porous) MOF film places 0.6 micromoles of electrochemically addressable catalyst within a micron or less of the electrode surface. In contrast, the millimolar homogeneous solution of Fe-TPP places 1 nanomol/cm^2 of catalyst—600x less—within a micron or less of the electrode (albeit, with the likelihood of fresh catalyst diffusing in as the initial catalyst undergoes reaction).

The comparatively weak dependence of the MOF-derived catalytic current on electrode potential implies that even as the potential is made less negative and the TOF for the *homogeneous* catalyst sharply drops, the heterogeneous process remains largely limited by diffusive charge transport rather than molecular-scale kinetics for catalytic conversion. Consequently, at slightly lower overpotentials, TOF values for the homogeneous catalyst become smaller than those of the heterogeneous version.

Thus, the TOF value for the MOF-immobilized catalyst at E = −1.25 V is 0.12 s^{-1} (compared to 0.3 s^{-1} for the homogeneous catalyst), and at −1.2 V, 0.11 s^{-1} (compared to 0.043 s^{-1} for the homogeneous catalyst). Nevertheless, for the heterogenized catalyst to match or exceed the catalytic current density achieved by the homogeneous catalyst at E = −1.3 V, it is clear that faster charge transport (charge diffusion) will be required. Understanding what limits redox-based charge transport through MOF materials is the focus of ongoing studies, as are investigations of methods for boosting rates of charge diffusion. While not explored here, we find that charge transport through Fe_MOF-525, as indicated by apparent diffusion coefficients, is about 20x faster when based on the Fe(III/II) couple than on the catalytically relevant Fe(I/0) couple. We will report elsewhere on the chemical basis for this large difference.

Finally, Fig. 5a implies that after five hours of CPE, the MOF-based catalyst has largely degraded. In contrast, based on Fig. 6, the homogeneous catalysis appears to degrade only slightly, if at all, over the course of six hours of CPE. It is important to note, however, that the total amount of catalyst present in the homogeneous CPE experiment is about 50-fold greater than in the heterogeneous experiment. Assuming that degradation is associated with catalytic cycling and recognizing that catalyst molecules in homogeneous solution both freely diffuse and are subjected to controlled convection (solution stirring), very few homogeneous catalyst molecules will experience the number of catalytic turnovers experienced by MOF-immobilized catalyst molecules.

8.3   Conclusions

Electrophoretic deposition of crystallites of appropriately chosen MOFs is an effective means of heterogenizing and surface-concentrating catalysts for the electrochemical reduction of CO_2. Using Fe_MOF-525, we find that the well-known CO_2 reduction catalyst Fe-TPP can be installed on electrode surfaces at high areal concentrations equivalent to *ca.* 900 monolayers of surface adsorbed Fe-TPP —and almost an order of magnitude higher than the highest previous report on heterogenized molecular CO_2 reduction catalysts. Importantly, the well-defined nanoscale porosity of the MOF facilitates solvent, reactant, and electrolyte access to the surfeit of catalytic sites. The MOF's metallo-porphyrinic linkers serve as both electrocatalysts and as redox-hopping-based conduits for the delivery of reducing equivalents to catalytic sites that are not in direct contact with the underlying electrode.

CV measurements indicate that the MOF is capable of electrocatalysis, exhibiting in CO_2-saturated solutions a catalytic wave at and before that for the catalytically active Fe(I/0) redox couple. CPE at a CO_2/CO overpotential of about 650 mV yielded current densities of a few to several mA/cm^2, corresponding to the formation of CO and H_2, in roughly equal amounts, with a Faradaic efficiency of ~100%. These products constitute a potential feedstock for Fischer-Tropsch synthesis of hydrocarbons. The observed catalytic currents are limited by the rate of charge diffusion through the MOF, rather than by the molecular-scale kinetics of reaction of CO_2 with Fe-TPP. Enhancing the rate of diffusion clearly will be necessary for fully realizing the promise of Fe_MOF-525 or related materials as electrocatalysts; this is a

focus of current work. In the presence of a 1 M TFE as a weakly acidic proton donor, electrocatalysis persists for about five hours (albeit, with gradual decay, due to catalyst chemical degradation[28]).

We believe that our work represents a significant step forward in the heterogenization of molecular electrocatalysts for energy-relevant reactions under high flux conditions. We are currently evaluating the broader utility of this approach to electrocatalysis, with an eye toward applications relevant to solar energy conversion. Future studies will include developing a MOF thin film for use with our Mn bipyridine catalysts, which should allow for high rates of CO_2 reduction at low overpotential in aqueous electrolyte.

8.4   Experimental

Instrumentation. Thin-film XRD patterns were measured on a Rigaku ATX-G thin-film diffraction workstation. UV-Vis spectroscopy of Fe_MOF-525 films was obtained using a Cary 5000 spectrophotometer (VARIAN). Scanning electron microscopy (SEM) images and energy dispersive X-ray spectroscopy (EDS) were collected on a Hitachi SU8030 instrument.

All cyclic voltammetry (CV) experiments were performed on either a Solarton Analytical Modulab Potentiostat or a Gamry Epsilon Potentiostat. A three-electrode electrochemical setup was used, with a platinum mesh counter electrode, Ag/AgCl/KCl (sat'd) electrode as reference electrode, and the Fe_MOF-525 thin-

film/FTO working electrode (active area of 1 cm^2). For all measured CVs, the scan rate was 100 mV/sec.

Electrophoretic Deposition of MOF Thin Films.[21,42] 10 mg of MOF powder were suspended in a 20 mL toluene solution and sonicated for 30 sec. Two identical fluorine-doped tin oxide (FTO) glass substrates (15 Ω/sq, Hartford Glass) were dipped in the deposition solution (1 cm separation distance) and a constant DC voltage of 130 V was applied using an Agilent E3 612A DC power supply. The duration of deposition was 3 hours. **Caution:** Electrical sparking due to accidental contact of electrodes and/or their leads can result in ignition of toluene. The electrophoretic deposition procedure should be done in a fume hood, clear of flammables.

Post-Metalation of the MOF-525 Thin Films. 10 mg of iron chloride was dissolved in 10 mL of DMF in an 8-dram vial. The MOF-525 thin film was placed into the vial, and the closed vial was placed into an oven at 80 ^{o}C for 24 h. The obtained thin film was removed from the solution, washed with DMF and acetone for several times and dried under vacuum.

Bulk Electrolysis Measurements. CPE experiments (at ca. −1.30 V vs. NHE) were carried out in a 60-mL Gamry 5-neck cell with a three-electrode setup – platinum counter electrode in a fritted glass compartment, a leakless Ag/AgCl reference electrode (eDAQ), and either the Fe_MOF-525 thin-film/FTO working electrode (active area of 1 cm^2) or a glassy carbon rod working electrode (surface area = 7.4 cm^2). A BASi Epsilon potentiostat was used to apply constant potential and record current. These CPE experiments were carried out in 30 mL of total electrolyte solution

(1 M TBAPF$_6$ in acetonitrile or DMF; for our purposes, the Fe-TPP molecular catalyst proved insufficiently soluble in acetonitrile). Electrochemical solutions were first bubbled with N$_2$ for 5 minutes and then bubbled with CO$_2$ for 15 mins before experiments. Solutions were constantly stirred (at a consistent rate for all experiments) throughout each CPE experiment. Gas analysis for CPE experiments were performed using 1 mL sample injections on a Hewlett-Packard 7890A Series gas chromatograph with two molsieve columns (30 m × 0.53 mm ID × 25 μm film). The 1 mL injection was split between two columns, one with N$_2$ as the carrier gas and one with He as the carrier gas, in order to quantify both H$_2$ and CO simultaneously in each run. Gas chromatography calibration curves were made by sampling known volumes of CO and H$_2$ gas. CPE experiments for Fe_MOF-525 films were done in a similar manner.

Synthesis of MOF-525. 105 mg of ZrOCl$_2$×8H$_2$O (0.30 mmol) and 2.7 g (22 mmol) of benzoic acid were mixed in 8 mL of DMF (in a 6-dram vial) and ultrasonically dissolved. The clear solution was incubated in an oven at 80 ºC for 2 hours. After cooling down to room temperature 47 mg (0.06 mmol) of H$_4$TCPP was added to this solution and the mixture was sonicated for 20 min. The purple suspension was heated in an oven at 70 ºC for 24 hours. After cooling down to room temperature, purple-red polycrystalline material was isolated by filtration and washed 3 times with DMF and Subsequently, the solid residue was washed three times with acetone and soaked in acetone for additional 12 hours. MOF-525 was filtered, briefly dried on a filter paper and activated at 80 ºC under vacuum for 12 hours.

Controlled Potential Electrolysis. CPE experiments (at ca. −1.30 V vs. NHE) were carried out in a 60-mL Gamry 5-neck cell equipped with 3 Ace-Thred ports to hold each electrode and two joints capable of being sealed with septa for gas sparging. This setup included the Fe_MOF-525 film on FTO as the working electrode (ca. 0.5 cm^2 surface area), a Pt wire counter electrode (flame annealed with a butane torch before use and separated from the bulk solution by fine glass frit), and a Ag/AgCl reference electrode (leakless assembly, eDAQ). Outside of the electrolyte solution, a bare portion of the FTO working electrode was attached to a Cu wire by a minimal amount of non-conductive, chemically-resistant epoxy in order to attach the FTO glass to the potentiostat leads. A BASi Epsilon potentiostat was used to apply constant potential and record current. These CPE experiments were carried out in 30 mL of total electrolyte solution (1 M TBAPF$_6$ in either acetonitrile or DMF). Electrochemical solutions were first sparged with N$_2$ for 5 mins then sparged with CO$_2$ for 15 mins before experiments. Both gases were pre-dried through a custom Drierite/3Å molecular sieves column before use. For experiments with added TFE, the appropriate amount of TFE was added to the electrolyte solution before the experiment. Acetonitrile and DMF solvents for CPE were sparged with argon, dried on a custom dry solvent system over alumina columns, and stored over molecular sieves before use. TBAPF$_6$ electrolyte used for CPE experiments (Aldrich, 98%) was twice recrystallized from methanol (MeOH) and dried under a vacuum at 90 °C overnight before use. Solutions were constantly stirred (at a consistent rate between all experiments) throughout each CPE experiment. Gas analysis for CPE experiments

were performed using 1 mL sample injections on a Hewlett-Packard 7890A Series gas chromatograph with two molsieve columns (30 m × 0.53 mm ID × 25 μm film). The 1 mL injection was split between two columns, one with N_2 as the carrier gas and one with He as the carrier gas, in order to quantify both H_2 and CO simultaneously in each run. Gas chromatography calibration curves were made by sampling known volumes of CO and H_2 gas.

Fe_MOF-525 **Spectroelectrochemistry.** Spectroelectrochemical measurements were done by recording UV−visible (UV−vis) spectra of the MOF thin films at various applied potentials, using a 3-electrode electrochemical setup coupled with a Shimadzu 1601 UV−vis spectrometer.

Fe-TPP Foot of the Wave Analysis.[41] Foot of the wave analysis allows the use of measured CVs of catalytic reactions in order to determine TOF and TON, regardless of any side-effects such as substrate consumption, which may interfere with the obtained results at high current densities. Consequently, one could extract TOF vs. η Tafel plots for a specific homogeneous molecular catalyst.

A second order catalytic reaction rate constant (k) can be calculated using E8.1. Here, i is the catalytic current under CO_2 at a given applied potential E, i_p^0 is the current under N_2 at the formal potential of the catalyst, $E_{FeI/0}$, R is the universal gas constant, T is temperature, F is Faraday's constant, v is scan rate (0.1 V/s in this case), and C_{CO2} is 0.23 M in DMF. By plotting i/i_p^0 vs. $(1 + \exp[(F/RT)(E - E_{FeI/0})])^{-1}$ and fitting the early linear portion of the curve (see Figure 8.14a), one can calculate k from the curve's slope. Then, TOF for each overpotential (η) can be obtained using E8.2.

As a result, a logTOF vs. η Tafel plot can be plotted (see Figure 8.14b), showing the dependence of TOF with η.

$$\frac{i}{i_p^0} = \frac{2.24\sqrt{\frac{RT}{Fv}2kC_{CO2}}}{1+\exp\left[\frac{F}{RT}\left(E-E_{Fe I/0}\right)\right]} \tag{E8.1}$$

$$TOF = \frac{2k}{1+\exp\left[\frac{F}{RT}\left(E_{CO2/CO}-E_{Fe I/0}-\eta\right)\right]} \tag{E8.2}$$

Much of the material for this chapter comes directly from a manuscript entitled: "Fe-Porphyrin-Based Metal-Organic Framework Films as High-Surface Concentration, Heterogeneous Catalysts for Electrochemical Reduction of CO_2" by Idan Hod, Matthew D. Sampson, Pravas Deria, Clifford P. Kubiak, Omar K. Farha, and Joseph T. Hupp, which has been published in *ACS Catal.*, **2015**, 5, 6302–6309. http://dx.doi.org/ 10.1021/acscatal.5b01767. The dissertation author is a contributing author of this manuscript.

8.5   References

(1) Chen, Z. F.; Concepcion, J. J.; Jurss, J. W.; Meyer, T. J. *J. Am. Chem. Soc.* **2009**, 131, 15580-15581.

(2) Lieber, C. M.; Lewis, N. S. *J. Am. Chem. Soc.* **1984**, 106, 5033-5034.

(3) Yoshida, T.; Tsutsumida, K.; Teratani, S.; Yasufuku, K.; Kaneko, M. *J. Chem. Soc., Chem. Commun.* **1993**, 631-633.

(4) Parkin, A.; Seravalli, J.; Vincent, K. A.; Ragsdale, S. W.; Armstrong, F. A. *J. Am. Chem. Soc.* **2007**, 129, 10328-+.

(5) Yao, S. A.; Ruther, R. E.; Zhang, L. H.; Franking, R. A.; Hamers, R. J.; Berry, J. F. *J. Am. Chem. Soc.* **2012**, 134, 15632-15635.

(6) Kang, P.; Zhang, S.; Meyer, T. J.; Brookhart, M. *Angew. Chem., Int. Ed.* **2014**, 53, 8709-8713.

(7) Blakemore, J. D.; Gupta, A.; Warren, J. J.; Brunschwig, B. S.; Gray, H. B. *J. Am. Chem. Soc.* **2013**, 135, 18288-18291.

(8) Otoole, T. R.; Sullivan, B. P.; Bruce, M. R. M.; Margerum, L. D.; Murray, R. W.; Meyer, T. J. *J. Electroanal. Chem.* **1989**, 259, 217-239.

(9) Cabrera, C. R.; Abruna, H. D. *J. Electroanal. Chem.* **1986**, 209, 101-107.

(10) Otoole, T. R.; Margerum, L. D.; Westmoreland, T. D.; Vining, W. J.; Murray, R. W.; Meyer, T. J. *J. Chem. Soc., Chem. Commun.* **1985**, 1416-1417.

(11) Collombdunandsauthier, M. N.; Deronzier, A.; Ziessel, R. *Inorg. Chem.* **1994**, 33, 2961-2967.

(12) Portenkirchner, E.; Gasiorowski, J.; Oppelt, K.; Schlager, S.; Schwarzinger, C.; Neugebauer, H.; Knor, G.; Sariciftci, N. S. *ChemCatChem* **2013**, 5, 1790-1796.

(13) Sende, J. A. R.; Arana, C. R.; Hernandez, L.; Potts, K. T.; Keshevarzk, M.; Abruna, H. D. *Inorg. Chem.* **1995**, 34, 3339-3348.

(14) Sathrum, A. J.; Kubiak, C. P. *J. Phys. Chem. Lett.* **2011**, 2, 2372-2379.

(15) Kumar, B.; Llorente, M.; Froehlich, J.; Dang, T.; Sathrum, A.; Kubiak, C. P. *Annu Rev Phys Chem* **2012**, 63, 541-569.

(16) Betard, A.; Fischer, R. A. *Chem. Rev.* **2012**, 112, 1055-1083.

(17) Wang, C.; Xie, Z. G.; deKrafft, K. E.; Lin, W. L. *J. Am. Chem. Soc.* **2011**, 133, 13445-13454.

(18) Wang, D. K.; Huang, R. K.; Liu, W. J.; Sun, D. R.; Li, Z. H. *ACS Catal.* **2014**, 4, 4254-4260.

(19) Zhang, T.; Lin, W. B. *Chem. Soc. Rev.* **2014**, 43, 5982-5993.

(20) Ahrenholtz, S. R.; Epley, C. C.; Morris, A. J. *J. Am. Chem. Soc.* **2014**, 136, 2464-2472.

(21) Hod, I.; Bury, W.; Karlin, D. M.; Deria, P.; Kung, C.-W.; Katz, M. J.; So, M.; Klahr, B.; Jin, D.; Chung, Y.-W.; Odom, T. W.; Farha, O. K.; Hupp, J. T. *Adv. Mater.* **2014**, 26, 6295-6300.

(22) Wade, C. R.; Li, M. Y.; Dinca, M. *Angew. Chem., Int. Ed.* **2013**, 52, 13377-13381.

(23) Usov, P. M.; Fabian, C.; D'Alessandro, D. M. *Chem. Commun.* **2012**, 48, 3945-3947.

(24) Hod, I.; Bury, W.; Gardner, D. M.; Deria, P.; Roznyatovskiy, V.; Wasielewski, M. R.; Farha, O. K.; Hupp, J. T. *J. Phys. Chem. Lett.* **2015**, 586-591.

(25) Kosal, M. E.; Chou, J. H.; Wilson, S. R.; Suslick, K. S. *Nat. Mater.* **2002**, 1, 118-121.

(26) Bhugun, I.; Lexa, D.; Saveant, J. M. *J. Phys. Chem.* **1996**, 100, 19981-19985.

(27) Bhugun, I.; Lexa, D.; Saveant, J. M. *J. Am. Chem. Soc.* **1994**, 116, 5015-5016.

(28) Hammouche, M.; Lexa, D.; Momenteau, M.; Saveant, J. M. *J. Am. Chem. Soc.* **1991**, 113, 8455-8466.

(29) Costentin, C.; Drouet, S.; Robert, M.; Saveant, J. M. *Science* **2012**, 338, 90-94.

(30) Morris, W.; Volosskiy, B.; Demir, S.; Gandara, F.; McGrier, P. L.; Furukawa, H.; Cascio, D.; Stoddart, J. F.; Yaghi, O. M. *Inorg. Chem.* **2012**, 51, 6443-6445.

(31) Kung, C.-W.; Chang, T.-H.; Chou, L.-Y.; Hupp, J. T.; Farha, O. K.; Ho, K.-C. *Chem. Commun.* **2015**, 51, 2414-2417.

(32) Mondloch, J. E.; Katz, M. J.; Planas, N.; Semrouni, D.; Gagliardi, L.; Hupp, J. T.; Farha, O. K. *Chem. Commun.* **2014**, 50, 8944-8946.

(33) DeCoste, J. B.; Peterson, G. W.; Jasuja, H.; Glover, T. G.; Huang, Y. G.; Walton, K. S. *J. Mater. Chem. A* **2013**, 1, 5642-5650.

(34) Silva, C. G.; Luz, I.; Xamena, F. X. L. I.; Corma, A.; Garcia, H. *Chem. Eur. J.* **2010**, 16, 11133-11138.

(35) Vermoortele, F.; Ameloot, R.; Vimont, A.; Serre, C.; De Vos, D. *Chem. Commun.* **2011**, 47, 1521-1523.

(36) Cardona, C. M.; Li, W.; Kaifer, A. E.; Stockdale, D.; Bazan, G. C. *Adv. Mater.* **2011**, 23, 2367-2371.

(37) Dry, M. E. *Catal. Today* **2002**, 71, 227-241.

(38) Bhugun, I.; Lexa, D.; Saveant, J. M. *J. Am. Chem. Soc.* **1996**, 118, 1769-1776.

(39) Costentin, C.; Drouet, S.; Passard, G.; Robert, M.; Saveant, J. M. *J. Am. Chem. Soc.* **2013**, 135, 9023-9031.

(40) Bonin, J.; Robert, M.; Routier, M. *J. Am. Chem. Soc.* **2014**, 136, 16768-16771.

(41) Costentin, C.; Drouet, S.; Robert, M.; Saveant, J. M. *J. Am. Chem. Soc.* **2012**, 134, 11235-11242.

(42) Hwang, Y.; Sohn, H.; Phan, A.; Yaghi, O. M.; Candler, R. N. *Nano Lett.* **2013**, 13, 5271-5276.

8.6   Appendix
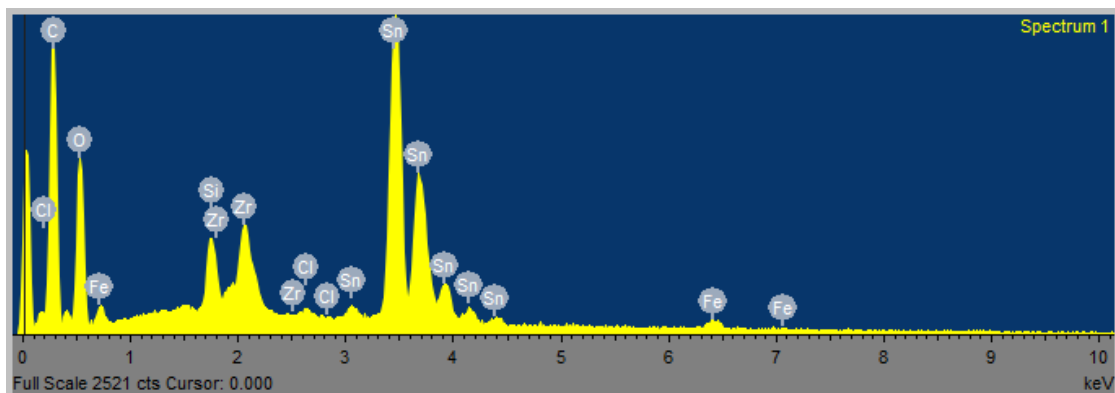
Figure 8.7 EDS spectra of a Fe_MOF-525 thin film, which resulted in a Zr_6 to Fe elemental ratio of 2.8.
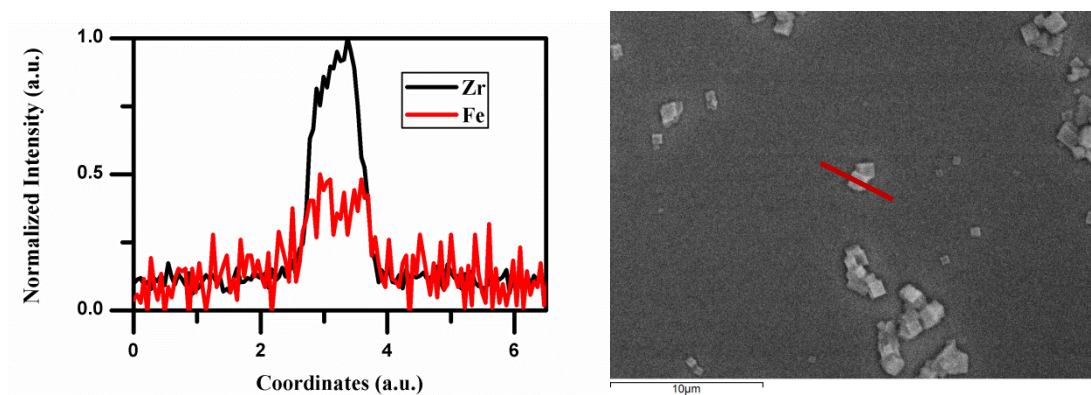
Figure 8.8 EDS mapping of single Fe_MOF-525 particle, showing an even distribution of Fe within the MOF.
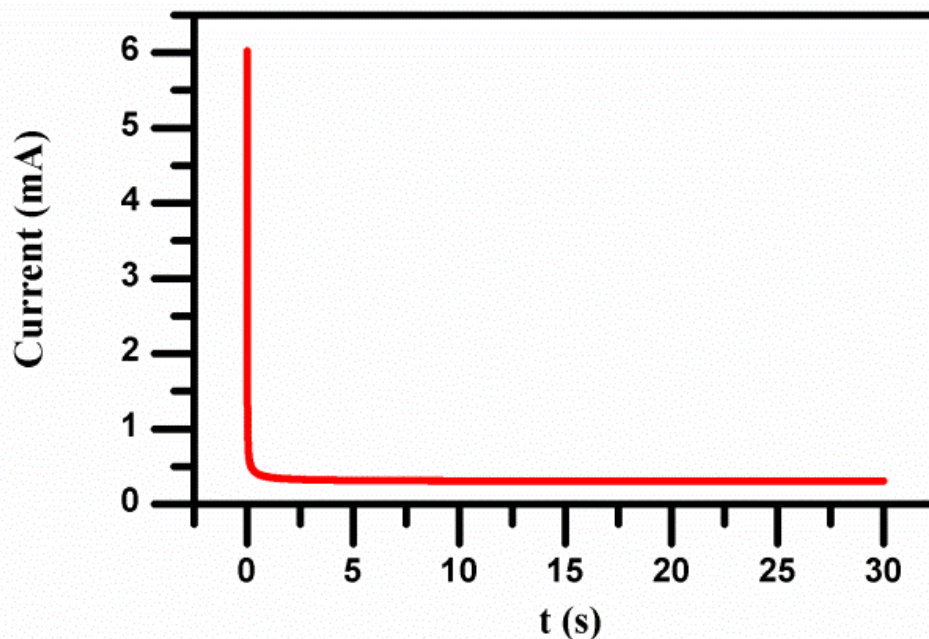
Figure 8.9 Current decay vs. time upon a reductive potential step of Fe_MOF-525 film from 0.2 V to −0.5 V vs. NHE. The amount of charge passed during this process was used to calculate the electroactive concentration of catalyst in the film.
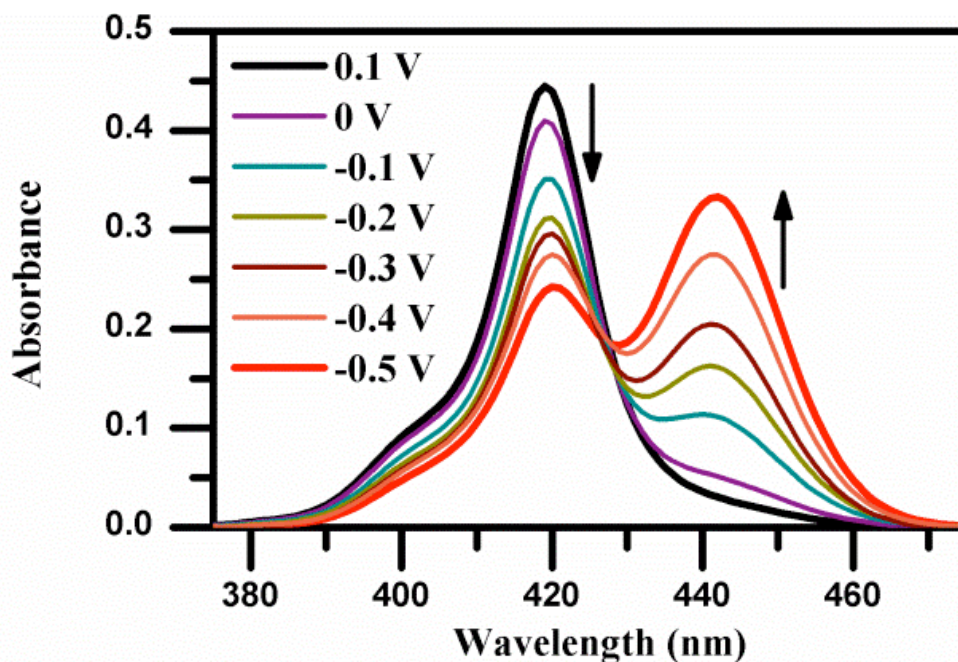
Figure 8.10 Visible region SEC of Fe_MOF-525 film in 1 M TBAPF$_6$/MeCN. Stepping the potential from 0.1 V (Fe(III)-porphyrin) to −0.5 V (Fe(II)-porphyrin), the peak at 419 nm diminishes while a new peak arises at 441 nm, corresponding to 77% electroactive porphyrin linkers in the MOF film.
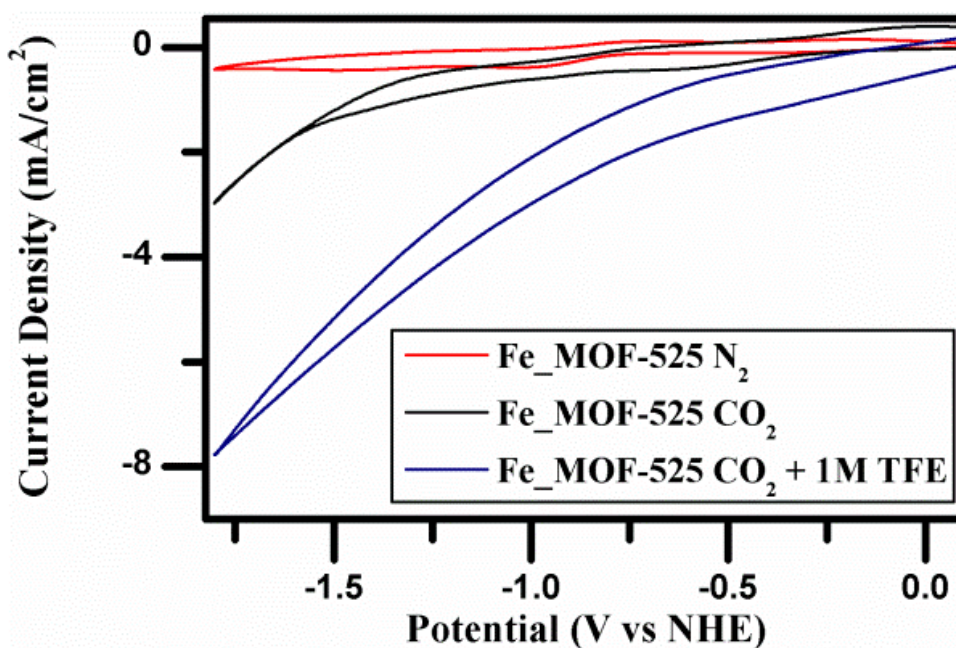
Figure 8.11 Cyclic voltammograms comparing between Fe_MOF-525 under N_2 and CO_2 atmospheres, with and without added proton source (1 M TFE).
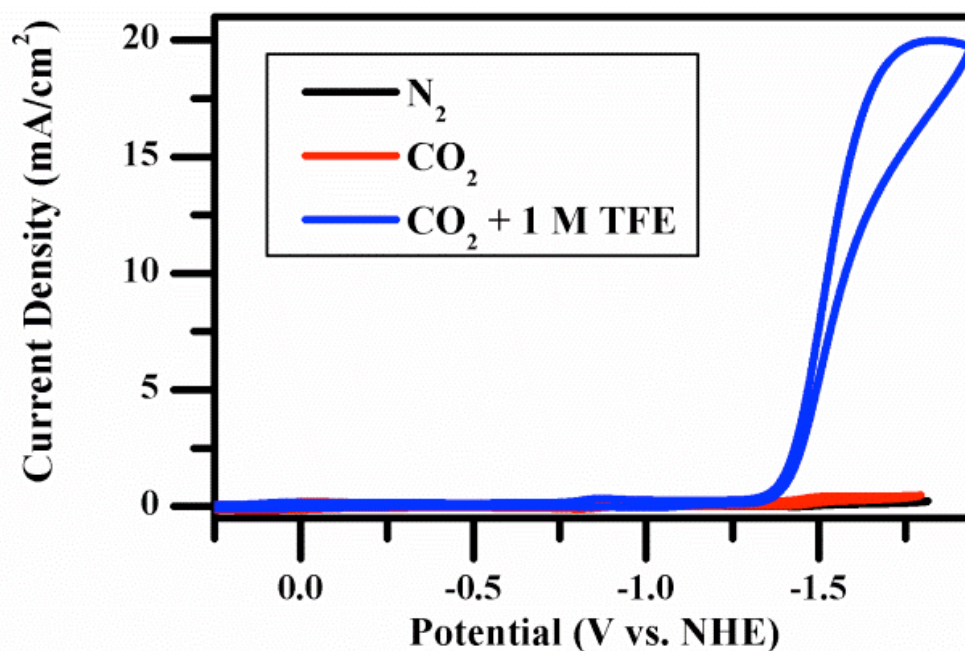
Figure 8.12 Cyclic voltammograms of homogeneous Fe-TPP (1 mM) in DMF (scan rate: 0.1 V/s), a) comparison between N_2 (black) and CO_2 atmosphere, with no added proton source (red), with 1 M added TFE proton source (blue), showing the catalytic wave rise with added TFE.
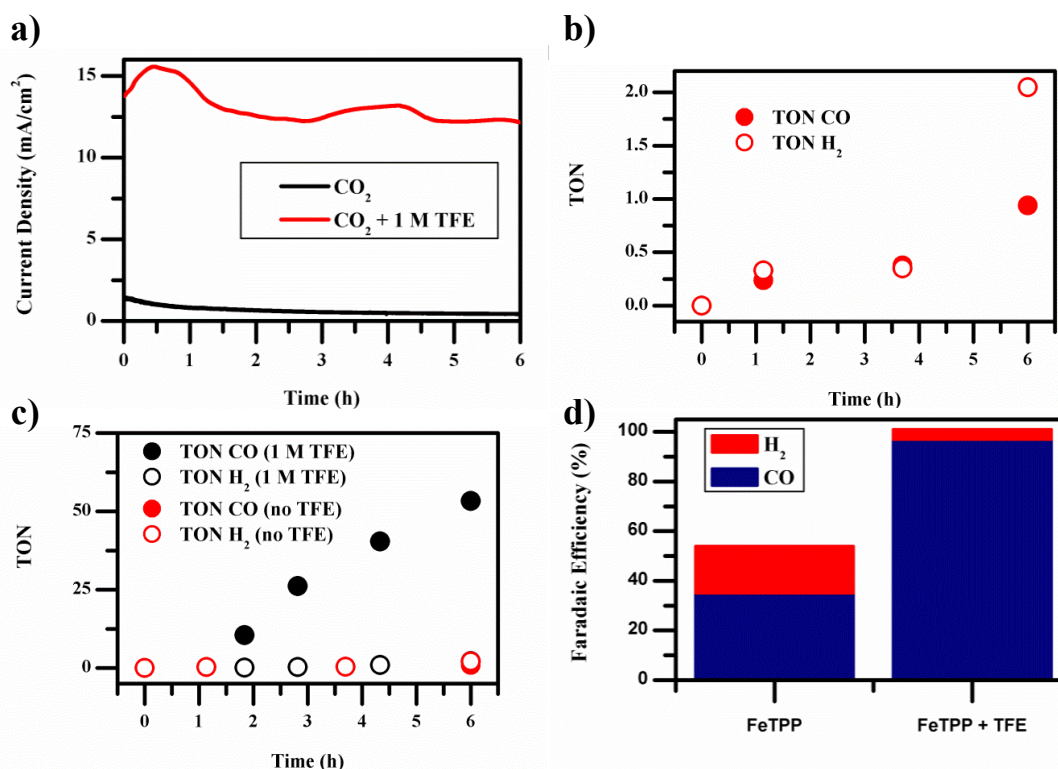
Figure 8.13 Controlled potential electrolysis for homogeneous Fe-TPP (1 mM) in DMF, (a) current vs. time plot, comparing Fe-TPP under CO_2 with and without 1 M TFE proton source (b) CO/H_2 TON for Fe-TPP with no added TFE (c) comparison between CO/H_2 TON for Fe-TPP with and without added TFE (d) CO/H_2 Faradaic efficiency with and without added TFE.
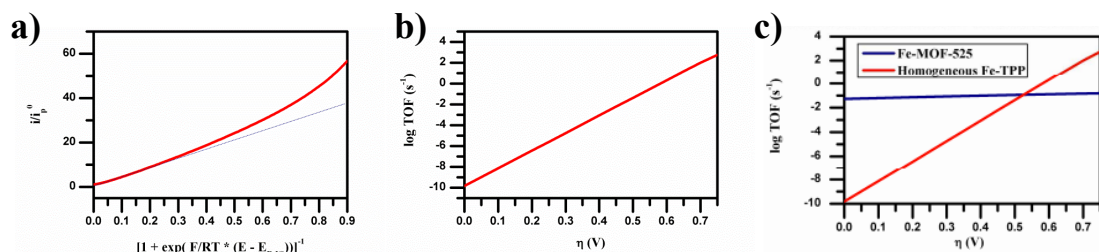
Figure 8.14 Foot of the wave analysis of homogeneous Fe-TPP in 1 M $TBAPF_6$ in DMF: (a) i/i_p^0 vs. $(1+ \exp[(F/RT)(E - E_{FeI/0})])^{-1}$ plot used to calculate the second order catalytic rate constant, k (2420 M^{-1} s^{-1}), (b) plot of TOF (s^{-1}) vs. overpotential for homogeneous Fe-TPP in 1 M $TBAPF_6$ in DMF, derived from the foot-of-the-wave analysis of Fe-TPP cyclic voltammograms, (c) plot of logTOF (s^{-1}) vs. overpotential, comparing homogeneous Fe-TPP and heterogeneous Fe-MOF-525.
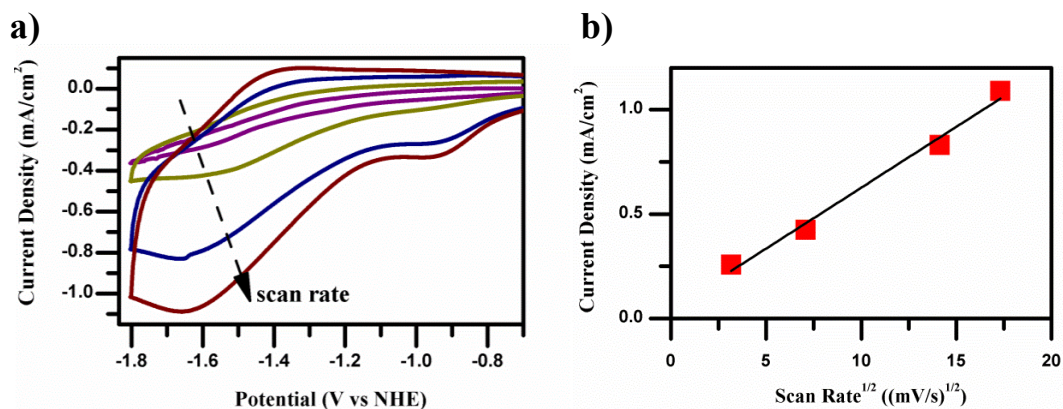
Figure 8.15 (a) Scan rate dependent cyclic voltammograms of Fe_MOF-525 under N_2. (b) Fe(I/0) peak current vs. square root of scan rate, showing a linear relation typical of diffusion-limited electron transfer reaction.
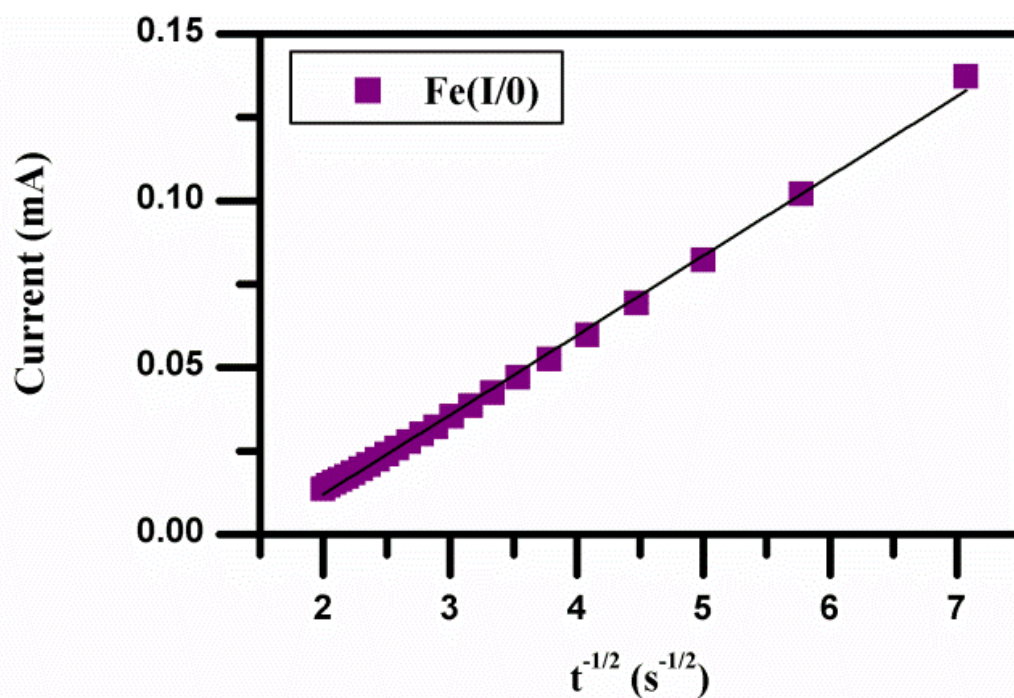
Figure 8.16 Cottrell plot (current vs. $t^{-1/2}$) for Fe(I/0) redox wave, which resulted in an electron hopping diffusion coefficient for Fe(I/0) redox wave = 4.8 x 10^{-13} cm^2 s^{-1}.

Chapter 9

Future directions: Towards a system capable of implementation on an industrial scale.

9.1 Introduction

Although there has been significant market penetration of electric vehicles in the personal transportation market in recent years, and although this penetration is likely to grow into the future, transportation sectors such as air travel, oceanic shipping, and many military applications will continue to depend on liquid fuel in the foreseeable future. At this stage, even considering a technological breakthrough, batteries simply do not possess a great enough energy density to be utilized for long distance travel applications (see Figure 9.1).[1] Therefore, creating a technology to produce synthetic liquid fuel from renewable sources, such as carbon dioxide (CO_2)

and water (H_2O), at an economically competitive cost should be of major effort in energy research.
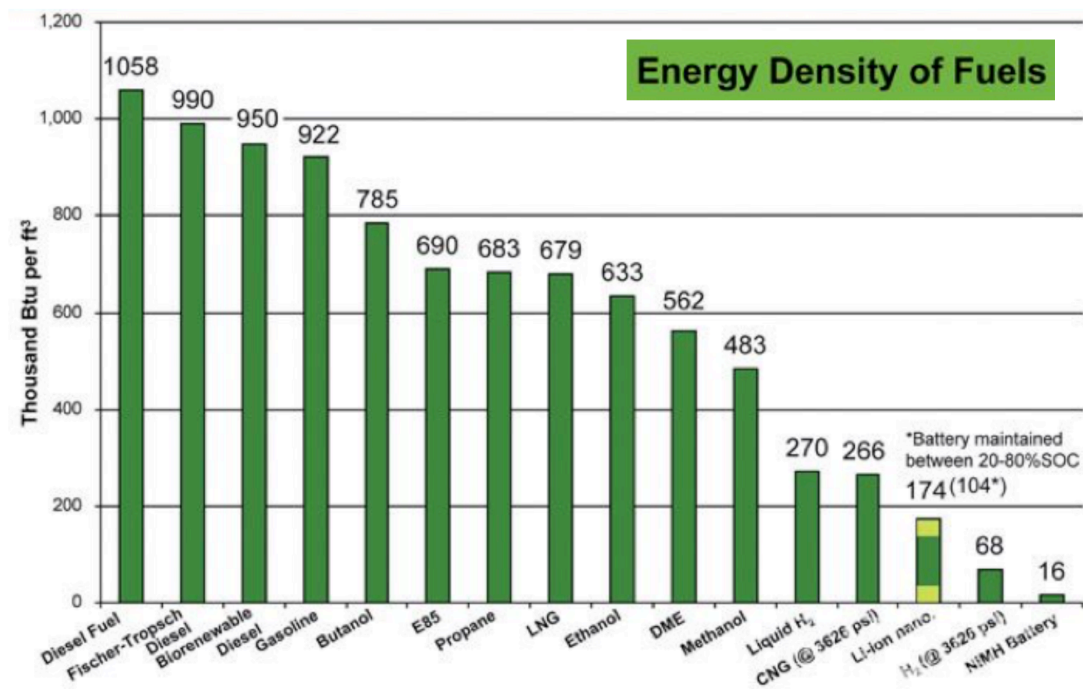
Figure 9.1 Energy density of fuels in thousands of BTU (British Thermal Units) per cubic foot. Figure adapted from Ref. 1.

A tremendous amount of knowledge and advancement has been made in regards to Re and Mn bipyridine (bpy) molecular catalysts for electrochemical CO_2 reduction; however, there still holds room for improvement in order to move closer to advancing these catalytic systems to a level capable of incorporation into a deployable device for CO_2 reduction and eventually incorporated on an industrial scale. In order to move these catalytic systems to a deployable level, we will need to translate the system into a heterogeneous form without sacrificing activity or selectivity. Many strategies can be pursued to heterogenize these Re and Mn bpy catalysts in metal-

organic frameworks (MOFs), similarly to our work on the Fe-porphyrin-functionalized MOF described in Chapter 8. MOFs, due to their highly functional nature, can be thought of as artificial metalloenzymes, where in the struts and nodes of the MOFs can be functionalized with secondary and outer coordination sphere units to provide a variety of interactions that enhance catalysis (see Figure 9.2). In contrast to a densely packed polymerized film or a catalyst anchored via an organic linker, a MOF creates an ordered, porous heterogeneous network, which allows for free permeation of electrolyte ions and dissolved CO_2 into the interior of the film.
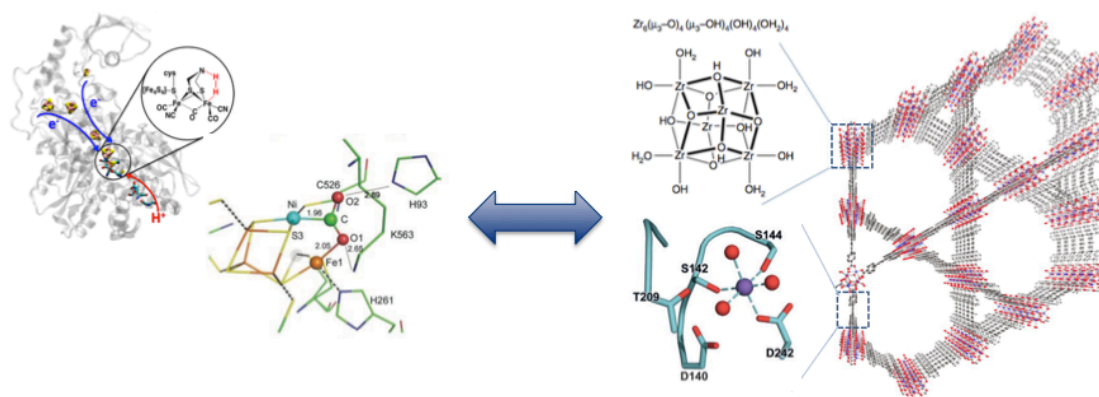
Figure 9.2 Comparison between metalloenzymes and a highly-functional metal-organic framework (MOF), wherein an immobilized molecular catalyst in a MOF can serve as the active site of a metalloenzyme and functional groups within the MOF can serve as secondary and outer coordination sphere interactions.

Finally, when considering the development of a heterogeneous device (incorporating an immobilized molecular catalyst) for CO_2 reduction using solar energy, care will need to be taken to match the incoming power and the limiting current densities of the catalyst.[2-3] Photoelectrochemical systems are currently being developed, which couple H_2O oxidation at a photoanode to CO_2 reduction at a cathode;[4] however, most of the photoelectrochemical CO_2 reduction studies reported

thus far utilize expensive, third-row transition metals. In addition to H_2O oxidation, a potential device could employ other oxidation reactions, such as conversion of lignin to useful chemicals,[5] at the photoanode in order to match current densities with CO_2 reduction at the cathode. Currently, there is a demanding need for the development and optimization of photoelectrochemical devices that utilize earth-abundant catalysts and materials.

9.2 Immobilizing Rhenium and Manganese Bipyridine Catalysts in Metal-Organic Framework Films

Due to their high activities and selectivities, Re and Mn bpy complexes are among the most promising molecular catalysts for future applications involving electrochemical CO_2 reduction. In order to transition laboratory studies to an commercially-viable level, means for heterogenizing these molecular systems must be developed. As previously stated, MOF thin films are currently gaining traction as supports for molecular catalysts due to their conductivity, high functionality, and ability to immobilize a high concentration of molecular species. Continuing from our work on Fe-porphyrin-based MOF thin films, the next steps for these studies involve immobilizing Re(bpy-R)(CO)$_3$Cl and Mn(bpy-R)(CO)$_3$Br in MOF films.

Many attachment strategies can be proposed to anchor Re(bpy-R)(CO)$_3$Cl and Mn(bpy-R)(CO)$_3$Br within MOFs. Two promising initial strategies are via attachment to the Zr nodes of a MOF via the bpy ligand of the Re or Mn catalyst. Phosphonate ($-PO_3^{2-}$) derivatized bpy ligands have recently been reported,[6] and their synthesis is

fairly straight forward. In order to separate the attachment group ($-PO_3{}^{2-}$) from the bpy ligand, a single methylene spacer can be used. A phosphonate derivatized bpy (like the one shown in Figure 9.3) could be easily attached to the Zr node of a MOF. Additionally, carboxylate ($-CO_2{}^-$) groups could also be used as means for attachment to Zr nodes (see Figure 9.3). Bpy ligands with either one or two carboxylic acid groups attached at the 4,4′-positions are commercially available. Specifically, a mono-substituted carboxylate bpy ligand, containing a methyl group at the opposite position of the carboxylate, is a promising choice for attachment. The methyl group would likely offset any electron-withdrawing character of the carboxylate groups, which could interfere with catalysis. One could also envision separating the carboxylate group from the bpy ligand via a methylene linker (similarly as the phosphonate derivatized bpy ligand). Either the phosphonate or carboxylate derivatized bpy ligands should be able to be attached to the Zr nodes in a MOF by simple heating in DMF overnight.
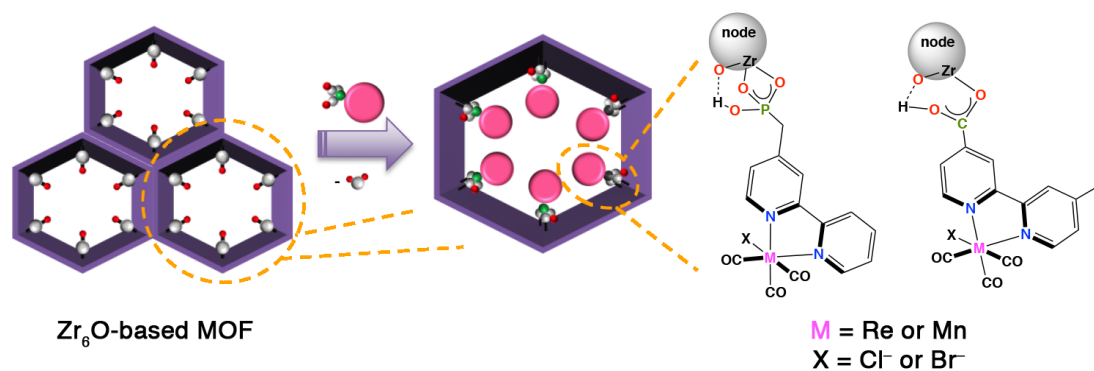
Figure 9.3 Strategies to attach M(bpy-R)(CO)$_3$X (M = Re or Mn, X = Cl$^-$ or Br$^-$) molecular catalysts to nodes of a Zr$_6$O-based MOF through the bpy ligand.

I have begun initial studies on a carboxylate functionalized Mn(bpy) catalyst, Mn(bpy-[COOH]$_1$)(CO)$_3$Br (Figure 9.3 right, M= Mn, X=Br$_-$), in the hopes to immobilize this catalyst in a MOF thin film. Cyclic voltammograms (CVs) of the molecular complex under N$_2$ atmosphere show two irreversible one-electron reductions and an oxidation peak (corresponding to oxidative cleave of Mn(0)–Mn(0) dimer), which is very similar to other Mn(bpy-R)(CO)$_3$Br complexes (Figure 9.4a).[7] Under CO$_2$ with added trifluoroethanol as a proton source, an increase in current is observed at the second one-electron reduction, consist with catalytic CO$_2$ reduction (Figure 9.4b).
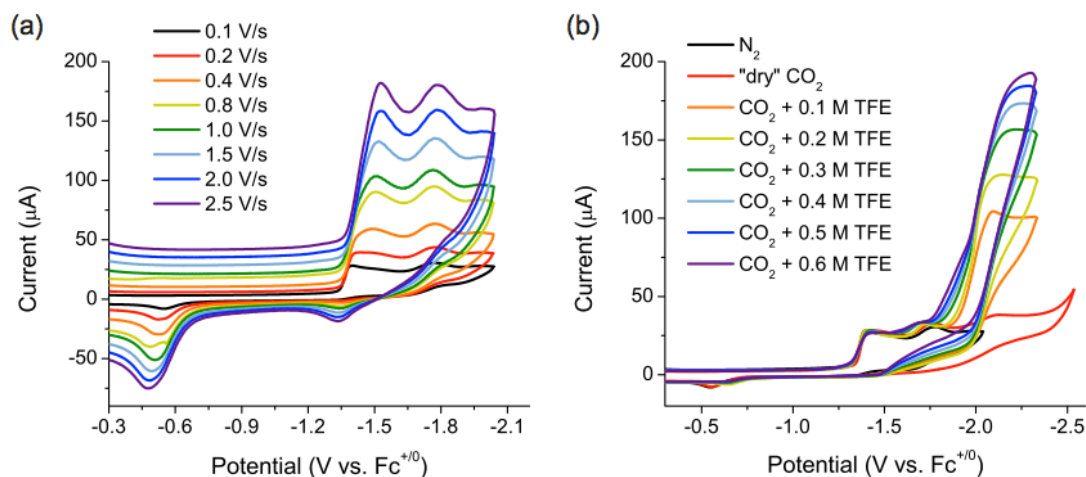
Figure 9.4 Cyclic voltammograms (CVs) of Mn(bpy-[COOH]$_1$)(CO)$_3$Br (bpy-[COOH]$_1$ = 4′-methyl-2,2′-bipyridine-4-carboxylic acid) showing (a) scan rate dependence under N$_2$ atmosphere and (b) electrocatalytic CO$_2$ reduction under CO$_2$ with added trifluoroethanol (TFE) at 0.1 V/s. Conditions: 1 mM Mn complex, 0.1 M tetrabutylammonium hexafluorophosphate (TBAPF$_6$) in MeCN.

Immobilization of this Mn catalyst in a MOF thin film would eliminate dimerization, which has been shown to decrease the operating potential for this family of catalysts by 300-400 mV.[8] Additionally, heterogenizing this catalyst would allow

for CO_2 reduction in a variety of solvents, such as aqueous electrolyte. Typically, these Mn complexes are only soluble in polar organics, and therefore, to this date, CO_2 reduction in H_2O with these catalysts has not been achieved. When considering a catalyst for scale-up and commercial use, operating in H_2O is much more appealing due to cost and environmental ramifications. Currently, we are targeting heterogenation in the highly stable, mesoporous MOF PCN-222, which contains porphyrin linkers to facilitate electron transfer throughout the MOF film.[9] This MOF contains one of the largest known 1D open channels (diameter = 3.7 nm), which should allow for facile electrolyte and substrate/product transport through the MOF.

9.3   Functionalizing Metal-Organic Frameworks Films to Provide Catalytic Enhancements for Immobilized Molecular Catalysts

There are many advantages to heterogenizing these molecular catalysts in MOFs rather than using "traditional" methods for attaching metal complexes to electrode surfaces, such as polymerization or covalent attachment via an organic linker.[10] Thus far, in the relatively early stages of developing redox active MOFs, electron transfer through MOF thin films seems to be much faster than electron transfer through a disordered polymer or a simple organic linker. Both the nodes and linkers in a MOF can be tuned to facilitate electron transport throughout a film. Many research groups have been developing redox active MOF thin films for a wide variety of applications. Some of the redox active linkers that have shown to be promising are

tetrakis(4-carboxypheny)porphyrin (TCPP),[11-13] bis-(pyraolyl)naphthalene diimide,[14] 2,5-dioxido-1,4-benzenedicarboxylate,[15] and pyrazine-2,3-dithiolate[15] (see Figure 9.5).
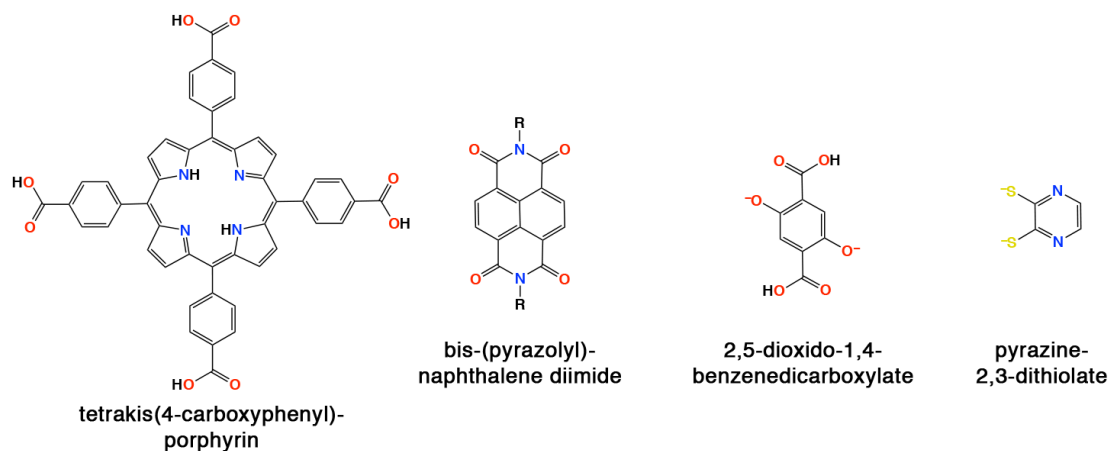
Figure 9.5 Examples of metal-organic framework (MOF) linkers, which have been used in redox-active MOF thin films.

Along with improved conductivity, MOFs provide a route to achieve high surface concentration of active catalyst on an electrode surface. Traditional routes to surface attachment only allow a monolayer, at most, of catalyst to be deposited. In terms of Fe tetraphenylporphyrin (as discussed in Chapter 8), utilizing MOFs increased the amount of active catalyst at the electrode surface by ~3 orders of magnitude, as compared to a monolayer of catalyst immobilized on the same flat electrode.[11] With optimization and more controlled film growth, I have confidence that this amount can be further increased to achieve even higher surface coverages of active catalyst.

MOFs can be thought of as highly-structured mimics to metalloenzymes, wherein the ordered, porous heterogeneous network of MOFs can facilitate solvent, reactant, and electrolyte delivery to/from the immobilized catalyst. In metalloenzymes,

hydrophobic/hydrophilic channels aid in transporting substrates and products to/from the active sites as well as aid in protecting the highly reactive metal centers of these active sites by excluding water, oxygen, or other species. Early studies have been reported involving MOFs, which possess bias-switchable permselectivity,[16] or the ability to exclude certain species from the MOF channels by redox switching. Figure 9.6 shows an example of a redox active ferrocene-functionalized MOF, which displays bias-switchable permselectivity of cations.[16] With informed design, this strategy of permselectivity can be extended to hydrophobic or hydrophilic channels as well as electrostatic interactions within channels, which would alter the local potential near an immobilized catalyst. Electrostatic interactions have been shown to change the selectivity of reactions catalyzed by both solid-state and molecular catalysts.[17-19] These interactions would influence ion pairing and solvent effects, which would have cooperative effects on catalysis.
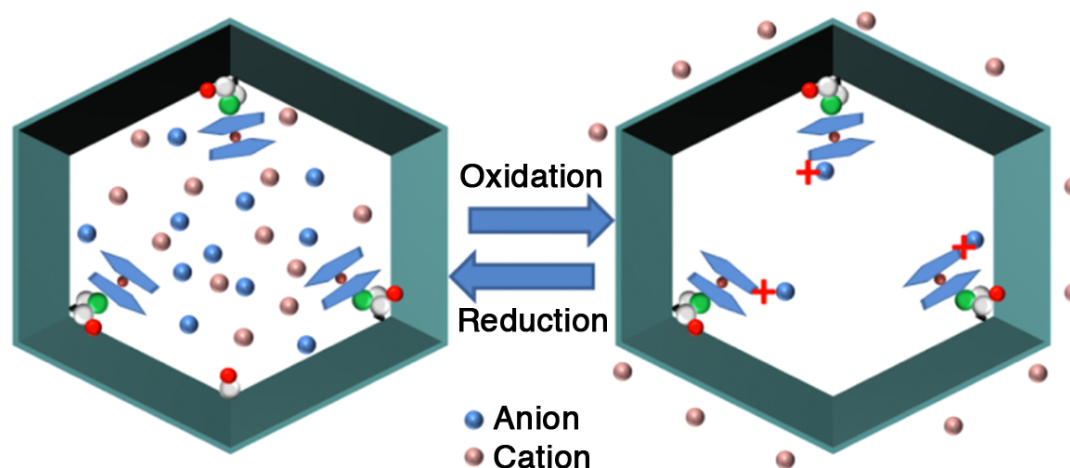

Figure 9.6 Bias-switchable permselectivity of a redox active ferrocene-functionalized metal-organic framework (MOF), displaying exclusion of cations in the MOF channels upon oxidation. Figure adapted from Ref. 16.

The highly functional nature of MOFs allows for endless possibilities to add co-catalysts and favorable functional groups at the nodes and linkers in the framework (see Figure 9.7) in order to mimic the outer and secondary coordination sphere effects in the active sites of metalloenzymes. The active sites of metalloenzymes contain a variety of functional groups that facilitate catalysis, such as electron transport mediators, hydrogen-bonding interactions, and local proton relays. The functional groups in the outer and secondary coordination environments are essential to the function of these metalloenzymes. These interactions both help lower operating potentials to near thermodynamic potentials and significantly increase the rates of catalysis by stabilizing the active state, facilitating substrate/product transfer to/from the active state, and facilitating the formation/breaking of crucial bonds in the bound substrate. Electron shuttles, such as ferrocene units or other redox mediators, could further increase conductivity in MOF films. Hydrogen bonding interactions, such as amino acid residues, could help stabilize highly reactive catalytic intermediates, aid in the formation/breaking of chemical bonds in bound substrate, and facilitate substrate/product transfer to/from the immobilized catalyst. Additionally, local proton relays, such as phenolic groups, can be positioned inside MOF channels to aid in proton-coupled reactions.[20] For simplicity, the Fe-porphyrin-based MOF-525 film, which we have previously studied for CO_2 reduction, can be used as a test system with these functional groups.
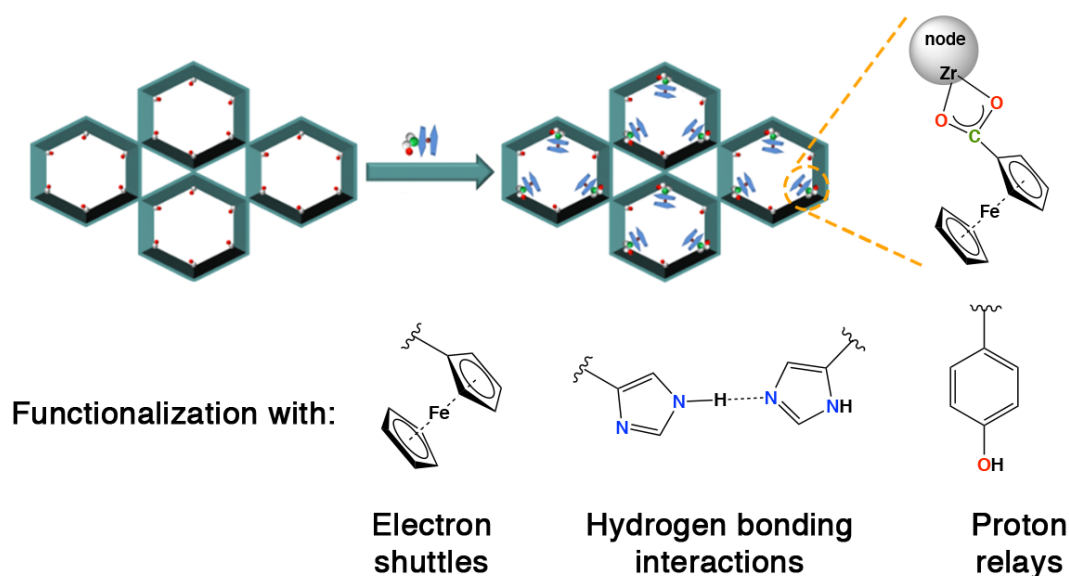
Figure 9.7 Examples of adding functionality to metal-organic frameworks (MOFs), such as electron shuttles (ferrocene units), hydrogen-bonding interactions (two histidine residues), and proton relays (phenolic proton group). Figure adapted from Ref. 16.

9.4 Pairing a Molecular-Catalyst-Incorporated Heterogeneous Device with Solar Energy

We have developed highly active and robust molecular catalysts for CO_2 reduction to carbon monoxide (CO). Specifically, our work on Mn(bpy-R)(CO)$_3$Br catalysts incorporating a bulky bipyridine ligand has combined the following necessities for a commercially viable catalyst: (1) the catalyst is cheap (earth-abundant metal), the catalyst operates at low overpotential (only ~0.2 V with a Mg^{2+} co-catalyst), and the catalyst is highly active (turnover frequencies >20 s^{-1} at ~0.2 V overpotential and >5,000 s^{-1} at ~0.8 V overpotential). Heterogenizing this molecular catalyst would also likely provide high stability. The bandgaps of various semiconductors at pH 1 (V vs. NHE) are listed in Figure 9.8. A few of these

semiconductor bandgaps align well with the operating potentials of commonly used molecular catalysts for CO_2 reduction (Figure 9.8). Here, it's important to note that these molecular catalysts, with the exception of $[Ni(cyclam)]^{2+}$, do not operate in aqueous electrolyte, and $[Pd_2(triphos)_2]^{2+}$ requires the use of strong acid to function, which significantly raises the thermodynamic potential for CO_2 reduction. It is clear from Figure 9.8, that a molecular catalyst with a low operating potential would be much more ideal than a catalyst with a high operating potential simply because it could be optimized for use with a variety of semiconductors. In this regard, $Mn(mesbpy)(CO)_3Br$ with Mg^{2+} co-catalyst is one of the most promising candidates to pair with a semiconductor and be utilized in a photoelectrochemical device.
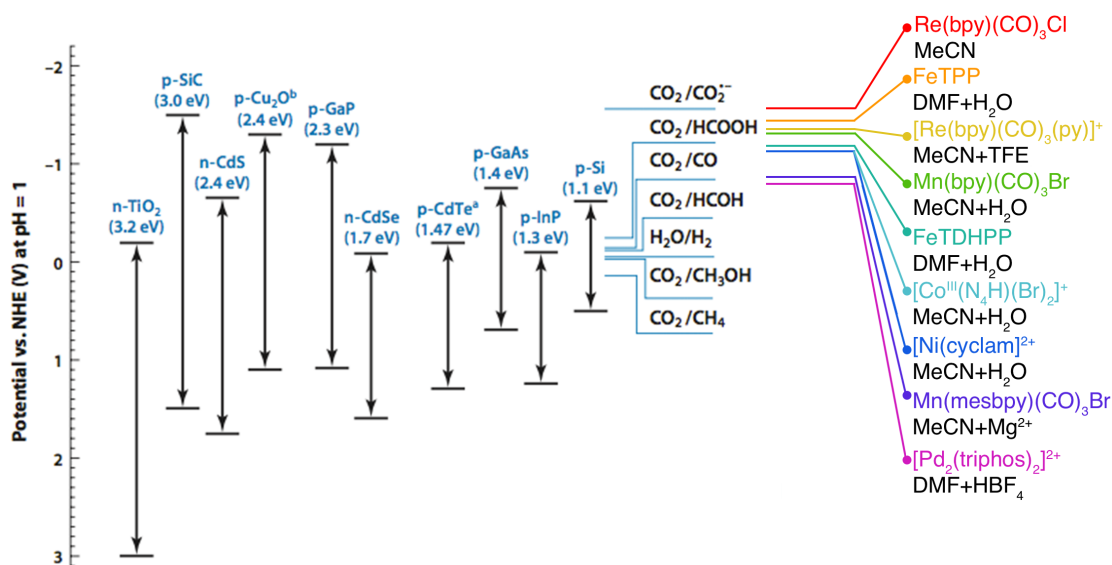
Figure 9.8 Position of the conduction and valence bands of several semiconductors at pH = 1 vs. NHE. Thermodynamic potentials for CO_2 reduction to different products at pH = 1 vs. NHE are shown next to the band edge positions, and the operating potentials of several commonly studied molecular catalysts for CO_2 reduction are shown at the right. It's important to note that all of the molecular catalysts, besides $[Ni(cyclam)]^{2+}$, do not operate in aqueous electrolyte in their homogeneous states. $[Pd_2(triphos)_2]^{2+}$ requires the use of strong acid to function, which significantly raises the thermodynamic potential for CO_2 reduction. Data obtained from Ref. 3,20-22.

Molecular catalysts are ideal to pair with semiconductors for photoelectrochemical CO_2 reduction in order to control selectivity of these inorganic semiconductors, which typically are non-selective for CO_2 reduction vs. proton reduction. The best photovoltaic or photoelectrochemical materials can sustain current densities in the range of 10–20 mA cm^{-2}. In contrast, a monolayer of molecular catalyst on an electrode surface for a two-electron catalytic processes cannot sustain sufficient current densities to pair with these materials.[3] Our previous work on heterogenizing molecular catalysts in MOFs (i.e. for Fe-porphyrin) and our strategies for heterogenizing Mn bpy catalysts (discussed earlier) allow much higher surface coverages of active catalyst than a single monolayer. Recent reports of covalent-organic frameworks (COF) films with immobilized Co-porphyrin catalysts provide evidence that adequate current densities for these applications are possible via this strategies.[12] With optimizing, I believe these surface coverages could reach levels capable of pairing with today's best photovoltaic or photoelectrochemical materials.

An abundant amount of research effort has focused on multijunction photoelectrochemical cells for water splitting. Specifically, Reece *et al.* used a triple-junction, amorphous Si solar cell with electrodeposited catalysts for water reduction (NiMoZn) and oxidation (amorphous cobalt oxide).[23] Khaselev *et al.* used Pt catalysts in a wired arrangement.[24] Walter *et al.* developed a wireless approach, in which at least one of the photoelectrodes incorporated semiconductor nanowires functionalized with catalysts.[25] Similar research efforts towards CO_2 photoelectrochemical reduction are lacking.

Studies have been reported on photoelectrochemical reduction of CO_2 in the absence of an immobilized molecular catalysts.[3] In terms of a tandem device, taking into account both cathodic and anodic reactions, Kang *et al.* demonstrated successful photoelectrochemical reduction of CO_2 to formate with simultaneous oxidation of H_2O to oxygen via a p-type $CuFeO_2$ semiconductor.[26] There have been even fewer studies on utilizing molecular catalysts for these photoelectrochemical reactions. Work by our own group, Kumar *et al.*, [27-28] has shown photoelectrochemical reduction of CO_2 on p-type Si utilizing Re(bpy-*t*Bu)(CO)$_3$Cl as a molecular catalyst in solution. Additionally, Arai *et al.* has displayed successful photoelectrochemical CO_2 reduction to formate utilizing a p-type InP-Zn photocathode modified with a polymerized Ru molecular catalyst.[29] The development of photoelectrochemical devices utilizing earth-abundant molecular catalysts for CO_2 reduction is of paramount importance. There also exists a need for the optimization of photoactivity and reaction selectivity in these photoelectrochemical reactions.

Interestingly, photovoltaic photoelectrolysis cells have photovoltages that are independent of pH,[3] which could be an important factor when pairing with pH-sensitive catalyst-mediated CO_2 reduction. Another type of device design is shown in Figure 9.9. Here, a photoanode is used for H_2O oxidation and a separated cathode with an immobilized molecular catalyst (in this case, a molecular catalyst immobilized in a MOF film) for CO_2 reduction. In this cell, the photoanode absorbs light, which ejects electrons in the CB. Holes in the valence band (VB) perform water oxidation, and the injected electrons are transferred to the cathode side of the cell. The immobilized

molecular catalyst is reduced by the transferred electrons and performs CO_2 reduction. Protons generated from H_2O oxidation are passed to the cathode compartment through a proton-conductive membrane (PEM). Concepcion *et al.* recently proposed a similar device design, using a dye-sensitized light absorber bound to the surface of a high band gap semiconductor (i.e. TiO_2) for the photoanode and a molecular catalyst tethered to the surface of the cathode.[4] One could also envision this device as a wireless, monolithic, two-compartment cell with a single dual-face photoelectrode (water oxidation in one compartment, CO_2 reduction in the other compartment).[3,25]
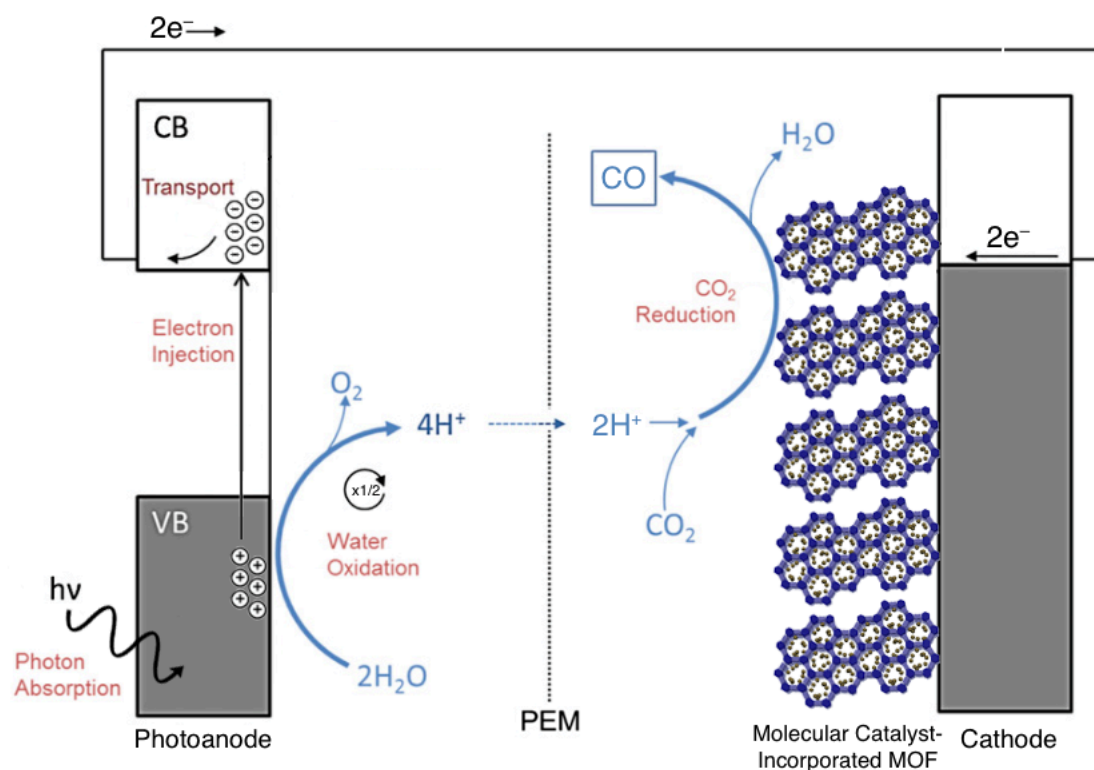
Figure 9.9 Schematic of a photoelectrosynthesis cell. In this cell, a photoanode for H_2O oxidation absorbs light, which injects electrons into the conduction band (CB). Holes in the valence band (VB) perform water oxidation, and the injected electrons are transferred to a separate cathode. The cathode is coated with a molecular catalyst-incorporated metal-organic framework (MOF) thin film, which performs electrocatalytic reduction of CO_2 to CO. PEM = proton exchange membrane. Figure adapted with permission from Ref. 4.

9.5   Conclusions and Final Thoughts

In order for the conversion of CO_2 to liquid fuels to be technologically relevant, a competent, solar-powered device that utilizes earth-abundant materials driving CO_2 reduction and H_2O oxidation must be developed. Molecular catalysts are essential for these photoelectrochemical reactions, in order to overcome the kinetic barriers required for CO_2 reduction as well as to control the selectivity of inorganic semiconductors. Government-supported research programs have abandoned the use of molecular catalysts for these applications (i.e. the Joint Center for Artificial Photosynthesis, JCAP) – in my opinion, primarily because immobilization strategies were too conventional. But let's be clear, the challenge to develop a device of this source is immense.

Some of the most promising molecular catalysts to drive these CO_2 reduction reactions are those of the type Mn(bpy-R)(CO)$_3$Br. These Mn catalysts are highly active and selective for CO_2 reduction to CO even in high concentrations of weak acid. We have gained a vast amount of knowledge regarding how these catalysts operate and how to tailor them to increase their activities, decrease overpotentials, and increase stabilities. Immobilization of these catalysts via a MOF film scaffold should generate a heterogeneous catalyst that operates at low overpotential, at high activity, and in neutral aqueous electrolyte. Once proof-of-concept studies have completed MOF films can be tailored in numerous ways via their highly functional linkers and nodes to create a catalyst system that mimics an artificial enzyme.

9.6   References

(1) *Annual Energy Review*; U.S. Energy Information Administration, 2011.

(2) Sathrum, A. J.; Kubiak, C. P. *J. Phys. Chem. Lett.* 2011, 2, 2372-2379.

(3) Kumar, B.; Llorente, M.; Froehlich, J.; Dang, T.; Sathrum, A.; Kubiak, C. P. *Annu. Rev. Phys. Chem.* 2012, 63, 541-569.

(4) Concepcion, J. J.; House, R. L.; Papanikolas, J. M.; Meyer, T. J. *Proc. Natl. Acad. Sci. U. S. A.* 2012, 109, 15560-15564.

(5) Barta, K.; Ford, P. C. *Acc. Chem. Res.* 2014, 47, 1503-1512.

(6) Norris, M. R.; Concepcion, J. J.; Glasson, C. R. K.; Fang, Z.; Lapides, A. M.; Ashford, D. L.; Templeton, J. L.; Meyer, T. J. *Inorg. Chem.* 2013, 52, 12492-12501.

(7) Smieja, J. M.; Sampson, M. D.; Grice, K. A.; Benson, E. E.; Froehlich, J. D.; Kubiak, C. P. *Inorg. Chem.* 2013, 52, 2484-2491.

(8) Sampson, M. D.; Nguyen, A. D.; Grice, K. A.; Moore, C. E.; Rheingold, A. L.; Kubiak, C. P. *J. Am. Chem. Soc.* 2014, 136, 5460-5471.

(9) Feng, D.; Gu, Z.-Y.; Li, J.-R.; Jiang, H.-L.; Wei, Z.; Zhou, H.-C. *Angew. Chem., Int. Ed.* 2012, 51, 10307-10310.

(10) Corma, A.; García, H.; Llabrés i Xamena, F. X. *Chem. Rev.* 2010, 110, 4606-4655.

(11) Hod, I.; Sampson, M. D.; Deria, P.; Kubiak, C. P.; Farha, O. K.; Hupp, J. T. *ACS Catal.* 2015, 6302-6309.

(12) Lin, S.; Diercks, C. S.; Zhang, Y.-B.; Kornienko, N.; Nichols, E. M.; Zhao, Y.; Paris, A. R.; Kim, D.; Yang, P.; Yaghi, O. M.; Chang, C. J. *Science* 2015, 349, 1208-1213.

(13) Ahrenholtz, S. R.; Epley, C. C.; Morris, A. J. *J. Am. Chem. Soc.* 2014, 136, 2464-2472.

(14) Wade, C. R.; Li, M.; Dincă, M. *Angew. Chem., Int. Ed.* 2013, 52, 13377-13381.

(15) Bloch, E. D.; Murray, L. J.; Queen, W. L.; Chavan, S.; Maximoff, S. N.; Bigi, J. P.; Krishna, R.; Peterson, V. K.; Grandjean, F.; Long, G. J.; Smit, B.; Bordiga, S.; Brown, C. M.; Long, J. R. *J. Am. Chem. Soc.* 2011, 133, 14814-14822.

(16) Hod, I.; Bury, W.; Gardner, D. M.; Deria, P.; Roznyatovskiy, V.; Wasielewski, M. R.; Farha, O. K.; Hupp, J. T. *J. Phys. Chem. Lett.* 2015, 586-591.

(17) Gorin, C. F.; Beh, E. S.; Kanan, M. W. *J. Am. Chem. Soc.* 2012, 134, 186-189.

(18) Gorin, C. F.; Beh, E. S.; Bui, Q. M.; Dick, G. R.; Kanan, M. W. *J. Am. Chem. Soc.* 2013, 135, 11257-11265.

(19) Lau, V. M.; Gorin, C. F.; Kanan, M. W. *Chem. Sci.* 2014, 5, 4975-4979.

(20) Costentin, C.; Drouet, S.; Robert, M.; Savéant, J.-M. *Science* 2012, 338, 90-94.

(21) Smieja, J. M.; Kubiak, C. P. *Inorg. Chem.* 2010, 49, 9283-9289.

(22) Wong, K.-Y.; Chung, W.-H.; Lau, C.-P. *J. Electroanal. Chem.* 1998, 453, 161-169.

(23) Reece, S. Y.; Hamel, J. A.; Sung, K.; Jarvi, T. D.; Esswein, A. J.; Pijpers, J. J. H.; Nocera, D. G. *Science* 2011, 334, 645-648.

(24) Khaselev, O.; Bansal, A.; Turner, J. A. *International Journal of Hydrogen Energy* 2001, 26, 127-132.

(25) Walter, M. G.; Warren, E. L.; McKone, J. R.; Boettcher, S. W.; Mi, Q.; Santori, E. A.; Lewis, N. S. *Chem. Rev.* 2010, 110, 6446-6473.

(26) Kang, U.; Choi, S. K.; Ham, D. J.; Ji, S. M.; Choi, W.; Han, D. S.; Abdel-Wahab, A.; Park, H. *Energ. Environ. Sci.* 2015, 8, 2638-2643.

(27) Kumar, B.; Smieja, J. M.; Kubiak, C. P. *J. Phys. Chem. C* 2010, 114, 14220-14223.

(28) Kumar, B.; Smieja, J. M.; Sasayama, A. F.; Kubiak, C. P. *Chem. Commun.* 2012, 48, 272-274.

(29) Arai, T.; Sato, S.; Uemura, K.; Morikawa, T.; Kajino, T.; Motohiro, T. *Chem. Commun.* 2010, 46, 6944-6946.